Can your phone improve your health? *p. 1306*

Vitamin C and cancer cell metabolism *pp. 1317 & 1391*

In search of stem cells *p. 1319*

Science

$10
11 DECEMBER 2015
sciencemag.org

AAAS

Machine intelligence

AI learns to read and write letters *p. 1332*

CONTENTS

11 DECEMBER 2015 • VOLUME 350 • ISSUE 6266

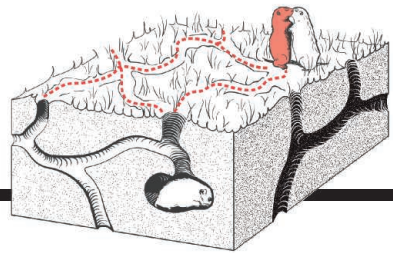

1310 & 1371
Memory and monogamy

These isolated Korubo people made peaceful contact in 1996, but other Korubo have recently faced violence.

PHOTO: BRAZILPHOTOS.COM/ALAMY

NEWS

IN BRIEF

1296 News at a glance

IN DEPTH

1299 **GERMLINE EDITING DOMINATES DNA SUMMIT**
Prospect of heritable changes sparks questions about safety, ethics, and rationale *By J. Travis*

1300 **A WHALE'S LIFE, INSCRIBED IN BALEEN**
Fibrous keratin can store a chemical record of pregnancies and stress
By R. Kessler

1302 **CUBESATS PROMISE TO FILL WEATHER DATA GAP**
Companies bet on a GPS technique and an agency shift to commercial data
By E. Hand

1303 **CONTROVERSIAL TEST FINDS NO SIGN OF A HOLOGRAPHIC UNIVERSE**
Speculative effort was destined to fail, critics say *By A. Cho*

1304 **DEADLY ATTACK ON ISOLATED TRIBE**
Isolated people recovering from conflict with settled neighbors in the Brazilian Amazon *By B. Fraser*

1305 **HIV/AIDS CARE FOR ALL—ON A BUDGET**
Zimbabwe meeting promotes ways to cut clinic visits and tests without compromising treatment
By J. Cohen

FEATURE

1306 **MIND THE PHONE**
Devices that monitor and coach users bring promise and peril *By K. Servick*

INSIGHTS

PERSPECTIVES

1310 **DISSECTING DIVERSITY IN THE SOCIAL BRAIN**
Male prairie voles with poor memory skills are less faithful to their partners
By G. E. Robinson
▸ REPORT P. 1371

1312 **SHARING BY DESIGN: DATA AND DECENTRALIZED COMMONS**
Overcoming legal and policy obstacles *By J. L. Contreras and J. H. Reichman*

1314 **MATCHED FILTERING OF ULTRASHORT PULSES**
Optical signal processing can help reduce noise in detection of ultrafast electrical pulses *By M. Vasilyev*
▸ REPORT P. 1343

1316 **OPENING THE GATE ON SUPERCONDUCTIVITY**
Superconducting two-dimensional materials are found to be remarkably robust *By H. J. Suderow*
▸ REPORT P. 1353

1317 **REVISITING VITAMIN C AND CANCER**
A high dose of vitamin C kills certain colon cancer cells
By C. R. Reczek and N. S. Chandel
▸ REPORT P. 1391

1319 **WHAT IS AN ADULT STEM CELL?**
Tissues may use diverse mechanisms to replace lost cells
By H. Clevers

1321 **IN THE WAKE OF COLLISION**
When atoms collide with metal surfaces, electron-hole pair excitations dissipate the adsorption energy
By H. Brune
▸ REPORT P. 1346

BOOKS *ET AL.*

1322 **MEL CHEMISTRY**
Reviewed by J. Fahrenkamp-Uppenbrink

1323 **ADA LOVELACE**
Reviewed by A. Robinson

LETTERS

1325 **FLYING FOXES FACE CULL DESPITE EVIDENCE**
By F. B. V. Florens

1325 **LIFE IN SCIENCE: THE FORCE OF ETHICS AWAKENS**
By M. J. Guitton

Science Staff 1294
New Products 1397
Science Careers 1398

Published by AAAS

CONTENTS

1387
Immune cells recognize cancer mutations

11 DECEMBER 2015 • VOLUME 350 • ISSUE 6266

1326 MARINE PROTECTED AREAS MISS THE BOAT
By R. Hilborn

1326 TECHNICAL COMMENT ABSTRACTS

RESEARCH

IN BRIEF

1327 From *Science* and other journals

REVIEW

1330 MICROBIOME
The global ocean microbiome
M. A. Moran
REVIEW SUMMARY; FOR FULL TEXT:
dx.doi.org/10.1126/science.aac8455

RESEARCH ARTICLES

1331 PROTEIN STRUCTURE
Principles of assembly reveal a periodic table of protein complexes
S. E. Ahnert et al.
RESEARCH ARTICLE SUMMARY; FOR FULL TEXT:
dx.doi.org/10.1126/science.aaa2245

1332 COGNITIVE SCIENCE
Human-level concept learning through probabilistic program induction
B. M. Lake et al.
▸ PODCAST

1338 PHYSICAL CHEMISTRY
Spectroscopic characterization of isomerization transition states
J. H. Baraban et al.

REPORTS

1343 SIGNAL PROCESSING
Subnoise detection of a fast random event *V. Ataie* et al.
▸ PERSPECTIVE P. 1314

1346 SURFACE SCIENCE
Electron-hole pair excitation determines the mechanism of hydrogen atom adsorption *O. Bünermann* et al.
▸ PERSPECTIVE P. 1321

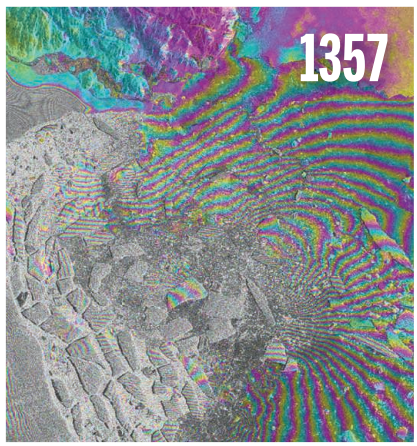

1349 GEOPHYSICS
Viscosity jump in Earth's mid-mantle
M. L. Rudolph et al.

1353 SUPERCONDUCTIVITY
Evidence for two-dimensional Ising superconductivity in gated MoS_2
J. M. Lu et al.
▸ PERSPECTIVE P. 1316

1357 ICE SHEETS
Fast retreat of Zachariæ Isstrøm, northeast Greenland *J. Mouginot* et al.

1361 NEURONAL DYNAMICS
High-speed recording of neural spikes in awake mice and flies with a fluorescent voltage sensor *Y. Gong* et al.

1367 RESEARCH INVESTMENT
Wrapping it up in a person: Examining employment and earnings outcomes for Ph.D. recipients *N. Zolas* et al.

1371 SOCIAL BEHAVIOR
Sexual fidelity trade-offs promote regulatory variation in the prairie vole brain *M. Okhovat* et al.
▸ PERSPECTIVE P. 1310

1375 AGING
Cell nonautonomous activation of flavin-containing monooxygenase promotes longevity and health span
S. F. Leiser et al.

1379 SIGNAL TRANSDUCTION
Oscillatory stress stimulation uncovers an Achilles' heel of the yeast MAPK signaling network *A. Mitchell* et al.

1383 TRANSCRIPTION
RNA polymerase II–associated factor 1 regulates the release and phosphorylation of paused RNA polymerase II *M. Yu* et al.

1387 CANCER IMMUNOTHERAPY
Immunogenicity of somatic mutations in human gastrointestinal cancers
E. Tran et al.

1391 VITAMIN C RESEARCH
Vitamin C selectively kills *KRAS* and *BRAF* mutant colorectal cancer cells by targeting GAPDH
J. Yun et al.
▸ PERSPECTIVE P. 1317

DEPARTMENTS

1295 EDITORIAL
Whither (wither?) tenure?
By Marcia McNutt

1434 WORKING LIFE
The M.D.-Ph.D. double agent
By Jessica W. Tsai

ON THE COVER

Illustration of character sorting by a computational model (tall piles, simple characters; short piles, more complex ones). People learn to recognize and draw simple visual concepts (such as a letter in a foreign alphabet) from only a few examples, whereas machine learning algorithms typically require tens or hundreds of examples. See page 1332 for more on representing concepts as programs that can generate a range of new letters.
Illustration: Eiko Ojala

SCIENCE (ISSN 0036-8075) is published weekly on Friday, except the last week in December, by the American Association for the Advancement of Science, 1200 New York Avenue, NW, Washington, DC 20005. Periodicals mail postage (publication No. 484460) paid at Washington, DC, and additional mailing offices. Copyright © 2015 by the American Association for the Advancement of Science. The title SCIENCE is a registered trademark of the AAAS. Domestic individual membership and subscription (51 issues): $153 ($74 allocated to subscription). Domestic institutional subscription (51 issues): $1282; Foreign postage extra: Mexico, Caribbean (surface mail) $55; other countries (air assist delivery) $85. First class, airmail, student, and emeritus rates on request. Canadian rates with GST available upon request, GST #1254 88122. Publications Mail Agreement Number 1069624. **Printed in the U.S.A.**
Change of address: Allow 4 weeks, giving old and new addresses and 8-digit account number. **Postmaster:** Send change of address to AAAS, P.O. Box 96178, Washington, DC 20090–6178. **Single-copy sales:** $10.00 current issue, $15.00 back issue prepaid includes surface postage; bulk rates on request. **Authorization to photocopy** material for internal or personal use under circumstances not falling within the fair use provisions of the Copyright Act is granted by AAAS to libraries and other users registered with the Copyright Clearance Center (CCC) Transactional Reporting Service, provided that $30.00 per article is paid directly to CCC, 222 Rosewood Drive, Danvers, MA 01923. The identification code for *Science* is 0036-8075. *Science* is indexed in the *Reader's Guide to Periodical Literature* and in several specialized indexes.

Published by AAAS

Science
AAAS
1200 New York Avenue, NW, Washington, DC 20005
Bateman House, 82-88 Hills Road, Cambridge, UK CB2 1LQ

Editor-in-Chief Marcia McNutt
Executive Editor Monica M. Bradford **News Editor** Tim Appenzeller
Managing Editor, Research Journals Katrina L. Kelner
Deputy Editors Barbara R. Jasny, Andrew M. Sugden(UK), Valda J. Vinson, Jake S. Yeston

Research and Insights

SR. EDITORS Caroline Ash(UK), Gilbert J. Chin, Lisa D. Chong, Julia Fahrenkamp-Uppenbrink(UK), Pamela J. Hines, Stella M. Hurtley(UK), Paula A. Kiberstis, Marc S. Lavine(Canada), Kristen L. Mueller, Ian S. Osborne(UK), Beverly A. Purnell, L. Bryan Ray, Guy Riddihough, H. Jesse Smith, Jelena Stajic, Peter Stern(UK), Phillip D. Szuromi, Brad Wible, Nicholas S. Wigginton, Laura M. Zahn **ASSOCIATE EDITORS** Brent Grocholski, Keith T. Smith, Sacha Vignieri **ASSOCIATE BOOK REVIEW EDITOR** Valerie B. Thompson **ASSOCIATE LETTERS EDITOR** Jennifer Sills **CHIEF CONTENT PRODUCTION EDITOR** Cara Tate **SR. CONTENT PRODUCTION EDITOR** Harry Jach, Lauren Kmec **CONTENT PRODUCTION EDITORS** Jeffrey E. Cook, Chris Filiatreau, Cynthia Howe, Barbara P. Ordway, Catherine Wolner **SR. EDITORIAL COORDINATORS** Carolyn Kyle, Beverly Shields **EDITORIAL COORDINATORS** Ramatoulaye Diop, Joi S. Granger, Lisa Johnson, Anita Wynn **PUBLICATIONS ASSISTANTS** Aneera Dobbins, Jeffrey Hearn, Dona Mathieu, Le-Toya Mayne Flood, Shannon McMahon, Scott Miller, Jerry Richardson, Rachel Roberts(UK), Alice Whaley(UK), Brian White **EXECUTIVE ASSISTANT** Anna Bashkirova **ADMINISTRATIVE SUPPORT** Janet Clements(UK), Lizanne Newton(UK), Maryrose Madrid, Laura-Nadine Schuhmacher (UK, Intern), Alix Welch (Intern), John Wood(UK)

News

NEWS MANAGING EDITOR John Travis **INTERNATIONAL EDITOR** Richard Stone **DEPUTY NEWS EDITORS** Daniel Clery(UK), Robert Coontz, Elizabeth Culotta, David Grimm, David Malakoff, Leslie Roberts **CONTRIBUING EDITOR** Martin Enserink(Europe) **SR. CORRESPONDENTS** Jeffrey Mervis, Elizabeth Pennisi **NEWS WRITERS** Adrian Cho, Jon Cohen, Jennifer Couzin-Frankel, Carolyn Gramling, Eric Hand, Jocelyn Kaiser, Catherine Matacic, Kelly Servick, Robert F. Service, Erik Stokstad(Cambridge, UK), Emily Underwood **INTERNS** Hanae Armitage, Emily DeMarco, Annick Laurent, Laura Olivieri, Juan David Romero **CONTRIBUTING CORRESPONDENTS** Michael Balter(Paris), John Bohannon, Ann Gibbons, Mara Hvistendahl, Sam Kean, Eli Kintisch, Kai Kupferschmidt(Berlin), Andrew Lawler, Christina Larson(Beijing), Mitch Leslie, Charles C. Mann, Eliot Marshall, Virginia Morell, Dennis Normile(Tokyo), Heather Pringle, Tania Rabesandratana(London), Gretchen Vogel(Berlin), Lizzie Wade(Mexico City) **CAREERS** Donisha Adams, Rachel Bernstein **COPY EDITORS** Julia Cole, Jennifer Levin (Chief) **ADMINISTRATIVE SUPPORT** Jessica Williams

Executive Publisher Rush D. Holt
Publisher Kent R. Anderson **Chief Digital Media Officer** Rob Covey

BUSINESS OPERATIONS AND PORTFOLIO MANAGEMENT DIRECTOR Sarah Whalen **BUSINESS SYSTEMS AND FINANCIAL ANALYSIS DIRECTOR** Randy Yi **MANAGER OF FULFILLMENT SYSTEMS** Neal Hawkins **SYSTEMS ANALYST** Nicole Mehmedovich **ASSISTANT DIRECTOR, BUSINESS OPERATIONS** Eric Knott **MANAGER, BUSINESS OPERATIONS** Jessica Tierney **BUSINESS ANALYSTS** Cory Lipman, Cooper Tilton, Celeste Troxler **FINANCIAL ANALYST** Robert Clark **RIGHTS AND PERMISSIONS ASSISTANT DIRECTOR** Emilie David **PERMISSIONS ASSOCIATE** Elizabeth Sandler **RIGHTS, CONTRACTS, AND LICENSING ASSOCIATE** Lili Kiser

MARKETING DIRECTOR Elise Swinehart **ASSOCIATE DIRECTOR OF ACQUISITION AND RETENTION** Julianne Wielga **MARKETING ASSOCIATE** Elizabeth Sattler **SR. MARKETING EXECUTIVE** Jennifer Reeves **ASSOCIATE DIRECTOR, CREATIVE SERVICES** Tzeitel Sorrosa **ART ASSOCIATE** Seil Lee **JR. ART ASSOCIATE** Kim Huynh **ASSISTANT COMMERCIAL EDITOR** Selby Frame **MARKETING PROJECT MANAGER** Angelissa McArthur **PROGRAM DIRECTOR, AAAS MEMBER CENTRAL** Peggy Mihelich **FULFILLMENT SYSTEMS AND OPERATIONS** membership@aaas.org **MANAGER, MEMBER SERVICES** Pat Butler **SPECIALISTS** LaToya Casteel, Terrance Morrison, Latasha Russell **MANAGER, DATA ENTRY** Mickie Napoleoni **DATA ENTRY SPECIALISTS** JJ Regan, Brenden Aquilino, Fiona Giblin

DIRECTOR, SITE LICENSING Tom Ryan **DIRECTOR, CORPORATE RELATIONS** Eileen Bernadette Moran **SR. PUBLISHER RELATIONS SPECIALIST** Kiki Forsythe **PUBLISHER RELATIONS MANAGER** Catherine Holland **PUBLISHER RELATIONS, EASTERN REGION** Keith Layson **PUBLISHER RELATIONS, WESTERN REGION** Ryan Rexroth **SALES RESEARCH COORDINATOR** Aiesha Marshall **MANAGER, SITE LICENSE OPERATIONS** Iquo Edim **SENIOR PRODUCTION SPECIALIST** Robert Koepke **SENIOR OPERATIONS ANALYST** Lana Guz **FULFILLMENT ANALYST** Judy Lillibridge **ASSOCIATE DIRECTOR, MARKETING** Christina Schlecht **MARKETING ASSOCIATES** Thomas Landreth, Isa Sesay-Bah

WEB TECHNOLOGIES SR. DEVELOPER Chris Coleman **DEVELOPERS** Dan Berger, Jimmy Marks, Ryan Jensen **SR. PROJECT MANAGER** Trista Smith

MULTIMEDIA DIRECTOR OF ANALYTICS Enrique Gonzales **SR. WEB PRODUCER** Sarah Crespi **WEB PRODUCER** Alison Crawford **VIDEO PRODUCER** Nguyen Nguyen **SOCIAL MEDIA PRODUCER** Brice Russ

DIRECTOR OF OPERATIONS PRINT AND ONLINE Lizabeth Harman **DIGITAL/PRINT STRATEGY MANAGER** Jason Hillman **QUALITY TECHNICAL MANAGER** Marcus Spiegler **PROJECT ACCOUNT MANAGER** Tara Kelly **DIGITAL PRODUCTION MANAGER** Lisa Stanford **ASSISTANT MANAGER DIGITAL/PRINT** Rebecca Doshi **SENIOR CONTENT SPECIALISTS** Steve Forrester, Antoinette Hodal, Lori Murphy, Anthony Rosen **CONTENT SPECIALISTS** Jacob Hedrick, Kimberley Oster

DESIGN DIRECTOR Beth Rakouskas **DESIGN EDITOR** Marcy Atarod **SENIOR DESIGNER** Garvin Grullón **DESIGNER** Chrystal Smith **GRAPHICS MANAGING EDITOR** Alberto Cuadra **SENIOR SCIENTIFIC ILLUSTRATORS** Chris Bickel, Katharine Sutliff **SCIENTIFIC ILLUSTRATOR** Valerie Altounian **SENIOR ART ASSOCIATES** Holly Bishop, Nathalie Cary, Preston Huey **SENIOR PHOTO EDITOR** William Douthitt **PHOTO EDITORS** Leslie Blizard, Christy Steele

DIRECTOR, GLOBAL COLLABORATION, CUSTOM PUBLICATIONS, ADVERTISING Bill Moran **EDITOR, CUSTOM PUBLISHING** Sean Sanders: 202-326-6430 **ASSISTANT EDITOR, CUSTOM PUBLISHING** Tianna Hicklin: 202-326-6463 **ADVERTISING MARKETING MANAGER** Justin Sawyers: 202-326-7061 science_advertising@aaas.org **ADVERTISING MARKETING ASSOCIATE** Javia Flemmings **ADVERTISING SUPPORT MANAGER** Karen Foote: 202-326-6740 **ADVERTISING PRODUCTION OPERATIONS MANAGER** Deborah Tompkins **SR. PRODUCTION SPECIALIST/GRAPHIC DESIGNER** Amy Hardcastle **PRODUCTION SPECIALIST** Yuse Lajiminmuhip **SR. TRAFFIC ASSOCIATE** Christine Hall **SALES COORDINATOR** Shirley Young **ASSOCIATE DIRECTOR, COLLABORATION, CUSTOM PUBLICATIONS/CHINA/TAIWAN/KOREA/SINGAPORE** Ruolei Wu: +86-186 0082 9345, rwu@aaas.org **COLLABORATION/ CUSTOM PUBLICATIONS/JAPAN** Adarsh Sandhu + 81532-81-5142 asandhu@aaas.org **EAST COAST/E. CANADA** Laurie Faraday: 508-747-9395, FAX 617-507-8189 **WEST COAST/W. CANADA** Lynne Stickrod: 415-931-9782, FAX 415-520-6940 **MIDWEST** Jeffrey Dembski: 847-498-4520 x3005, Steven Loerch: 847-498-4520 x3006 **UK EUROPE/ASIA** Roger Goncalves: TEL/FAX +41 43 243 1358 **JAPAN** Katsuyoshi Fukamizu(Tokyo): +81-3-3219-5777 kfukamizu@aaas.org **CHINA/TAIWAN** Ruolei Wu: +86-186 0082 9345, rwu@aaas.org

WORLDWIDE ASSOCIATE DIRECTOR OF SCIENCE CAREERS Tracy Holmes: +44 (0) 1223 326525, FAX +44 (0) 1223 326532 tholmes@science-int.co.uk **CLASSIFIED** advertise@sciencecareers.org **U.S. SALES** Tina Burks: 202-326-6577, Nancy Toema: 202-326-6578 **SALES ADMINISTRATOR** Marci Gallun **EUROPE/ROW SALES** Axel Gesatzki, Sarah Lelarge **SALES ASSISTANT** Kelly Grace **JAPAN** Hiroyuki Mashiki(Kyoto): +81-75-823-1109 hmashiki@aaas.org **CHINA/TAIWAN** Ruolei Wu: +86-186 0082 9345 rwu@aaas.org **MARKETING MANAGER** Allison Pritchard **MARKETING ASSOCIATE** Aimee Aponte

AAAS BOARD OF DIRECTORS RETIRING PRESIDENT, CHAIR Gerald R. Fink **PRESIDENT** Geraldine (Geri) Richmond **PRESIDENT-ELECT** Barbara A. Schaal **TREASURER** David Evans Shaw **CHIEF EXECUTIVE OFFICER** Rush D. Holt **BOARD** Bonnie L. Bassler, May R. Berenbaum, Carlos J. Bustamante, Stephen P.A. Fodor, Claire M. Fraser, Michael S. Gazzaniga, Laura H. Greene, Elizabeth Loftus, Mercedes Pascual

SUBSCRIPTION SERVICES For change of address, missing issues, new orders and renewals, and payment questions: 866-434-AAAS (2227) or 202-326-6417, FAX 202-842-1065. Mailing addresses: AAAS, P.O. Box 96178, Washington, DC 20090-6178 or AAAS Member Services, 1200 New York Avenue, NW, Washington, DC 20005

INSTITUTIONAL SITE LICENSES 202-326-6730 **REPRINTS:** Author Inquiries 800-635-7181 **COMMERCIAL INQUIRIES** 803-359-4578 **PERMISSIONS** 202-326-6765, permissions@aaas.org **AAAS Member Services** 202-326-6417 or http://membercentral.aaas.org/discounts

Science serves as a forum for discussion of important issues related to the advancement of science by publishing material on which a consensus has been reached as well as including the presentation of minority of conflicting points of view. Accordingly, all articles published in *Science*—including editorials, news and comment, and books reviews—are signed and reflect the individual views of the authors and not official points of view adopted by AAAS or the institutions with which the authors are affiliated.

INFORMATION FOR AUTHORS See pages 678 and 679 of the 6 February 2015 issue or access www.sciencemag.org/about/authors

SENIOR EDITORIAL BOARD

Robert H. Grubbs, *California Institute of Technology,* **Gary King,** *Harvard University*
Susan M. Rosenberg, *Baylor College of Medicine,* **Ali Shilatifard,** *Northwestern University Feinberg School of Medicine,* **Michael S. Turner**, *U. of Chicago*

BOARD OF REVIEWING EDITORS (Statistics board members indicated with **(S)**

Adriano Aguzzi, *U. Hospital Zürich*
Takuzo Aida, *U. of Tokyo*
Leslie Aiello, *Wenner-Gren Foundation*
Judith Allen, *U. of Edinburgh*
Sonia Altizer, *U. of Georgia*
Sebastian Amigorena, *Institut Curie*
Kathryn Anderson, *Memorial Sloan-Kettering Cancer Center*
Meinrat O. Andreae, *Max-Planck Inst. Mainz*
Paola Arlotta, *Harvard U.*
Johan Auwerx, *EPFL*
David Awschalom, *U. of Chicago*
Clare Baker, *University of Cambridge*
Jordi Bascompte, *University of Zurich*
Facundo Batista, *London Research Inst.*
Ray H. Baughman, *U. of Texas, Dallas*
David Baum, *U. of Wisconsin*
Carlo Beenakker, *Leiden U.*
Kamran Behnia, *ESPCI-ParisTech*
Yasmine Belkaid, *NIAID, NIH*
Philip Benfey, *Duke U.*
Stephen J. Benkovic, *Penn State U.*
May Berenbaum, *U. of Illinois*
Gabriele Bergers, *U. of California, San Francisco*
Bradley Bernstein, *Massachusettes General Hospital*
Peer Bork, *EMBL*
Bernard Bourdon, *Ecole Normale Supérieure de Lyon*
Chris Bowler, *École Normale Supérieure*
Ian Boyd, *U. of St. Andrews*
Emily Brodsky, *U. of California, Santa Cruz*
Ron Brookmeyer, *U. of California Los Angeles* **(S)**
Christian Büchel, *U. Hamburg-Eppendorf*
Joseph A. Burns, *Cornell U.*
Carter Tribley Butts, *U. of California, Irvine*
Gyorgy Buzsaki, *New York U. School of Medicine*
Blanche Capel, *Duke U.*
Mats Carlsson, *U. of Oslo*
Ib Chorkendorff, *U. of Denmark*
David Clapham, *Children's Hospital Boston*
David Clary, *U. of Oxford*
Joel Cohen, *Rockefeller U., Columbia U.*
James J. Collins, *MIT*
Robert Cook-Deegan, *Duke U.*
Alan Cowman, *Walter & Eliza Hall Inst.*
Robert H. Crabtree, *Yale U.*
Roberta Croce, *Vrije Universiteit*
Janet Currie, *Princeton U.*
Jeff L. Dangl, *U. of North Carolina*
Tom Daniel, *U. of Washington*
Frans de Waal, *Emory U.*
Stanislas Dehaene, *Collège de France*
Robert Desimone, *MIT*
Claude Desplan, *New York U.*
Ap Dijksterhuis, *Radboud U. of Nijmegen*
Dennis Discher, *U. of Pennsylvania*
Gerald W. Dorn II, *Washington U. School of Medicine*
Jennifer A. Doudna, *U. of California, Berkeley*
Bruce Dunn, *U. of California, Los Angeles*
William Dunphy, *Caltech*
Christopher Dye, *WHO*
Todd Ehlers, *U. of Tuebingen*
David Ehrhardt, *Carnegie Inst. of Washington*
Tim Elston, *U. of North Carolina at Chapel Hill*
Gerhard Ertl, *Fritz-Haber-Institut, Berlin*
Barry Everitt, *U. of Cambridge*
Ernst Fehr, *U. of Zurich*
Anne C. Ferguson-Smith, *U. of Cambridge*
Michael Feuer, *The George Washington U.*
Toren Finkel, *NHLBI, NIH*
Kate Fitzgerald, *U. of Massachusetts*
Peter Fratzl, *Max-Planck Inst.*
Elaine Fuchs, *Rockefeller U.*
Daniel Geschwind, *UCLA*
Karl-Heinz Glassmeier, *TU Braunschweig*
Ramon Gonzalez, *Rice U.*
Julia R. Greer, *Caltech*
Elizabeth Grove, *U. of Chicago*
Nicolas Gruber, *ETH Zurich*
Kip Guy, *St. Jude's Children's Research Hospital*
Taekjip Ha, *U. of Illinois at Urbana-Champaign*
Christian Haass, *Ludwig Maximilians U.*
Michael Hasselmo, *Boston U.*
Martin Heimann, *Max-Planck Inst. Jena*
Yka Helariutta, *U. of Cambridge*
James A. Hendler, *Rensselaer Polytechnic Inst.*
Janet G. Hering, *Swiss Fed. Inst. of Aquatic Science & Technology*
Kai-Uwe Hinrichs, *U. of Bremen*
Kei Hirose, *Tokyo Inst. of Technology*
David Hodell, *U. of Cambridge*
David Holden, *Imperial College*
Lora Hooper, *UT Southwestern Medical Ctr. at Dallas*
Raymond Huey, *U. of Washington*
Auke Ijspeert, *EPFL Lausanne*
Steven Jacobsen, *U. of California, Los Angeles*
Kai Johnsson, *EPFL Lausanne*
Peter Jonas, *Inst. of Science & Technology (IST) Austria*
Matt Kaeberlein, *U. of Washington*
William Kaelin Jr., *Dana-Farber Cancer Inst.*
Daniel Kahne, *Harvard U.*
Daniel Kammen, *U. of California, Berkeley*
Masashi Kawasaki, *U. of Tokyo*
V. Narry Kim, *Seoul National U.*
Joel Kingsolver, *U. of North Carolina at Chapel Hill*
Robert Kingston, *Harvard Medical School*
Etienne Koechlin, *Ecole Normale Suprieure*
Alexander Kolodkin, *Johns Hopkins U.*
Leonid Kruglyak, *UCLA*
Thomas Langer, *U. of Cologne*
Mitchell A. Lazar, *U. of Pennsylvania*
David Lazer, *Harvard U.*
Thomas Lecuit, *IBDM*
Virginia Lee, *U. of Pennsylvania*
Stanley Lemon, *U. of North Carolina at Chapel Hill*
Ottoline Leyser, *Cambridge U.*
Wendell Lim, *U.C. San Francisco*
Marcia C. Linn, *U. of California, Berkeley*
Jianguo Liu, *Michigan State U.*
Luis Liz-Marzan, *CIC biomaGUNE*
Jonathan Losos, *Harvard U.*
Ke Lu, *Chinese Acad. of Sciences*
Christian Lüscher, *U. of Geneva*
Laura Machesky, *CRUK Beatson Inst. for Cancer Research*
Anne Magurran, *U. of St. Andrews*
Oscar Marin, *CSIC & U. Miguel Hernández*
Charles Marshall, *U. of California, Berkeley*
C. Robertson McClung, *Dartmouth College*
Graham Medley, *U. of Warwick*
Tom Misteli, *NCI*
Yasushi Miyashita, *U. of Tokyo*
Mary Ann Moran, *U. of Georgia*
Richard Morris, *U. of Edinburgh*
Alison Motsinger-Reif, *NC State U.* **(S)**
Thomas Murray, *The Hastings Center*
James Nelson, *Stanford U. School of Med.*
Daniel Neumark, *U. of California, Berkeley*
Kitty Nijmeijer, *U. of Twente*
Pär Nordlund, *Karolinska Inst.*
Helga Nowotny, *European Research Advisory Board*
Ben Olken, *MIT*
Joe Orenstein, *U. of California Berkeley & Lawrence Berkeley National Lab*
Harry Orr, *U. of Minnesota*
Andrew Oswald, *U. of Warwick*
Steve Palumbi, *Stanford U.*
Jane Parker, *Max-Planck Inst. of Plant Breeding Research*
Giovanni Parmigiani, *Dana-Farber Cancer Inst.* **(S)**
Donald R. Paul, *U. of Texas, Austin*
John H. J. Petrini, *Memorial Sloan-Kettering Cancer Center*
Samuel Pfaff, *Salk Institute for Biological Studies*
Joshua Plotkin, *U. of Pennsylvania*
Albert Polman, *FOM Institute AMOLF*
Philippe Poulin, *CNRS*
Jonathan Pritchard, *Stanford U.*
David Randall, *Colorado State U.*
Colin Renfrew, *U. of Cambridge*
Felix Rey, *Institut Pasteur*
Trevor Robbins, *U. of Cambridge*
Jim Roberts, *Fred Hutchinson Cancer Research Ctr.*
Barbara A. Romanowicz, *U. of California, Berkeley*
Amy Rosenzweig, *Northwestern University*
Jens Rostrup-Nielsen, *Haldor Topsoe*
Mike Ryan, *U. of Texas, Austin*
Mitinori Saitou, *Kyoto U.*
Shimon Sakaguchi, *Kyoto U.*
Miquel Salmeron, *Lawrence Berkeley National Lab*
Jürgen Sandkühler, *Medical U. of Vienna*
Alexander Schier, *Harvard U.*
Randy Seeley, *U. of Cincinnati*
Vladimir Shalaev, *Purdue U.*
Robert Siliciano, *Johns Hopkins School of Medicine*
Denis Simon, *Arizona State U.*
Uri Simonsohn, *U. of Pennsylvania*
Alison Smith, *John Innes Centre*
Richard Smith, *U. of North Carolina* **(S)**
John Speakman, *U. of Aberdeen*
Allan C. Spradling, *Carnegie Institution of Washington*
Jonathan Sprent, *Garvan Inst. of Medical Research*
Eric Steig, *U. of Washington*
Paula Stephan, *Georgia State U. and National Bureau of Economic Research*
Molly Stevens, *Imperial College London*
V. S. Subrahmanian, *U. of Maryland*
Ira Tabas, *Columbia U.*
Sarah Teichmann, *Cambridge U.*
John Thomas, *North Carolina State U.*
Shubha Tole, *Tata Institute of Fundamental Research*
Christopher Tyler-Smith, *The Wellcome Trust Sanger Inst.*
Herbert Virgin, *Washington U.*
Bert Vogelstein, *Johns Hopkins U.*
Cynthia Volkert, *U. of Göttingen*
Douglas Wallace, *Dalhousie U.*
David Wallach, *Weizmann Inst. of Science*
Ian Walmsley, *U. of Oxford*
Jane-Ling Wang, *U. of California, Davis*
David A. Wardle, *Swedish U. of Agric. Sciences*
David Waxman, *Fudan U.*
Jonathan Weissman, *U. of California, San Francisco*
Chris Wikle, *U. of Missouri* **(S)**
Ian A. Wilson, *The Scripps Res. Inst.* **(S)**
Timothy D. Wilson, *U. of Virginia*
Rosemary Wyse, *Johns Hopkins U.*
Jan Zaanen, *Leiden U.*
Kenneth Zaret, *U. of Pennsylvania School of Medicine*
Jonathan Zehr, *U. of California, Santa Cruz*
Len Zon, *Children's Hospital Boston*
Maria Zuber, *MIT*

BOOK REVIEW BOARD

David Bloom, *Harvard U.*, **Samuel Bowring,** *MIT,* **Angela Creager,** *Princeton U.,* **Richard Shweder,** *U. of Chicago,* **Ed Wasserman,** *DuPont*

Published by AAAS

EDITORIAL

Whither (wither?) tenure?

The system of tenure for university faculty in the United States arose in the late 19th to early 20th centuries to guarantee that academics would not be capriciously dismissed if they conducted research on controversial topics, pursued "unpromising" research, or did not conform to conventional beliefs. Much in the world has changed in the past 100 years, from the demographics of the academic workforce and the scale of the educational enterprise, to the pace of discovery and the legal statutes surrounding retirement. These changes prompt a reexamination: Is tenure the best way to nurture scholarly growth and academic freedom, or has its cost become too much to bear?

"...has its cost become too much to bear?"

Fortunately, the makeup of university faculty has changed over the past 100 years as well. Today, the proportion of women scientists as professors has grown. However, they are still underrepresented among tenured faculty as compared to, for example, the number of women in similar positions that do not require tenure, such as government scientists or university lecturers. A major reason is that young academics must concentrate on their careers to earn tenure at the same time as they would be starting their families, and this issue affects women disproportionately more. The year that I came up for tenure at the Massachusetts Institute of Technology, I was told that no woman who had taken time out for childbirth had ever been granted tenure. My twins were born on Monday; I was back in the office on Thursday. Whether women see the tenure hurdle and opt out for family instead, or just never opted in to begin with, the result is that there are too few women for a diverse academic enterprise, and if this process does not evolve, how can the highest institutes of learning promote academic freedom and progress?

Because higher education is essential for the best employment prospects, colleges and universities have expanded to meet the demand. However, the growth has not been primarily in tenure-track faculty, but rather in lecturers, adjunct professors, and staff who generally experience lower pay and benefits, are excluded from university governance, and survive on short-term contracts. Universities have found that this approach enables facile changes that complement the teaching staff as enrollment shifts and needs change. Nimble faculty can also change with the times, but not all tenured faculty are motivated to stay abreast of new developments. What might have been a booming job market 20 years ago when a faculty member earned tenure may be entirely moribund now. In some countries, such as the United States, the problem of obsolescence is exacerbated by the fact that retirement is no longer mandated at a certain age. Average life expectancy has increased since tenure was first instituted. Today, tenured professors can continue to hold their positions 40 to 50 years past the date when they received tenure.

Revising the tenure system to a more flexible form of employment is not going to be easy. Those in a position to change the system are the ones who personally benefited from it. Those hurt by the system are powerless. But it's time for universities to discuss unilateral action and institute some other mechanism. For example, promotion to associate professor could be rewarded with a longer-term contract (10 years), followed by a series of renewable 10-year contracts (or in rare cases, longer contracts) as a full professor. The contracts would be nonbinding, giving the faculty member flexibility to consider opportunities at other institutions. Such a change would encourage faculty to experience the intellectual boost that comes from interaction with different colleagues at a new university and would also facilitate institutional renewal. An appeals process (through a national university association) could adjudicate contract disputes or cases of dismissal on grounds of intellectual disagreements.

The long-standing debate on tenure has not yet resulted in any serious push to change things. At what cost?

– Marcia McNutt

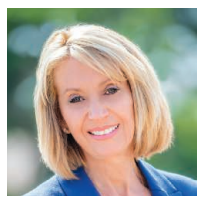

Marcia McNutt
Editor-in Chief
Science *Journals*

PHOTO: (RIGHT) STACEY PENTLAND PHOTOGRAPHY; (INSET) ENIS AKSOY/ISTOCKPHOTO.COM

Downloaded from www.sciencemag.org on December 14, 2015

10.1126/science.aad9966

Published by AAAS

NEWS

> “Froome’s values are close to what we believe are the upper limits for VO_2 peak in humans.”
>
> **Phillip Bell** of the GlaxoSmithKline Human Performance Lab, to *Esquire*, on measuring oxygen uptake by repeat Tour de France winner Chris Froome, who is regularly accused of doping or using illegal bikes.

IN BRIEF

Hawaii telescope in legal limbo

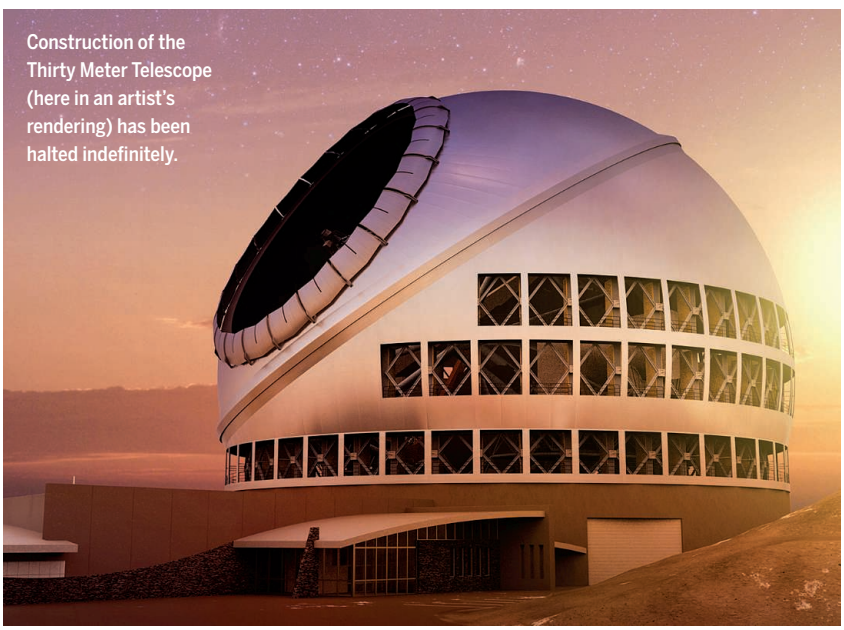

Construction of the Thirty Meter Telescope (here in an artist’s rendering) has been halted indefinitely.

The effort to build the largest optical observatory in the United States, the Thirty Meter Telescope (TMT) in Hawaii, was halted indefinitely on 2 December after the state’s supreme court ruled that the project’s building permits were invalid. Chief Justice Mark Recktenwald decided that the state Board of Land and Natural Resources (BLNR) had wrongly approved the permits in 2011 before a contested case hearing could be resolved, thus not allowing opponents due process. The decision supersedes a lower court’s ruling in 2014 that upheld the permits. The BLNR must now allow the contested case hearing to be held before a new permit is issued. David Callies, a law professor at the University of Hawaii, Manoa, says opponents will likely stretch out the process with new litigation. “In that case, you’re talking more than 1 or 2 years,” he says. Native Hawaiian opponents of the project say the 18-story TMT structure at the summit of the Mauna Kea volcano would be further desecration of one of their most sacred places. Protesters have been blocking construction workers’ access to the site since March; about 70 people have been arrested.

AROUND THE WORLD

Reproducibility study trimmed

CHARLOTTESVILLE, VIRGINIA AND PALO ALTO, CALIFORNIA | An ambitious effort to check the reproducibility of 50 top papers in cancer biology is scaling back because of higher than expected costs. The Reproducibility Project: Cancer Biology, run by the Center for Open Science in Charlottesville, Virginia, and Science Exchange in Palo Alto, California, set out 2 years ago to replicate key experiments from highly cited cancer papers published from 2010 to 2012 (*Science*, 25 June, p. 1411). But the $1.3 million it had from a foundation to redo the studies was not enough, and last week the project’s managers noted online that 13 of the 50 replications have been put on hold. Most involve costly animal experiments. If funding can be found, efforts to reproduce the studies will resume.

Progress on Red-Dead conduit

AMMAN | Israel and Jordan last week issued requests for proposals to build an $800 million water project that would include a pipeline linking the Red Sea and the endangered Dead Sea (below). The project, which has drawn criticism from environmental scientists, has been on the drawing board for 3 decades and is slated to be completed around 2020. Jordanian water and irrigation minister Hazim El-Nasser and Israeli Vice Prime Minister

PHOTOS: (LEFT TO RIGHT) THIRTY METER TELESCOPE; TSAIPROJECT/FLICKR

Downloaded from www.sciencemag.org on December 14, 2015

Published by AAAS

Silvan Shalom unveiled the project, intended to provide potable water to the region. Planners envision a desalination plant in Aqaba, Jordan, that will have an initial capacity of 65 million cubic meters of water per year. Jordan and Israel will share that water, and Shalom believes the project can also help "save" the Dead Sea, where levels are dropping by about 1 meter per year, by transporting in brine from the Red Sea. But critics fear minerals in the transported water could harm the fragile Dead Sea ecosystem, or that pumping could affect organisms in the Red Sea. Advocates for Palestinian farmers also object to the exclusion of the Palestinian National Authority from the deal.

Japan defends whaling plan

TOKYO | Japan has resumed its controversial lethal research whaling in the Southern Ocean, because it wants to determine how many minke whales can be harvested sustainably and also study the Antarctic environment, Joji Morishita, the nation's representative to the International Whaling Commission (IWC), told a press conference 7 December. "We did our best to try to meet the criteria established by the ICJ [International Court of Justice] and we have decided to implement our research plan because we are confident we have completed our scientific homework," Morishita said. In March 2014, the ICJ had ordered the nation to halt its research whaling, ruling that its program at the time, which sought to take 850 minke whales, 50 fin whales, and 50 humpback whales, did not meet stipulated standards of whaling for purposes of scientific research. The country unveiled a new program in November 2014 that calls for taking 333 minke whales; IWC's Scientific Committee examined the new program but last June reported that it could not reach a consensus.

Virus may cause birth defects

BRASÍLIA | The Zika virus, an emerging virus that is causing an unprecedented epidemic in Brazil and is quickly spreading through Latin America, may be responsible for a spike in severe birth defects. Transmitted by mosquitoes, Zika usually causes relatively mild symptoms, including fever and rashes. But the Brazilian government warned last week that the virus may be responsible for a dramatic increase in cases of microcephaly, a severe birth defect in which the brain fails to develop properly and the head is much smaller than normal. The connection is not yet proven, but several lines of evidence point toward Zika as a culprit: The virus has been found in the amniotic fluid of two fetuses diagnosed with microcephaly via ultrasound, and has also been found in tissues of a baby with microcephaly that died shortly after birth. http://scim.ag/Zikamicrocephaly

The secret to cuttlefish 'invisibility'

When threatened by predators, cuttlefish (such as *Sepia officinalis*, below) stop breathing and freeze in place. That isn't just for visual camouflage, suggests a study in the *Proceedings of the Royal Society B.* Sharks can detect the electrical signals produced by an animal's gills—and less water flowing over the cuttlefish's gills makes it harder to detect, it turns out. In the lab, researchers measured electrical signals generated by cuttlefish—first, at rest on the floor of a tank, and then startled by videos of a looming predator. When the frightened creatures froze and covered the cavity leading to the gills with their tentacles, the voltage in the water dropped by about 80%. The tactic works beautifully on sharks, the team found: They simulated electrical signals from a fleeing cuttlefish, a cuttlefish at rest, and a cuttlefish holding its breath. The sharks detected the fleeing cuttlefish 94% of the time and from up to 38 centimeters away; they sensed the resting cuttlefish from 20 centimeters away and struck 62% of the time, but they had to get within 15 centimeters of the frozen cuttlefish to detect it—and still only struck 30% of the time.

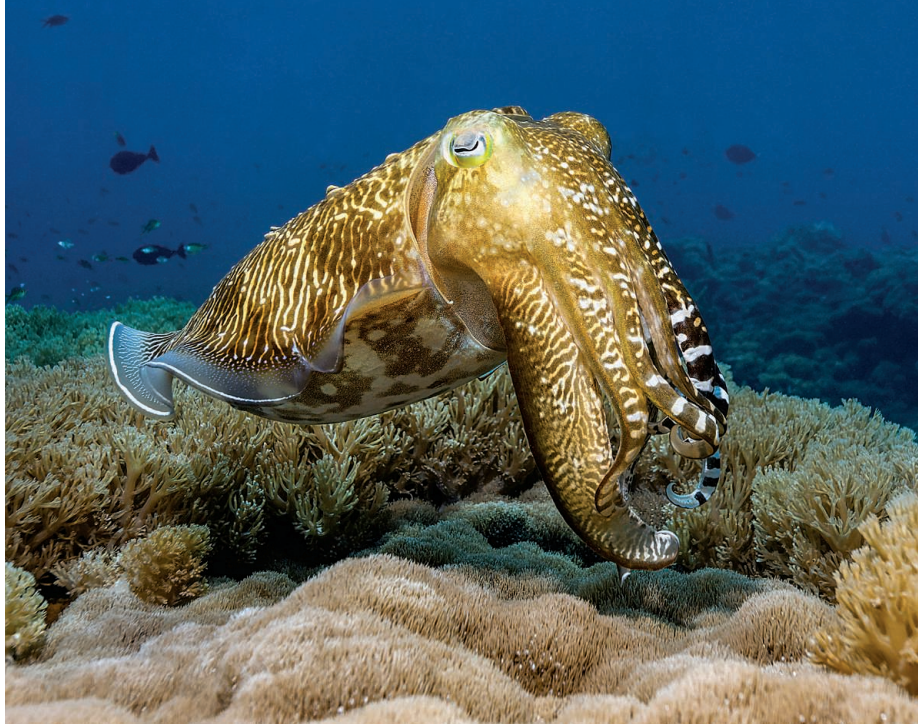

PHOTO: © IMAGEBROKER/ALAMY STOCK PHOTO

Second try at Venus finds success

TOKYO | A spacecraft designed to study Venus's atmosphere that missed its target 5 years ago has apparently succeeded in entering an orbit around the planet, according to the Japan Aerospace Exploration Agency (JAXA). An engine malfunction during its first rendezvous with Venus on 7 December 2010 sent the probe, named Atatsuki, on a 5-year, 10-orbit trip around the sun. Engineers used the time to develop a scheme to insert the craft into orbit using four small attitude control thrusters. JAXA reported that the thruster firing went as planned this week and that Akatsuki "is now in good health" and apparently circling Venus. Mission controllers will confirm the trajectory of the probe in the coming days.

NEWSMAKERS

Integrity office gets new head

The U.S. office that guards against fraud in federally funded biomedical research has a new chief. **Kathy Partin**, a basic neuroscientist and administrator at Colorado State University (CSU), Fort Collins, will become director of the federal Office of Research Integrity (ORI) the week of 27 December. Partin will replace David Wright, who

Published by AAAS

left ORI after 2 years in March 2014 after becoming frustrated with the federal bureaucracy and the little regard his office was given by the Department of Health and Human Services. ORI has often been criticized for moving too slowly to close cases and for meting out relatively light punishments for those found guilty of research misconduct. Partin studies glutamate receptors in the brain, is assistant vice president for research at CSU, and directs the university's research integrity office. http://scim.ag/PartinORI

Three Q's

The new open-access scientific journal *Matters* aims to publish single observations rather than complete stories. *Science* spoke with the journal's founder, **Lawrence Rajendran**, a cell biologist at the University of Zurich in Switzerland. http://scim.ag/Mattersjournal

Q: What motivated you to launch this new journal?
A: As a postdoc applying for jobs 8 years ago, I was shocked to discover that certain figures from retracted manuscripts had gotten published elsewhere. It made me wonder if the pressure to publish "good stories" could be nudging authors to tweak data that doesn't neatly fit a storyline. I remember thinking: If people could just report the one thing they're comfortable with, they wouldn't have to be dishonest.

Q: Tell us about *Matters*' submission and review process.
A: We're focusing on cell biology, biochemistry, biophysics, neuroscience, and genetics. The first 500 submissions to the journal will be free; after that, *Matters* will charge $150 per submission from universities and other nonprofits, and $300 per submission from for-profit entities. We use a triple-blind peer-review process and will publish all scientifically sound observations—even negative data and confirmatory data—within 2 weeks of submission.

Q: But there's a good reason many journals publish "stories"—people *like* stories.
A: An initial finding can be extended with subsequent observations by the original authors or others, who can then build narratives from the collection of findings. It will be like Twitter—you can always go back to who said it first. Our tagline is not "stories don't matter"—it's "stories can wait."

PHOTO: NASA/JOHNS HOPKINS UNIVERSITY APPLIED PHYSICS LABORATORY/SOUTHWEST RESEARCH INSTITUTE

Pluto mission reveals best images yet

NASA's New Horizons spacecraft has returned the best pictures of Pluto the world may ever see. The new images, at resolutions of about 80 meters per pixel, show a striking shoreline, where smooth plains of nitrogen ice from Pluto's "heart" rub up against water ice mountains several kilometers high. The jumbled-up rubble at the base of the ice mountains helps confirm team members' theories that the mountains are, in fact, giant icebergs that have moved around on more plastic layers of nitrogen ice below. The spacecraft made its closest approach to the dwarf planet in July. But because of the great distances and the spacecraft's low-power antenna, some of the best data are reaching Earth only now.

BY THE NUMBERS

55

Percent of giant exoplanets spotted by NASA's Kepler mission that are false positives—not planets but another object such as a brown dwarf, said scientists at the Extreme Solar Systems III conference last week in Hawaii.

$730 million

Amount, in U.S. dollars, of Australia's new National Innovation and Science Agenda, announced 7 December to help reverse deep cuts to science made by the previous administration. http://scim.ag/Ausboom

€5 billion

Total amount of investment in R&D per year, by both public and private sources, that the Irish government aims for by 2020. Last year, the total spent was €2.9 billion.

Published by AAAS

Scientists, physicians, ethicists, and others debated human gene editing at the Washington, D.C., summit.

GENETIC ENGINEERING

Germline editing dominates DNA summit

Prospect of heritable changes sparks questions about safety, ethics, and rationale

By **John Travis**

A congressman's warning. The long shadow of eugenics. Philosophical, ethical, and moral debates. Uncertain science and patchy regulations. And a cast that included scientists expected to share a Nobel Prize for a new DNA-changing technology, commonly called CRISPR. All was on display last week at the International Summit on Human Gene Editing, held at the U.S. National Academy of Sciences (NAS) in Washington, D.C.

"CRISPR and related technologies have the potential to revolutionize the treatment of diseases but could be used in many ways not beneficial to society," noted Representative Bill Foster (D–IL), the only Ph.D. physicist in the U.S. Congress, as the summit opened.

The gathering ended on a similar note: The organizing committee strongly endorsed the use of CRISPR and similar methods for basic research that involves altering DNA of human sperm, eggs, and embryos, but concluded that producing a pregnancy from such modified cells or embryos is currently "irresponsible" because of ongoing safety concerns and a lack of societal consensus. Yet the group—12 biologists, physicians, and bioethicists—did not flatly rule out future use of such "germline editing," in which the DNA changes would be passed down from one generation to the next.

Much of the summit's discussions revolved around whether germline modifications could be justified to prevent the inheritance of disease or, more controversially, to produce "enhancements" such as higher IQ or a reduced need for sleep. In fact, the organizers called for an "ongoing international forum" to regularly revisit the issue of germline editing. "The unthinkable has become conceivable," declared biologist David Baltimore of the California Institute of Technology in Pasadena, the chairperson of the organizing committee.

The new molecular toolkit motivating the summit, CRISPR, consists of a DNA-cutting enzyme called a nuclease and a piece of RNA that homes in on a DNA sequence, enabling researchers to create precisely targeted mutations, corrections to mutations, or other alterations. Along with two earlier genome editors, zinc finger nucleases and TALENs, CRISPR is transforming basic biology and aiding the development of new crops and farm animals. Earlier this year, a Chinese team became the first to publicly report using CRISPR to alter the DNA of human embryos—nonviable ones—from in vitro fertilization (IVF) clinics, and a U.K. group said it wanted to do similar research in the United Kingdom. In response, NAS, the U.S. National Academy of Medicine, the United Kingdom's Royal Society, and the Chinese Academy of Sciences rushed to convene the summit.

> *"The unthinkable has become conceivable."*
>
> **David Baltimore**, California Institute of Technology

By tweaking CRISPR's RNA or nuclease components, researchers expect to make the tool, developed from an immune system found in bacteria, still more precise. And "there are likely more powerful systems still out there in nature," noted Feng Zhang of the Broad Institute in Cambridge, Massachusetts, who at one point shared the stage with other CRISPR pioneers, Jennifer Doudna of University of California, Berkeley, and Emmanuelle Charpentier of the Max Planck Institute for Infection Biology in Berlin. Many predict the trio will win a Nobel for developing the system.

Few at the summit had qualms about using CRISPR and its rivals in somatic cells to treat disease. By applying zinc finger nucleases to immune cells in vitro, groups have already deactivated the gene for CCR5, a protein that the AIDS virus uses to invade the cells; the modified cells were then returned to HIV-infected people. And last month, a team reported on using TALENs to edit cancer-fighting immune cells that subsequently arrested leukemia in a 1-year-old girl. Speakers also discussed plans to use CRISPR on blood stem cells to reverse disorders such as sickle cell anemia and beta thalassemia by fixing hemoglobin gene mutations.

Biologist Janet Rossant of The Hospital for Sick Children in Toronto, Canada, among others, spoke of the need to go further and use gene editing to do basic re-

PHOTO: NATIONAL ACADEMY OF SCIENCES/PAM RISDON

Downloaded from www.sciencemag.org on December 14, 2015

Published by AAAS

search on human embryos—work that the U.S. National Institutes of Health is currently prevented by law from funding and that could get scientists imprisoned in Germany. Such studies, she explained, could probe the causes of miscarriages, birth defects, and developmental disorders. "We still have a lot more to learn about the human embryo and preimplantation stages," Rossant said. Attendees largely agreed, but differed about whether spare IVF embryos are good enough for such work, or whether the door should be open to creating embryos just for research.

Germline gene editing to produce babies stirred deeper debate. The summit heard a primer on the dark history of eugenics, but John Harris, a philosopher at the University of Manchester in the United Kingdom, later argued that nothing is sacred about the germline. All forms of assisted reproduction affect future generations, he said, and normal reproduction is a "genetic lottery" that often produces birth defects and disease.

For now, the best argument for germline editing may be its potential to correct known genetic errors and allow parents to have healthy children. That did not sway Catholic theologian Hille Haker of Loyola University Chicago in Illinois, who contended that no one has a right to have genetically related children and called for a ban on all human germline editing research.

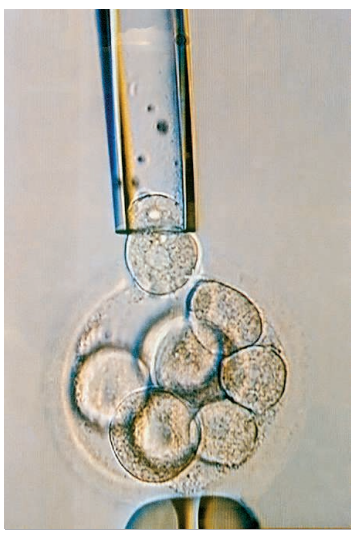

Preimplantation genetic diagnosis of human embryos (shown here) offers an alternative to editing their DNA.

Also stirring discussion was the question of whether germline editing is actually the best way to prevent the transmission of genetic diseases. Many cited a potential alternative: preimplantation genetic diagnosis (PGD), a relatively new procedure in which cells removed from IVF embryos are screened for inherited mutations; only healthy embryos are then implanted. In most cases in which one or both parents have a known inheritable disease, Mendelian genetics imply that some fraction of their embryos will be free of the responsible mutation(s). With PGD, those healthy embryos could be identified and implanted. Baltimore crystallized the issue, asking: "Is it more ethical to edit embryos or screen a lot of embryos and throw many away?"

In some cases, however, no IVF embryos would be normal, rendering PGD useless. For example, if both parents have cystic fibrosis, an autosomal recessive disorder, any offspring would carry double mutations. Similarly, a person with two dominant mutations, such as those causing Huntington disease, would pass on one. Speakers raised other scenarios that might call for germline editing, including bids to reverse infertility and parents seeking a "savior sibling" to provide matched, healthy bone marrow for a sick older child.

For now, few would say genome editing is safe enough for such uses. In the human embryo experiment, CRISPR cut many nontargeted genes. And Rudolf Jaenisch of the Massachusetts Institute of Technology in Cambridge noted that when CRISPR repairs one copy of a disease gene, it sometimes mutates the healthy copy. Eric Lander of the Broad Institute pointed out that if editing is attempted in early-stage human embryos, rather than in sperm or eggs, it might only reach some cells, not all, resulting in a mosaic embryo with some mutant tissues.

Technology may not be a showstopper, however Zhang and others at the summit were optimistic about reducing CRISPR's worrisome off-target edits. But Lander, who was on the summit's organizing committee, reminded attendees that the issues go well beyond technical skill, especially when it comes to genetic enhancement. We know far too little about the human genome's role in cognition and other traits to try to mess with it, he said. "The conclusion is simply humility. Before we make permanent changes to the human gene pool, we should exercise considerable caution."

Even if some parents and clinicians eventually decide it's safe and sensible to do germline engineering, they face a pastiche of conflicting laws and regulations around the world. More than 40 countries outlaw tampering with the germline in IVF efforts, although many others, including the United States, do not. The U.S. government will not fund clinical trials of such work, but gives free rein to private IVF clinics. Near the end of the summit, Barbara Evans of the University of Houston Law Center in Texas noted that "the 'science' of regulation is more precarious and uncertain than the science of gene editing." ■

MARINE MAMMALS

A whale's life, inscribed in baleen

Fibrous keratin can store a chemical record of pregnancies and stress

By **Rebecca Kessler**

In 2004, a collision with a ship cut short the life of an endangered North Atlantic right whale. Many lamented the death of Stumpy, as scientists called her—all the more because she was pregnant. But Stumpy's demise could ultimately help other whales. Researchers are using plates of her tough, hairlike baleen to develop a new method of reconstructing a whale's life story—much as scientists use growth rings to reveal a tree's past. The nascent technique could make it easier to study, and perhaps protect, whales.

Deriving whale biographies from baleen is just one concept to be discussed next week at the 21st Biennial Conference on the Biology of Marine Mammals in San Francisco, California. Some 3000 researchers will share insights into some of the world's most charismatic creatures, including first-time audio recordings of rare species and updates on struggling populations. They'll also discuss novel ways of assessing the health and physiology of free-swimming mammals that can be hard to study in the wild.

That's where the work involving Stumpy—and a second right whale named Staccato—will come in. Over the past decade or so, wildlife researchers have been figuring out how to pry life history information out of tissues based on keratin, the fibrous protein found in nails, hair, feathers, horns, claws, hooves, and skin. Researchers have used hair, for example, to study past drug use in humans and exposure to toxins in wildlife.

Keratin is also a major component of baleen, the comblike structures on the upper jaws of about 14 whale species that help the animals catch food. The tips of baleen plates—the comb's teeth—wear away over time, so whales continuously grow new keratin to replace what's lost. The new baleen stores chemicals, such as hormones or contaminants, which are circulating in the

PHOTO: BENOÎT RAJAU/SCIENCE SOURCE

Published by AAAS

Hormones stored in the baleen of this bowhead whale, killed by Native Alaskan hunters, can help tell its life story.

whale's blood at the time. That makes each plate—which can represent years or decades of growth—a time capsule, recording important life events such as pregnancies or exposure to stressful situations.

Such information can be crucial to conserving rare species such as North Atlantic right whales, which number just about 500. When it comes to large whales, "there's no other animal on the planet where we know [so] little about basic reproduction," says Kathleen Hunt, a research scientist at the New England Aquarium in Boston. For example, scientists don't know how long female right whales carry their calves, or how frequently they become fertile. They also can't easily tell whether the whales are experiencing harmful stress resulting from ocean noise, pollution, or other factors.

Hunt and Rosalind Rolland, a colleague at the aquarium, have already developed noninvasive ways to measure whale hormones associated with stress and reproduction. They involve going to sea to scoop up fresh dung or to collect "whale blow"—the air and droplets an animal exhales through its blowhole. But such samples provide only a snapshot of a whale's current physiological state. Hormone measurements from baleen promised a fuller backstory.

Last year, the researchers published their first results from a pilot study of 16 bowhead whales killed as part of a legal hunt by native Alaskans. Bowheads are a long-lived species, and their baleen can record about 25 years of growth. In *Conservation Physiology*, a team led by Hunt and Rolland reported that not only could they detect two hormones in baleen—the stress hormone cortisol, and the reproductive hormone progesterone—they could also use them to distinguish males from females, and identify pregnant females. They also saw progesterone spikes that looked suspiciously like signatures of past pregnancies.

To know whether those signatures were real, the researchers needed baleen results they could match against documented whale pregnancies. Enter Stumpy and Staccato, also killed by a ship, in 1999. As a result of efforts by government agencies and conservation groups to monitor and protect right whales, scientists had records indicating when each whale had given birth to some of her calves.

In San Francisco, Hunt and her colleagues will unveil new results that suggest researchers can read baleen like a history book. When they analyzed plates from Stumpy and Staccato recording about 10 years of growth, they found that progesterone levels spiked in material dating to documented pregnancies, and then dropped for several years while the mothers were known to be raising calves and later traveling solo. The pattern was "incredibly striking and obvious," Hunt says. That was a huge contrast to the "very subtle patterns" she's used to seeing in other kinds of whale data, she says. "Yeah! Most exciting results I'd ever seen in my career."

The team has also been able to measure cortisol in the baleen, and they see patterns suggesting that stressors, such as getting entangled in commercial fishing gear, can interfere with a whale's ability to get pregnant. Stumpy's baleen, for instance, showed elevated cortisol levels after one pregnancy, and she didn't get pregnant again until the cortisol levels dropped.

Assuming the technique works in other baleen whales, researchers say it would be a welcome new tool. Currently, the only other way to reconstruct a whale's past is by analyzing the layers of wax that accrete in some whale ears. Both the wax and baleen can be collected only from dead animals, but Hunt notes that the wax doesn't last long and is rarely collected. In contrast, baleen is sturdy and long lasting. That could enable researchers to see far back in time by analyzing museum specimens of baleen, some of which are more than a century old, or whale remains found at archaeological sites.

Such "specimens are a treasure trove of biological information just waiting to be unlocked," says ecotoxicologist Thea Bechshoft, a postdoctoral researcher at the University of Alberta, Edmonton, in Canada. The baleen work, she says, "adds to the growing evidence of how amazingly useful keratinous tissue … can be." ■

Baleen from Stumpy, a right whale killed by a ship, yielded a record of her pregnancies.

Rebecca Kessler is a journalist in Providence.

PHOTOS (TOP TO BOTTOM): © GREGORY BULL/AP/CORBIS; REGINA CAMPBELL-MALONE, WOODS HOLE OCEANOGRAPHIC INSTITUTION

Published by AAAS

WEATHER FORECASTING

CubeSats promise to fill weather data gap

Companies bet on a GPS technique and an agency shift to commercial data

By **Eric Hand**

The massive weather satellites that plumb the atmosphere are facing a swarm of tiny competitors. Data from shoebox-sized private satellites, exploiting a new technique for probing the atmosphere, could significantly reduce forecast errors, researchers say. But national weather agencies, used to generating their own data, have so far been reluctant customers. At a workshop this week, the U.S. National Oceanic and Atmospheric Administration (NOAA) hoped to address some of the stumbling blocks.

The big government systems are becoming increasingly fragile and unaffordable. Witness the $11.3 billion Joint Polar Satellite System (JPSS) at NOAA: It is drastically over budget and behind schedule for the planned 2017 launch of its JPSS-1 satellite, jeopardizing the flow of crucial weather data.

Companies say they can fill the gap with data from cheap CubeSats, small satellites the size of one or several 10-centimeter cubes (*Science*, 10 April, p. 172). Last week, Boulder, Colorado–based PlanetiQ booked a 2016 flight for its first two weather satellites. And after the successful launch of four satellites in September, San Francisco, California–based Spire says it is in negotiations to license its data to both government and private entities. Yet NOAA has been hesitant to support the satellite weather startups, says Mariel Borowitz, a space policy researcher at the Georgia Institute of Technology in Atlanta. "They have said, 'Build it and once it's in operation, then we'll decide if we want it or not.'"

One reason is NOAA's concern that the private companies would restrict its ability to share data freely with other agencies and governments. This week's workshop built on a draft commercial space policy the agency released in September, which suggests that data buys should comply with a guiding principle of open and free data.

The companies are taking advantage of one of the most promising remote sensing techniques of the last 20 years: GPS radio occultation. Dozens of GPS satellites circle the globe in medium-Earth orbit, constantly broadcasting the radio signals used to locate everything from cellphones to drones. When the signals pass through Earth's atmosphere, they bend slightly, like light refracting in water. A satellite in low-Earth orbit can pick up signals that have skimmed the atmosphere, calculate the bending from their travel time, and use it to infer temperature, pressure, and humidity at particular altitudes. A constellation of small satellites could measure thousands of these vertical profiles each day as GPS satellites constantly rise and set on the horizon.

Weather balloons offer similar data, but they are released mostly over land in the Northern Hemisphere. Radio occultations, by contrast, occur day and night and are evenly distributed around the globe. Occultations also offer advantages over the infrared and microwave data collected by massive satellites like JPSS. Infrared sounders cannot see through clouds, and microwave sounders are confused by moisture, which adds uncertainty to predictions of hurricane paths and intensities.

What's more, because occultation measurements depend only on the timing of an arriving GPS signal, it is easy to compare data from different satellites and campaigns without complex corrections. Once a few decades of data are in place, radio occultations could even track global warming trends. "You don't need to bias-correct the system," says Sean Healy, a scientist at the European Centre for Medium-range Weather Forecasting (ECMWF) in Reading, U.K. "That's why it should be useful for climate monitoring."

> ***"Every single GPS radio occultation profile we can get our hands on ... will save lives and money."***
> **Peter Platzer**, CEO, Spire

As countries expand their GPS networks (China and India are rapidly building their own systems), the potential for radio-occultation data grows. Healy says the ECMWF currently primes its forecasts with as many as 3000 daily radio occultation profiles, gathered by a handful of satellites—but the agency wants more. A 2013 study found that including 16,000 daily profiles in the ECMWF model could significantly reduce forecast errors, and that benefits continued to accrue with as many as 128,000. So far, the data have come from government satellites, but the startup companies see an opportunity. "GPS radio occultation is the best candidate for attempting commercialization of a weather satellite system," Borowitz says.

Some want the agency-owned approach to continue. A public, $100 million system of six satellites called COSMIC, launched in 2006, pioneered the technique, and its leaders have secured $450 million from Taiwan, the U.S. Air Force, and NOAA for COSMIC-2, a new system of 12 satellites. Rick Anthes, who helped develop COSMIC when he was president of the University Corporation for Atmospheric Research in Boulder, thinks the public approach is the better bet. "There are definite plans and definite

Bent over the horizon

By picking up GPS signals passing through the atmosphere, small GPS radio occultation (GPS-RO) satellites can gather weather data.

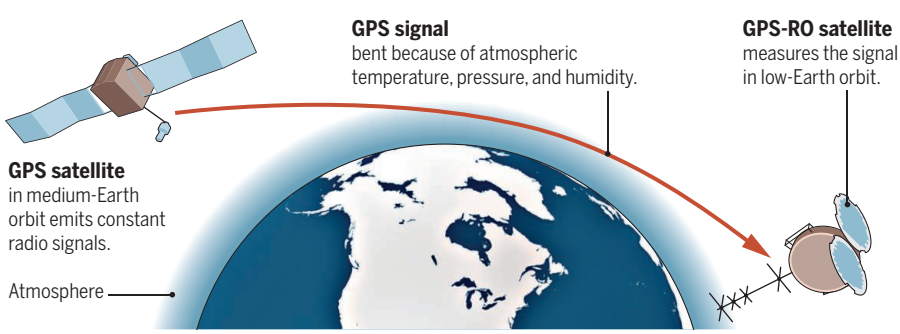

ILLUSTRATION: P. HUEY/*SCIENCE*

Downloaded from www.sciencemag.org on December 14, 2015

Published by AAAS

instruments and definite data quality," he says. He notes that COSMIC-2 satellites, at 70 kilograms, are bigger than the private companies' CubeSats. A bigger satellite can carry a bigger antenna and better receivers, which boosts signal quality, he says.

But Spire, with $80 million in investor funding and a nimble, Silicon Valley approach, believes that a bigger constellation can overcome any limitations in data quality. In September, four of its "Lemur" satellites—each a 5-kilogram "3U" box taking up three CubeSats' worth of space—reached orbit on an Indian rocket. "All are nominal, fully functioning, and delivering data to us," says founder and CEO Peter Platzer. He would not say how many profiles the Lemurs are producing, only that four to eight additional Lemurs are likely to be launched every month for the next 2 years, and that the company is on track to produce 20,000 profiles a day by the end of 2016. He says more than half of the world's 10 largest weather-forecasting agencies have sent Spire letters of intent for data licensing agreements.

With a 10-kilogram, 6U CubeSat design, PlanetiQ's satellites are twice the size of Spire's—a difference that CEO Chris McCormack says makes possible better data quality. His bigger satellites can tune in to multiple GPS networks, whereas Spire's first Lemurs listen only to the U.S. system. With $5 million in investor funding, PlanetiQ says that by the end of 2017 it will be operating a constellation of 12 satellites capable of generating 34,000 profiles a day.

McCormack is palpably frustrated with NOAA's reluctance to encourage commercial data. "They have not been a supporter of data buys whatsoever," he says. "They don't like change." The agencies so far are insisting on freely shareable commercial data. Platzer says he would be happy to offer such a licensing agreement—but that it would be much more expensive. The companies hope to profit by selling data to multiple buyers, both private and public. Borowitz says, however, that the global data-sharing protocols specify that all "essential" data be shared freely—a word that could offer agencies some interpretive wiggle room.

NOAA declined to make officials available for an interview. In a statement, spokesperson John Leslie said the agency is reviewing comments in response to its draft commercial space policy. But Platzer is confident that agreements can be reached. "The global weather community can use every single GPS radio occultation profile we can get our hands on," he says. "Every single one will save lives and money." ■

PHOTO: FERMILAB

PHYSICS

Controversial test finds no sign of a holographic universe

Speculative effort was destined to fail, critics say

By **Adrian Cho**

Even proponents admitted the experiment was a long shot. Working with a few lasers and mirrors, physicists at Fermi National Accelerator Laboratory (Fermilab) in Batavia, Illinois, claimed they could test perhaps the wildest idea from string theory: that our universe may be like an enormous hologram (*Science*, 13 April 2012, p. 147). Others scoffed that the experiment couldn't possibly probe the "holographic principle."

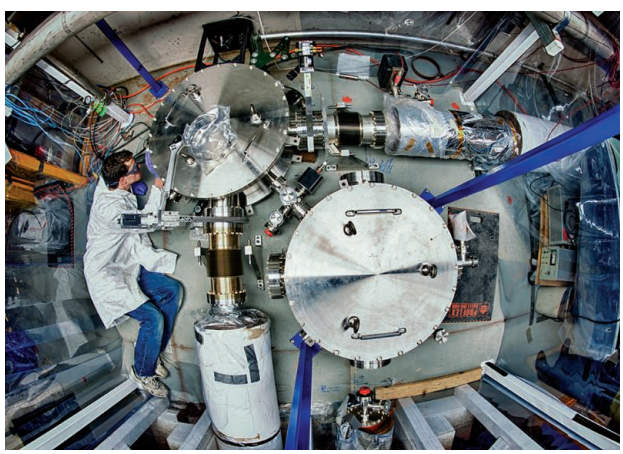

The Fermilab Holometer was built on a shoestring in an abandoned tunnel.

So last week, when experimenters with the $2.5 million Fermilab Holometer reported that they had seen no evidence to support the principle, critics were unimpressed.

"Not surprising, as the idea underlying it is nonsense," tweeted Sabine Hossenfelder, a theorist at the Nordic Institute for Theoretical Physics in Stockholm. However, Yanbei Chen, a theorist at the California Institute of Technology in Pasadena, says the experiment and its inventor, Fermilab theorist Craig Hogan, deserve credit for trying. "At least he's making some effort to make an experimental test," Chen says. "If the string theorists complain that this is not testing what they're doing, well, they can come up with their own tests."

The holographic principle springs from the theory of black holes, spherical regions where gravity is so intense that not even light can escape. In theory, a black hole has an amount of disorder, or entropy, that is proportional to its surface area. As entropy is related to information content, some theorists have conjectured that the maximum amount of information in any volume of space and time, or spacetime, may be proportional to its surface area. The universe would then work like a like a hologram, in which a 2D pattern captures a 3D image. The idea could guide string theorists in their quest to meld the theories of gravity and quantum mechanics.

In 2009 Hogan dreamt up a way to test the idea. The holographic principle might come about, he argued, if coordinates in different directions—up-down, forward-backward, right-left—obey a quantum mechanical uncertainty relationship like the Heisenberg uncertainty principle, which says it is impossible to know both the position and momentum of a particle such as an electron. It would then be impossible to define position, at least on scales of 10^{-35} meters.

Hogan figured he could spot the effect using L-shaped optical devices known as interferometers, which serve as ultraprecise rulers. If position really is hazy, then "holographic noise" should cause the output of an interferometer to jiggle at millions of cycles per second, he claims. If two interferometers were nestled one inside the other to probe the same volume of spacetime, their holographic noise would show telltale correlations—if the noise existed. However, using two interferometers with 39-meter arms, Hogan, Fermilab experimenter Aaron Chou, and colleagues saw no such correlated noise.

Critics say Hogan's idea is half-baked and has nothing to do with the holographic principle. Hogan is undaunted. "For me, the big news is that we have a technique for measuring spacetime at this level," he says. He plans to reconfigure the holometer to look for another possible sign of quantum gravity: an uncertainty in angular orientation within spacetime. ■

Published by AAAS

A Korubo man and boys made contact with officials in the Brazilian Amazon this fall.

PHOTO: CGIIRC/FUNAI

ANTHROPOLOGY

Deadly attack on isolated tribe

Isolated people recovering from conflict with settled neighbors in the Brazilian Amazon

By **Barbara Fraser**

This fall, some members of the settled Matis tribe saw a group of naked strangers along the riverbank near their village of Tawaya in the Amazon rainforest of western Brazil. The Matis, who first made contact with the wider world in the 1970s, have shotguns and wear Western-style clothes. But they knew from previous encounters who the strangers were: Members of the Korubo tribe, who live deep in the forest, follow a traditional way of life, and typically shun interactions with outsiders. The Matis took the 10 Korubo—five adults, a young man, and four children—back to their village and contacted FUNAI, the Brazilian government agency responsible for indigenous peoples.

To FUNAI, this was a health emergency. Isolated people lack immunity to common diseases, so workers arrived 3 days later to provide medical care to that first group of Korubo and more who came to the village a week later. As they talked with the Korubo, FUNAI officials heard some disturbing news: Some tribespeople said they had survived an attack by members of the Matis tribe in December 2014. At least eight Korubo were killed in what was apparently revenge for the deaths of two Matis men, also last December. The Matis alerted FUNAI after their people were killed, but the agency did not authorize contact.

These revelations, made public only late last month by FUNAI, have rekindled a broader debate that divides experts inside and outside Brazil as isolated indigenous peoples increasingly emerge from the forest, displaced by mining, logging, and illegal activities (*Science*, 5 June, pp. 1061, 1072, 1080). After deliberate contacts in the last century often proved catastrophic, with disease and violence killing two-thirds of the members of some newly contacted groups, FUNAI resolved not to initiate contact. "The goal is not to keep them isolated," says Carlos Travassos, who heads the agency's office for people in isolation in Brasília. "The goal is to protect them so they can decide if they want to establish contact or not."

But in this case, some say that FUNAI should have taken the initiative and contacted the group. Anthropologist Robert Walker of the University of Missouri, Columbia, says the tragic deaths of the Matis and the Korubo are "a good example of why the 'leave them alone' strategy doesn't work."

The events are the latest in a series of sometimes hostile encounters between the Matis and isolated Korubo. Their territories have long overlapped in what is now the Vale do Javari Indigenous Territory, home to 16 isolated groups as well as about 4500 settled indigenous people, according to FUNAI. In 2011, a group of Matis established a village in an area known to be used by the Korubo. FUNAI workers encouraged the Matis to avoid contact with the Korubo, who sometimes appeared along the river.

Then in December 2014, a group of isolated Korubo killed two Matis men with wooden clubs, apparently after some Korubo died of illnesses that they blamed on an encounter with the Matis, Travassos says. Some of the Matis then requested permission to establish contact with the Korubo, according to a letter from the Matis Indigenous Association to the Brazilian Attorney General's Office. But FUNAI officials believed that the Korubo's hostility indicated that they did not want contact. To prevent conflict, the agency instead convinced the Matis to relocate to Tawaya, Travassos says. He adds that FUNAI learned of the revenge killings of the Korubo and their original deaths from illness only after speaking with tribespeople this fall, and that details of the December encounters are still unclear.

Health workers are continuing to provide health care for the Korubo. Respiratory illnesses—which are the most common cause of death in cases of recent contact—were reported, according to Douglas Rodrigues, a physician and public health expert at the Federal University of São Paulo, who is in contact with the FUNAI team on the ground. Officials moved the Korubo camp away from the village to help prevent any additional disease transmission, and the illnesses are now under control, Rodrigues says, adding that a Korubo baby was born. Medical care and long-term monitoring are crucial, he says, because it can take four or five generations for people to develop natural resistance to diseases.

But the Matis fear further conflict. On 1 December, the Matis association issued a statement calling for a meeting with the president of FUNAI and for the agency to send two teams to the area. The statement says that Matis villagers saw more Korubo near Tawaya in early November, and that stronger action by FUNAI is needed to avoid more deaths. If attacked, "the Matis will retaliate," the statement said. Travassos says that FUNAI takes this situation very seriously but that the agency's limited resources must stretch to cover many other isolated groups.

Antenor Vaz, a former FUNAI official, says the events show that FUNAI needs to improve on-the-ground monitoring and respond more readily when contact is likely. "Within the policy of protection, contact is foreseen," he says. "The government and society should be prepared for it." ■

Barbara Fraser is a freelance writer in Lima.

Downloaded from www.sciencemag.org on December 14, 2015

Published by AAAS

INFECTIOUS DISEASES

HIV/AIDS care for all—on a budget

Meeting promotes ways to cut clinic visits and tests without compromising treatment

By **Jon Cohen**, *in Harare*

Every 2 months, a Land Cruiser stuffed with health care workers leaves Chidamoyo Hospital here early in the morning and drives 90 minutes east across washboard roads to the farming village of Nyamutora. Boxes of antiretroviral (ARV) drugs and medical records crowd the back of the vehicle. Sitting on pews at a Salvation Army church, nearly 150 HIV-infected people are waiting for the nurses and counselors. By the time the Land Cruiser leaves about 6 hours later, all will have received enough drugs to last until the team's next visit, had their weight documented, and spoken with a nurse. Some will have had blood drawn for later analyses to test how they're responding to treatment.

This routine departs from the usual model of HIV treatment, in which patients receive ARVs at frequent clinic visits. Yet the 143 Nyamutora villagers who have been given their ARVs every 2 months through this 3-year outreach effort have done remarkably well, Benjamin Chimukangara, a molecular virologist at the Biomedical Research and Training Institute in Harare, reported here last week at the International Conference on AIDS and STIs in Africa. Only two have died from AIDS—both began treatment when they were very ill—and all but four others, or 96%, have reduced their "viral load" to the level that the World Health Organization (WHO) uses to define treatment success—less than 1000 virus particles per milliliter of blood. "They've shown an unbelievable adherence and response," said study leader David Katzenstein of Stanford University in Palo Alto, California.

The result is good news for efforts to lower the cost of HIV treatment, so that poor countries like Zimbabwe can come closer to achieving a new goal: universal treatment for HIV. Until today, most governments have reserved ARVs for people who have shown at least some immune system damage from HIV. But new evidence shows that immediate treatment staves off AIDS, and in September WHO called on countries to offer the drugs to all HIV-infected people. There are an estimated 21 million untreated people, 12 million of whom live in Africa. Without a bolus of new cash, which no one expects, governments will have to come up with ways to cut costs without compromising the quality of care. The Nyamutora project is precisely the sort of simple, innovative "alternative delivery model" that can help. "The paradigm should be services going to people, and today, most people are going to services," Michel Sidibé, head of the Joint United Nations Programme on HIV/AIDS, told *Science*.

Sidibé, who spoke at the meeting, noted that the world now spends $22 billion on HIV/AIDS a year, and yet the cost of drugs is only $80 to $100 per person a year in poor countries. Most of the global expenses are for clinic visits and lab tests. "It's difficult for me to think we'll be able to change completely the scale of our treatment programs by continuing the traditional high-cost approach," he said. A new buzzword, "differentiated care," calls for providing intensive services only to those who are ill or failing on medication: Those doing well can cut clinic visits back to twice a year and receive up to a 6-month supply of ARVs.

The Nyamutora project, conceived by the local Salvation Army church and Chidamoyo Hospital, shows how efficient that approach can be. Before the project began, people would either have to find round-trip transportation—which often meant paying $6, a hefty sum for most—or walk for an entire day to receive a month or two's supply of medication. What the villagers call "Chidamoyo day" also saves the hospital staff time and money: The village visit is an efficient way to see many patients in one fell swoop, and their main extra cost is $35 for gas.

One reason patients can forgo frequent clinics visits is that routine monitoring of CD4s, the white blood cells that HIV targets and destroys, is increasingly being seen as a pointless money sink. At the meeting WHO recommended "stopping routine CD4 count testing" for people who are stable on ARVs and instead monitoring viral loads as rarely as once a year. Using "dried blood spot" technology, which requires a simple finger prick rather than collecting venous blood to monitor viral load, could save even more money. Zimbabwe alone could save millions of dollars each year by using the dried blood spot strategy instead of routine CD4 measurements, according to a model presented by Paul Revill of the University of York in the United Kingdom.

HIV-infected people in a remote Zimbabwean village receive antiretroviral drugs at the local church once every 2 months.

PHOTO: TJ MAPOSHERE

Less skilled workers can often do the same quality work as better-paid professionals, several speakers said. Pharmacists, for example, need not distribute ARVs. Doctors Without Borders trained community health workers in rural Malawi to perform viral load tests accurately. "We have to explore every single piece of how to get as many people on treatment right now with the resources we have," Deborah Birx, head of the U.S. President's Emergency Plan for AIDS Relief, told *Science*.

Birx urged countries to put the new recommendations into effect "within weeks, not years." She also sees other opportunities for savings. "You could visualize in these remote areas drones carrying drugs and drones carrying dried blood spots," she suggests. "There are a lot of different innovations we haven't even attempted." ■

Reporting for this story was supported by the Pulitzer Center on Crisis Reporting.

Downloaded from www.sciencemag.org on December 14, 2015

Published by AAAS

Corrected 10 December 2015; see full text.

FEATURES

MIND THE PHONE

Devices that monitor and coach users bring promise and peril to the science of behavior change

By **Kelly Servick**

Fitbit activity trackers come with a "manifesto." Over a photo of a fierce-eyed jogger, the company's website proclaims: "Every moment matters and every bit makes a big impact. Because fitness is the sum of your life."

Roughly 20 million people have found that message compelling enough to order a Fitbit. Many more seek out other devices and smartphone apps designed to count their steps, their calories, or their hours of sleep; to help them quit smoking, drinking, or stressing; or to help manage chronic illness. The distillation of daily life into a motivational stream of stats has become a booming industry—the world of the quantified self.

This life-tracking craze has produced something that many clinical researchers covet: a deluge of intimate data about individuals' moment-to-moment behavior in "the wild," as researchers sometimes call the world outside the controlled environment of the lab or the clinic. "It's sort of opening a window into parts of people's lives we haven't really had access to before," says Ida Sim, a physician and informaticist at the University of California, San Francisco.

Once, peeking through that window required equipping subjects with elaborate motion and heart rate monitors designed specifically for research. But now that roughly two-thirds of U.S. adults own smartphones equipped with GPS systems, cameras, and light and motion sensors, "people are thinking, 'Oh, well maybe I could just get [data] off somebody's phone while it's in their purse," Sim says. "It's bringing in a whole new group of people who are asking new questions."

ILLUSTRATION: JOHN HOLCROFT

Downloaded from www.sciencemag.org on December 14, 2015

Published by AAAS

For example, researchers wonder whether they can finally discover just how much exercise—and what kind—makes for a healthy heart, and what strategies help people stop smoking for good. For many researchers, the hope is that mobile devices will allow them to go beyond collecting data to influencing behavior on a massive scale. Through activities built into an app or strategically timed alerts and messages, researchers can attempt to monitor and modify the habits of thousands of people simultaneously. Major university health centers and government funding agencies hope "mHealth" will finally make a dent in intractable public health problems, from obesity to tobacco use to depression. Sim, for example, collaborates on a 4-year, 11-university project funded by a $10.8 million grant from the U.S. National Institutes of Health (NIH), to design new analytical tools for interpreting mobile data and using them to combat disease. The team is already developing mobile technologies to help people manage congestive heart failure and quit smoking.

But harnessing the self-tracking trend to promote healthier behavior is far from a sure bet. The world of commercial self-improvement apps is "the world of the cowboys," says clinical health psychologist Bonnie Spring of Northwestern University Feinberg School of Medicine in Chicago, Illinois. Commercial app designers "are really unbothered by the kind of standards of evidence that we care about," says Spring, who studies behavioral treatments for obesity and tobacco addiction and collaborates on the NIH project. Few commercial apps have actually been shown to help change users' behavior, improve their health, or even take accurate measurements.

Researchers hoping to bring rigor to the Wild West of mobile sensors are still wading through fundamental questions: Do the raw data from a phone or wearable device reliably measure behavior? Does getting feedback about their behavior really help people change it? And how do you keep the download-happy masses from quickly losing interest or ignoring your app? Sim says it's hard not to let expectations about mobile health research soar beyond the evidence. "I think right now it's still a lot of excitement, and a lot of hype."

IN THE 1960s, walking clubs in Japan adopted a new fad: a commercial pedometer called *manpo-kei*, literally meaning "10,000-step meter." Researchers were soon exploring the health benefits of the handy-but-arbitrary goal of 10,000 steps per day. Today, it's the default goal on every new Fitbit.

But scientists still don't know whether it's the right exercise goal, says Euan Ashley, a cardiologist at Stanford University in Palo Alto, California. "Is it better to do vigorous exercise on weekends, or is it better to accumulate 10,000 steps a day? We don't know," he says. "It's almost like we have something more powerful than any drug that we have for cardiovascular disease—physical activity—but we don't know how to dose it." He believes that the answer could lie in mobile health data.

Research that relates behavior to health has often relied on crude surveys that ask patients to remember and report what they've been up to. "'What did you do on Monday? How many flights of stairs did you do on Tuesday?' That's literally how these studies are carried out," Ashley says. "I can barely remember what I had for breakfast, never mind what I did last Wednesday." Even big, successful, longitudinal studies like the famous 67-year-old Framingham Heart Study have relied on occasional surveys to spot correlations between behaviors and measures of health.

Other studies have taken people out of "the wild" for stints of close observation. Participants in sleep research may spend days or weeks in the lab, sometimes wired up with sensors or lying in magnetic resonance imaging scanners, for example. But the effort and cost of recruiting and compensating subjects makes large-scale studies impossible.

Mobile phones and wearable sensors offer a much cheaper way to get huge sample sizes … if they measure what they say they measure. "If we're going to do science with these devices, we really want to validate them ourselves," says Ashley, who is in the middle of that unglamorous task. He has rounded up all the major commercial fitness trackers to see how they compare with clinical grade equipment on their measures of heart rate and calories burned. His preliminary finding, which matches other recent studies, is that devices tend to agree on heart rate, but calorie counts are "kind of all over the place."

Ashley is also experimenting with a new system for gathering health and activity information from iPhone users. He's one of more than a dozen investigators who have launched apps using ResearchKit, Apple's open-source software platform for scientists, unveiled in March. His team's app, called MyHeart Counts, pulls data from phone accelerometers, which track daily step counts and can record participants' performance on a 6-minute test of walking speed. The researchers can then explore how those readings correlate with participant-reported cardiovascular risk factors, diet, and mood. In its first month, the app recruited 30,000 participants, all of whom opted to share data through an informed consent form on their phones. By now more than 47,000 have signed up.

Ashley is just beginning to analyze the data, but his group is already developing a new version of the app. It turns the phone from a monitor into a coach, nudging participants to do more exercise.

Psychologists like Spring welcome such efforts to wrestle behavior-change strategies onto our tiny screens. They say that although pocket-sized counseling or coaching is unlikely to replace traditional in-person sessions, it might extend the reach of such interventions. "We know that the people we're helping are in some ways those least in need—the ones who can afford to come, who have the time, who can pay for the parking," she says.

In one early attempt, Spring and her colleagues designed an app that draws on principles of the Diabetes Prevention Program—a clinically tested curriculum that she calls "the most successful weight loss approach ever." Central to that approach is getting participants to religiously count their fat and calorie intake and track their weight, Spring

Encouraging words

Many behavior-change programs designed for mobile phones rely on motivational texts to engage users all day. The U.K.-based txt2stop service tailors messages about quitting smoking to a user's responses.

Day4=Big day - cravings still strong? Don't worry tomorrow will be easier! Keep your mind & hands busy. Save this txt so u can txt CRAVE to us at any time during the programme.

txt2stop service

Cravings last less than 5 minutes on average. To help distract yourself, try sipping a drink slowly until the craving is over.

txt2stop, Response to text "crave"

Don't feel bad or guilty if you've slipped. You've achieved a lot by stopping for a while. Slip-ups can be a normal part of the quitting process. Keep going, you can do it!

txt2stop, Response to text "lapse"

Published by AAAS

Corrected 10 December 2015; see full text.

Healthy habits

MIT researchers tracked undergraduates' lifestyles and well-being by asking them to report their activities on their phones over 30 days; the calmest 20% and most stressed 20% of students, as sorted by an end-of-month evaluation, had some different habits.

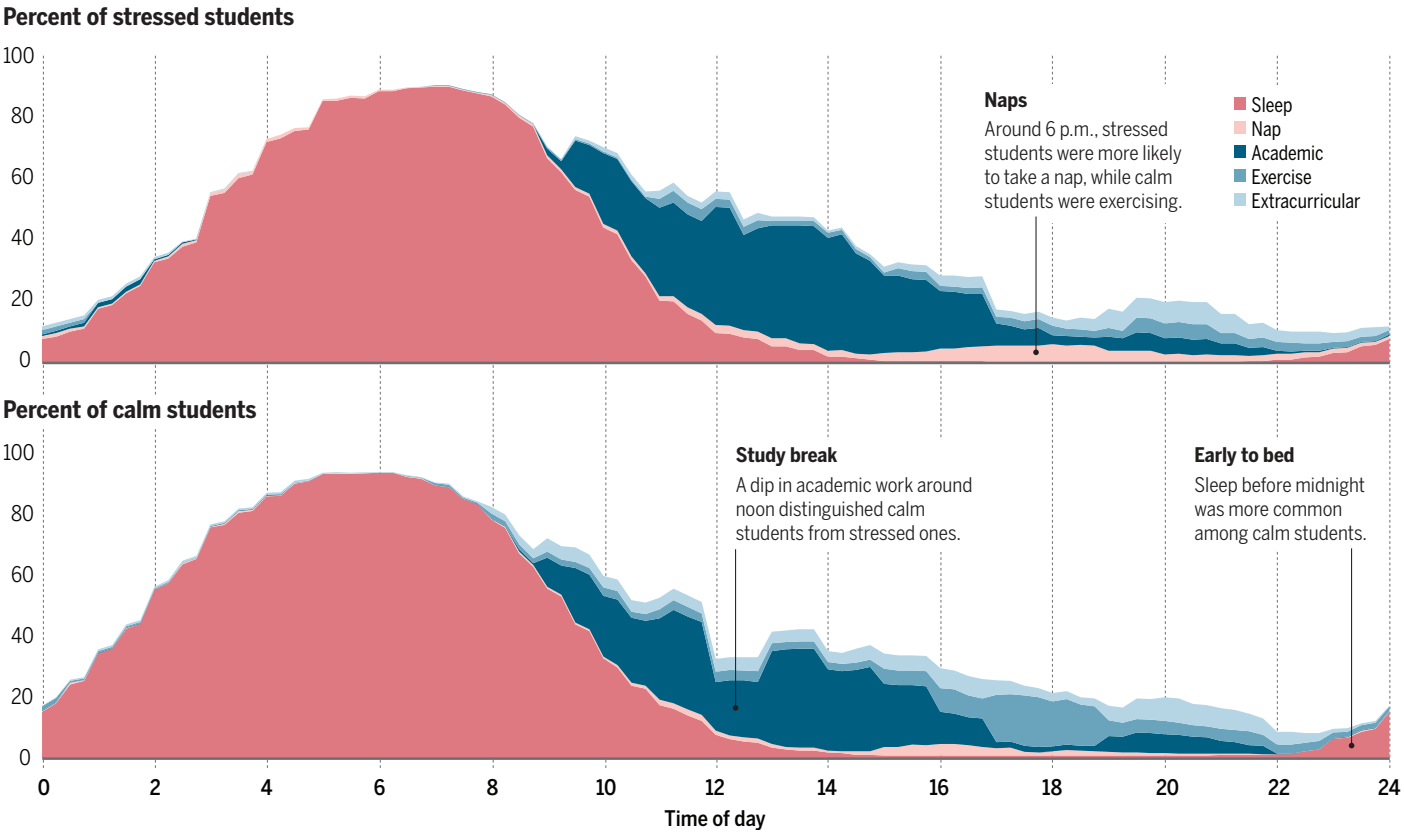

GRAPHIC: ADAPTED FROM SNAPSHOT STUDY/MIT MEDIA LAB AFFECTIVE COMPUTING GROUP/HTTP://SNAPSHOT.MEDIA.MIT.EDU/C. SMITH/*SCIENCE*

says, which can be a challenge. Hoping to keep users engaged, her group's app depicts calorie and fat allowances in colorful meters that fill up over the course of the day.

Other researchers are testing apps meant to help recently abstinent smokers avoid relapse. A U.K.-based program called txt2stop simply sends tailored text messages, such as "Day4=Big day - cravings still strong? Don't worry tomorrow will be easier! Keep your mind & hands busy." Users can text the word "crave" at any time to get additional reinforcement, and "lapse" if they have smoked and need coaching through a slip-up.

That approach depends on users to reach out or engage with their phones when they're tempted, however. "When people need the most help, they are not the ones likely to ask for it," says Santosh Kumar, a computer scientist at the University of Memphis in Tennessee who leads the big NIH-funded project known as Mobile Data to Knowledge (MD2K). Ideally, he says, an app would sense the user's context—including the presence of potential temptations—to figure out when someone needs guidance and then provide a so-called "just-in-time intervention."

MD2K collaborators are working on one such system. It will infer stress—a known risk factor for a lapse in attempts to quit smoking—from heartbeat intervals in electrocardiogram data collected by a chest band. (Kumar notes that data from a smartwatch could also work, provided the watch's heart monitor delivers reliable data.) The MD2K system will also detect when people smoke without their having to report it, by combining breathing patterns from the chest band with readings of arm motion gathered by a motion-sensing wristband. The hope is that stress-relieving exercises can be timed to moments when a person is most vulnerable to an urge or most receptive to encouragement.

Another context-dependent smoking app, called Q Sense, is under development in the lab of Felix Naughton, a health psychologist at the University of Cambridge in the United Kingdom. The app first uses a phone's GPS system to tune into a person's habits and learn where they are most likely to smoke—for example, in the pub or outside the workplace. Once people start to quit, they'll receive tailored messages of encouragement when they breach a certain radius of these locations. Being in the workplace, for example, might trigger instructions for a stress-reduction technique.

DESPITE THE FLURRY OF RESEARCH, the first generation of behavior-change apps has a spotty report card. The U.K. antismoking app txt2stop showed some benefit in a randomized study of 5524 participants. It doubled the rate of successful quit attempts after 6 months—from about 5% in the control group to about 10% of text recipients. Although that may sound like meager progress, it's cost-effective for health systems: The service costs £16,120 but gains about 18 life-years per 1000 enrolled participants.

Spring's weight loss app, meanwhile, inspired an astounding level of self-tracking in its users. They entered their weight on more than 90% of days, she says. "I've never seen this. It was unimaginable." But when she compared app users with people who tracked their weight and food intake with paper and pencil, the app seemed to provide no additional benefit in terms of pounds lost—both groups saw modest weight loss.

Spring suspects that self-tracking makes users more careful with their diets, but only to a point. Perhaps participants maxed out the benefit they could get from seeing their own data, so the app provided no advantage. If the researchers want more clinical im-

Published by AAAS

provements, Spring says, they'll have to add in some other approach.

Other app studies have struggled to reveal any long-term benefits at all. A recent meta-analysis of 14 mobile weight interventions found an average weight loss of only about 1.4 kilograms compared with control groups. And a 2013 review of 21 randomized controlled trials of mobile interventions for obesity, diabetes management, smoking, and other health challenges found that less than half led to improvements in a relevant measure of health.

"Frankly, this is so new that I'm not sure that we know that it works—that it makes a difference," says Arthur Stone, a behavioral scientist at the University of Southern California in Los Angeles, who co-authored the review. In the 1990s, Stone was an early pioneer of real-time health tracking, having developed a method known as "ecological momentary assessment" that encourages participants to log their activity and describe their moods right when they experience them. The goal was to give researchers a more detailed picture of subjects' psychological symptoms. But as smartphones take data gathering to its extreme, he finds himself among the skeptics. "Do we need the incredible density of data that we seem to automatically want to go to?" he wonders. "A lot of times, we're measuring things because we can measure them, and we don't know exactly why we're measuring them."

The new generation of just-in-time interventions faces other hurdles. In a recent feasibility study to learn how smokers would use his Q Sense app, Naughton found that about half the time, users didn't open the app for more than 30 minutes after they received a notification. That means the intervention likely wasn't reaching people at the intended moment.

The question of how and when a phone should interrupt a person has become a field of study in itself. Computer scientist Veljko Pejović at the University of Ljubljana and colleagues have tried to model users' "interruptibility" by gathering their feedback about messages and alerts at various points in the day. So far, his results can't offer a generalizable strategy. "It's very personalized," he says. People may engage with or ignore a message based on their location, the time of day, the kind of activity they're involved in, and whether they're starting or finishing a task.

The MD2K team worries that users won't be able to focus on an alert when they need it most: at times of stress. So in January they'll launch a new study of their system, involving 75 smokers, which will be "micro-randomized." A given user will sometimes receive an alert telling him or her to do a stress management exercise at moments of high stress; at other times, the alert will arrive when stress is deemed low. Combined with records of smoking from wearable sensors, the data might reveal which strategy has the greatest impact.

It may turn out that no one behavior-change strategy will work for everyone. The MD2K team, for example, plans to eventually personalize the timing of alerts for each participant. As apps bring in richer data about each individual user, it's becoming clear that "what predicts behavior in groups doesn't necessarily predict behavior in individuals," Naughton says.

Rosalind Picard, a computer scientist at the Massachusetts Institute of Technology (MIT) in Cambridge, is developing highly personalized interventions that would be sensitive to users' state of mind.

Picard was motivated by a tragedy: In 2013, she learned that a former graduate student had taken his own life. Her team started thinking about how wearable sensors could relieve stress and prevent depression. "It's one thing to study all this," she says. "It's another to build it into a form that people can start changing their lives around." With support from a memorial fund organized by her former student's mother, Picard's lab has begun studying work-related stress and strategies for relieving it.

A first step, published this year, tracks a group of MIT undergrads over 30 days, collecting data from wearable wrist sensors on movement, skin conductivity, and temperature, as well as smartphone records of location, calls, and text messages. The team then related these measurements to self-ratings of stress, health, energy, alertness, and happiness (see graph, p. 1308). Initial insights were far from shocking: Spending extra time outdoors and getting ample, consistent sleep were among the factors predictive of happiness, for example.

But the technology Picard envisions down the road is more elaborate: a system that trains itself to forecast an oncoming anxiety attack or a bout of depression, based on sensor-derived signals that are unique to an individual, and that alerts wearers when they might be in trouble. For example, if a person's sensor and mobile data showed that she was sleeping irregularly or using her phone late at night at times when she felt down, the system might automatically send a reassurance or suggest that she get more sleep.

It remains to be seen whether such a system could be reliable, not to mention how government regulators would view it. "We're kind of where weather forecasting was 150 years ago. People looked at the farmer's almanac, and then the city got wiped out that night by a storm and they didn't see it coming," Picard says. But she thinks the technology is now good enough for researchers to think about predicting human behavior. "It's not as good as weather forecasting yet, but it's better than random." ■

ILLUSTRATION: JOHN HOLCROFT

Published by AAAS

Sharing data by design p. 1312
Vitamin C and cancer p. 1317 ▸

PERSPECTIVES

EVOLUTION

Dissecting diversity in the social brain

Male prairie voles with poor memory skills are less faithful to their partners

By **Gene E. Robinson**

Soon after launching an ambitious 25-year study of the population cycles of rodents in the fields and prairies near the University of Illinois at Urbana–Champaign in 1971, Lowell Getz saw something strange. Adult male and female prairie voles (*Microtus ochrogaster*) often appeared in the same live trap, unlike the meadow vole, whose sexes were more segregated. Moreover, the same pairs were often retrapped months later. Using radio tracking, Getz and his co-workers found that most trapped pairs were long-term partners living together in underground nests and sharing common home ranges (*1*). So began almost 50 years of pathbreaking research into the biology of prairie vole monogamy, in one of fewer than 5% of mammalian species with a monogamous lifestyle (*2*, *3*). On page 1371 of this issue, Okhovat *et al.* (*4*) use the prairie vole model system to investigate individual differences in this social behavior. Differences in social behavior are widely observed but poorly understood in most species.

A hallmark of the prairie vole model is its strong multidisciplinarity, from the field to the lab, and perhaps eventually to the clinic (*3*). Soon after his initial findings, Getz

PHOTO: YVA MOMATIUK & JOHN EASTCOTT/MINDEN PICTURES/NEWSCO

Carl R. Woese Institute for Genomic Biology, Department of Entomology, Neuroscience Program, University of Illinois at Urbana–Champaign, Urbana, IL 61801, USA. E-mail: generobi@illinois.edu

Downloaded from www.sciencemag.org on December 14, 2015

Published by AAAS

teamed up with neurobiologist Sue Carter to show that prairie vole mating in the laboratory results in the kind of robust partner preference that would lead to long-term pair-bonding in nature (*2*). Neurobiologists began to use prairie voles to study the role of the neuropeptide oxytocin in female monogamy (*5*). Focusing on the male prairie vole brain, Insel and Shapiro showed that the distribution of a receptor for the closely related vasopressin, V1aR, differed strikingly from closely related polygynous species, with a hot spot of expression in the ventral pallidum, a part of the basal ganglia known to mediate reward and motivation (*3*). Insel, Young, and their co-workers demonstrated that increased V1aR expression in the ventral pallidum increased partner preference in transgenic voles and mice (*3*).

Okhovat *et al*. now return to the field, blending genomics with ecological and evolutionary analyses made possible by behavioral studies in seminatural enclosures. They take advantage of the fact that prairie voles differ in their degree of monogamy. Some stray from their mate and engage in frequent extra-pair fertilization (EPF); others are more faithful, engaging mostly in intra-pair fertilization (IPF). Phelps and colleagues (*6*) showed earlier that EPF males have lower levels of V1aR expression than IPF males, but with a twist on the original V1aR findings: The lower levels of V1aR expression are not seen in the ventral pallidum but rather in parts of the brain involved in spatial learning, including the retrosplenial cortex.

Phelps and colleagues (*4*) confirm these findings and conclude that they are likely due to differences in the regulation of *avpr1a*, the gene encoding V1aR. They base this conclusion on DNA sequencing of the *avpr1a* region of the prairie vole genome, chromatin immunoprecipitation, bisulfite sequencing, and bioinformatic analysis. In the course of these experiments, the authors discovered four genetically linked single-nucleotide polymorphisms (SNPs) in putative enhancer regions for *avpr1a*, which puts them in the right places to influence *avpr1a* expression. They also found behaviorally related differences in methylation in various parts of the *avpr1a* gene, with enhancer methylation correlated with retrosplenial cortex *avpr1a* expression.

Consistent with best practices in behavioral genetics, the authors replicated the behavior-SNP associations with animals from a different population. Nonetheless, it will be important to further examine the causal relationship between genetic and behavioral variation. Surely CRISPR/Cas9 prairie voles will not be long in coming.

Okhovat *et al*. also use radio-tracking data to show that EPF males have relatively larger home ranges, which overlap with the territories of other males. Are EPF males more amorous, gregarious, or novelty-seeking? We do not know yet, but the authors use their neuroanatomical data to argue for a more prosaic explanation: poor spatial memory.

The idea builds on an earlier suggestion (*7*) that IPF males might remember painfully well the locations of rough encounters with other males and thus stay closer to home, whereas EPF males are less inhibited by unpleasant spatial memories and continue to roam (see the figure). This speculation provided the basis for Okhovat *et al*.'s hypothesis that the well-known behavioral ecological trade-off between siring additional offspring and being cuckolded while out and about op-

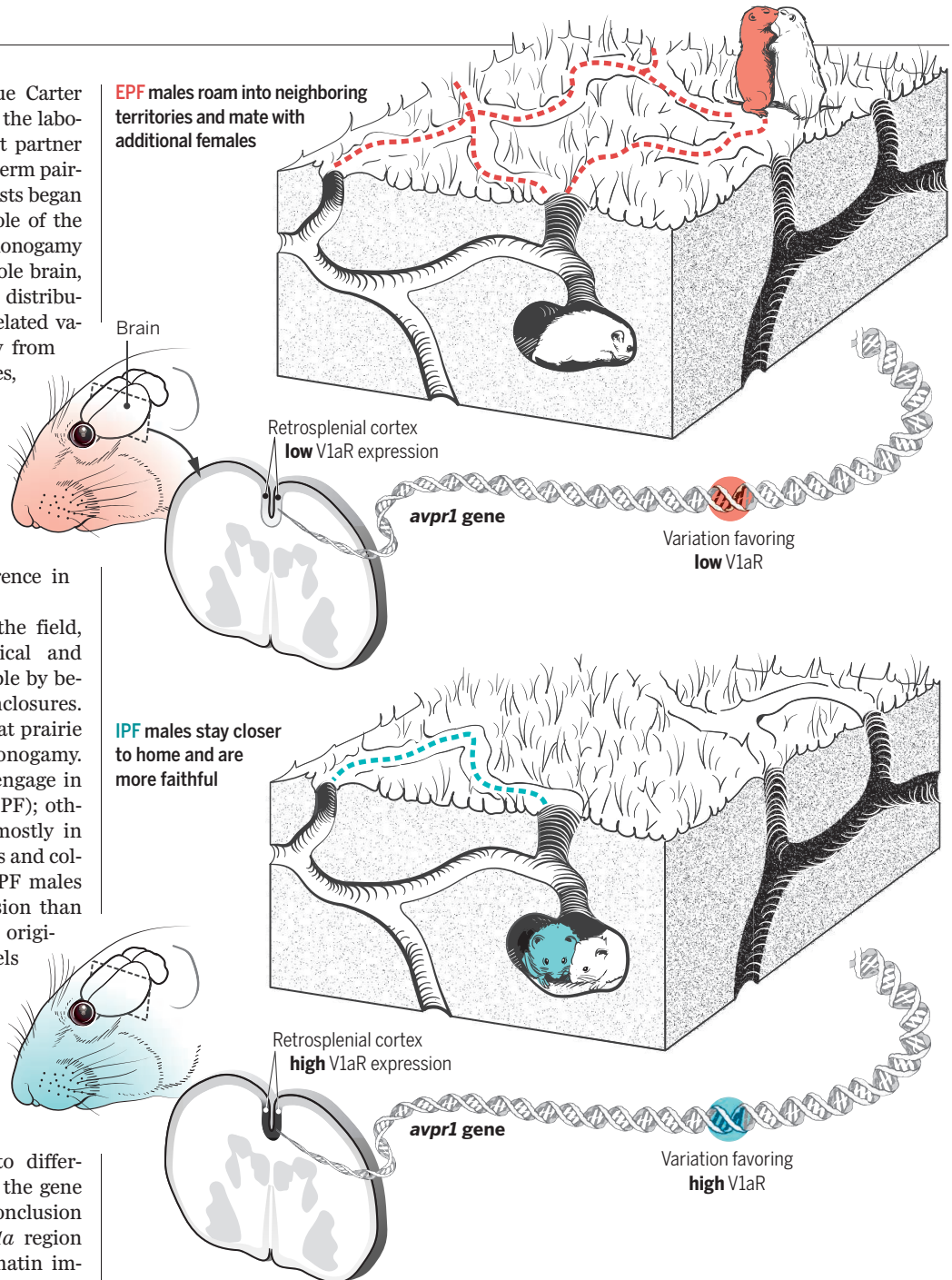

Degrees of faithfulness. Okhovat *et al*. report behavioral, neurobiological, genomic, and evolutionary analyses that explain individual differences in male prairie vole monogamy. They attribute the finding that less faithful (EPF) males range more widely than more faithful (IPF) males to poorer spatial memory skills, which are related to striking differences in the regulation of *avpr1a* and the expression of V1aR in the brain.

ILLUSTRATION: K. SUTLIFF/*SCIENCE*

Published by AAAS

erates for prairie voles. They report a positive correlation between how often a male intrudes on a neighboring male's territory and how often his own territory is intruded upon by another wandering male. An EPF male encounters more females than IPF males and thus more opportunities for mating, but so does his partner back home. This trade-off is etched in the genome, with evidence of balancing selection for the above-mentioned *avpr1a* SNPs, but no such evidence at several other locations in the prairie vole genome.

Okhovat *et al.* propose that high population densities favor genetic variants resulting in lower V1aR expression, poorer spatial memory, and more expansive home ranges to capitalize on enhanced possibilities of extra-pair matings. Low population densities would favor the inverse of these traits. In other words, the evolutionary explanation for the persistence of both EPF and IPF males points to the very same cycles of population density that originally motivated Getz's field studies.

The study by Okhovat *et al.* impressively bridges mechanistic and evolutionary analyses to provide a detailed picture of individual differences in social behavior. Future studies should try to integrate the spatial learning and partner preference narratives for both males and females; the joint evolutionary dynamics of male and female traits must be considered to fully understand a mating system (*8*). With the availability of the prairie vole genome, future analyses also will no doubt include efforts to identify other genes that interact with *avpr1a*, in both mechanistic and evolutionary contexts (*9*). Measuring the effects of changes in population density on gene expression throughout the brain will help us better understand how nature and nurture shape social life (*10*). *M. ochrogaster* has come a long way from the traps on the prairie and clearly has much more to teach us. ■

REFERENCES AND NOTES

1. J. E. Hofmann, L. L. Getz, L. Gavish, *Am. Midland Nat.* **112**, 314 (1984).
2. C. S. Carter, L. L. Getz, *Sci. Am.* **268** (6), 100 (1993).
3. Z. R. Donaldson, L. J. Young, *Science* **322**, 900 (2008).
4. M. Okhovat *et al.*, *Science* **350**, 1371 (2015).
5. D. M. Witt *et al.*, *J. Neuroendocrinol.* **3**, 155 (1991).
6. A. G. Ophir, J. O. Wolff, S. M. Phelps, *Proc. Natl. Acad. Sci. U.S.A.* **105**, 1249 (2008).
7. S. M. Phelps, A. G. Ophir, in *Cognitive Ecology II*, R. Dukas, J. M. Ratcliffe, Eds. (Univ. of Chicago Press, Chicago, 2009), chap. 9.
8. S. Gavrilets, *Proc. Natl. Acad. Sci. U.S.A.* **109**, 9923 (2012).
9. C. C. Rittschof, G. E. Robinson, *Anim. Behav.* **192**, 263 (2014).
10. G. E. Robinson *et al.*, *Science* **322**, 896 (2008).

ACKNOWLEDGMENTS

I thank C. S. Carter, Z. R. Donaldson, L. L. Getz, and T. R. Insel for historical information, C. C. Lutz for comments that improved the manuscript, and M. Lee for expert assistance with the graphics.

10.1126/science.aad8071

DATA ACCESS

Sharing by design: Data and decentralized commons

Overcoming legal and policy obstacles

By **Jorge L. Contreras[1]* and Jerome H. Reichman[2]**

POLICY

Ambitious international data-sharing initiatives have existed for years in fields such as genomics, earth science, and astronomy. But to realize the promise of widespread sharing of scientific data, intellectual property, data privacy, national security, and other legal and policy obstacles must be overcome (*1*). Although these issues have attracted much attention in some circles, they have often taken a back seat to addressing technical challenges. Yet failure to account for legal and policy issues at the outset of a large transborder data-sharing project can lead to undue resource expenditures and data-sharing structures that may offer fewer benefits than hoped. Drawing on our experience with the Belmont Forum, a multinational earth change–research program, we propose a framework to help plan data-sharing arrangements with a focus on early-stage decisions including options for legal interoperability.

> *"Even if resources do not exist ... technically, there are advantages to fostering legal interoperability among distributed repositories."*

A rich literature beginning with the work of Ostrom (*2*) addresses the organization and governance of common pool resources shared by communities of users in contexts ranging from the global environment to communal living spaces. More recent work has expanded these principles to knowledge commons: collections of intangible resources, such as digital libraries, scholarly publications, and scientific data (*3*). Responding to calls for increased international scientific collaboration, several expert bodies have developed high-level principles for transborder data sharing (*4*–*6*). Although these efforts lay the groundwork for broad data-pooling initiatives, critical design decisions must be made before larger issues of governance and operation.

A SPECTRUM OF CENTRALIZATION. Although little empirical research exists on commons structures for data sharing and related costs, we have observed four basic structural models for scientific data pools along a continuum ranging from the most to the least centralized (see the table).

(i) *fully centralized*: all data are aggregated in a single, centrally managed repository;

(ii) *intermediate distributed*: repositories are distributed and separately maintained, but may be interconnected by a central access portal, share technical service components, and utilize a common data-exchange format [sometimes called a federated database system (*7*)];

(iii) *fully distributed*: repositories are maintained locally and are not technically integrated, but share a common legal and policy framework that allows access on uniform terms and conditions (legal interoperability);

(iv) *noncommons*: repositories are largely disaggregated and lack technical and legal interoperability and, at most, may share a common index.

Centralized repositories with curation, analytics, and quality control can enhance the value of the data they contain [e.g., the GenBank repository of DNA and RNA sequence data (*8*)]. Centralized structures, however, come at a cost and may be impractical in many transborder collaborations because of political, legal, and organizational issues. But the alternative to a fully centralized commons need not be a noncommons. The shortfalls of noncommons models include incompatible data formats, inability to search across data sets, underutilization of data resources, individualized and inefficient access requirements, and difficulties moving data across national boundaries. Distributed commons structures, however, offer a meaningful subset of benefits with lower cost and resource commitments than fully centralized models.

For example, an online portal through which researchers can access multiple inde-

[1]*S. J. Quinney College of Law and Department of Human Genetics, University of Utah, Salt Lake City, UT, USA.*
[2]*School of Law, Duke University, Durham, NC, USA.*
**E-mail: jorge.contreras@law.utah.edu*

Published by AAAS

pendent repositories may feel like a centralized commons to users, but avoids the cost and governance overhead of a centralized repository [e.g., the Global Earth Observation System of Systems (GEOSS)]. Portal-based structures may make it easier for a central administrator to provide users with value-added services and aggregated statistics [e.g., the World Data Center for Microorganisms (*9*)], and allow users to more easily query, combine, and analyze multiple data sources (*7*).

Even if resources do not exist to link repositories technically, there are advantages to fostering legal interoperability among distributed repositories (*10*). To achieve this across jurisdictions, rules for data access and usage must be compatible with each other, must comply with laws and regulations of relevant jurisdictions, and must address rights of ownership and control granted to data generators (*11*). Legal interoperability can enable researchers to access and use data across multiple repositories without seeking authorization on a case-by-case basis, which increases the likelihood that more data will be put to productive use.

Perhaps the most straightforward path to legal interoperability is simply to contribute data to the public domain and waive all future rights to control it (*11*). This approach has been advocated by more than 250 organizations that have endorsed the 2010 Panton Principles for open data in science (*12*). Alternatively, researchers who wish to receive attribution credit for their contributions, but are otherwise willing to relinquish control over them, have released data under standardized Creative Commons licenses that have been widely used for other online content, including open-source code software, music, and photographs.

Despite the simplicity and appeal of these approaches, they are not always feasible. Data will often remain subject to legal regulation that, for instance, explicitly or implicitly reveal personally identifiable information, were obtained from human research subjects, relate to sensitive technologies, or disclose infrastructural details. Wilbanks and others, recognizing these requirements, have called for new models of informed consent and privacy protection to facilitate broad, socially beneficial sharing of at least some categories of such data (*13*).

DESIGN CONSIDERATIONS. If a collaborative research project has sufficient resources to create a centralized data repository with accompanying infrastructure and staffing (potentially millions of dollars up-front and thereafter for fully staffed and curated repositories), important benefits can be achieved. In most cases, however, this level of funding will not be available and a distributed data commons could be a desirable alternative. We found, in our experience with the Belmont Forum, that the project's leadership gave substantial weight to early aspirational statements regarding broad data sharing. Sufficient consideration may not have been given to potentially useful distributed data structures. When, at the conclusion of a lengthy planning stage, it became apparent that a centralized commons was beyond budgetary constraints, the decision was made to settle for no commons at all and rely on lofty but nonspecific data-sharing principles to motivate researchers to share data on their own (*14*). To help avoid such dilemmas in the future, we offer the following actionable framework for evaluating distributed data commons early in the project-planning phase:

How many data repositories are under consideration? If the number is small, then fully distributed, unlinked repositories (i.e., no commons) may suffice. Researchers may easily access each repository, and the cost of a commons structure can be avoided.

Are there resources to develop a common data portal? As the number of repositories increases, some form of commons structure will likely facilitate data sharing and usage. Although the cost is not trivial, a common portal can enhance the value and usability of the data. If funding for a data portal is not available, planners may wish to consider a fully distributed commons with legal interoperability.

Structural models for scientific data pools

Data-sharing options

BENEFITS AND COSTS	CENTRALIZED	INTERMEDIATE DISTRIBUTED	FULLY DISTRIBUTED	NONCOMMONS
Incremental research benefits				
Data access	Access to all data in unified manner	Access to multiple repositories through central portal	Access to each repository separately, but under a common usage/access policy and single approval	Ad hoc coordination with other repositories only
Data analytics	Most powerful search, analysis, quality assurance of aggregated data	Cross-repository searching and analytics; Metadata and aggregate statistics can be developed by central authority	Index/catalog only	Index/catalog only
Costs				
Up-front costs	Structure and build centralized repository; Develop data interoperability mechanisms; Develop common usage policy	Develop data interoperability mechanisms; Develop common usage policy	Develop common usage policy	Few up-front costs
Ongoing centralized costs	Operating and maintaining central repository; administering policies	Operating and maintaining portal; administering policies	Administering policies	No central costs
Ongoing distributed costs	Few distributed costs	Operating and maintaining repositories	Operating and maintaining repositories	Operating and maintaining repositories
Governance overhead	Central repository	Central portal/services, each distributed repository, and interrelationships	Each distributed repository and interrelationships	Each distributed repository with minimal coordination

Published by AAAS

Are data regulated in the relevant jurisdictions? This question is relevant no matter which commons structure is selected. If data are not regulated or subject to human-subject, privacy, health, or similar legal regimes, consider releasing data to the public domain or licensing under a common-use license. If data are regulated in one or more relevant jurisdictions, planners should consider engaging legal experts to develop a common data access and use policy that complies with regulations in each jurisdiction. For example, if data include human genetic information, both genetic nondiscrimination laws and data privacy regulations should be considered. Legal interoperability, and the ability for users to access and use all data on consistent terms via a single authorization, will be achieved only if the most stringent jurisdiction's regulations are observed in each case or are otherwise addressed (*13*).

Although the Belmont Forum will doubtless produce a wealth of valuable earth science data, initial appreciation of data-sharing options might have facilitated decision-making and planning among its many national participants and might have resulted in a more robust data-sharing structure. Addressing these design choices early—while acknowledging budgetary, legal, and political constraints—can save planning and implementation costs later.

REFERENCES AND NOTES

1. J. H. Reichman, P. F. Uhlir, *Law Contemp. Probl.* **66**, 315 (2003).
2. E. Ostrom, *Governing the Commons: The Evolution of Institutions for Collective Action* (Cambridge Univ. Press, Cambridge, 1990).
3. B. M. Frischmann, M. J. Madison, K. J. Strandburg, *Governing Knowledge Commons* (Oxford Univ. Press, New York, 2014), chap. 1.
4. Policy RECommendations for Open Access to Research Data in Europe (RECODE), http://recodeproject.eu.
5. International Council for Science, World Data System Strategic Plans 2014–2018 (ICSU, Paris, 2011).
6. B. M. Knoppers *et al.*, *Genome Med.* **3**, 46 (2011).
7. Institute of Medicine, *Sharing Clinical Trial Data: Maximizing Benefits, Minimizing Risk* (National Academies Press, Washington, DC, 2015), chap. 6.
8. J. L. Contreras, *Science* **329**, 393 (2010).
9. J. H. Reichman, P. F. Uhlir, T. Dedeurwaerdere, *Governing Digitally Integrated Genetic Resources, Data, and Literature: Global Intellectual Property Strategies for a Redesigned Microbial Research Commons* (Cambridge Univ. Press, New York, forthcoming 2016), chap. 8.
10. J. Palfrey, U. Gasser, *Interop: The Promise and Perils of Highly Interconnected Systems* (Basic Books, New York, 2012).
11. Group on Earth Observations (GEOSS), "Mechanisms to share data as part of the GEOSS data-core" (White paper, GEOSS, Geneva, 2015); http://bit.ly/GEOSSdata-sharing.
12. P. Murray-Rust, C. Neylon, R. Pollock, J. Wilbanks, "Panton Principles: Principles for open data in science" (2010); http://pantonprinciples.org.
13. J. Wilbanks, in *Privacy, Big Data, and the Pubic Good* (Cambridge Univ. Press, Cambridge, 2014), chap. 11.
14. Belmont Forum Steering Committee, "A place to stand: e-Infrastructures and data management for global change research" (Belmont Forum Secretariat, Paris, 2015).

ACKNOWLEDGMENTS

J.H.R. has received support from the National Human Genome Research Institute (award no. P50HG003391). J.L.C. and J.H.R. served as members of the U.S. delegation to the Belmont Forum organized by NSF.

10.1126/science.aaa7485

PHOTO: PEOPLEIMAGES/ISTOCK PHOTO

SIGNAL PROCESSING

Matched filtering of ultrashort pulses

Optical signal processing can help reduce noise in detection of ultrafast electrical pulses

By **Michael Vasilyev**

The need to detect a small signal obscured by a large amount of noise is like the problem Prince Charming faced in his search for Cinderella. Fortunately, he had the magic glass slipper that perfectly fit only her. In signal detection and estimation theory, such a magic glass slipper that perfectly fits only the signal of interest is called a "matched filter." Because every change in the signal shape requires a change of the matched filter, it would be highly advantageous for the filter to be dynamically reconfigured according to the expected signal. For ultrashort (<100 ps) electrical signals that are near the limits of today's electronics, such reconfigurable matched filters become extremely challenging to make. On page 1343 of this issue, Ataie *et al.* (*1*) show how optical signal processing could help to achieve this goal. They demonstrate the detection of a single 80-ps pulse in the presence of a large amount of noise by converting electrical signals to optical signals and subsequently approximating the matched filter with a potentially reconfigurable optical scheme.

The matched-filter concept arises in the context of optimal detection of a signal $x(t)$ (see the figure, panels A and B) that is possibly scaled in magnitude, shifted in time, and degraded by additive noise (panel C). The optimal receiver correlates its input with the matched filter for a time-shift τ [$x(t - \tau)^*$] producing the correlation function (panel D) with a tall and narrow peak at $\tau = 0$, thereby permitting easy detection. In the frequency domain, this is equivalent to multiplying the received spectrum by the matched filter in the shape of the complex conjugate of the expected signal spectrum. For received signals shifted in time, the matched time-domain filter is shifted accordingly, or the frequency-domain filter is multiplied by a linear phase response. It is well known (*2*) that for a signal degraded by white noise, the matched filter maximizes the signal-to-noise ratio (SNR) in the optimal receiver. Optical receivers with matched filtering have been demonstrated to operate within a fraction of a decibel from the quantum sensitivity limit (*3*) and are being considered for use in future near-Earth and interplanetary laser communication links.

Physically, the use of the matched filter integrates all of the signal's temporal or spectral components in such a way that they add up coherently (they are in phase) to create the peak of the correlation function, whereas the noise's components add incoherently (they have random phases). Thus, the resulting SNR is improved relative to the SNR of the individual components. The matched filter not only recovers the arrival time of the signal, but also compensates for the spectral phase distortions caused by signal propagation (dispersion) in microwave transmission lines and optical fibers, which, if left uncompensated, lead to unwanted pulse broadening (see the figure, panel B) as well as chirping and ringing effects in time domain that further drown the signal in the noise (panel C).

The signal domain can be straightforwardly expanded to two-dimensional images. Here, the linear phase response in

Department of Electrical Engineering, University of Texas, Arlington, TX 76019, USA. E-mail: vasilyev@uta.edu

Published by AAAS

the spatial frequency domain corresponds to image translation, whereas the parabolic phase response represents distortions caused by free-space propagation (diffraction in paraxial approximation). A simple example of a filter with matched phase response that is easily reconfigurable for various signals is the lens of the human eye. It compensates for the parabolic phase shift caused by the free-space image propagation to ensure that different spatial frequency components of the image arrive in phase (in focus) at each pixel of the retina. The eye's lens easily accommodates (reconfigures) for focusing on object planes at various distances, and, if such a distance is beyond the eye's accommodation range, the matched phase filtering can be provided by eyeglasses or a loupe (see the photo).

Another example is a two-dimensional amplitude filter that dramatically facilitates the detection of a word message, as shown in panel E of the figure. This filter is only partially matched because it accepts different letters within each transmission window, and hence can receive different messages. A filter that is 100% matched to a message will have the amplitude windows in the shapes of the specific letters of the message, which maximizes the correlation and SNR when the filter is aligned with the message.

One of the applications most sensitive to the accuracy of the matched-filter shape is the homodyne detection of a quantum state of a particular temporal or spatial mode (*4*). Here, the mode of the homodyne local oscillator, when mixed with the signal, serves as the matched filter, and even small errors in its shape could couple considerable extra noise to the photocurrent. This noise could potentially destroy the detection of quantum states manifesting themselves in fragile photocurrent features with amplitudes below the shot-noise level. Recent extensive efforts have identified the matched-filter shapes for temporally multimode (*5*–*7*) and spatially multimode (*8*–*11*) quantum states produced by various nonlinear processes.

The scheme implemented by Ataie *et al.* nearly noiselessly replicates ultrashort electrical signal in the form of multiple frequency-shifted optical clones. The amplitudes and phases of all frequency components of the signal can be measured simultaneously and independently by relatively slow, narrowband optical homodyne detection of the cloned signals. The local oscillators are supplied by the individual frequency components of a frequency comb. After compensating the linear phase response representing temporal shift, the amplitudes of the signal's frequency components are coherently added together, while noises add incoherently, which improves the SNR. This addition is equivalent to using a partially matched filter with the optimum phase response but with a flat amplitude response.

The approach of Ataie *et al.* builds on recent remarkable advances in optical combs and coherent signal processing technologies, and it offers flexibility that can potentially be used to adaptively synthesize matched filters for extremely short electrical pulses of arbitrary shapes. For example, the demonstrated scheme could be extended to make a 100% matched filter by properly weighing the added amplitudes. Moreover, because the addition is done by a digital signal processor, it can be easily reconfigured to match amplitude and phase profiles of a variety of signals. In particular, it could compensate for a temporal signal shape distortion caused by group-velocity dispersion by performing parabolic rather than linear approximation of the phases of a signal's frequency components. Such an adaptive filter synthesis for processing ultrashort signals is very desirable in many applications, such as determining neutrino velocities by accurately detecting their arrival times (*12*) or hiding and uncovering in the noise a secure signal with a scrambled phase response [steganography (*13*)]. ■

REFERENCES

1. V. Ataie *et al.*, *Science* **350**, 1343 (2015).
2. A. Papoulis, S. U. Pillai, *Probability, Random Variables, and Stochastic Processes* (McGraw-Hill, New York, ed. 4, 2002).
3. D. O. Caplan, *J. Opt. Fiber Commun. Res.* **4**, 225 (2007).
4. J. H. Shapiro, A. Shakeel, *J. Opt. Soc. Am. B* **14**, 232 (1997).
5. W. Wasilewski *et al.*, *Phys. Rev. A* **73**, 063819 (2006).
6. C. J. McKinstrie, *Opt. Commun.* **282**, 583 (2009).
7. G. Patera *et al.*, *Eur. Phys. J. D* **56**, 123 (2010).
8. B. Chalopin *et al.*, *Opt. Express* **19**, 4405 (2011).
9. M. Annamalai *et al.*, *Opt. Express* **19**, 26710 (2011).
10. M. Annamalai *et al.*, *Opt. Express* **21**, 28134 (2013).
11. A. R. Bhagwat *et al.*, *Opt. Lett.* **38**, 2858 (2013).
12. N. Yu. Agafonova *et al.*, *Phys. Rev. Lett.* **109**, 070801 (2012).
13. B. B. Wu, E. E. Narimanov, *Opt. Express* **14**, 3738 (2006).

10.1126/science.aad7804

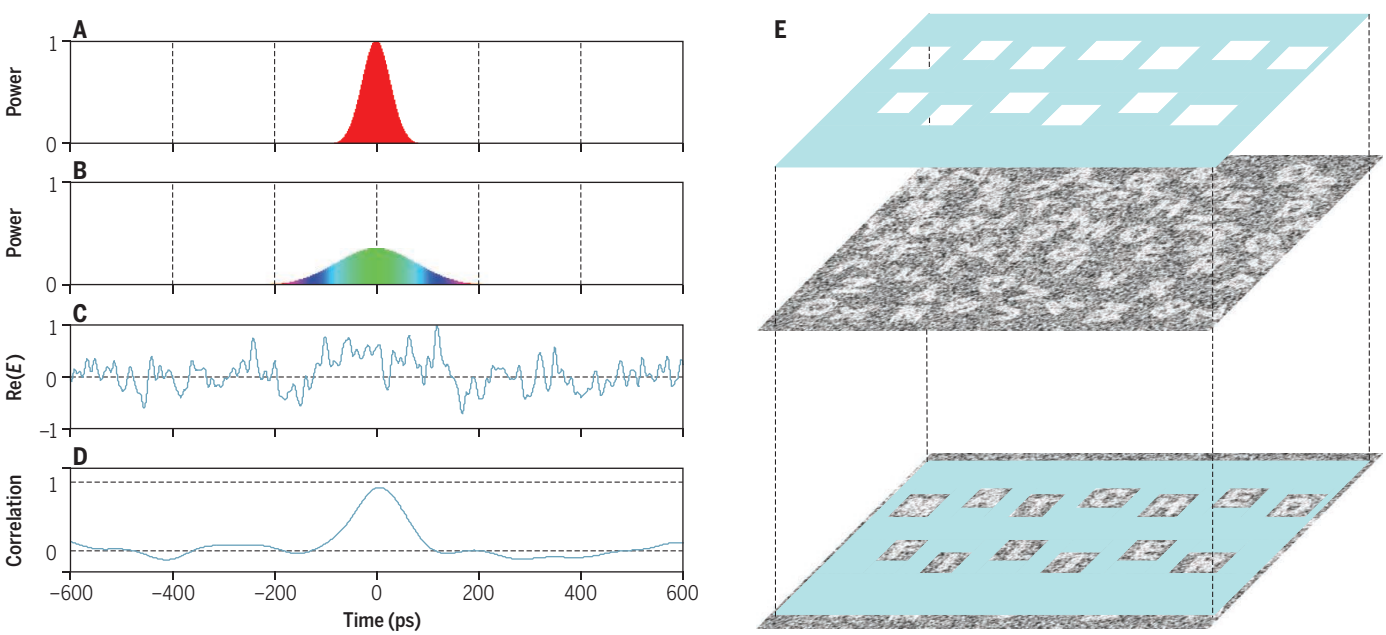

ILLUSTRATION: P. HUEY/*SCIENCE*

Matched filtering in the temporal and spatial domains. (**A**) A transform-limited (as short as possible for its bandwidth) pulse (red) and (**B**) the same pulse broadened by dispersion (colors represent phases). (**C**) The measured real part of the latter pulse's electric field Re(*E*) can be easily lost in the noise. However, correlation (**D**) of such a noisy dispersed pulse with a time-shifted matched filter $x(t-\tau)^*$ creates a readily detected peak at $\tau = 0$. (**E**) A message is hidden under clutter and noise but can be easily read by using a (partially) matched amplitude filter.

Published by AAAS

PHYSICS

Opening the gate on superconductivity

Superconducting two-dimensional materials are found to be remarkably robust

By **Hermann J. Suderow**

The deleterious effect of the magnetic field on superconductivity has plagued researchers and engineers alike for more than a century (*1*). Quantized vortices appear in most superconductors when applying a magnetic field and move under a current, creating dissipation that destroys the superconducting state. By pinning their motion through complex materials engineering, powerful magnets can be built for use in resonance imaging for medicine or to levitate trains. However, the magnetic field also perturbs superconductivity through the electron's magnetic property (known as spin). Superconductivity requires electrons to form Cooper pairs, in which the spins point oppositely to form a singlet state. Lu *et al.* (*2*) on page 1353 of this issue and another recent study (*3*) show that two-dimensional (2D) superconductors such as MoS_2 can circumvent the negative effects of the magnetic field on Cooper pairs' spin. To induce superconductivity in MoS_2, a transistor with two gates was used—a solid-state gate and a liquid gate—where moving ions generate a highly inhomogeneous electric field on top of thin MoS_2 flakes. The resulting superconductor is extremely thin, just one MoS_2 layer thick, and is remarkably robust to parallel magnetic fields. Although there are other thin superconductors robust to parallel magnetic fields, the mechanism providing insensitivity to the magnetic field is a new advance.

Monolayers of the material MoS_2 are of broad interest. For example, they are direct band-gap semiconductors, whose gap magnitude lies in the visible optical range (*4*). Conduction and valence bands are located at the corners of the Brillouin zone in two inequivalent sites K and K′ (red and blue semicircles) (see the figure, panel B). This band structure is very similar to that of graphene, but there is an important difference—the heavy Mo atoms provide strong spin-orbit coupling (*5*). This, together with the absence of in-plane inversion symmetry in single layers of MoS_2 (see the figure, panel A), provides strong coupling between the spins of electrons lying at K and K′ sites (*6*). The splitting of the bands for each spin polarization is inverted at the two sites. Because of the splitting, the spins of electrons having the same energy and opposite momenta are oriented in opposite directions. This behavior mimics the spin and momentum structure of a singlet Cooper pair (two electrons with opposite momenta and spin). By gating the split bands of the semiconductor to the Fermi level, Cooper pairs form, and the relative orientation of their spin and momenta is fixed by the coupling between electrons among K and K′ sites enforced by the band structure. Because the splitting between the bands of opposite spin polarity is so large, the spins of the Cooper pairs remain effectively protected from external magnetic fields.

The effects of the magnetic field on the Cooper pairs' spin (*7*) have remained notoriously difficult to control experimentally. It is thus of little surprise that many scientists active in superconductivity tend to think of vortices when discussing a superconductor in a magnetic field. This can lead to strange situations when meeting experts in magnetism, who often have in mind that magnetic fields act mainly on electrons' spin. I encountered such an expert when I was trying to convince a selection panel during a job interview a few years ago about the importance of vortices. The expert stopped me and said that there was no point in discussing vortices to explain the effect on superconductivity in the magnetic field. He argued that the energy of the electrons shifted depending on the orientation of their spin relative to the magnetic field. Thus, one could only maintain a singlet Cooper pair if the energy shift is smaller than the superconducting gap. Fortunately, I was able to convince the panel that vorti-

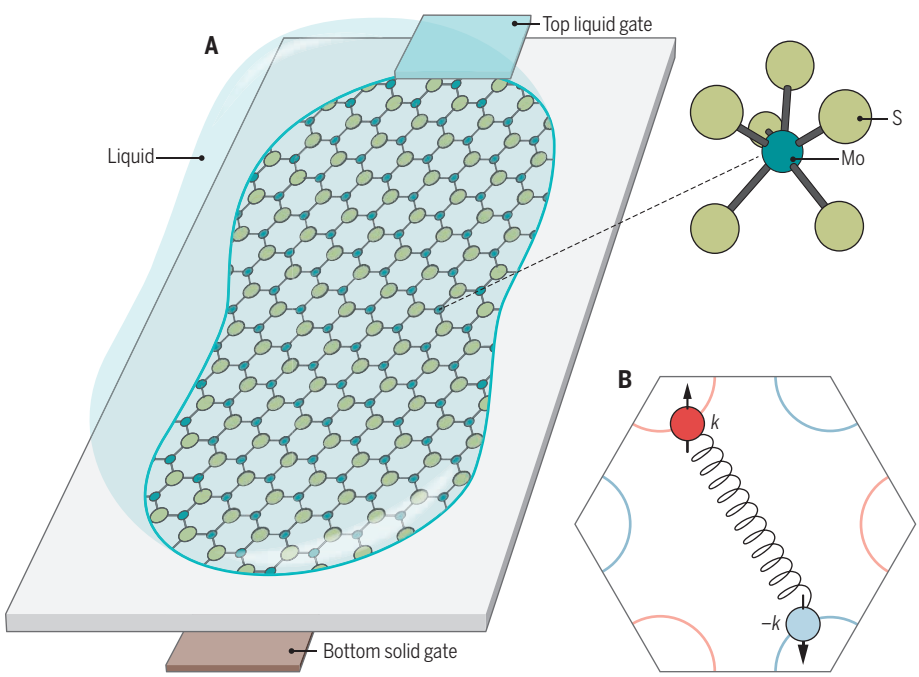

Ready to switch on. (**A**) Thin semiconducting MoS_2 is gated from below with a solid-state gate and from above with a liquid gate. By controlling the gate voltages, a 2D superconductor is formed in which Mo (dark green) and S (light green) atoms comprise a structure with no in-plane inversion symmetry. (**B**) The Cooper pair electrons are represented by colored spheres and their spin by perpendicular arrows. Cooper pairs form with opposite momenta (k and $-k$). The black hexagon represents the first Brillouin zone. The Fermi surface consists of pockets at the edges (blue and red semicircles). Spin-orbit coupling and lack of inversion symmetry conspire to fix the spin of each electron to their momentum's direction.

ILLUSTRATION: P. HUEY/*SCIENCE*

Laboratorio de Bajas Temperaturas, Departamento de Física de la Materia Condensada, Instituto Nicolás Cabrera, Center for Condensed Matter Physics (IFIMAC), Unidad Asociada CSIC, Universidad Autónoma de Madrid, Spain. E-mail: hermann.suderow@uam.es

Downloaded from www.sciencemag.org on December 14, 2015

Published by AAAS

ces are important, and that was enough to get the job. However, the insights presented by the experiments of Lu *et al.* show that the expert was partly right.

Admittedly, there have been many demonstrations of the connection between magnetism and superconductivity, in particular when superconductors containing a magnetic element were found: for instance, in the rare-earth nickel borocarbides (*8*), in ferromagnetic superconductors (*9*), or in the recent Fe-based materials (*10*). In these cases, time-inversion symmetry is broken in some form, particularly in the ferromagnetic superconductors, where triplet Cooper pairs are required (with spins of the same orientation). However, the spin locking in MoS_2 preserves time-reversal symmetry. The same occurs in systems with so-called Rashba spin-orbit coupling. Such coupling arises in the absence of inversion symmetry and in materials with heavy elements and again locks electron's spin and momenta. It is related to the electric-field gradient leading to spin-orbit coupling. The "fictitious" magnetic field generated by Rashba spin-orbit coupling is oriented in the plane of the Cooper pair electrons' momentum. This can eventually favor mixtures of singlet and triplet Cooper pairs (*11*). Estimates for the size of this effect, however, provide very small values for MoS_2 (*2, 3*). By contrast, the effect discussed in MoS_2 is a direct consequence of the inequivalence of K and K′ sites on the Fermi surface.

Monolayers of the related material $NbSe_2$, another transition-metal dichalcogenide, show similar behavior (*12*). Yet another recent work discovers amazing properties of 2D vortices in ionic gate-induced superconductivity in ZrNCl (*13*). It seems that a gate is being opened, likely showing beautiful vistas of superconductivity through a looking glass, where the crystal lattice is trump. ■

REFERENCES AND NOTES

1. D. van Delft, P. Kes, *Phys. Today* **63**, 38 (2010).
2. J. M. Lu *et al.*, *Science* **350**, 1353 (2015).
3. Y. Saito *et al.*, http://arxiv.org/abs/1506.04146 (2015).
4. K. F. Mak *et al.*, *Phys. Rev. Lett.* **105**, 136805 (2010).
5. D. Xiao *et al.*, *Phys. Rev. Lett.* **108**, 196802 (2012).
6. R. Roldán *et al.*, *Phys. Rev. B* **88**, 054515 (2013).
7. A. I. Buzdin, *Rev. Mod. Phys.* **77**, 935 (2005).
8. P.C. Canfield *et al.*, *Phys. Today* **51**, 40 (1998).
9. D. Aoki, J. Flouquet, *J. Phys. Soc. Jap.* **81**, 011003 (2011).
10. A. Chubukov, P. J. Hirschfeld, *Phys. Today* **68**, 46 (2015).
11. E. Bauer, M. Sigrist, Eds., *Non-Centrosymmetric Superconductors*, Lecture Notes in Physics 847 (Springer, Berlin, 2012).
12. X. Xi *et al.*, *Nat. Phys.* 10.1038/nphys3538 (2015).
13. Y. Saito *et al.*, *Science* **350**, 409 (2015)

ACKNOWLEDGMENTS

Supported by Mineco (FIS2014-54498-R) and Region of Madrid (S2013/MIT-2850).

10.1126/science.aad7086

CANCER

Revisiting vitamin C and cancer

A high dose of vitamin C kills certain colon cancer cells

By **Colleen R. Reczek** *and* **Navdeep S. Chandel**

In the early 1970s, the two-time Nobel Prize–winning chemist Linus Pauling proposed that high doses of vitamin C (ascorbic acid) can act as an antioxidant to reduce cancer. Pauling and his colleague Ewan Cameron reported that cancer patients given intravenous vitamin C (10 g/day) followed by oral delivery had an increased rate of survival (*1*). This led to two large clinical trials carried out by the Mayo Clinic in the late 1970s and mid-1980s (*2, 3*), which demonstrated that oral administration of a high dose of vitamin C had no efficacy as a cancer therapeutic. Furthermore, dietary antioxidants have failed as anticancer agents in clinical trials (*4*). However, on page 1391 in this issue, Yun *et al.* (*5*) show that high doses of vitamin C selectively kill colorectal cancer cells carrying activating mutations in the oncogenes *KRAS* or *BRAF*, which are often refractory to approved targeted therapies.

"...the study...provides a mechanistic rationale for how vitamin C selectively kills...cancer cells."

Vitamin C is taken up by cells through sodium-dependent vitamin C transporters, whereas the oxidized form of vitamin C, dehydroascorbate (DHA), moves into cells via glucose transporters such as GLUT1 (*5, 6*). Once inside the cell, DHA is reduced back to vitamin C by glutathione (GSH), which consequently becomes oxidized glutathione (GSSG). Subsequently, GSSG is converted back to GSH by reduced nicotinamide adenine dinucleotide phosphate (NADPH) (see the figure). High doses of vitamin C can increase the amount of reactive oxygen species (ROS) in cancer cells and exert antitumorigenic activity (*7*). However, the molecular mechanisms by which vitamin C inhibits tumorigenesis remained unknown.

Yun *et al.* observed that vitamin C was oxidized to DHA in cell culture media lacking reducing agents, and was subsequently imported into human colon cancer cells harboring oncogenic *KRAS* or *BRAF* mutations by GLUT1. Moreover, the authors showed that high doses of vitamin C that resulted in a peak plasma concentration of 30 mM when administered intraperitoneally reduced the intestinal tumor burden in mice bearing conditional oncogenic activating forms of *Kras* and *adenomatous polyposis coli* (*Apc*) mutations, but not in mice with the conditional *Apc* mutation alone. Tumors from the double conditional *Kras* and *Apc* mutant mice expressed more GLUT1 than tumors from mice harboring only the *Apc* mutation. Furthermore, the pan-antioxidant *N*-acetylcysteine prevented the vitamin C–mediated decrease in tumor burden, indicating that elevated ROS amounts due to vitamin C were responsible for reducing tumorigenesis in vivo.

Yun *et al.* report that the increased uptake of DHA into the *KRAS* or *BRAF* mutant cancer cells, which express more GLUT1 compared to normal cells, leads to the rapid conversion of DHA to vitamin C, resulting in the depletion of GSH and NADPH and an increase in ROS. Metabolite analysis revealed an increase in glucose carbons into the oxidative pentose phosphate pathway, a major cytosolic mechanism to generate NADPH. Indeed, increases in ROS have been shown to activate the oxidative pentose phosphate pathway within minutes (*8*). Additionally, metabolite analysis revealed an increase in glycolytic intermediates such as glyceraldehyde-3-phosphate (G3P) upstream of glyceraldehyde 3-phosphate dehydrogenase (GAPDH). Concomitantly, Yun *et al.* observed a decrease in metabolites downstream of the GAPDH reaction, suggesting GAPDH inhibition by ROS as a result of the increased DHA flux into *KRAS* or *BRAF* mutant colon cancer cells. GAPDH is a redox-sensitive protein, as its active-site cysteine residue can be targeted by ROS. Inhibition of GAPDH decreases the generation of glycolytic adenosine 5′-triphosphate (ATP) and pyruvate, a major substrate required to drive ATP production in the mitochondria. However, pyruvate supplementation can rescue the cell death and energetic

Department of Medicine and Robert H. Lurie Cancer Center, Feinberg School of Medicine, Northwestern University, Chicago, IL 60611, USA. E-mail: nav@northwestern.edu

Published by AAAS

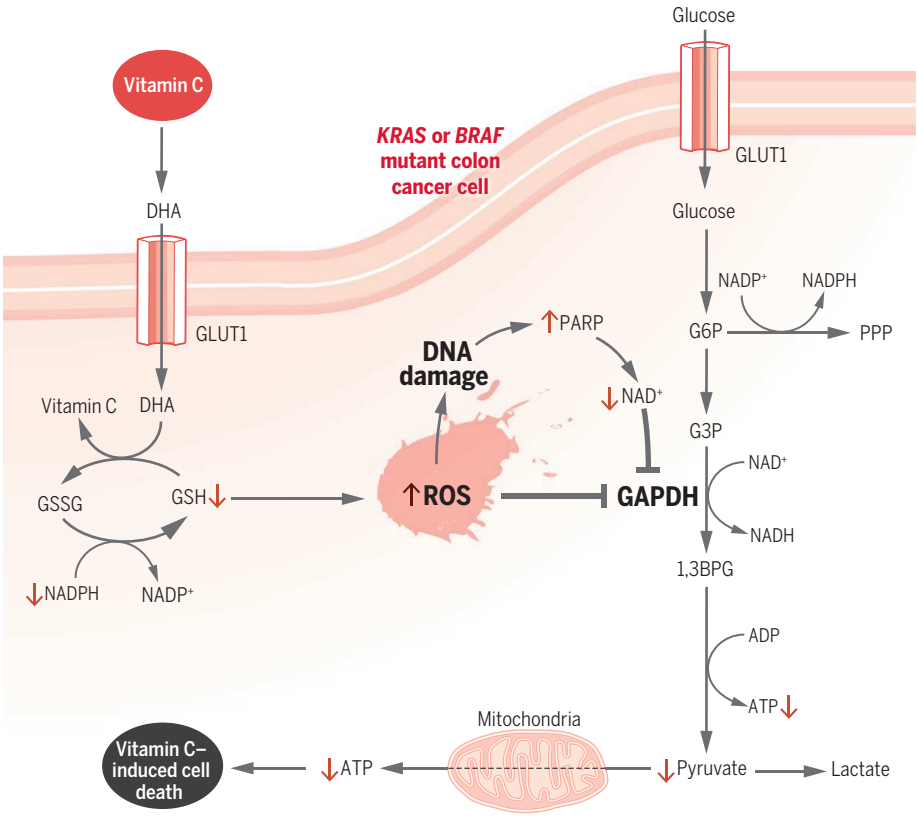

Vitamin C and cell metabolism. The uptake of vitamin C by *KRAS* and *BRAF* mutant colon cancer cells is shown. The resulting increase in ROS production blocks glucose metabolism (in addition to other effects shown). Cells shift their glycolytic flux into the pentose phosphate pathway (PPP), but ultimately, the cells become depleted of ATP, inducing an energetic crisis that leads to cell death.

crisis caused by GAPDH inhibition. Thus, these results suggest that high doses of vitamin C impair glycolysis and could be combined with the antidiabetic drug metformin, which can also diminish tumor burden by inhibiting mitochondrial complex I (*9*).

In addition to oxidizing GAPDH, the elevated ROS amounts induced by vitamin C cause DNA damage, resulting in poly(ADP-ribose) polymerase (PARP) activation and NAD^+ consumption. Notably, the GAPDH enzymatic reaction utilizes NAD^+ to convert G3P to 1,3-bisphosphoglycerate (1,3BPG). Therefore, the decrease in NAD^+ due to PARP activation further diminishes the GAPDH reaction. Inhibition of PARP or administration of nicotinamide mononucleotide, a precursor of NAD^+ synthesis, partially rescued cell viability after vitamin C treatment in vitro. Collectively, these findings suggest that in *KRAS* and *BRAF* mutant cells, vitamin C–induced endogenous ROS inhibits the GAPDH reaction directly (oxidizing GAPDH) as well as indirectly (reducing the NAD^+ pool), leading to an energetic crisis that triggers cell death.

High GLUT1 expression alone, however, does not make a cell more susceptible to vitamin C cytotoxicity. Wild-type *KRAS* and *BRAF* colon cancer cells overexpressing GLUT1 were resistant to vitamin C–induced cell death, implying that oncogenic *KRAS*- or *BRAF*-induced metabolic reprogramming, in addition to high GLUT1 expression, is needed for toxicity. One metabolic liability of oncogenic *KRAS*-driven tumors is their increased rate of mitochondrial and cytosolic NADPH oxidase–generated ROS compared to wild-type cells, which initiate localized signaling pathways necessary for tumor cell proliferation and tumorigenesis (*10*). Consequently, these cancer cells increase their antioxidant defense system by up-regulating the expression of the transcription factor nuclear factor (erythroid-derived 2) related factor-2 (NRF2) to buffer the accumulation of ROS and prevent damage (*4*). The impairment of NRF2 or disabling antioxidant proteins in oncogenic *KRAS*-driven cancer cells would allow for excessive amounts of ROS to accumulate and incur cell death, resulting in reduced tumor growth (*11, 12*). The results by Yun *et al.* are consistent with previous findings that increasing endogenous ROS with high doses of vitamin C reduces the tumor growth of oncogenic *KRAS*-driven pancreatic cancer cells (*13*). Thus, tumors that exhibit a high rate of ROS generation coupled with increased GLUT1 expression are likely to benefit from treatment with a high dose of vitamin C.

An important difference between the study by Yun *et al.* and many previous studies is the mode of vitamin C delivery. Oral ingestion of high concentrations of vitamin C, 100 times the recommended dietary allowance, rarely exceeds a plasma concentration greater than 200 μM due to limited absorption and renal excretion. By contrast, vitamin C administered intravenously can reach a plasma concentration of up to 10 mM and is safe in humans. Yun *et al.* injected vitamin C intraperitoneally in mice that reached millimolar concentrations in the plasma. A recent pilot phase IIa clinical trial using intravenous administration of vitamin C in conjunction with conventional paclitaxel-carboplatin therapy demonstrated a benefit in a small number of patients (*14*). Furthermore, metastatic tumor cells can survive the hostile oxidizing environment of the blood by increasing their antioxidant defenses (*15*). Thus, infusion of vitamin C may be an effective therapeutic strategy to induce the cell death of circulating metastatic tumor cells.

One drawback of intravenous administration of vitamin C is that patients will have to visit the clinic for vitamin C infusions daily for months. However, the development of a new oral formulation of vitamin C that can achieve high plasma concentrations may circumvent this concern. Nevertheless, the study by Yun *et al.* provides a mechanistic rationale for how vitamin C selectively kills *KRAS* and *BRAF* mutant colorectal cancer cells. These findings warrant high-dose vitamin C clinical trials with selectivity for patients with a high GLUT1 expression combined with *KRAS* or *BRAF* oncogene–induced metabolic reprogramming. After all these years, it seems that Pauling may have been correct on the use of high doses of vitamin C for cancer therapy but for the wrong reasons—not as an antioxidant, but as a pro-oxidant anticancer agent. ■

REFERENCES

1. E. Cameron, L. Pauling, *Proc. Natl. Acad. Sci. U.S.A.* **73**, 3685 (1976).
2. C. G. Moertel *et al.*, *N. Engl. J. Med.* **312**, 137 (1985).
3. E. T. Creagan *et al.*, *N. Engl. J. Med.* **301**, 687 (1979).
4. N. S. Chandel, D. A. Tuveson, *N. Engl. J. Med.* **371**, 177 (2014).
5. J. Yun *et al.*, *Science* **350**, 1391 (2015).
6. W. Tian *et al.*, *J. Biol. Chem.* **289**, 3339 (2014).
7. Q. Chen *et al.*, *Proc. Natl. Acad. Sci. U.S.A.* **105**, 11105 (2008).
8. A. Kuehne *et al.*, *Mol. Cell* **59**, 359 (2015).
9. W. W. Wheaton *et al.*, *eLife* **3**, e02242 (2014).
10. F. Weinberg *et al.*, *Proc. Natl. Acad. Sci. U.S.A.* **107**, 8788 (2010).
11. G. M. DeNicola *et al.*, *Nature* **475**, 106 (2011).
12. A. Glasauer, L. A. Sena, L. P. Diebold, A. P. Mazar, N. S. Chandel, J. Clin. *Invest.* **124**, 117 (2014).
13. M. G. Espey *et al.*, *Free Radic. Biol. Med.* **50**, 1610 (2011).
14. Y. Ma *et al.*, *Sci. Transl. Med.* **6**, 222ra18 (2014).
15. E. Piskounova *et al.*, *Nature* **527**, 186 (2015).

10.1126/science.aad8671

ILLUSTRATION: K. SUTLIFF/*SCIENCE*

Published by AAAS

STEM CELLS

What is an adult stem cell?

Tissues may use diverse mechanisms to replace lost cells

By **Hans Clevers**

The paradigm of the hematopoietic stem cell (HSC) has become deeply engrained in our minds, ever since bone marrow transplantation technology narrowed in on this almost magical multipotent entity that gives rise to all blood cells. The HSC's ability to "self-renew" as well as to proceed down hierarchical differentiation pathways involves a rigidly choreographed flow of events. The HSC paradigm currently serves as a template to interpret experimental observations on any other mammalian tissue. Yet, it is not obvious why evolution would have come up with the very same solution for the renewal of all tissues. Attempts to fit observations on solid tissues into the HSC hierarchy mold have led to confusing theories, terminologies, experimental approaches, and heated debates, many of which remain unresolved. Organs differ in size, architecture, and function, and are subject to markedly different biological and physical challenges. It therefore appears plausible that tissues, with their different regenerative demands, have evolved different ways to restore cell numbers.

After the atomic bombing of Hiroshima, experiments in irradiated mice established that bone marrow transplantation protected against the drop in the number of white blood cells. Therapeutic bone marrow transplantation technology allowed scientists to reduce a qualitative phenomenon—the rescue of blood cell production by foreign bone marrow—to the properties of a physical entity, the HSC. Development of a surrogate, quantitative assay for HSCs in vivo (the spleen focus-forming assay) was followed by various in vitro assays for clonogenic HSCs and lineage-restricted progenitors. All of this has led to a consensus on the defining characteristics of HSCs and the differentiation hierarchy it fuels.

The HSC is rare and it divides infrequently (it is "quiescent"), as DNA replication carries the risk of mutation. HSC division occurs asymmetrically, yielding one actively dividing daughter progenitor and a new, quiescent stem cell. The HSC has the unique, defining capacity to self-renew and is therefore long-lived. Dividing progenitors migrate down the hierarchy to become progressively lineage-restricted, eventually yielding the various mature blood cells. Thus, cells flow unidirectionally through the system, away from the HSC. These insights were obtained decades before tissue-renewal in other mammalian tissues could be studied. What have we learned since?

Department of Developmental Biology and Stem Cell Research, Hubrecht Institute and University Medical Center, Netherlands. E-mail: h.clevers@hubrecht.eu

DISTRIBUTED STEM CELL FUNCTION. The development of cell culture technologies in the 1970s allowed extensive expansion of proliferative epidermal cells into large sheets. As autologous transplants, these sheets have saved the lives of many burn patients, a dramatic demonstration of stem cell potential. Yet to date, the identity of the epidermal stem cell has remained controversial. It gives rise to a single cell type—the keratinocyte—which disqualifies it as stem cell, as it is not multipotent. But behind this semantic issue, a deeper problem exists.

> ***"...the search for stem cells as a physical entity may need to be replaced by the search for stem cell function..."***

It has remained impossible to pinpoint a rare, quiescent stem cell, hidden between the abundance of proliferative progenitors that constitute the epidermal stratum basale. Indeed, random labeling of these proliferative cells yields epidermal clones of constantly changing shapes and sizes, which can persist lifelong (*1*).

Similar situations occur in the esophagus (*2*), intestinal crypts (*3*), stomach glands (*4*) and the testis (*5*). These tissues harbor large populations of proliferating stemlike cells of equal potency, each intrinsically capable of generating a long-lived lineage of cellular offspring. These constantly proliferating stem cells compete for niche space. Chance decides which cell will persist long-term; all others will eventually disappear. These active stem cells do not fit the defining characteristics of the HSC: They are abundant (not rare), cycling (not quiescent), mostly divide symmetrically (not asymmetrically), and their life span is not predetermined but subject to stochastic events. Thus, while these tissues harbor an explicit tissue-renewal function, this function is distributed over a large cell population. At the single-cell level, there exists no rare, hardwired stem cell with the prototypic stem cell characteristics.

QUIESCENCE. This state of nonproliferation, experimentally defined by the ability to retain chemical DNA labels, is widely used as a defining stem cell characteristic. Yet, the overwhelming majority of our cells are nondividing, rendering quiescence a rather nondiscriminatory parameter. Furthermore, it appears somewhat counterintuitive that cells whose only raison d'être is the generation of daughter cells, would rarely divide.

Good examples of quiescent stem cells do exist. The first stem cell to be defined in the hair follicle bulge is quiescent (*6*). Striated muscle contains the poster child of quiescence, the satellite cell (*7*). Healthy muscle fibers are large, long-lived, nonproliferative syncytia. Closely apposed to these fibers are small, nondividing cells barely larger than a nucleus. These satellite cells lay dormant for years, called into action only upon muscle damage. By asymmetric cell division, the satellite cell renews itself while also creating its offspring, the contractile muscle fiber.

In the intestinal crypt, the continuously proliferating Lgr5 stem cells (see the figure) are located at the base, while a "reserve" quiescent stem cell resides at position +4 counted from the crypt base (*3*). In one view, these cells occupy the apex of the hierarchy, giving rise to the proliferative Lgr5 cells. Recent genetic tracing studies have unveiled an alternative mechanism: +4 cells represent daughters that have exited the cell cycle to terminally differentiate into secretory cells (*8, 9*). Acute loss of the Lgr5 stem cells can coax +4 cells to settle at the crypt base and reacquire a multipotent Lgr5 stem cell phenotype. Individually, these quiescent +4 cells are short-lived as they will differentiate and die. But as a population, these transiting cells serve as a reserve stem cell pool by violating the rule that the flow through a stem cell hierarchy should be unidirectional.

PLASTICITY. The +4 secretory precursor may be said to exhibit plasticity. Similar observations have been made in other tissues. Thus, luminal secretory cells of the airway epithelium revert to a multipotent stem cell state when the pool of basal stem cells is lost (*10*). Terminally differentiated, pepsinogen-producing chief cells located at the stomach

Downloaded from www.sciencemag.org on December 14, 2015

Published by AAAS

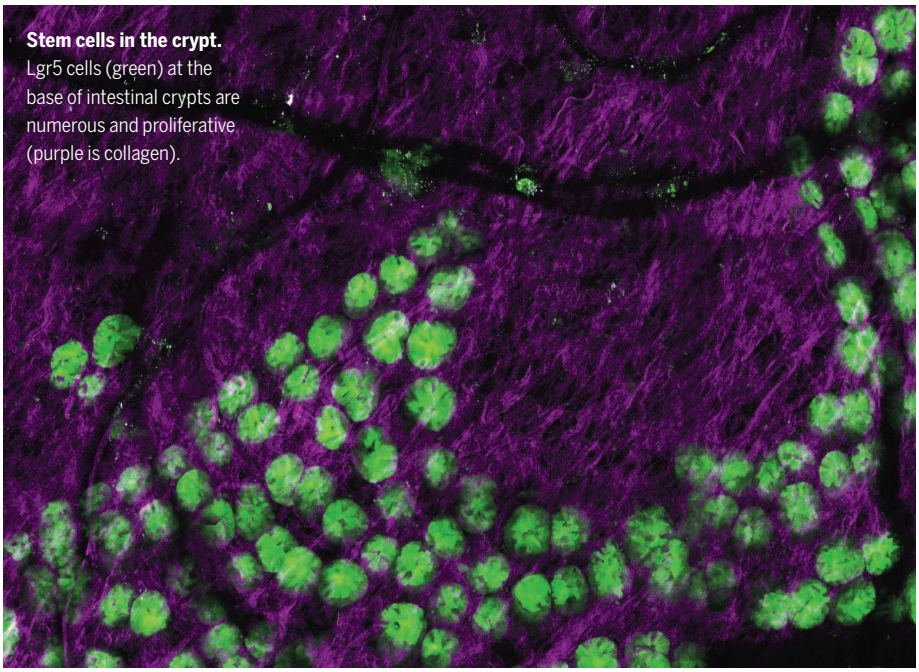

Stem cells in the crypt. Lgr5 cells (green) at the base of intestinal crypts are numerous and proliferative (purple is collagen).

gland base revert at an inconspicuously slow rate to a multipotent stem cell fate, a process that strongly accelerates upon loss of the proliferative stem cell pool (*11*). In these examples, "quiescent" cells play a crucial role in tissue renewal upon damage. In their unperturbed state, however, these cells have ceased to divide while differentiating, not because they are stem cells.

COEXISTING STEM CELL TYPES. The adult hair follicle is home to a host of stem cell types, each in its distinct location (*6*). During hair follicle maintenance, these stem cells only produce the specialized cell types required at their specific location. But upon damage, they reveal a remarkable level of plasticity by generating almost any component of the epidermis. Two classic studies on mammary stem cells have followed the HSC paradigm. Transplantation of single sorted mammary epithelial cells into their niche, the fat pad, have identified rare cells that, on their own, build a complete, functional mammary gland, consisting of the two main layers: the basal (or myoepithelial) layer and the luminal layer (*12, 13*). Although studies using genetic marking in vivo have confirmed the presence of such multipotent stem cells [e.g. (*14, 15*)], another study has demonstrated that the basal and luminal lineages are maintained by independent stem cells (*16*). A similarly confusing situation exists in the prostate stem cell field, where multipotent stem cells have alternatively been reported to reside in the basal or in the luminal layer, while a recent study indicates that basal and luminal lineages are maintained over the long term by independent stem cells (*17*). None of these observations agree easily with a classically designed stem cell hierarchy.

RENEWAL BY DIFFERENTIATED CELLS. The liver is the "champion" of mammalian tissue regeneration. Upon hemihepatectomy, hepatocytes in the remaining liver enter the cell division cycle without dedifferentiation. Within weeks, original liver mass and function are restored, upon which all cells return to their nonproliferative state. Few would use the term "self-renewal" for the rapid replacement of surgically removed hepatocytes by remaining hepatocytes (*18*). An alternative, more mundane mechanism of liver repair becomes active when noxious agents (such as toxins or viruses) simultaneously affect the health of all hepatocytes. Under these circumstances of global damage, cells from the bile duct tree revert to a bipotent stem cell state ("oval cells") capable of regenerating hepatocytes and biliary cells (*18*). Great efforts have been made to identify "professional" stem cells—cells with no other function—in the liver, but it may well be that the healthy liver does not contain such stem cells and that it relies entirely on the proliferative capacity of the two differentiated cell types. Similar considerations may apply to other internal organs that exhibit little proliferative activity in the healthy state, such as the pancreas or the kidney.

HOW TO DEFINE STEM CELL FUNCTION? Central to the HSC paradigm is the concept that the maintenance and restoration of blood cell numbers are exclusively executed (and can be exclusively transferred) by a discrete, rare, physical entity, the HSC. The success and the esthetic appeal of the HSC paradigm have been overwhelming. Subsequent studies in other tissues have almost inescapably been devoted to discovering an HSC equivalent. Discussions over the general applicability of the HSC paradigm as a stereotypic template have essentially not occurred. The examples given here present some of the best-studied models of mammalian tissue renewal. None of these match easily to the HSC paradigm. Rather, with some notable exceptions such as the muscle satellite cell or the bulge stem cell, the search for rare, hard-wired professional stem cells has been futile in most tissues.

In a more open approach, the focus on the search for stem cells as a physical entity may need to be replaced by the search for stem cell function, operationally defined as the ability of an organ to replace lost tissue. An opportunistic experimental starting point should probably focus on those cell populations that exhibit proliferative activity during tissue renewal and on the origins of those cells. Stem cell function may indeed be embodied in hard-wired professional stem cells in some tissues. But stem cell function may also diffusely be contained within much larger populations of neutrally competing, undifferentiated cells. It may be executed by facultative stem cells, opportunistically recruited from committed or even from fully differentiated cell populations. Tissues might avoid the use of undifferentiated stem cells altogether, by allowing differentiated cells to proliferate directly and thus to replace lost tissue. In the end, there may be no general rules as to how tissues are renewed, as there is no end to the inventive power of evolution.

REFERENCES

1. E. Clayton *et al.*, *Nature* **446**, 185 (2007).
2. D. P. Doupé *et al.*, *Science* **337**, 1091 (2012).
3. H. Clevers, *Cell* **154**, 274 (2013).
4. M. Leushacke *et al.*, *Cell Rep.* **5**, 349 (2013).
5. A. M. Klein *et al.*, *Cell Stem Cell* **7**, 214 (2010).
6. V. Jaks, M. Kasper, R. Toftgard, *Exp. Cell Res.* **316**, 1422 (2010).
7. A. S. Brack, T. A. Rando, *Cell Stem Cell* **10**, 504 (2012).
8. S. J. Buczacki *et al.*, *Nature* **495**, 65 (2013).
9. J. H. van Es *et al.*, *Nat. Cell Biol.* **14**, 1099 (2012).
10. P. R. Tata *et al.*, *Nature* **503**, 218 (2013).
11. D. E. Stange *et al.*, *Cell* **155**, 357 (2013).
12. J. Stingl *et al.*, *Nature* **439**, 993 (2006).
13. M. Shackleton *et al.*, *Nature* **439**, 84 (2006).
14. A. C. Rios, N. Y. Fu, G. J. Lindeman, J. E. Visvader, *Nature* **506**, 322 (2014).
15. D. Wang *et al.*, *Nature* **517**, 81 (2015).
16. A. Van Keymeulen *et al.*, *Nature* **479**, 189 (2011).
17. D. W. Strand, A. S. Goldstein, *Endocr. Relat. Cancer* **22**, T187 (2015).
18. B. Z. Stanger, *Annu. Rev. Physiol.* **77**, 179 (2015).

10.1126/science.aad7016

PHOTO: SASKIA ELLENBROEK/HUBRECHT INSTITUTE

Published by AAAS

CHEMISTRY

In the wake of collision

When atoms collide with metal surfaces, electron-hole pair excitations dissipate the adsorption energy

By **Harald Brune**

When a metal atom with thermal kinetic energy hits a metal surface, it adsorbs on it with a probability of one. Moreover, it sticks to its impact site and makes not even a single jump to neighboring lattice sites (*1*). The mechanism behind this observation is not fully understood. On page 1346 of this issue, Bünermann *et al.* study a simpler system that can help to elucidate the metal/metal case. In their study, energetic hydrogen atoms impact on a gold surface. Only a fraction of the H atoms adsorb on the surface (see the figure), but the reflected atoms still lose a substantial fraction of their incident kinetic energy. The authors unequivocally identify electron-hole pair excitation as the main dissipation mechanism in these collisions (*2*). Apart from its obvious model character, the H/metal system is important for fields as diverse as heterogeneous catalysis, interstellar H_2 production, and H storage.

For the metal/metal case, field ion microscopy studies have shown that the adsorption energy is dissipated instantaneously. Atoms deposited at low temperature (20 K) onto a close-packed single crystal surface populate two nonequivalent adsorption sites with equal probability, even when the two sites have slightly different binding energies (*3*). If the atoms were able to make only one lateral jump, the higher binding energy site would be occupied more often than the low-energy one. When the surface is heated to 45 K, thermal diffusion leads to the exclusive occupation of the energetically more favorable site. The complete absence of transient mobility at low temperature requires the entire adsorption energy—on the order of several electron volts (eV)—to be dissipated instantaneously. It is unlikely that collective lattice vibrations are fast enough to dissipate this energy. As in the H/metal system, electronically nonadiabatic effects, such as electron-hole pair excitations, are thus likely to play the dominant role.

In a binary collision of H and Au atoms, only 2% of the kinetic energy is transferred from H to Au. This is a result of the very different masses of both atoms. For the incident kinetic energy chosen in Bünermann *et al.*'s experiment, the expected energy loss from a binary ballistic collision on Au is 56 meV. However, the observed energy loss is almost 20 times higher, and the energy-loss distribution is much broader. It is centered at 910 meV and the maximum energy loss is larger than 2.0 eV, explaining why some atoms stick and therefore why this reaction takes place at all.

To illustrate the role of electron-hole pair excitation, the authors compare the reaction on a clean Au surface with one that has a thick layer of solid Xe adsorbed onto it. On Xe, the binary collision model gives an energy loss of 83 meV, and the observed loss is comparable (46 meV). Therefore, the H-Xe collision can be treated as a ballistic collision, but the H-Au collision clearly cannot.

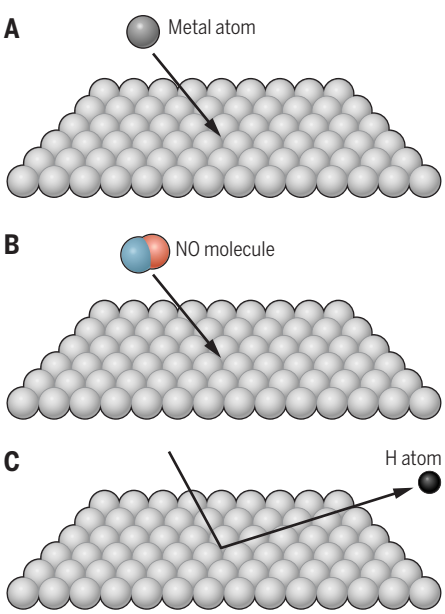

Surface collisions. (**A**) When metal atoms collide with a metal surface with very small incident kinetic energy, every atom sticks. (**B**) For molecule-metal collisions, electron-hole pair excitations are the main mechanism through which adsorption energy is dissipated. (**C**) Hydrogen/metal collisions are similar to metal/metal ones; if the incident kinetic energy is small, every atom would probably stick. At the higher energies used by Bünermann *et al.*, only very few stick, making it possible to measure the energy of the backscattered atoms and to determine how much energy they have lost. The authors show that as for molecule/metal collisions, electron-hole pair excitation is the dominant mechanism for energy dissipation.

Molecular dynamics calculations without electronic excitations essentially yield the ballistic loss spectrum that is in disagreement with the scattering data from Au(111). Once electron-hole pair creation is included, the calculations give excellent agreement with experiment. Similar to the experiment, these simulations are very demanding, because many trajectories have to be considered on a high-dimensional potential energy surface. The beauty of H as adsorbate is that it reduces the complexity because there is only translational kinetic energy; no rotations, vibrations, or steric effects such as orientations of the molecular axes need to be considered. The theory uses the ab initio potential energy surface in classical molecular dynamics simulations and applies the known scheme to introduce electronic friction (*4*). It thus has no adjustable parameters.

The interactions of molecules with metal surfaces are much more complicated because the molecules can dissociate, there might be activation barriers for this dissociation, and steric effects can play a role. However, energy dissipation in nondissociative molecular adsorption is in a way simpler than in atomic adsorption (*5*). The molecule gets distorted when binding to the surface starts to become significant. For example, near a surface, the bond in a simple diatomic molecule gets weakened and therefore stretched, thereby exciting the molecule's vibrational degrees of freedom. From this excited state, the energy can very efficiently be transferred to electronically nonadiabatic behavior, such as electron-hole pair excitation in the metal.

The central insight from the work of Bünermann *et al.* is that translational motion can be damped in the same way as intramolecular excitations (*6*). This is important in the energy dissipation of hot reaction products (*7*, *8*). Electron-hole pair creation is also behind regular dry friction, and its effect can be suppressed by putting one of the sliding bodies into a superconducting state (*9*). Electron-hole pair excitations control the time and energy scale of surface chemical reactions, obviously also for the most elementary one of H on Au(111). ■

Institute of Condensed Matter Physics, Ecole Polytechnique Fédérale de Lausanne (EPFL), Station 3, CH-1015 Lausanne, Switzerland. E-mail: harald.brune@epfl.ch

ILLUSTRATION: P. HUEY/*SCIENCE*

REFERENCES

1. H. Brune, in *Physics of Covered Solid Surfaces*, H. P. Bonzel, Ed. (Springer, Berlin, 2001), vol. III/42 Subvolume A, Part 1 of Landolt Börnstein New Series, Group III: Condensed Matter, pp. 217–258.
2. O. Bünermann *et al.*, *Science* **350**, 1346 (2015).
3. A. Gölzhäuser, G. Ehrlich, *Phys. Rev. Lett.* **77**, 1334 (1996).
4. S. M. Janke *et al.*, *J. Chem. Phys.* **143**, 124708 (2015).
5. K. Golibrzuch *et al.*, *Ann. Rev. Phys. Chem.* **66**, 399 (2015).
6. S. P. Rittmeyer *et al.*, *Phys. Rev. Lett.* **115**, 046102 (2015).
7. H. Brune *et al.*, *Phys. Rev. Lett.* **68**, 624 (1992).
8. J. Wintterlin *et al.*, *Phys. Rev. Lett.* **77**, 123 (1996).
9. M. Kisiel *et al.*, *Nat. Mater.* **10**, 119 (2011).

10.1126/science.aad8005

Downloaded from www.sciencemag.org on December 14, 2015

Published by AAAS

BOOKS *et al.*

In one of the kit's experiments, a zinc pellet placed in a tin chloride solution becomes a tin "hedgehog."

CHEMISTRY

A kid's guide to chemistry

The classic chemistry set gets a 21st-century upgrade

By **Julia Fahrenkamp-Uppenbrink**

Chemistry sets used to be all the rage, but today, children are more likely to be found at their computers or tablets than doing experiments. Furthermore, existing sets tend to present chemistry as miraculous, without explaining the observations in any detail. A new take on the old staple is trying to change that. MEL Science's chemistry set currently targets the home-schooling market, providing a starter kit and 36 individual experiment sets intended for children aged 12 years and older. The experiments are sent out in packs of three over the course of 12 months, and can currently be shipped to addresses in the United States, United Kingdom, and Russia. The kits were developed by a group of self-described "science geeks," with the help of schoolchildren and teachers at a London secondary school to make sure that the science is presented at an appropriate level.

The reviewer is on staff at Science *magazine, AAAS Science International, Cambridge CB2 1LQ, UK. E-mail: jfahrenkamp@science-int.co.uk*

For this review, my daughter and her school friend first picked the "Colorful chemistry" set. The set contains two experiments that were easy to perform and that worked exactly as expected. In one experiment, addition of glycerol to a potassium permanganate solution changes its color gradually from purple to orange as the permanganate reacts with the glycerol. In the other, the thymol blue dye changes the color of a solution depending on its acidity. My daughter made the connection to an acid-base chart from her science class and was thrilled to have recreated it herself.

For our second session, two other friends joined us, as word had got around at school about the cool new chemistry set being tested. This time, we made a tin "hedgehog" by placing a zinc pellet in a tin chloride solution. We watched little spikes grow all over the pellet as the zinc reacted with the tin chloride and the tin precipitated from the solution. In the second experiment, we watched tin dendrites grow in tin chloride solution exposed to an electric current. The children were very impressed by the results. From start to finish, each set took about 1 hour to complete.

MEL Chemistry
Starter kit: $73.80,
individual sets: $11.95
https://melscience.com

Each set comes with detailed, easy-to-follow instructions and brief explanations, including the main chemical equations that underlie the observations. The ones we tested were meticulously prepared and of high quality. I loved the level of attention to detail: For example, a paper clip provided for pricking the tops of reagent bottles comes in its own little bag, pre-bent to allow easy pricking. With only a few exceptions—such as calling one experiment "Magic liquid" and one set "Chemistry of monsters"—they are refreshingly free of silliness.

The sets are designed to work with smartphones in a number of ways that are likely to make them fascinating for young people. For example, we had fun taking close-up pictures of the tin hedgehog with the smartphone macro lens provided in the starter kit. There is also a dedicated phone and tablet app that provides more detailed explanations for each experiment. The explanation for the tin set was detailed and well presented. The explanations for the colorful chemistry set were more limited in the trial kit that we received, but when I followed up with the kit's creators, I learned that they have since been updated.

The app also shows the chemical structures of all reagents, including stereoviews of stick and space-filling models. A stereoviewer is provided as part of the starter kit, and although it took some effort to get it to work, it did impress the young people. This functionality illustrates the ambition of the project, which goes well beyond a traditional chemistry set.

At times during our sessions, I did feel slightly overwhelmed trying to use a phone, tablet, and stereoviewer while simultaneously supervising the experiments, but I quickly relaxed as I saw the children enjoying themselves. The app is a great resource for follow-up questions, and the reagent viewing can also be left to a later date.

Having done two sets of experiments, I feel we have only just scratched the surface of what the set has to offer. My daughter and her rapidly growing group of chemistry enthusiast friends are looking forward to exploring chemical erasers and the zinc-carbon battery set next. I will leave the chemical monsters to last.

10.1126/science.aad9017

PHOTO: MEL SCIENCE

Downloaded from www.sciencemag.org on December 14, 2015

Published by AAAS

EXHIBITION

The enchantress of numbers

Two hundred years after her birth, a new exhibition explores the life of Ada Lovelace

Ada Lovelace
Science Museum, London
Through 31 March 2016

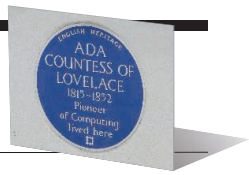

By **Andrew Robinson**

Any visitor to the London Library inevitably walks past a commemorative blue plaque attached to a neighboring house in which once lived the remarkable Ada, Countess of Lovelace (1815–1852). Ada Lovelace is well known for three reasons. She was the daughter of the Romantic poet Lord Byron, who separated from her mother when Ada was just 1 month old. (Despite his early abandonment, she ultimately chose to be buried next to Byron in the family tomb.) She was also the first person to discuss the concept of programming a computer: In the 1840s, she issued an extensive and farsighted commentary on a calculating machine known as the Analytical Engine, created by the mathematician and inventor Charles Babbage.

Those who are unfamiliar with Lovelace's biography may recognize her name nonetheless: In 1980, a high-level computer programming language, Ada, was created for the U.S. Department of Defense. The language is still widely used today. With the recent establishment of Ada Lovelace Day on 13 October, she has become something of an iconic figure for those whose goal is to increase the profile of women in science, technology, and mathematics.

For the bicentenary of her birth, the Science Museum in London, which holds Babbage's Difference Engine and Analytical Engine, is displaying a small but intriguing exhibition about Lovelace's brief life and mathematical work. In addition to a prototype of the Difference Engine and the unfinished Analytical Engine, the exhibition includes a model of a Jacquard loom. Whereas the punch cards of the loom wove flowers and leaves, those of the engine would weave algebraic patterns, she once observed.

The exhibition also features two color portraits of Lovelace, each depicting her as a fashion-conscious young lady. She was not overly fond of either portrait; one of them prompted her to comment that her jaw looked large enough to write the word "mathematics" on it.

According to Lovelace, this portrait, painted in 1836, rendered her jaw large enough to write the word "mathematics" upon.

Originals of her letters from the collections of the British Library and the Bodleian Library appear alongside a digital display, which allows the visitor to follow the progress of her work and her interactions with Babbage, Michael Faraday, and others.

Speaking of the Analytical Engine, she once pointed out that, because the engine generates numerical data, many people might mistakenly assume that it is only useful for arithmetic. On the contrary, she argued, "The engine can arrange and combine its numerical quantities exactly as if they were letters or any other general symbols; and in fact it might bring out its results in algebraical notation, were provisions made accordingly."

In a remark that presciently foreshadows the digitization of music, she goes on: "Supposing, for instance, that the fundamental relations of pitched sounds in the science of harmony and of musical composition were susceptible of such expression and adaptations, the engine might compose elaborate and scientific pieces of music of any degree of complexity or extent."

Several historians of computing, including Doron Swade, one of the advisers to the exhibition, have observed that Lovelace had a rather high opinion of her own intellect (*1*). For example, in 1843 she informed Babbage that "the more I study, the more insatiable do I feel my genius for it to be." Comparing herself with her father, she wrote: "I do *not* believe that my father was (or ever could have been) such a *Poet* as I shall be an *Analyst* (& Metaphysician)." The exhibition organizers downplay this conceit, diplomatically stating that "Her distinctive mixture of mathematical analysis and unbridled imagination brought unique insights into what the Analytical Engine could achieve."

Sadly, because Babbage never completed the engine, for lack of public funding, we shall never know what it might have produced. And since Lovelace died from cancer in her 30s, her potential, too, went unfulfilled. But despite her untimely death, her legacy as a "prophet of the computer age" is very much alive today.

The reviewer is the author of The Last Man Who Knew Everything *(Pi Press, New York, 2005). E-mail: andrew.robinson33@virgin.net*

REFERENCES

1. D. Swade, *The Cogwheel Brain: Charles Babbage and the Quest to Build the First Computer* (Little, Brown, London, 2000).

10.1126/science.aad6636

PHOTO: PURCHASE OF 4TH EARL OF LYTTON VIA LEGGATT BROS. JUNE 1953

Downloaded from www.sciencemag.org on December 14, 2015

Published by AAAS

Flying foxes face cull despite evidence

FLYING FOXES (*PTEROPUS niger*, also known as Mauritius fruit bats) are currently listed as Vulnerable by the World Conservation Union (IUCN) (*1*). Originally inhabitants of all three Mascarene Islands, the *P. niger* population was driven extinct on Réunion and Rodrigues, leaving only the population on Mauritius (*2*) [although a few animals did stray from Mauritius to Réunion recently (*1*)]. Mauritius, meanwhile, has lost two of its three flying fox species as a result of habitat destruction and hunting by humans (*2*, *3*). Yet, disregarding scientific evidence, the Parliament in Mauritius recently decided to cull thousands of the island's remaining flying foxes, which consume fruit and nectar, in an effort to increase the profits of fruit producers (*4*). The IUCN warned that the cull would force an immediate reassessment of the species' Red List Category, possibly even to Critically Endangered, damaging Mauritius's reputation (*3*). The IUCN, Bat Conservation International, and others have called for an evidence-based decision instead, but so far in vain (*3*, *5*).

To justify the cull, the government is using exaggerated figures of population size and damage to fruits (*3*–*5*). The Honorable Minister has cited a population ranging from 90,000 (*4*) to more than 1 million fruit bats (*6*). Research by experts indicates that the population is only 50,000 (*3*, *4*). If the government uses its own estimates instead of scientific evidence to determine the number of fruit bats to cull, the targeted 20% could amount to 18,000 fruit bats (or more, if higher estimates are used). This would not be 20%, but closer to 40% of the actual population. Worse, the cull is scheduled to take place at the onset of the cyclonic season.

Other factors, including impacts of invasive alien species (e.g., rats, parakeets, and mynahs), destroy more fruits than flying foxes (*7*), but are not targeted by the cull, casting further doubts on its effectiveness. Aside from elevating the species' extinction risks, the cull would exacerbate the already critical situation of Mauritian biodiversity (*8*), because flying foxes are the sole surviving seed disseminator for several important native tree species (*9*–*11*).

Mauritius should not allow its fruit production and export industry to damage threatened species and the environment. The international community can help encourage Mauritius to reinstate evidence-based decisions and stop the cull.

F. B. Vincent Florens

Faculty of Science, University of Mauritius, Réduit, Mauritius. E-mail: Vin.Florens@uom.ac.mu

REFERENCES

1. The IUCN Red List of Threatened Species, *Pteropus niger* (www.iucnredlist.org/details/18743/0).
2. A. S. Cheke, J. P. Hume, *Lost Land of the Dodo: An Ecological History of Mauritius, Réunion, and Rodrigues* (T & AD Poyser, London, 2008).
3. IUCN, IUCN SSC position statement on the culling of the Mauritius Fruit Bat (www.iucn.org/es/noticias/noticias_por_fecha/?22044/IUCN-SSC-position-statement-on-the-culling-of-the-Mauritius-Fruit-Bat).
4. Republic of Mauritius, Sixth National Assembly, Parliamentary Debates (http://mauritiusassembly.govmu.org/English/hansard/Documents/2015/hansard3315.pdf).
5. Bat Conservation International, Bat Conservation International's Position on the proposed control of Mauritius Fruit Bats *Pteropus niger* (www.batcon.org/files/BCI_MauritiusBat_Culling_20152.pdf).
6. "Production Fruitère: Le ministre Seeruttun rassure par rapport à l'exercice d'élimination contrôlée des chauves-souris," *Le Mauricien* (2015); www.lemauricien.com/article/production-fruitere-ministre-seeruttun-rassure-rapport-lexercice-delimination-controlee-des- [in French].
7. R. Oleksy, "The impact of the Mauritius Fruit Bat (*Pteropus niger*) on commercial fruit farms and possible mitigation measures" (Detailed final report to The Rufford Foundation, 2015); www.rufford.org/files/14099-B%20Detailed%20Final%20Report.pdf.
8. F. B. V. Florens, in *Conservation Biology: Voices from the*

PHOTO: © LUCASFILM/SUNSET BOULEVARD/CORBIS

LIFE IN SCIENCE

The Force of ethics awakens

"Would creating an army of clones to battle droids be ethically acceptable? As the Chancellor Palpatine suggested to Anakin Skywalker, could creating life or indefinitely prolonging life be considered morally legitimate? If so, then why did the Jedi's moral code strictly prevent all forms of research on altering life itself and ban the acquisition of such knowledge?" I pause to allow my students to absorb these questions. They regard me, wide-eyed.

Summoning Master Yoda, Obi-Wan Kenobi, or even—may the Force protect us!—the Emperor in a class on the ethics of biomedical research might at first sound a bit out of place. But upon closer look, the Jedi and the Sith could well be welcome there. *Star Wars* presents an almost continuous collection of life-related moral dilemmas, each of them serving as a perfect starting point for discussions in a biomedical classroom. From massive cloning and species destruction or creation, to mind-control and knowledge being kept by (and for) a limited elite, *Star Wars* provides examples for almost all of the challenges we want students to consider. The vast majority of students are highly familiar with the popular culture phenomenon that is *Star Wars*, and they are motivated to actively engage in the debate process.

With biomedical science moving so fast that it might sound like fiction, one of our missions is to prepare students—the future scientists—for the ethical challenges they might encounter in their career. Popular culture is just a tool we can use to approach such essential questions. Still, awakening the Force in the classroom might help our students avoid becoming seduced by the Dark Side.

Matthieu J. Guitton

Faculty of Medicine, Laval University, Quebec City, QC, G1V 0A6, Canada. E-mail: Matthieu.Guitton@fmed.ulaval.ca

Downloaded from www.sciencemag.org on December 14, 2015

Published by AAAS

Tropics, N. S. Sodhi *et al.*, Eds. (John Wiley & Sons, 2013), pp. 40–50.
9. F. B. V. Florens *et al.*, *Biodivers. Conserv.* **21**, 2139 (2012).
10. D. M. Hansen, M. Galetti, *Science* **324**, 42 (2009).
11. D. F. Nyhagen *et al.*, *Biol. Conserv.* **122**, 491 (2005).

Marine Protected Areas miss the boat

IN THEIR POLICY Forum "Making waves: The science and politics of ocean protection" (23 October, p. 382; Published online 15 October 2015), J. Lubchenco and K. Grorud-Colvert discuss recent progress in establishing and enforcing Marine Protected Areas, in which extractive activities are illegal. We should make sure that the focus on Marine Protected Areas does not divert attention from other strategies of ocean protection. The major threats to the ocean are global warming, ocean acidification, pollution, illegal fishing, land-based runoff of sediments, and plastics (*1*, *2*). Other threats include noise pollution and whale collisions resulting from ship traffic (*3*, *4*). Marine Protected Areas provide absolutely no protection from any of these threats. The major "threat" they address is legal fishing, which is now well regulated in almost all of the areas where large Marine Protected Areas are being implemented (*5*) and unlikely to be effectively enforced where fisheries are not well regulated (*6*).

Ray Hilborn

School of Aquatic and Fishery Sciences, University of Washington, Seattle, WA 98195, USA.
E-mail: rayh@u.washington.edu

REFERENCES

1. R. Hilborn, *Adv. Mar. Biol.* **69**, 1 (2014).
2. W. J. Fletcher, R. E. Kearney, B. S. Wise, W. J. Nash, *Ecol. Appl.* **25**, 1187 (2014).
3. D. W. Laist, A. R. Knowlton, J. G. Mead, A. S. Collet, M. Podesta, *Mar. Mammal Sci.* **17**, 35 (2001).
4. D. Malakoff, *Science* **291**, 576 (2001).
5. R. Hilborn, D. Ovando, *ICES J. Mar. Sci.* **71**, 1040 (2014).
6. G. J. Edgar *et al.*, *Nature* **506**, 216 (2014).

TECHNICAL COMMENT ABSTRACTS

Comment on "Atlantic and Pacific multidecadal oscillations and Northern Hemisphere temperatures"

S. Kravtsov, M. G. Wyatt, J. A. Curry, A. A. Tsonis

Steinman *et al.* (Reports, 27 February 2015, p. 988) argue that appropriately rescaled multimodel ensemble-mean time series provide an unbiased estimate of the forced climate response in individual model simulations. However, their procedure for demonstrating the validity of this assertion is flawed, and the residual intrinsic variability so defined is in fact dominated by the actual forced response of individual models.

Full text at http://dx.doi.org/10.1126/science.aab3570

Response to Comment on "Atlantic and Pacific multidecadal oscillations and Northern Hemisphere temperatures"

B. A. Steinman, L. M. Frankcombe, M. E. Mann, S. K. Miller, M. H. England

Kravtsov *et al.* claim that we incorrectly assess the statistical independence of simulated samples of internal climate variability and that we underestimate uncertainty in our calculations of observed internal variability. Their analysis is fundamentally flawed, owing to the use of model ensembles with too few realizations and the fact that no one model can adequately represent the forced signal.

Full text at http://dx.doi.org/10.1126/science.aac5208

TECHNICAL COMMENT

CLIMATE CHANGE

Comment on "Atlantic and Pacific multidecadal oscillations and Northern Hemisphere temperatures"

S. Kravtsov,[1]* M. G. Wyatt,[2] J. A. Curry,[3] A. A. Tsonis[1]

Steinman *et al*. (Reports, 27 February 2015, p. 988) argue that appropriately rescaled multimodel ensemble-mean time series provide an unbiased estimate of the forced climate response in individual model simulations. However, their procedure for demonstrating the validity of this assertion is flawed, and the residual intrinsic variability so defined is in fact dominated by the actual forced response of individual models.

The central result of Steinman *et al*.'s analysis (*1*) is the demonstration of an apparent consistency among the responses of different models to variable forcing in the 20th-century climate simulations. In particular, they claim that regional multimodel ensemble-mean time series defines the universal forced signal, which can be linearly rescaled to provide unbiased estimates of the regional forced responses for individual models. Such a consistency is surprising because the models have different physical parameterizations and the simulations may use different forcing subsets. If their claim were true, it would add much confidence to the authors' semi-empirical attribution of the observed multidecadal climate variability to the forced and intrinsic sources. However, the implied uniqueness of the forced signal defined by their regional regression method is an artifact of their analysis procedure, and the actual uncertainty of the semi-empirical estimates of the observed multidecadal intrinsic variability is much larger than these authors have inferred.

Consider M time series of length T, corresponding to M different climate simulations: $x_m^{(t)}; m = 1, ..., M; t = 1, ..., T$. Let the bar denote averaging across the time dimension (t) and square brackets denote averaging across the ensemble member dimension (m). For example, the time mean of each ensemble member $\overline{x_m}$ and the ensemble average time series $[x^{(t)}]$ are defined as follows

$$\overline{x_m} = \frac{1}{T}\sum_{t=1}^{T} x_m^{(t)} \qquad (1)$$

$$[x^{(t)}] = \frac{1}{M}\sum_{m=1}^{M} x_m^{(t)} \qquad (2)$$

Consider a decomposition of $x_m^{(t)}$ into the forced signal $f_m^{(t)}$ and residual intrinsic variability $\epsilon_m^{(t)}$

$$x_m^{(t)} = f_m^{(t)} + \epsilon_m^{(t)} \qquad (3)$$

Without loss of generality, we can assume $\overline{x_m} = \overline{f_m} = 0$, hence $\overline{\epsilon_m} = 0$. If the estimated forced signal $f_m^{(t)}$ is unbiased, then the time series $\epsilon_{m_1}^{(t)}$ and $\epsilon_{m_2}^{(t)}$ of residual intrinsic variability in any pair of simulations m_1 and m_2 must be uncorrelated (independent). Furthermore, if the distribution of $\epsilon_m^{(t)}$ has mean 0 and variance σ^2, the ensemble mean residual time series $[\epsilon^{(t)}]$ will have the distribution with mean 0 and variance σ^2/M. Hence, one can quantitatively assess the statistical independence of different realizations of simulated intrinsic variability by comparing the actual dispersion $[\epsilon]^2$ of the ensemble mean time series $[\epsilon^{(t)}]$ with its theoretical prediction $[\overline{\epsilon^2}]/M$, where we estimated $\sigma^2 \sim [\overline{\epsilon^2}]$. Large values of $[\epsilon]^2$ would indicate that assumption of statistical independence between different realizations of intrinsic variability $\epsilon_m^{(t)}$ is violated due to biases in the estimated forced signal $f_m^{(t)}$, so that at least a portion of the common true forced signal manifests in the estimated "intrinsic" residuals $\epsilon_m^{(t)}$.

Steinman *et al*. considered, among others, the following two methods for estimating the forced signal, both based on the multimodel ensemble mean time series

$$f_m^{(t)} = [x^{(t)}] \qquad (4A)$$

$$f_m^{(t)} = a_m [x^{(t)}] \qquad (4B)$$

The differencing method (Eqs. 3 and 4A) simply identifies the forced signal with the multimodel ensemble mean $[x^{(t)}]$. The regression method (Eqs. 3 and 4B) rescales the first-guess forced signal $[x^{(t)}]$ for a given simulation by finding a_m via least squares to minimize $\overline{\epsilon_m^2}$ in Eq. 3.

Steinman *et al*. further claimed that both of these methods provided independent realizations of residual intrinsic variability in climate-model simulations, based on the fact that the resulting variance $[\epsilon]^2$ of the ensemble mean residual time series was much smaller than the theoretical value of $[\overline{\epsilon^2}]/M$. However, it is easy to show that, due to the choice of forcing derived using either Eq. 4A or Eq. 4B, this ensemble mean residual time series is identically zero

$$[\epsilon^{(t)}] = 0; t = 1, ..., T \qquad (5)$$

and so is its variance $[\overline{\epsilon}]^2 = 0$. Hence, the extreme smallness of the dispersion of ensemble average intrinsic variability attributed in (*1*) to the statistical independence of its different realizations is actually an artifact of the algebraic constraint (Eq. 5) [see (*2*–*5*)]. This flaw does not mean that the residuals are necessarily correlated (not independent), but a different test is required to determine that.

We now show directly that the regional regression approach (*1*) of defining the forced signal leads to the correlated samples of residual intrinsic variability in the individual-model ensembles (subensembles of simulations using a single model with fixed physics package and an identical forcing history). For these subensembles, it is the expression (Eq. 4A) that naturally gives an unbiased estimate of the forced variability. We considered 18 such subensembles from the Coupled Model Intercomparison Project Phase 5 (CMIP5) models with four or more 20th-century simulations (*6*), totaling 116 individual simulations out of the 170 available simulations. The multimodel ensemble mean based on these 116 simulations is nearly identical to the one computed using all of the available 170 simulations. We defined two alternative sets of the model-simulated intrinsic variability. In method A, we formed realizations of intrinsic variability by subtracting the 5-year low-pass-filtered ensemble mean of each model from this model's individual simulations (i.e., Eq. 4A applied separately to individual model ensembles). The second set (method B) defined the residual intrinsic variability using the forced signal estimated from regional multimodel regression (*1*) (i.e., Eq. 4B applied to the whole ensemble of 116 simulations).

To quantify independence of different realizations of intrinsic variability in the individual-model ensembles, we introduced an ensemble correlation measure C by summing positive correlations among all possible pairs of an individual model's M ensemble members

$$C = \frac{2}{M(M-1)}\sum_{m>l} C_{ml}\, H(C_{ml}) \qquad (6)$$

where $H(x)$ is the Heaviside step function (*7*); the quantity C ranges from 0 (no positive correlations between individual ensemble members) to 1 (all ensemble members are perfectly correlated). The correlation measure (Eq. 6) was computed for raw and low-pass-filtered intrinsic variability defined using methods A and B [Fig. 1, A to C shows results for the Geophysical

[1]Department of Mathematical Sciences, Atmospheric Science group, University of Wisconsin-Milwaukee, Post Office Box 413, Milwaukee, WI 53201, USA. [2]Department of Geological Sciences, University of Colorado, Boulder, CO, USA. [3]School of Earth and Atmospheric Sciences, Georgia Institute of Technology, Atlanta, GA, USA.
*Corresponding author: kravtsov@uwm.edu

Downloaded from www.sciencemag.org on December 14, 2015

Fluid Dynamics Laboratory (GFDL) CM3 model; see (*8*)]. Method A produces intrinsic variability with C values well within the range expected from random uncorrelated red-noise samples generated using an autoregressive model of order 3 (AR-3) (*9*). In contrast, Steinman *et al.*'s method B results in samples that are significantly correlated due to their systematic difference from the true forced signal.

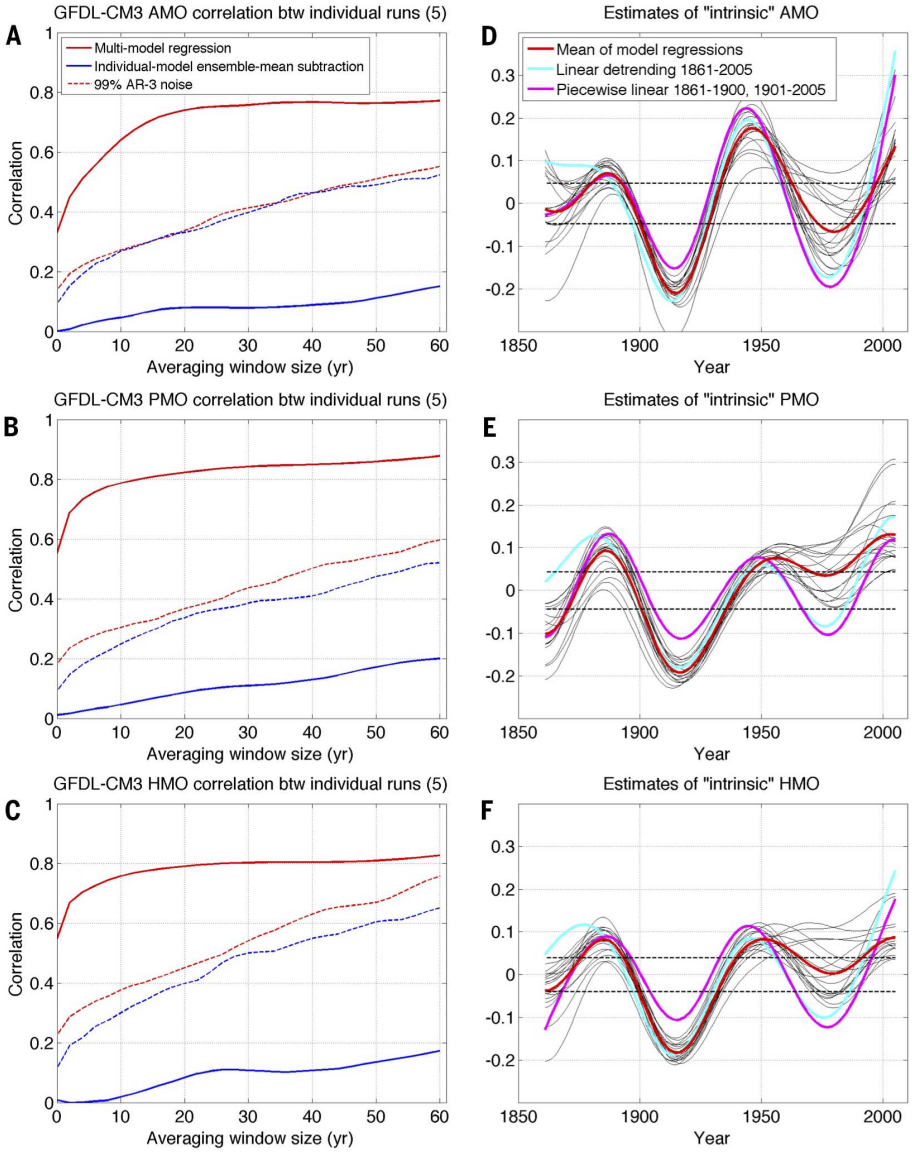

Fig. 1. Intrinsic variability in the 20th-century model simulations with four or more ensemble members identified using two different methods for estimating the forced signal: the classical subtraction of the individual-model ensemble mean (method A) and the multimodel regional regression method (*1*) (method B). (**A** to **C**) The correlation measure (Eq. 6) of statistical independence between multiple realizations of the GFDL CM3 model (five realizations) for (A) Atlantic Multidecadal Oscillation (AMO), (B) Pacific Multidecadal Oscillation (PMO), and (C) Northern Hemisphere Multidecadal Oscillation (HMO) indices; these correlations were computed for running-mean low-pass-filtered residual time series (which characterize intrinsic variability) and are plotted here against the averaging window size. Low correlation measure indicates statistical independence of intrinsic residuals. Dashed lines show the 99th percentile of the correlation measure based on the 1000 simulations of the corresponding AR-3 red-noise model. (**D** to **F**) Estimates of the observed multidecadal intrinsic variability for (D) AMO, (E) PMO, and (F) HMO. The semi-empirical estimates (thin black lines) were computed as in (*1*) based on the forced signals obtained using method A for each of the 18 model ensembles considered, with the heavy red line indicating the average over these individual estimates. Additional heavy lines (see legend) are for results based on linear detrending. The distance between the black dashed lines in each plot shows the 95th percentile of the standard deviations for multidecadal intrinsic variability estimated using method A for each of 116 simulations considered.

We then used 18 versions of the forced signal, estimated by the unbiased method A, to isolate intrinsic variability in observed surface temperatures via Eq. 3 and Eq. 4B (Fig. 1, D to F). The spread among the 18 estimates of intrinsic variability in observations is much larger than the tight bootstrap-based error bounds on the semi-empirical estimates of the observed intrinsic variability in figure 3 in (*1*). Hence, the actual uncertainty of the semi-empirical attribution by SMM is also much larger (*10*), thereby preventing any clear inferences about the cause of the "false pause" in the global warming (*11*, *12*).

REFERENCES AND NOTES

1. B. A. Steinman, M. E. Mann, S. K. Miller, *Science* **347**, 988–991 (2015).
2. The standard deviation of intrinsic variability computed in Steinman *et al.* (*1*) is small, but not exactly zero because of their using a data adaptive low-pass filter before averaging intrinsic variability among different simulations.
3. Steinman *et al.* also used weighted ensemble means to define a version of their model-based forced signal. In this case, the constraint (Eq. 5) would not be exact but would still be approximately valid, because the weighted and nonweighted estimates of the forced signal are in fact very close (not shown here).
4. Comment (*3*) above also applies to a possible variation of the regression method (Eq. 4B) in which, instead of scaling each individual simulation by its own factor a_m, one would estimate and use the single scaling factor for all simulations of each model; this scaling factor can be defined, for example, as the ensemble mean of a_m estimates computed for individual simulations of a given model.
5. One way to try to alleviate constraint (Eq. 5) would be to estimate the forced signal for a given subset of models using the ensemble mean time series of the complement subset of models. However, this would only be effective if the sizes of these two subsets are comparable. Otherwise, the multimodel averaging over the much larger complement subset of models would also be very close to the all-model ensemble mean, and the algebraic constraint (Eq. 5) would still approximately hold.
6. There are 13 models with four or more 20th-century simulations in the CMIP5 data set, but considering separately the ensembles of the Goddard Institute for Space Studies (GISS) models with different physics packages makes up 18 independent ensembles.
7. The Heaviside step function is used here merely to streamline the mathematical notations in the multiple correlation measure (Eq. 6) by zeroing out negative terms in the sum of correlations, leaving positive terms unchanged.
8. Other models exhibit a similar behavior; see the corresponding images at https://pantherfile.uwm.edu/kravtsov/www/downloads/KWCT2015/TIFF_FILES.
9. If one does not divide the large ensembles of the GISS models into the subensembles with different physics (*6*), the correlation-measure diagnosis does identify the dependency between the model realizations, because the true forced responses in these versions of the model are different from the grand ensemble mean response, and similar long-term biases across the same-physics model simulations ensue.
10. The bootstrap resampling used in (*1*) is equivalent to considering subensembles of about two-thirds of independent models (or simulations), thus effectively averaging out the intramodel uncertainty of the forced response emphasized in our Fig. 1, D to F.
11. This is exacerbated further by the unfortunate linear extrapolation of the CMIP5 runs from 2005 to 2012 used in (*1*) to estimate recent intrinsic trends.
12. B. Rajaratnam, J. Romano, M. Tsiang, N. S. Diffenbaugh, *Clim. Change* **133**, 129–140 (2015).

ACKNOWLEDGMENTS

We thank Steinman *et al.* for making their data and analysis code publicly available. This research was supported by NSF grants OCE-1243158 (S.K.) and AGS-1408897 (S.K. and A.A.T.). All data and MATLAB (MathWorks, Natick, MA) scripts for this paper are available for downloading from http://pantherfile.uwm.edu/kravtsov/www/downloads/KWCT2015.

15 April 2015; accepted 6 November 2015
10.1126/science.aab3570

TECHNICAL RESPONSE

CLIMATE CHANGE

Response to Comment on "Atlantic and Pacific multidecadal oscillations and Northern Hemisphere temperatures"

B. A. Steinman,[1]*† L. M. Frankcombe,[2]† M. E. Mann,[3] S. K. Miller,[3] M. H. England[2]

Kravtsov *et al*. claim that we incorrectly assess the statistical independence of simulated samples of internal climate variability and that we underestimate uncertainty in our calculations of observed internal variability. Their analysis is fundamentally flawed, owing to the use of model ensembles with too few realizations and the fact that no one model can adequately represent the forced signal.

Kravtsov *et al*. (*1*) wrongly claim (i) that our assertion of statistical independence among estimates of the internal variability in regional temperature change in climate models (*2*) is an artifact of a flawed procedure. They further suggest (ii) that robust assessments of simulated internal variability cannot rely on a multimodel ensemble mean (MMEM) that differs from the true forced signal of the individual models, because the residuals of the two forced signals masquerade as low-frequency internal variability, which leads to correlation among ensemble members. Finally, they claim (iii) that we substantially underestimate the uncertainty in the semi-empirical estimate of internal variability derived using the MMEM to approximate the forced signal.

Regarding their first point, Kravtsov *et al*. assert (in their second reference/note) that the standard deviation of the mean of internal variability is not exactly zero only because the data were filtered before analysis [figure 2 and figures S2 to S4 in (*2*)]. This is true, however, only if the full ensemble of realizations, N, is used in the calculation. If $(N-1)$ realizations are instead used, as is the case in our analysis, the standard deviation of the mean is not zero (regardless of whether the data are filtered beforehand) (*3*). Our method for assessing statistical independence is valid.

Regarding their second point, Kravtsov *et al*. claim that internal variability calculated using the regional regression method and a scaled MMEM introduces errors because each model has a different forced response. Instead, they use a single-model ensemble mean (SMEM) for models with four or more historical runs and show that the internal variability calculated in this manner has a lower variance and lower intramodel correlation than that determined using a MMEM [figure 1, A to F, in (*1*)]. They assert that this occurs because the difference between the MMEM and the true forced signal for individual models introduces extra internal variability at low frequencies. Although this could be true in principle, this point is irrelevant because the ensembles of simulated internal variability determined using regional regression nevertheless universally satisfy the requirements for statistical independence [figure 2 in (*2*)].

Moreover, we show that more than four (indeed, more than 10) ensemble members are required for a robust estimate of the forced signal from a SMEM, and thus the lower variance of the internal variability estimates is due to the small ensemble size, which leads to the removal of too much of the internal variability. We demonstrate this point using synthetic autoregressive-1 time series (Fig. 1, A and B), each with the same forced signal, and a different realization of red noise (*4*). We divide the 160-member ensemble into subsets of four- or ten-member ensembles, which were smoothed using a 5-year low-pass filter. Using the code provided by Kravtsov *et al*., we show that the application of small ensemble SMEMs results in lower variance of internal variability (Fig. 1A), even though in this case we know that the large ensemble yields a far more accurate estimate of the forced signal (Fig. 1B). This idealized example reveals that the higher variance obtained when using the MMEM relative to using the SMEM is in fact due to the removal of too much internal variability when using the SMEM.

Regarding their third point, Kravtsov *et al*. claim that there is a wide range of possible semi-empirical estimates of observed internal variability resulting from the range of possible SMEM estimates of the forced signal. They attempt to assess the uncertainty in the Atlantic Multidecadal Oscillation (AMO), Pacific Multidecadal Oscillation (PMO), and Northern Hemisphere Multidecadal Oscillation (NMO) by applying the mean of individual model ensembles with four or more realizations and claim that the resulting spread of these separate estimates defines uncertainty inherent in the regional regression method (*5*). However, as we have shown, none of these SMEMs is in itself a robust estimate of the forced signal, because none of the models have enough ensemble members for suitable cancellation of the different realizations of internal variability [which also explains the narrow 2σ range in their figure 1, G to I (*1*)]. More importantly, it is unreasonable to expect an individual model to have a better representation of the forced signal than the multimodel ensemble. In fact, the spread in the internal variability estimates of Kravtsov *et al*. [figure 1, G to I in (*1*)] supports this assertion, indicating that regional regression–based estimates of internal variability and their uncertainties are intrinsically dependent on the choice of the forced signal and therefore that only robust estimates derived from a large number of models or realizations should be used for this assessment. The MMEMs from the Coupled Model Intercomparison Project Phase 5 [CMIP5-All (all models) and CMIP5-AIE (models that include the first and second aerosol indirect effects)] applied in our study fulfill these requirements, whereas the SMEMs do not. By this rationale, the CMIP5-All mean provides the best overall estimate of the forced signal, with an uncertainty that can be estimated (among other methods) using bootstrap resampling [figure 3C in (*2*)].

Although the use of SMEMs based on a small number of realizations is an inherently flawed method, we nonetheless show that both the MMEM and SMEM regression-based methods provide better estimates of the internal signal than simple linear detrending, which produces a large overestimation of the variance of the internal variability, especially in recent decades [magenta curves in Fig. 1, A and C, and figure 1, G to I in (*1*)]. Indeed, this is one of the key points of our original Report and is a principal focus of Frankcombe *et al*. (*6*). This recent study concludes that linear detrending introduces large biases in both the amplitude and phase of the internal variability and that regression-based approaches that rely on large historical simulation ensembles to estimate the forced signal produce less biased estimates of internal variability.

The use of different MMEM and large ensemble SMEM estimates of the forced series (*5*) produces internal variability trends that are generally consistent [see figure 3 and figure S6 in (*2*)]. For example, the AMO, PMO, and NMO behavior over the most recent two decades are in each case largely similar to one another (e.g., in the most recent decade: PMO decreasing, NMO decreasing, AMO flat) (*7*) and inconsistent with estimates of

[1]Large Lakes Observatory and Department of Earth and Environmental Sciences, University of Minnesota Duluth, Duluth, MN, USA. [2]Australian Research Council Centre of Excellence for Climate System Science and Climate Change Research Centre, University of New South Wales, Sydney, New South Wales, Australia. [3]Department of Meteorology and Earth and Environmental Systems Institute, Pennsylvania State University, University Park, PA, USA.
*Corresponding author. E-mail: bsteinma@d.umn.edu
†These authors contributed equally to this work.

Downloaded from www.sciencemag.org on December 14, 2015

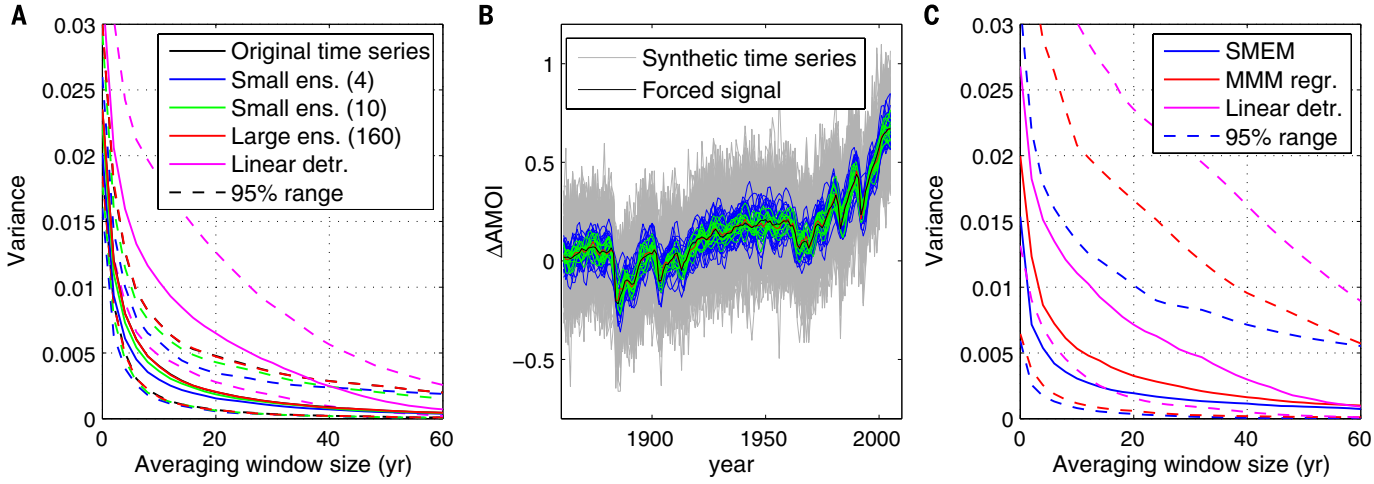

Fig. 1. Estimates of AMO variance based on ensemble size and smoothing window. (**A**) The variance of internal variability in synthetic AMO time series produced using the same forced signal and different realizations of red noise. The mean variance (solid lines) and 2σ range (dashed lines) of the large ensemble (red, 160 members) and small ensembles (green, 10 members; blue, 4 members) are shown as a function of the time-averaging window size. The small ensembles consist of random groupings taken from the large ensemble. Also shown are the variance of the original synthetic time series (not including the forced signal; black, almost coinciding with the red curve) and the variance obtained after linear detrending (magenta). (**B**) Individual estimates of the forced signal from the large and small ensembles means [colors as in (A)] shown with the true forced signal (black). Note the extremely high level of agreement between the large ensemble mean and the true forced signal relative to that of the small ensemble means. The synthetic time series (including the forced signal) are shown in gray. (**C**) The variance of semi-empirical estimates of AMO variability from the 18 CMIP5 models considered in Kravtsov *et al*. using multimodel ensemble mean regression (red), individual model ensemble mean subtraction (blue), and linear detrending (magenta). Ensemble mean variance (solid lines) and 2σ ranges (dashed lines) are shown as a function of the time-averaging window size.

internal variability derived from simple statistical methods (i.e., detrending, with the exception of, perhaps, the PMO). Furthermore, the principal conclusions of Steinman *et al*. (*2*) (regarding the recent slowdown in surface warming) have been supported by at least eight other prominent studies (*8*–*15*), of which the most recent (*15*) uses a semi-empirical method (in which the forced signal is estimated using a MMEM) that is very similar to the target region regression method of Steinman *et al*. (*2*).

In short, we find no merit to the criticisms of Kratsov *et al*. We once again emphasize that the linear detrending procedure used in their past work (*16*) leads to extremely biased estimates of internal variability and should not be employed. Our regression-based approach (*2*, *6*), by contrast, yields faithful estimates of the internal variability.

REFERENCES AND NOTES

1. S. Kravtsov, M. G. Wyatt, J. A. Curry, A. A. Tsonis, *Science* **350**, 1326 (2015).
2. B. A. Steinman, M. E. Mann, S. K. Miller, *Science* **347**, 988–991 (2015).
3. In our original analysis, we incorrectly assessed the standard deviation of the mean of the internal variability estimates by including all realizations (N = 170, in the case of CMIP5-All) rather than (N – 1) realizations in demonstrating that only the regional regression approach satisfies the requirement for statistical independence. However, the correct calculation results in an insignificant difference in the results that has no effect on our findings and conclusions. The manuscript, code, and results have been updated to reflect this correction.
4. The forced signal is the Coupled Model Intercomparison Project Phase 5 all model (CMIP5-All) ensemble mean North Atlantic time series. The realizations of red noise are scaled to match the average autocorrelation of the North Atlantic series in the CMIP5 models.
5. We agree, in part, that the true uncertainty in semi-empirical estimates of internal variability is best assessed using multiple, equally valid estimates of the forced signal based on different models with a large number of realizations. We addressed this specific point in our manuscript through the inclusion of five separate estimates of internal variability based on five individual SMEMs consisting of 10 or more realizations [our ensembles include CMIP5-All (all models)/CMIP5-GISS (GISS model E2 ensemble)/CMIP5-AIE (models that include the first and second aerosol indirect effects)/five different SMEMs with more than 10 members] [figure S6 in (*2*)].
6. L. M. Frankcombe, M. H. England, M. E. Mann, B. A. Steinman, *J. Clim.* **28**, 8184–8202 (2015).
7. The linear extrapolation method used to extend model series from 2005 through 2012 produces results that are generally consistent with simple propagation of the 2005 value. The claim in reference/note 11 in Kravtsov *et al*. (*1*) that our methodology here is "unfortunate" is therefore inappropriate. This issue was addressed in detail by Mann *et al*. (*8*).
8. M. E. Mann, B. A. Steinman, S. K. Miller, *Geophys. Res. Lett.* **41**, 3211–3219 (2014).
9. Y. Kosaka, S.-P. Xie, *Nature* **501**, 403–407 (2013).
10. M. H. England *et al*., *Nature Clim. Change* **4**, 222–227 (2014).
11. K. E. Trenberth, J. T. Fasullo, *Earth's Future* **1**, 19–32 (2013).
12. X. Chen, K.-K. Tung, *Science* **345**, 897–903 (2014).
13. V. Guemas, F. J. Doblas-Reyes, I. Andreu-Burillo, M. Asif, *Nat. Clim. Chang.* **3**, 649–653 (2013).
14. G. A. Meehl, A. Hu, J. M. Arblaster, J. Fasullo, K. E. Trenberth, *J. Clim.* **26**, 7298–7310 (2013).
15. A. Dai, J. C. Fyfe, S.-P. Xie, X. Dai, *Nat. Clim. Change* **5**, 555–559 (2015).
16. M. G. Wyatt, S. Kravtsov, A. A. Tsonis, *Clim. Dyn.* **38**, 929–949 (2012).

ACKNOWLEDGMENTS

We thank Kravtsov *et al*. for providing the MATLAB code used for their analyses. All raw data, MATLAB code, and results from our analysis are available at the supplementary website www.meteo.psu.edu/holocene/public_html/supplements/Science2015.

14 May 2015; accepted 6 November 2015
10.1126/science.aac5208

RESEARCH

Predicting protein quaternary structure

Ahnert et al., *p. 1331*

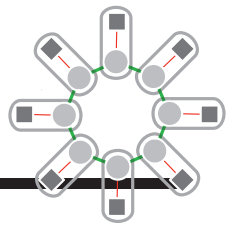

IN *SCIENCE* JOURNALS

Edited by **Stella Hurtley**

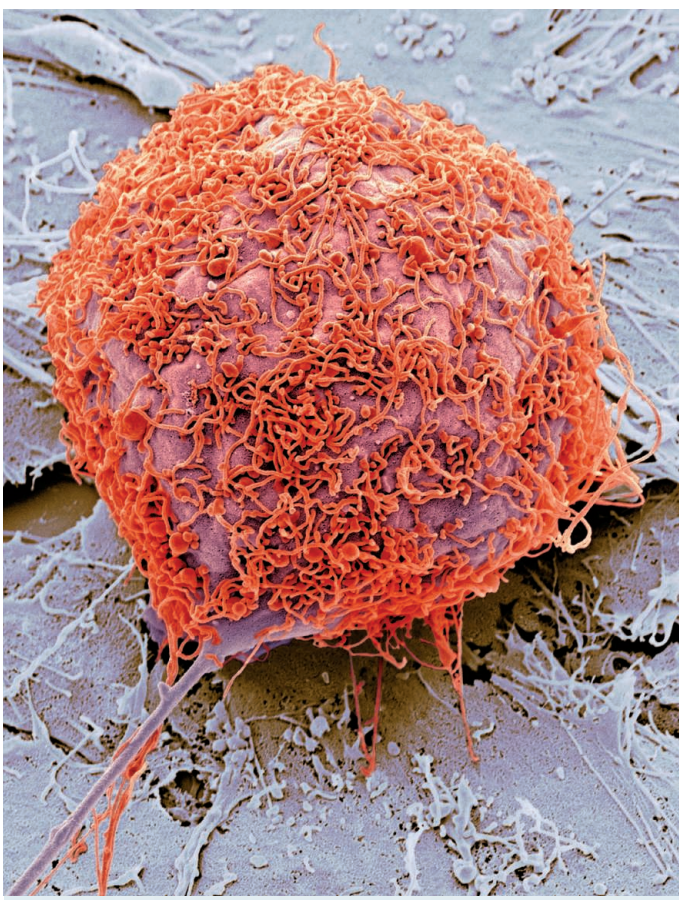

Colored scanning electron micrograph of an osteosarcoma cancer cell

CANCER

Out-RANKing osteosarcoma

Osteosarcoma, the most common primary bone cancer, can be difficult to treat, especially in patients with metastatic disease. Chen *et al.* developed genetically engineered mouse models of osteosarcoma and used them to demonstrate that receptor activator of nuclear factor κB ligand (RANKL) signaling contributes to the progression of this disease. Furthermore, denosumab, an antibody against RANKL already used in patients with other bone diseases, inhibited osteosarcoma in mouse models and so is a viable candidate for future testing in human patients. — YN

Sci. Transl. Med. **7**, 317ra197 (2015).

CANCER IMMUNOTHERAPY

Low mutation rate okay for T cells

Cancers that tend to have high numbers of mutations, such as melanoma and smoking-induced lung cancer, respond well to immunotherapies, whereas those with fewer mutations, such as pancreatic cancer, do not. Tran *et al*. searched for tumor mutation–reactive T cells in 10 patients with metastatic gastrointestinal cancers, which have relatively low mutation burdens, and discovered that 9 out of 10 harbored such cells. T cells from one patient recognized a mutation common to many types of cancers. Engineering T cells to express this particular mutation-reactive T cell receptor may extend adoptive cell immunotherapy to a larger pool of patients than previously anticipated. — KLM

Science, this issue p. 1387

AGING

Aging: All in the head—and the gut

The effects of hypoxia and caloric restriction, both of which extend life span in *Caenorhabditis elegans*, converge on the activation of an enzyme in cells of the intestine. Leiser *et al*. show that the life-extending effects of hypoxia begin in neurons with transcriptional activation by hypoxia-inducible factor–1 and increased serotonergic signaling. These effects lead to increased production of flavin-containing monooxygenase-2 (FMO-2) in the intestine, which increased longevity. Finding the relevant targets of FMO-2, which also accumulates in mammals under conditions that promote longevity, may elucidate further mechanisms that promote healthy aging. — LBR

Science, this issue p. 1375

ICE SHEETS

Shrinking shelf and faster flow

Zachariæ Isstrøm, a large glacier in northeast Greenland, began a rapid retreat after detaching from a stabilizing sill in the late 1990s. Mouginot *et al*. report that between 2002 and 2014, the area covered by the glacier's ice shelf shrank by 95%; since 1999, the glacier's flow rate has nearly doubled; and its acceleration increased threefold in the fall of 2012. These dramatic changes appear to be the result of a combination of warmer air and ocean temperatures and the topography of the ocean floor at the head of the glacier. Rising sea levels should continue to destabilize the marine portion of Zachariæ Isstrøm for decades. — HJS

Science, this issue p. 1357

Greenland's ice flows over the varied underlying terrain near the coast

Downloaded from www.sciencemag.org on December 14, 2015

PHOTOS: (FROM TOP) AHNERT *ET AL.*; STEVE GSCHMEISSNER/SCIENCE SOURCE; NASA/GSFC/JEFFERSON BECK

Published by AAAS

SOCIAL BEHAVIOR

From faithfulness to spatial memory

Natural selection shapes traits to be as adaptive as possible for a given environment. Okhovat *et al*. show that such varying selection also shapes variation in social behavior and the brain (see the Perspective by Robinson). Variation in male fidelity among monogamous prairie voles reflects differences in the expression, regulation, and epigenetic status of a vasopressin receptor that functions in spatial memory. Thus, the trade-offs males face between fidelity and infidelity may promote heritable variation that is important for spatial memory and maintain variation in their levels of fidelity. — SNV

Science, this issue p. 1371; see also p. 1310

CANCER

Growing blood vessels in gliomas

Aggressive gliomas have a high density of abnormal blood vessels that enables tumor growth and damages the brain. Zhang *et al.* analyzed patient data and correlated increased levels of a secreted factor called pleiotrophin with more aggressive grades of glioma and decreased survival. When implanted in mice, glioma cells that released pleiotrophin formed larger tumors with more blood vessels. Mice developed smaller gliomas and survived longer when treated with inhibitors of ALK, a receptor for pleiotrophin. — WW

Sci. Signal. **8**, ra125 (2015).

GEOPHYSICS

A mysterious mid-mantle slowdown

The viscosity of Earth's deep interior plays a key role in mediating plate tectonics. Rudolph *et al*. combined several geophysical data sets to model the viscosity of the mantle. Mantle viscosity abruptly increases below 1000 km. The increase could explain the stalling of subducting slabs and the deflections of hot upwelling plumes around this depth. Although the viscosity increase explains some recent unexpected observations, the origin of the jump itself remains a mystery. — BG

Science, this issue p. 1349

SUPERCONDUCTIVITY

Locking the spins in a superconductor

In Cooper pairs—pairs of electrons responsible for the exotic properties of superconductors—the two electrons' spins typically point in opposite directions. A strong-enough external magnetic field will destroy superconductivity by making the spins point in the same direction. Lu *et al*. observed a two-dimensional superconducting state in the material MoS_2 that was surprisingly immune to a magnetic field applied in the plane of the sample (see the Perspective by Suderow). The band structure of MoS_2 and its spin-orbit coupling conspired to create an effective magnetic field that reinforced the electron pairing, with spins aligned perpendicular to the sample. — JS

Science, this issue p. 1353; see also p. 1316

COGNITIVE SCIENCE

Handwritten characters drawn by a model

Not only do children learn effortlessly, they do so quickly and with a remarkable ability to use what they have learned as the raw material for creating new stuff. Lake *et al*. describe a computational model that learns in a similar fashion and does so better than current deep learning algorithms. The model classifies, parses, and recreates handwritten characters, and can generate new letters of the alphabet that look "right" as judged by Turing-like tests of the model's output in comparison to what real humans produce. — GJC

Science, this issue p. 1332

IN OTHER JOURNALS

Edited by **Kristen Mueller** *and* **Jesse Smith**

Planting marsh grasses in a clumped, rather than dispersed, pattern can improve outcomes when restoring wetlands

PHOTO: © NICO VAN KAPPEL/BUITEN-BEELD/MINDEN PICTURES/CORBIS

RESTORATION ECOLOGY

Planting to enhance positive interactions

Rising sea levels and human development threaten coastal ecosystems worldwide. Efforts to protect and restore these environments include a range of physical and biological measures, including reestablishing vegetation to stabilize the habitat and restore ecosystem function. Silliman *et al*. report the results of experiments in coastal wetlands in Florida and the Netherlands, showing that the simple pattern of planting (clumped versus dispersed) marsh grasses influences the success of restoration. Compared to a dispersed pattern of planting, planting marsh grasses in a clumped pattern enhanced their survival, biomass, and density. Clumped plants interacted positively; for instance, they reduced their anoxia stress, and neighboring roots shared oxygen more readily, effectively producing a more oxygen-rich microenvironment than isolated individual plants can achieve. — AMS

Proc. Natl. Acad. Sci. U.S.A. **112**, 14297 (2015).

Published by AAAS

GEOPHYSICS

Setting the table for an old plate

New pictures of Earth's interior reveal an ancient tectonic plate sinking toward the bottom of the mantle. Simmons *et al.* find the structure in seismic tomography images under the data-limited region of the Indian Ocean. Complete subduction of the plate occurred more than 100 million years ago. This observation suggests that old plates can hang around in the mantle longer than previously thought. It also provides a new piece of information for reconstructing plate motions and landmass locations in the distant past. — BG

Geophys. Rev. Lett. 10.1002/2015GL066237 (2015).

BEHAVIOR

Empathy is for the birds

Many species empathize with one other by state matching, a process whereby an individual shifts its physiological state to match another's. Increasing evidence suggests that empathy occurs across mammals, but whether other vertebrates empathize is unclear. Birds are prime candidates for state matching, given their extensive parental care, pair bonding, and sociality. Perez *et al*. now show that in highly monogamous zebra finches, females match their state of stress (as measured by glucocorticoids) to that of their male mate, as perceived only through changes in his call. No match appeared when females listened to the calls of unknown males, which suggests that the close bond facilitates empathy. — SNV

Horm. Behav. 10.1016/j.yhbeh.2015.09.002 (2015).

Monogamous zebra finches empathize through song

PHOTOS: (FROM TOP): ©WEGNER. JÖRG & PETRA/ANIMALS ANIMALS; KICHIGIN/ISTOCK PHOTO

AGING

A circadian secret to a long life

Dietary restriction (reduced nutrient intake without malnutrition) increases life span in multiple species, including fruit flies, but how this occurs is largely unknown. Katewa *et al*. now find that in flies, changes in the expression of genes that regulate the circadian clock underlie the life-extending effect of dietary restriction. Dietary restriction increased the amplitude of daily cycles of clock gene expression in tissues such as the fly head and body. In flies with mutated clock genes, dietary restriction failed to increase longevity. Moreover, genetically increasing the periodicity of circadian gene expression also extended the life span of flies. Further analysis indicated that circadian gene expression contributes to changes in metabolism that mediate the effects of dietary restriction on life span. — LBR

Cell Metab. 10.1016/j.cmet.2015.10.014 (2015)

CATALYSIS

Upgrading ethanol without adding hydrogen

An issue with ethanol–usage mandates for gasoline is the "blend wall": Many vehicles can only use up to 10 to 15% ethanol. In order to use more ethanol as a fuel, it must be converted to hydrocarbons that blend into gasoline, but existing processes have suffered from the need to add hydrogen or produce a high fraction of undesirable small hydrocarbons. Narula *et al*. report the conversion of ethanol to larger hydrocarbons suitable for use in gasoline, as well as diesel and jet fuels, with a ZSM-5 zeolite containing indium and vanadium. A hydrocarbon pool mechanism appears to operate without dehydration steps. — PDS

Sci. Rep. 10.1038/srep16039 (2015).

Catalytic conversion to hydrocarbons allows more ethanol to be used in automobile fuel

NEPHROLOGY

A circulating harbinger of kidney disease

Chronic kidney disease affects 600 million people worldwide. Initially asymptomatic, the disease often follows a progressive course that can lead to heart disease and kidney failure. An easily measured biomarker that identifies people at high risk of developing kidney disease would allow doctors to intervene earlier so that patients' disease progresses at a slower rate. Toward that end, Hayek *et al*. examined the predictive capacity of suPAR, a protein previously linked to a certain type of kidney disease. They serially monitored plasma levels of suPAR in a large group of patients, many with normal kidney function at the study's start, and found that elevated levels of the protein correlated with a decline in kidney function and with new-onset chronic kidney disease. — PAK

N. Engl. J. Med. **373**, 1916 (2015).

PHYSICS

Studying magnetism in an atomic chain

When we think of magnets, solid materials generally come to mind, but researchers can also study magnetism by placing individual atoms in an egg-crate–like potential created by lasers: an optical lattice. This approach, however, requires extraordinarily low temperatures. To circumvent that requirement, Murmann *et al.* studied a string of three or four fermionic ^{6}Li atoms in an elongated optical trap. In this one-dimensional system, no lattice was needed because the atoms, tuned to interact strongly, spontaneously formed an ordered chain. The researchers first placed three atoms in a particular spin configuration and then tilted the trap to let the outermost atom tunnel out. The spin state of the tunneling atom revealed that the atoms were initially in an antiferromagnetic state. — JS

Phys. Rev. Lett. **115**, 215301 (2015).

Published by AAAS

ALSO IN *SCIENCE* JOURNALS

Edited by **Stella Hurtley**

MICROBIOME

The ocean microbial system

The vast translucent oceans are teeming with microscopic life that drives significant life processes and elemental cycling on Earth. Yet how climate change will affect the functioning of this microbiome is not well understood. Moran reviews progress and the transformative discoveries made recently in marine microbiology that have led environmental, plant, animal, and even human microbiome research. — CA

Science, this issue p. 1330

PROTEIN STRUCTURE

The principles of protein assembly

A knowledge of protein structure greatly enhances our understanding of protein function. In many cases, function depends on oligomerization. Ahnert *et al*. used mass spectrometry data together with a large-scale analysis of structures of protein complexes to examine the fundamental steps of protein assembly. Systematically combining assembly steps revealed a large set of quaternary topologies that were organized into a periodic table. Based on this table, the authors accurately predicted the expected frequencies of quaternary structure topologies. — VV

Science, this issue p. 1331

PHYSICAL CHEMISTRY

Shaking out details of transition states

Chemists liken reaction energetics to a landscape with hills and valleys. In this context, the transition state represents the highest barrier that reagents must pass over en route to forming products. Baraban *et al*. introduce a framework for extracting details about the transition state of rearrangement reactions directly from vibrational spectral data. They identified a characteristic pattern in the spacing between vibrational energy levels near the transition state, which revealed its energy as well as the specific motions involved in surmounting the barrier. — JSY

Science, this issue p. 1338

SIGNAL PROCESSING

Detecting a transient needle in a haystack

Discriminating signals within a noisy environment is an issue crucial to many disciplines, from observational astronomy to secure communication and imaging. If the signal is periodic, then averaging over many measurements can help enhance the signal-to-noise ratio. However, for signals that present as a single transient event, the detection capability has been limited. Ataie *et al*. developed a detector that can lift that limitation by combining signal cloning with frequency combs and signal-processing techniques (see the Perspective by Vasilyev). Their detector could detect signals buried within noise that would otherwise be undetectable. — ISO

Science, this issue p. 1343; see also p. 1314

SURFACE SCIENCE

Sticking hydrogen atoms to surfaces

The simplest case of adsorption at a surface—that of a hydrogen atom—is actually quite complicated. This is because it is not clear how this light atom can transfer enough momentum to the heavy surface that it can slow down and stick. Bünermann *et al*. prepared highly energetically controlled hydrogen atoms (see the Perspective by Brune). On a gold surface, inelastic collisions occurred during adsorption, but not when an insulating layer of xenon atoms was used. — PDS

Science, this issue p. 1346; see also p. 1321

NEURONAL DYNAMICS

In vivo imaging of neuronal voltage spikes

Neuroscientists have long sought tools that allow optical imaging of individual neurons' membrane voltage dynamics in awake behaving animals. Gong *et al*. genetically engineered a protein voltage indicator that can report action potentials with <1-ms precision and orders of magnitude lower spike detection error rates than were previously possible. They were thus able to record action potentials and membrane voltage dynamics in the brains of awake mice and fruit flies. — PRS

Science, this issue p. 1361

RESEARCH INVESTMENT

Tracking the knowledge economy

Although the U.S investment in scientific research can be documented readily, its output is harder to track. Zolas *et al*. combined data obtained from eight universities on their doctorate recipients with data from business registries and the U.S. Census Bureau. This allowed them to link Ph.D. recipients to all their subsequent employers. Doctoral recipients tended to stay in academia or join large companies with high salaries. Roughly 20% stayed in the state in which they received their degree. In the year after receiving a Ph.D., mathematicians and computer scientists received the highest salaries, and biologists received the lowest. — BJ

Science, this issue p. 1367

SIGNAL TRANSDUCTION

Altering timing perturbs cell signaling

Biological regulatory systems have been optimized by evolution to accommodate environmental variation. Yet these systems may also have fragile aspects that can be exposed by variation in the timing of signaling events. Mitchell *et al*. studied the properties of the yeast signaling system that allows cells to adapt to changing osmotic conditions. The same properties also made the system sensitive to hyperactivation and the consequent inhibition of cell growth if exposed to oscillations in osmotic conditions with a particular frequency. The identification of similar fragility in other regulatory pathways might prove useful in the development of therapeutic strategies against diseases in which signaling is perturbed, such as cancer and diabetes. — LBR

Science, this issue p. 1379

TRANSCRIPTION

"Please release me, let me go."

RNA polymerase II (Pol II) is

Published by AAAS

the principal protein complex required for gene transcription in metazoan cells. Many genes have a "paused" Pol II near their promoters, waiting to be released so they can start messenger RNA synthesis. Yu *et al*. show that Pol II–associated factor 1 (PAF1) plays a central role in regulating the activation of these paused Pol II complexes. The positive transcription elongation factor b helps recruit PAF1 to the paused Pol II. This facilitates the phosphorylation of Pol II on its C-terminal domain, freeing it to start transcription in earnest. — GR

Science, this issue p. 1383

VITAMIN C RESEARCH

Getting all stressed out by vitamin C

Few experimental cancer therapies have incited as much debate as vitamin C. Yet the mechanistic effect of vitamin C on cancer cells is still poorly understood. Yun *et al*. studied human colorectal cancer cells with KRAS or BRAF mutations and found that they "handle" vitamin C in a different way than other cells, ultimately to their detriment (see the Perspective by Reczek and Chandel). Because a certain receptor is up-regulated in the mutant cells, they take up the oxidized form of vitamin C (dehydroascorbate). This leads to oxidative stress, inactivation of a glycolytic enzyme required by the mutant cells for growth, and finally cell death. Whether the selective toxicity of vitamin C to these mutant cells can be exploited therapeutically remains unclear. — PAK

Science, this issue p. 1391; see also p. 1317

Published by AAAS

REVIEW SUMMARY

MICROBIOME

The global ocean microbiome

Mary Ann Moran

BACKGROUND: Oceanographers began studying the ocean microbiome in earnest over four decades ago, when it was recognized that microbes are responsible for nearly all of the energy flux in this largest and most dilute biological system on Earth. Much has been learned about the microbes that play key roles in every marine element cycle, but much is still unknown about the factors regulating their activity. Although the number of marine microbes per liter of seawater reaches into the billions, their small size means that, statistically, each microbe is separated by 100 to 200 body lengths from its closest neighbors. Yet recognition of microscale structuring of both microbial communities and marine organic matter suggests that the ocean microbiome does not operate as stand-alone cells in a watery soup.

ADVANCES: Several decades of 16*S* ribosomal RNA gene analysis has revealed distinct and recurring bacterial communities in the ocean. More recent characterizations of marine archaea, protists, and viruses are filling out the taxonomic inventories of the ocean microbiome and showing that membership is predictable over seasons, ocean depth, and organic matter features. The retrieval of proteorhodopsin—a gene that allows cells to harvest energy from sunlight without complex photosynthetic machinery—from an uncultured ocean microbe marked the first exciting discovery from the use of "meta-omics" methodologies in the ocean. Now these techniques are the central tools for converting inventories of organisms and functions into explicit linkages between the two. Substantial progress has been made toward unraveling how and where microbes participate in ocean biogeochemical processes, as well as toward recognizing new categories of nonpredatory microbial alliances that operate based on the exchange of nitrogen, vitamins, hormones, and antibiotics.

Several characteristics of the ocean microbiome distinguish it from microbiomes on or in animals, plants, and soils. First, the primary producers that fuel the ocean are exclusively microbial and thus are a part of the microbiome. This is the case for photosynthesis in the surface ocean and for chemosynthesis carried out in deeper waters. The ocean microbiome is responsible for half of all primary production occurring on Earth. Second, trophic categories are particularly difficult to assign in the ocean microbiome, with no clear division of organisms into canonical autotrophic and heterotrophic roles. Proteorhodopsin, anoxygenic phototrophy, and chemolithotrophic energy acquisition from inorganic compounds create trophic mayhem among members of the ocean microbiome. Having multiple strategies for meeting metabolic requirements may be an advantage in this chemically dilute and physically dynamic environment. Last, heterogeneity in the structure of seawater organic matter has become a foundational concept for the ocean microbiome because it aligns with differences in microbial attributes. Bacteria and archaea that live singly in seawater differ from those that intermingle on the various marine polymer networks and organic surfaces in terms of phylogenetic affinity, metabolism, and capabilities for motility, chemotaxis, and defense. Single bacteria and archaea are numerically dominant in terms of cells, genes, and transcripts, but those clustered near surfaces have higher per-cell rates of metabolism and growth. The importance of material exchanges and signaling networks between neighboring cells in the ocean, as well as the consequences spatial arrangements impose on biogeochemical processing, are not yet understood.

ON OUR WEB SITE

Read the full article at http://dx.doi.org/10.1126/science.aac8455

OUTLOOK: Earth's changing climate is predicted to decrease carbon fixation by microbial primary producers, favor smaller picophytoplankton over larger nano- and microphytoplankton, and impose stress on photosynthetic microbes that form calcium carbonate shells. The structure of phytoplankton communities, in turn, has implications for the abundance and composition of organic substrates for heterotrophic microbes, as well as for dictating which trophic strategies will be under selection in the future ocean. Taking stock of the ocean microbiome in terms of cells, genes, transcripts, and proteins now has a long tradition in oceanography. Linking these stocks with the regulation of critical ecosystem functions is the next challenge. One key step in this process is the identification of the molecules that pass between microbes as substrates, nutrients, signaling molecules, and defensive compounds; these are the "currencies" of ocean microbiome function. ■

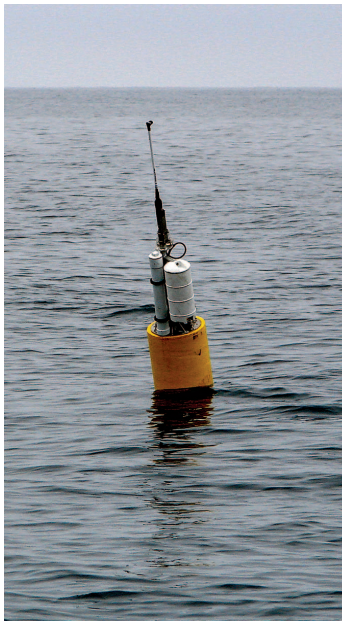

Sampling the ocean microbiome. (**Left**) New instruments such as the Environmental Sample Processor (ESP) (Monterey Bay Aquarium Research Institute) autonomously sample ocean microbes and environmental conditions while deployed at sea. (**Right**) Microbial cells preserved in metal pucks inside the ESP are removed for gene expression analysis.

The list of author affiliations is available in the full article online.
E-mail: mmoran@uga.edu
Cite this article as M. A. Moran, *Science* **350**, aac8455 (2015). DOI: 10.1126/science.aac8455

PHOTOS: (LEFT) J. MOTARD-CÔTÉ; (RIGHT) A. BURNS

Downloaded from www.sciencemag.org on December 14, 2015

REVIEW

MICROBIOME

The global ocean microbiome

Mary Ann Moran

The microbiome of the largest environment on Earth has been gradually revealing its secrets over four decades of study. Despite the dispersed nature of substrates and the transience of surfaces, marine microbes drive essential transformations in all global elemental cycles. Much has been learned about the microbes that carry out key biogeochemical processes, but there are still plenty of ambiguities about the factors important in regulating activity, including the role of microbial interactions. Identifying the molecular "currencies" exchanged within the microbial community will provide key information on microbiome function and its vulnerability to environmental change.

The ocean microbiome is a highly dilute microbial system that covers the majority of Earth's surface and extends an average of 3600 m down to the seafloor. As one of the first microbiomes to be studied, the diversity and distribution of its members is now becoming familiar. Key questions remain, however, regarding how functional capabilities are distributed and what biotic and environmental factors control their rates.

A consistent link is emerging between ocean temperature and both the composition (*1*, *2*) and productivity (*3*) of microbes inhabiting surface seawater. Stratification of the ocean into more discrete layers and consequent reduction in the mixing of nutrient-rich deeper waters to the surface may be one key mechanism behind this link (*3*). Decreases in ocean pH, a direct chemical outcome of increased absorption of CO_2 from the atmosphere, affect the energetic costs to microbes of obtaining inorganic carbon for photosynthesis and the availability of $CaCO_3$ for forming calcareous shells (*4*). To expand our evolving knowledge of the ocean microbiome, recent work has been directed toward explaining how the resident microbes will be affected by the predicted impacts of climate change on the ocean ecosystem.

In 1974, the idea that microorganisms are the major consumers of energy in the sea was formally articulated (*5*). Marine microbes <60 μm in diameter had gradually been recognized as responsible for nearly all of the primary production and respiration occurring in the ocean. This "new paradigm" proposed four decades ago marked the first conceptualization of the ocean microbiome, a community of microorganisms inhabiting 71% of Earth's surface (*6*) and taking part in every one of its major elemental cycles.

Despite population numbers reaching into the billions per liter of seawater, marine bacteria in today's ocean are separated from their closest neighbor by an average of 200 body lengths, due to their small size. The larger but less abundant microbial eukaryotes are separated by an average of ~100 body lengths (*7*). Early views of the ocean microbiome were therefore premised on the idea that interactions between members were indirect, except in predator-prey relationships. Microbes added and removed organic and inorganic materials from the pool of nonliving matter in seawater, and their interactions were mediated largely through the compounds in this pool. Yet the groundwork for recognizing the presence of structured microbial communities, even in dilute ocean waters, had already been laid (*8*). Bacteria were shown to exhibit chemotaxis to phytoplankton exudates (*9*) and to gain energy benefits when clustered around patches of concentrated organic matter (*10*). These were early hints that the ocean microbiome does not operate as stand-alone cells in a watery soup.

The organic matter continuum

The microscale structure of organic materials in seawater that is relevant at the microbial scale, although daunting in its complexity, is now better understood. At the low end of the size range, seawater harbors a pool of dissolved organic molecules released from plankton or leaked during predatory interactions. There are tens of thousands of different structures of these dissolved compounds (*11*), an overwhelming diversity whose origin and fate are only beginning to be understood (*12*, *13*). Intermediate structures include three-dimensional polymer networks, or "microgels" (*14*), that can serve as loci for microbial clustering (*15*), followed by "macrogels" (larger polymer networks, often dominated by polysaccharides). At the upper end of the size range are eukaryotic plankton cells, both alive and dying. Although eukaryotic microbes typically are not heavily colonized by bacteria or archaea when healthy (*16*), the larger cells create zones of concentrated dissolved organic matter extending from their surfaces—these zones are referred to as "phycospheres" (*9*) (Fig. 1). Fecal pellets and other remnants of multicellular organisms also contribute to the organic matter matrix.

The heterogeneity in the structure of seawater organic matter is a foundational concept for the ocean microbiome because it aligns with differences in composition, metabolism, and genome content of the member microbes. Bacteria and archaea that live singly in the ocean passively encounter small molecules and efficiently scavenge them at low concentrations (*17*). Those that intermingle with the various types of polymer networks and organic surfaces have better access to substrates but more neighbors to contend with compared to the free-living cells (Fig. 1). Along with differences in phylogenetic affiliation (*18*) and metabolic capabilities (*19*, *20*), these bacteria and archaea, compared to their free-living counterparts, have genes biased toward capabilities such as signal transduction, defense, anaerobic metabolism, and carbohydrate processing (*21*, *22*) and use motility and chemotaxis to find substrate-rich plumes and filaments associated with the organic matrix (*23*, *24*). In some ways it is surprising that these differences consistently emerge, despite the fact that bacteria and archaea are quite coarsely assigned their place in the organic matter continuum based on passage through a filter: Those passing through a pore of a few micrometers in diameter (typically 2.0 μm) are considered free-living, whereas those retained are considered matrix-associated. Eukaryotic plankton are also divided across this size-based boundary. Small eukaryotes (picoeukaryotes) are collected with the free-living bacteria and archaea by virtue of their small size (*25*). Larger eukaryotic microbes (nano- and microeukaryotes) are collected with matrix-associated bacteria and archaea.

How do inventories and activities compare between microbes associated with different organic matter features of the ocean microbiome? As a general rule of thumb, free-living bacteria and archaea account for more cells (~80%) and more genes and transcripts per volume of seawater (*26*) than those that are matrix-associated (Fig. 2). Yet per-cell rates of metabolism and growth (*27*, *28*) coincident with per-cell inventories of genes and transcripts (*26*, *29*) are higher in the organic matrix-associated bacteria and archaea. Cyanobacteria and picoeukaryotes, minute enough to pass through a 2.0-μm filter pore, are the smallest photosynthetic organisms of the ocean. In seawater, picoeukaryotes are typically an order of magnitude fewer in number than cyanobacteria, but they contribute more biomass per cell (*30*) and can produce nearly equivalent numbers of transcripts (Fig. 2). The larger eukaryotes are generally most abundant where nutrient levels are high, such as in coastal oceans or upwelling regions, and can sometimes rival heterotrophic bacteria in their contribution of microbial genes and transcripts to seawater (Fig. 2).

The assemblage

Early studies typically used the word "assemblage" to refer to microbes in seawater; this term indicates that encounters might be too infrequent

Department of Marine Sciences, University of Georgia, Athens, GA 30602-3636, USA.
E-mail: mmoran@uga.edu

and random to be considered a structured ecological community. Eventually, distinct and predictable microbial communities were identified in the ocean, enabled by new methodologies that did not depend on cultivation. In the first application of a 16*S* ribosomal RNA (rRNA) gene amplicon surveying to a natural ecosystem, three previously unidentified bacterial lineages were discovered among just 12 sequences amplified from Sargasso Sea surface waters (*31*). The SAR11 lineage was uncovered in this pioneering survey and is now recognized as the most abundant bacterial group in the world's oceans (*32*, *33*). Several decades of 16*S* rRNA gene analysis have made us quite knowledgeable about the identity, relative abundance, and patterns of occurrence of marine bacteria and archaea (*2*, *34*, *35*). Most marine microbial communities are composed of few dominant species and a long tail of rare ones (*36*), and species are divided into coexisting populations that imply fine-scale dissection of available resources (*37*, *38*). Latitudinal patterns in species richness similar to those for macroorganisms have been observed (*1*), and community composition is predictable over time (*39*), depth (*40*), and in relation to the structure and composition of seawater organic matter (*18*, *41*–*43*).

More recently, attention has turned to the taxonomic characterization of protists [recognized in 1974 as important in ocean microbial communities (*1*)], viruses [joining the ocean microbiome in 1989 (*44*, *45*)], and archaea [joining in 1992 (*46*, *47*)]. A recent comprehensive accounting of ocean microbes by the *Tara* Oceans expedition found 37,000 bacterial and archaeal species [based on 16 million metagenomic 16*S* rRNA genes (*2*)], 100,000 protist groups [based on 580 million amplified 18*S* rRNA genes (*48*)], and 5500 viral populations [based on 2 million metagenomic sequences and considering only double-stranded DNA bacterial and archaeal viruses (*49*)]. If each sample in this survey is representative of a 0.25-km^3 homogeneous parcel of seawater (*35*), we now have a snapshot in time of a 26-millionth of the ocean microbiome.

Functions in the ocean

A gene retrieved from an uncultured coastal ocean bacterium in 1999 challenged perceptions about energy acquisition by the ocean microbiome (*50*). This gene encodes a rhodopsin protein—belonging to a family previously known only from microbes living in extreme environments—that allows cells without photosynthetic machinery to harvest energy through sunlight-driven proton pumping. The discovery overturned a fundamental distinction between microbes obtaining energy from sunlight versus from organic matter and was a "tip-of-the-iceberg" moment that hinted at other notable microbial physiologies yet to be discovered. Before this study, the main strategy for linking microbes to their roles in the ocean was through "guilt by association," with functional roles of organisms known only by their 16*S* rRNA gene sequences inferred from the physiology of their cultured relatives (if they existed). But the discrepancies in evolutionary history between the highly conserved phylogenetic marker genes and the highly diverse accessory genes (more easily shaped by forces of selection, drift, and horizontal transfer) made this an unsatisfying approach. Further, it confined progress in functional understanding to physiologies known from a narrow suite of cultured microbes.

The proteorhodopsin discovery emerged from the idea to clone random fragments of bacterial DNA from seawater (*51*) and then sequence the regions flanking 16*S* rRNA genes (*50*). Eventually, capabilities for this proteorhodopsin-based energy transduction were found in >40% of bacterial cells in the surface ocean (*52*), representing all major heterotrophic bacterial lineages (*53*), as well as in marine archaea (*54*), microbial eukaryotes (*55*, *56*), and even viruses (*57*). The fact that such a fundamental energy-acquisition mechanism had gone unnoticed for decades was equally sobering and exhilarating.

Metagenomics and other "meta-omics" methodologies thus became central tools for turning disjointed inventories of organisms and functions into explicit linkages between them. For example, our understanding of nitrogen controls on marine primary production was advanced when a widespread unicellular N_2-fixing cyanobacterium, known only by its nitrogenase gene sequence, was successfully hunted down (*58*). Metagenomic sequencing of an enrichment of these elusive UCYN-A cells revealed a surprising cyanobacterial genome lacking genes for photosystem II and carbon fixation and therefore represented a novel category of ocean microbial

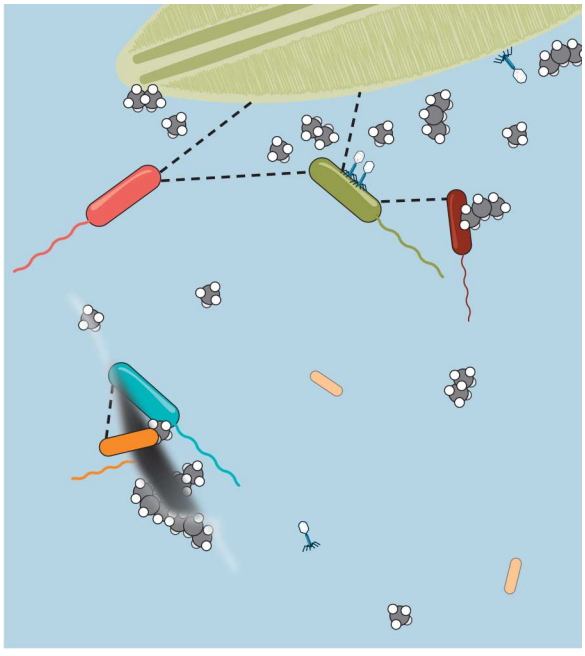

Fig. 1. Microscale structure of the ocean microbiome. The ocean microbiome is dispersed across a dilute matrix of organic matter, populated by bacterial, archaeal, and eukaryotic cells using complex trophic strategies and fueled by microbially fixed carbon. Molecules, gels, and a living diatom represent the organic matter matrix of seawater. Dashed lines indicate predatory or nonpredatory interactions between microbiome members.

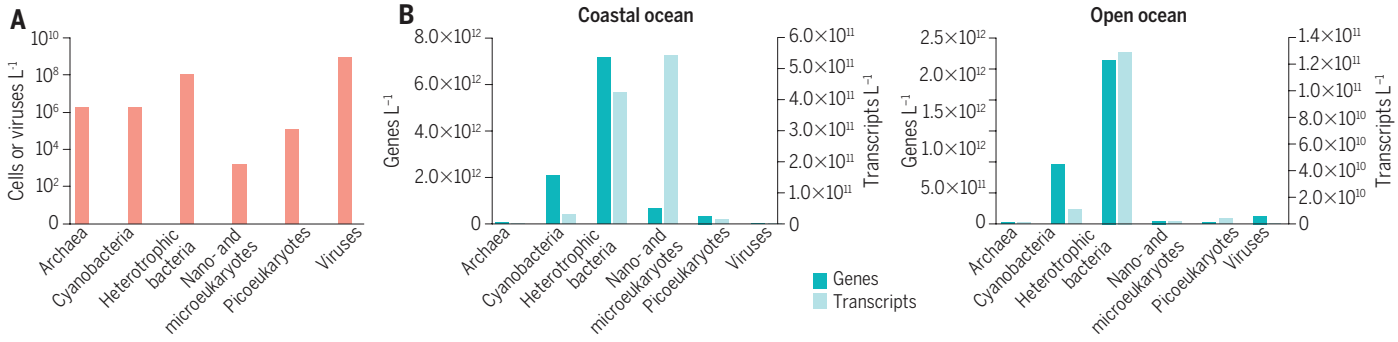

Fig. 2. Organisms and "omics." (**A**) Typical inventory of microbial cells and (**B**) microbial genes and transcripts per liter of ocean water (*26*, *29*).

function that potentially decoupled carbon and nitrogen fixation (58). Similarly, characterization of the marine bacteria responsible for metabolizing a sulfur-containing phytoplankton osmolyte (dimethylsulfoniopropionate) began with gene discovery efforts in cultured marine strains (59–61), followed by metagenomic data mining (52, 59) and then autonomous ocean sensing (62). Regulation of these bacterial genes affects the primary source of biogenic sulfur emissions to the atmosphere (63) and influences sulfur cycling on a global scale (64, 65).

The Global Ocean Sampling data set released in 2004 consists of 1 gigabyte of metagenomic sequence data from the North Atlantic Ocean (66); the *Tara* Oceans data set released in 2015 consists of 7200 gigabytes of metagenomic data from multiple locations and depths across the globe (2). Our knowledge of marine microbial function has been rapidly propelled by the availability of these and other marine meta-omic data sets (67, 68). They provide windows into the multitude of organisms, genes, and transcripts of the ocean microbiome that run the global elemental cycles, buffer atmospheric CO_2 concentrations, and are on the front line of Earth's changing climate (3, 69).

Neighborhood associations

The assemblage perspective of early researchers has given way to a growing understanding of the diverse mechanisms by which ocean microbes interact. Even though microbial cells occupy only ~0.0001% of seawater volume (70), predatory activities are surprisingly efficient. Between 20 and 50% of bacterial cells are killed each day in the ocean by viral infection (71), and a similar amount are consumed by protist grazers (72). Microbial predators and prey are engaged in sophisticated evolutionary arms races; for example, cyanobacterial viruses carry copies of photosynthesis genes, originally captured from their hosts, that ensure a sufficient number of light-harvesting proteins during later stages of infection (73). Whole new categories of nonpredatory microbial alliances are also being recognized. These include

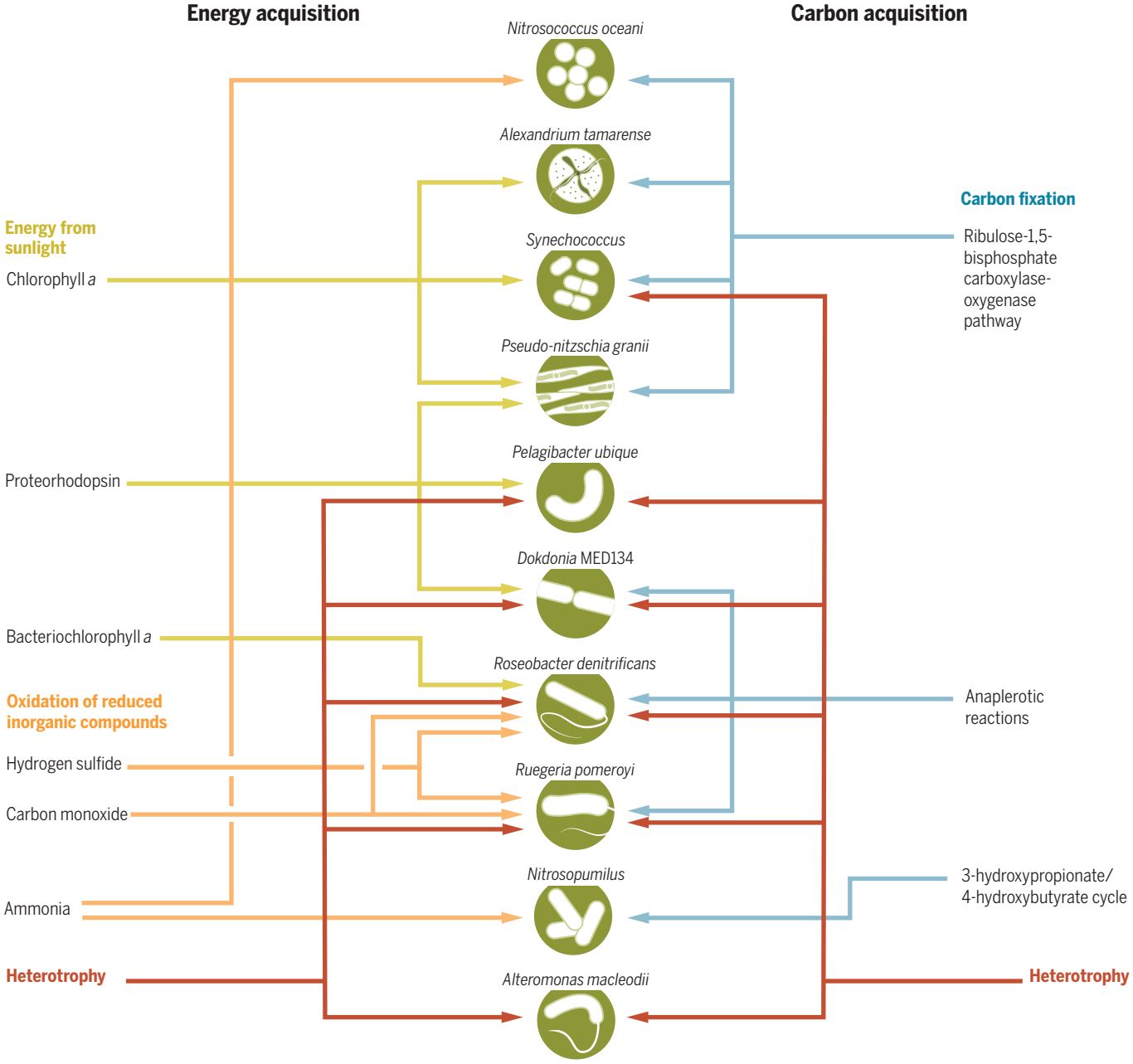

Fig. 3. Trophic categories of the ocean microbiome. The mechanisms by which microbes of oxygenated seawater obtain energy and carbon are grouped in unconventional ways in the trophic hodgepodge of the ocean microbiome (50, 55, 93, 95, 107, 108).

bacteria that release a hormone promoting phytoplankton cell division (*74*); phytoplankton that synthesize novel organic molecules that only certain bacterial species can use as substrates (*75*); nitrogen-fixing cyanobacteria that are endosymbiotic (*76*) or episymbiotic (*77*) with eukaryotic hosts; ciliates that borrow functional chloroplasts from their otherwise-digested prey (*78*); microbes that rely on neighboring cells for essential vitamins and defensive enzymes because they have lost their own capability for synthesis (*79*, *80*); and bacteria that attack neighboring microbes through the production of algicides (*81*), antibacterial compounds (*82*), or both (*83*). At the level of community assembly, there is evidence of patterns in microbial composition and function over time frames of tidal cycles, days, and seasons (*40*, *84*, *85*). The limitation of relying on filters to distinguish microbial roles in the ocean microbiome is now being complemented by methods that track individual cells moving through seawater (*86*), quantify metabolite exchanges between two microbes (*87*), and sequence parasite or symbiont genomes inside a single host microbial cell (*88*). Our appreciation of the richness of microbial interactions in the ocean and their relevance to microbial function is in the very early stages.

An unusual microbiome

Several combined features of the ocean microbiome distinguish it from those on or in animals, plants, and soils. First, the organisms responsible for fueling the system through primary production are exclusively microbial and, thus, part of the microbiome rather than external to it. This is the case for photosynthesis orchestrated by bacteria and eukaryotes in the surface ocean and also for chemosynthesis carried out by archaea and bacteria (*89*). The ocean microbiome is responsible for half of all primary production occurring on Earth (*90*).

Trophic categories are particularly difficult to assign in the ocean microbiome (Fig. 3). The division of organisms into strict autotrophic and heterotrophic roles began to unravel with the realization that proteorhodopsin allowed otherwise heterotrophic microbes to harvest light energy (*91*). It continued with the discovery of anoxygenic phototrophic bacteria in the ocean that acquire energy from sunlight, using bacteriochlorophyll *a* and associated photosynthetic reaction centers. However, unlike photosynthetic microbes, these bacteria are unable to fix CO_2 (*92*–*94*). Other ocean microbes are able to obtain energy from the oxidation of both inorganic compounds, such as carbon monoxide and sulfide, and organic compounds (*95*). One hypothesis to explain the choreographed trophic mayhem of the ocean microbiome is that variability in organic matter and light, as microbes are mixed into and out of surface waters and sink to deep ocean layers, creates an advantage for organisms with numerous metabolic mechanisms. Another is that very low concentrations and supply rates of the individual organic resources in oligotrophic seawater select for microbes that can take advantage of many different energy and carbon sources.

Finally, because the majority of microbes in the ocean microbiome are free-living, only those cells populating the organic matter matrix experience physical interactions at the scale typical of most other microbiomes (Fig. 1). Questions regarding how close microbes need to be to establish networks of signaling and material exchange (*96*–*98*) and what consequences spatial arrangements impose on biogeochemical processing (*24*, *99*, *100*) are still awaiting answers.

Earth's changing climate will affect characteristics of the ocean microbiome. Strengthening of stratification under a warming climate is widely predicted to decrease carbon fixation rates of the ocean's microbial primary producers (*67*) and to favor picophytoplankton over larger nano- and microphytoplankton because the former are better competitors for nutrients (*101*, *102*). Members of the phytoplankton community that form calcium carbonate shells are anticipated to be negatively affected by increasing seawater pH (*103*). In turn, phytoplankton composition has implications for the abundance and composition of the polymer networks and organic surfaces that are the substrates for heterotrophic microbes (*104*). Picophytoplankton may be of insufficient size to create phycospheres detectable by chemosensory mechanisms (*105*), and their dominance would favor free-living over matrix-associated bacteria and archaea (*104*). Certainly, the intricate trophic schemes of marine microorganisms will be subject to redesign in the future ocean, with changes in surface seawater temperature (*95*), CO_2 concentrations (*96*), O_2 concentrations (*95*), nutrient regimes (*68*), and light availability (*97*) shifting the physiological and ecological payoffs of a microbe's life history strategy.

Conclusions

The ocean microbiome fits the definition of an ecological community of microorganisms that share an environment (*106*). As is true for all microbiomes, it is considerably easier to inventory microbial parts (cells, genes, transcripts, proteins, regulatory molecules) than to link the parts with their functions in the community or to understand the give-and-take relationships with a shifting environment. Identifying the molecules—whether as substrates, nutrients, signaling molecules, or defensive compounds—that pass between microbes is an emerging area of microbiome research that will focus attention on the "currencies" of microbial activity. Ultimately, the flux of materials, both among microbes and between microbes and their surroundings, constitutes microbiome function and determines its response to external changes.

REFERENCES AND NOTES

1. J. A. Fuhrman *et al*., A latitudinal diversity gradient in planktonic marine bacteria. *Proc. Natl. Acad. Sci. U.S.A.* **105**, 7774–7778 (2008). doi: 10.1073/pnas.0803070105; pmid: 18509059
2. S. Sunagawa *et al*., Structure and function of the global ocean microbiome. *Science* **348**, 1261359 (2015). doi: 10.1126/science.1261359; pmid: 25999513
3. M. J. Behrenfeld *et al*., Climate-driven trends in contemporary ocean productivity. *Nature* **444**, 752–755 (2006). doi: 10.1038/nature05317; pmid: 17151666
4. S. C. Doney, V. J. Fabry, R. A. Feely, J. A. Kleypas, Ocean acidification: The other CO_2 problem. *Annu. Rev. Mar. Sci.* **1**, 169–192 (2009). doi: 10.1146/annurev.marine.010908.163834; pmid: 21141034
5. L. R. Pomeroy, Oceans food web, a changing paradigm. *Bioscience* **24**, 499–504 (1974). doi: 10.2307/1296885
6. B. W. Eakins, G. F. Sharman, "Volumes of the world's oceans from ETOPO1" (NOAA National Geophysical Data Center, Boulder, CO, 2010).
7. Body length calculations assume 1×10^9 bacterial cells per liter of 0.5-μm average diameter and 1×10^6 microbial eukaryote cells per liter of 100-μm average diameter.
8. F. Azam, Microbial control of oceanic carbon flux: The plot thickens. *Science* **280**, 694–696 (1998). doi: 10.1126/science.280.5364.694
9. W. Bell, R. Mitchell, Chemotactic and growth responses of marine bacteria to algal extracellular products. *Biol. Bull.* **143**, 265–277 (1972). doi: 10.2307/1540052
10. F. Azam, J. Ammerman, in *Flows of Energy and Materials in Marine Ecosystems*, M. J. R. Fasham, Ed. (Springer, 1984), vol. 13, chap. 14, pp. 345–360.
11. B. P. Koch, M. R. Witt, R. Engbrodt, T. Dittmar, G. Kattner, Molecular formulae of marine and terrigenous dissolved organic matter detected by electrospray ionization Fourier transform ion cyclotron resonance mass spectrometry. *Geochim. Cosmochim. Acta* **69**, 3299–3308 (2005). doi: 10.1016/j.gca.2005.02.027
12. J. M. Arrieta *et al*., Dilution limits dissolved organic carbon utilization in the deep ocean. *Science* **348**, 331–333 (2015). doi: 10.1126/science.1258955; pmid: 25883355
13. O. J. Lechtenfeld, N. Hertkorn, Y. Shen, M. Witt, R. Benner, Marine sequestration of carbon in bacterial metabolites. *Nat. Commun.* **6**, 6711 (2015). doi: 10.1038/ncomms7711; pmid: 25826720
14. W.-C. Chin, M. V. Orellana, P. Verdugo, Spontaneous assembly of marine dissolved organic matter into polymer gels. *Nature* **391**, 568–572 (1998). doi: 10.1038/35345
15. P. Verdugo *et al*., The oceanic gel phase: A bridge in the DOM-POM continuum. *Mar. Chem.* **92**, 67–85 (2004). doi: 10.1016/j.marchem.2004.06.017
16. M. R. Droop, K. G. R. Elson, Are pelagic diatoms free from bacteria? *Nature* **211**, 1096–1097 (1966). doi: 10.1038/2111096a0
17. S. J. Giovannoni, J. Cameron Thrash, B. Temperton, Implications of streamlining theory for microbial ecology. *ISME J.* **8**, 1553–1565 (2014). doi: 10.1038/ismej.2014.60; pmid: 24739623
18. E. F. DeLong, D. G. Franks, A. L. Alldredge, Phylogenetic diversity of aggregate-attached vs. free-living marine bacterial assemblages. *Limnol. Oceanogr.* **38**, 924–934 (1993). doi: 10.4319/lo.1993.38.5.0924
19. A. L. Alldredge, Y. Cohen, Can microscale chemical patches persist in the sea? Microelectrode study of marine snow, fecal pellets. *Science* **235**, 689–691 (1987). doi: 10.1126/science.235.4789.689; pmid: 17833630
20. K. Ziervogel, C. Arnosti, Polysaccharide hydrolysis in aggregates and free enzyme activity in aggregate-free seawater from the north-eastern Gulf of Mexico. *Environ. Microbiol.* **10**, 289–299 (2008). doi: 10.1111/j.1462-2920.2007.01451.x; pmid: 18093165
21. F. M. Lauro *et al*., The genomic basis of trophic strategy in marine bacteria. *Proc. Natl. Acad. Sci. U.S.A.* **106**, 15527–15533 (2009). doi: 10.1073/pnas.0903507106; pmid: 19805210
22. H. Luo, M. A. Moran, How do divergent ecological strategies emerge among marine bacterioplankton lineages? *Trends Microbiol.* **23**, 577–584 (2015). pmid: 26051014
23. T. Kiørboe, G. A. Jackson, Marine snow, organic solute plumes, and optimal chemosensory behavior of bacteria. *Limnol. Oceanogr.* **46**, 1309–1318 (2001). doi: 10.4319/lo.2001.46.6.1309
24. R. Stocker, Marine microbes see a sea of gradients. *Science* **338**, 628–633 (2012). doi: 10.1126/science.1208929; pmid: 23118182
25. A. Z. Worden, J. K. Nolan, B. Palenik, Assessing the dynamics and ecology of marine picophytoplankton: The importance of the eukaryotic component. *Limnol. Oceanogr.* **49**, 168–179 (2004). doi: 10.4319/lo.2004.49.1.0168
26. B. M. Satinsky *et al*., Microspatial gene expression patterns in the Amazon River Plume. *Proc. Natl. Acad. Sci. U.S.A.* **111**, 11085–11090 (2014). pmid: 25024226

27. J. Iriberri, M. Unanue, I. Barcina, L. Egea, Seasonal variation in population density and heterotrophic activity of attached and free-living bacteria in coastal waters. *Appl. Environ. Microbiol.* **53**, 2308–2314 (1987). pmid: 16347451
28. H. P. Grossart, K. W. Tang, T. Kiørboe, H. Ploug, Comparison of cell-specific activity between free-living and attached bacteria using isolates and natural assemblages. *FEMS Microbiol. Lett.* **266**, 194–200 (2007). doi: 10.1111/j.1574-6968.2006.00520.x; pmid: 17233730
29. B. M. Satinsky *et al*., The Amazon continuum dataset: Quantitative metagenomic and metatranscriptomic inventories of the Amazon River plume, June 2010. *Microbiome* **2**, 17 (2014). doi: 10.1186/2049-2618-2-17; pmid: 24883185
30. M. L. Cuvelier *et al*., Targeted metagenomics and ecology of globally important uncultured eukaryotic phytoplankton. *Proc. Natl. Acad. Sci. U.S.A.* **107**, 14679–14684 (2010). doi: 10.1073/pnas.1001665107; pmid: 20668244
31. S. J. Giovannoni, T. B. Britschgi, C. L. Moyer, K. G. Field, Genetic diversity in Sargasso Sea bacterioplankton. *Nature* **345**, 60–63 (1990). doi: 10.1038/345060a0; pmid: 2330053
32. R. M. Morris *et al*., SAR11 clade dominates ocean surface bacterioplankton communities. *Nature* **420**, 806–810 (2002). doi: 10.1038/nature01240; pmid: 12490947
33. M. V. Brown *et al*., Global biogeography of SAR11 marine bacteria. *Mol. Syst. Biol.* **8**, 595 (2012). doi: 10.1038/msb.2012.28; pmid: 22806143
34. S. J. Giovannoni, U. Stingl, Molecular diversity and ecology of microbial plankton. *Nature* **437**, 343–348 (2005). doi: 10.1038/nature04158; pmid: 16163344
35. J. A. Fuhrman, Microbial community structure and its functional implications. *Nature* **459**, 193–199 (2009). doi: 10.1038/nature08058; pmid: 19444205
36. C. Pedrós-Alió, The rare bacterial biosphere. *Annu. Rev. Mar. Sci.* **4**, 449–466 (2012). doi: 10.1146/annurev-marine-120710-100948; pmid: 22457983
37. S. G. Acinas *et al*., Fine-scale phylogenetic architecture of a complex bacterial community. *Nature* **430**, 551–554 (2004). doi: 10.1038/nature02649; pmid: 15282603
38. N. Kashtan *et al*., Single-cell genomics reveals hundreds of coexisting subpopulations in wild *Prochlorococcus*. *Science* **344**, 416–420 (2014). doi: 10.1126/science.1248575; pmid: 24763590
39. J. A. Fuhrman *et al*., Annually reoccurring bacterial communities are predictable from ocean conditions. *Proc. Natl. Acad. Sci. U.S.A.* **103**, 13104–13109 (2006). doi: 10.1073/pnas.0602399103; pmid: 16938845
40. S. J. Giovannoni, K. L. Vergin, Seasonality in ocean microbial communities. *Science* **335**, 671–676 (2012). doi: 10.1126/science.1198078; pmid: 22323811
41. S. G. Acinas, J. Antón, F. Rodríguez-Valera, Diversity of free-living and attached bacteria in offshore Western Mediterranean waters as depicted by analysis of genes encoding 16S rRNA. *Appl. Environ. Microbiol.* **65**, 514–522 (1999). pmid: 9925576
42. J. N. Rooney-Varga *et al*., Links between phytoplankton and bacterial community dynamics in a coastal marine environment. *Microb. Ecol.* **49**, 163–175 (2005). doi: 10.1007/s00248-003-1057-0; pmid: 15688258
43. H. Teeling *et al*., Substrate-controlled succession of marine bacterioplankton populations induced by a phytoplankton bloom. *Science* **336**, 608–611 (2012). doi: 10.1126/science.1218344; pmid: 22556258
44. O. Bergh, K. Y. Børsheim, G. Bratbak, M. Heldal, High abundance of viruses found in aquatic environments. *Nature* **340**, 467–468 (1989). doi: 10.1038/340467a0; pmid: 2755508
45. L. M. Proctor, J. A. Fuhrman, Viral mortality of marine bacteria and cyanobacteria. *Nature* **343**, 60–62 (1990). doi: 10.1038/343060a0
46. J. A. Fuhrman, K. McCallum, A. A. Davis, Novel major archaebacterial group from marine plankton. *Nature* **356**, 148–149 (1992). doi: 10.1038/356148a0; pmid: 1545865
47. E. F. DeLong, Archaea in coastal marine environments. *Proc. Natl. Acad. Sci. U.S.A.* **89**, 5685–5689 (1992). doi: 10.1073/pnas.89.12.5685; pmid: 1608980
48. C. de Vargas *et al*., Eukaryotic plankton diversity in the sunlit ocean. *Science* **348**, 1261605 (2015). doi: 10.1126/science.1261605; pmid: 25999516
49. J. R. Brum *et al*., Patterns and ecological drivers of ocean viral communities. *Science* **348**, 1261498 (2015). doi: 10.1126/science.1261498; pmid: 25999515
50. O. Béjà *et al*., Bacterial rhodopsin: Evidence for a new type of phototrophy in the sea. *Science* **289**, 1902–1906 (2000). doi: 10.1126/science.289.5486.1902; pmid: 10988064
51. T. M. Schmidt, E. F. DeLong, N. R. Pace, Analysis of a marine picoplankton community by 16S rRNA gene cloning and sequencing. *J. Bacteriol.* **173**, 4371–4378 (1991). pmid: 2066334
52. E. C. Howard, S. Sun, E. J. Biers, M. A. Moran, Abundant and diverse bacteria involved in DMSP degradation in marine surface waters. *Environ. Microbiol.* **10**, 2397–2410 (2008). doi: 10.1111/j.1462-2920.2008.01665.x; pmid: 18510552
53. O. Béjà, J. Pinhassi, J. L. Spudich, in *Encyclopedia of Biodiversity*, S. A. Levin, Ed. (Academic Press, Waltham, MA, 2013), vol. 6, pp. 280–285.
54. N. U. Frigaard, A. Martinez, T. J. Mincer, E. F. DeLong, Proteorhodopsin lateral gene transfer between marine planktonic Bacteria and Archaea. *Nature* **439**, 847–850 (2006). doi: 10.1038/nature04435; pmid: 16482157
55. A. Marchetti, D. Catlett, B. M. Hopkinson, K. Ellis, N. Cassar, Marine diatom proteorhodopsins and their potential role in coping with low iron availability. *ISME J.* **9**, 2745–2748 (2015). doi: 10.1038/ismej.2015.74; pmid: 26023874
56. X. Shi *et al*., Rhodopsin gene expression regulated by the light dark cycle, light spectrum and light intensity in the dinoflagellate Prorocentrum. *Front. Microbiol.* **6**, 555 (2015). doi: 10.3389/fmicb.2015.00555; pmid: 26082770
57. N. Yutin, E. V. Koonin, Proteorhodopsin genes in giant viruses. *Biol. Direct* **7**, 34 (2012). doi: 10.1186/1745-6150-7-34; pmid: 23036091
58. J. P. Zehr *et al*., Globally distributed uncultivated oceanic N_2-fixing cyanobacteria lack oxygenic photosystem II. *Science* **322**, 1110–1112 (2008). doi: 10.1126/science.1165340; pmid: 19008448
59. E. C. Howard *et al*., Bacterial taxa that limit sulfur flux from the ocean. *Science* **314**, 649–652 (2006). doi: 10.1126/science.1130657; pmid: 17068264
60. A. R. J. Curson, J. D. Todd, M. J. Sullivan, A. W. B. Johnston, Catabolism of dimethylsulphoniopropionate: Microorganisms, enzymes and genes. *Nat. Rev. Microbiol.* **9**, 849–859 (2011). doi: 10.1038/nrmicro2653; pmid: 21986900
61. C. R. Reisch *et al*., Novel pathway for assimilation of dimethylsulphoniopropionate widespread in marine bacteria. *Nature* **473**, 208–211 (2011). doi: 10.1038/nature10078; pmid: 21562561
62. V. A. Varaljay *et al*., Single-taxon field measurements of bacterial gene regulation controlling DMSP fate. *ISME J.* **9**, 1677–1686 (2015). doi: 10.1038/ismej.2015.23; pmid: 25700338
63. R. Simó, Production of atmospheric sulfur by oceanic plankton: Biogeochemical, ecological and evolutionary links. *Trends Ecol. Evol.* **16**, 287–294 (2001). doi: 10.1016/S0169-5347(01)02152-8; pmid: 11369106
64. R. P. Kiene, L. J. Linn, J. A. Bruton, New and important roles for DMSP in marine microbial communities. *J. Sea Res.* **43**, 209–224 (2000). doi: 10.1016/S1385-1101(00)00023-X
65. P. K. Quinn, T. S. Bates, The case against climate regulation via oceanic phytoplankton sulphur emissions. *Nature* **480**, 51–56 (2011). doi: 10.1038/nature10580; pmid: 22129724
66. J. C. Venter *et al*., Environmental genome shotgun sequencing of the Sargasso Sea. *Science* **304**, 66–74 (2004). doi: 10.1126/science.1093857; pmid: 15001713
67. E. F. DeLong, Microbial community genomics in the ocean. *Nat. Rev. Microbiol.* **3**, 459–469 (2005). doi: 10.1038/nrmicro1158; pmid: 15886695
68. S. M. Gifford, S. Sharma, J. M. Rinta-Kanto, M. A. Moran, Quantitative analysis of a deeply sequenced marine microbial metatranscriptome. *ISME J.* **5**, 461–472 (2011). doi: 10.1038/ismej.2010.141; pmid: 20844569
69. C. M. Moore *et al*., Processes and patterns of oceanic nutrient limitation. *Nat. Geosci.* **6**, 701–710 (2013). doi: 10.1038/ngeo1765
70. The percent of seawater volume occupied by microbial biomass was estimated by assuming average volumes of 0.1, 2, and 550 μm^3 for marine heterotrophic bacteria, cyanobacteria, and protists, respectively. Average cell numbers are assumed to be 1×10^9, 1×10^7, and 1×10^6 cells per liter, respectively.
71. J. A. Fuhrman, Marine viruses and their biogeochemical and ecological effects. *Nature* **399**, 541–548 (1999). doi: 10.1038/21119; pmid: 10376593
72. E. Sherr, B. Sherr, in *Microbial Ecology of the Oceans*, D. L. Kirchman, Ed. (Wiley, Hoboken, NJ, 2008), pp. 27–44.
73. D. Lindell, J. D. Jaffe, Z. I. Johnson, G. M. Church, S. W. Chisholm, Photosynthesis genes in marine viruses yield proteins during host infection. *Nature* **438**, 86–89 (2005). doi: 10.1038/nature04111; pmid: 16222247
74. S. A. Amin *et al*., Interaction and signalling between a cosmopolitan phytoplankton and associated bacteria. *Nature* **522**, 98–101 (2015). doi: 10.1038/nature14488; pmid: 26017307
75. B. P. Durham *et al*., Cryptic carbon and sulfur cycling between surface ocean plankton. *Proc. Natl. Acad. Sci. U.S.A.* **112**, 453–457 (2015). doi: 10.1073/pnas.1413137112; pmid: 25548163
76. T. A. Villareal, Nitrogen-fixation by the cyanobacterial symbiont of the diatom genus *Hemiaulus*. *Mar. Ecol. Prog. Ser.* **76**, 201–204 (1991). doi: 10.3354/meps076201
77. A. W. Thompson *et al*., Unicellular cyanobacterium symbiotic with a single-celled eukaryotic alga. *Science* **337**, 1546–1550 (2012). doi: 10.1126/science.1222700; pmid: 22997339
78. D. K. Stoecker, A. E. Michaels, L. H. Davis, Large proportion of marine planktonic ciliates found to contain functional chloroplasts. *Nature* **326**, 790–792 (1987). doi: 10.1038/326790a0
79. J. J. Morris, Z. I. Johnson, M. J. Szul, M. Keller, E. R. Zinser, Dependence of the cyanobacterium *Prochlorococcus* on hydrogen peroxide scavenging microbes for growth at the ocean's surface. *PLOS ONE* **6**, e16805 (2011). doi: 10.1371/journal.pone.0016805; pmid: 21304826
80. E. M. Bertrand *et al*., Phytoplankton-bacterial interactions mediate micronutrient colimitation at the coastal Antarctic sea ice edge. *Proc. Natl. Acad. Sci. U.S.A.* **112**, 9938–9943 (2015). doi: 10.1073/pnas.1501615112; pmid: 26221022
81. X. Mayali, P. J. S. Franks, F. Azam, Cultivation and ecosystem role of a marine roseobacter clade-affiliated cluster bacterium. *Appl. Environ. Microbiol.* **74**, 2595–2603 (2008). doi: 10.1128/AEM.02191-07; pmid: 18326670
82. J. B. Bruhn, L. Gram, R. Belas, Production of antibacterial compounds and biofilm formation by *Roseobacter* species are influenced by culture conditions. *Appl. Environ. Microbiol.* **73**, 442–450 (2007). doi: 10.1128/AEM.02238-06; pmid: 17098910
83. M. R. Seyedsayamdost, R. J. Case, R. Kolter, J. Clardy, The Jekyll-and-Hyde chemistry of *Phaeobacter gallaeciensis*. *Nat. Chem.* **3**, 331–335 (2011). doi: 10.1038/nchem.1002; pmid: 21430694
84. S. M. Gifford, S. Sharma, M. A. Moran, Linking activity and function to ecosystem dynamics in a coastal bacterioplankton community. *Front. Microbiol.* **5**, 185 (2014). doi: 10.3389/fmicb.2014.00185; pmid: 24795712
85. E. A. Ottesen *et al*., Multispecies diel transcriptional oscillations in open ocean heterotrophic bacterial assemblages. *Science* **345**, 207–212 (2014). doi: 10.1126/science.1252476; pmid: 25013074
86. R. Stocker, J. R. Seymour, A. Samadani, D. E. Hunt, M. F. Polz, Rapid chemotactic response enables marine bacteria to exploit ephemeral microscale nutrient patches. *Proc. Natl. Acad. Sci. U.S.A.* **105**, 4209–4214 (2008). doi: 10.1073/pnas.0709765105; pmid: 18337491
87. R. A. Foster *et al*., Nitrogen fixation and transfer in open ocean diatom-cyanobacterial symbioses. *ISME J.* **5**, 1484–1493 (2011). doi: 10.1038/ismej.2011.26; pmid: 21451586
88. R. Stepanauskas, Wiretapping into microbial interactions by single cell genomics. *Front. Microbiol.* **6**, 258 (2015). doi: 10.3389/fmicb.2015.00258; pmid: 25904902
89. M. Pester, C. Schleper, M. Wagner, The Thaumarchaeota: An emerging view of their phylogeny and ecophysiology. *Curr. Opin. Microbiol.* **14**, 300–306 (2011). doi: 10.1016/j.mib.2011.04.007; pmid: 21546306
90. D. A. Hansell, C. A. Carlson, D. J. Repeta, R. Schlitzer, Dissolved organic matter in the ocean: A controversy stimulates new insights. *Oceanography* **22**, 202–211 (2009). doi: 10.5670/oceanog.2009.109
91. M. A. Moran, W. L. Miller, Resourceful heterotrophs make the most of light in the coastal ocean. *Nat. Rev. Microbiol.* **5**, 792–800 (2007). doi: 10.1038/nrmicro1746; pmid: 17828280
92. O. Béjà *et al*., Unsuspected diversity among marine aerobic anoxygenic phototrophs. *Nature* **415**, 630–633 (2002). doi: 10.1038/415630a; pmid: 11832943
93. Z. S. Kolber *et al*., Contribution of aerobic photoheterotrophic bacteria to the carbon cycle in the ocean. *Science* **292**, 2492–2495 (2001). doi: 10.1126/science.1059707; pmid: 11431568

94. N. Yutin *et al*., Assessing diversity and biogeography of aerobic anoxygenic phototrophic bacteria in surface waters of the Atlantic and Pacific Oceans using the Global Ocean Sampling expedition metagenomes. *Environ. Microbiol.* **9**, 1464–1475 (2007). doi: 10.1111/j.1462-2920.2007.01265.x; pmid: 17504484
95. M. A. Moran *et al*., Genome sequence of *Silicibacter pomeroyi* reveals adaptations to the marine environment. *Nature* **432**, 910–913 (2004). doi: 10.1038/nature03170; pmid: 15602564
96. S. A. Amin *et al*., Photolysis of iron-siderophore chelates promotes bacterial-algal mutualism. *Proc. Natl. Acad. Sci. U.S.A.* **106**, 17071–17076 (2009). doi: 10.1073/pnas.0905512106; pmid: 19805106
97. L. Gram, H. P. Grossart, A. Schlingloff, T. Kiørboe, Possible quorum sensing in marine snow bacteria: Production of acylated homoserine lactones by *Roseobacter* strains isolated from marine snow. *Appl. Environ. Microbiol.* **68**, 4111–4116 (2002). doi: 10.1128/AEM.68.8.4111-4116.2002; pmid: 12147515
98. O. P. Persson *et al*., High abundance of virulence gene homologues in marine bacteria. *Environ. Microbiol.* **11**, 1348–1357 (2009). doi: 10.1111/j.1462-2920.2008.01861.x; pmid: 19207573
99. H. Geng, R. Belas, Molecular mechanisms underlying roseobacter-phytoplankton symbioses. *Curr. Opin. Biotechnol.* **21**, 332–338 (2010). doi: 10.1016/j.copbio.2010.03.013; pmid: 20399092
100. J. Hollibaugh, F. Azam, Microbial degradation of dissolved proteins in seawater. *Limnol. Oceanogr.* **28**, 1104–1116 (1983). doi: 10.4319/lo.1983.28.6.1104
101. I. Marinov, S. C. Doney, I. D. Lima, Response of ocean phytoplankton community structure to climate change over the 21st century: Partitioning the effects of nutrients, temperature and light. *Biogeosciences* **7**, 3941–3959 (2010). doi: 10.5194/bg-7-3941-2010
102. G. T. Taylor *et al*., Ecosystem responses in the southern Caribbean Sea to global climate change. *Proc. Natl. Acad. Sci. U.S.A.* **109**, 19315–19320 (2012). doi: 10.1073/pnas.1207514109; pmid: 23071299
103. U. Riebesell, A. Körtzinger, A. Oschlies, Sensitivities of marine carbon fluxes to ocean change. *Proc. Natl. Acad. Sci. U.S.A.* **106**, 20602–20609 (2009). doi: 10.1073/pnas.0813291106; pmid: 19995981
104. H. Luo, M. Csuros, A. L. Hughes, M. A. Moran, Evolution of divergent life history strategies in marine alphaproteobacteria. *mBio* **4**, e00373-13 (2013). doi: 10.1128/mBio.00373-13; pmid: 23839216
105. G. A. Jackson, Simulating chemosensory responses of marine microorganisms. *Limnol. Oceanogr.* **32**, 1253–1266 (1987). doi: 10.4319/lo.1987.32.6.1253
106. J. Lederberg, A. T. McCray, 'Ome sweet 'omics - A genealogical treasury of words. *The Scientist* **15**, 8 (2001).
107. J. Palovaara *et al*., Stimulation of growth by proteorhodopsin phototrophy involves regulation of central metabolic pathways in marine planktonic bacteria. *Proc. Natl. Acad. Sci. U.S.A.* **111**, E3650–E3658 (2014). doi: 10.1073/pnas.1402617111; pmid: 25136122
108. W. D. Swingley *et al*., The complete genome sequence of *Roseobacter denitrificans* reveals a mixotrophic rather than photosynthetic metabolism. *J. Bacteriol.* **189**, 683–690 (2007). doi: 10.1128/JB.01390-06; pmid: 17098896

ACKNOWLEDGMENTS

J. T. Hollibaugh, K. Ross, M. Landa, A. Burns, and B. Nowinski provided helpful discussions and C. English assisted with graphics. This work was supported by NSF grants OCE-1356010 and OCE-1342694 and, in part, by the Gordon and Betty Moore Foundation through grant 538.01.

10.1126/science.aac8455

RESEARCH ARTICLE SUMMARY

PROTEIN STRUCTURE

Principles of assembly reveal a periodic table of protein complexes

Sebastian E. Ahnert,* Joseph A. Marsh,* Helena Hernández, Carol V. Robinson, Sarah A. Teichmann†

INTRODUCTION: The assembly of proteins into complexes is crucial for most biological processes. The three-dimensional structures of many thousands of homomeric and heteromeric protein complexes have now been determined, and this has had a broad impact on our understanding of biological function and evolution. Despite this, the organizing principles that underlie the great diversity of protein quaternary structures observed in nature remain poorly understood, particularly in comparison with protein folds, which have been extensively classified in terms of their architecture and evolutionary relationships.

RATIONALE: In this work, we sought a comprehensive understanding of the general principles underlying quaternary structure organization. Our approach was to consider protein complexes in terms of their assembly. Many protein complexes assemble spontaneously via ordered pathways in vitro, and these pathways have a strong tendency to be evolutionarily conserved. Furthermore, there are strong similarities between protein complex assembly and evolutionary pathways, with assembly pathways often being reflective of evolutionary histories, and vice versa. This suggests that it may be useful to consider the types of protein complexes that have evolved from the perspective of what assembly pathways are possible.

RESULTS: We first examined the fundamental steps by which protein complexes can assemble, using electrospray mass spectrometry experiments, literature-curated assembly data, and a large-scale analysis of protein complex structures. We found that most assembly steps can be classified into three basic types: dimerization, cyclization, and heteromeric subunit addition. By systematically combining different assembly steps in different ways, we were able to enumerate a large set of possible quaternary structure topologies, or patterns of key interfaces between the proteins within a complex. The vast majority of real protein complex structures lie within these topologies. This enables a natural organization of protein complexes into a "periodic table," because each heteromer can be related to a simpler symmetric homomer topology. Exceptions are mostly the result of quaternary structure assignment errors, or cases where sequence-identical subunits can have different interactions and thus introduce asymmetry. Many of these asymmetric complexes fit the paradigm of a periodic table when their assembly role is considered. Finally, we implemented a model based on the periodic table, which predicts the expected frequencies of each quaternary structure topology, including those not yet observed. Our model correctly predicts quaternary structure topologies of recent crystal and electron microscopy structures that are not included in our original data set.

ON OUR WEB SITE

Read the full article at http://dx.doi.org/10.1126/science.aaa2245

CONCLUSION: This work explains much of the observed distribution of known protein complexes in quaternary structure space and provides a framework for understanding their evolution. In addition, it can contribute considerably to the prediction and modeling of quaternary structures by specifying which topologies are most likely to be adopted by a complex with a given stoichiometry, potentially providing constraints for multi-subunit docking and hybrid methods. Lastly, it could help in the bioengineering of protein complexes by identifying which topologies are most likely to be stable, and thus which types of essential interfaces need to be engineered. ■

The list of author affiliations is available in the full article online.
*These authors contributed equally to this work.
†Corresponding author. E-mail: saraht@ebi.ac.uk
Cite this paper as S.E. Ahnert *et al.*, *Science* 350, aaa2245 (2015). DOI: 10.1126/science.aaa2245

Protein assembly steps lead to a periodic table of protein complexes and can predict likely quaternary structure topologies. Three main assembly steps are possible: cyclization, dimerization, and subunit addition. By combining these in different ways, a large set of possible quaternary structure topologies can be generated. These can be arranged on a periodic table that describes most known complexes and that can predict previously unobserved topologies.

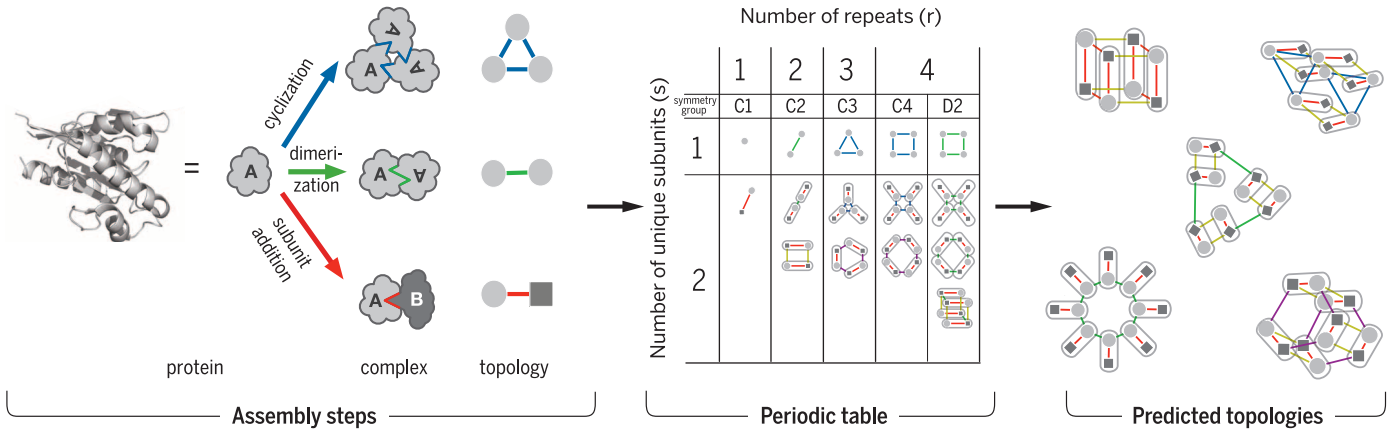

Downloaded from www.sciencemag.org on December 14, 2015

RESEARCH ARTICLE

PROTEIN STRUCTURE

Principles of assembly reveal a periodic table of protein complexes

Sebastian E. Ahnert,[1]* Joseph A. Marsh,[2,3]* Helena Hernández,[4] Carol V. Robinson,[4] Sarah A. Teichmann[1,3,5]†

Structural insights into protein complexes have had a broad impact on our understanding of biological function and evolution. In this work, we sought a comprehensive understanding of the general principles underlying quaternary structure organization in protein complexes. We first examined the fundamental steps by which protein complexes can assemble, using experimental and structure-based characterization of assembly pathways. Most assembly transitions can be classified into three basic types, which can then be used to exhaustively enumerate a large set of possible quaternary structure topologies. These topologies, which include the vast majority of observed protein complex structures, enable a natural organization of protein complexes into a periodic table. On the basis of this table, we can accurately predict the expected frequencies of quaternary structure topologies, including those not yet observed. These results have important implications for quaternary structure prediction, modeling, and engineering.

Evolution has given rise to an enormous variety of protein complexes (*1*–*3*). The organizing principles that underlie this diversity remain poorly understood, particularly in comparison with protein folds, which have been classified extensively in terms of their architecture (*4*–*6*) and evolution (*7*, *8*). However, network models have shown considerable promise in recent years for characterizing and comparing protein complexes. For example, complexes are often represented as networks of associations between proteins, with little consideration for structure or stoichiometry. Alternatively, a graph representation, which we introduced several years ago, can be used to capture the main features of quaternary structure topology (*9*). In this model, the nodes are the polypeptide chains, defined by their amino acid sequence and often referred to as subunits, and the edges are the interfaces between physically interacting chains, weighted according to size.

Many protein complexes assemble spontaneously via ordered pathways in vitro, and we have shown that these assembly pathways have a strong tendency to be evolutionarily conserved (*10*, *11*). Furthermore, there are strong similarities between protein complex assembly and evolutionary pathways, with assembly pathways often being reflective of evolutionary histories, and vice versa (*12*). Thus, quaternary structure evolution essentially can be thought of as an assembly process occurring on an evolutionary time scale. This suggests that it may be useful to consider the types of protein complexes that have evolved from the perspective of assembly pathways.

In this work, we attempted to understand and explain the organization of protein complexes in quaternary structure space, using the principles of assembly. First, by characterizing the assembly pathways of a large number of protein complexes, we found that assembly can be explained generally by three basic steps: dimerization, cyclization, and subunit addition. Combinations of these steps allow us to exhaustively enumerate possible quaternary structure topologies within a given region of quaternary structure space.

To achieve this, we considered each polypeptide chain as a distinct self-assembly building block and considered all the ways in which interfaces can be distributed across the chains that are present in the complex. The large variety of possible topologies generated by this approach were then compared to observed structures. We found that ~92% of known protein complex structures are compatible with this model.

A major benefit of this assembly-centric view of protein complexes is that it enables a natural organization of complexes into a "periodic table," ordered by the number of subunit repeats (r) and the number of subunit types that are unique within a given complex (s). Exceptions are primarily the result of quaternary structure assignment errors or cases where sequence-identical subunits can have different interactions and thus introduce asymmetry. Many of these asymmetric complexes fit the paradigm of a periodic table when their assembly role (rather than their subunit identity) is considered.

Finally, by combining the periodic table with our enumeration, we introduced a model to predict the expected frequencies of different quaternary structure topologies. Not only does this model effectively replicate the relative frequencies of known protein complex structures, it also predicts the new topologies that are most likely to be observed in the future.

A survey of transitions in the assembly pathways of protein complexes

To understand the principles that underlie quaternary structure organization, it is useful to begin by considering the different ways in which protein complexes can assemble. We therefore first sought to determine the assembly and disassembly ["(dis)assembly"] pathways for as many protein complexes as possible. Previously, we have used electrospray mass spectrometry to characterize the (dis)assembly of eight homomers (*10*) and eight heteromers (*11*, *13*). Whereas the homomers followed simple pathways, more diversity was observed for the heteromeric complexes. For this reason, in this study, we experimentally characterized the (dis)assembly pathways of nine additional heteromers with widely varying quaternary structures (Fig. 1). In all of these cases, well-defined intermediate subcomplexes could be identified under at least one set of experimental conditions. All eight homomers and 15 of the 17 heteromers characterized by electrospray mass spectrometry to date have stoichiometries under native conditions that are consistent with the published biological units in the Protein Data Bank (PDB).

We also searched the literature for protein complexes of known structure for which experimental (dis)assembly data are available, as we have done previously (*10*, *11*). Often, these are cases where at least two different oligomeric states have been observed under equilibrium conditions. In total, we identified 11 homomers and 13 heteromers for which some (dis)assembly information is available in the literature.

We obtained further information on protein assembly by considering the large number of protein complexes of known structure. We searched for pairs of protein complexes where the quaternary structure of one complex could be described as a subset of the other. Such pairs include, for example, a homodimer and a homotetramer with highly similar or identical sequences, suggesting that the tetramer assembles via a dimeric intermediate. Also included are homomer-heteromer pairs, where the heteromer has acquired a subunit with respect to the homomers. In total, this approach identified 154 homomers and 263 heteromers with putative structure-based assembly information.

We recognize that the structure-based pathways do not represent direct characterization of assembly. Instead, they indicate that two or more different quaternary structure states have been observed, and we assume that assembly transitions can occur between them. Even for biophysically characterized assembly pathways, we do not always have evidence that they are physiologically relevant. However, the fact that the biophysical and structure-based pathways have a strong tendency to reflect evolutionary history (*10*) and to

[1]Theory of Condensed Matter Group, Cavendish Laboratory, University of Cambridge, JJ Thomson Avenue, Cambridge CB3 0HE, UK. [2]Medical Research Council Human Genetics Unit, Institute of Genetics and Molecular Medicine, University of Edinburgh, Western General Hospital, Edinburgh EH4 2XU, UK. [3]European Molecular Biology Laboratory–European Bioinformatics Institute, Wellcome Trust Genome Campus, Hinxton, Cambridge CB10 1SD, UK. [4]Physical and Theoretical Chemistry Laboratory, Department of Chemistry, University of Oxford, South Parks Road, Oxford OX1 3QZ, UK. [5]Wellcome Trust Sanger Institute, Wellcome Trust Genome Campus, Hinxton, Cambridge CB10 1SA, UK.
*These authors contributed equally to this work. †Corresponding author. E-mail: saraht@ebi.ac.uk

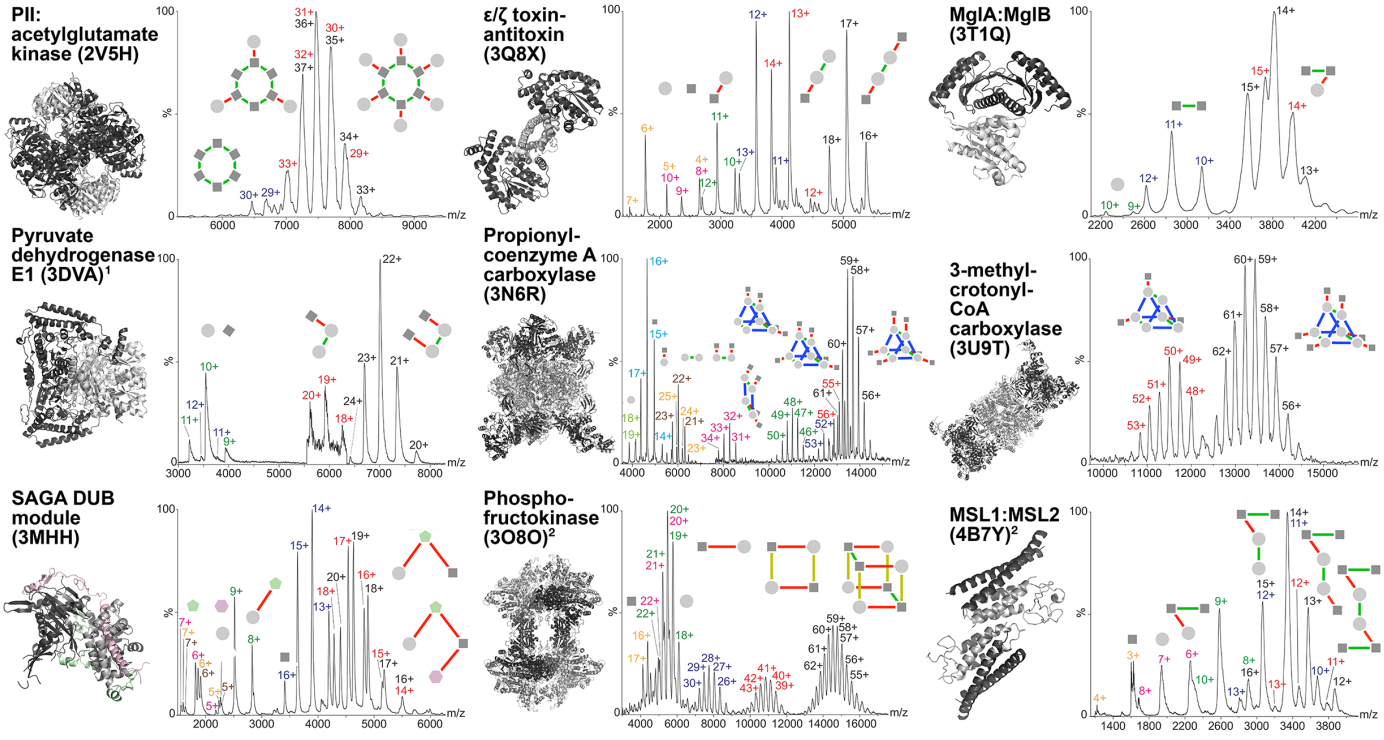

Fig. 1. Mass spectrometry characterization of heteromer (dis)assembly pathways. For each characterized complex, the known three-dimensional structure is shown with a representative mass spectrum, accompanied by graph representations of the full complex and subcomplexes. In all cases, the full complex is represented by the rightmost graph. A full list of subcomplexes is provided in table S1. The structures of 3DVA, 3O8O, and 4B7Y shown here differ from those in the PDB: 3DVA is missing the γ subunit, because it was not present in our sample, and the 4:4 model of 3O8O and the 4:2 model of 4B7Y were built from the unit cell to match the mass spectrometry data. Colors in the graph representations indicate homomeric isologous (green), homomeric heterologous (blue), and heteromeric heterologous (red) interfaces; shapes indicate different subunit types.

be evolutionarily conserved (*11*) does suggest that they have a functional relevance.

Given this large set of assembly data, we next asked what quaternary structure transitions (assembly steps) tend to be observed. For homomeric complexes, we classified all possible transitions into three types (Fig. 2A, left). First, there is dimerization, where a doubling of the complex occurs and a twofold axis of rotational symmetry is formed (e.g., monomer-to-dimer or dimer-to-tetramer). Second, there is cyclization, which involves the assembly of a ring-like quaternary structure with higher-order rotational symmetry (e.g., monomer-to-trimer or monomer-to-tetramer). Third, there is fractional transition, an inherently asymmetric step in which the quaternary structure changes by a non-integer ratio (e.g., dimer-to-timer or trimer-to-tetramer).

For each homomer with assembly data, we identified all the assembly steps that could account for the transitions between the free monomers, the observed subcomplexes, and the full complex (see Methods). The distributions of these three different assembly steps are shown in Fig. 2B. All three data sets show a similar trend, with dimerization being the most common step, cyclization being the next most common, and fractional transitions being rare. This is consistent with previous observations of the favorable assembly and evolutionary transitions between homomers with different symmetries (*10*).

In heteromers, there are two further assembly steps that are possible, in addition to the three steps observed for homomers. These are illustrated in Fig. 2A (right): subunit addition, in which a new subunit is acquired (e.g., monomer-to-heterodimer); and nonstoichiometric transition, in which the types of subunits within the heteromer remain the same, but their relative ratios change (e.g., assembly from 1:1 to 2:1 stoichiometry).

The distributions of all five possible assembly steps for heteromers are shown in Fig. 2C. The same trend is observed among the three homomeric steps, with dimerization being the most common and few fractional transitions. However, across all five possible steps, the most common observed step for heteromers from all three data sets is heteromeric subunit addition.

Within the heteromers, there is a difference between the transitions observed in the mass spectrometry data and those recorded in the other data sets. Specifically, nonstoichiometric transitions are much more common in mass spectrometry data, as evident from the considerable number of subcomplex intermediates with uneven stoichiometry (different numbers of each subunit type) shown in Fig. 1. This can be attributed to two factors: the sensitivity of the mass spectrometry measurements to low-populated assembly intermediates, and the way in which the mass spectrometry experiments are performed—namely, over a range of destabilizing solution conditions designed to progressively disrupt the quaternary structure of the complex. We know that such nonstoichiometric transitions must occur in many cases where they are not observed. For example, consider the transition from an AA homodimer to a BAAB heterotetramer, where there is no interaction between the two B subunits. In this case, an AAB assembly intermediate should form, given that it is highly improbable that two separate B subunits would bind simultaneously. However, this asymmetric subcomplex is unlikely to be observed under non-destabilizing conditions and without highly sensitive mass spectrometry measurements.

Enumeration of the topological space of protein complexes

Next, we explored quaternary structure space by combining different assembly steps to determine which protein complex topologies are possible. Given that the protein complex assembly pathways described above are dominated by dimerization, cyclization, and subunit addition, we focused on these three steps.

An important consideration is interface symmetry. Dimerization results in a twofold axis of rotational symmetry, and therefore the interface formed by dimerization will be isologous (symmetric or head-to-head) and will involve two

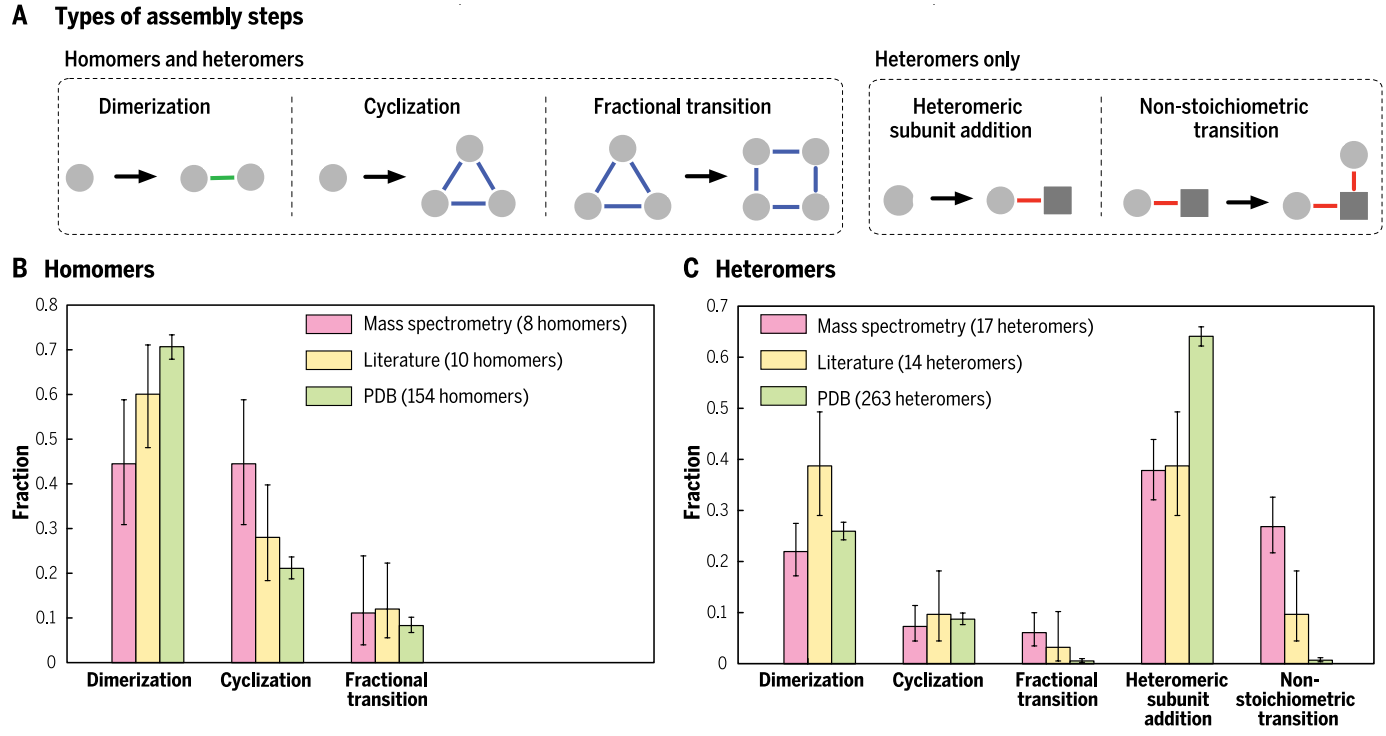

Fig. 2. Types of assembly steps observed in homomeric and heteromeric complexes. (**A**) The five possible types of assembly steps. (**B** and **C**) Distribution of observed assembly steps for homomers and heteromers from mass spectrometry experiments, from assembly pathways identified in the literature, and from complexes with varying quaternary structures in the PDB. Error bars represent 68% Clopper-Pearson confidence intervals.

identical surfaces on subunits of the same type (*14*). In contrast, cyclization results in higher-order rotational symmetry and is associated with interfaces that are heterologous (asymmetric or head-to-tail) and that involve two different surfaces on the same type of subunit. In addition, there are heteromeric interfaces, formed between two distinct polypeptide chains and hence by definition also heterologous.

Proteins are inherently asymmetric at the level of individual polypeptide chains, so we can assume that the same interface surface cannot appear on the same protein twice, or on two structurally different proteins. Together with this fundamental assumption, the three transitions (dimerization, cyclization, and subunit addition) all lead to symmetric protein complexes with even subunit stoichiometry. This is because subunit addition can be viewed as the formation of a larger multiprotein subunit, or protomer, which means that we can extend the homomeric definitions of dimerization and cyclization to homomers formed of these multiprotein subunits, leading to equal multiples of each type of protein (Fig. 3).

Every homomeric complex (of single-protein or multiprotein subunits) can have at most two isologous or heterologous interfaces, because each new homomeric interface imposes a new axis of rotational symmetry. In other words, symmetry constrains the number of homomeric interface types to a maximum of two. One or two interfaces of two possible types give us five scenarios: (i) one isologous, (ii) one heterologous, (iii) two isologous, (iv) two heterologous, and (v) one isologous and one heterologous.

To elucidate all possible heteromeric topologies that can arise under these constraints, we started by enumerating all tree-like topologies of s subunits, in which each subunit type occurs exactly once (Fig. 3). We used trees rather than all possible graphs, because we wanted to distinguish between essential and nonessential ("circumstantial") interfaces in the complex (see next section and Methods for details). For each of the five scenarios described above, we then considered all topologically distinct ways (that is, distinct under symmetry operations on the tree) in which the interfaces can be distributed across the set of subunits and pairs of subunits on the tree. The final step was to construct the topologies of the complexes from these distributions of interfaces across the tree. Some of these are isomorphic (taking into account interface types and subunit identities), which reduces the overall number of topologies.

An important difference between our idealized model and real protein complexes is that real complexes can have more interfaces. However, we can directly relate real protein topologies to the above idealized forms if we consider some of the weaker intersubunit contacts to be circumstantial. In other words, stronger, essential interfaces exist that bind the complex together by themselves. We can distinguish between the essential and circumstantial interfaces by successively cutting away, in increasing order of size, as many interfaces as possible without giving rise to disconnected components of the complex (see Methods for details), thereby producing the simplest possible graph representation of a quaternary structure topology. This contrasts with the previous approach of 3D Complex (*9*), in which all intersubunit interfaces are considered. Thus, this representation effectively sits above the more detailed classification of 3D Complex: A single simplified topology used here can correspond to multiple 3D Complex topologies.

Most real protein complexes are compatible with our model: 92.5% of homomers and 91.7% of heteromers have topologies identified in our exhaustive enumeration (Fig. 4). In these complexes, structurally identical proteins inhabit the same topological environment, meaning the same local environment in terms of the interfaces that they form with other subunits in a complex. We therefore define as bijective those complexes that have a one-to-one correspondence between their polypeptide sequence and their topological environment.

In contrast, all of the real protein complexes not compatible with our enumeration are nonbijective, meaning that sequence-identical subunits exist in nonequivalent topological environments (Fig. 4). The difference between bijective and nonbijective complexes is further illustrated in fig. S1.

Unlike our simple enumeration model that requires only three types of assembly steps, nonbijective complexes would require other asymmetric fractional transition and nonstoichiometric transition assembly steps. To explore this, we performed an exhaustive enumeration of all possible bijective and nonbijective topologies for complexes with specific stoichiometries. We found that for complexes with 2:2 stoichiometry, there are two possible bijective topologies, compared with seven possible nonbijective topologies (fig. S2). For

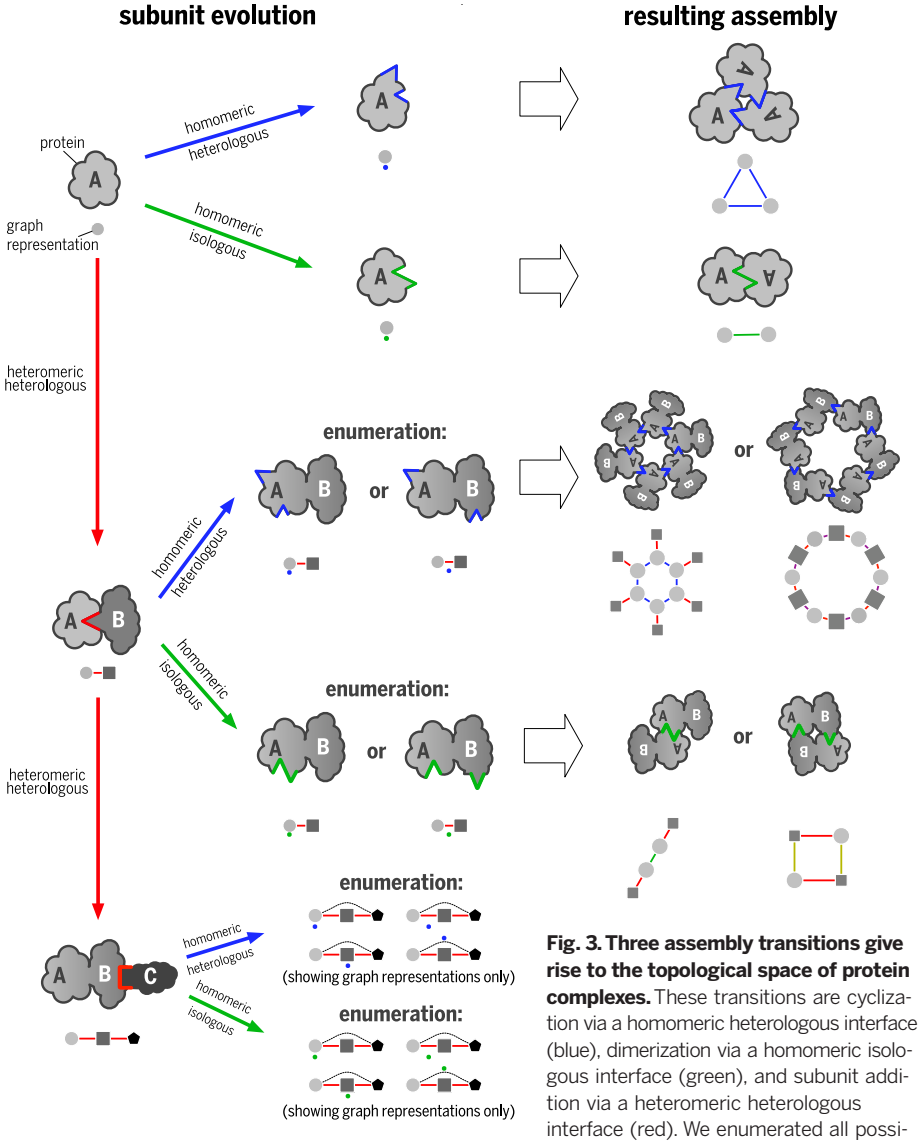

Fig. 3. Three assembly transitions give rise to the topological space of protein complexes. These transitions are cyclization via a homomeric heterologous interface (blue), dimerization via a homomeric isologous interface (green), and subunit addition via a heteromeric heterologous interface (red). We enumerated all possible topologies arising from these steps by calculating all ways in which a cyclic or dihedral interface can be distributed across a heteromer with 1:1 stoichiometry. For heterodimers, there are two such ways for both the cyclization and the dimerization steps. For heterotrimers, there are four such ways for each step. In the graph representation of the enumeration step, the possible locations of the distributed interfaces are indicated by colored dots.

complexes with 3:3 stoichiometry, there are also two possible bijective topologies, whereas the number of possible nonbijective topologies rises sharply to 250 (fig. S3). This illustrates a major benefit of our approach: By limiting our model to only three simple assembly steps, we are able to cover most observed protein complexes with a much smaller set of possible quaternary structure topologies.

To further justify our classification into bijective and nonbijective complexes, we used the fact that the quaternary structure assigned to a protein complex is often incorrect and does not represent the quaternary structure in solution or within the cell (*15*, *16*). Using a database of manually confirmed quaternary structure assignments (*17*), complemented by additional manual assignments of our own, we compared error rates for bijective and nonbijective homomers and heteromers (Fig. 4). We found that, whereas bijective complexes have a low rate of quaternary structure error (~10%), more than half of the nonbijective structures are the result of errors. Thus, most nonbijective protein complex structures are not genuine examples of biological asymmetry but instead are due to artifacts or errors in the structure determination process. This also suggests that a protein complex's nonbijective status could be very useful for identifying likely quaternary structure assignment errors.

The nonbijective complexes with uneven stoichiometry are an exception to the above, with only a 20% quaternary structure error rate. We recently studied these in detail and determined several different structural mechanisms by which they can form, which include varying degrees of pseudosymmetry, steric occlusion, and subunit flexibility leading to conformational differences between identical subunits (*18*). We found that those complexes for which a structural mechanism for uneven stoichiometry could not be ascertained were mostly the result of quaternary structure assignment errors (*18*).

A periodic table of protein complexes

Analysis of the real and enumerated quaternary structure topologies above shows that all bijective heteromers can be related to simpler homomeric topologies. Specifically, if the different subunit types are grouped together as protomers, then the interactions between protomers will be equivalent to a bijective homomer topology or, for cases with no subunit repeats, to a monomer. This suggests a natural classification for protein complexes: in one dimension, by the number of their repeats, and within that, by their equivalent homomeric topologies; and in the other dimension, by the number of unique subunits. Figure 5 illustrates this periodic table of protein complexes for all topologies with ≤12 repeats and ≤4 unique subunits. In this classification, complexes related to the equivalent homomers are contained in the same column of the table, thus allowing the similarities between different heteromeric complexes to be easily recognized.

Most symmetry groups are associated with a single homomeric topology, except dihedral groups for ≥6 subunits and tetrahedral groups (12 subunits), which both have two topologies each. Higher-order symmetries, such as the octahedral and icosahedral groups, only appear for 24 or more subunits and can have three or more topologies each. Although the graph representation of the topology incorporates similarities between binding surfaces based on the identities of interacting residues, it does not require any nonlocal geometric information. Our graph representations therefore inherently include the symmetry group information of a complex, and they constitute the first network representation of complexes to do this.

Figure S4 shows the frequencies of each equivalent homomer symmetry group for complexes with varying numbers of unique subunits. Complexes with different numbers of unique subunits have similar distributions. Thus, homomers and heteromers populate the horizontal axis of the periodic table in a similar manner, although complexes with more unique subunits do tend to have fewer repeats.

The regions of the periodic table that correspond to higher numbers of repeats and subunits are sparsely populated. This can be attributed to two factors. First, there is a considerable bias among structurally characterized protein complexes toward those with smaller numbers of unique subunits, whereas evidence suggests that protein complexes in vivo will tend to have more unique components (*19*, *20*). Second, as shown in fig. S4, topologies toward the right of the periodic table tend to be less common, which suggests that cyclic or dihedral complexes with more repeated subunits may be less stable or more difficult to evolve. These regions can also be expected to be

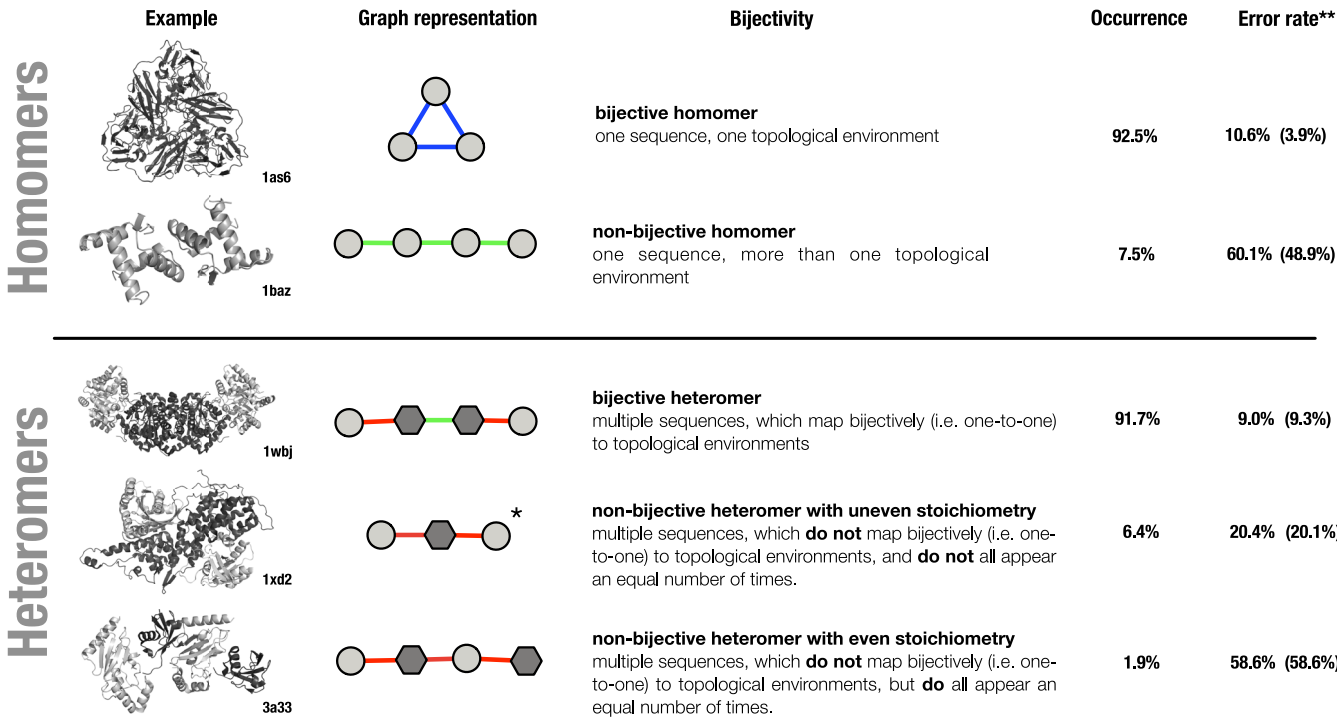

* In this example the central protein forms two different interfaces with the two outer proteins due to the inherent asymmetry of proteins. The topological environments of the outer proteins therefore differ.

** values in brackets exclude 'probably yes' and 'probably no' error assignments in PiQSi from the analysis

Fig. 4. Frequencies of protein complex types and their quaternary structure assignment error rates. Among nonbijective heteromers, we further distinguished between those with even stoichiometry and those with uneven stoichiometry. The former are much more like to be the result of quaternary structure assignment errors. The latter are more likely to represent a biologically relevant quaternary structure. In the last column, we give alternative error rates in brackets that exclude the PiQSi (*17*) error assignments "probably yes" and "probably no" from the analysis. These error rates follow the same pattern for nonbijective heteromers of both even and uneven stoichiometries.

filled in coming years, at least to a certain extent. Figure 5A shows the rate at which new topologies have been discovered—roughly four per year for the past 20 years, with no signs of slowing. To illustrate the space of possible topologies, the number of discovered topologies versus the number possible as determined through exhaustive enumeration is shown in each cell of the periodic table (an example is shown in Fig. 5B).

This table is not "periodic" in the same sense as the periodic table of the elements, because it is in principle open-ended, as opposed to periodic with respect to atomic number. There are no theoretical limitations to quaternary structure topology space in either dimension, although the vast majority of known structures can be placed on the table in Fig. 5. In fig. S5, we have provided an expanded version of the periodic table, where complexes with up to 14 unique subunits and 48 subunit repeats can be visualized. We believe that the analogy to the periodic table of the elements is useful, because it provides a means of organizing quaternary structure topologies and visualizing similarities. Furthermore, just as the periodic table of the elements has successfully predicted many new chemical elements, our periodic table of proteins has considerable predictive power by revealing the regions of quaternary structure space that remain to be populated.

We showed above that the majority of nonbijective complexes are the result of quaternary structure assignment errors. The exception to this is complexes with uneven stoichiometry, most of which represent genuine cases of biological asymmetry. Therefore, we sought to reconcile uneven stoichiometry with our periodic table. We found that if we consider the periodic table at the level of local topological environments, rather than at the level of subunits, then two sequence-identical subunits can play different roles within the graph representing the complex. Examination of the topologies of nonbjiective complexes revealed that many of them were equivalent to the same symmetric homomer topologies observed for the bijective periodic table. Figure S6 illustrates this with a periodic table made for nonbijective heteromers with 2:1 subunit stoichiometry. For these cases, the 2:1 protomer can be considered analogous to a heterotrimer with three unique subunits. The only difference between 2:1 heteromers here and 1:1:1 heteromers from the main periodic table (the third row in Fig. 5) is that in the 2:1 heteromers, sequence-identical subunits sometimes can still form isologous interfaces, despite existing in different local environments. Thus, the results of our quaternary structure enumeration can be easily applied to complexes with uneven stoichiometry, if the repeated subunits from the protomer are considered to be different subunit types in our enumeration model.

Predicting likely yet unobserved quaternary structure topologies

The exhaustive enumeration allows us to determine what quaternary structure topologies are possible, but it does not tell us which are most likely or should be most abundant in nature. To address this, we adapted our enumeration procedure to produce topologies according to the observed distribution in the periodic table. We know that each cell on the periodic table can be defined by a specific set of assembly steps needed to build the topologies within that cell. Combining the steps in different ways can produce all the topologies compatible with a given cell. Therefore, we sampled cells of the periodic table according to the observed distribution in real complexes, each time randomly combining the assembly steps associated with each cell. This was repeated 3×10^7 times (details are provided in the Methods).

All of the quaternary structure topologies present on the periodic table were observed at least once in our calculations. In addition to the previously observed quaternary structure topologies, our model also predicted 579 topologies that were not seen in any of the complexes in our data set. To independently validate this result, we

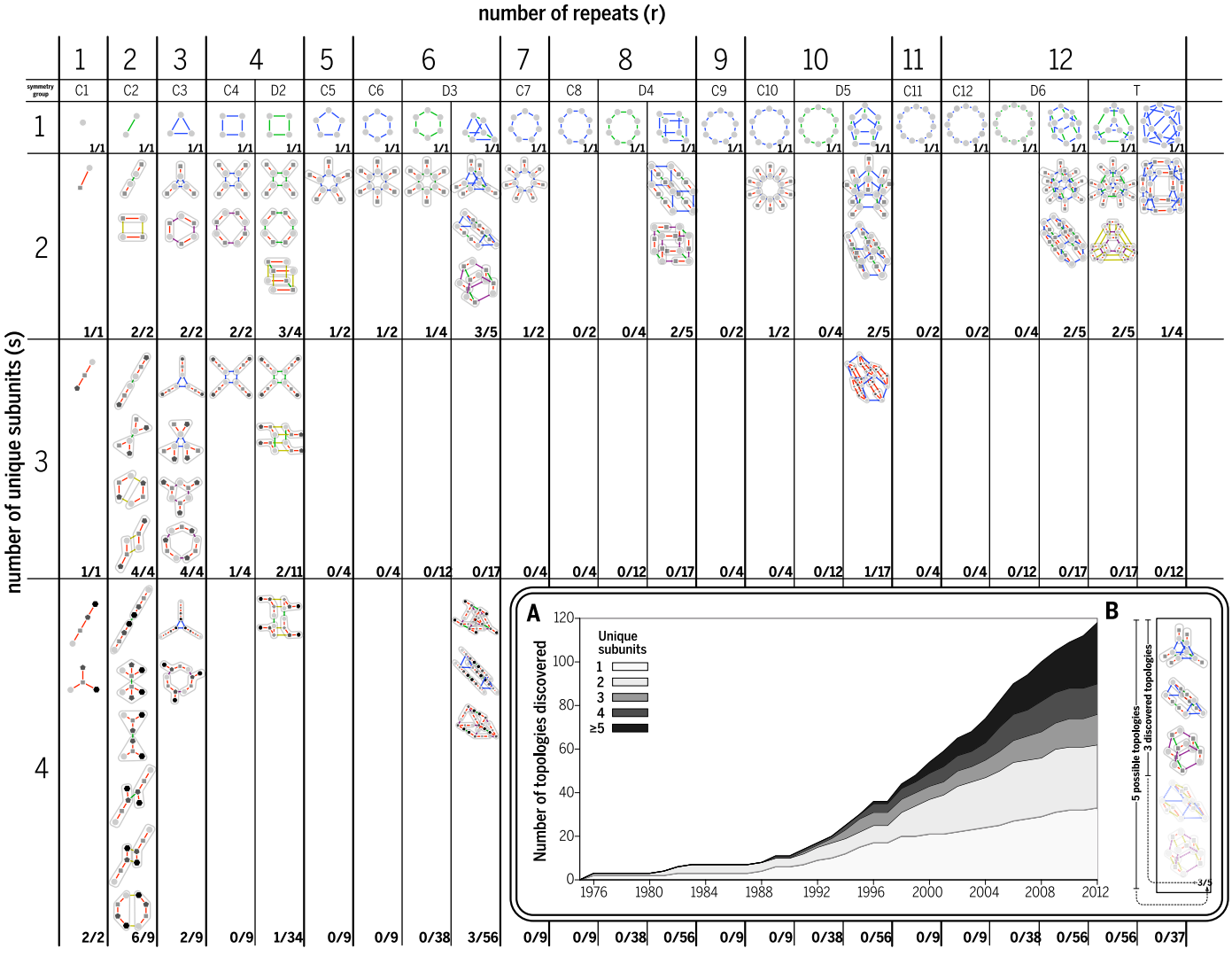

Fig. 5. Periodic table of protein complexes. All bijective protein complex topologies can be arranged according to the number of different subunit types (*s*) and the number of times these subunits are repeated (*r*). Isologous interfaces between the same subunits (dihedral interfaces) are shown in green, and heterologous interfaces between subunits of the same types (cyclic interfaces) are shown in blue. Heteromeric interfaces are shown in red, apart from those that correspond to a symmetric dimerization (yellow) or to higher-order cyclization (purple). The topologies in the $s = 1$ row are the equivalent homomers of the heteromeric structures in the $s > 1$ rows. To clarify this equivalence, subunits in the heteromers are grouped according to the repeated subcomplexes. In addition, the yellow and purple interfaces of the heteromeric complexes highlight interfaces that are dihedral (green) and cyclic (blue) in the equivalent homomers. The ratio in the bottom right of each cell indicates the number of topologies that have been observed and the total number of possible topologies of this type. The table shown here is an excerpt ($s < 5$; $r < 13$) of the full table. An interactive version of this table with information on the structures represented by each topology can be found at http://www.periodicproteincomplexes.org/. [Inset (A)] Number of discovered topologies as a function of time, which has been steadily increasing at a rate of about four topologies per year for the past two decades. [Inset (B)] An illustration of observed topologies versus all possible topologies with six repeats and two subunits ($r = 6$; $s = 2$). Three of the possible five topologies have been observed thus far.

compiled an extended set of heteromeric complexes not present in our original data set because they were published more recently, because they were determined with electron microscopy (which we did not initially include), or because they were originally excluded based on structural criteria (see Methods).

The extended set of heteromers contained 53 different quaternary structure topologies, 14 of which were not present in the main data set. These 14 tended to be among the most highly predicted topologies in our model. For example, six of them were observed among the top 20 most likely predicted topologies (Fig. 6), out of a total of 579 predicted ($P = 2 \times 10^{-6}$; Fisher's exact test). Figure S7 illustrates how the observed topologies cluster within the most highly predicted rankings, thus supporting the predictive utility of our model.

We also used a complementary approach for the prediction of the relative abundances of topologies within a given cell, which makes fewer assumptions but also yields less specific predictions. We considered the number of distributed interfaces (that is, single interfaces that are spread across two subunits) and the number of topological equivalents (marked by red crosses in fig. S8) of a given interface distribution. We compared topologies pairwise within cells of the periodic table with ≤4 unique subunits and ≤12 subunit repeats, and we counted the instances in which topology A had fewer distributed interfaces and equal or more topological equivalents than topology B, or fewer or equal distributed interfaces and more topological equivalents. Out of the 30 such instances, topology A was more abundant that topology B 21 times (70% of instances). This is because distributed interfaces restrict the order in which evolutionary steps can happen, making topologies

with more such interfaces rarer. Larger numbers of topological equivalents, on the other hand, make topologies more common, because there are more ways in which such complexes can evolve.

Finally, to further validate our predictive model, we compared the predicted frequencies of heteromeric quaternary structure topologies with those observed in both the main and extended data sets (fig. S9). Overall, the correlations are strong, with the predictions recapitulating the observed frequencies. Although the predictions are partially fitted to the frequencies of topologies observed in the main data set, the high correlation with the extended data set provides strong independent validation of our model.

Conclusion

In this study, we have shown that the assembly of protein complexes is dominated by three main transition types, which in combination can explain most observed quaternary structure topologies. This also allows a natural organization of protein complexes in a periodic table, in which heteromeric protein complexes are grouped according to their equivalent homomeric quaternary structure topologies. The periodic table illustrates both the variety of observed protein complexes and the space of possible topologies through exhaustive enumeration, analogous to previous strategies of investigating network topologies (*21*, *22*). Given that new topologies have been discovered at a fairly constant rate of four per year over the past two decades (Fig. 5A), we can expect new additions to the unfilled or partially filled cells of the periodic table in the near future. These unfilled or partially filled cells constrain the total space of expected protein complexes, similar to the proposed upper bound of 10,000 total types of interacting domain pairs (*23*).

A major practical application of the periodic table will be in predicting and modeling the quaternary structure of protein complexes. Specifically, our results show that bijective quaternary structure topologies are far more likely to occur than nonbijective topologies, despite the fact that there are far more possible nonbijective topologies. We also provide predictions for the relative likelihoods of different bijective topologies. This knowledge can inform the interpretation of high-throughput interaction experiments (*24*) or structure-based interaction predictions (*25*) by highlighting the quaternary structure topologies that are possible and most likely to occur. Homology information can aid these quaternary structure predictions and give further insight into the evolution and assembly of complexes, because subcomplexes often arise as evolutionary precursors and assembly intermediates (*12*). Similarly, the periodic table can tell us which evolutionary precursor topologies are likely to have given rise to a specific complex. The periodic table can also provide constraints for multi-subunit docking or modeling, both on the relative arrangements of subunits and on the overall complex symmetry (*26*–*29*). Such constraints could be further integrated into hybrid methods that combine different experimental measurements (*30*), such as electrospray (*31*) or cross-linking (*32*) mass spectrometry.

This work could be of substantial utility in the bioengineering of protein complexes. The self-assembly formalism introduced here allows specification of exactly which essential interfaces would need to be engineered to form a protein complex of a given topology. This could facilitate de novo engineering of oligomeric assemblies (*33*–*35*) and allow for directed modulation of existing quaternary structures, stepping either across or down the periodic table in an incremental manner.

Despite its strong predictive power, the basic periodic table model does not account for ~8% of known protein complex structures. More than half of these exceptions arise as a result of quaternary structure assignment errors. A benefit of this approach is that it highlights likely quaternary structure misassignments, particularly by identifying

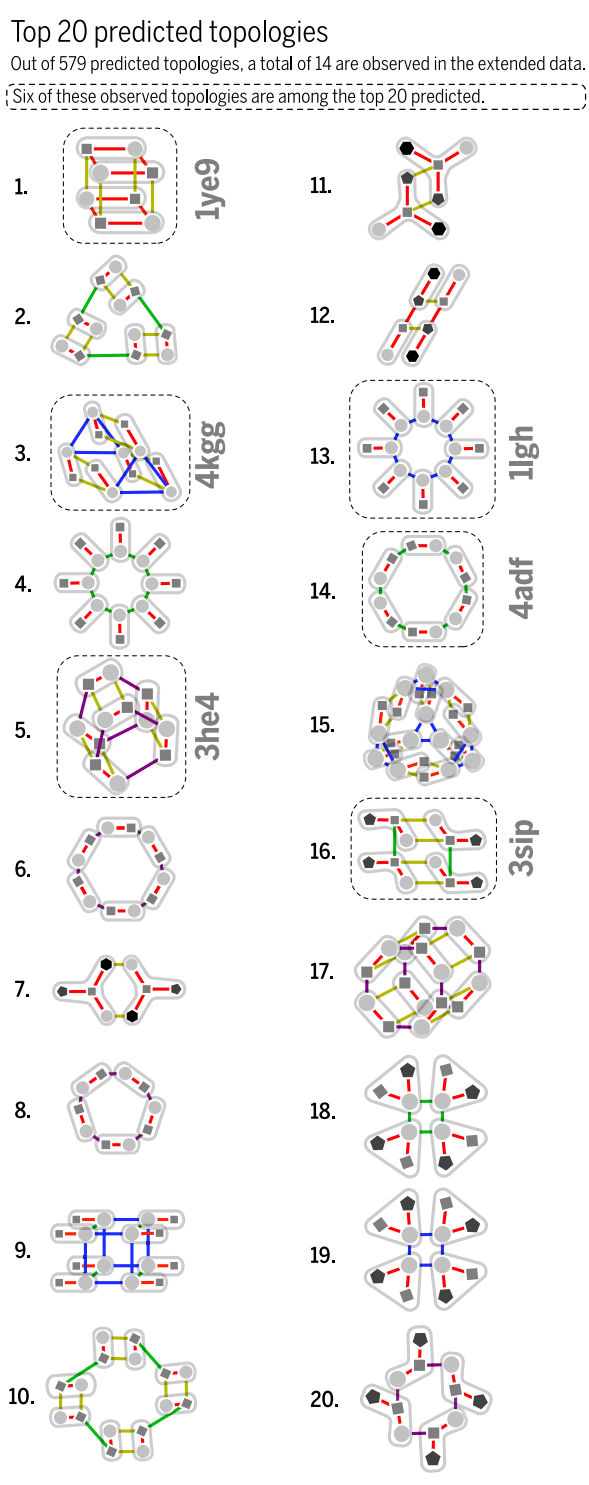

Fig. 6. The top 20 most likely quaternary structure topologies from our model that are not observed in the main data set. Of these top 20, six are observed in the extended data set, validating the power of the model ($P = 2 \times 10^{-6}$). The other 14 topologies in the top 20 are also expected to occur relatively frequently in nature and thus to be observed soon in experimentally determined structures. The distribution of all new topologies observed in the extended data set compared with the expected frequencies of all predicted topologies is shown in fig. S7.

nonbijective complexes with even subunit stoichiometry. However, this still leaves ~4% of known structures that are correct but are not compatible with the periodic table.

Although nonbijective complexes are possible, they are rare, and this should be given consideration in any protein modeling or engineering attempts. Related to this, it would be particularly interesting to see whether chaperones are more frequently involved in the assembly of nonbijective complexes to stabilize the required asymmetric transitions. To model the nonbijective protein complexes, additional assembly steps involving fractional and nonstoichiometric transitions are needed. However, as we showed, this would also greatly expand the number of possible quaternary structure topologies. Therefore, we consider the periodic table in its current implementation to be a reasonable compromise, allowing the vast majority of existing quaternary structure topologies to be explained and the most likely unobserved topologies to be predicted.

Methods

Mass spectrometry experiments

The complexes were kindly donated as follows: *Saccharomyces cerevisiae* SAGA deubiquitinating module [PDB accession number (ID), 3MHH; C. Wolberger, John Hopkins University School of Medicine]; *Thermus thermophilus* MglA/MglB complex (PDB ID, 3T1Q; A. Wittinghofer, Max Planck Institute for Molecular Physiology); *Geobacillus stearothermophilus* PDH E1 subunit (PDB ID, 3DVA; B. Luisi, University of Cambridge); *Streptococcus pyogenes* toxin-antitoxin complex (PDB ID, 3Q8X; A. Meinhart, Max Planck Institute for Medical Research); *Saccharomyces cerevisiae* phosphofructokinase (PDB ID, 3O8O; T. Schöneberg, University of Leipzig); *Ruegeria pomeroyi* propionyl-CoA carboxylase (PDB ID, 3N6R; L. Tong, Columbia University); *Homo sapiens* MSL1-MSL2 complex (PDB ID, 4B7Y; J. Kadlec, European Molecular Biology Laboratory); *Synechococcus elongatus* acetylglutamate kinase/PII complex (PDB ID, 2V5H; V.Rubio, Instituto de Biomedicina de Valencia); and *Pseudomonas aeruginosa* 3-methylcrotonyl-CoA carboxylase (PDB IDs, 3U9T and 3U9S; L. Tong, Columbia University).

The nano-electrospray ionization mass spectrometry experiments on complex disassembly and reassembly were performed as previously described using quadrupole time-of-flight mass spectrometers modified for high–mass/charge ratio operation (*11*). A list of all (sub)complexes observed under various experimental conditions is provided in table S1.

Protein complex data sets

The full set of protein x-ray crystal structures was taken from the PDB on 8 August 2012. Only polypeptide chains with at least 30 residues were considered. Backbone-only models were ignored, as were structures containing nucleic acids or >10% non-water heteroatoms. Heteromeric protein complexes formed by polypeptide cleavage were also ignored. In addition, this approach had the effect of removing complexes with protein chains that lack unique "db_id" sequence identifiers in the PDB. Complexes with >59 subunits or that were split over multiple PDB entries were excluded. In total, the final data set contained 30,469 monomers, 28,935 homomers, and 5543 heteromers. Manual quaternary structure assignments came from PiQSi entries with errors assigned as "probably yes" or "probably no" (*17*) and from additional manual searching of the literature.

The size of the interface between each pair of subunits from all protein complexes was calculated with AREAIMOL (*36*). For each complex, all interfaces of the same type were identified by calculating the correlation between atom-specific buried surface areas for each pair of interfaces. Only interfaces >200 $Å^2$ were considered. Two interfaces were considered to be of the same type if the Pearson correlation between the buried surface areas (in terms of equivalent amino acids) was >0.7. Interface sizes were averaged over all interfaces of the same type. Similarly, homomeric interfaces were classified as isologous if the correlation between the residue-specific buried surface area for each subunit was >0.7.

The extended set of quaternary structure topologies, used to validate our predictive model, was taken from a more recent set of protein complex structures from the PDB on 16 December 2014. In addition to the crystal structures used in the main set, electron microscopy structures were also considered here. The constraints on the main data set were loosened, so that complexes formed via cleavage, as well as complexes containing nucleic acids or other heteroatoms, were also included (although only protein chains were considered). In total, this extended set possessed 4214 bijective heteromers (with ≤4 unique subunits and ≤12 subunit repeats) not present in the main data set. Within this set, there were 53 different quaternary structure topologies, 14 of which are new.

For certain analyses, we used nonredundant subsets of the full and extended data sets. Proteins were filtered for redundancy at the 50% sequence identity level, essentially following a previous approach (*18*, *20*). The nonredundant sets were used for the histogram in fig. S4, for the comparison between observed and predicted results in fig. S9, and for fitting the expected distribution of periodic table quaternary structures in our model.

Both the main set and the extended set of quaternary structure topologies used in this study are provided in table S2, in the form of pairwise interfaces formed between subunits.

Determination of assembly pathways

All of the mass spectrometry and literature-identified (dis)assembly pathways involved protein complexes of known structure for which the subunit composition of at least one subcomplex intermediate could be identified. To complement this, we also performed a structural analysis in which we identified similar protein complexes with different quaternary structures. Starting from the full set of homomeric and heteromeric complexes in our main data set, we searched for complexes for which another complex could be considered as a subset of the full complex. For example, a homodimer was considered to be a subset of a homotetramer if the subunits shared >90% sequence identity. All of these subset complexes were considered to be similar to the experimentally identified subcomplexes for the purpose of defining assembly transitions. All of the experimentally identified subcomplexes and structural subsets are provided in table S3.

Although we observed the subcomplexes formed during (dis)assembly, we did not directly observe the assembly or disassembly steps that occur in solution. However, we inferred these from the subcomplexes identified. For every subcomplex and full complex, we identified the largest subcomplex that can be considered to be a subset of that (sub) complex. If no subcomplex was observed, then (dis)assembly was assumed to occur via free monomers. We then assigned the transition between the two states into one of the five categories from Fig. 2. All (dis)assembly transitions are provided in table S4.

Interface cutting procedure

To distinguish subunit interfaces that are circumstantial from those that are essential to the self-assembly process, we removed interfaces from the weighted subunit contact graph of a given complex, in increasing order of interface size. We skipped interfaces if cutting them would result in the complex becoming disconnected, and we stopped when no further interfaces could be cut.

This procedure does not necessarily result in a tree-like graph, because the same interface may appear several times in the same complex. For example, a cyclic ring will not be cut further, because all interfaces, which are of the same size, would have to be cut at once.

The advantages of this approach are that (i) it greatly simplifies the number of possible topologies and unifies similar topologies that would be treated differently if all interfaces were taken into account; (ii) it is less arbitrary than conventional thresholds of interface size, and therefore it is a more fundamental description of a complex; and (iii) symmetry emerges directly from the graph topology through the number of distinct interfaces of a subunit.

Topological enumeration procedure

The combinations of different interface types that can be present in a homomeric structure include one symmetric interface (C_2 symmetry), one asymmetric interface (cyclic symmetry with more than two subunits), one symmetric and one asymmetric interface (dihedral or tetrahedral symmetry), two symmetric interfaces (dihedral symmetry), and two asymmetric interfaces (only in tetrahedral symmetry). Larger numbers of interface types are not possible in homomers, because of the constraints placed on the symmetry of the complex by these interface types.

As explained above, any heteromer that is formed using a combination of cyclization, dimerization, and subunit addition can be represented as a homomer of multiple copies of the same heteromeric module, in which each subunit

type appears exactly once. We therefore enumerated all possible heteromeric topologies by carrying out the following procedure (illustrated in fig. S8).

1) We enumerated all trees of s unique subunits. These are the heteromeric modules, multiple copies of which are joined together into "homomers." The reason for restricting ourselves to trees instead of all possible graphs is that we aimed to consider only the most important interfaces in the original complexes, by using the interface cutting procedure outlined above. This will always lead to tree-like structures as the repeated heteromeric modules.

2) For each of the five possible combinations of interface types in homomers discussed above, we considered all topologically distinct ways in which the interfaces can be distributed across the set of subunits and pairs of subunits of the tree. Here, topologically distinct means that we cannot convert two distributions of interfaces into each other by only using symmetry operations of the tree.

3) We constructed the topologies of the complexes from these distributions of interfaces across the tree. For this, we also needed to consider the possible number of repetitions for each cyclic interface (for example, in the case of the ring-like complexes of varying size). In complexes with 12 or more subunits, there can be more than one pair of divisors with at least one even divisor (e.g., in the case of 12 subunits, three and four, and two and six), which leads to several possible topologies for the same total number of subunits (for example, D_6 and T in the r = 12 column of the s = 1 row of the periodic table).

4) We distinguished isomorphic topologies. In some cases, different distributions of interfaces in the enumeration procedure led to isomorphic topologies. These were easily identified using an isomorphism check, giving us the final enumeration of topologies.

The numbers in the bottom right of each cell in the periodic table (Fig. 5) give the observed and total numbers of different topologies for that particular symmetry group and number of subunits s.

Enumeration of all possible bijective and nonbijective topologies

We enumerated all possible bijective and nonbijective topologies with 2:2 stoichiometry, and all possible bijective and nonbijective topologies with 3:3 stoichiometry and up to six interfaces. We did this by considering all possible four-node graphs with three to six edges (2:2), shown in fig. S2, and all six-node graphs with five or six edges (3:3), shown in fig. S3. For these, we considered all distributions of equal numbers of two node colors (corresponding to the two protein species). In addition, for all edges between nodes of the same color, we considered two possibilities, corresponding to isologous and heterologous interfaces. Edges can thus have three colorings (heteromeric, homomeric-isologous, and homomeric-heterologous). We also considered different interface sizes by considering all possible relative size ranks (including equal ranks) of the different edges and subsequently cutting interfaces according to the same procedure followed in the periodic table. An isomorphism check (which includes the colorings of nodes and edges) was then used to identify distinct topologies in this enumeration. Two additional constraints were (i) that an equal interface size can appear more than once only for one type of subunit pair, and (ii) that the same interface size can only appear once on each subunit for homomeric-isologous and heteromeric interfaces and once or twice for homomeric-heterologous interfaces.

Prediction of expected frequencies of quaternary structure topologies

To predict the expected frequencies of quaternary structure topologies, we attempted to recapitulate the observed distribution of complexes within cells on the periodic table, considering complexes with ≤12 subunit repeats and ≤4 unique subunits. This prediction procedure can be divided into three parts.

1) Selecting a cell from the periodic table. We first randomly selected a structure from the nonredundant set of complexes and monomers. The row of the periodic table (the number of unique subunits s) was directly taken from this randomly selected structure. However, the column of the periodic table was not taken directly from this structure. This is because the sampling of cells on the periodic table is sparse for the lower rows, and thus we would have missed cells with no current structures. Instead, each structure was classified into one of three groups: first column (monomeric or no repeated subunits), cyclic (including C_2), or dihedral or tetrahedral. Then, another structure was randomly selected from those in the first row of the table (a monomer or homomer) that belong to the same group. This structure was used to define the column of the periodic table. Thus, the distribution of homomers defines the distribution of predicted heteromers in the horizontal axis, with a correction for the fact that complexes with more subunit repeats tend to be less likely to have cyclic or dihedral subunit repeats.

2) Defining the assembly steps. Each cell of the periodic table is associated with a specific set of subunit addition, dimerization, and/or cyclization assembly steps required to get to it from a monomer. Therefore, to generate a random quaternary structure topology that was compatible with a given cell, we first randomized the order of the assembly steps. There are two exceptions to this: (i) for dihdedral topologies where the homomer has at least six subunits and only isologous interfaces (e.g., a trimer of dimers rather than a dimer of trimers), the dimerization step must occur before the cyclization step; and ii) for tetrahedral complexes, the cyclic trimerization must occur before the tetramerization.

3) Constructing a quaternary structure topology, given a defined set of assembly steps. A new interface was added to the quaternary structure topology for each assembly step. When the subcomplex is heteromeric, there are multiple ways an interface could be formed. In these cases, the subunit(s) to be involved were randomly selected. For example, if a dimerization step was applied to an A-B subcomplex, then a new isologous interface could be formed between two A subunits or two B subunits, or a pair of identical heteromeric interfaces could be formed between each pair of A and B subunits. In the latter case, the isologous interface is distributed across two subunits. In fig. S10, we illustrate the random construction process of the quaternary structure topology for a single cell of the periodic table.

All predicted quaternary structure topologies are provided in table S5.

Enumeration-based shorthand notation of protein complex topologies

The representation of interface distributions across the subunits, as shown in Fig. 3 and fig. S9, allows for a natural shorthand notation of topologies. The subunits are labeled A, B, C, etc., and cyclic, dihedral, and heteromeric interfaces are denoted c, d, and h. The location of an interface follows the type, and in the case of distributed interfaces, both subunits are given. A cyclic homomer therefore is cA, the first cyclic structure with two subunits in Fig. 3 is cA hAB, and the last structure with three subunits in the same figure is dAC hAB hBC.

REFERENCES AND NOTES

1. D. S. Goodsell, A. J. Olson, Structural symmetry and protein function. *Annu. Rev. Biophys. Biomol. Struct.* **29**, 105–153 (2000). doi: 10.1146/annurev.biophys.29.1.105; pmid: 10940245
2. J. Janin, R. P. Bahadur, P. Chakrabarti, Protein-protein interaction and quaternary structure. *Q. Rev. Biophys.* **41**, 133–180 (2008). doi: 10.1017/S0033583508004708; pmid: 18812015
3. J. A. Marsh, S. A. Teichmann, Structure, dynamics, assembly, and evolution of protein complexes. *Annu. Rev. Biochem.* **84**, 551–575 (2015). doi: 10.1146/annurev-biochem-060614-034142; pmid: 25494300
4. M. Levitt, C. Chothia, Structural patterns in globular proteins. *Nature* **261**, 552–558 (1976). doi: 10.1038/261552a0; pmid: 934293
5. C. A. Orengo, D. T. Jones, J. M. Thornton, Protein superfamilies and domain superfolds. *Nature* **372**, 631–634 (1994). doi: 10.1038/372631a0; pmid: 7990952
6. W. R. Taylor, A 'periodic table' for protein structures. *Nature* **416**, 657–660 (2002). doi: 10.1038/416657a; pmid: 11948354
7. A. G. Murzin, S. E. Brenner, T. Hubbard, C. Chothia, SCOP: A structural classification of proteins database for the investigation of sequences and structures. *J. Mol. Biol.* **247**, 536–540 (1995). doi: 10.1016/S0022-2836(05)80134-2; pmid: 7723011
8. C. A. Orengo *et al.*, CATH—a hierarchic classification of protein domain structures. *Structure* **5**, 1093–1109 (1997). doi: 10.1016/S0969-2126(97)00260-8; pmid: 9309224
9. E. D. Levy, J. B. Pereira-Leal, C. Chothia, S. A. Teichmann, 3D Complex: A structural classification of protein complexes. *PLOS Comput. Biol.* **2**, e155 (2006). doi: 10.1371/journal.pcbi.0020155; pmid: 17112313
10. E. D. Levy, E. Boeri Erba, C. V. Robinson, S. A. Teichmann, Assembly reflects evolution of protein complexes. *Nature* **453**, 1262–1265 (2008). doi: 10.1038/nature06942; pmid: 18563089
11. J. A. Marsh *et al.*, Protein complexes are under evolutionary selection to assemble via ordered pathways. *Cell* **153**, 461–470 (2013). doi: 10.1016/j.cell.2013.02.044; pmid: 23582331
12. J. A. Marsh, S. A. Teichmann, Parallel dynamics and evolution: Protein conformational fluctuations and assembly reflect evolutionary changes in sequence and structure. *BioEssays* **36**, 209–218 (2014). doi: 10.1002/bies.201300134; pmid: 24272815
13. Z. Hall, A. Politis, C. V. Robinson, Structural modeling of heteromeric protein complexes from disassembly pathways and ion mobility-mass spectrometry. *Structure* **20**, 1596–1609 (2012). doi: 10.1016/j.str.2012.07.001; pmid: 22841294
14. J. Monod, J. Wyman, J.-P. Changeux, On the nature of allosteric transitions: A plausible model. *J. Mol. Biol.* **12**, 88–118

(1965). doi: 10.1016/S0022-2836(65)80285-6; pmid: 14343300
15. K. Henrick, J. M. Thornton, PQS: A protein quaternary structure file server. *Trends Biochem. Sci.* **23**, 358–361 (1998). doi: 10.1016/S0968-0004(98)01253-5; pmid: 9787643
16. E. Krissinel, K. Henrick, Inference of macromolecular assemblies from crystalline state. *J. Mol. Biol.* **372**, 774–797 (2007). doi: 10.1016/j.jmb.2007.05.022; pmid: 17681537
17. E. D. Levy, PiQSi: Protein quaternary structure investigation. *Structure* **15**, 1364–1367 (2007). doi: 10.1016/j.str.2007.09.019; pmid: 17997962
18. J. A. Marsh, H. A. Rees, S. E. Ahnert, S. A. Teichmann, Structural and evolutionary versatility in protein complexes with uneven stoichiometry. *Nat. Commun.* **6**, 6394 (2015). doi: 10.1038/ncomms7394; pmid: 25775164
19. T. Perica *et al*., The emergence of protein complexes: Quaternary structure, dynamics and allostery. *Biochem. Soc. Trans.* **40**, 475–491 (2012). doi: 10.1042/BST20120056; pmid: 22616857
20. J. A. Marsh, S. A. Teichmann, Protein flexibility facilitates quaternary structure assembly and evolution. *PLOS Biol.* **12**, e1001870 (2014). doi: 10.1371/journal.pbio.1001870; pmid: 24866000
21. S. S. Shen-Orr, R. Milo, S. Mangan, U. Alon, Network motifs in the transcriptional regulation network of *Escherichia coli*. *Nat. Genet.* **31**, 64–68 (2002). doi: 10.1038/ng881; pmid: 11967538
22. W. Ma, A. Trusina, H. El-Samad, W. A. Lim, C. Tang, Defining network topologies that can achieve biochemical adaptation. *Cell* **138**, 760–773 (2009). doi: 10.1016/j.cell.2009.06.013; pmid: 19703401
23. P. Aloy, R. B. Russell, Ten thousand interactions for the molecular biologist. *Nat. Biotechnol.* **22**, 1317–1321 (2004). doi: 10.1038/nbt1018; pmid: 15470473
24. P. C. Havugimana *et al*., A census of human soluble protein complexes. *Cell* **150**, 1068–1081 (2012). doi: 10.1016/j.cell.2012.08.011; pmid: 22939629
25. Q. C. Zhang *et al*., Structure-based prediction of protein-protein interactions on a genome-wide scale. *Nature* **490**, 556–560 (2012). doi: 10.1038/nature11503; pmid: 23023127
26. Y. Inbar, H. Benyamini, R. Nussinov, H. J. Wolfson, Prediction of multimolecular assemblies by multiple docking. *J. Mol. Biol.* **349**, 435–447 (2005). doi: 10.1016/j.jmb.2005.03.039; pmid: 15890207
27. F. DiMaio, A. Leaver-Fay, P. Bradley, D. Baker, I. André, Modeling symmetric macromolecular structures in Rosetta3. *PLOS ONE* **6**, e20450 (2011). doi: 10.1371/journal.pone.0020450; pmid: 21731614
28. J. Esquivel-Rodríguez, D. Kihara, Evaluation of multiple protein docking structures using correctly predicted pairwise subunits. *BMC Bioinformatics* **13**, S6 (2012). doi: 10.1186/1471-2105-13-S2-S6; pmid: 22536869
29. B. G. Pierce *et al*., ZDOCK server: Interactive docking prediction of protein-protein complexes and symmetric multimers. *Bioinformatics* **30**, 1771–1773 (2014). doi: 10.1093/bioinformatics/btu097; pmid: 24532726
30. F. Alber, F. Förster, D. Korkin, M. Topf, A. Sali, Integrating diverse data for structure determination of macromolecular assemblies. *Annu. Rev. Biochem.* **77**, 443–477 (2008). doi: 10.1146/annurev.biochem.77.060407.135530; pmid: 18318657
31. H. Hernández, C. V. Robinson, Determining the stoichiometry and interactions of macromolecular assemblies from mass spectrometry. *Nat. Protoc.* **2**, 715–726 (2007). doi: 10.1038/nprot.2007.73; pmid: 17406634
32. J. Rappsilber, The beginning of a beautiful friendship: Cross-linking/mass spectrometry and modelling of proteins and multi-protein complexes. *J. Struct. Biol.* **173**, 530–540 (2011). doi: 10.1016/j.jsb.2010.10.014; pmid: 21029779
33. N. P. King *et al*., Computational design of self-assembling protein nanomaterials with atomic level accuracy. *Science* **336**, 1171–1174 (2012). doi: 10.1126/science.1219364; pmid: 22654060
34. Y.-T. Lai, D. Cascio, T. O. Yeates, Structure of a 16-nm cage designed by using protein oligomers. *Science* **336**, 1129 (2012). doi: 10.1126/science.1219351; pmid: 22654051
35. J. Zhang, F. Zheng, G. Grigoryan, Design and designability of protein-based assemblies. *Curr. Opin. Struct. Biol.* **27**, 79–86 (2014). doi: 10.1016/j.sbi.2014.05.009; pmid: 24952313
36. M. D. Winn *et al*., Overview of the *CCP*4 suite and current developments. *Acta Crystallogr. D Biol. Crystallogr.* **67**, 235–242 (2011). doi: 10.1107/S0907444910045749; pmid: 21460441

ACKNOWLEDGMENTS

We thank C. Wolberger, A. Wittinghofer, B. Luisi, A. Meinhart, T. Schöneberg, L. Tong, J. Kadlec, and V. Rubio for providing protein complex samples; H. Rees for assistance with manual quaternary structure assignments and identification of literature-derived assembly pathways; and P. Beltrao, S. Edelstein, T. Flock, D. Gfeller, M. Hein, F. Krueger, R. Laskowski, E. Levy, S. MacKinnon, I. Moal, E. Natan, T. Perica, B. Stauch, S. Velankar, S. Wodak, and X. Zhang for helpful discussions and comments on the manuscript. This work was supported by the Royal Society (S.E.A. and C.V.R.), the Human Frontier Science Program (J.A.M.), the Medical Research Council (grant G1000819 to H.H. and C.V.R.), and the Lister Institute for Preventative Medicine (S.A.T.).

SUPPLEMENTARY MATERIALS

www.sciencemag.org/content/350/6266/aaa2245/suppl/DC1
Figs. S1 to S10
Tables S1 to S5

17 March 2015; accepted 29 October 2015
10.1126/science.aaa2245

RESEARCH ARTICLES

COGNITIVE SCIENCE

Human-level concept learning through probabilistic program induction

Brenden M. Lake,[1]* Ruslan Salakhutdinov,[2] Joshua B. Tenenbaum[3]

People learning new concepts can often generalize successfully from just a single example, yet machine learning algorithms typically require tens or hundreds of examples to perform with similar accuracy. People can also use learned concepts in richer ways than conventional algorithms—for action, imagination, and explanation. We present a computational model that captures these human learning abilities for a large class of simple visual concepts: handwritten characters from the world's alphabets. The model represents concepts as simple programs that best explain observed examples under a Bayesian criterion. On a challenging one-shot classification task, the model achieves human-level performance while outperforming recent deep learning approaches. We also present several "visual Turing tests" probing the model's creative generalization abilities, which in many cases are indistinguishable from human behavior.

Despite remarkable advances in artificial intelligence and machine learning, two aspects of human conceptual knowledge have eluded machine systems. First, for most interesting kinds of natural and man-made categories, people can learn a new concept from just one or a handful of examples, whereas standard algorithms in machine learning require tens or hundreds of examples to perform similarly. For instance, people may only need to see one example of a novel two-wheeled vehicle (Fig. 1A) in order to grasp the boundaries of the new concept, and even children can make meaningful generalizations via "one-shot learning" (*1*–*3*). In contrast, many of the leading approaches in machine learning are also the most data-hungry, especially "deep learning" models that have achieved new levels of performance on object and speech recognition benchmarks (*4*–*9*). Second, people learn richer representations than machines do, even for simple concepts (Fig. 1B), using them for a wider range of functions, including (Fig. 1, ii) creating new exemplars (*10*), (Fig. 1, iii) parsing objects into parts and relations (*11*), and (Fig. 1, iv) creating new abstract categories of objects based on existing categories (*12*, *13*). In contrast, the best machine classifiers do not perform these additional functions, which are rarely studied and usually require specialized algorithms. A central challenge is to explain these two aspects of human-level concept learning: How do people learn new concepts from just one or a few examples? And how do people learn such abstract, rich, and flexible representations? An even greater challenge arises when putting them together: How can learning succeed from such sparse data yet also produce such rich representations? For any theory of

[1]Center for Data Science, New York University, 726 Broadway, New York, NY 10003, USA. [2]Department of Computer Science and Department of Statistics, University of Toronto, 6 King's College Road, Toronto, ON M5S 3G4, Canada. [3]Department of Brain and Cognitive Sciences, Massachusetts Institute of Technology, 77 Massachusetts Avenue, Cambridge, MA 02139, USA.
*Corresponding author. E-mail: brenden@nyu.edu

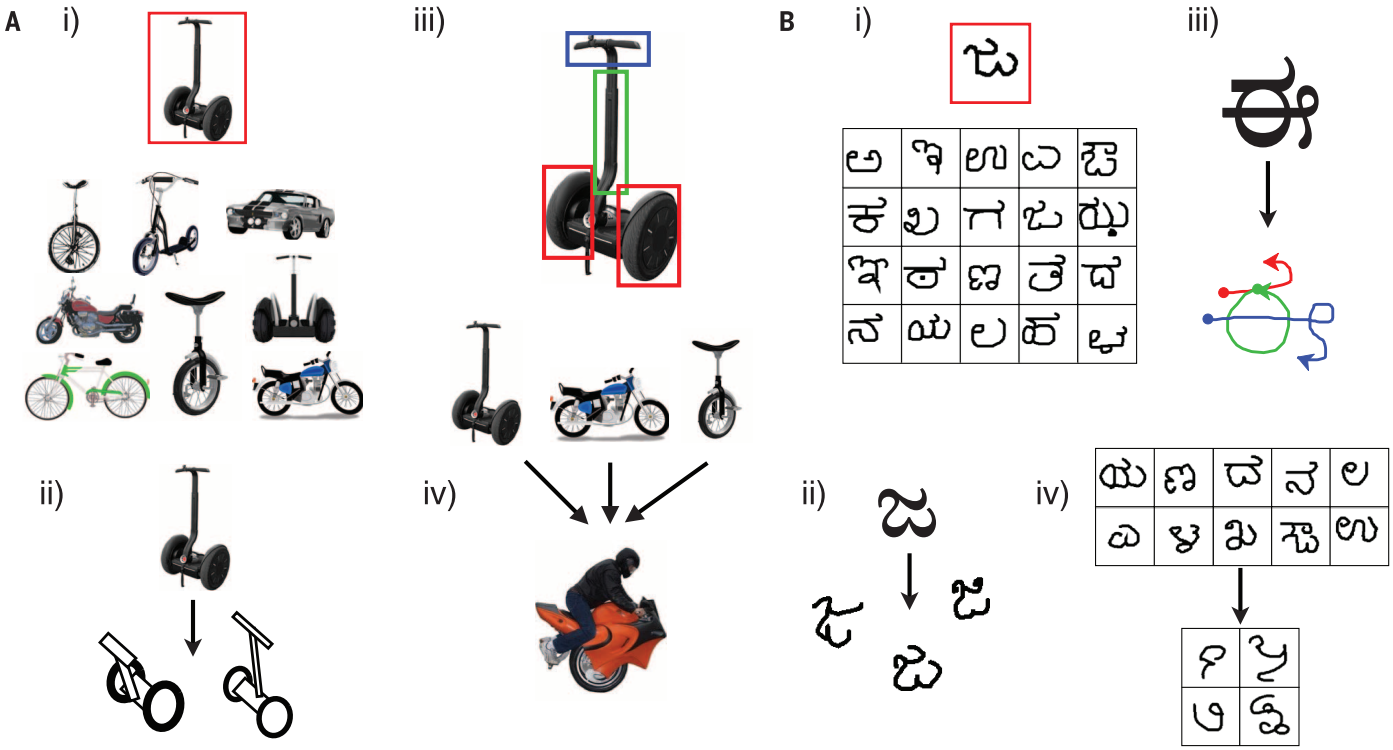

Fig. 1. People can learn rich concepts from limited data. (**A** and **B**) A single example of a new concept (red boxes) can be enough information to support the (i) classification of new examples, (ii) generation of new examples, (iii) parsing an object into parts and relations (parts segmented by color), and (iv) generation of new concepts from related concepts. [Image credit for (A), iv, bottom: With permission from Glenn Roberts and Motorcycle Mojo Magazine]

Downloaded from www.sciencemag.org on December 14, 2015

learning (*4*, *14*–*16*), fitting a more complicated model requires more data, not less, in order to achieve some measure of good generalization, usually the difference in performance between new and old examples. Nonetheless, people seem to navigate this trade-off with remarkable agility, learning rich concepts that generalize well from sparse data.

This paper introduces the Bayesian program learning (BPL) framework, capable of learning a large class of visual concepts from just a single example and generalizing in ways that are mostly indistinguishable from people. Concepts are represented as simple probabilistic programs—that is, probabilistic generative models expressed as structured procedures in an abstract description language (*17*, *18*). Our framework brings together three key ideas—compositionality, causality, and learning to learn—that have been separately influential in cognitive science and machine learning over the past several decades (*19*–*22*). As programs, rich concepts can be built "compositionally" from simpler primitives. Their probabilistic semantics handle noise and support creative generalizations in a procedural form that (unlike other probabilistic models) naturally captures the abstract "causal" structure of the real-world processes that produce examples of a category. Learning proceeds by constructing programs that best explain the observations under a Bayesian criterion, and the model "learns to learn" (*23*, *24*) by developing hierarchical priors that allow previous experience with related concepts to ease learning of new concepts (*25*, *26*). These priors represent a learned inductive bias (*27*) that abstracts the key regularities and dimensions of variation holding across both types of concepts and across instances (or tokens) of a concept in a given domain. In short, BPL can construct new programs by reusing the pieces of existing ones, capturing the causal and compositional properties of real-world generative processes operating on multiple scales.

In addition to developing the approach sketched above, we directly compared people, BPL, and other computational approaches on a set of five challenging concept learning tasks (Fig. 1B). The tasks use simple visual concepts from Omniglot, a data set we collected of multiple examples of 1623 handwritten characters from 50 writing systems (Fig. 2) (see acknowledgments). Both images and pen strokes were collected (see below) as detailed in section S1 of the online supplementary materials. Handwritten characters are well suited for comparing human and machine learning on a relatively even footing: They are both cognitively natural and often used as a benchmark for comparing learning algorithms. Whereas machine learning algorithms are typically evaluated after hundreds or thousands of training examples per class (*5*), we evaluated the tasks of classification, parsing (Fig. 1B, iii), and generation (Fig. 1B, ii) of new examples in their most challenging form: after just one example of a new concept. We also investigated more creative tasks that asked people and computational models to generate new concepts (Fig. 1B, iv). BPL was compared with three deep learning models, a classic pattern recognition algorithm, and various lesioned versions of the model—a breadth of comparisons that serve to isolate the role of each modeling ingredient (see section S4 for descriptions of alternative models). We compare with two varieties of deep convolutional networks (*28*), representative of the current leading approaches to object recognition (*7*), and a hierarchical deep (HD) model (*29*), a probabilistic model needed for our more generative tasks and specialized for one-shot learning.

Bayesian Program Learning

The BPL approach learns simple stochastic programs to represent concepts, building them compositionally from parts (Fig. 3A, iii), subparts (Fig. 3A, ii), and spatial relations (Fig. 3A, iv). BPL defines a generative model that can sample new types of concepts (an "A," "B," etc.) by combining parts and subparts in new ways. Each new type is also represented as a generative model, and this lower-level generative model produces new examples (or tokens) of the concept (Fig. 3A, v), making BPL a generative model for generative models. The final step renders the token-level variables in the format of the raw data (Fig. 3A, vi). The joint distribution on types ψ, a set of M tokens of that type $\theta^{(1)}, \ldots, \theta^{(M)}$, and the corresponding binary images $I^{(1)}, \ldots, I^{(M)}$ factors as

$$P(\psi, \theta^{(1)}, \ldots, \theta^{(M)}, I^{(1)}, \ldots, I^{(M)}) = P(\psi)\prod_{m=1}^{M} P(I^{(m)}|\theta^{(m)})P(\theta^{(m)}|\psi) \quad (1)$$

The generative process for types $P(\psi)$ and tokens $P(\theta^{(m)}|\psi)$ are described by the pseudocode in Fig. 3B and detailed along with the image model $P(I^{(m)}|\theta^{(m)})$ in section S2. Source code is available online (see acknowledgments). The model learns to learn by fitting each conditional distribution to a background set of characters from 30 alphabets, using both the image and the stroke data, and this image set was also used to pretrain the alternative deep learning models. Neither the production data nor any alphabets from this set are used in the subsequent evaluation tasks, which provide the models with only raw images of novel characters.

Handwritten character types ψ are an abstract schema of parts, subparts, and relations. Reflecting the causal structure of the handwriting process, character parts S_i are strokes initiated by pressing the pen down and terminated by lifting it up (Fig. 3A, iii), and subparts $s_{i1}, \ldots, s_{in_i}$ are more primitive movements separated by brief pauses of

Fig. 2. Simple visual concepts for comparing human and machine learning. 525 (out of 1623) character concepts, shown with one example each.

the pen (Fig. 3A, ii). To construct a new character type, first the model samples the number of parts κ and the number of subparts n_i, for each part $i = 1, ..., \kappa$, from their empirical distributions as measured from the background set. Second, a template for a part S_i is constructed by sampling subparts from a set of discrete primitive actions learned from the background set (Fig. 3A, i), such that the probability of the next action depends on the previous. Third, parts are then grounded as parameterized curves (splines) by sampling the control points and scale parameters

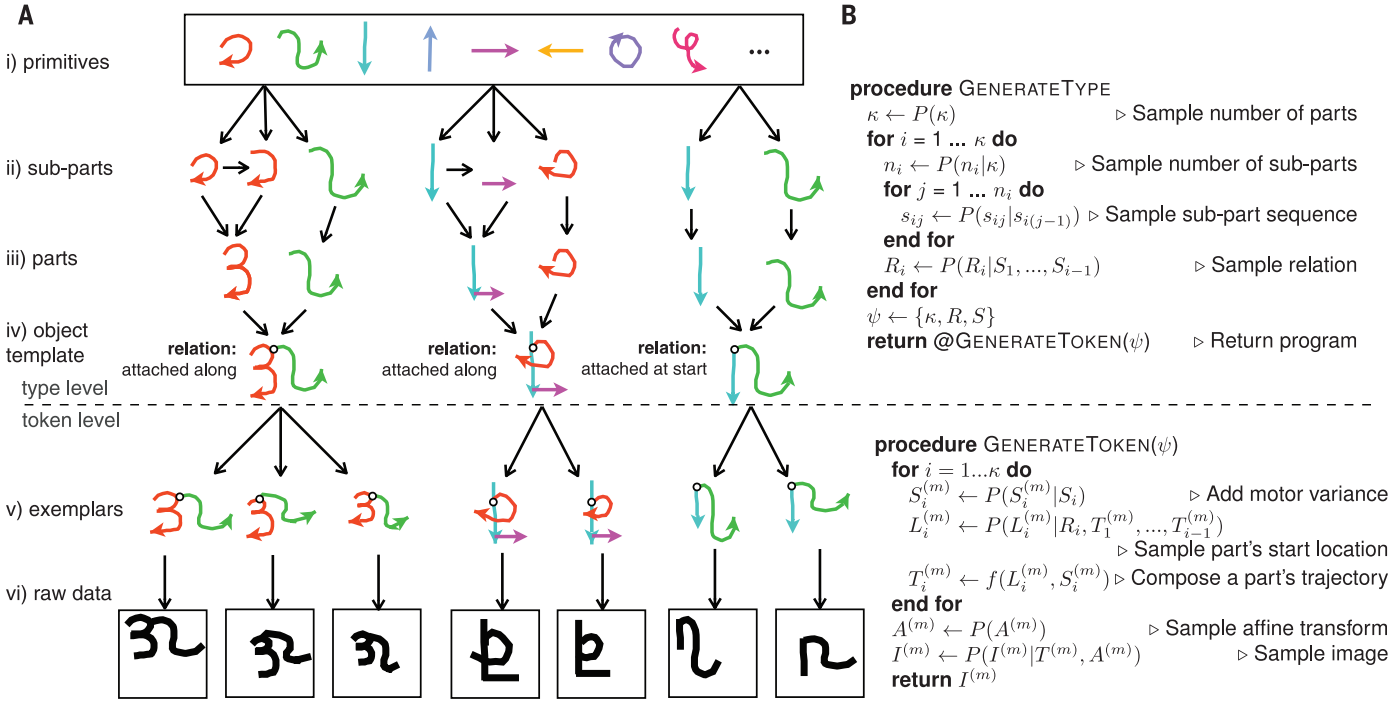

Fig. 3. A generative model of handwritten characters. (**A**) New types are generated by choosing primitive actions (color coded) from a library (i), combining these subparts (ii) to make parts (iii), and combining parts with relations to define simple programs (iv). New tokens are generated by running these programs (v), which are then rendered as raw data (vi). (**B**) Pseudocode for generating new types ψ and new token images $I^{(m)}$ for $m = 1, ..., M$. The function $f(\cdot, \cdot)$ transforms a subpart sequence and start location into a trajectory.

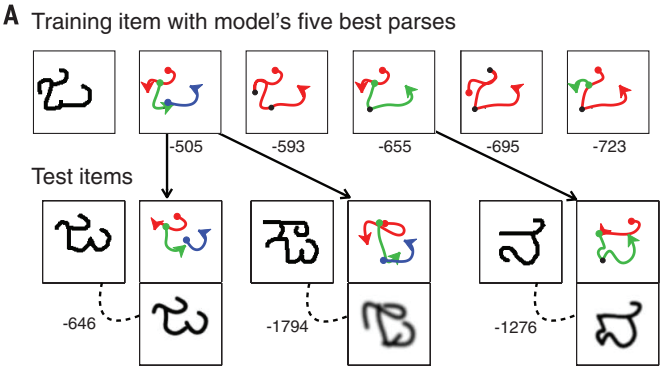

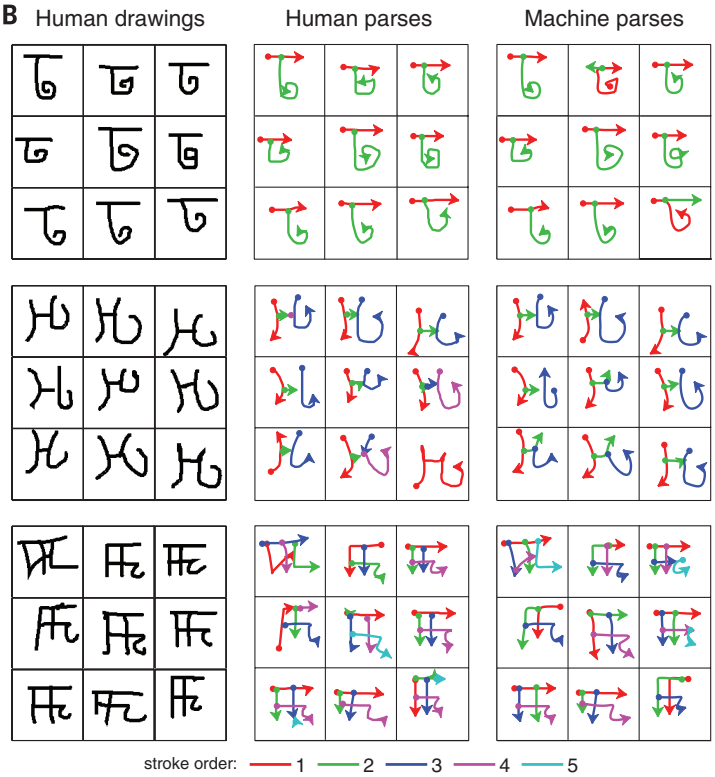

Fig. 4. Inferring motor programs from images. Parts are distinguished by color, with a colored dot indicating the beginning of a stroke and an arrowhead indicating the end. (**A**) The top row shows the five best programs discovered for an image along with their log-probability scores (Eq. 1). Subpart breaks are shown as black dots. For classification, each program was refit to three new test images (left in image triplets), and the best-fitting parse (top right) is shown with its image reconstruction (bottom right) and classification score (log posterior predictive probability). The correctly matching test item receives a much higher classification score and is also more cleanly reconstructed by the best programs induced from the training item. (**B**) Nine human drawings of three characters (left) are shown with their ground truth parses (middle) and best model parses (right).

for each subpart. Last, parts are roughly positioned to begin either independently, at the beginning, at the end, or along previous parts, as defined by relation R_i (Fig. 3A, iv).

Character tokens $\theta^{(m)}$ are produced by executing the parts and the relations and modeling how ink flows from the pen to the page. First, motor noise is added to the control points and the scale of the subparts to create token-level stroke trajectories $S^{(m)}$. Second, the trajectory's precise start location $L^{(m)}$ is sampled from the schematic provided by its relation R_i to previous strokes. Third, global transformations are sampled, including an affine warp $A^{(m)}$ and adaptive noise parameters that ease probabilistic inference (*30*). Last, a binary image $I^{(m)}$ is created by a stochastic rendering function, lining the stroke trajectories with grayscale ink and interpreting the pixel values as independent Bernoulli probabilities.

Posterior inference requires searching the large combinatorial space of programs that could have generated a raw image $I^{(m)}$. Our strategy uses fast bottom-up methods (*31*) to propose a range of candidate parses. The most promising candidates are refined by using continuous optimization and local search, forming a discrete approximation to the posterior distribution $P(\psi, \theta^{(m)}|I^{(m)})$ (section S3). Figure 4A shows the set of discovered programs for a training image $I^{(1)}$ and how they are refit to different test images $I^{(2)}$ to compute a classification score $\log P(I^{(2)}|I^{(1)})$ (the log posterior predictive probability), where higher scores indicate that they are more likely to belong to the same class. A high score is achieved when at least one set of parts and relations can successfully explain both the training and the test images, without violating the soft constraints of the learned within-class variability model. Figure 4B compares the model's best-scoring parses with the ground-truth human parses for several characters.

Results

People, BPL, and alternative models were compared side by side on five concept learning tasks that examine different forms of generalization from just one or a few examples (example task Fig. 5). All behavioral experiments were run through Amazon's Mechanical Turk, and the experimental procedures are detailed in section S5. The main results are summarized by Fig. 6, and additional lesion analyses and controls are reported in section S6.

One-shot classification was evaluated through a series of within-alphabet classification tasks for 10 different alphabets. As illustrated in Fig. 1B, i, a single image of a new character was presented, and participants selected another example of that same character from a set of 20 distinct characters produced by a typical drawer of that alphabet. Performance is shown in Fig. 6A, where chance is 95% errors. As a baseline, the modified Hausdorff distance (*32*) was computed between centered images, producing 38.8% errors. People were skilled one-shot learners, achieving an average error rate of 4.5% ($N = 40$). BPL showed a similar error rate of 3.3%, achieving better performance than a deep convolutional network (convnet; 13.5% errors) and the HD model (34.8%)—each adapted from deep learning methods that have performed well on a range of computer vision tasks. A deep Siamese convolutional network optimized for this one-shot learning task achieved 8.0% errors (*33*), still about twice as high as humans or our model. BPL's advantage points to the benefits of modeling the underlying causal process in learning concepts, a strategy different from the particular deep learning approaches examined here. BPL's other key ingredients also make positive contributions, as shown by higher error rates for BPL lesions without learning to learn (token-level only) or compositionality (11.0% errors and 14.0%, respectively). Learning to learn was studied separately at the type and token level by disrupting the learned hyperparameters of the generative model. Compositionality was evaluated by comparing BPL to a matched model that allowed just one spline-based stroke, resembling earlier analysis-by-synthesis models for handwritten characters that were similarly limited (*34*, *35*).

The human capacity for one-shot learning is more than just classification. It can include a suite of abilities, such as generating new examples of a concept. We compared the creative outputs produced by humans and machines through "visual Turing tests," where naive human judges tried to identify the machine, given paired examples of human and machine behavior. In our most basic task, judges compared the drawings from nine humans asked to produce a new instance of a concept given one example with nine new examples drawn by BPL (Fig. 5). We evaluated each model based on the accuracy of the judges, which we call their identification (ID) level: Ideal model performance is 50% ID level, indicating that they cannot distinguish the model's behavior from humans; worst-case performance is 100%. Each judge ($N = 147$) completed 49 trials with blocked feedback, and judges were analyzed individually and in aggregate. The results are shown in Fig. 6B (new exemplars). Judges had only a 52% ID level on average for discriminating human versus BPL behavior. As a group, this performance was barely better than chance [$t(47) = 2.03$, $P = 0.048$], and only 3 of 48 judges had an ID level reliably above chance. Three lesioned models were evaluated by different groups of judges in separate

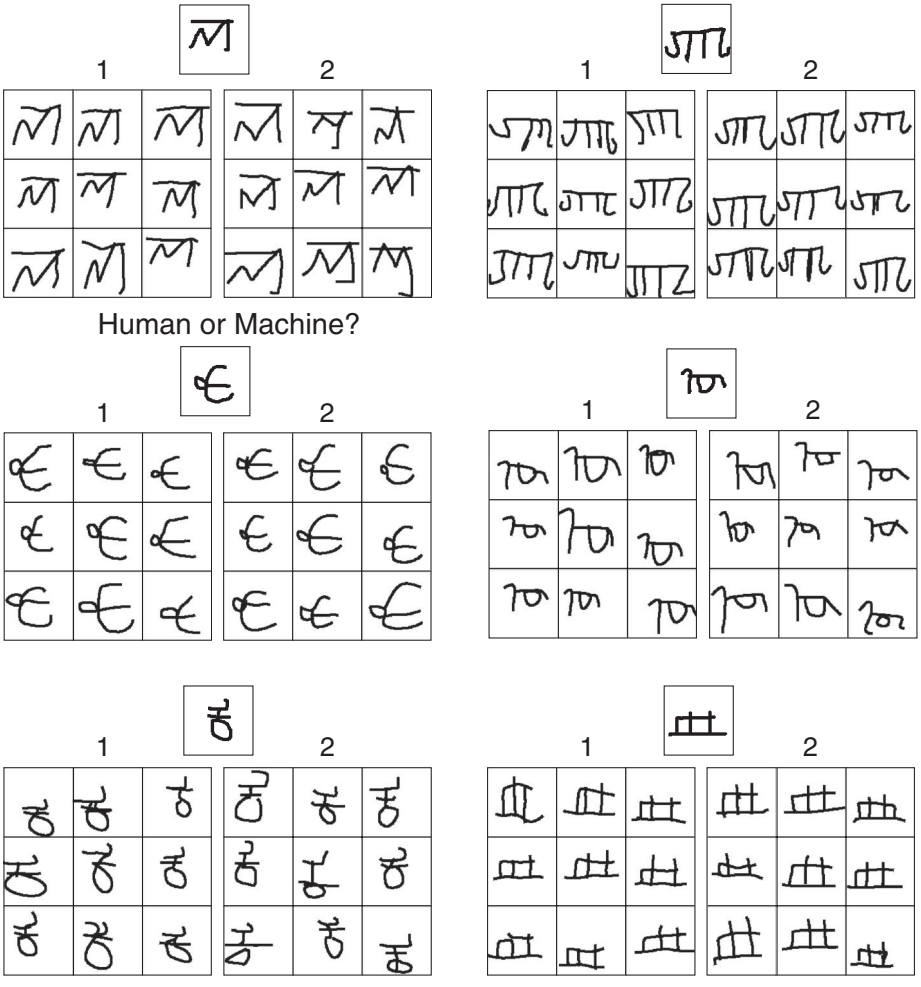

Fig. 5. Generating new exemplars. Humans and machines were given an image of a novel character (top) and asked to produce new exemplars. The nine-character grids in each pair that were generated by a machine are (by row) 1, 2; 2, 1; 1, 1.

conditions of the visual Turing test, examining the necessity of key model ingredients in BPL. Two lesions, learning to learn (token-level only) and compositionality, resulted in significantly easier Turing test tasks (80% ID level with 17 of 19 judges above chance and 65% with 14 of 26, respectively), indicating that this task is a nontrivial one to pass and that these two principles each contribute to BPL's human-like generative proficiency. To evaluate parsing more directly (Fig. 4B), we ran a dynamic version of this task with a different set of judges (N = 143), where each trial showed paired movies of a person and BPL drawing the same character. BPL performance on this visual Turing test was not perfect (59% average ID level; new exemplars (dynamic) in Fig. 6B), although randomizing the learned prior on stroke order and direction significantly raises the ID level (71%), showing the importance of capturing the right causal dynamics for BPL.

Although learning to learn new characters from 30 background alphabets proved effective, many human learners will have much less experience: perhaps familiarity with only one or a few alphabets, along with related drawing tasks. To see how the models perform with more limited experience, we retrained several of them by using two different subsets of only five background alphabets. BPL achieved similar performance for one-shot classification as with 30 alphabets (4.3% and 4.0% errors, for the two sets, respectively); in contrast, the deep convolutional net performed notably worse than before (24.0% and 22.3% errors). BPL performance on a visual Turing test of exemplar generation (N = 59) was also similar on the first set [52% average ID level that was not significantly different from chance $t(26) = 1.04$, $P > 0.05$], with only 3 of 27 judges reliably above chance, although performance on the second set was slightly worse [57% ID level; $t(31) = 4.35$, $P < 0.001$; 7 of 32 judges reliably above chance]. These results suggest that although learning to learn is important for BPL's success, the model's structure allows it to take nearly full advantage of comparatively limited background training.

The human productive capacity goes beyond generating new examples of a given concept: People can also generate whole new concepts. We tested this by showing a few example characters from 1 of 10 foreign alphabets and asking participants to quickly create a new character that appears to belong to the same alphabet (Fig. 7A). The BPL model can capture this behavior by placing a nonparametric prior on the type level, which favors reusing strokes inferred from the example characters to produce stylistically consistent new characters (section S7). Human judges compared people versus BPL in a visual Turing test (N = 117), viewing a series of displays in the format of Fig. 7A, i and iii. The judges had only a 49% ID level on average [Fig. 6B, new concepts (from type)], which is not significantly different from chance [$t(34) = 0.45$, $P > 0.05$]. Individually, only 8 of 35 judges had an ID level significantly above chance. In contrast, a model with a lesion to (type-level) learning to learn was successfully detected by judges on 69% of trials in a separate condition of the visual Turing test, and was significantly easier to detect than BPL (18 of 25 judges above chance). Further comparisons in section S6 suggested that the model's ability to produce plausible novel characters, rather than stylistic consistency per se, was the crucial factor for passing this test. We also found greater variation in individual judges' comparisons of people and the BPL model on this task, as reflected in their ID levels: 10 of 35 judges had individual ID levels significantly below chance; in contrast, only two participants had below-chance ID levels for BPL across all the other experiments shown in Fig. 6B.

Last, judges (N = 124) compared people and models on an entirely free-form task of generating novel character concepts, unconstrained by a particular alphabet (Fig. 7B). Sampling from the prior distribution on character types $P(\psi)$ in BPL led to an average ID level of 57% correct in a visual Turing test (11 of 32 judges above chance); with the nonparametric prior that reuses inferred parts from background characters, BPL achieved a 51% ID level [Fig. 7B and new concepts (unconstrained) in Fig. 6B; ID level not significantly different from chance $t(24) = 0.497$, $P > 0.05$; 2 of 25 judges above chance]. A lesion analysis revealed that both compositionality (68% and 15 of 22) and learning to learn (64% and 22 of 45) were crucial in passing this test.

Discussion

Despite a changing artificial intelligence landscape, people remain far better than machines at learning new concepts: They require fewer examples and use their concepts in richer ways. Our work suggests that the principles of compositionality, causality, and learning to learn will be critical in building machines that narrow this gap. Machine learning and computer vision researchers are beginning to explore methods based on simple program induction (*36*–*41*), and our results show that this approach can perform one-shot learning in classification tasks at human-level accuracy and fool most judges in visual Turing tests of its more creative abilities. For each visual Turing test, fewer than 25% of judges performed significantly better than chance.

Although successful on these tasks, BPL still sees less structure in visual concepts than people do. It lacks explicit knowledge of parallel lines, symmetry, optional elements such as cross bars in "7"s, and connections between the ends of strokes and other strokes. Moreover, people use their concepts for other abilities that were not studied here, including planning (*42*), explanation (*43*), communication (*44*), and conceptual combination (*45*). Probabilistic programs could capture these richer aspects of concept learning and use, but only with more abstract and complex structure than the programs studied here. More-sophisticated programs could also be suitable for learning compositional, causal representations of many concepts beyond simple perceptual categories. Examples include concepts for physical artifacts, such as tools, vehicles, or furniture, that are well described by parts, relations, and the functions

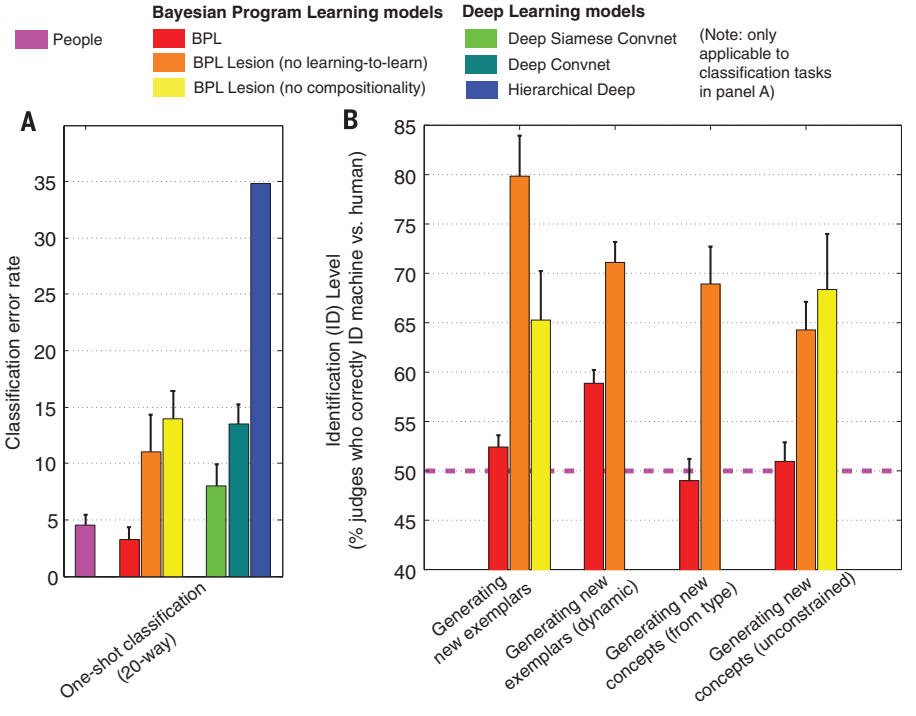

Fig. 6. Human and machine performance was compared on (A) one-shot classification and (B) four generative tasks. The creative outputs for humans and models were compared by the percent of human judges to correctly identify the machine. Ideal performance is 50%, where the machine is perfectly confusable with humans in these two-alternative forced choice tasks (pink dotted line). Bars show the mean ± SEM [N = 10 alphabets in (A)]. The no learning-to-learn lesion is applied at different levels (bars left to right): (A) token; (B) token, stroke order, type, and type.

these structures support; fractal structures, such as rivers and trees, where complexity arises from highly iterated but simple generative processes; and even abstract knowledge, such as natural number, natural language semantics, and intuitive physical theories (*17*, *46*–*48*).

Capturing how people learn all these concepts at the level we reached with handwritten characters is a long-term goal. In the near term, applying our approach to other types of symbolic concepts may be particularly promising. Human cultures produce many such symbol systems, including gestures, dance moves, and the words of spoken and signed languages. As with characters, these concepts can be learned to some extent from one or a few examples, even before the symbolic meaning is clear: Consider seeing a "thumbs up," "fist bump," or "high five" or hearing the names "Boutros Boutros-Ghali," "Kofi Annan," or "Ban Ki-moon" for the first time. From this limited experience, people can typically recognize new examples and even produce a recognizable semblance of the concept themselves. The BPL principles of compositionality, causality, and learning to learn may help to explain how.

To illustrate how BPL applies in the domain of speech, programs for spoken words could be constructed by composing phonemes (subparts) systematically to form syllables (parts), which compose further to form morphemes and entire words. Given an abstract syllable-phoneme parse of a word, realistic speech tokens can be generated from a causal model that captures aspects of speech motor articulation. These part and subpart components are shared across the words in a language, enabling children to acquire them through a long-term learning-to-learn process. We have already found that a prototype model exploiting compositionality and learning to learn, but not causality, is able to capture some aspects of the human ability to learn and generalize new spoken words (e.g., English speakers learning words in Japanese) (*49*). Further progress may come from adopting a richer causal model of speech generation, in the spirit of classic "analysis-by-synthesis" proposals for speech perception and language comprehension (*20*, *50*).

Although our work focused on adult learners, it raises natural developmental questions. If children learning to write acquire an inductive bias similar to what BPL constructs, the model could help explain why children find some characters difficult and which teaching procedures are most effective (*51*). Comparing children's parsing and generalization behavior at different stages of learning and BPL models given varying background experience could better evaluate the model's learning-to-learn mechanisms and suggest improvements. By testing our classification tasks on infants who categorize visually before they begin drawing or scribbling (*52*), we can ask whether children learn to perceive characters more causally and compositionally based on their own proto-writing experience. Causal representations are prewired in our current BPL models, but they could conceivably be constructed through learning to learn at an even deeper level of model hierarchy (*53*).

Last, we hope that our work may shed light on the neural representations of concepts and the development of more neurally grounded learning models. Supplementing feedforward visual processing (*54*), previous behavioral studies and our results suggest that people learn new handwritten characters in part by inferring abstract motor programs (*55*), a representation grounded in production yet active in purely perceptual tasks, independent of specific motor articulators and potentially driven by activity in premotor cortex (*56*–*58*). Could we decode representations structurally similar to those in BPL from brain imaging of premotor cortex (or other action-oriented regions) in humans perceiving and classifying new characters for the first time? Recent large-scale brain models (*59*) and deep recurrent neural networks (*60*–*62*) have also focused on character recognition and production tasks—but typically learning from large training samples with many examples of each concept. We see the one-shot learning capacities studied here as a challenge for these neural models: one we expect they might rise to by incorporating the principles of compositionality, causality, and learning to learn that BPL instantiates.

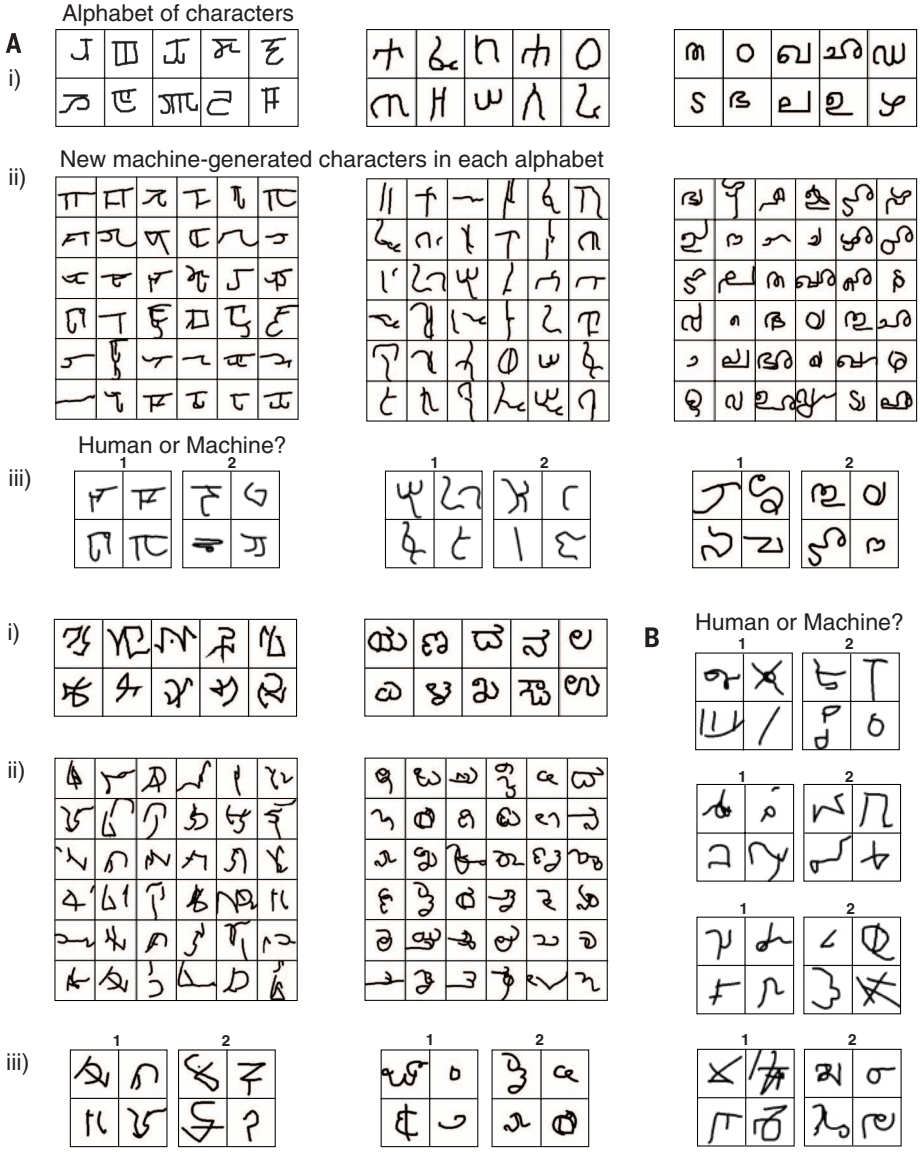

Fig. 7. Generating new concepts. (**A**) Humans and machines were given a novel alphabet (i) and asked to produce new characters for that alphabet. New machine-generated characters are shown in (ii). Human and machine productions can be compared in (iii). The four-character grids in each pair that were generated by the machine are (by row) 1, 1, 2; 1, 2. (**B**) Humans and machines produced new characters without a reference alphabet. The grids that were generated by a machine are 2; 1; 1; 2.

REFERENCES AND NOTES

1. B. Landau, L. B. Smith, S. S. Jones, *Cogn. Dev.* **3**, 299–321 (1988).
2. E. M. Markman, *Categorization and Naming in Children* (MIT Press, Cambridge, MA, 1989).
3. F. Xu, J. B. Tenenbaum, *Psychol. Rev.* **114**, 245–272 (2007).
4. S. Geman, E. Bienenstock, R. Doursat, *Neural Comput.* **4**, 1–58 (1992).
5. Y. LeCun, L. Bottou, Y. Bengio, P. Haffner, *Proc. IEEE* **86**, 2278–2324 (1998).

6. G. E. Hinton *et al.*, *IEEE Signal Process. Mag.* **29**, 82–97 (2012).
7. A. Krizhevsky, I. Sutskever, G. E. Hinton, *Adv. Neural Inf. Process. Syst.* **25**, 1097–1105 (2012).
8. Y. LeCun, Y. Bengio, G. Hinton, *Nature* **521**, 436–444 (2015).
9. V. Mnih *et al.*, *Nature* **518**, 529–533 (2015).
10. J. Feldman, *J. Math. Psychol.* **41**, 145–170 (1997).
11. I. Biederman, *Psychol. Rev.* **94**, 115–147 (1987).
12. T. B. Ward, *Cognit. Psychol.* **27**, 1–40 (1994).
13. A. Jern, C. Kemp, *Cognit. Psychol.* **66**, 85–125 (2013).
14. L. G. Valiant, *Commun. ACM* **27**, 1134–1142 (1984).
15. D. McAllester, in *Proceedings of the 11th Annual Conference on Computational Learning Theory (COLT)*, Madison, WI, 24 to 26 July 1998 (Association for Computing Machinery, New York, 1998), pp. 230–234.
16. V. N. Vapnik, *IEEE Trans. Neural Netw.* **10**, 988–999 (1999).
17. N. D. Goodman, J. B. Tenenbaum, T. Gerstenberg, *Concepts: New Directions*, E. Margolis, S. Laurence, Eds. (MIT Press, Cambridge, MA, 2015).
18. Z. Ghahramani, *Nature* **521**, 452–459 (2015).
19. P. H. Winston, *The Psychology of Computer Vision*, P. H. Winston, Ed. (McGraw-Hill, New York, 1975).
20. T. G. Bever, D. Poeppel, *Biolinguistics* **4**, 174 (2010).
21. L. B. Smith, S. S. Jones, B. Landau, L. Gershkoff-Stowe, L. Samuelson, *Psychol. Sci.* **13**, 13–19 (2002).
22. R. L. Goldstone, in *Perceptual Organization in Vision: Behavioral and Neural Perspectives*, R. Kimchi, M. Behrmann, C. Olson, Eds. (Lawrence Erlbaum, City, NJ, 2003), pp. 233–278.
23. H. F. Harlow, *Psychol. Rev.* **56**, 51–65 (1949).
24. D. A. Braun, C. Mehring, D. M. Wolpert, *Behav. Brain Res.* **206**, 157–165 (2010).
25. C. Kemp, A. Perfors, J. B. Tenenbaum, *Dev. Sci.* **10**, 307–321 (2007).
26. R. Salakhutdinov, J. Tenenbaum, A. Torralba, in *JMLR Workshop and Conference Proceedings*, vol. 27, *Unsupervised and Transfer Learning Workshop*, I. Guyon, G. Dror, V. Lemaire, G. Taylor, D. Silver, Eds. (Microtome, Brookline, MA, 2012), pp. 195–206.
27. J. Baxter, *J. Artif. Intell. Res.* **12**, 149 (2000).
28. Y. LeCun *et al.*, *Neural Comput.* **1**, 541–551 (1989).
29. R. Salakhutdinov, J. B. Tenenbaum, A. Torralba, *IEEE Trans. Pattern Anal. Mach. Intell.* **35**, 1958–1971 (2013).
30. V. K. Mansinghka, T. D. Kulkarni, Y. N. Perov, J. B. Tenenbaum, *Adv. Neural Inf. Process. Syst.* **26**, 1520–1528 (2013).
31. K. Liu, Y. S. Huang, C. Y. Suen, *IEEE Trans. Pattern Anal. Mach. Intell.* **21**, 1095–1100 (1999).
32. M.-P. Dubuisson, A. K. Jain, in *Proceedings of the 12th IAPR International Conference on Pattern Recognition, Vol. 1, Conference A: Computer Vision and Image Processing*, Jerusalem, Israel, 9 to 13 October 1994 (IEEE, New York, 1994), pp. 566–568.
33. G. Koch, R. S. Zemel, R. Salakhutdinov, paper presented at ICML Deep Learning Workshop, Lille, France, 10 and 11 July 2015.
34. M. Revow, C. K. I. Williams, G. E. Hinton, *IEEE Trans. Pattern Anal. Mach. Intell.* **18**, 592–606 (1996).
35. G. E. Hinton, V. Nair, *Adv. Neural Inf. Process. Syst.* **18**, 515–522 (2006).
36. S.-C. Zhu, D. Mumford, *Foundations Trends Comput. Graphics Vision* **2**, 259–362 (2006).
37. P. Liang, M. I. Jordan, D. Klein, in *Proceedings of the 27th International Conference on Machine Learning*, Haifa, Israel, 21 to 25 June 2010 (International Machine Learning Society, Princeton, NJ, 2010), pp. 639–646.
38. P. F. Felzenszwalb, R. B. Girshick, D. McAllester, D. Ramanan, *IEEE Trans. Pattern Anal. Mach. Intell.* **32**, 1627–1645 (2010).
39. I. Hwang, A. Stuhlmüller, N. D. Goodman, http://arxiv.org/abs/1110.5667 (2011).
40. E. Dechter, J. Malmaud, R. P. Adams, J. B. Tenenbaum, in *Proceedings of the 23rd International Joint Conference on Artificial Intelligence*, F. Rossi, Ed., Beijing, China, 3 to 9 August 2013 (AAAI Press/International Joint Conferences on Artificial Intelligence, Menlo Park, CA, 2013), pp. 1302–1309.
41. J. Rule, E. Dechter, J. B. Tenenbaum, in *Proceedings of the 37th Annual Conference of the Cognitive Science Society*, D. C. Noelle *et al.*, Eds., Pasadena, CA, 22 to 25 July 2015 (Cognitive Science Society, Austin, TX, 2015), pp. 2051–2056.
42. L. W. Barsalou, *Mem. Cognit.* **11**, 211–227 (1983).
43. J. J. Williams, T. Lombrozo, *Cogn. Sci.* **34**, 776–806 (2010).
44. A. B. Markman, V. S. Makin, *J. Exp. Psychol. Gen.* **127**, 331–354 (1998).
45. D. N. Osherson, E. E. Smith, *Cognition* **9**, 35–58 (1981).
46. S. T. Piantadosi, J. B. Tenenbaum, N. D. Goodman, *Cognition* **123**, 199–217 (2012).
47. G. A. Miller, P. N. Johnson-Laird, *Language and Perception* (Belknap, Cambridge, MA, 1976).
48. T. D. Ullman, A. Stuhlmuller, N. Goodman, J. B. Tenenbaum, in *Proceedings of the 36th Annual Conference of the Cognitive Science Society*, Quebec City, Canada, 23 to 26 July 2014 (Cognitive Science Society, Austin, TX, 2014), pp. 1640–1645.
49. B. M. Lake, C.-y. Lee, J. R. Glass, J. B. Tenenbaum, in *Proceedings of the 36th Annual Conference of the Cognitive Science Society*, Quebec City, Canada, 23 to 26 July 2014 (Cognitive Science Society, Austin, TX, 2014), pp. 803–808.
50. U. Neisser, *Cognitive Psychology* (Appleton-Century-Crofts, New York, 1966).
51. R. Treiman, B. Kessler, *How Children Learn to Write Words* (Oxford Univ. Press, New York, 2014).
52. A. L. Ferry, S. J. Hespos, S. R. Waxman, *Child Dev.* **81**, 472–479 (2010).
53. N. D. Goodman, T. D. Ullman, J. B. Tenenbaum, *Psychol. Rev.* **118**, 110–119 (2011).
54. S. Dehaene, *Reading in the Brain* (Penguin, New York, 2009).
55. M. K. Babcock, J. J. Freyd, *Am. J. Psychol.* **101**, 111–130 (1988).
56. M. Longcamp, J. L. Anton, M. Roth, J. L. Velay, *Neuroimage* **19**, 1492–1500 (2003).
57. K. H. James, I. Gauthier, *Neuropsychologia* **44**, 2937–2949 (2006).
58. K. H. James, I. Gauthier, *J. Exp. Psychol. Gen.* **138**, 416–431 (2009).
59. C. Eliasmith *et al.*, *Science* **338**, 1202–1205 (2012).
60. A. Graves, http://arxiv.org/abs/1308.0850 (2014).
61. K. Gregor, I. Danihelka, A. Graves, D. J. Rezende, D. Wierstra, in *Proceedings of the International Conference on Machine Learning (ICML)*, Lille, France, 6 to 11 July 2015 (International Machine Learning Society, Princeton, NJ, 2015), pp. 1462–1471.
62. J. Chung *et al.*, *Adv. Neural Inf. Process. Syst.* **28**, (2015).

ACKNOWLEDGMENTS

This work was supported by a NSF Graduate Research Fellowship to B.M.L.; the Center for Brains, Minds, and Machines funded by NSF Science and Technology Center award CCF-1231216; Army Research Office and Office of Naval Research contracts W911NF-08-1-0242, W911NF-13-1-2012, and N000141310333; the Natural Sciences and Engineering Research Council of Canada; the Canadian Institute for Advanced Research; and the Moore-Sloan Data Science Environment at NYU. We thank J. McClelland, T. Poggio and L. Schulz for many valuable contributions and N. Kanwisher for helping us elucidate the three key principles. We are grateful to J. Gross and the Omniglot.com encyclopedia of writing systems for helping to make this data set possible. Online archives are available for visual Turing tests (http://github.com/brendenlake/visual-turing-tests), Omniglot data set (http://github.com/brendenlake/omniglot), and BPL source code (http://github.com/brendenlake/BPL).

SUPPLEMENTARY MATERIALS

www.sciencemag.org/content/350/6266/1332/suppl/DC1
Materials and Methods
Supplementary Text
Figs. S1 to S11
References (*63–80*)

1 June 2015; accepted 15 October 2015
10.1126/science.aab3050

PHYSICAL CHEMISTRY

Spectroscopic characterization of isomerization transition states

Joshua H. Baraban,[1]* P. Bryan Changala,[1]† Georg Ch. Mellau,[2] John F. Stanton,[3] Anthony J. Merer,[4,5] Robert W. Field[1]‡

Transition state theory is central to our understanding of chemical reaction dynamics. We demonstrate a method for extracting transition state energies and properties from a characteristic pattern found in frequency-domain spectra of isomerizing systems. This pattern—a dip in the spacings of certain barrier-proximal vibrational levels—can be understood using the concept of effective frequency, ω^{eff}. The method is applied to the cis-trans conformational change in the S_1 state of C_2H_2 and the bond-breaking HCN-HNC isomerization. In both cases, the barrier heights derived from spectroscopic data agree extremely well with previous ab initio calculations. We also show that it is possible to distinguish between vibrational modes that are actively involved in the isomerization process and those that are passive bystanders.

The central concept of the transition state in chemical kinetics is familiar to all students of chemistry. Since its inception by Arrhenius (*1*) and later development into a full theory by Eyring, Wigner, Polanyi, and Evans (*2–5*), the idea that the thermal rate depends primarily on the highest point along the lowest-energy path from reactants to products has remained essentially unchanged. Most of chemical dynamics is now firmly based on this idea of the transition state, notwithstanding the emergence of unconventional reactions such as roaming (*6*, *7*), where a photodissociated atom wanders before abstracting from the parent fragment. Despite the clear importance of the transition state to the field of chemistry, direct experimental studies of the transition state and its properties are scarce (*8*).

Here, we report the observation of a vibrational pattern, a dip in the trend of quantum level spacings, which occurs at the energy of the saddle point. This phenomenon is expected to provide a generally applicable and accurate method for characterizing transition states. Only a subset of vibrational states exhibit a dip; these states contain excitation along the reaction coordinate and are barrier-proximal, meaning that they are more

[1]Department of Chemistry, Massachusetts Institute of Technology, Cambridge, MA 02139, USA. [2]Physikalisch-Chemisches Institut, Justus-Liebig-Universität Giessen, D-35392 Giessen, Germany. [3]Department of Chemistry and Biochemistry, University of Texas, Austin, TX 78712, USA. [4]Department of Chemistry, University of British Columbia, Vancouver, BC V6T 1Z1, Canada. [5]Institute of Atomic and Molecular Sciences, Academia Sinica, Taipei 10617, Taiwan. *Present address: Department of Chemistry and Biochemistry, University of Colorado, Boulder, CO 80309, USA. †Present address: JILA, National Institute of Standards and Technology, and Department of Physics, University of Colorado, Boulder, CO 80309, USA. **‡Corresponding author. E-mail: rwfield@mit.edu**

susceptible than other states to the effects of the isomerization barrier. Experimental evidence for this concept is drawn from our studies of two prototypical systems: the HCN ↔ HNC isomerization and the cis-trans conformational change in the first electronically excited singlet state of acetylene.

Effective frequency and the isomerization dip

The effective frequency ω^{eff} is the central quantity in our model for the spectroscopic signature of isomerizing systems. In a one-dimensional system, the effective frequency is the derivative of the energy with respect to the quantum number n,

$$\omega^{eff}(n) = \frac{\partial E}{\partial n} = \frac{\Delta E}{\Delta n} \quad (1)$$

where ω^{eff} is evaluated discretely for quantized systems. ω^{eff} is a dynamic quantity that can change as excitation increases, unlike quantities such as harmonic frequency, ω, or fundamental frequency, ν, which are often listed as molecular constants. As such, it is a useful diagnostic of the behavior of the system.

Applications of effective frequency date back a long way. For example, the effective frequencies $\omega^{eff}(n)$ of a state of a diatomic molecule are its vibrational intervals, which decrease to zero at the dissociation limit. The sum of the effective frequencies is therefore the dissociation energy. In most cases it is not possible to observe $\omega^{eff}(n)$ all the way to the dissociation limit, but a linear extrapolation to $\omega^{eff} = 0$ allows a very good estimate of the dissociation energy, notwithstanding nonlinearities in the trend of vibrational intervals near dissociation. This is the basis of the Birge-Sponer plot (*9*) where the area under a graph of the vibrational intervals, $\omega^{eff}(n)$, against n gives the dissociation energy. Leroy and Bernstein (*10*) have given a protocol for extrapolating the effective frequencies, which takes account of the exact long-range shape of the vibrational potential near dissociation. This procedure is found to give very accurate dissociation energies (*11*).

Effective frequencies also play a large part in our understanding of quasi-linear molecules. A quasi-linear molecule has a nonlinear equilibrium geometry but a comparatively small potential barrier to linearity. The pattern of the lowest vibrational levels is that of a bent molecule, but with increasing bending vibrational excitation, this changes smoothly into the pattern for a linear molecule, vibrating with large amplitude. Dixon (*12*) modeled a quasi-linear potential as a two-dimensional harmonic oscillator perturbed by a Gaussian hump at the linear configuration, and calculated its energy levels. These levels may be assigned vibrational (v) and angular momentum (K) quantum numbers (*13*). If the vibrational intervals (effective frequencies) for a given K value are plotted against v, they pass through a minimum at the energy of the potential barrier, thereby allowing determination of its value. The depth of this "Dixon dip" is greatest for $K = 0$ and decreases with increasing K. The reason is that the angular momentum results in a K-dependent centrifugal barrier at the linear configuration, which the molecule must avoid.

We now illustrate the concept of effective frequency in more detail, with the four types of potential shown in Fig. 1. For the harmonic oscillator,

$$\omega^{eff} = \frac{\partial}{\partial n}\left[\omega\left(n+\frac{1}{2}\right)\right] = \omega \quad (2a)$$

and

$$\frac{\partial \omega^{eff}}{\partial n} = 0 \quad (2b)$$

indicating that the dynamics of the system do not change as a function of energy. For a Morse oscillator, the potential is $V(r) = D_e[1 - \exp(-ar)]^2$, where D_e is the dissociation energy, a is a length parameter, and r is the bond length displacement. In this case,

$$\omega^{eff} = \frac{\partial}{\partial n}\left[\omega\left(n+\frac{1}{2}\right) + x\left(n+\frac{1}{2}\right)^2\right] = \omega + x + 2nx \quad (3a)$$

and

$$\frac{\partial \omega^{eff}}{\partial n} = 2x \quad (3b)$$

where x is always negative. This linear decrease of ω^{eff} with n reflects the migration of the Morse wave functions toward the softer outer turning point. When ω^{eff} reaches zero at the dissociation limit, it becomes clear that the Morse and harmonic oscillators display very different dynamics.

Simple expressions for ω^{eff} and $\partial\omega^{eff}/\partial n$ cannot be derived for the other cases in Fig. 1, but these illustrate the most important feature even more clearly: The effective frequency goes to zero at the energy of each stationary point on the potential. Classically, this can be understood by imagining a ball released to roll on a double-minimum surface. If the ball starts on one side at exactly the height of a local maximum, it will reach that maximum with zero kinetic energy and stop. Because the ball never returns, the oscillation period is infinite and the frequency is therefore zero. We see immediately that this applies to the Morse oscillator as well: ω^{eff} reaches zero at the dissociation limit, which is a horizontal asymptote of $V(r)$. It is clear that this phenomenon is quite general and that zeros or

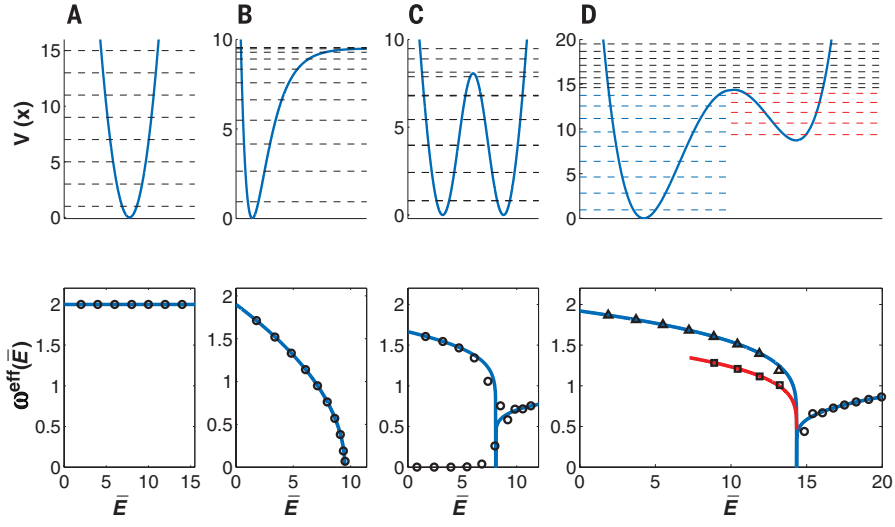

Fig. 1. Effective frequency plots below their associated model potentials. (**A**) Harmonic oscillator. (**B**) Morse oscillator. (**C**) Symmetric double minimum potential. (**D**) Asymmetric double minimum potential. In the top row, the quantized energy levels are marked with dashed lines. In the bottom row, the classical ω^{eff} is shown as a solid line, with the quantum level spacings plotted as open circles versus $\bar{E}$ (the midpoint energy for each interval). In (C), the upper and lower series of circles correspond to the vibrational level spacings and tunneling splittings, respectively. In (D), the ω^{eff} curve and energy levels for the second minimum are shown in red, and the quantum level spacings are overlaid on the ω^{eff} curves as triangles and squares.

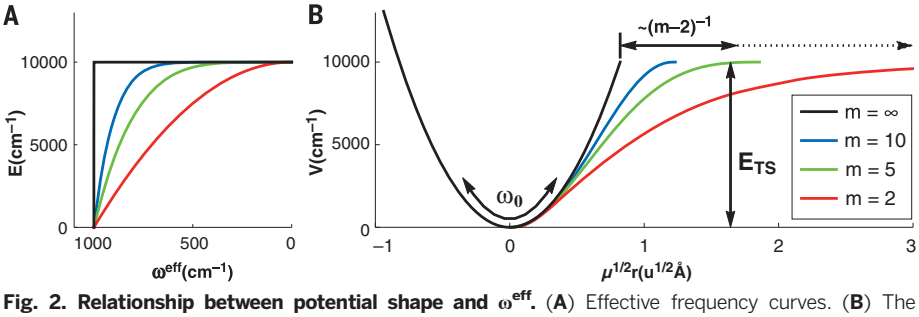

Fig. 2. Relationship between potential shape and ω^{eff}. (**A**) Effective frequency curves. (**B**) The corresponding potentials as a function of the shape parameter m in Eq. 4.

abrupt changes in ω^{eff} signal important changes in the dynamics of the system.

In their quantum and semiclassical analysis of highly excited states of HCP, Jacobson and Child (*14*) mentioned a dip in ω^{eff} as the signature of an approach to a saddle point. Because the HCP ↔ HPC potential energy surface exhibits some unusual features (HPC is a saddle point rather than a second minimum) and is not a true isomerization (*15*), the observed ω^{eff} trend was categorized as a peculiar "Dixon dip" rather than being recognized as the universal signature proposed here. Similarly, the onset of internal rotation in the ground state of SiC_2 (*16*) is not an isomerization, although the ideas presented here are applicable to it. More generally, the behavior of systems as they encounter stationary points has been investigated from other perspectives as well (*17*–*20*). For our purposes, it suffices that this dip in ω^{eff} provides a marker of the chemically relevant transition state energy, as we demonstrate below.

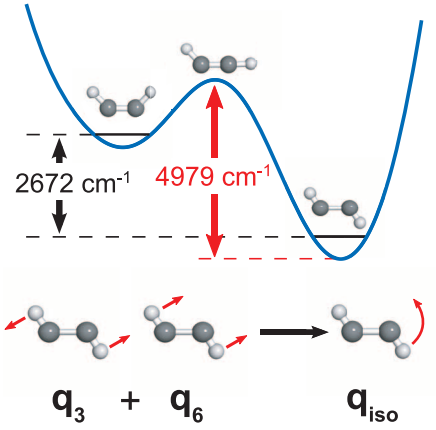

Fig. 3. Salient features of the cis-trans isomerization in S_1 C_2H_2. The barrier height and energy difference between the two conformers are shown, as well as the combination of trans normal modes (q_3 and q_6) that corresponds to the isomerization coordinate.

A model for measurement of the transition state energy

To determine the transition state energy, we propose the following semiempirical formula for ω^{eff} as a function of energy, $\overline{E}$, defined as the midpoint energy for each vibrational interval:

$$\omega^{eff}(\overline{E}) = \omega_0\left(1 - \frac{\overline{E}}{E_{TS}}\right)^{1/m}$$

$$\omega_0, E_{TS} \geq 0;\ 2 \leq m \leq \infty;\ \overline{E} \leq E_{TS} \qquad (4)$$

where ω_0 is the effective frequency at $\overline{E} = 0$ for the progression being analyzed, E_{TS} is the energy of the transition state, and m is a parameter related to the barrier shape. For the Morse oscillator (Fig. 1B), $m = 2$ analytically (*21*–*23*), $E_{TS} = D_e$, and $\omega_0 = \omega$, the harmonic frequency. Equation 4 can be regarded as a generalization of the Morse formula where m is allowed to take values greater than 2. The formula also satisfies the required physical boundary conditions of a limiting harmonic frequency ω_0 at $\overline{E} = 0$ and $\omega^{eff} = 0$ at $\overline{E} = E_{TS}$.

The dependence of the m parameter on potential shape is illustrated in Fig. 2 (see supplementary text for further details). The lower limit is $m = 2$, the Morse oscillator, where the asymptote is approached infinitesimally with r. The other limit is a truncated harmonic oscillator where the potential abruptly becomes constant at E_{TS}. In such a case, ω^{eff} falls instantly to zero and $m = \infty$.

Dissociation versus isomerization

The physical arguments presented here regarding the behavior of ω^{eff} versus $\overline{E}$ (and therefore Eq. 4) pertain only up to $\overline{E} = E_{TS}$. Above that energy, ω^{eff} can either remain at zero for an unbound system (as with the Morse oscillator) or rise again (in a bound system). The above-barrier behavior of ω^{eff} depends on the outer walls of the potential and is not described by Eq. 4. The mth root form of Eq. 4 suggests the presence of a branch point at E_{TS}, which separates the above-barrier and below-barrier eigenspectra into two distinct energy regions (*19*, *24*).

A semiclassical analysis of long-range interatomic potentials of the form $D - (C/r^n)$ was performed by LeRoy and Bernstein (*10*) more than 40 years ago. They derived an expression that relates the change in energy per quantum number (i.e., the effective frequency) near the dissociation limit to a quantity proportional to $[1 - (E/D)]^{(n+2)/2n}$. This expression is clearly similar to our effective frequency formula, but the two models treat dynamically and mathematically distinct regimes. For inverse power-law potentials where $n = \{1, 2, 3, 4, \ldots\}$, the corresponding m values are $\{{}^2/_3, 1, {}^6/_5, {}^4/_3, \ldots\}$. In the limit $n \to \infty$, the effective m value approaches 2 from below. In contrast, our model has a lower limit of $m = 2$. In other words, these two similar effective frequency expressions treat essentially disjoint classes of potentials. The key difference is how the stationary point (or dissociation limit) is approached. For long-range potentials with inverse power-law forms, the stationary point at $r \to \infty$ is approached only polynomially. Our treatment considers potentials where stationary points are local maxima and are therefore approached over a finite domain. The common system, the Morse potential, has a stationary point at $r \to \infty$ but approaches it exponentially (i.e., faster than any power law) and is in some sense simultaneously long-range and local. Graphically, the dynamical distinction corresponds to positive curvature (LeRoy-Bernstein) versus negative curvature (our model) on a Birge-Sponer plot, with the linear plot of the Morse oscillator dividing the two regimes.

Practical application

What is the best way to extract the desired saddle point energy from spectroscopically measured quantities? From the frequency-domain spectrum we measure the energies of a series of quantized vibrational levels, and take the average $\overline{E}$ and

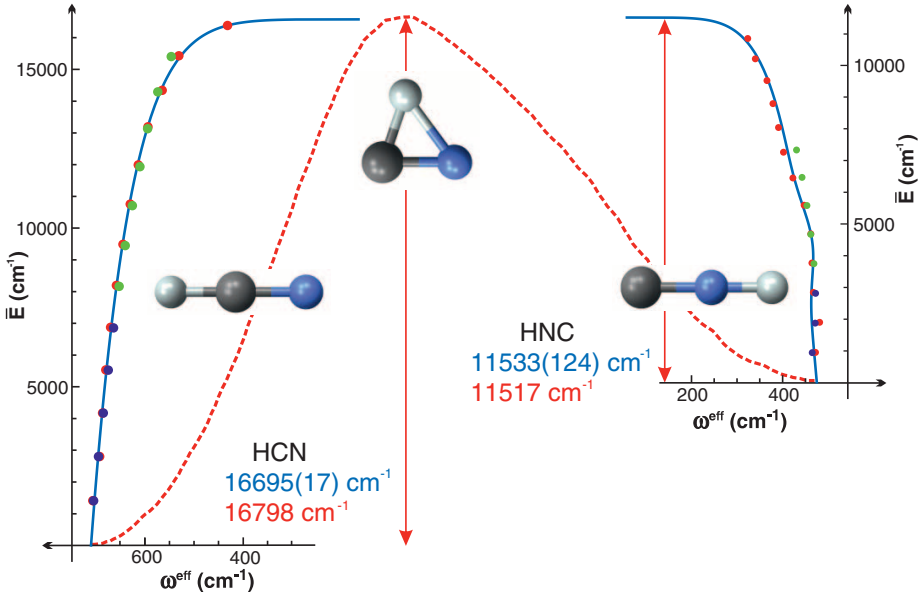

Fig. 4. The ω_2^{eff} ($\ell = 0$) effective frequency analysis for HCN and HNC. Shown are experimental data points (blue), Dunham polynomial expansion predictions using only experimental data (green), and the assigned ab initio data points (red) (*26*) (see supplementary text for details). The fitted E_{TS} parameters using Eq. 4 (blue) are compared with the ab initio barrier heights (red). A one-dimensional cut through the potential energy surface is shown as a red dashed line. The unusual shapes of the HNC potential and ω^{eff} plot near 5000 cm^{-1} result from interaction with a low-lying excited diabatic electronic state (*44*).

difference ω^{eff} of adjacent level energies to obtain a set of ($\overline{E}$, ω^{eff}) data points (*25*). Equivalently, time domain spectroscopy may provide alternative or more direct ways to obtain vibrational periods or frequencies versus energy, especially for larger systems. A plot of these ($\overline{E}$, ω^{eff}) data reveals any dynamical trend in ω^{eff}, whether constant, linear, or nonlinear. If a stationary point is present within the data range of $\overline{E}$, the plot will dip to a minimum as the energy of the stationary point is approached, although in a bound quantum system there will never be a point with ω^{eff} equal to zero.

In principle, only this bare minimum of information is necessary to apply Eq. 4. A value for E_{TS} can then be obtained, which in favorable cases should have an uncertainty of 5 to 10% of the effective frequency, depending on the extent and quality of the input data. High resolution and detailed spectroscopic assignments are not a requirement, nor are ab initio calculations, although these can help to identify the active vibrations and the nature of the transition state. Even in larger molecules, where full spectroscopic and computational analyses are impractical, the problem must simplify to a very small number of vibrational modes that form the reaction coordinate and lead to the transition state. These active vibrations reveal themselves by their isomerization dips.

To demonstrate the capabilities of our method, we applied the model to two prototypical isomerizing molecules, HCN and the S_1 state of C_2H_2. These systems have been spectroscopically characterized in great detail, such that we can apply the isomerization dip method and Eq. 4 to them with confidence. We emphasize that the levels of knowledge and quality of data available for these systems are not necessary in general for the application of our method. Furthermore, despite the small sizes of HCN and C_2H_2, they exhibit many of the complications expected in larger molecules.

The examples of S_0 HCN ↔ HNC and S_1 C_2H_2

The potential surface for the electronic ground state of the [H,C,N] system has two minima: the linear HCN and HNC isomers, separated by approximately 5200 cm^{-1}. The reaction coordinate of the bond-breaking HCN-HNC isomerization corresponds mainly to the ν_2 bending vibration, and the barrier to isomerization is nearly 17,000 cm^{-1} above the HCN minimum. Extensive experimental term values for both isomers are available up to 10,000 cm^{-1} above the HCN minimum (*26*). To continue the analysis up to and beyond the barrier energy, we used spectroscopically assigned ab initio eigenenergies (*26*–*28*). In (*26*), levels with high bending excitation were reported to deviate unexpectedly from effective Hamiltonian predictions, reflecting the presence of the double-well potential.

The S_1 state of C_2H_2 supports cis and trans conformers, with the cis conformer lying about 2672 cm^{-1} above the trans. As illustrated in Fig. 3, the transition state is planar and nearly half-linear (*29*). The bare saddle point energy is calculated to be 4979 cm^{-1} above the trans minimum, but with an uncertainty of hundreds of cm^{-1}, even for the most accurate calculations to date (*30*). A torsional isomerization path might have been expected on the basis of cis-trans isomerizations in other molecules, but this is not found here.

The height of the barrier relative to the fundamental frequencies leads us to expect at least some normal vibrational structure, even in the shallower cis well. Thus far, several cis vibrational levels have been identified, in reasonable agreement with ab initio calculations (*31*–*33*). In the trans well, almost all of the vibrational levels below the barrier have been assigned (*33*). Of the six trans conformer vibrational modes, four are fairly well behaved: the Franck-Condon active vibrations ν_2 (CC stretch) and ν_3 (trans bend) (*34*), and the CH stretching modes ν_1 and ν_5 (*35*, *36*). On the other hand, a large portion of the trans vibrational manifold can only be understood within the framework of bending polyads $B^{n=(v_4+v_6)}$ (*37*), because of the Darling-Dennison and Coriolis interactions between the low-frequency ungerade bending modes, ν_4 (torsion) and ν_6 (cis bend).

Despite the success of the polyad model in reproducing the level structures associated with the bending vibrations, there are disturbing exceptions. As illustrated in figure 13 of (*38*), the series of 3^nB^2 polyads exhibits a surprising trend, with the energy of the lowest member of the polyad decreasing rapidly relative to the energies of the other polyad members. Although inexplicable by conventional models, this occurrence turns out to be intimately related to the isomerization dynamics discussed here.

Determination of the barrier height

We now apply the isomerization dip concept, and in particular Eq. 4, to the barrier proximal energy levels discussed above. Figure 4 shows the results of the pure bending (ω_2^{eff}) effective frequency analysis for HCN-HNC. The barrier heights for both wells are found to be within 1% of the ab initio values. To compare E_{TS} to calculated barrier heights, either the ab initio zero point energy must be subtracted from the calculated barrier height, or an effective zero point energy must be added to the fitted E_{TS} value (see supplementary text). A consistency check of the HCN-HNC analysis stems from another dynamical parameter that affects ω_2^{eff} and the effective barrier height: the vibrational angular momentum, ℓ. The fitted E_{TS} barrier heights are summarized in table S5 and, as expected, the barrier height increases approximately quadratically with ℓ.

Figure 5A shows plots of ω_3^{eff} and ω_6^{eff} for the 3^n6^2 series of C_2H_2, where Eq. 4 can be seen to fit the observed data very well (see tables S1 and S2 for details of the fits). The 3^n6^2 levels experience the effects of the barrier most strongly, whereas the 3^n levels are completely uninfluenced by it, because a combination of q_3 and q_6 is required to access the transition state geometry. Both ω_3^{eff} and ω_6^{eff} can be obtained as a function of ν_6 as well, reading the array of term values in table S2 horizontally rather than vertically. The same {$\overline{E}$, ω^{eff}} data are obtained, but in different sets.

Reaction path analysis

Several possibilities arise when the ω^{eff} analysis is extended to additional vibrational progressions. The first, shown in Fig. 5C, is that of differentiating between isomerization pathways. We

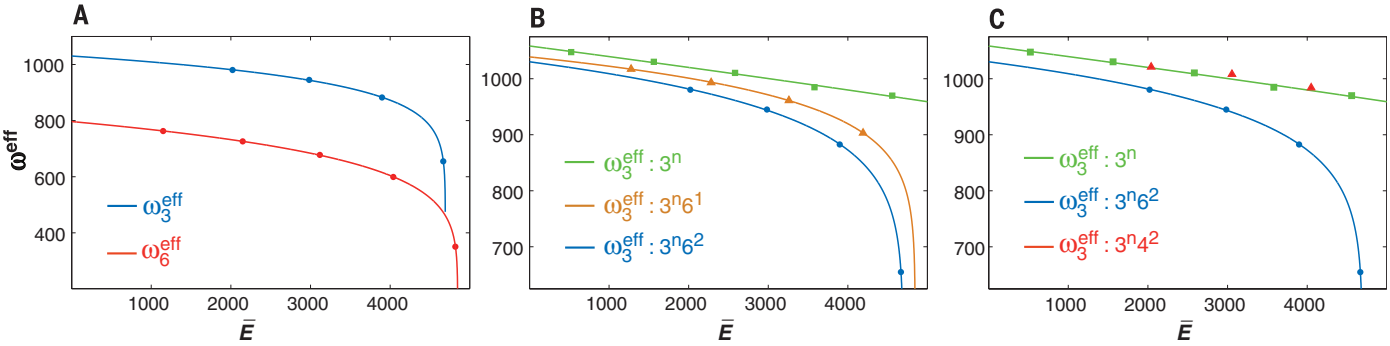

Fig. 5. The ω^{eff} analysis for S_1 C_2H_2. The dip is expected near the ab initio value of 4979 cm^{-1}. Data are from tables S1 to S3. (**A**) Experimental ω^{eff} for the 3^n6^2 levels, shown with fits to Eq. 4. ω_3^{eff} is obtained directly from the progression of 3^n6^2 levels, and ω_6^{eff} is derived from the 3^n6^2 and 3^n6^1 levels at a given n_3. (**B**) Experimental ω_3^{eff} for the 3^n6^2 levels as compared to ω_3^{eff} for other progressions with varying quanta of ν_6, shown with fits to Eq. 4. The 3^n6^2 series has the sharpest dip, in close analogy to the $K = \ell = 0$ series in the "Dixon dip" (*12*). (**C**) ω_3^{eff} plots for the 3^n, 3^n4^2, and 3^n6^2 progressions. The 3^n4^2 series follows the normal behavior of the 3^n levels, despite the isomerization dip observed in the 3^n6^2 levels. This shows that the torsional mode ν_4 is not involved in the isomerization process at these energies.

have noted already that certain progressions, such as the 3^n of *trans*-C_2H_2, show no sign of an isomerization dip. Here we see that surprisingly, the 3^n4^2 levels exhibit the same ω_3^{eff} as the 3^n, from which we conclude that the torsional cis-trans isomerization pathway is closed at these energies. This observation is consistent with the harmonic behavior in ν_4 noted in (*37*). Furthermore, the very strong interactions between ν_4 and ν_6, as well as the inevitable evolution of the torsion as the molecule straightens, would have led us to predict some kind of nonlinear behavior of the ω_3^{eff} from the 3^n4^2 levels. The absence of any such effects implies that the torsion is a spectator mode independent of the isomerization occurring in ν_3 and ν_6. Unlike in many other molecules, torsion does not play a role in this cis-trans isomerization. It appears that the residual π bond, despite its incomplete complement of substituents, leads to the preference for in-plane isomerization (Fig. 3).

The clear distinction between spectator modes and isomerizing modes suggests that other properties of the saddle point may be obtainable from ω^{eff} analysis. Consider a separable system that consists of an asymmetric double minimum in x and a harmonic oscillator in y: $V(x, y) = V(x) + (ky^2/2)$. Because the Hamiltonian is separable, $E = E_x + E_y$, and therefore ω_x^{eff} does not depend on y, in the same way that ω_3^{eff} does not depend on ν_4 in *trans*-S_1 C_2H_2. This means that the ω_y of the transition state is unchanged from that of the minimum. We can then imagine a case where $[\partial^2V(x, y)]/\partial y^2$ varies with x. In such a case it is possible to extract a value for ω_y of the transition state from the spacing of the ω_x^{eff} curves, or by plotting ω_y^{eff} directly, including data from above the saddle point energy (*39*). To give a specific example from a rotational degree of freedom, a quadratic fit of the ℓ-dependence of the $0\nu_20$ HCN barrier height (table S5) yields $(A - \overline{B})_{TS} = 11.1\ (\pm 0.9)\ cm^{-1}$ for the transition state, which agrees well with the ab initio value of 12.2 cm^{-1}. These hitherto unmeasurable transition state rotational constants and frequencies, in addition to the saddle point energy, are critical inputs to the expression for the rate constant in transition state theory (*2*).

The ideas about spectator modes articulated here are confirmed by analysis of the HCN-HNC stretching mode progressions; neither shows any dip up to 19,000 cm^{-1} above the HCN minimum. Furthermore, the shifts in the fitted barrier heights for ν_2 progressions built upon excitation in ν_1 and ν_3 match well with the one-dimensional pseudopotentials $V_{\nu_1,\nu_3}(\theta)$ from (*40*–*42*) and the stretching frequencies (table S4).

Implications and outlook

The method described here provides qualitative and quantitative information about the isomerization mechanism and the transition state solely on the basis of experimental data. The reaction coordinate can be identified from the isomerization dips shown by active vibrations, and quantitative information about the energy, vibrational frequencies, and rotational constants of the transition state becomes available. It is especially promising that this analysis stems entirely from a small subset of the vibrational levels; in other words, a full vibrational analysis is not necessary. Special states exist that encode chemically important information, although it may not always be easy to recognize them.

The most exciting outcome of the excellent fits using Eq. 4 is the determination of the transition state energies. The uncertainties in E_{TS} are at least as good as what is currently available from theory. In many cases, experiments might only confirm theoretical predictions, but we expect them to sharpen our understanding, and the potential value of our method goes well beyond validating theory. For example, we envision that this approach is a step toward establishing kinetics on the same firm experimental foundation as that already enjoyed by thermochemistry, where precise information is broadly available. This could aid in modeling complex reaction networks as well as provide benchmarks for theoretical calculations.

The next stages in developing the concepts of isomerization dip and effective frequency will require more experimental data for model systems as well as refinement of the basic ideas. For example, it is clear that ω^{eff} is a multidimensional quantity, which could be treated by suitable multidimensional analysis. However, it is not yet clear how to define $\overline{E}$ in many dimensions. On the experimental side, the MgNC ↔ MgCN isomerization (*43*) is similar to HCN ↔ HNC, although with a much lower barrier; with higher resolution than has been used so far, it should be possible to get detailed information on the isomerizing levels all the way to the barrier and beyond.

The most promising prospect is the application of this approach to larger molecular systems. For example, the principles presented in this work will provide a framework for experimental characterization of the transition state and detailed mechanism in other reactions, such as cis-trans isomerization, as epitomized by stilbene, and 1,2 hydrogen shifts, which are ubiquitous in organic chemistry. Remarkably little frequency-domain spectroscopy has been done at the high energies relevant to chemical kinetics. Partly this is because it was not clear previously what could be learned, and partly it is because the spectra rapidly become very complicated at such energies, so it is difficult to recognize the important patterns. In time it is likely that new classes of experiments will sample the information about isomerization that is encoded in time- or frequency-domain spectra of larger molecules. Our hope is that the concepts and examples described here will be viewed as templates for the characterization of isomerizing systems, thereby challenging and guiding spectroscopists to attack similar problems of chemical interest.

REFERENCES AND NOTES

1. S. Arrhenius, *Z. Phys. Chem.* **4**, 226–248 (1889).
2. H. Eyring, *J. Chem. Phys.* **3**, 107 (1935).
3. H. Eyring, M. Polanyi, *Z. Phys. Chem. B* **12**, 279 (1931).
4. M. G. Evans, M. Polanyi, *Trans. Faraday Soc.* **31**, 875 (1935).
5. E. Wigner, *Trans. Faraday Soc.* **34**, 29 (1938).
6. D. Townsend *et al.*, *Science* **306**, 1158–1161 (2004).
7. J. M. Bowman, B. C. Shepler, *Annu. Rev. Phys. Chem.* **62**, 531–553 (2011).
8. J. C. Polanyi, A. H. Zewail, *Acc. Chem. Res.* **28**, 119–132 (1995).
9. R. T. Birge, H. Sponer, *Phys. Rev.* **28**, 259–283 (1926).
10. R. J. LeRoy, R. B. Bernstein, *J. Chem. Phys.* **52**, 3869 (1970).
11. R. J. Leroy, R. B. Bernstein, *Chem. Phys. Lett.* **5**, 42–44 (1970).
12. R. N. Dixon, *Trans. Faraday Soc.* **60**, 1363 (1964).
13. The angular momentum quantum number K plays two roles here: that of the asymmetric top rotational quantum number and the linear molecule vibrational angular momentum quantum number, ℓ.
14. M. P. Jacobson, M. S. Child, *J. Chem. Phys.* **114**, 262 (2001).
15. H. Ishikawa *et al.*, *Annu. Rev. Phys. Chem.* **50**, 443–484 (1999).
16. S. C. Ross, T. J. Butenhoff, E. A. Rohlfing, C. M. Rohlfing, *J. Chem. Phys.* **100**, 4110 (1994).
17. M. S. Child, *Adv. Chem. Phys.* **136**, 39–94 (2008).
18. S. Yang, V. Tyng, M. E. Kellman, *J. Phys. Chem. A* **107**, 8345–8354 (2003).
19. N. Moiseyev, *Non-Hermitian Quantum Mechanics* (Cambridge Univ. Press, 2011).
20. D. Larese, F. Iachello, *J. Mol. Struct.* **1006**, 611–628 (2011).
21. M. S. Child, M. P. Jacobson, C. D. Cooper, *J. Phys. Chem. A* **105**, 10791–10799 (2001).
22. N. B. Slater, *Nature* **180**, 1352–1353 (1957).
23. D. W. Oxtoby, S. A. Rice, *J. Chem. Phys.* **65**, 1676 (1976).
24. M. S. Child, *J. Phys. Math. Gen.* **31**, 657–670 (1998).
25. Regarding ω^{eff} versus $\overline{E}$ as opposed to ω^{eff} versus n: Using n simplifies derivations, but $\overline{E}$ is more practical for actual use. Furthermore, plotting against $\overline{E}$ gives more direct information about the potential energy surface.
26. G. Ch. Mellau, *J. Chem. Phys.* **134**, 234303 (2011).
27. T. van Mourik *et al.*, *J. Chem. Phys.* **115**, 3706 (2001).
28. G. J. Harris, J. Tennyson, B. M. Kaminsky, Y. V. Pavlenko, H. R. A. Jones, *Mon. Not. R. Astron. Soc.* **367**, 400–406 (2006).
29. J. F. Stanton, C.-M. Huang, P. G. Szalay, *J. Chem. Phys.* **101**, 356 (1994).
30. J. H. Baraban, A. R. Beck, A. H. Steeves, J. F. Stanton, R. W. Field, *J. Chem. Phys.* **134**, 244311 (2011).
31. A. J. Merer, A. H. Steeves, J. H. Baraban, H. A. Bechtel, R. W. Field, *J. Chem. Phys.* **134**, 244310 (2011).
32. J. H. Baraban *et al.*, *Mol. Phys.* **110**, 2707–2723 (2012).
33. J. H. Baraban, J. F. Stanton, A. J. Merer, R. W. Field, *Mol. Phys.* **110**, 2725–2733 (2012).
34. J. K. G. Watson, M. Herman, J. C. Van Craen, R. Colin, *J. Mol. Spectrosc.* **95**, 101–132 (1982).
35. A. H. Steeves, A. J. Merer, H. A. Bechtel, A. R. Beck, R. W. Field, *Mol. Phys.* **106**, 1867–1877 (2008).
36. J. D. Tobiason, A. L. Utz, F. F. Crim, *J. Chem. Phys.* **99**, 928 (1993).
37. A. J. Merer *et al.*, *J. Chem. Phys.* **129**, 054304 (2008).
38. A. H. Steeves *et al.*, *J. Mol. Spectrosc.* **256**, 256–278 (2009).
39. In a real system, reaction path curvature could occur, such that the normal modes of the minima are not identical to those of the transition state. This would complicate matters, but the modes necessarily evolve smoothly from minimum to transition state.
40. M. Joyeux, S. Y. Grebenshchikov, J. Bredenbeck, R. Schinke, S. C. Farantos, *Adv. Chem. Phys.* **130**, 267–303 (2005).
41. Z. Bačić, J. C. Light, *J. Chem. Phys.* **86**, 3065 (1987).
42. J. C. Light, Z. Bačić, *J. Chem. Phys.* **87**, 4008 (1987).
43. M. Fukushima, T. Ishiwata, *J. Chem. Phys.* **135**, 124311 (2011).
44. D. Lauvergnat, A. Simon, P. Maître, *Chem. Phys. Lett.* **350**, 345–350 (2001).

ACKNOWLEDGMENTS

We thank M. Joyeux for providing the HCN-HNC pseudopotentials. Supported by NSF Graduate Research Fellowship DGE 1144083 (P.B.C.), an Alexander von Humboldt Foundation Feodor Lynen fellowship for experienced researchers (G.C.M.), and U.S. Department of Energy grant DE-FG0287ER13671.

SUPPLEMENTARY MATERIALS

www.sciencemag.org/content/350/6266/1338/suppl/DC1
Supplementary Text
Figs. S1 and S2
Tables S1 to S6
References (*45*–*60*)

1 September 2015; accepted 29 October 2015
10.1126/science.aac9668

REPORTS

SIGNAL PROCESSING

Subnoise detection of a fast random event

V. Ataie, D. Esman, B. P.-P. Kuo, N. Alic, S. Radic*

Observation of random, nonrepetitive phenomena is of critical importance in astronomy, spectroscopy, biology, and remote sensing. Heralded by weak signals, hidden in noise, they pose basic detection challenges. In contrast to repetitive waveforms, a single-instance signal cannot be separated from noise through averaging. Here, we show that a fast, randomly occurring event can be detected and extracted from a noisy background without conventional averaging. An isolated 80-picosecond pulse was received with confidence level exceeding 99%, even when accompanied by noise. Our detector relies on instantaneous spectral cloning and a single-step, coherent field processor. The ability to extract fast, subnoise events is expected to increase detection sensitivity in multiple disciplines. Additionally, the new spectral-cloning receiver can potentially intercept communication signals that are presently considered secure.

The spontaneous decay of a molecule (*1*), a fast radio-astronomy burst (*2*), or the arrival of a secure communication packet (*3*) are examples of nonrepetitive events that pose similar challenges for observers. In addition to requiring a fast and sensitive detector, a randomly occurring signal must be extracted from the background noise in either the optical or electrical domain. If the event is repetitive, this noise can be substantially eliminated by classical averaging (*4*). When noise is temporally uncorrelated, the summation of a sufficiently large number of signal instances can lead to an arbitrary signal-to-noise ratio (SNR) improvement (*4*). Simple to implement, averaging plays a critical role in the capture of fast, weak, or noisy signals. A powerful generalization of the averaging concept was developed for cyclostationary signals accompanied by spectrally uncorrelated noise (*5*). In contrast to temporal averaging, cyclostationary and cumulant analysis recognizes that noise spectral components can be rejected if the signal is cyclically modulated. Intuitively, a similar treatment could be extended to a single-instance signal if it can be temporally replicated. In earlier work (*6*), a recirculating loop was used to create multiple, serialized signal outputs that can be independently detected and subsequently averaged. Such replication requires an amplifier to overcome coupling losses, thus injecting excess (amplification) noise. Unfortunately, all known temporal replication mechanisms (*6*, *7*) are inherently lossy and are subject to this basic limitation.

However, a single event can be replicated to frequency nondegenerate copies (spectral clones) in a nearly noiseless manner (*8*). We show that an isolated pulse can be extracted from noise by single-step processing of its spectral clones. To demonstrate single-event detection, an 80-ps-long pulse was cloned and processed in order to increase the received SNR by 14.1 dB. To separate signal from noise, the experiment varied the number of spectral copies from 6 to 36, proving that background rejection can be progressively increased even when the random event is immersed in a high level of background noise.

When a repetitive signal $s(t)$ is accompanied by noise $n(t)$, its estimate can be reached by coherent summation (*4*): $\sum_{k-1}^{N} \frac{1}{N\Delta T}\int_{t_k-\Delta T/2}^{t_k+\Delta T/2}[s(t)+n(t)]dt$, where t_k and ΔT indicate the signal instance and observation (detection) interval, respectively. For a sufficiently large occurrence count ($N \gg 1$), when noise is a zero-mean uncorrelated process (*4*), this estimate can be arbitrarily accurate because $\sum_{k-1}^{N} \frac{1}{N\Delta T}\int_{t_k-\Delta T/2}^{t_k+\Delta T/2} n(t)dt \to 0$. In the case of a single event ($N = 1$), noise cannot be repeatedly measured but can still be discriminated from the signal in the spectral domain. Indeed, whereas two distinct signal spectral components have a deterministic relation, the same is not true for noise components. This important difference was recognized (*5*) and used to discriminate δ-correlated noise from the signal. In the simplest cyclostationary receiver implementation, the product of two spectral components is integrated over many signal cycles in order to acquire the correlation between any pair of spectral components. The correlation collapses when only noise is received, thus allowing for signal feature extraction (*5*).

Cyclostationary detection fails to reject the noise accompanying an isolated (single-cycle) event because no correlation can be drawn at any time instance beyond the event duration. However, by replicating such a signal in a substantially noiseless manner, one can still exploit the fact that the signal possesses spectral correlation, whereas the received noise does not (Fig. 1). To describe noise discrimination in this case, let us assume that a set of lossless narrow filters with bandwidth δf can be constructed over the full span of a Δf-wide signal (Fig. 1). The spectral decomposition (*9*) of the received field $r(t) = s(t) + n(t)$ can be described by the short-time Fourier transform (STFT) $R(t, k\delta f) = \int_{-1/2\delta f}^{+1/2\delta f} w(t-\tau)r(\tau)e^{j2\pi k\delta f\tau}d\tau$, where $w(t) = \sin(\pi\delta f t)/\pi t$ is the δf-wide band-pass window function. STFT is a slowly varying complex function that, when sampled within the detection interval $[t \pm 1/(2\delta f)]$ (*9*), represents the received spectral component centered at f_k as the phasor sum $\boldsymbol{R_k} = \boldsymbol{S_k} + \boldsymbol{n_k}$. In the absence of noise, its magnitude is a measure of the signal spectral density $\tilde{S}(f_k)$; in the absence of the signal, the magnitude and phase of this phasor is defined by the statistics of the interfering noise field.

The STFT cannot be realized by mere filtering centered at f_k because it will result in the carrier-specific phase rotation $2\pi f_k t$. To address this, the differential phasor rotation must be stopped by frequency shifting each output to the baseband (*9*). Consequently, phasor summation across the entire bandpass set leads to a noise-sensitive outcome. For a noiseless, transform-limited signal pulse, this summation results in collinear vector addition. In contrast, when only noise is present this summation resembles a random walk in the complex plane, (Fig. 1, inset Σ). Consequently, the effective SNR increase provided by a spectrally cloning detector should scale with the replica count N as $\sim (N/\sqrt{N})^2$ (*10*).

Although the single-event detector is conceptually simple, its realization faces a set of basic challenges. In the first of these challenges, the spectral decomposition process must be distortionless and lossless. This requirement is easily satisfied for slow, microsecond-scale events that can be quantized with high precision (*11*, *12*). In this case, the digitized field can be used to calculate the sampled STFT and emulate the coherent subband summation (Fig. 1). However, when the event is fast (subnanosecond), signal quantization imposes a fundamental resolution limit (*11*, *12*), eliminating such a computational approach. Its alternative, physical channelization (*13*), is neither distortionless nor lossless.

Recognizing these limits, we mapped the received signal onto widely separated frequency carriers (ΔF) and performed spectral decomposition by means of a strictly periodic bandpass process (Fig. 1). In the optical domain, the received spectrum can be parametrically cloned (*8*) and subsequently decomposed by a single physical filter (*14*). This strategy cannot be applied in spectral ranges where efficient, low-noise parametric mixers (*15*, *16*) do not exist. Among those ranges, the microwave range (0.3 to 100 GHz) is arguably the most important because it hosts commercial (*17*), scientific (*17*), and defense (*17*, *18*) signals. To construct a single-event detector operating in this band, we mapped the received field onto a highly coherent frequency comb (Fig. 2).

In the first experiment, a single-instance signal was represented by a 12-GHz-wide pulse and was

Department of Electrical and Computer Engineering, University of California, San Diego, La Jolla, CA 92093, USA.
*Corresponding author. E-mail: sradic@ucsd.edu

Downloaded from www.sciencemag.org on December 14, 2015

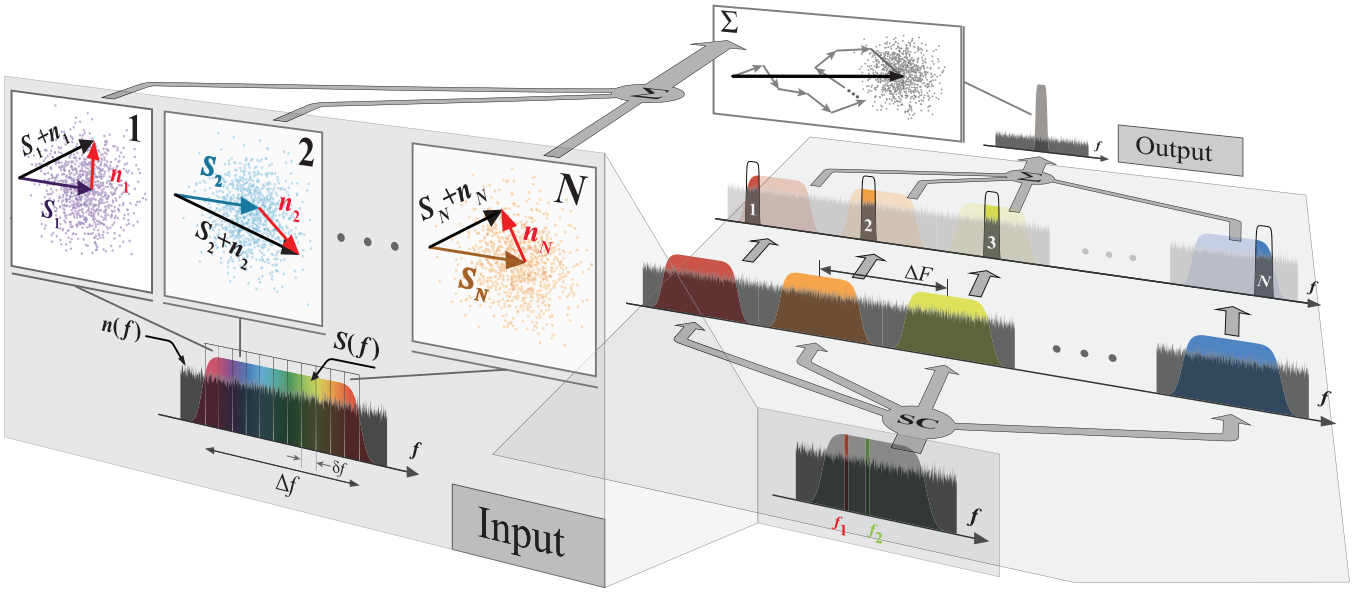

Fig. 1. Single-event noise discrimination. A set of lossless bandpass filters (δ*f*) spectrally decomposes the signal and noise fields into a set of $\mathbf{S_k}$ and $\mathbf{n_k}$ phasors. In the reference frame of the signal carrier, these phasors are not synchronous and rotate at different rates $\omega = 2\pi f_k$ ($k = 1, N$); Spectral cloning (SC) maps the received field onto a widely spaced grid (Δ*F*) and enables lossless spectral decomposition by means of a single periodic process (filter). To coherently sum signal (noise) phasors, differential phasor rotation must be arrested by means of a frequency-invariant baseband process.

cloned to six spectral replicas. The pulse was centered at 6.5 GHz and combined with broadband noise generated by a photodiode that receives amplified spontaneous emission from an erbium-doped fiber amplifier. The signal and noise were combined and used to modulate a tunable optical frequency comb (TOC_1), replicating the noise-loaded signal onto its frequency modes. Each mode had an optical SNR in excess of 40 dB, measured within a 12.5-GHz bandwidth and at 1550 nm. TOC_1 had a continuously variable frequency pitch (*19*) that was set to $\Delta F = 50$ GHz. The second (Vernier) optical comb (TOC_2) was used as a local-oscillator (LO) array, with frequency pitch differing by $\delta f = 2$ GHz from the signal comb. Both optical combs were seeded by a single master oscillator with a spectral linewidth of 3 kHz, guaranteeing a high degree of mutual coherence (*20*) during the longest signal capture time (~256 μs). The ability to continuously tune the frequency pitch of both optical combs is critical because it defines the offset between a specific spectral replica and the distinct LO mode. When combined in a detector with bandwidth δf_D, the beating between the k^{th} replica and the LO mode selects a δf_D-wide spectral segment that is centered $f_k = k \times \delta f$ away from the replica carrier. If the detector bandwidth and the comb frequency offset are matched ($\delta f_D = \delta f$), the comb-assisted cloning becomes equivalent to the spectral decomposition (Fig. 1). Two wavelength-demultiplexing elements (WDMs) were used to route the spectrally overlapping copy and LO mode to a coherent detector (D). A matched detector bandwidth, defined by the ratio of the pulse bandwidth ($\Delta f = 12$ GHz) and the spectral replica count $N = 6$, defines the frequency offset between the signal (TOC_1) and Vernier combs (TOC_2), $\delta f = \Delta f / N = 2$ GHz. Last, the output of each detector D is sampled and used to perform coherent summation in order to discriminate the pulse from the noise, as detailed in (*21*).

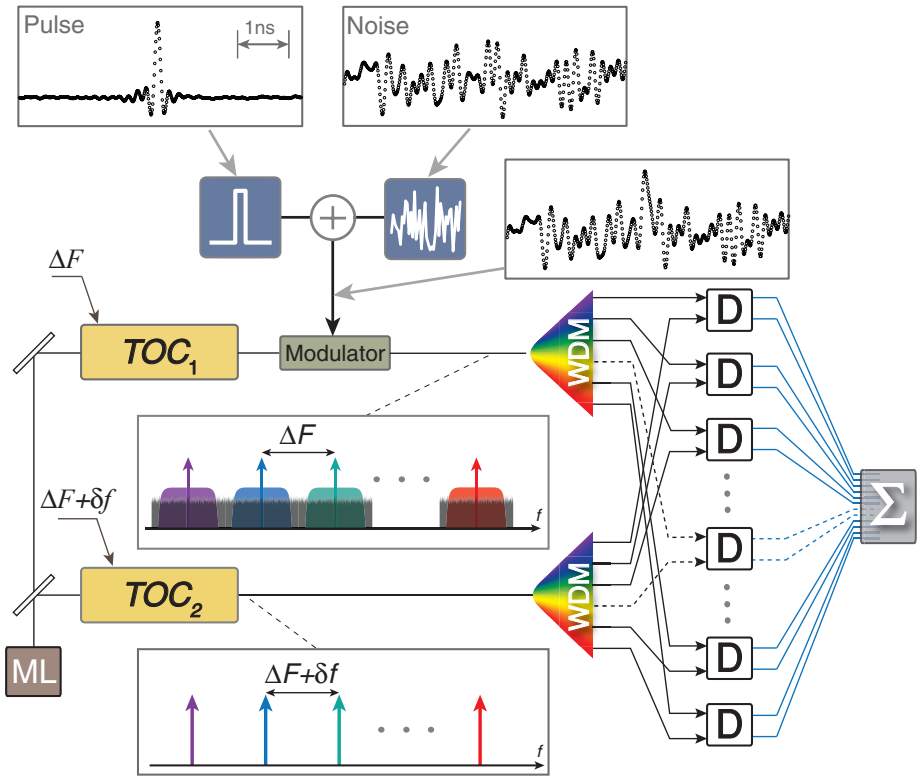

Fig. 2. Spectral cloning receiver. Two frequency-tunable optical combs (TOC_1 and TOC_2) are derived from a single master laser (ML). A single pulse is combined with noise and used to modulate TOC_1 with frequency pitch Δ*F*. The Vernier comb TOC_2, with frequency pitch $\Delta F + \delta f$, serves as local oscillator array and is combined with the received signal at the subrate detector array (D).

The first measurement generated six spectral copies of an 80-ps pulse accompanied by various levels of interfering noise (Fig. 3A). The input SNR (SNR_{IN}) was defined as the ratio of the signal and noise powers, measured within the observation interval $N/\Delta f = 500$ ps. We performed

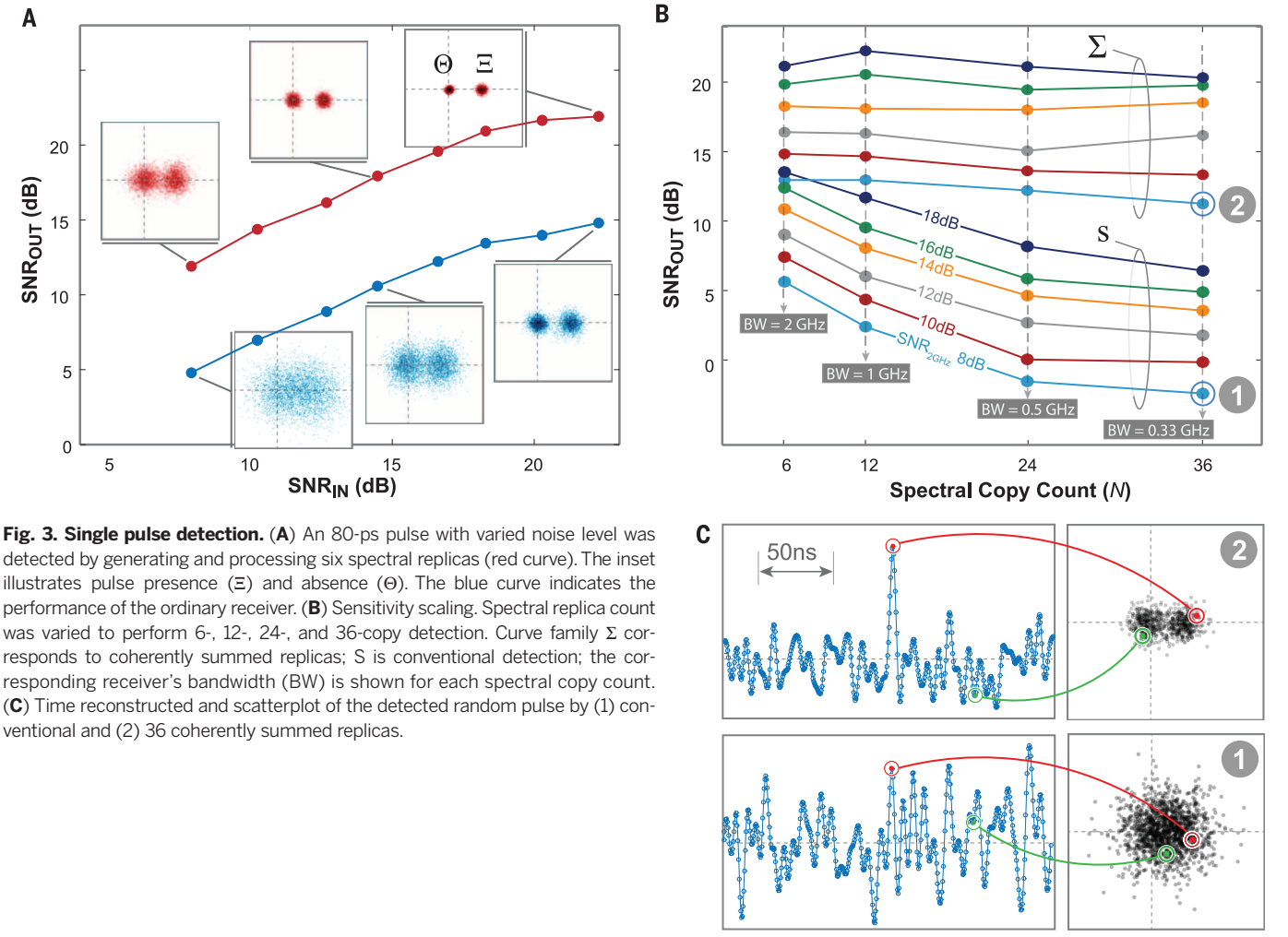

Fig. 3. Single pulse detection. (**A**) An 80-ps pulse with varied noise level was detected by generating and processing six spectral replicas (red curve). The inset illustrates pulse presence (Ξ) and absence (Θ). The blue curve indicates the performance of the ordinary receiver. (**B**) Sensitivity scaling. Spectral replica count was varied to perform 6-, 12-, 24-, and 36-copy detection. Curve family Σ corresponds to coherently summed replicas; S is conventional detection; the corresponding receiver's bandwidth (BW) is shown for each spectral copy count. (**C**) Time reconstructed and scatterplot of the detected random pulse by (1) conventional and (2) 36 coherently summed replicas.

4720 detections to quantify the ability to distinguish signal from noise. Measurements (Fig. 3A) are shown with each point in the scatter plot corresponding to a single detection outcome. Intuitively, the detection of a low-noise pulse corresponds to highly distinguishable ensemble scatters. As an example, the measurement ensemble Ξ (Fig. 3A) corresponds to the detection of a signal with SNR_{IN} = 22.3 dB, whereas in Θ, the signal was absent. The less overlap between these scatters reflects a higher confidence level (*22*) with which one can differentiate between pulse presence and absence, as detailed in (*21*). To quantify the spectral-cloning receiver performance, we define the output SNR (SNR_{OUT}) as the ratio between the square of the scatter mean separation and its variance. As an illustration, a pulse with SNR_{IN} = 7.9 dB is detected with SNR_{OUT} = 11.9 dB, indicating a 4-dB increase in the level of detection confidence. To compare the performance of the spectral cloning and conventional detector, we did not perform coherent decomposition and summation in a subsequent set of measurements. Instead, the output of each detector was recorded and its average was plotted (Fig. 3A). The increase in SNR_{OUT} between the two cases varies from 7.1 dB (SNR_{IN} = 22.3 dB) to 7.5 dB (SNR_{IN} = 18.3 dB), which is in agreement with the value predicted previously for six (N = 6) spectral replicas ~ $(N/\sqrt{N})^2$ ~ 7.8 dB.

Last, to test the main hypothesis, which predicts that the sensitivity increases with spectral clone count, we constructed receivers with 12, 24, and 36 replicas. To circumvent the physical scaling of the subrate detector array, interfering noise was synthesized by using a 64-GS/s digital-to-analog-converter (DAC) and combined with a 12-GHz-wide pulse, as described in (*21*). Clone-scaling measurements (Fig. 3B) indicate that an average sensitivity gain of 10.4, 13.1, and 14.1 dB was achieved when 12, 24, and 36 copies were generated, respectively. These measurements agree remarkably well with the predicted sensitivity gains $(N/\sqrt{N})^2$ ~ 10.8, 13.8, and 15.6 dB, when N = 12, 24, and 36, respectively.

These results prove the importance of low-noise, low-distortion spectral replication for the detection of a random, nonrepetitive signal. Although we describe the detection of a single pulse, it is not difficult to recognize that spectral cloning can be used for considerably more complex analyses of random events, in both the microwave and optical domains. Besides discriminating noise, the ability to accurately replicate a fast, random event onto an arbitrary frequency map paves the way for low-latency, computation-free Fourier processing beyond simple coherent summation.

REFERENCES AND NOTES

1. J. R. Lakowicz, *Principles of Fluorescence Spectroscopy* (Springer, New York, 2006).
2. D. Thornton *et al.*, *Science* **341**, 53–56 (2013).
3. G. J. Pendock, D. D. Sampson, *IEEE Photon. Technol. Lett.* **7**, 1504–1506 (1995).
4. R. N. McDonough, A. D. Whalen, *Detection of Signals in Noise* (Academic Press, San Diego, CA, 1995).
5. W. A. Gardner, A. Napolitano, L. Paura, *Signal Process.* **86**, 639–697 (2006).
6. A. Jolly, J. F. Gleyze, J. C. Jolly, *Opt. Commun.* **264**, 89–96 (2006).
7. W. R. Donaldson, J. R. Marciante, R. G. Roides, *IEEE J. Quantum Electron.* **46**, 191–196 (2010).
8. Z. Tong, S. Radic, *Adv. Opt. Photon.* **5**, 318–384 (2013).
9. J. B. Allen, *IEEE Trans. Acoust. Speech Signal Process.* **25**, 235–238 (1977).
10. Y. Rozanov, *Probability Theory, Random Processes and Mathematical Statistics* (Springer, New York, 1995).
11. R. H. Walden, *IEEE J. Sel. Areas Comm.* **17**, 539–550 (1999).
12. B. Murmann, *ADC Performance Survey* 1997–2015; available at http://web.stanford.edu/~murmann/adcsurvey.html (2015).
13. G. W. Anderson, D. C. Webb, A. E. Spezio, J. N. Lee, *Proc. IEEE* **79**, 355–388 (1991).
14. C.-S. Bres, A. O. J. Wiberg, S. Zlatanovic, S. Radic, *J. Lightwave Technol.* **30**, 3192–3198 (2012).
15. M. E. Marhic, *Optical Parametric Amplifiers, Oscillators and Related Devices* (Cambridge Univ. Press, 2008).
16. Z. Tong *et al.*, *Nat. Photonics* **5**, 430–436 (2011).
17. J. D. Taylor, *Ultrawideband Radar: Applications and Design* (CRC Press, 2012).

18. C. Weitkamp, *Lidar: Range-Resolved Optical Remote Sensing of the Atmosphere* (Springer, New York, 2014).
19. E. Myslivets, B. P.-P. Kuo, N. Alic, S. Radic, *Opt. Express* **20**, 3331–3344 (2012).
20. V. Ataie, E. Myslivets, B. P.-P. Kuo, N. Alic, S. Radic, *J. Lightwave Technol.* **32**, 840–846 (2014).
21. Material and methods are available as supplementary materials on *Science* Online.
22. G. Jacobsen, *Noise in Digital Optical Transmission Systems* (Artech House, Boston, 1994).

ACKNOWLEDGMENTS

This work is funded in part by the Defense Advanced Research Projects Agency. University of California has filed a patent on the method and applications of random signal detection and coherent analysis.

SUPPLEMENTARY MATERIALS

www.sciencemag.org/content/350/6266/1343/suppl/DC1
Materials and Methods
Figs. S1 to S7
References (*23*–*29*)

20 August 2015; accepted 12 October 2015
10.1126/science.aac8446

SURFACE SCIENCE

Electron-hole pair excitation determines the mechanism of hydrogen atom adsorption

Oliver Bünermann,[1,2,3]* Hongyan Jiang,[1] Yvonne Dorenkamp,[1] Alexander Kandratsenka,[1,2] Svenja M. Janke,[1,2] Daniel J. Auerbach,[1,2] Alec M. Wodtke[1,2,3]

How much translational energy atoms and molecules lose in collisions at surfaces determines whether they adsorb or scatter. The fact that hydrogen (H) atoms stick to metal surfaces poses a basic question. Momentum and energy conservation demands that the light H atom cannot efficiently transfer its energy to the heavier atoms of the solid in a binary collision. How then do H atoms efficiently stick to metal surfaces? We show through experiments that H-atom collisions at an insulating surface (an adsorbed xenon layer on a gold single-crystal surface) are indeed nearly elastic, following the predictions of energy and momentum conservation. In contrast, H-atom collisions with the bare gold surface exhibit a large loss of translational energy that can be reproduced by an atomic-level simulation describing electron-hole pair excitation.

Adsorption of atomic hydrogen (H) is the simplest reaction in surface chemistry. Langmuir's study of this reaction ushered in the era of modern surface science (*1*). Hydrogen adsorption is important for many fields, ranging from heterogeneous catalysis (*2*) to interstellar molecular hydrogen production (*3*). Adsorbed H atoms can stabilize surfaces of intrinsically reactive solids, healing dangling bonds and making them suitable for industrial processing (*4*). Adsorption is also central to hydrogen storage technologies (*5*), and it is the basis for a chemical means of manipulating the band gap in graphene (*6*).

Despite more than a century of study, we still do not have a fundamental understanding of how H-atom adsorption takes place. Adsorption involves the H atom coming to rest at the surface, losing its initial translational energy, and dissipating the energy of the chemical bond formed with the solid (Fig. 1A). Because of its light mass, energy and momentum conservation requires that the transfer of H-atom translational energy to heavy surface atoms is inefficient; for example, an H atom colliding with a gold atom at a Au(111) surface is expected to transfer only 2% of its translational energy per collision (Fig. 1B). How then can the H atom lose sufficient translational energy to adsorb? As early as 1979, speculations were made, supported by theoretical analysis, that the mechanism of H-atom adsorption at metals could involve the conversion of H-atom translational energy to electronic excitation of the solid (*7*). This requires a failure of the Born-Oppenheimer approximation (BOA), which assumes that electronic motions are much faster than nuclear motions and can be treated separately (*8*). Although failure of the BOA is not without precedence—for example, infrared linewidths of chemisorbed H atoms on metals are believed to be broadened by electronic interactions (*9*), and "chemicurrents" have been detected at Schottky diode junctions (*10*–*12*)—there are no experimental measurements of the translational inelasticity of H atoms with any solid. Moreover, translational excitation of electron-hole pairs occurring because of collisions of atoms or molecules with surfaces has never been observed in the absence of efficient phonon excitation (*13*).

Previous experiments on BOA failure showed that highly vibrationally excited molecules exhibit efficient vibrational relaxation when they collide with a clean single-crystal metal surface, whereas little relaxation is seen with insulators (*14*, *15*). This comparison showed the importance of electronic excitation by molecular vibration, a phenomenon that could also be investigated with first-principles theory (*16*, *17*). Although vibrational relaxation studies tell us nothing about adsorption, they suggest an approach to the problem. If BOA failure were important in H-atom adsorption, we would expect inelastic H-atom scattering from metals and insulators to exhibit dramatic differences in their translational energy loss; furthermore, we could only describe the inelasticity with modern theoretical methods that account for electronic excitation (*18*–*20*).

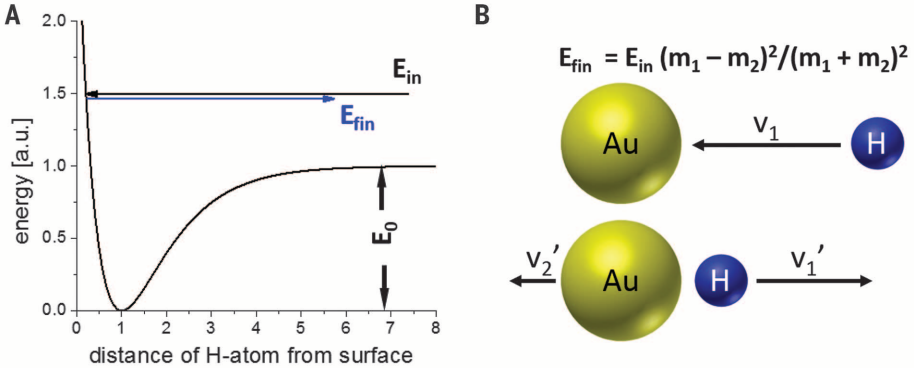

Fig. 1. Adsorption of H atom requires loss of translational energy. (**A**) The incident H atom must lose its initial translational energy, E_{in}, and dissipate the chemical potential energy, E_0, that it discovers in binding to the surface. (**B**) Conserving linear momentum and translational energy in a simple collinear binary collision model leads to a simple relation between E_{in} and the final kinetic energy of the H atom, E_{fin}, that depends only on the masses of the atoms. For the example of H ($m_1 = 1$) colliding with Au ($m_2 = 198$), the H atom retains 98% of its initial energy.

[1]Institute for Physical Chemistry, Georg-August University of Göttingen, Tammannstrasse 6, 37077 Göttingen, Germany. [2]Department of Dynamics at Surfaces, Max Planck Institute for Biophysical Chemistry, Am Faßberg 11, 37077 Göttingen, Germany. [3]International Center for Advanced Studies of Energy Conversion, Georg-August University of Göttingen, Tammannstrasse 6, 37077 Göttingen, Germany.
***Corresponding author. E-mail: oliver.buenermann@chemie.uni-goettingen.de**

Experiments probing inelastic H-atom scattering from surfaces are extremely challenging. Previous studies on H-atom scattering from solids used discharge-based H-atom sources and, in some cases, electromagnetic velocity filters (*21*, *22*). These approaches yield relatively broad H-atom velocity distributions that peak at low translational energies. Detecting H atoms is also challenging: Bolometers (*22*), photographic plates (*23*), and ZnO conductivity detectors (*24*) were sensitive enough to observe surface scattering, but their slow temporal response precludes the study of inelastic scattering. These experimental limitations help explain why, since the first successful observations of H atom scattering from surfaces (*23*), additional studies have measured spatially resolved diffraction rather than inelastic scattering.

Here, we show that the translational energy loss of H atoms colliding at a metal surface predominantly results from electronic excitation of the solid. We produced nearly monoenergetic incident beams of H atoms by laser photolysis, the energy of which can be varied (*25*, *26*), and obtained scattering-angle resolved, translational energy loss spectra by the Rydberg-atom neutral time-of-flight (TOF) method (*27*). Our measurements show that collisions of H atoms at metal surfaces are strongly inelastic. In contrast, H-atom collisions at an insulator are nearly elastic. For the insulator, the small inelasticity can be understood as a simple binary collision between a light and heavy atom where linear momentum is conserved. For H-atom energy loss at a metal, we used a recently developed full-dimensional molecular dynamics (MD) method (*20*) capable of describing both excitation of the solid lattice and electron-hole pairs. This model gives good agreement with experimental results. Switching off electron-hole pair excitation in the simulations resulted in energy loss far less than observed.

A schematic diagram of our apparatus (Fig. 2) shows the pulsed molecular beam expansion that efficiently cooled HI to its ground state, where ultraviolet (UV) laser photolysis produced nearly mono-energetic H atoms. A small fraction of these atoms passed through two differential pumping chambers (not shown), entered an ultrahigh vacuum (UHV) chamber, and collided with a gold (Au) single crystal. The incidence angles, ϑ_i and φ_i, were varied by tilting the Au crystal, which was held in a six-axis UHV manipulator. Recoiling H atoms were subjected to Rydberg tagging (*27*); that is, they were excited by two laser pulses to the long-lived n = 34 Rydberg state, which lies just ~10 meV below the ionization level. These neutral atoms passed a detector aperture and traveled 25 cm in a field-free region, and then through a grounded wire mesh, to encounter a weak (~7 kV/cm) ionizing field just in front of an ion counting detector. H-atom TOFs were recorded by a multichannel scalar. The detector could be rotated so that TOF data could be obtained at many scattering angles, ϑ_s.

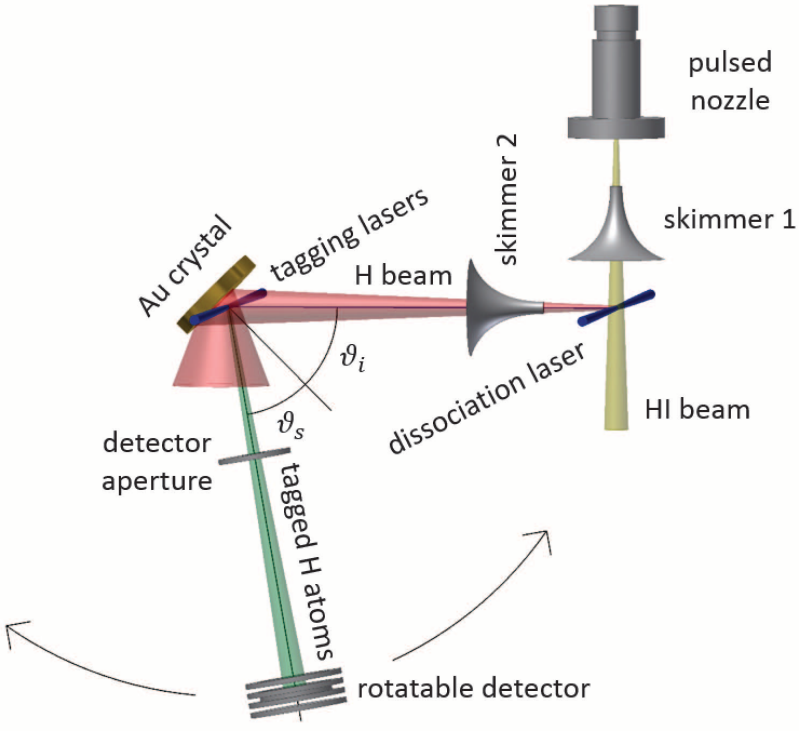

Fig. 2. Schematic of the experimental apparatus. A molecular beam of rotationally cold HI is formed in a pulsed molecular beam expansion. After skimmer 1, the HI beam is crossed by the dissociation laser beam. A small fraction of the H-atom photoproducts pass skimmer 2, pass through two differential pumping stages (not shown), and enter a UHV chamber. Here, they hit the surface of a Au single crystal held on a six-axis manipulator that allows the variation of the polar (ϑ_i) and azimuthal (φ_i) incidence angles. Scattered H atoms are tagged in a two-step process: first, a 121.57-nm photon brings the H atoms into the 2p state. Second, a 365.90-nm photon transfers the atoms into the n = 34 Rydberg state. A fraction of the tagged H atoms pass the detector aperture and travel 25 cm before they reach the detector, where their time of arrival is recorded. The detector is rotatable, allowing the variation of the scattering angle ϑ_s.

The Au surface was cleaned by cycles of Ar-ion sputtering and annealing at 1000 K. Auger electron spectroscopy (AES) and low-energy electron diffraction (LEED) were used to determine the cleanliness and orientation of the Au(111) surface. The Au sample could also be cooled to 45 K with cold gaseous He, allowing Xe condensation. We used a 300-Langmuir exposure (10^{-6} mbar Xe gas for 5 min) to produce a thick Xe layer (an insulating surface) whose structure was not influenced by the underlying Au crystal. Warming easily removed the Xe layer, allowing H-atom scattering measurements from metal and insulator to be made within minutes of one another.

Figure 3A shows representative TOF data for H-atom scattering from Au (open squares) and solid Xe (filled squares). The scattering conditions were E_{in} = 2.76 eV, $\vartheta_i = 45°$, $\vartheta_s = 45°$, and $\varphi_i = 0°$ with respect to the $[10\,\bar{1}]$ direction. Figure 3B shows the translational energy loss distributions derived from the TOF data using the appropriate Jacobian. The inset shows the measured translational energy distribution of the incident H atoms.

There is a stunning difference in the observed H-atom inelasticity for scattering from metallic Au and an insulating Xe layer. The most probable energy loss for H-atom scattering from solid Xe was 46 meV, somewhat lower than that expected for a collinear binary elastic collision between a H and a single Xe atom (83 meV, shown as a vertical arrow in Fig. 3). For H-atom scattering from gold, the average energy loss was 20 times as high (910 meV). This energy loss is far too large to be compatible with the expectation for a H/Au binary collision model (56 meV), yet it is still far too small to be the result of H-atom trapping followed by thermal desorption. Furthermore, in contrast to the H/Xe scattering, which shows a very specific energy loss, the energy loss distribution for H scattering from Au was remarkably broad, extending out to at least 2.0 eV, suggesting that a broad continuum of acceptor states in the solid contributes to the translational inelasticity. These remarkable observations are compelling evidence that H-atom translational energy is efficiently converted to electronic excitation in collisions with solid gold.

Although a binary electronically adiabatic collision model is sufficient to understand the essence of the H-atom scattering from solid Xe, more involved theory is needed to treat H-atom scattering from a metal (*18*, *19*). Accurately describing metal atom motion and electron-hole pair excitation are the two key challenges. Recently, we have developed an approach to MD simulations that self-consistently treats mechanical energy transfer to Au lattice motion

and electronic excitation (*20*). The MD is carried out on a global full-dimensional potential energy surface (PES) based on effective medium theory (EMT) fitted to ab initio electronic energies. Because the EMT intrinsically contains the embedded electron densities, we can self-consistently describe electronically nonadiabatic behavior on the level of the local-density electronic friction approximation (LDFA) (*28*), with no adjustable parameters. We performed MD calculations for several million trajectories, enough to make comparisons with the measurements of angle-resolved inelastic scattering.

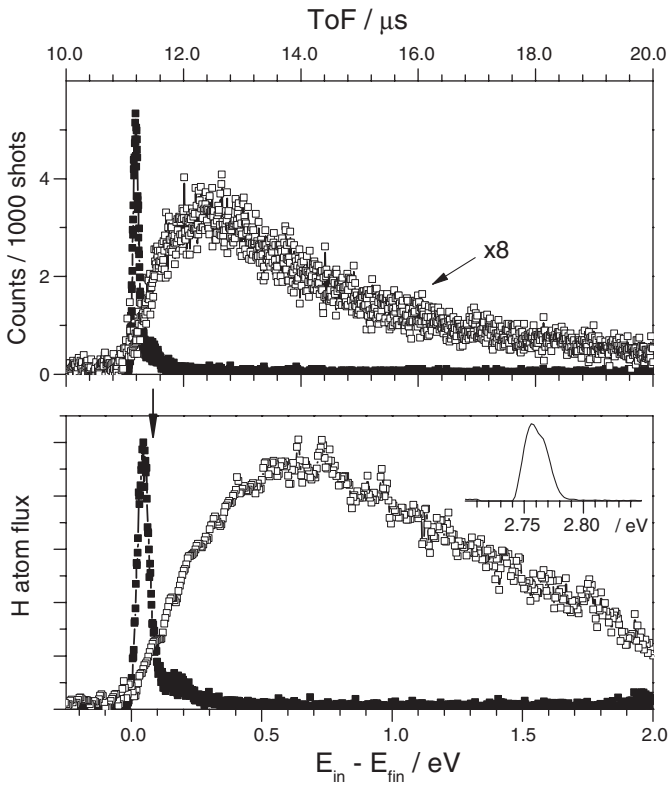

Fig. 3. Translational inelasticity for H-atom collisions with an insulator and a metal. (**Top**) Measured TOF spectra for H atoms scattered from Au(111) (open squares) and solid Xe (filled squares). The channel width is 8 ns for Au and 4 ns for Xe. (**Bottom**) Corresponding kinetic energy loss spectra obtained by Jacobian transformation of the TOF data. The inset shows the kinetic energy distribution of the incident H-atom beam. The vertical arrow marks the expected energy loss for a binary collision between an H and a Xe atom. The experimental conditions are E_{in} = 2.76 eV, ϑ_i = 45°, ϑ_s = 45° and ϕ_i = 0°, with respect to the [10$\bar{1}$] direction.

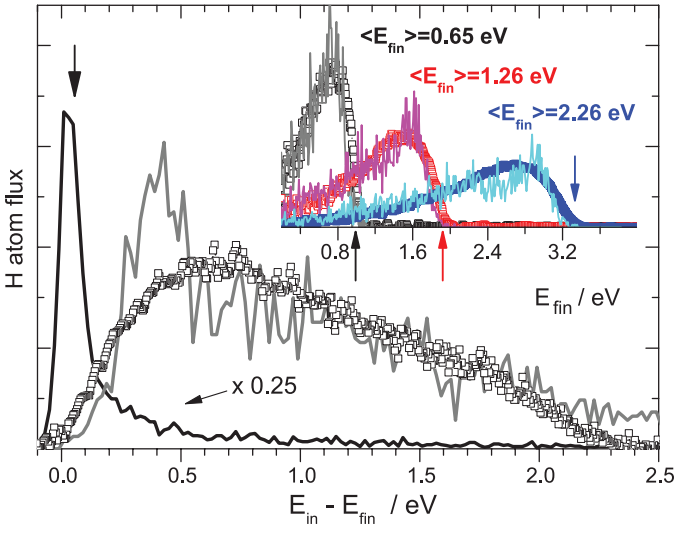

Fig. 4. Comparison of the experimentally obtained kinetic energy loss spectrum to theoretical simulations. Theoretical energy loss found when neglecting (solid black line) and including (solid gray line) electronic excitation. Experimental energy loss for E_{in} = 2.76 eV are shown as open squares. The vertical arrow marks the expected energy loss for a binary collision between an H and an Au atom. The inset shows the incidence energy dependence, E_{in}, of the experimentally derived translational inelasticity (open squares) and comparison to theory (solid lines): E_{in} = 3.33 eV (blue), 1.92 eV (red), and 0.99 eV (black). Colored arrows mark the three incidence energies. Also shown are the average final translational energies, $\langle E_{fin} \rangle$. The scattering angles are ϑ_i = 45°, ϑ_s = 45°, and φ_i = 0° with respect to the [10$\bar{1}$] direction. In all cases, the scattered H atoms remain unthermalized with the solid, emerging with a substantial fraction of their incidence translational energy.

Figure 4 shows some of these comparisons for H-atom scattering from Au(111). The solid black line shows the theoretical prediction, neglecting electronic excitation. The narrow energy loss distribution, peaking near the expected value for a binary collision of H with Au (56 meV, shown as a vertical arrow), clearly fails to capture the observed magnitude of the H-atom translational energy loss. The gray solid line shows the simulated energy loss distribution when electronic excitation is included in the MD simulations at the level of the LDFA. Here, the theoretical energy loss distribution captures the experimental result remarkably well. We have made extensive comparisons between experiment and theory, like those shown in Fig. 4 for a range of scattering angles, ϑ_i, φ_i, and ϑ_s; the agreement is uniformly good.

The inset to Fig. 4 shows how the translational inelasticity depends on the incidence energy and compares to electronically nonadiabatic MD simulations. At all incidence energies, agreement between experiment and theory is good and the energy loss is dominated by electronic excitation. We note that the fractional energy loss, $(E_{in} - \langle E_{fin} \rangle)/E_{in}$ = 0.33 ± 0.01, is nearly independent of E_{in}, meaning that electron-hole pair excitation remains important even at reduced incidence energies. This theoretical modeling confirms the qualitative statement made above: H-atom translational energy is efficiently converted to electronic excitation in collisions with solid gold.

The good agreement between experiment and theory is evidence for the validity of the approximations made in the MD simulations. Furthermore, the ability of the simulations to reproduce these experiments lends weight to the predictions made in (*20*). Most interesting among these are the predictions that electron-hole pair excitation increases the sticking probability and determines the adsorption mechanism, which occurs by penetration resurfacing. Here, H-atom adsorption occurs by initial population of subsurface binding sites (where electronic excitation is most efficient) followed by migration to the strongest binding sites, which are at the surface. This work also invalidates a previous alternative hypothesis, one where multiple electronically adiabatic collisions resulting from a conversion of normal to parallel H-atom momentum lead to sticking (*29*). Inspection of individual trajectories shows that such adsorption behavior occurs only when electronic excitation is included in the simulations (*20*).

This study demonstrates the importance of electronic excitation in atomic scattering at metal surfaces and provides a valuable benchmark for first-principles theories of energy transfer and adsorption. The prospect of using an experimentally validated electronically nonadiabatic theory of H interactions at a solid metal is exciting and could lead to progress on important problems, including H-atom diffusion in bulk metals and on metal surfaces, adsorbate influences on surface reconstruction, quantum dynamics of adsorption, and energetic atom diffusion and surface

penetration. More generally, chemical reactions at a metal surface are nearly always modeled within the adiabatic Born-Oppenheimer approximation; see, for example, (*30*). Our work suggests that theories of surface chemistry capable of describing electron excitation may be crucial to understanding atomic-scale motion occurring in surface reactions, especially if H-atom translation is involved.

REFERENCES AND NOTES

1. I. Langmuir, *J. Am. Chem. Soc.* **34**, 1310–1325 (1912).
2. M. P. Andersson *et al.*, *J. Catal.* **255**, 6–19 (2008).
3. D. Hollenbach, E. E. Salpeter, *Astrophys. J.* **163**, 155 (1971).
4. G. S. Higashi, Y. J. Chabal, G. W. Trucks, K. Raghavachari, *Appl. Phys. Lett.* **56**, 656–658 (1990).
5. S. M. Lee *et al.*, *Synth. Met.* **113**, 209–216 (2000).
6. D. Haberer *et al.*, *Nano Lett.* **10**, 3360–3366 (2010).
7. J. K. Norskov, B. I. Lundqvist, *Surf. Sci.* **89**, 251–261 (1979).
8. M. Born, R. Oppenheimer, *Annalen Der Physik* **84**, 457–484 (1927).
9. C. L. A. Lamont, B. N. J. Persson, G. P. Williams, *Chem. Phys. Lett.* **243**, 429–434 (1995).
10. H. Nienhaus *et al.*, *Phys. Rev. Lett.* **82**, 446–449 (1999).
11. B. Gergen, H. Nienhaus, W. H. Weinberg, E. W. McFarland, *Science* **294**, 2521–2523 (2001).
12. D. M. Bird, M. S. Mizielinski, M. Lindenblatt, E. Pehlke, *Surf. Sci.* **602**, 1212–1216 (2008).
13. A. Amirav, M.J. Cardillo, *Phys. Rev. Lett.* **57**, 2299 (1986).
14. Y. Huang, C. T. Rettner, D. J. Auerbach, A. M. Wodtke, *Science* **290**, 111–114 (2000).
15. K. Golibrzuch, N. Bartels, D. J. Auerbach, A. M. Wodtke, *Annu. Rev. Phys. Chem.* **66**, 399–425 (2015).
16. N. Shenvi, S. Roy, J. C. Tully, *Science* **326**, 829–832 (2009).
17. R. Cooper *et al.*, *Angew. Chem. Int. Ed.* **51**, 4954–4958 (2012).
18. M. Pavanello *et al.*, *Journal of Physical Chemistry Letters* **4**, 3735–3740 (2013).
19. G. J. Kroes, M. Pavanello, M. Blanco-Rey, M. Alducin, D. J. Auerbach, *J. Chem. Phys.* **141**, 054705 (2014).
20. S. M. Janke, D. J. Auerbach, A. M. Wodtke, A. Kandratsenka, *J. Chem. Phys.* **143**, 124708 (2015).
21. H. U. Finzel *et al.*, *Surf. Sci.* **49**, 577–605 (1975).
22. G. Caracciolo, S. Iannotta, G. Scoles, U. Valbusa, *J. Chem. Phys.* **72**, 4491–4499 (1980).
23. T. H. Johnson, *Phys. Rev.* **37**, 847–861 (1931).
24. K. Haberrecker *et al.*, *Nucl. Instrum. Methods* **57**, 22–28 (1967).
25. L. Schnieder *et al.*, *Faraday Discuss.* **91**, 259–269 (1991).
26. T. Kinugawa, T. Arikawa, *Jpn. J. Appl. Phys.* **2** (Part 2, No. 4A), L550–L552 (1993).
27. L. Schnieder, W. Meier, K. H. Welge, M. N. R. Ashfold, C. M. Western, *J. Chem. Phys.* **92**, 7027–7037 (1990).
28. Y. Li, G. Wahnström, *Phys. Rev. B* **46**, 14528–14542 (1992).
29. J. Strömquist, L. Bengtsson, M. Persson, B. Hammer, *Surf. Sci.* **397**, 382–394 (1998).
30. A. Hellman *et al.*, *J. Phys. Chem. B* **110**, 17719–17735 (2006).

ACKNOWLEDGMENTS

We thank X. Yang and C. Xiao for helping to set up Rydberg Atom Tagging, R. Bürsing for helping to design the experimental apparatus, and G.-J. Kroes for assisting in the development of the theory. A.M.W. and D.J.A. gratefully acknowledge support from the Humboldt Foundation. We acknowledge support from the Sonderforschungsbereich 1073 under project A04; from the Deutsche Forschungsgemeinschaft (DFG) and the Agence Nationale de la Recherché (ANR) under grant no. WO 1541/1-1; and from the DFG, the Ministerium für Wissenschaft und Kultur (MWK) Niedersachsen, and the Volkswagenstiftung under grant no. INST 186/902-1.

21 September 2015; accepted 30 October 2015
Published online 26 November 2015
10.1126/science.aad4972

GEOPHYSICS

Viscosity jump in Earth's mid-mantle

Maxwell L. Rudolph,[1]* Vedran Lekić,[2] Carolina Lithgow-Bertelloni[3]

The viscosity structure of Earth's deep mantle affects the thermal evolution of Earth, the ascent of mantle plumes, settling of subducted oceanic lithosphere, and the mixing of compositional heterogeneities in the mantle. Based on a reanalysis of the long-wavelength nonhydrostatic geoid, we infer viscous layering of the mantle using a method that allows us to avoid a priori assumptions about its variation with depth. We detect an increase in viscosity at 800- to 1200-kilometers depth, far greater than the depth of the mineral phase transformations that define the mantle transition zone. The viscosity increase is coincident in depth with regions where seismic tomography has imaged slab stagnation, plume deflection, and changes in large-scale structure and offers a simple explanation of these phenomena.

The viscosity of Earth's mantle controls the rate and pattern of mantle convection and, through it, the dynamics of our planet's deep interior, including degassing of and heat transport from the interior, mixing of compositional heterogeneity, plume ascent and passive upwelling, and slab descent. The long-wavelength nonhydrostatic geoid is a key geophysical constraint on Earth's internal viscosity structure. At the largest spatial scales (spherical harmonic degrees 2 to 7), the geoid is most sensitive to density structure and viscosity contrasts in the lower mantle. At smaller scales, the geoid becomes increasingly sensitive to upper mantle structure, which is primarily associated with subducting slabs. Because lateral viscosity variations have minor effects on the geoid at large spatial scales (*1*, *2*)—though they may become more important at shorter length scales (*3*)—it is possible to infer deep mantle viscous layering from geoid observations. However, most studies of Earth's mantle viscosity structure impose layer interfaces to be coincident with seismic velocity discontinuities. Thus, these studies may not resolve viscous layering whose origin is distinct from that of pressure-induced phase changes (e.g., at 410- and 660-km depth), or may miss phase transitions not clearly associated with seismic discontinuities.

We use the long-wavelength nonhydrostatic geoid to infer the mantle radial viscosity structure in a manner distinct from that of previous attempts in three key ways. First, we employ a transdimensional, hierarchical, Bayesian inversion procedure (*4*) that does not specify at the outset the number or location of interfaces in our layered viscosity structure. The Bayesian approach is very attractive for this inverse problem because it yields a posterior probability distribution that can be analyzed to quantify uncertainties of and trade-offs between model parameters (e.g., layer depth and viscosity contrast). Second, we explore various choices for the conversion between seismic velocity anomalies and density anomalies, including depth-dependent conversion factors based on thermodynamic principles, calculated using HeFESTo (*5*). Finally, we use a recent whole-mantle tomographic model, SEMUCB-WM1 (*6*), developed with waveform tomography using highly accurate wave propagation computations, to infer mantle density structure and a modern geoid model based on 10 years of GRACE satellite observations, combined with revised estimates of the hydrostatic flattening of Earth (*7*, *8*).

A posterior probability density function for the radial profile of viscosity is shown in Fig. 1, where the mean (taken in log-space) viscosity at each depth is shown as a purple curve. In this particular inversion, we find evidence for relatively uniform viscosity throughout the upper mantle and transition zone. Below the mantle transition zone, there is a region of lower viscosity and an increase in viscosity between 670- and 1000-km depth. The preferred depth of this viscosity increase can be inferred from Fig. 1B and is centered about 1000 km.

We carried out multiple inversions to explore the effects of (i) our treatment of data and model uncertainty, (ii) the degree of truncation of the spherical harmonic expansion of the geoid used to constrain our models, and (iii) the density scaling $R_{\rho,S} = d \ln \rho / d \ln V_S$ (Fig. 1). We consider features of the viscosity profiles to be robust if they are common among the separate inversions. We find that all solutions place the depth of viscosity increase considerably below 670-km depth, most often near 1000-km depth. This result appears to be independent of assumptions made, including maximum spherical harmonic degree l_{max}, choice of depth-dependent or constant $R_{\rho,S}$, or treatment of data and model covariance (*7*). Other features of the solutions are sensitive to these choices and, therefore, their robustness is proportional to the likelihood of the assumptions from which they result. Inversions with $l_{max} = 7$ (dashed curves in Fig. 2) generally have a more pronounced peak in viscosity in the mid-mantle, underlain by a weaker region between 1500- and 2500-km depth and an increase in viscosity in

[1]Department of Geology, Portland State University, Post Office Box 751, Portland, OR 97207, USA. [2]Department of Geology, University of Maryland, College Park, MD 20742, USA. [3]Department of Earth Sciences, University College London, London WC1E 6BT, UK.
*Corresponding author. E-mail: maxwell.rudolph@pdx.edu

the lowermost mantle. Several solutions, using depth-dependent $R_{\rho,S}$ or $R_{\rho,S} = 0.4$, feature a lower-viscosity layer between 670- and 1000-km depth. Some solutions include a high-viscosity "hill" in the mid-mantle between 1000- and 1500-km depth, separating upper and lower mantles of lower viscosity.

Many early studies advocated for layered mantle convection with an interface at or somewhat below 670-km depth, and in particular Wen and Anderson (*9*) noted that the amplitude and pattern of the long-wavelength geoid and surface topography could be well reproduced using mantle flow models with an imposed barrier to flow about 250 km deeper than the 670-km seismic discontinuity. However, tomographic images of relict Farallon and Tethys slabs in the lower mantle suggest that the concept of layered mantle convection is at best incomplete, and we emphasize that our mantle flow calculations do not impose layered convection.

Our results favor viscosity structures in which the overall increase in viscosity is a factor of 10 to 150, in agreement with previous studies. All of our results favor the location (interface depth) of this viscosity increase lying below 670-km depth, and most models place this viscosity increase deeper still, in the vicinity of 1000-km depth. This result is particularly intriguing given the observation that most actively subducting slabs stagnate below the 670-km seismic discontinuity, at depths of 1000 km (*10*). For instance, both the GAP-P4 model (*11*) and SEMUCB-WM1 reveal slabs stagnating above the 670-km discontinuity in the Northern Honshu arc, but passing through the 670-km discontinuity and stagnating above 1000-km depth along the Tonga and Kermadec arcs. In at least one region, Central America, the slab appears to enter the lower mantle without stagnation. The mechanism responsible for this slab stagnation is unclear, as there is no velocity discontinuity at this depth in one-dimensional (1D) seismic models (*12*), nor a known phase transition.

Two mechanisms have been recently suggested for slab stagnation in the mid-mantle. First, King *et al.* (*13*) have suggested that the pyroxene to majoritic garnet phase transition in subducted slabs is kinetically hindered, and thus older, colder, slabs are more prone to stagnation. Marquardt and Miyagi (*14*), based on high-pressure deformation experiments of (Mg,Fe)O, argued that viscosity in the regions surrounding settling slabs in the shallow-most 900 km of the lower mantle may be about two orders of magnitude higher than previously expected, causing slabs to spread laterally and to settle very slowly through this region. Our results indicate that there may be a viscosity increase in the mid-mantle, and many of our inversions have viscosity contrasts at depths comparable to those suggested (*14*). However, we note that the observation of regional differences in slab behavior, and in particular the speculation that old, cold, slabs preferentially stagnate, cannot be explained using our 1D viscosity structure or by a viscosity contrast that would occur in the mantle surrounding all slabs, irrespective of age, without invoking additional mantle dynamic processes or subduction zone histories, such as the prevalence of trench rollback.

Previous inversions for layered viscosity structure with prescribed layer interfaces depths revealed some indication of an increase in viscosity at or around 1000-km depth. In particular, King and Masters (*15*) inverted for layered viscosity structure constrained by the geoid using a uniform velocity to density conversion factor, with velocity anomalies inferred from *S*-wave tomographic models, and found evidence for a viscosity increase of ~20 at 670-km depth and a second increase of ~5 at 1022-km depth. Forte and Peltier (*16*) also found, using a combination of a slab density model and lower-mantle tomographic model, that the agreement between modeled and observed geoid was better for a layered viscosity structure with an interface at 1200-km depth than at 670-km depth. Kido *et al.* (*17*) performed inversions for layered mantle viscosity structure

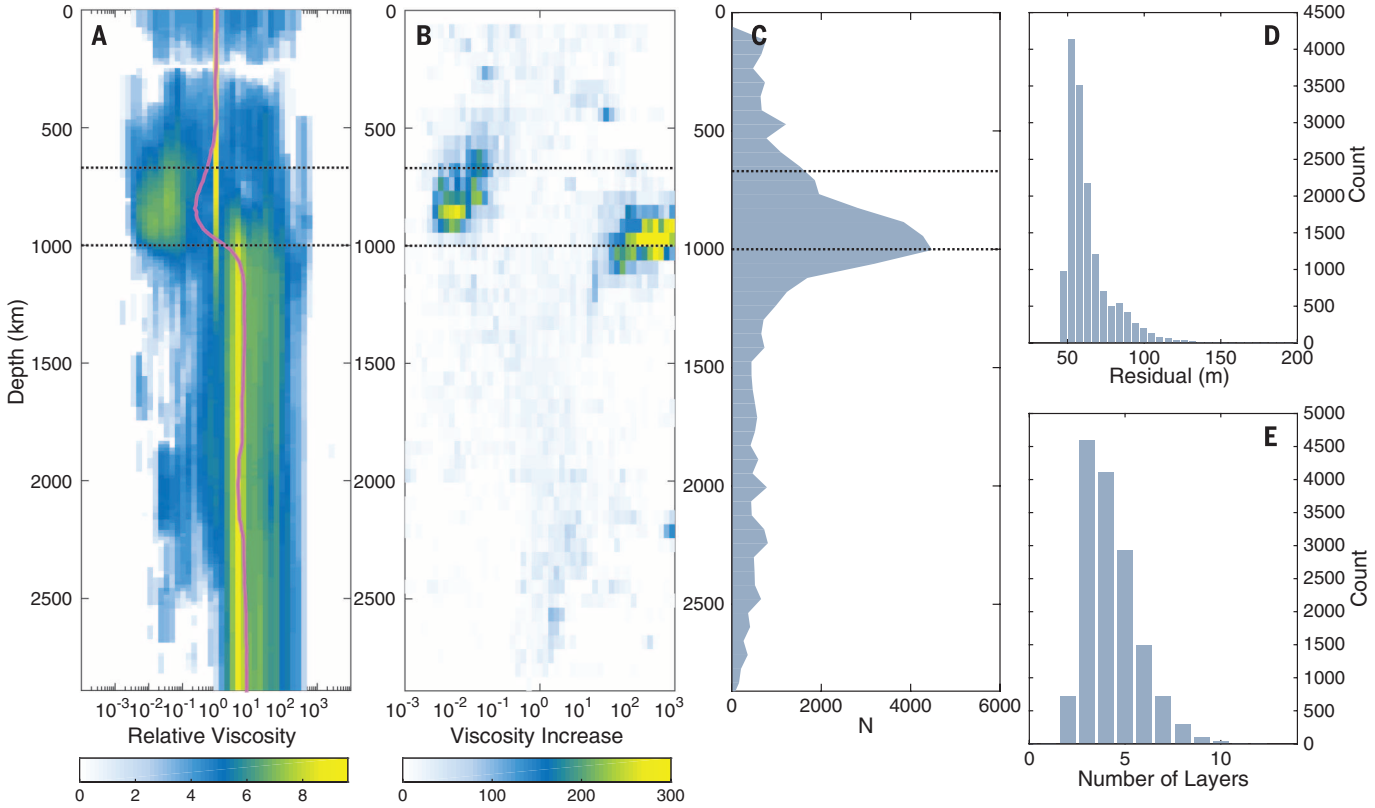

Fig. 1. Properties of ensemble solution. Viscosity inversion using depth-dependent $R_{\rho,S}$ from HeFESTo, l_{max} = 3, and assumption of uncorrelated errors yields radial viscosity profiles with a viscosity increase at 1000-km depth and a lower-viscosity channel between 670 and 1000 km. (**A**) A 2D histogram showing the posterior likelihood of viscosity and depth values. Horizontal dotted lines indicate depths of 670 and 1000 km. (**B**) A 2D histogram showing the posterior likelihood of layer interface depth and viscosity increase (>1 means viscosity increases with increasing depth). (**C**) Posterior likelihood of having a layer interface at each depth. (**D**) Distribution of residuals of solutions in ensemble solution. (**E**) Distribution of number of layers in models in the ensemble solution.

(with prescribed layer depths) using a genetic algorithm and found evidence for a decrease in viscosity at 670-km depth and subsequent increase in viscosity at 1000-km depth. Our study is different in that we do not prescribe at the outset the number or locations of layer interfaces in our layered viscosity structure and as a result, we place the largest viscosity contrast in the model somewhat deeper than previous studies.

Many studies from the 1980s and 1990s employed layered structures with layering identical to that of the tomographic models then available (~11 layers), or layered structures with layers at the major seismic discontinuities. Subsequent models have introduced additional layers [for instance, 25 in (*18*)]. To justify such parameterizations, either additional observational constraints, such as rates of glacial isostatic adjustment, plate motions, or patterns of seismic anisotropy, or additional assumptions about the smoothness of the mantle viscosity structure, are required. Paulson *et al.* (*19*, *20*) used geoid and relative sea-level data as constraints on a Monte-Carlo inversion for mantle viscosity structure with one, two, and three layers. One of the central conclusions was that the GRACE and relative sea-level data cannot be used to uniquely constrain a layered mantle viscosity structure with more than two layers. Two markedly different two-layer models were permitted by these inversions (with prescribed interface depth at 670 km), one having an upper mantle with viscosity around 5×10^{20} Pa-s and a lower mantle ~4.33 more viscous and the other having an upper mantle viscosity about an order of magnitude smaller and a viscosity contrast of ~1500, similar to what was found by Ricard *et al.* (*21*). Our results generally support the suggestion that the geoid alone cannot uniquely constrain the viscosity of more than a handful of layers. Indeed, many individual models in the posterior population for each of our inversions do have more than five layers (e.g., Fig. 1), but owing to trade-offs, the layer properties of these more complex structures cannot be uniquely constrained. The posterior distribution of solutions inherently captures these trade-offs between model parameters, and the precise viscosity structures of these inversions are largely dependent on assumptions in the inversion (*7*).

A viscosity contrast at 1000-km depth has important implications for the dynamics of convection in Earth's mantle, including its thermal and chemical evolution. As ascending plumes encounter abrupt changes in viscosity (in numerical models), they can be laterally deflected and thinned. Similarly, downwellings in numerical simulations become elongated laterally and compressed vertically as they encounter viscosity increases. Deflection of upwellings is observed in some tomographic models. For instance, recent tomographic images obtained by full waveform tomography with sophisticated forward-modeling approaches reveal apparent deflection at 1000-km depth of the seismically slow structures both regionally beneath the Iceland hotspot (*22*) and globally (*23*). Indeed, examples of apparent deflected upwellings, such as the feature beneath the Macdonald hotspot in the South Pacific (Fig. 3), are globally not uncommon (*23*). In both studies (*22*, *23*), the apparent radius of plumes also decreases from the lower to the upper mantle. The decrease in radius appears to be coincident with the deflection at 1000-km depth. Upwelling structures in numerical simulations of mantle convection with an imposed increase in viscosity at 1000-km depth show similar behavior (Fig. 3).

Other studies use the mantle radial correlation function (*24*) to analyze tomographic models and to compare tomographic and geodynamic models (*24*, *25*). Radial correlation functions calculated for SEMUCB-WM1, as well as for the global *P*-wave tomographic model GAP-P4 (*10*) for spherical harmonic degrees 1 to 3 (Fig. 4, A and B), show a high degree of correlation throughout the lower mantle at depths greater than 1000 km and a rapid decrease in correlation at 1000-km depth. Nearly identical behavior is also present in the average of *S*-wave tomographic models SMEAN (*25*) (fig. S10). Other tomographic models show a change in radial correlation around this depth as well as a change in velocity heterogeneity, particularly at spherical harmonic degree 4 (*25*), and an independent test based on voxel tomography favors a vertical coherence minimum around 800-km depth, below the base of the transition zone (*26*).

Changes in the radial correlation function may be related to changes in viscosity. Numerical simulations of convection in spherical shell geometry show that endothermic phase changes (*24*) and depth-dependent viscosity can both cause corresponding changes in the radial correlation. We find that a viscosity increase at 1000 km (Fig. 4C)

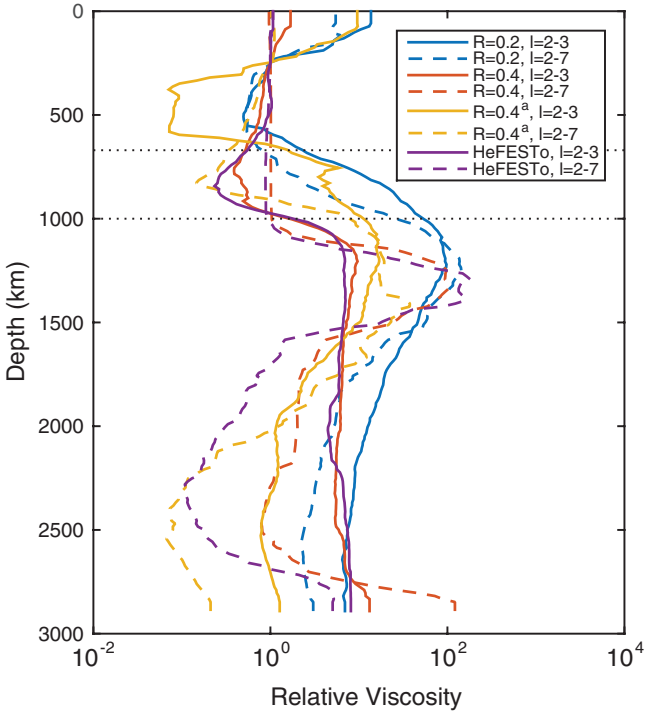

Fig. 2. Results from multiple inversions. Mean radial profiles of viscosity obtained in eight inversions varying $R_{p,S}$, l_{max}, and eliminating buoyancy contributions from the lowermost 1000 km of the mantle (denoted by a superscript "a") all exhibit an increase in viscosity between 670- and 1000-km depth. Models with $l_{max} = 7$ are characterized by low viscosity in the mid–lower mantle.

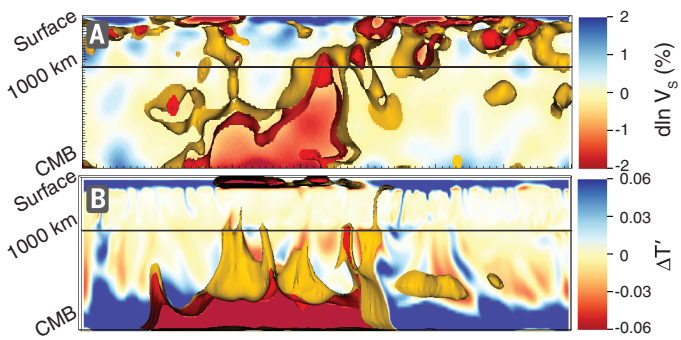

Fig. 3. Observed and modeled upwellings. (**A**) Shear velocity anomaly isocontours delineate deflected downwellings at 1000-km depth (horizontal line) near McDonald hotspot in SEMUCB-WM1. (**B**) Dimensionless temperature (T') anomaly isocontours (and pseudocolor) show similar deflection and thinning of upwellings in a numerical geodynamic model with a viscosity increase at 1000-km depth. Cool and warm colors trace dimensionless temperature variations in (B) and denote seismically fast or slow regions in (A).

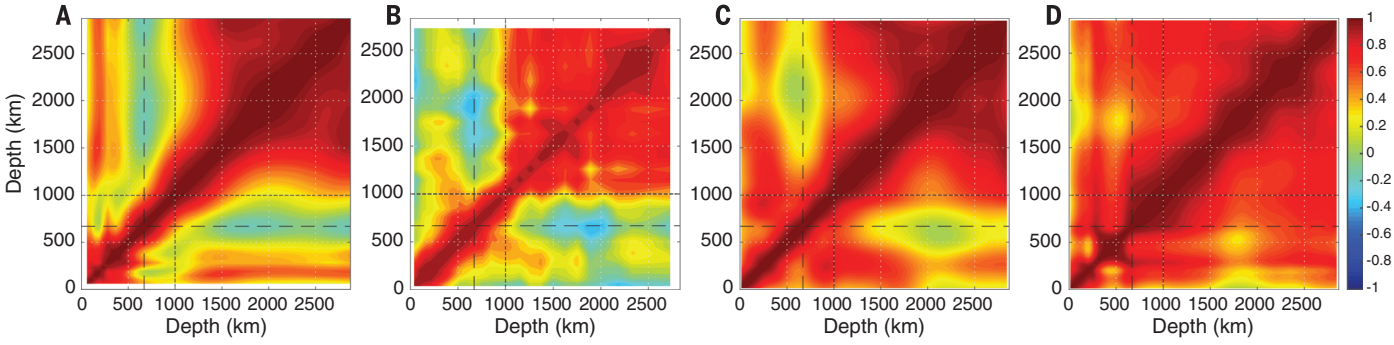

Fig. 4. Radial correlation functions of tomographic and geodynamic models. (**A**) Radial correlation functions for spherical harmonic degrees 1 to 3 from SEMUCB-WM1 and (**B**) GAP-P4 show an abrupt decorrelation of structure across 1000-km depth. Very similar radial correlation functions are seen in the temperature field from numerical mantle convection simulations with imposed plate motions, including a viscosity contrast at 1000-km depth (**C**), but not when the viscosity contrast is smaller and shallower, at 670-km depth (**D**).

yields a radial correlation structure much more similar to that found in tomographic models (Fig. 4, A and B) than does a viscosity increase at 670 km (Fig. 4D). The rapid change in radial correlation at 1000-km depth in tomographic models thus suggests a contrast in viscosity, because no change in phase is known to occur at this depth. We emphasize that these models include simplified representations of mantle viscosity structure (fig. S7) and that a more gradual increase in viscosity may also be compatible with the observations. Other, more complex viscosity structures can also alter the behavior of upwellings and downwellings and consequently change the radial correlation structure. Convection simulations run with a "second asthenosphere," a weak zone extending from 670- to 1000-km depth as suggested in some of our inversions (Fig. 1) as well as in inversions by Kido *et al.* (*17*), show a greater tendency toward layered convection (*27*), which promotes decorrelation.

The viscosity contrast at a 1000-km depth provides a physical mechanism for the observation that slabs and plumes stagnate or become deflected deeper than the transition zone in the absence of a pervasive compositional barrier or another endothermic phase change. It may also reconcile observations of changes in seismic structure (*28*) that led to a proposed hot abyssal layer (*29*), though this was originally placed at greater depths. Given the present state of understanding in mineral physics, no unique mechanism can be identified for this increase in viscosity, and our observation should motivate further experimental and computational studies. First principles calculations have indicated a continuous though gentle increase in the viscosity of bridgmanite due to greater vacancy diffusion starting at around 40 GPa (~1000 km) and continuing until the postperovskite phase transition (*30*). The increase in the strength of ferropericlase observed by Marquardt and Miyagi (*14*) is the first positive experimental evidence for a possible change in rheology at these depths. Whether this effect, which is localized in high–strain-rate regions (surrounding slabs), should be expected to contribute to the viscosity inferred on the basis of the very-long-wavelength components of the geoid, remains to be determined. The spin transition in ferropericlase occurs at much greater depths, and first-principles simulations suggest that the higher-pressure phase (low spin) should have increased diffusion and lower viscosity (*31*), with a viscosity minimum near 1500-km depth (*32*).

Two possible intriguing (though speculative) solutions remain. Changes in the relative abundance of ferric versus ferrous iron due to disproportionation (*33*) at these depths or gradually over a depth range might change the bonding strength in bridgmanite enough to markedly strengthen it. Perhaps of greater interest and of more pervasive dynamical consequence might be the gradual drying of the bridgmanite perovskite as the solubility of water in the structure decreases with pressure (*34*), becoming more viscous at 1000-km depth.

REFERENCES AND NOTES

1. S. Zhong, *J. Geophys. Res.* **106**, 703 (2001).
2. R. Moucha, A. M. Forte, J. X. Mitrovica, A. Daradich, *Geophys. J. R. Astron. Soc.* **169**, 113–135 (2007).
3. A. Ghosh, T. W. Becker, S. J. Zhong, *Geophys. Res. Lett.* **37**, 01301 (2010).
4. M. Sambridge, T. Bodin, K. Gallagher, H. Tkalcic, *Philos. Trans. A Math. Phys. Eng. Sci.* **371**, 20110547 (2013).
5. L. Stixrude, C. Lithgow-Bertelloni, *Earth Planet. Sci. Lett.* **263**, 45–55 (2007).
6. S. W. French, B. A. Romanowicz, *Geophys. J. Int.* **199**, 1303–1327 (2014).
7. Methods can be found in the supplementary materials on *Science* Online.
8. F. Chambat, Y. Ricard, B. Valette, *Geophys. J. Int.* **183**, 727–732 (2010).
9. L. Wen, D. L. Anderson, *Earth Planet. Sci. Lett.* **146**, 367 (1997).
10. Y. Fukao, M. Obayashi, *J. Geophys. Res. B* **118**, 5920–5938 (2013). 10.1002/2013JB010466
11. M. Obayashi *et al.*, *Geophys. Res. Lett.* **40**, 5652–5657 (2013).
12. A. M. Dziewonski, D. L. Anderson, *Phys. Earth Planet. Inter.* **25**, 297–356 (1981).
13. S. D. King, D. J. Frost, D. C. Rubie, *Geology* **43**, 231–234 (2015).
14. H. Marquardt, L. Miyagi, *Nat. Geosci.* **8**, 311–314 (2015).
15. S. D. King, G. Masters, *Geophys. Res. Lett.* **19**, 1551–1554 (1992).
16. A. M. Forte, R. Peltier, *J. Geophys. Res.* **96**, 20131 (1991).
17. M. Kido, D. A. Yuen, O. Čadek, T. Nakakuki, *Phys. Earth Planet. Inter.* **107**, 307–326 (1998).
18. J. X. Mitrovica, A. M. Forte, *Earth Planet. Sci. Lett.* **225**, 177–189 (2004).
19. A. Paulson, S. Zhong, J. Wahr, *Geophys. J. Int.* **168**, 1195–1209 (2007).
20. A. Paulson, S. Zhong, J. Wahr, *Geophys. J. Int.* **171**, 497–508 (2007).
21. Y. Ricard, C. Vigny, C. Froidevaux, *J. Geophys. Res.* **94** (B10), 13739 (1989).
22. F. Rickers, A. Fichtner, J. Trampert, *Earth Planet. Sci. Lett.* **367**, 39 (2013).
23. S. W. French, B. Romanowicz, *Nature* **525**, 95–99 (2015).
24. T. H. Jordan, P. Puster, G. A. Glatzmaier, P. J. Tackley, *Science* **261**, 1427–1431 (1993).
25. T. W. Becker, L. Boschi, *Geochem. Geophys. Geosyst.* **3**, 1003 (2002).
26. L. Boschi, T. W. Becker, *Geophys. Res. Lett.* **38**, L20306 (2011).
27. L. Cserepes, D. Yuen, *Geophys. Res. Lett.* **24**, 181–184 (1997).
28. H. Kárason, R. D. van der Hilst, *Science* **283**, 1885–1888 (1999).
29. L. H. Kellogg, B. H. Hager, R. D. van der Hilst, R. D. van der Hilst, *Science* **283**, 1881–1884 (1999).
30. M. W. Ammann, J. P. Brodholt, J. Wookey, D. P. Dobson, *Nature* **465**, 462–465 (2010).
31. M. W. Ammann, J. P. Brodholt, D. P. Dobson, *Earth Planet. Sci. Lett.* **302**, 393–402 (2011).
32. R. M. Wentzcovitch *et al.*, *Proc. Natl. Acad. Sci. U.S.A.* **106**, 8447–8452 (2009).
33. D. J. Frost *et al.*, *Nature* **428**, 409–412 (2004).
34. N. Bolfan-Casanova, H. Keppler, D. C. Rubie, *Geophys. Res. Lett.* **30**, 1905 (2003).

ACKNOWLEDGMENTS

We thank T. Becker and C. O'Neill for developing and releasing the source code to HC and the Computational Infrastructure for Geodynamics (geodynamics.org) for distributing software, Y. Ricard for enlightening discussion, and three anonymous reviewers. This project was initiated at the 2014 CIDER workshop at the Kavli Institute for Theoretical Physics, University of California, Santa Barbara. This work was supported by NSF grant EAR/1135452 and Natural Environment Research Council NE/K006061/1, as well as a Packard Science and Engineering Fellowship to V.L. All data are available in the manuscript and supplementary materials. The GRACE gravity model GGM05S can be obtained at: ftp://ftp.csr.utexas.edu/pub/grace.

SUPPLEMENTARY MATERIALS

www.sciencemag.org/content/350/6266/1349/suppl/DC1
Materials and Methods
Figs. S1 to S10
Table S1
References (*35*–*56*)

6 August 2015; accepted 30 October 2015
10.1126/science.aad1929

SUPERCONDUCTIVITY

Evidence for two-dimensional Ising superconductivity in gated MoS_2

J. M. Lu,[1] O. Zheliuk,[1] I. Leermakers,[2] N. F. Q. Yuan,[3] U. Zeitler,[2] K. T. Law,[3] J. T. Ye[1]*

The Zeeman effect, which is usually detrimental to superconductivity, can be strongly protective when an effective Zeeman field from intrinsic spin-orbit coupling locks the spins of Cooper pairs in a direction orthogonal to an external magnetic field. We performed magnetotransport experiments with ionic-gated molybdenum disulfide transistors, in which gating prepared individual superconducting states with different carrier dopings, and measured an in-plane critical field B_{c2} far beyond the Pauli paramagnetic limit, consistent with Zeeman-protected superconductivity. The gating-enhanced B_{c2} is more than an order of magnitude larger than it is in the bulk superconducting phases, where the effective Zeeman field is weakened by interlayer coupling. Our study provides experimental evidence of an Ising superconductor, in which spins of the pairing electrons are strongly pinned by an effective Zeeman field.

In conventional superconductors, applying a sufficiently high magnetic field above the upper critical field B_{c2} is a direct way to destroy superconductivity by breaking Cooper pairs via the coexisting orbital and Pauli paramagnetic mechanisms. The orbital contribution originates from the coupling between the magnetic field and the electron momentum, whereas the paramagnetic contribution is caused by spin alignment in Cooper pairs by an external magnetic field. When the orbital effect is weakened or eliminated, either by having a large electron mass (*1*) or by reducing dimensionality (*2*), B_{c2} is solely determined by the interaction between the magnetic field and the spin degree of freedom of the Cooper pairs. In superconductors where Cooper pairs are formed by electrons with opposite spins, aligning the electron spins by the external magnetic field increases the energy of the system; therefore, B_{c2} cannot exceed the Clogston-Chandrasekhar limit (*3*, *4*) or the Pauli paramagnetic limit (in units of tesla), $B_p \approx 1.86\ T_c(0)$. Here, $T_c(0)$ is the zero-field superconducting critical temperature (in units of kelvin) that characterizes the binding energy of a Cooper pair, which competes with the Zeeman splitting energy.

However, in some superconductors, the Pauli limit can be surpassed. For example, forming Fulde-Ferrell-Larkin-Ovchinnikov states with inhomogeneous pairing densities favors the presence of a magnetic field, even above B_p (*5*). In spin-triplet superconductors, the parallel-aligned spin configuration in Cooper pairs is not affected by Pauli paramagentism, and B_{c2} can easily exceed B_p (*6*–*8*). Spin-orbit interactions have also been shown to align spins to overcome the Pauli limit. Rashba spin-orbit coupling (SOC) in noncentrosymmetric superconductors will lock the spin to the in-plane direction, which can greatly enhance the out-of-plane B_{c2} (*9*); however, for an in-plane magnetic field, B_{c2} can only be moderately enhanced to $\sqrt{2}\,B_p$ (*10*). Alternatively, electron spins can be randomized by spin-orbit scattering (SOS), which weakens the effect of spin paramagnetism (*11*–*15*) and hence enhances B_{c2}.

Superconductivity in thin flakes of MoS_2 can be induced electrostatically using the electric field effect, mediated by moving ions in a voltage-biased ionic liquid placed on top of the sample [section 1 of (*16*); (*17*)]. Negative carriers (electrons) are induced by accumulating cations above the outermost layer of an MoS_2 flake, forming a capacitor ~1 nm thick (*17*–*22*). The potential gradient at the surface creates a planar homogenous electronic system

[1]Device Physics of Complex Materials, Zernike Institute for Advanced Materials, Nijenborgh 4, 9747 AG, Groningen, Netherlands. [2]High Field Magnet Laboratory, European Magnetic Field Laboratory (HFML-EMFL), and Institute of Molecules and Materials, Radboud University, Toernooiveld 7, 6525 ED Nijmegen, Netherlands. [3]Department of Physics, Hong Kong University of Science and Technology, Clear Water Bay, Hong Kong, China.
*Corresponding author. E-mail: j.ye@rug.nl

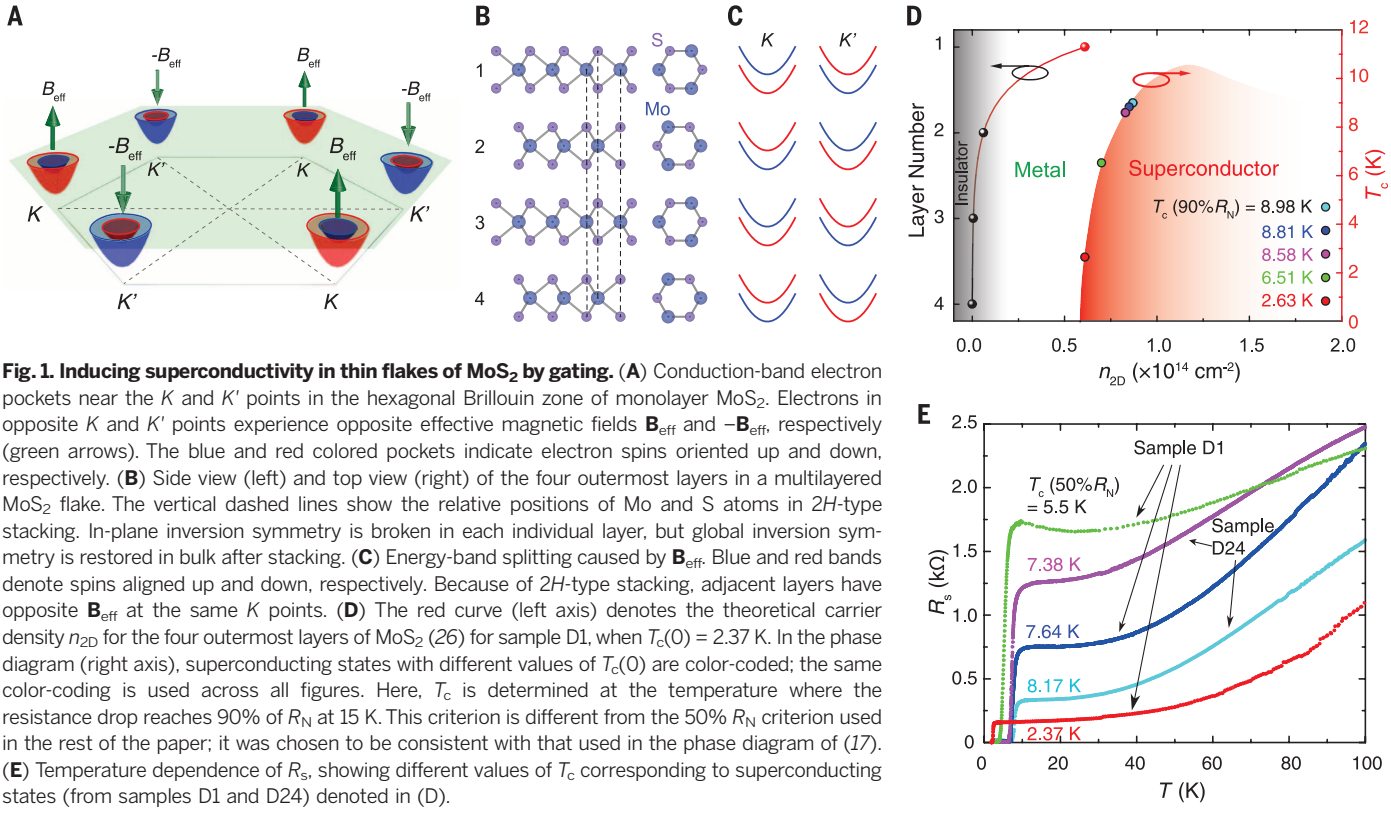

Fig. 1. Inducing superconductivity in thin flakes of MoS_2 by gating. (**A**) Conduction-band electron pockets near the *K* and *K*′ points in the hexagonal Brillouin zone of monolayer MoS_2. Electrons in opposite *K* and *K*′ points experience opposite effective magnetic fields $\mathbf{B}_{eff}$ and $-\mathbf{B}_{eff}$, respectively (green arrows). The blue and red colored pockets indicate electron spins oriented up and down, respectively. (**B**) Side view (left) and top view (right) of the four outermost layers in a multilayered MoS_2 flake. The vertical dashed lines show the relative positions of Mo and S atoms in 2*H*-type stacking. In-plane inversion symmetry is broken in each individual layer, but global inversion symmetry is restored in bulk after stacking. (**C**) Energy-band splitting caused by $\mathbf{B}_{eff}$. Blue and red bands denote spins aligned up and down, respectively. Because of 2*H*-type stacking, adjacent layers have opposite $\mathbf{B}_{eff}$ at the same *K* points. (**D**) The red curve (left axis) denotes the theoretical carrier density n_{2D} for the four outermost layers of MoS_2 (*26*) for sample D1, when $T_c(0) = 2.37$ K. In the phase diagram (right axis), superconducting states with different values of $T_c(0)$ are color-coded; the same color-coding is used across all figures. Here, T_c is determined at the temperature where the resistance drop reaches 90% of R_N at 15 K. This criterion is different from the 50% R_N criterion used in the rest of the paper; it was chosen to be consistent with that used in the phase diagram of (*17*). (**E**) Temperature dependence of R_s, showing different values of T_c corresponding to superconducting states (from samples D1 and D24) denoted in (D).

Downloaded from www.sciencemag.org on December 14, 2015

with an inhomogeneous vertical doping profile, where conducting electrons are predominantly doped into a few of the outermost layers, forming superconducting states near the K and K' valleys of the conduction band (Fig. 1A). The in-plane inversion symmetry breaking in a MoS_2 monolayer can induce SOC, manifested as a Zeeman-like effective magnetic field $\mathbf{B}_{eff}$ (~100 T) oppositely applied at the K and K' points of the Brillouin zone (*23*). Because electrons of opposite momentum experience opposite $\mathbf{B}_{eff}$, this SOC is then compatible with Cooper pairs also residing at the K and K' points (*24*). Therefore, spins of electrons in the Cooper pairs are polarized by this large out-of-plane Zeeman field, which is able to protect their orientation from being realigned by an in-plane magnetic field, leading to a large in-plane B_{c2}. This alternating spin configuration also provides the essential ingredient for establishing an Ising superconductor, where spins of electrons in the Cooper pairs are strongly pinned by an effective Zeeman field in an Ising-like fashion.

Because of the alternating stacking order in 2*H*-type single crystals of transition metal dichalcogenide (TMD) (Fig. 1B), electrons with the same momentum experience $\mathbf{B}_{eff}$ with opposite signs for adjacent layers, which weakens the effect of SOC by cancelling out $\mathbf{B}_{eff}$ mutually in the bulk crystal (Fig. 1C) (a comparison with bulk intercalated TMD is given in section 7 of (*16*)]. However, field-effect doping can strongly confine carriers to the outermost layer, reaching a two-dimensional (2D) carrier density n_{2D} of up to ~10^{14} cm^{-2} (*17*, *25*). Theoretical calculations for our devices indicate that the n_{2D} of individual layers decays exponentially from the channel surface (Fig. 1D, left axis), reducing the n_{2D} of the second-to-outermost layer by almost 90% in comparison with the outermost one (*26*). From the established phase diagram (*17*), if superconductivity is induced close to the quantum critical point (QCP; $n_{2D} \sim 6 \times 10^{13}$ cm^{-2}), the second layer is not even metallic, because metallic transport can be observed only when $n_{2D} > 8 \times 10^{12}$ cm^{-2}. Therefore, the outermost layer is well isolated by gating, mimicking a freestanding monolayer (*27*).

We obtained superconducting states across a range of doping concentrations (Fig. 1D, right axis) by varying the gate voltage (*17*); these states have different temperature dependences of sheet resistivity R_s (Fig. 1E). A superconducting state [T_c (at B = 0) = 2.37 K] at the onset of superconductivity (close to QCP) could be induced without suffering from the inhomogeneity usually encountered at low doping concentrations (Fig. 1E, red curve). Consistently, this well-behaved state also exhibits a high mobility of ~700 cm^2/Vs (measured at T = 15 K) before reaching zero resistance.

Angle-resolved photoemission spectroscopy (ARPES) measurements (*27*, *28*) and theoretical calculations (*25*, *29*) both showed that electron doping starts near the K points of the conduction band. The band structure is modified at higher doping (*25*, *29*), meaning that the simplest superconducting states in MoS_2, which are dominated by Cooper pairs at the K and K' points, should be prepared by minimizing doping [higher doping states are discussed in section 7 of (*16*)].

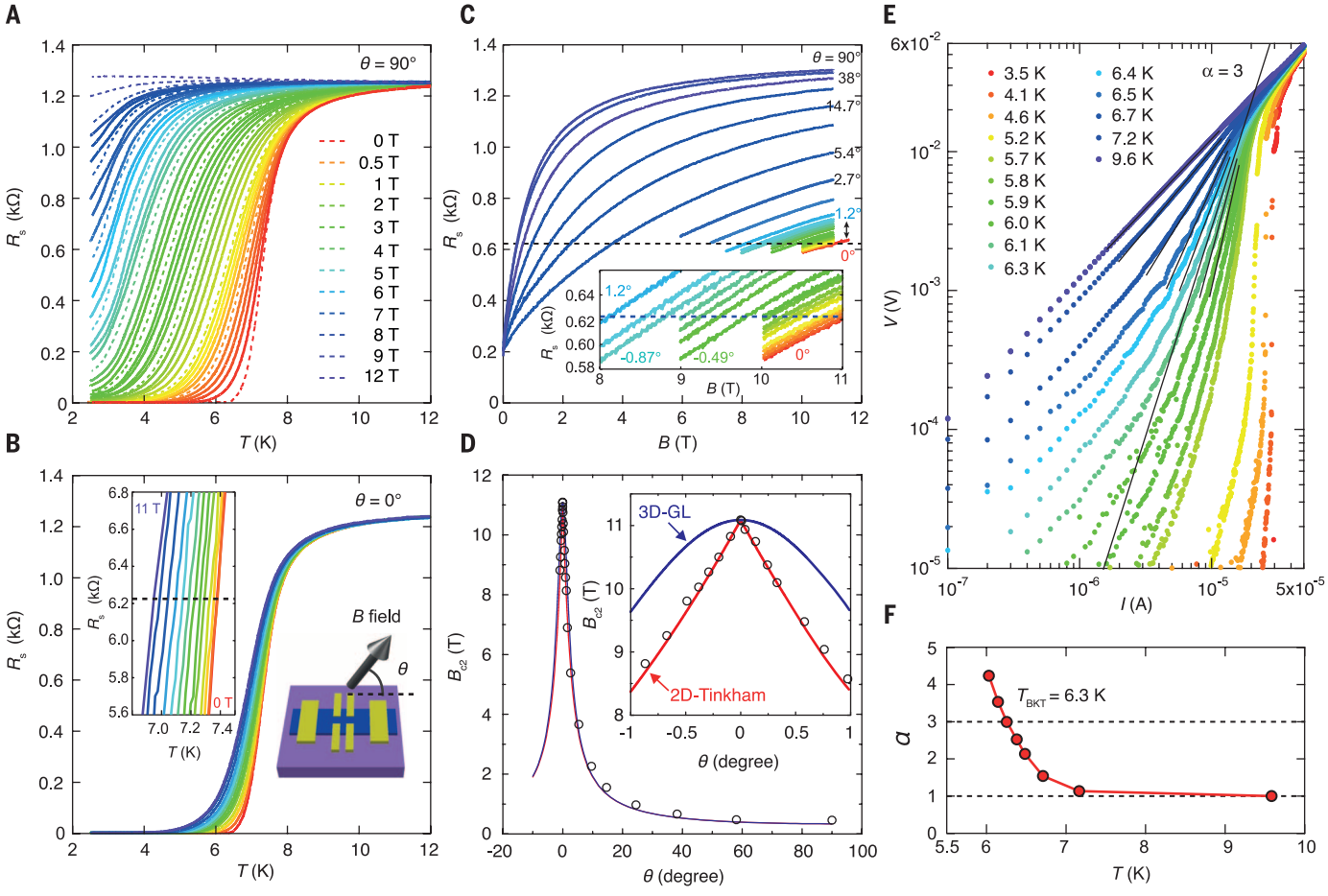

Fig. 2. 2D superconductivity in gated MoS_2 (sample D24). Temperature dependence of R_s under a constant out-of-plane (**A**) and in-plane (**B**) magnetic field, up to 12 T. In (B), the left inset shows a close-up view of the data near $R_N/2$ within 1 K. In the right inset, θ is the angle between the B field and the MoS_2 surface. (**C**) Angular dependence of R_s, where the dashed line denotes $R_s = R_N/2$. In the inset, the data are shown in detail within ±1° of the in-plane field configuration (θ = 0°). (**D**) Angular dependence of B_{c2}, which is fitted by both the 2D Tinkham model (red) and the 3D anisotropic GL model (blue). In the inset, the angular dependence of B_{c2} is shown in detail within ±1° of the in-plane field configuration (θ = 0°). (**E**) The V-I relationship at different temperatures close to T_c, plotted on a logarithmic scale. The black lines are fits close to metal-superconductor transitions. The long black line denotes $V \propto I^3$, which gives T_{BKT}. (**F**) Temperature dependence of α from fitting the power law dependence of $V \propto I^{\alpha}$ from the black lines in (E). T_{BKT} = 6.3 K is obtained for α = 3.

The charge distribution of our gated system implies that the superconducting state thus formed should exhibit a purely 2D nature. To demonstrate this dimensionality, we have characterized sample D24 [with $T_c(0)$ = 7.38 K] with a series of measurements. The temperature dependences of R_s under out-of- and in-plane magnetic fields (Fig. 2, A and B) are highly anisotropic. The angular dependence of B_{c2} at T = 6.99 K (Fig. 2D) was extracted from Fig. 2C. Curves fitted with the 2D Tinkham formula (red curve) (*30*) and the 3D anisotropic Ginzburg-Landau (GL) model (blue curve) (*2*) show that for $\theta > \pm 1°$ (where θ is the angle between the B field and the MoS_2 surface), the data are consistent with both models, whereas for $\theta < \pm 1°$ (Fig. 2D, inset), the cusp-shaped dependence can only be explained with a 2D model. These measurements show that our system exhibits 2D superconductivity, similar to $LaAlO_3$/$SrTiO_3$ interfaces (*31*) and ion-gated $SrTiO_3$ surfaces (*32*). From the voltage-current (*V-I*) dependence at different temperatures close to $T_c(0)$ (Fig. 2E), we determined that the Berezinskii-Kosterlitz-Thouless temperature T_{BKT} is 6.3 K for our 2D system (Fig. 2F). *V-I* characteristics in a magnetic field (fig. S3) exhibit similar critical behavior to the zero-field data, with their T_{BKT} values effectively reduced by increasing the magnetic field.

A moderate in-plane B field of up to 12 T shows little effect on the superconducting transition temperature [where $T_c(0)$ = 7.38 K and the Pauli limit B_P = 13.7 T (Fig. 2B)]; thus, the B_{c2} of the system must be far above B_P. To confirm this, we performed a high field measurement up to 37 T [section 2 of (*16*)] on sample D1 after observing a steep increase in B_{c2} near $T_c(0)$ = 5.5 K (Fig. 3C, green dots). By controlling the gating strength, superconducting states with $T_c(0)$ = 2.37 and 7.64 K were induced in sample D1. For $T_c(0)$ = 2.37 K, we obtained B_{c2} as the magnetic field required to reach 50% of the normal state resistivity (R_N) (Fig. 3A). B_{c2} is above 20 T at 1.46 K (Fig. 3C, red circles), which is more than four times the B_P. The data from the second gating [$T_c(0)$ = 7.64 K (Fig. 3B)] show only a weak reduction of T_c by ~1 K at even the highest magnetic field, 32.5 T (~ 2.3 × B_p).

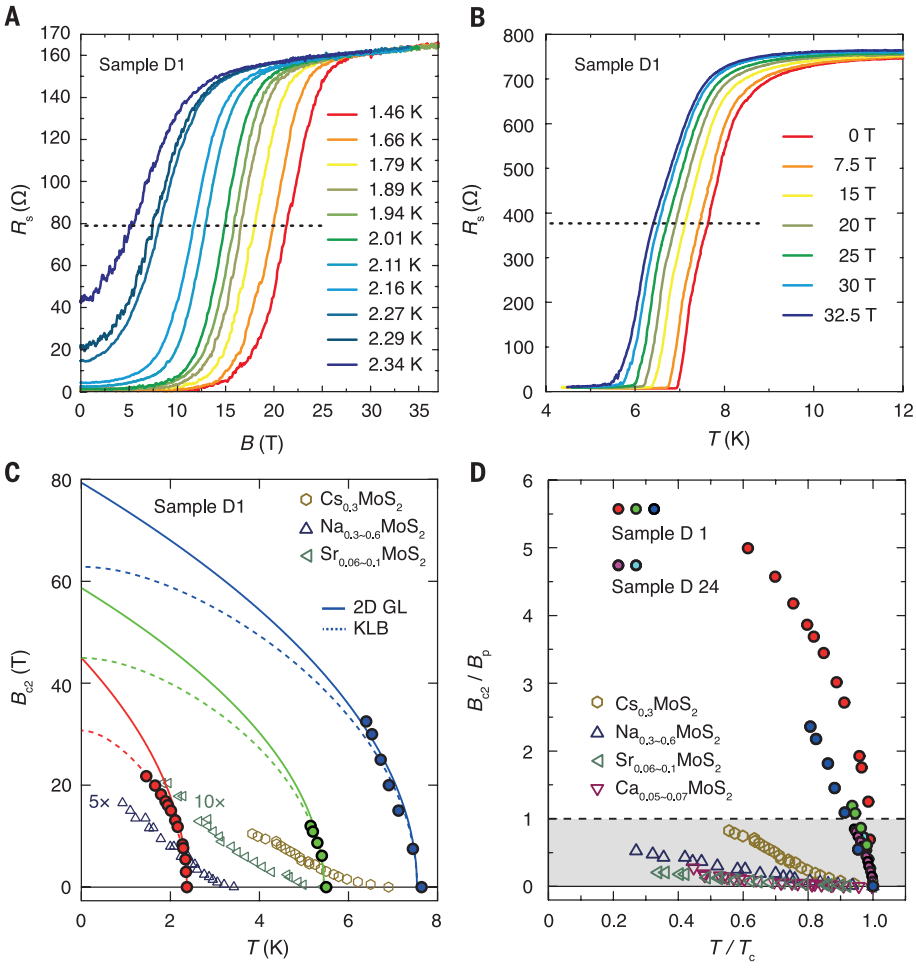

Fig. 3. Determining the in-plane upper critical field B_{c2} at different T_c (samples D1 and D24). (**A**) Magnetoresistance of sample D1 [with $T_c(0)$ = 2.37 K near the onset of the superconducting phase] as a function of an in-plane magnetic field up to 37 T, at various temperatures. (**B**) Temperature dependence of R_s for sample D1 [with $T_c(0)$ = 7.64 K] under different in-plane magnetic fields up to 32.5 T. The dashed lines in (A) and (B) indicate $R_N/2$. B_{c2} is determined as the intercept between dashed lines and R_s curves. (**C**) Temperature dependence of B_{c2} for superconducting states induced in sample D1 with different T_c [solid circles; colors follow (D)]. The B_{c2} for alkali metal–intercalated bulk MoS_2 compounds is from (*41*) and is shown for comparison. The B_{c2} for gate-induced states is fitted as a function of temperature using the 2D GL (solid line) and KLB (dashed line) models. (**D**) B_{c2} normalized by B_p, as a function of reduced temperature T/T_c, including superconducting states from alkali-doped bulk phases and gated-induced phases (samples D1 and D24). The dashed line denotes B_p and sets the boundary of the Pauli limited regime (shaded).

Our observation of a B_{c2} far above the Pauli limit is consistent with the conclusion drawn from Fig. 2 and previous theoretical calculations (*17*, *26*) and ARPES measurements (*27*, *28*) regarding predominant doping in the outermost layer. Curves fitted with the KLB theory yield a very short SOS time of ~24 fs (fig. S5), which is less than the total scattering time of 185 fs estimated from resistivity measurements at 15 K (table S2) and much shorter than the estimation of nanoseconds calculated for MoS_2 at the carrier density range accessed by this work (*34*). Short spin-orbit scattering times of ~40 to 50 fs have also been observed in organic molecule–intercalated TaS_2 (*35*–*37*), $(LaSe)_{1.14}(NbSe_2)$ (*38*, *39*), and the organic superconductor κ-$(ET)_4Hg_{2.89}Br_8$ [ET, bis(ethylenedithio)tetrathiafulvalene] (*40*).

The temperature dependence of B_{c2} in bulk superconducting MoS_2 intercalated by alkali metals (*41*) near $T_c(0)$ is linear instead of square root (Fig. 3C). The slight upturn of B_{c2} toward lower temperatures away from $T_c(0)$ is the evidence of crossover from 3D to 2D superconducting states (*12*, *33*, *36*–*38*) caused by the layered nature of the bulk crystal. In these bulk phases, the measured B_{c2} values are much smaller than or comparable (when Cs dopants are intercalated) to B_p (*41*).

This behavior is visualized in Fig. 3D, where the in-plane B_{c2} normalized by B_p for bulk superconducting phases falls within the shaded area bounded by the Pauli limit. In contrast, all gate-induced phases (from samples D1 and D24) are far above both B_p (dashed line) and bulk-phase B_{c2}. The D1 with $T_c(0)$ = 2.37 K, which is separated from the other gate-induced states, exhibits the largest enhancement. If the large SOS rate extracted from the KLB fitting (Fig. 3C) were the reason for the enhancement of B_{c2} in gate-induced phases, we would expect it to also enhance

B_{c2} in the bulk phases. The difference shown in Fig. 3D indicates that SOS is unlikely to be the origin of the enhancement of B_{c2} in the gated phases.

Excluding SOS as the principal mechanism for the strong enhancement of the in-plane B_{c2}, and taking into account recent developments in understanding the band structures of monolayer MoS_2 (*42*, *43*), we propose that this B_{c2} enhancement is mainly caused by the intrinsic spin-orbit coupling in MoS_2. Near the K points of the Brillouin zone (Fig. 1A) and on the basis of spin-up and -down electrons $[\psi_{k\uparrow}, \psi_{k\downarrow}]$, the normal-state Hamiltonian of monolayer MoS_2 in the presence of an external field can be described by (*24*)

$$H(\mathbf{k}+\epsilon\mathbf{K}) = \varepsilon_k + \epsilon\beta_{so}\sigma_z + \alpha_R \mathbf{g}_F \cdot \sigma + \mathbf{b}\cdot\sigma \quad (1)$$

Here, $\varepsilon_k = \frac{\mathbf{k}^2}{2m} - \mu$ denotes the kinetic energy with chemical potential μ; $\mathbf{k} = (k_x, k_y, 0)$ is the kinetic momentum of electrons in the K and K' valleys; $\mathbf{K}$ is the kinetic momentum of the K valley; m is the effective mass of the electrons; $\sigma = (\sigma_x, \sigma_y, \sigma_z)$ are the Pauli matrices; $\mathbf{g}_F = (k_y, -k_x, 0)$ denotes the Rashba vector (lying in-plane); α_R and β_{SO} are the strength of Rashba and intrinsic SOC, respectively; $\epsilon = \pm 1$ is the valley index (1 at the K valley and –1 at the K' valley); and $\mathbf{b} = \mu_B\mathbf{B}$ is the external Zeeman field (where μ_B is the Bohr magneton). The intrinsic SOC term $\epsilon\beta_{SO}\sigma_z$, due to in-plane inversion symmetry breaking, induces an effective magnetic field pointing out of the plane (z direction), which has opposite signs at opposite valleys (green arrows in Fig. 1A). This Zeeman-like effective magnetic field $\mathbf{B}_{eff} = \epsilon\beta_{SO}\hat{z}/g\mu_B$ (g, gyromagnetic ratio; $\hat{z}$, unit vector in the out-of-plane direction) will only appear in our multilayered system after applying a strong electric field, which isolates the outermost layers from the other layers (*17*, *44*), thus mimicking a monolayer system. The large electric field generated by gating reaches ~50 million volts/cm (*17*) in our system, causing additional out-of-plane inversion symmetry breaking and creating a Rashba-type effective magnetic field $\mathbf{B}_{Ra} = \alpha_R\mathbf{g}_F/g\mu_B$.

The total energy in a magnetic field is schematically shown in Fig. 4, A to D. If the electron spin aligned by $\mathbf{B}_{eff}$ ($\mathbf{B}_{Ra}$) stays parallel to the external magnetic field $\mathbf{B}_{ex}$ (Fig. 4, A and C), the system gains energy through coupling between spin and external fields as $\mu_B\mathbf{B}_{ex}$. Therefore, B_{c2} is limited by B_p (Fig. 4A), or it can reach $\sqrt{2}\,B_p$ (Fig. 4C) when coupling is reduced in a Rashba-type spin configuration (*10*). When $\mathbf{B}_{eff}$ and $\mathbf{B}_{Ra}$ are perpendicular to $\mathbf{B}_{ex}$, as respectively shown in Fig. 4, B and D, the spin aligned by both effective fields is orthogonal to $\mathbf{B}_{ex}$. Hence, the coupling between spin and $\mathbf{B}_{ex}$ is minimized, and B_{c2} can easily surpass B_p in these two cases.

To theoretically describe our system when subjected to an in-plane external magnetic field (combining the cases shown in Fig. 4, B and

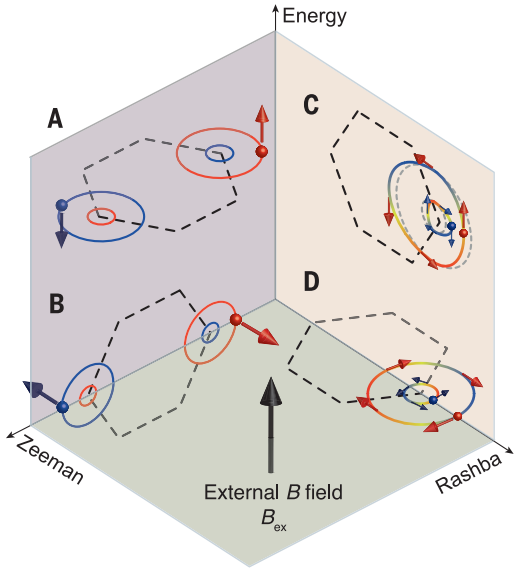

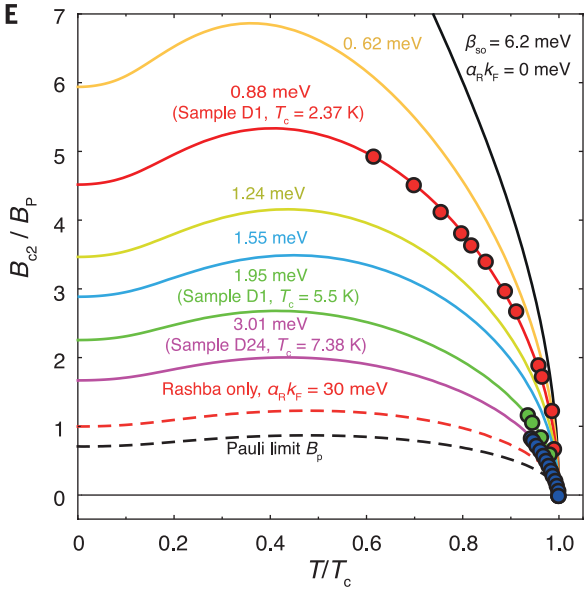

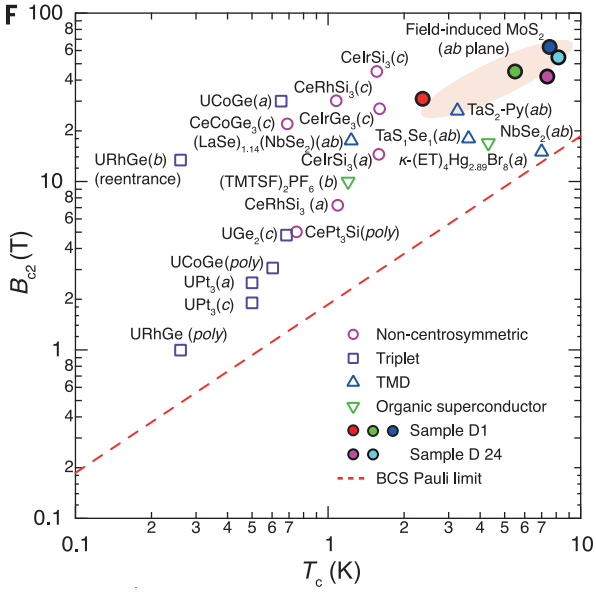

Fig. 4. Interplay between an external magnetic field and the spins of Cooper pairs aligned by Zeeman and Rashba-type effective magnetic fields. (**A** to **D**) Illustration of the acquisition of Zeeman energy through coupling between an external magnetic field and the spins of Cooper pairs formed near the K and K' points of the Brillouin zone (not to scale). When Rashba or Zeeman SOC aligns the spins of Cooper pairs parallel to the external field, the increase in Zeeman energy due to parallel coupling between the field and the spin eventually can cause the pair to break [(A) and (C)]. In (B) and (D), the acquired Zeeman energy is minimized as a result of the orthogonal coupling between the field and the aligned spins, which effectively protects the Cooper pairs from depairing. (**E**) Theoretical fitting of the relationship between B_{c2}/B_p and T/T_c for samples D1 [$T_c(0)$ = 2.37 K and 5.5 K] and D24 [$T_c(0)$ = 7.38 K], using a fixed effective Zeeman field (β_{SO} = 6.2 meV) and an increasing Rashba field ($\alpha_R k_F$ ranges from 10 to ~50% of β_{SO}) [section 6 of (*16*)]. Two dashed lines show the special cases calculated by equation S3, when only the Rashba field ($\alpha_R k_F$ = 30 meV; β_{SO} = 0) is considered (red), and when both the Zeeman and Rashba fields are zero (black). In the former case, a large $\alpha_R k_F$ causes a moderate increase of B_{c2} to ~$\sqrt{2}B_p$ (*10*). In the latter case, the conventional Pauli limit at zero temperature is recovered. (**F**) Plot of B_{c2} versus T_c for different superconductors [a magnetic field was applied along crystal axes *a*, *b*, or *c* or to a polycrystalline (*poly*)]. The data shown are from well-known systems including noncentrosymmetric (pink circles), triplet (purple squares) (*6*, *8*, *9*), low-dimensional organic (green triangles) (*40*, *50*–*52*), and bulk TMD superconductors (blue triangles) (*35*–*38*, *47*). The robustness of the spin protection can be measured by the vertical distance between B_{c2} and the red dashed line denoting B_p. Gate-induced superconductivity from samples D1 and D24 are among the states with the highest B_{c2}/B_p ratio. In $(LaSe)_{1.14}(NbSe_2)$, T_c was determined at 95% of R_N; T_c in organic molecule–intercalated TMDs was obtained by extrapolating to zero resistance; and all other systems use the standard of 50% of R_N.

C), we introduced the pairing potential terms $\Delta\psi_{k\uparrow}\psi_{-k\downarrow} + h.c.$ into $H(\mathbf{k})$ and solved the self-consistent mean field gap equation [section 6 of (*16*); *h.c.*, hermitian conjugate]. The in-plane B_{c2} for a sample with a given T_c can then be determined by including the intrinsic SOC term β_{SO} and the Rashba energy $\alpha_R k_F$, where k_F is the Fermi momentum.

For the most extensive data set from sample D1 [$T_c(0)$ = 2.37 K], the relationship between B_{c2}/B_p and the reduced temperature T/T_c, shown in Fig. 4E, can be fitted well with β_{SO} = 6.2 meV and $\alpha_R k_F$ = 0.88 meV. The value obtained for β_{SO} corresponds to an out-of-plane field of ~114 T, which is comparable to the value expected from theoretical calculation at the *K* point (3 meV) (*23*). The Rashba energy obtained can be regarded as an upper bound, because the present model does not include impurity scattering, which can also reduce B_{c2} (*45*).

The scale of B_{c2} enhancement is determined by a destructive interplay between intrinsic β_{SO} and $\alpha_R k_F$. Reaching higher $T_c(0)$ requires stronger doping under higher electric fields, with a concomitant increase of $\mathbf{B}_{Ra}$. As a result of this competition, the in-plane B_{c2} protection should be weakened with the increase of $T_c(0)$. To support this argument, we chose two other superconducting samples that showed consecutively higher $T_c(0)$ (from D1 and D24). By assuming identical β_{SO} (6.2 meV), B_{c2} from D1 with $T_c(0)$ = 5.5 K and B_{c2} from D24 with $T_c(0)$ = 7.38 K can be well fitted using $\alpha_R k_F$ = 1.94 and 3.02 meV, respectively; these values are consistent with the expected increase of $\alpha_R k_F$ with $T_c(0)$ (Fig. 4E).

The effective Zeeman field and its orthogonal protection in individual layers can also be induced by reducing the interlayer coupling in bulk superconducting TMDs (*33*, *35*, *38*, *46*, *47*). Therefore, a large in-plane B_{c2} was also observed in bulk when lattice symmetry was lowered by intercalating organic molecules and alkali elements with large radii (Cs-intercalated MoS_2 shows the highest B_{c2} among bulk phases in Fig. 3D) or by forming a charge density wave (*46*).

We compared our B_{c2} results with those obtained from other superconductors with enhanced B_{c2} under their maximum spin protection along the labeled crystal axis (Fig. 4F); we found that the Zeeman field–protected states in our samples are among the states that are most robust against external magnetic fields. Given the very similar band structures found in 2*H*-type TMDs with universal Zeeman-type spin splitting and the recent successes in inducing more TMD superconductors using the field effect (*17*, *48*, *49*), we would expect a family of Ising superconductors in 2*H*-type TMDs. The concept of the Ising superconductor is also applicable to other layered systems, where similar intrinsic SOC could be induced by symmetry breaking.

REFERENCES AND NOTES

1. G. R. Stewart, *Rev. Mod. Phys.* **56**, 755–787 (1984).
2. M. Tinkham, *Introduction to Superconductivity* (McGraw-Hill, 1996).
3. A. M. Clogston, *Phys. Rev. Lett.* **9**, 266–267 (1962).
4. B. S. Chandrasekhar, *Appl. Phys. Lett.* **1**, 7 (1962).
5. Y. Matsuda, H. Shimahara, *J. Phys. Soc. Jpn.* **76**, 051005 (2007).
6. D. Aoki *et al.*, *Nature* **413**, 613–616 (2001).
7. N. T. Huy *et al.*, *Phys. Rev. Lett.* **99**, 067006 (2007).
8. D. Aoki, J. Flouquet, *J. Phys. Soc. Jpn.* **81**, 011003 (2012).
9. E. Bauer, M. Sigrist, Eds., *Non-Centrosymmetric Superconductors* (Springer-Verlag, 2012).
10. L. P. Gor'kov, E. I. Rashba, *Phys. Rev. Lett.* **87**, 037004 (2001).
11. A. A. Abrikosov, L. P. Gor'kov, *Sov. Phys. JETP* **15**, 752 (1962).
12. R. A. Klemm, A. Luther, M. R. Beasley, *Phys. Rev. B* **12**, 877–891 (1975).
13. P. M. Tedrow, R. Meservey, *Phys. Rev. B* **25**, 171–178 (1982).
14. X. S. Wu, P. W. Adams, Y. Yang, R. L. McCarley, *Phys. Rev. Lett.* **96**, 127002 (2006).
15. R. A. Klemm, *Layered Superconductors: Volume 1* (International Series of Monographs on Physics 153, Oxford Univ. Press, 2011).
16. Materials and methods are available as supplementary materials on *Science* Online.
17. J. T. Ye *et al.*, *Science* **338**, 1193–1196 (2012).
18. K. Ueno *et al.*, *Nat. Mater.* **7**, 855–858 (2008).
19. H. Yuan *et al.*, *Adv. Funct. Mater.* **19**, 1046–1053 (2009).
20. J. T. Ye *et al.*, *Nat. Mater.* **9**, 125–128 (2010).
21. K. Ueno *et al.*, *Nat. Nanotechnol.* **6**, 408–412 (2011).
22. J. Ye *et al.*, *Proc. Natl. Acad. Sci. U.S.A.* **108**, 13002–13006 (2011).
23. A. Kormányos *et al.*, *Phys. Rev. B* **88**, 045416 (2013).
24. N. F. Q. Yuan, K. F. Mak, K. T. Law, *Phys. Rev. Lett.* **113**, 097001 (2014).
25. M. Rösner, S. Haas, T. O. Wehling, *Phys. Rev. B* **90**, 245105 (2014).
26. R. Roldán, E. Cappelluti, F. Guinea, *Phys. Rev. B* **88**, 054515 (2013).
27. T. Eknapakul *et al.*, *Nano Lett.* **14**, 1312–1316 (2014).
28. Y. Zhang *et al.*, *Nat. Nanotechnol.* **9**, 111–115 (2014).
29. Y. Ge, A. Y. Liu, *Phys. Rev. B* **87**, 241408 (2013).
30. M. Tinkham, *Phys. Rev.* **129**, 2413–2422 (1963).
31. N. Reyren *et al.*, *Appl. Phys. Lett.* **94**, 112506 (2009).
32. K. Ueno *et al.*, *Phys. Rev. B* **89**, 020508 (2014).
33. R. A. Klemm, *Physica C* **514**, 86–94 (2015).
34. L. Wang, M. W. Wu, *Phys. Lett. A* **378**, 1336–1340 (2014).
35. R. C. Morris, R. V. Coleman, *Phys. Rev. B* **7**, 991–1001 (1973).
36. R. V. Coleman, G. K. Eiserman, S. J. Hillenius, A. T. Mitchell, J. L. Vicent, *Phys. Rev. B* **27**, 125–139 (1983).
37. D. E. Prober, R. E. Schwall, M. R. Beasley, *Phys. Rev. B* **21**, 2717–2733 (1980).
38. P. Samuely *et al.*, *Physica C* **369**, 61–67 (2002).
39. J. Kačmarčík *et al.*, *Physica C* **468**, 543–546 (2008).
40. R. N. Lyubovskaya, R. B. Lyubovskii, M. K. Kakova, S. I. Pesotskii, *JETP Lett.* **51**, 361 (1990).
41. J. A. Woollam, R. B. Somoano, *Phys. Rev. B* **13**, 3843–3853 (1976).
42. D. Xiao, G.-B. Liu, W. Feng, X. Xu, W. Yao, *Phys. Rev. Lett.* **108**, 196802 (2012).
43. Z. Y. Zhu, Y. C. Cheng, U. Schwingenschlögl, *Phys. Rev. B* **84**, 153402 (2011).
44. H. Yuan *et al.*, *Nat. Phys.* **9**, 563–569 (2013).
45. L. N. Bulaevskii, A. A. Guseinov, A. I. Rusinov, *Sov. Phys. JETP* **44**, 1243 (1976).
46. S. Foner, E. J. McNiff Jr., *Phys. Lett. A* **45**, 429–430 (1973).
47. Y. Kashihara, A. Nishida, H. Yoshioka, *J. Phys. Soc. Jpn.* **46**, 1112–1118 (1979).
48. K. Taniguchi, A. Matsumoto, H. Shimotani, H. Takagi, *Appl. Phys. Lett.* **101**, 042603 (2012).
49. W. Shi *et al.*, *Sci. Rep.* **5**, 12534 (2015).
50. I. J. Lee, M. J. Naughton, G. M. Danner, P. M. Chaikin, *Phys. Rev. Lett.* **78**, 3555–3558 (1997).
51. I. J. Lee, P. M. Chaikin, M. J. Naughton, *Phys. Rev. B* **62**, R14669–R14672 (2000).
52. P. M. Chaikin, E. I. Chashechkina, I. J. Lee, M. J. Naughton, *J. Phys. Condens. Matter* **10**, 11301–11314 (1998).

ACKNOWLEDGMENTS

We acknowledge support from the High Field Magnet Laboratory Nijmegen (HFML-RU/FOM), a member of the European Magnetic Field Laboratory. J.T.Y. acknowledges funding from the European Research Council (consolidator grant no. 648855 lg-QPD). U.Z. was supported by the DESCO program (2-Dimensional Electron Systems in Complex Oxides, program no. 149) of the Foundation for Fundamental Research on Matter, which is part of the Netherlands Organization for Scientific Research. K.T.L. and N.F.Q.Y. were supported by the Hong Kong Research Grants Council and the Croucher Foundation through grants HKUST3/CRF/13G, 602813, 605512, and 16303014 and an Innovation Grant.

SUPPLEMENTARY MATERIALS

www.sciencemag.org/content/350/6266/1353/suppl/DC1
Materials and Methods
Figs. S1 to S5
Tables S1 and S2
References (*53*–*65*)

30 March 2015; accepted 21 October 2015
Published online 12 November 2015
10.1126/science.aab2277

ICE SHEETS

Fast retreat of Zachariæ Isstrøm, northeast Greenland

J. Mouginot,[1]* E. Rignot,[1,2] B. Scheuchl,[1] I. Fenty,[2] A. Khazendar,[2] M. Morlighem,[1] A. Buzzi,[1] J. Paden[3]

After 8 years of decay of its ice shelf, Zachariæ Isstrøm, a major glacier of northeast Greenland that holds a 0.5-meter sea-level rise equivalent, entered a phase of accelerated retreat in fall 2012. The acceleration rate of its ice velocity tripled, melting of its residual ice shelf and thinning of its grounded portion doubled, and calving is now occurring at its grounding line. Warmer air and ocean temperatures have caused the glacier to detach from a stabilizing sill and retreat rapidly along a downward-sloping, marine-based bed. Its equal-ice-volume neighbor, Nioghalvfjerdsfjorden, is also melting rapidly but retreating slowly along an upward-sloping bed. The destabilization of this marine-based sector will increase sea-level rise from the Greenland Ice Sheet for decades to come.

Zachariæ Isstrøm (ZI) and Nioghalvfjerdsfjorden glacier (NG), in northeast Greenland, drain a sector 198,380 km^2 in size, or 12% of the Greenland Ice Sheet (*1*). These two glaciers together drain the northeast Greenland ice stream, the only large, dynamic feature that extends continuously deep to the ice sheet interior near Greenland's summit (*2*). This marine-based sector holds a 1.1-m sea-level rise equivalent (*3*) (Fig. 1D).

We constructed a high-resolution bed topography of both glaciers (Fig. 1) using a mass conservation method over grounded ice (*3*) and airborne gravity inversion (*4*) over floating ice.

On ZI, we find that the grounding line in year 1996 (*5*) was positioned 450 m below sea level (bsl), on a previously unknown sill that crosses the entire glacier width. Seaward of the sill, the seafloor drops to 800-m bsl (Fig. 1D). Inland of the sill, the glacier bed remains between 400 and 700 m bsl for 30 km. The bed then rises to reach a ridge at sea level. The ridge is cut across by a 300-m-deep channel that connects with interior regions, where the bed remains 300 m bsl for another 150 km. On NG, the 1996 grounding line was 600 m bsl. We find no sill, and the bed is sloping upward until 45 km inland. Seismic data collected in the 1990s (*6*) indicate that the ice shelf floats on a 900-m bsl cavity. The seafloor rises to 200 m bsl to the east, where the ice front is anchored by islands and ice rises, and 600 m bsl to the north into Dijmphna Sund.

[1]Department of Earth System Science, University of California, Irvine, CA 92697, USA. [2]Jet Propulsion Laboratory, California Institute of Technology, Pasadena, CA 91109-8099, USA. [3]Center for Remote Sensing of Ice Sheets, University of Kansas, Lawrence, KS 66045, USA.
*Corresponding author. E-mail: jmougino@uci.edu

We use Landsat optical imagery (fig. S1) to document the ice-front positions over the past 40 years. ZI ice shelf was stable until 2002–2003, when a large section broke off (*7*) and ice debris cleared from Jøkelbugten fjord. The ice front retreated steadily until late 2012, when the northern and southern floating sections became disconnected. In 2013–2014, the ice-front retreat accelerated markedly and the glacier started to calve at its grounding line. By December 2014, the remaining shelf was 52 km^2 in size, or 95% smaller than in 2002. Meanwhile, the calving front of NG retreated by only a few km between 2002 and 2012 (*7*).

We map the glacier grounding lines from 1992 to 2015 (Fig. 1C and figs. S2 and S3) using differential satellite radar interferometry (DInSAR). The grounding line of ZI retreated by 3.5 km at its center between 1996 and 2010, and 3.5 km between 2011 and 2015 (Fig. 1C). The mean rate of grounding-line retreat therefore quadrupled from 230 m/year to 875 m/year before and after 2011. On NG, the grounding line retreated 1 km between 1992 and 2011 and has remained stable since. The DInSAR observations reveal a downward tilting of the ice-front surface of ZI by 75 cm between 16 to 20 December and 20 to 24 December 2014 in a section 1 km wide by 7 km long (Fig. 1C). We attribute this deformation to a buoyancy-driven rotation of the terminus depressed below flotation and facilitated by the propagation of basal crevasses to the water line (*8*).

We document 40 years of surface velocity using Landsat and SAR instruments (table S1 and fig. S4). The results show that after 25 years of stability, the speed of ZI increased by 50% from 2000 to 2014, with half of that increase taking place after 2012 (Fig. 2). The glacier sped up 125 m/year every year from 2012 to 2015, or three times as fast as between 2000 and 2012. NG exhibited smaller changes: Its speed increased by 8% between 1976 and 2014, with most of the acceleration occurring after 2006. The glacier accelerations are larger than seasonal variations and extend 80 km and 15 km upstream of the 1996 grounding lines of ZI and NG, respectively, indicating that the coastal changes affect a substantial portion of the drainage system (Fig. 2).

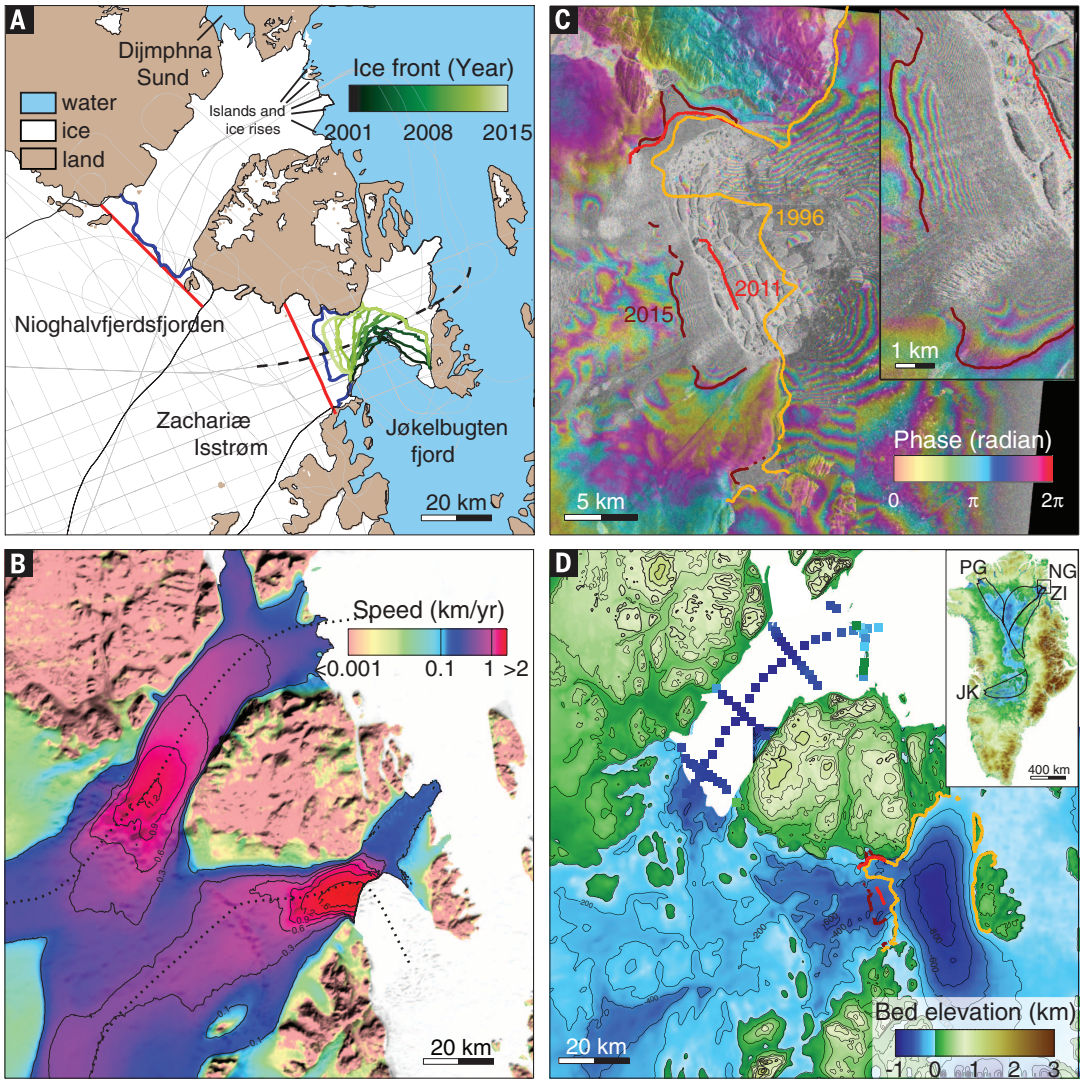

Fig. 1. Ice speed, bed topography, and grounding lines of ZI and NG. (**A**) Schematic view with Operation IceBridge and other NASA mission flight tracks in gray, basin boundaries in black, flux gates in thick blue and red (table S2), and the profile used in Fig. 2 in dashed black. (**B**) Ice surface speed from 2008 to 2009 (*1*), with velocity profiles used in Fig. 3 in black dots. The profiles in (A) and (B) are different. (**C**) Differential interferogram showing the tide-induced motion of ZI in December 2014. The inset shows detail about the pattern of tidal flexure at the grounding line. (**D**) Bed topography above the WGS84 ellipsoid derived from mass conservation on land (*3*) and gravity data at sea (*4*). The seafloor bathymetry beneath NG ice shelf (square) is from seismic measurements (*6*). Inset shows the drainage boundaries of three major marine-based basins in Greenland (*3*).

Repeat measurements of ice thickness (±10-m precision) and surface elevation (±10-cm precision) using radar and light detection and ranging (LIDAR) data (see the supplementary materials) from 1995 to 2014 provide precise information about ice thickness change during the retreat of ZI. About 4.5 km upstream from the 2014 grounding line of ZI, the ice-thinning rate doubled from 2.5 ± 0.1 m/year, consistent with (*9*), to 5.1 ± 0.3 m/year during 1999 to 2010 and 2010 to 2014, respectively. On the ice shelf, the change in ice thickness is large enough to be directly measured with radar (Fig. 3). After correction for dynamic thinning and changes in surface mass balance (SMB), we find that the ice-shelf thickness at the 1996 and 2011 grounding lines decreased by 161 ± 43 m and 100 ± 50 m, respectively, during 1999 to 2010 and 2010 to 2014, reflecting enhanced bottom melting by the ocean of 14.6 ± 4.1 m/year and 25 ± 12 m/year during those time periods (see the supplementary materials). Application of mass conservation on the ice shelf indicated that in the 1990s, the steady-state bottom melt rates of ZI and NG averaged 8 and 5 m/year, respectively, and reached 25 m/year within 10 km of the grounding lines (*5*). We conclude that ice-shelf bottom melting doubled in recent years compared with the 1990s and that half of the increase took place between 2010 and 2014.

On NG, 3.7 km upstream of the 1996 grounding line, ice thinned 0.9 ± 0.1 m/year and 1.4 ± 0.5 m/year during 1999 to 2012 and 2012 to 2014, respectively. The radar echograms show that 5 km downstream of the grounding line, the ice shelf lost 30% of its total thickness (fig. S5). This corresponds to a bottom melting of 13.3 ± 4 m/year in the past 15 years, or 50% above the melt rate from the 1990s (*5*). The ice shelf is therefore eroding rapidly from the bottom. We hypothesize that the erosion has not translated into an inland migration of the grounding line and ice-flow acceleration because the bed of NG rises inland and the ice-shelf front did not detach from bay walls, islands, and ice rises (fig. S5).

Combining surface velocity and ice thickness, we calculate the glacier ice discharge from 1976 to 2015 (Fig. 4 and fig. S6). On ZI, the ice flux increased from 10.3 ± 1.2 Gt/year in 1976 to 15.4 ± 1.7 Gt/year in 2015, or 50%. On NG, the ice discharge increased by 8% from 1976 to 2015. Comparing the ice discharge with net accumulation of mass over the drainage basins (fig. S7) using the regional climate model MAR (Modèle Atmosphérique Régional) (*10*) indicates that ZI was in a state of mass balance until 2003 and is now losing mass at about 5 Gt/year, whereas NG remains close to a state of mass balance (Fig. 4). Our discharge estimates for ZI supersede the overestimates in (*7*) for the period 1990 to 2012, which employed less reliable ice thickness data (figs. S8 and S9).

The MAR reconstruction shows that the mean surface runoff tripled from 0.6 to 1.8 Gt/year, respectively, during 1960 to 1990 and 2002 to 2014 (Fig. 4C) as a result of warmer air temperatures. Higher melting thins ice from the top and contributes to grounding-line retreat as floating ice achieves hydrostatic equilibrium farther upstream. Meltwater ponding on the ice shelf likely contributed to its break-up via hydrofracturing (*11*). Warmer air temperatures melted the ice mélange that keeps ice floes glued together in the fjord (*7*). Enhanced glacier runoff increased subglacial freshwater discharge at the grounding line, which drives a stronger thermohaline circulation at the ice underside and increases the rate of melt by the ocean (*12*).

Ocean in situ measurements over the period 1997 to 2010 show an increase of +1°C in mean temperature of the warm, salty subtropical-origin Atlantic Water (AW) advected from the North Atlantic toward the Arctic Ocean via the West Spitsbergen Current (WSC) (*13*). Although resolving the transport pathways and water-mass transformation of AW in the Northeast Atlantic and East Arctic Ocean is an area of active research (*14*, *15*), it is known that some fraction of these warm northward-flowing waters recirculates in the northern Greenland Sea and in the southern Nansen Basin to join the southward-flowing East Greenland Current (EGC) (*16*). Ocean temperatures observed from moored instruments spanning Fram Strait at 78°50′N from 1997 to the present (*17*) show that temperature anomalies in the northward-flowing WSC also appear in the southward-flowing EGC (*18*). Although high-resolution (2 to 4 km) ocean simulations show that ocean temperature anomalies on the EGC propagate from the continental shelf break into Belgica Trough to within 50 km of ZI (*19*), the seafloor bathymetry in these critical last 50 km is not known well enough to simulate ocean circulation close to the glacier. Yet observations from 1996–1997 (*6*) and 2009 (*20*) reveal the presence of warm AW at the mouth of the NG ice-shelf cavity. A 1°C increase in AW would have increased bottom melting by 10 (*21*) to 20 m/year (*22*), which is within the range of our observations. We conclude that ocean warming most probably played a major role in triggering the glacier retreat, more important than the sea-ice concentration decrease (*7*). Oceanographic observations near ZI are critically needed to address the effect of thermal ocean forcing on the glacier evolution in more detail.

ZI has now transformed into a tidewater glacier calving along an ice cliff as a result of warmer air and ocean temperatures. The mass loss is driven by the increase in ice discharge rather than a change in SMB (Fig. 4). The glacier detached from a stabilizing sill and retreated into a retrograde basin 700 m bsl. Tidewater glaciers are known to retreat rapidly along retrograde beds until the bed rises again (*23*). We project that ZI may continue retreating rapidly for another 20 to 30 years.

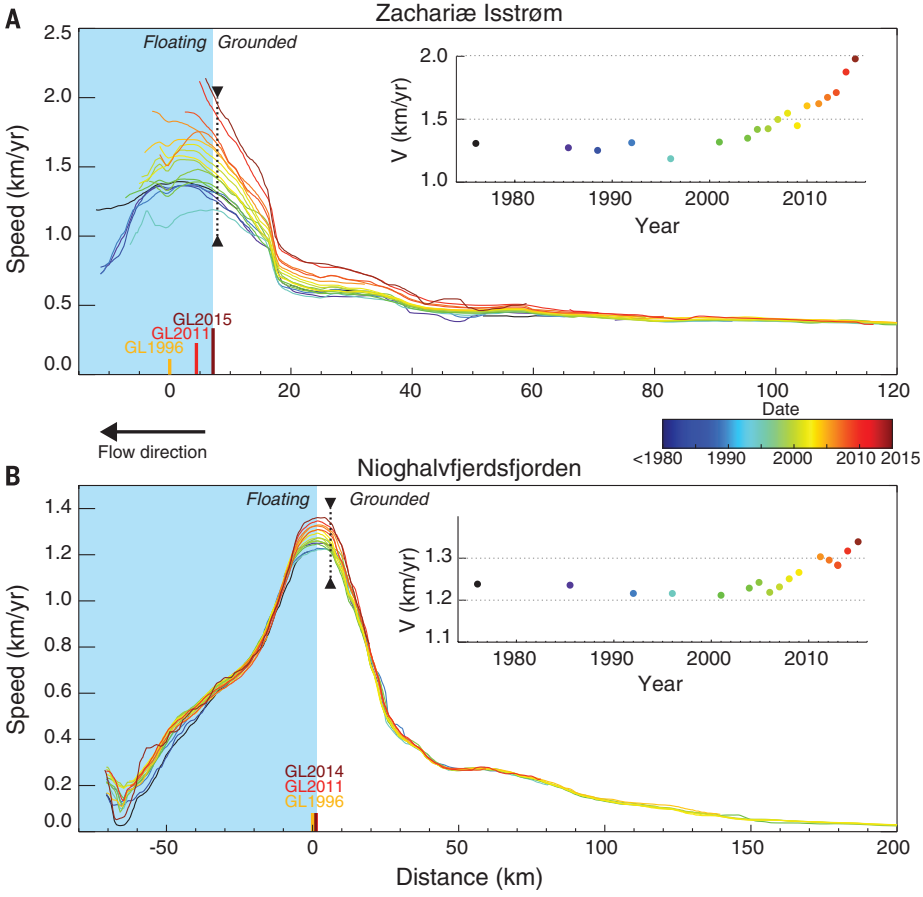

Fig. 2. Ice speed of ZI and NG from 1976 to 2015. (**A** and **B**) Ice speed along the profile in Fig. 1B color-coded from blue (1976) to red (2015). Thick vertical lines locate the grounding lines. The inset displays ice speed versus time at the location of the black dashed vertical line.

Its ice front will progressively widen from 19 km at present to 50 km about 30 km upstream, thereby increasing ice discharge. The height of the calving cliff will increase from its current 75 m to enhance the risk of ice fracture (*11*). With the formation of a calving cliff, the ocean-induced melt rates will increase considerably because buoyant meltwater plumes rise faster along a vertical face than along a near-horizontal ice-shelf bottom (*5*, *12*). Beyond 30 km, the retreat will be slowed down by a rising bed topography, but submarine channels will maintain the contact with the ocean into the deep interior.

The ZI/NG sector is one of three major marine-based basins in Greenland (fig. S10), along with Jakobshavn Isbræ (JI) and Petermann (PG)–Humboldt glaciers, each holding a 0.6-m sea-level equivalent. JI started a rapid retreat (18 km from 2001 to 2015) after the collapse of its ice shelf and has undergone massive calving events since 2010 (*24*) (fig. S11). The central channel of the PG ice shelf lost 250 m of ice from 2002 to 2010, and the ice front retreated 33 km from 2010 to 2012 (*25*). The NG ice shelf will become vulnerable to break-up in the near future if thinning continues. These observations combined suggest that all three major marine-based basins are undergoing substantial changes at present. JI and ZI have already transitioned to a tidewater glacier regime, with increased calf-ice production and ice melting by

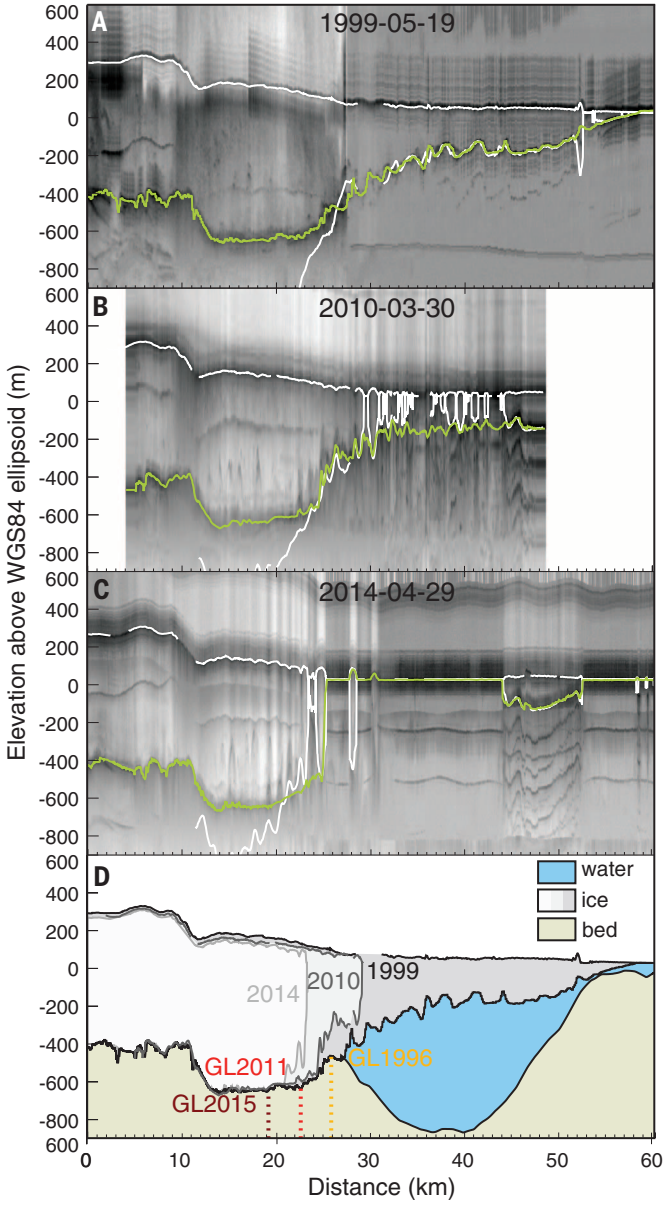

Fig. 3. Surface elevation and ice thickness of ZI from 1999 to 2014. (**A** to **C**) Radar echograms along the center-line profile in Fig. 1A. Ice surface and bottom (assuming flotation) from LiDAR data, respectively, are white. Bed elevation from radar data is green. (**D**) Evolution of ZI between 1999 and 2014, with successive ice-front positions color-coded from dark (1999) to light gray (2014), seawater in blue, and bedrock in light brown. Vertical dashed lines locate the grounding lines.

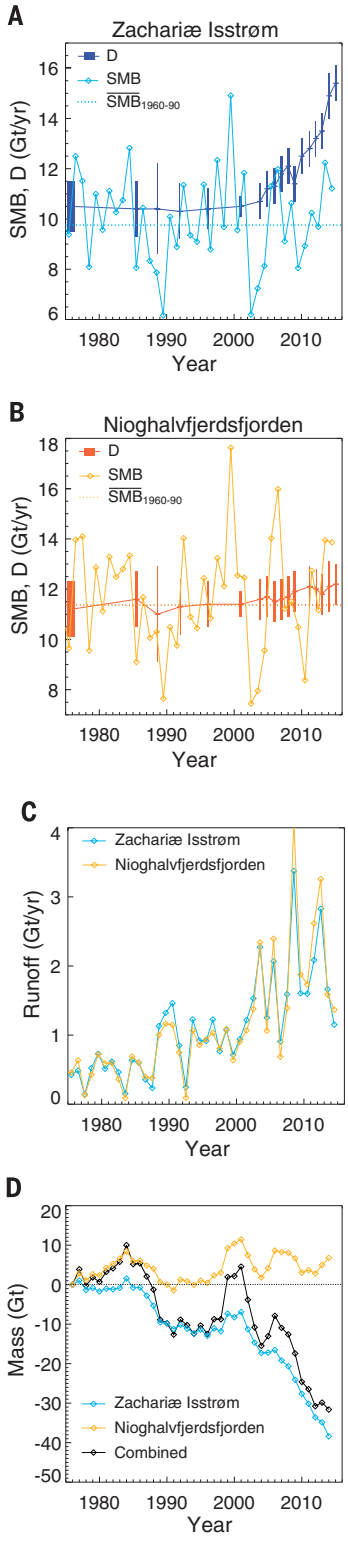

Fig. 4. Yearly ice discharge, surface mass balance, and runoff of ZI and NG from 1976 to 2015. (**A** and **B**) Ice flux [D] and SMB from the regional climate model MAR (*10*) for ZI and NG color-coded blue and orange, respectively. (**C**) Runoff from MAR (*10*). (**D**) Mass evolution of NG, ZI, and both combined. $\overline{SMB}_{1960-90}$ is the mean SMB for the time period 1960–1990.

the ocean. The retreat of these marine-based sectors is likely to increase sea-level rise from Greenland for decades to come.

REFERENCES AND NOTES

1. E. Rignot, J. Mouginot, *Geophys. Res. Lett.* **39**, L11501 (2012).
2. M. Fahnestock, W. Abdalati, I. Joughin, J. Brozena, P. Gogineni, *Science* **294**, 2338–2342 (2001).
3. M. Morlighem, E. Rignot, J. Mouginot, H. Seroussi, E. Larour, *Nat. Geosci.* **7**, 418–422 (2014).
4. J. R. Cochran, R. E. Bell, *J. Glaciol.* **58**, 540–552 (2012).
5. E. Rignot, S. Gogineni, I. Joughin, W. Krabill, *J. Geophys. Res.* **106** (D24), 34007 (2001).
6. C. Mayer, N. Reeh, F. Jung-Rothenhausler, P. Huybrechts, H. Oerter, *Geophys. Res. Lett.* **27**, 2289–2292 (2000).
7. S. A. Khan *et al.*, *Nat. Clim. Change* **4**, 292–299 (2014).
8. T. D. James, T. Murray, N. Selmes, K. Scharrer, M. O'Leary, *Nat. Geosci.* **7**, 593–596 (2014).
9. B. M. Csatho *et al.*, *Proc. Natl. Acad. Sci. U.S.A.* **111**, 18478–18483 (2014).
10. X. Fettweis *et al.*, *The Cryosphere* **7**, 469–489 (2013).
11. D. Pollard, R. M. DeConto, R. B. Alley, *Earth Planet. Sci. Lett.* **412**, 112–121 (2015).
12. Y. Xu, E. Rignot, I. Fenty, D. Menemenlis, M. M. Flexas, *Geophys. Res. Lett.* **40**, 4648–4653 (2013).
13. N. P. Holliday *et al.*, *Geophys. Res. Lett.* **35**, L03614 (2008).
14. K. Orvik, P. Niiler, *Geophys. Res. Lett.* **29**, 1896 (2002).
15. C. Mauritzen *et al.*, *Prog. Oceanogr.* **90**, 62–89 (2011).
16. L. de Steur, E. Hansen, C. Mauritzen, A. Beszczynska-Moeller, E. Fahrbach, *Deep Sea Res. Part I Oceanogr. Res. Pap.* **92**, 26–40 (2014).
17. U. Schauer *et al.*, in *Arctic-Subarctic Ocean Fluxes*, R. R. Dickson, J. Meincke, P. Rhines, Eds. (Springer, Dordrecht, Netherlands, 2008), pp. 65–85.
18. A. Beszczynska-Moeller, E. Fahrbach, U. Schauer, E. Hansen, *ICES J. Mar. Sci.* **69**, 852–863 (2012).
19. E. Rignot, I. Fenty, D. Menemenlis, Y. Xu, *Ann. Glaciol.* **53**, 257–266 (2012).
20. N. J. Wilson, F. Straneo, *Geophys. Res. Lett.* **42**, 7648–7654 (2015). 10.1002/2015GL064944
21. E. Rignot, S. S. Jacobs, *Science* **296**, 2020–2023 (2002).
22. P. R. Holland, A. Jenkins, D. M. Holland, *J. Clim.* **21**, 2558–2572 (2008).
23. M. F. Meier, A. Post, *J. Geophys. Res.* **92** (B9), 9051 (1987).
24. I. Joughin, B. E. Smith, D. E. Shean, D. Floricioiu, *The Cryosphere* **8**, 209–214 (2014).
25. A. Münchow, L. Padman, H. A. Fricker, *J. Glaciol.* **60**, 489–499 (2014).

ACKNOWLEDGMENTS

This work was performed under NASA grants NNX13AI84A (E.R.), NNX14AB93G (E.R.), NNX13AD53A (J.P.), and NNX15AD55G (M.M.), and NSF grant ANT-0424589 (J.P.). The work of I.F., A.K., and E.R. was carried at the Jet Propulsion Laboratory, California Institute of Technology, under a contract with NASA. We gratefully acknowledge European Space Agency, Canadian Space Agency, Japan Aerospace Exploration Agency, Agenzia Spaziale Italiana, National Aeronautics and Space Administration, and Deutsches Zentrum für Luft- und Raumfahrt e.V. for providing SAR data and Polar Space Task Group for coordination of SAR acquisitions.

SUPPLEMENTARY MATERIALS

www.sciencemag.org/content/350/6266/1357/suppl/DC1
Materials and Methods
Supplementary Text
Figs. S1 to S11
Tables S1 and S2
References (*26*–*43*)

10 June 2015; accepted 28 October 2015
Published online 12 November 2015
10.1126/science.aac7111

NEURONAL DYNAMICS

High-speed recording of neural spikes in awake mice and flies with a fluorescent voltage sensor

Yiyang Gong,[1,2,3]* Cheng Huang,[1] Jin Zhong Li,[1,2] Benjamin F. Grewe,[1,2] Yanping Zhang,[1,2,4] Stephan Eismann,[1,2] Mark J. Schnitzer[1,2,4]*

Genetically encoded voltage indicators (GEVIs) are a promising technology for fluorescence readout of millisecond-scale neuronal dynamics. Previous GEVIs had insufficient signaling speed and dynamic range to resolve action potentials in live animals. We coupled fast voltage-sensing domains from a rhodopsin protein to bright fluorophores through resonance energy transfer. The resulting GEVIs are sufficiently bright and fast to report neuronal action potentials and membrane voltage dynamics in awake mice and flies, resolving fast spike trains with 0.2-millisecond timing precision at spike detection error rates orders of magnitude better than previous GEVIs. In vivo imaging revealed sensory-evoked responses, including somatic spiking, dendritic dynamics, and intracellular voltage propagation. These results empower in vivo optical studies of neuronal electrophysiology and coding and motivate further advancements in high-speed microscopy.

To dissect the mechanisms of high-speed neuronal information processing in the live brain, neuroscientists need to track cellular and subcellular electrophysiological activity with millisecond-scale resolution in identified neuron types. Genetically encoded fluorescent Ca^{2+} indicators report isolated, individual action potentials from many cell types in live animals (*1*, *2*). However, Ca^{2+} indicators' slow kinetics (~50 to 1000 ms) precludes high-fidelity studies of fast-spiking cell types, determinations of spike waveforms, resolution of individual spikes in fast spike trains, and precise estimates of spike timing. Moreover, the magnitude of Ca^{2+} influx in response to an action potential varies across cell types and even within individual cells (*1*, *2*). In vivo Ca^{2+} imaging also poorly tracks subthreshold or dendritic voltage dynamics, due to insensitivity to hyperpolarizations and confounds from synaptic Ca^{2+} influx. Organic voltage-sensitive dyes typically have much faster kinetics than Ca^{2+} indicators but are generally highly phototoxic, allow neither genetically targeted delivery nor long-term imaging studies of single cells, and have been incapable of reporting single spikes in the live mammalian brain (*3*).

GEVIs combine genetic targeting and optical readout of transmembrane voltage (*3*, *4*), and in principle can sense spikes and subthreshold dynamics. Nevertheless, to date, GEVIs have lacked the capabilities to detect individual action potentials and fast spike trains in live animals (*3*, *4*).

[1]James H. Clark Center, Stanford University, Stanford, CA 94305, USA. [2]*CNC* Program, Stanford University, Stanford, CA 94305, USA. [3]Department of Biomedical Engineering, Duke University, Durham, NC 27708, USA. [4]Howard Hughes Medical Institute, Stanford University, Stanford, CA, USA.
***Corresponding author. E-mail: yiyang.gong@duke.edu (Y.G.); mschnitz@stanford.edu (M.J.S.)**

Past efforts fused fluorescent proteins to voltage-sensitive domains (VSDs) from voltage-sensitive phosphatases (*5*–*9*) or used Archaerhodopsin (Arch), which is both a fast VSD and a dim fluorophore (*10*). Although Arch variants work well in cultured neurons, the intense illumination required (1 to 10 $W \cdot mm^{-2}$) plus the consequent heating, autofluorescence, and photodamage have precluded imaging studies in intact tissue over wide fields of view (*10*).

Here, we present fast GEVIs (<1-ms response) that fuse the *Acetabularia acetabulum* rhodopsin (Ace) (*11*) and mNeonGreen (*12*) fluorescent protein to enable voltage-sensitive fluorescence resonance energy transfer (FRET) (Fig. 1A and table S1). We previously introduced this "FRET-opsin" configuration (*13*, *14*), which combines the fast kinetics of a rhodopsin VSD with a bright fluorophore and provides high-fidelity membrane potential and spike train readouts at illumination levels ~50 to 100 times lower than those used with Arch indicators. A FRET-opsin indicator based on *Leptosphaeria maculans* (Mac) rhodopsin and yellow fluorescent mCitrine reported fast neural spiking in brain slices and Purkinje neurons' dendritic activation in live mice (*13*). These results had suggested that optical recordings of action potentials and dendritic voltage dynamics in live animals might be attainable. Ace-mNeon indicators now enable high-fidelity imaging of individual spikes and fast spike trains in live mice and flies due to their faster kinetics and superior brightness compared with all prior GEVIs. Ace is about six times as fast as Mac, and mNeonGreen has a ~50% higher extinction coefficient than mCitrine and nearly threefold better photostability (*12*). We created Ace mutants (Ace1Q and Ace2N) with an inactivated proton pump; these have blue-shifted absorption spectra compared with Mac and Arch (*11*, *13*), yielding superior

FRET acceptors when paired with green or yellow emitters (figs. S1 and S2). When used together with protein trafficking signals, the fusions provide high FRET efficiency and minimal protein aggregation in live neurons (Fig. 1, A and B), key attributes of a FRET indicator (*13*, *14*).

We measured responses of Ace1Q-mNeon and Ace2N-mNeon to voltage depolarization steps in cultured human embryonic kidney–293T (HEK293T) cells. These sensors responded five to six times as fast as MacQ-mCitrine (*13*) and the ASAP1 indicator (*7*) (Fig. 1C and table S2). At termination of a step depolarization, Ace2N-mNeon exhibited some hysteresis during its relaxation back to baseline fluorescence levels (Fig. 1C, inset, and fig. S3). However, the steady-state response varied linearly with the transmembrane voltage within the physiological range of subthreshold potentials, and the initial peak response increased linearly between –100 mV and +30 mV (Fig. 1D). These relationships were similar to those of previous FRET-opsin sensors (Fig. 1D and fig. S3), but the faster kinetics of the Ace indicators enabled superior spike detection fidelity, even for rapid successions of spikes that would have blurred together with Ca^{2+} imaging (Fig. 2, A to E). During action potentials in cultured neurons, Ace2N-mNeon and Ace1Q-mNeon had peak changes in fluorescence intensity relative to baseline values ($\Delta F/F$) of 12.0 ± 0.8% (mean ± SEM; N = 12 cells) and 8.5 ± 0.7% (N = 10 cells), respectively, while leaving the spike waveform unperturbed (Fig. 2, A and B, and fig. S4). Photobleaching rates were those of the constituent mNeonGreen, which is as photostable as enhanced green fluorescent protein (*12*) and comparable to those of other brightly fluorescent voltage indicators (table S2).

To quantitatively compare multiple indicators, we used a metric of spike detection fidelity, d', from signal detection theory (*9*, *15*). This metric accounts for an indicator's optical waveform in response to a spike and thus captures rates of correct and false spike detection better than other metrics, such as signal-to-noise ratio (SNR) (*16*). Modest improvements in d' can have huge benefits for experimentation because false detection rates decline faster than exponentially with increases in d' (*9*, *15*). Compared to MacQ-mCitrine, the superior brightness and peak $\Delta F/F$ responses of the Ace indicators increased d' by factors of 2.2 to 3.0, with d' values of 100 ± 12 (Ace2N-mNeon, mean ± SEM) and 70 ± 8 (Ace1Q-mNeon) in cultured neurons (Fig. 2C). Our calculations predicted that this should be sufficient to image spikes >0.4 ms in duration, not only in brain slices but also in live animals (fig. S5).

Studies in mouse brain slices and live mice validated these predictions (Fig. 2, B to E, and Fig. 3, A to F). To facilitate spike detection, we sparsely expressed the GEVIs using the SAD-ΔG viral vector, which efficiently transduces neurons through axons (*17*). This labeling approach reduced background fluorescence from out-of-focal-plane or nonspecifically labeled sources. Previous studies with this virus have shown that there is minimal toxicity in neurons up to 10 days after infection (*17*). We imaged thick brain slices 3 to 5 days after viral injection and found that Ace2N-mNeon reported action potentials with $\Delta F/F$ = 6.5 ± 1.5% and d' = 32 ± 5 (mean ± SEM; n = 5 cells) (Fig. 2B). Neurons expressing the GEVI had statistically indistinguishable spike waveforms compared with nonfluorescent neurons in the same slices (fig. S4).

We next imaged Ace2N-expressing neurons in the mouse visual cortex, using an indicator variant (Ace2N-4AA-mNeon) with four extra amino acids in the linker domain (table S1). This variant yielded improved expression and superior visualization of individual cells' dynamics in live mice (Figs. 2D and 3A, inset). Because extending the linker left the VSD unchanged, the voltage-dependent kinetics were unaffected, although the increased distance between the FRET pairs reduced the peak $\Delta F/F$ response to neural spikes (fig. S6 and table S2). In anesthetized mice (Fig. 2, D and E) and awake mice (Fig. 3), we readily observed spiking waveforms in labeled neurons in cortical layer 2/3, with interspike intervals as brief as ~10 ms—i.e., an interval briefer by a factor of 20 than the signal integration time of the fast Ca^{2+} indicator GCaMP6f (*1*).

Ace2N-4AA-mNeon also provided a high level of spike detection fidelity (d' = 16 ± 1.5; mean ± SEM; N = 56 layer 2/3 neurons, ~150 μm below the brain surface; N = 20 awake mice), at which the frequency of spike detection errors is vastly less than with previous GEVIs. Imaging at a 1-kHz frame rate at a d' value of 16 corresponds to a mean rate of $<10^{-7}$ detection errors per day (*15*). Consistent with this, during simultaneous optical and loose-patch electrical recordings in the same neocortical neurons of anesthetized mice (Fig. 2D), the spike trains attained using

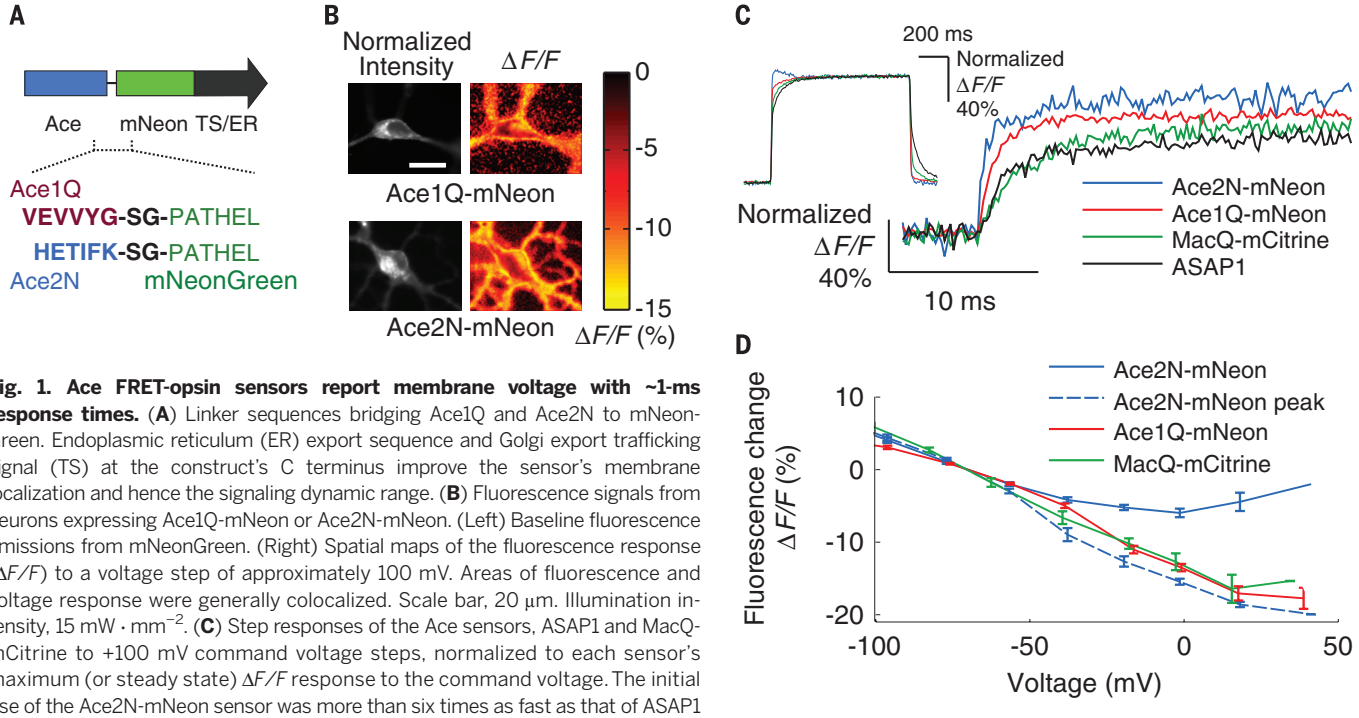

Fig. 1. Ace FRET-opsin sensors report membrane voltage with ~1-ms response times. (**A**) Linker sequences bridging Ace1Q and Ace2N to mNeonGreen. Endoplasmic reticulum (ER) export sequence and Golgi export trafficking signal (TS) at the construct's C terminus improve the sensor's membrane localization and hence the signaling dynamic range. (**B**) Fluorescence signals from neurons expressing Ace1Q-mNeon or Ace2N-mNeon. (Left) Baseline fluorescence emissions from mNeonGreen. (Right) Spatial maps of the fluorescence response ($\Delta F/F$) to a voltage step of approximately 100 mV. Areas of fluorescence and voltage response were generally colocalized. Scale bar, 20 μm. Illumination intensity, 15 mW · mm^{-2}. (**C**) Step responses of the Ace sensors, ASAP1 and MacQ-mCitrine to +100 mV command voltage steps, normalized to each sensor's maximum (or steady state) $\Delta F/F$ response to the command voltage. The initial rise of the Ace2N-mNeon sensor was more than six times as fast as that of ASAP1 and MacQ-mCitrine (table S2). (Inset) The full step response of all sensors. The trace for Ace2N-mNeon exhibits hysteresis ~40 to 200 ms after the voltage step, outside the interval shown in the main plot. Illumination intensity, 15 to 50 mW · mm^{-2}. Data acquisition rate, 5 kHz. Inset traces were down-sampled to 250 Hz. (**D**) Steady-state responses of FRET-opsin sensors as a function of membrane voltage in cultured neurons (N = 10 cells per trace). Because Ace2N-mNeon exhibited hysteric responses to voltage steps (fig. S2), we also plot its peak initial responses. Illumination intensity, 15 mW · mm^{-2}. Error bars, SEM.

Ace2N-4AA-mNeon and those from the electrical recordings were in perfect concordance (837 total spikes detected in dual recordings; N = 3 mice). Highlighting the importance of Ace2N's ~threefold increase in d' over the best previous GEVIs, in vivo imaging with a value threefold lower (d' = 5.3) leads to an unacceptable four spike-detection errors per second. The nearly vanishing error rate predicted at d' = 16 is unattainable over hours under true experimental conditions due to the indicator's finite photostability and nonstationary noise sources in the live brain other than photon shot noise. Nevertheless, this calculation underscores the huge effect of modest rises in d', in that Ace2N has an error rate that is orders of magnitude lower than previous GEVIs and is the first GEVI with acceptable error rates in the detection of single action potentials in live mammals.

Ace2N-4AA-mNeon also provided exquisite spike-timing accuracy, as determined from the dual optical and electrical recordings in live mice (Fig. 2E). Relative to the spike times in the electrical traces, the spike times in the optical traces differed by only 0.24 ± 0.01 ms (SEM; N = 837 spikes) (*16*). This degree of spike-timing accuracy approached the theoretical physical limits, 0.14 ± 0.03 ms, set by quantum mechanical photon shot noise (*9*, *15*, *16*).

We also examined in awake mice whether individual cells' ongoing fluctuations in baseline Ace2N-4AA-mNeon emissions reflect subthreshold membrane voltage dynamics. If so, periods of optically reported membrane hyperpolarization should have reduced spike rates, and periods of reported depolarization should have elevated firing rates. This prediction proved correct for all 56 layer 2/3 neurons imaged in awake mice (Fig. 3B). As determined optically, each neuron fired spikes from baseline voltage levels that were significantly higher than its median resting potential (P < 0.05 for all 56 cells; Wilcoxon rank-sum test). As a population, the 56 cells were far more likely to fire spikes when the optically reported membrane voltages were above median resting levels (P < 10^{-15}; Binomial test). Ace2N-4AA-mNeon also revealed submillisecond-scale features of dendritic voltage dynamics during spike generation (Fig. 3C and movie S1). Thus, Ace2N reports aspects of individual cells' subthreshold, dendritic, and high-speed membrane potential dynamics in the live brain.

We next studied visually evoked spiking responses. To illustrate targeting of specific subclasses of visual cortical neurons, we expressed Ace2N-4AA-mNeon selectively in cells of the primary visual area (V1) that sent axons to the lateromedial cortical area (LM) (denoted V1→LM neurons), one of 15 cortical areas in mice that receive inputs from V1 (*16*, *18*). We presented moving grating visual stimuli to awake mice and imaged the cells' evoked responses. Generally, layer 2/3 V1→LM neurons' evoked spiking was preferentially elicited by gratings of one orientation (4.1 ± 1.1 spikes · s^{-1}; mean ± SEM) versus the response (or suppression of activity) to gratings of the orthogonal orientation (1.0 ± 0.2 spikes · s^{-1}) (Fig. 3, D to F) (N = 7 neurons from 5 mice; P < 10^{-3}; permutation test for each cell; 10^5 permutations). The mean orientation selectivity index (0.82 ± 0.03; mean ± SEM), as determined from Ace2N-4AA-mNeon fluorescence traces, fit well

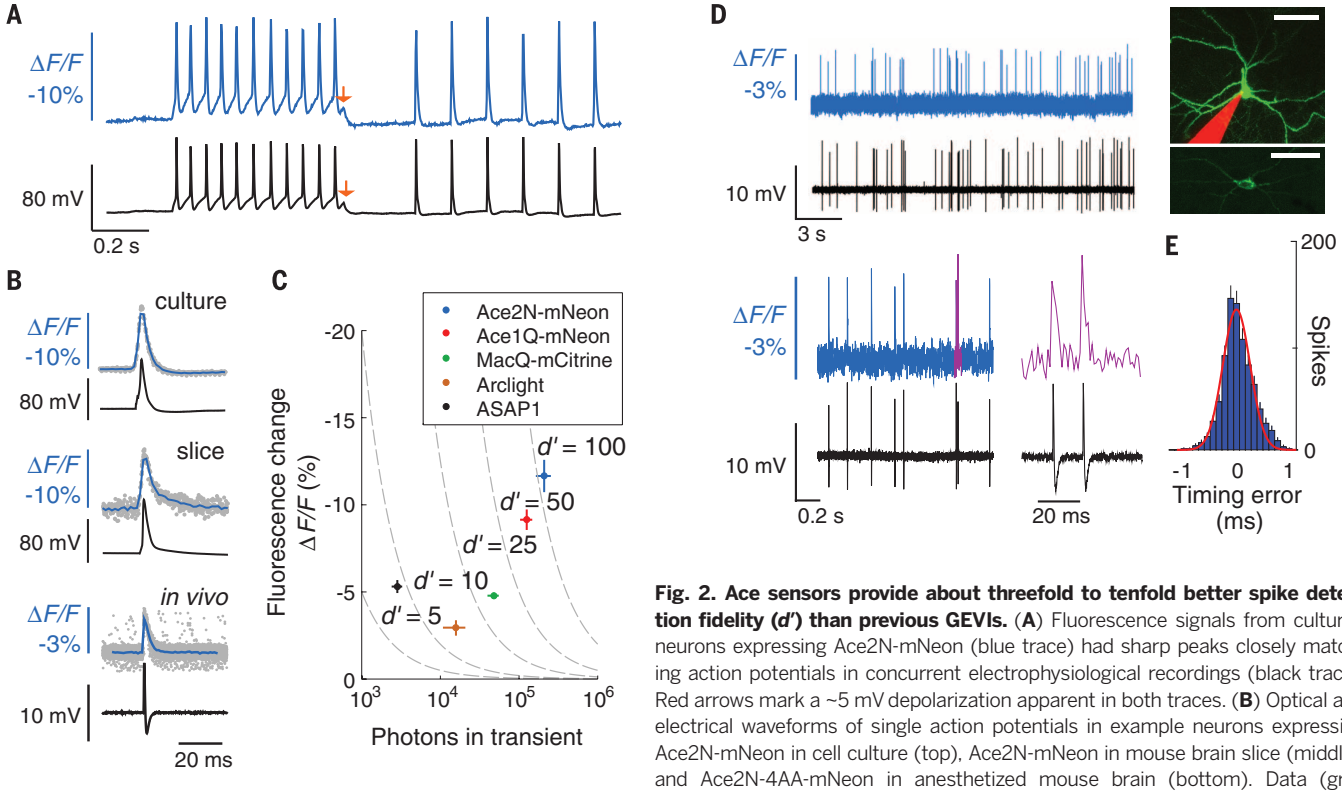

Fig. 2. Ace sensors provide about threefold to tenfold better spike detection fidelity (d') than previous GEVIs. (**A**) Fluorescence signals from cultured neurons expressing Ace2N-mNeon (blue trace) had sharp peaks closely matching action potentials in concurrent electrophysiological recordings (black trace). Red arrows mark a ~5 mV depolarization apparent in both traces. (**B**) Optical and electrical waveforms of single action potentials in example neurons expressing Ace2N-mNeon in cell culture (top), Ace2N-mNeon in mouse brain slice (middle), and Ace2N-4AA-mNeon in anesthetized mouse brain (bottom). Data (gray points) acquired optically from different spikes were temporally aligned to the corresponding peaks in the electrical traces. Mean waveforms of the optical data (blue traces; averaged over N = 30 spikes; resampled to 2 kHz) are aligned with the mean electrical waveforms (black traces; whole-cell patch recordings for cells in culture and brain slice; loose patch recording for live mouse). (**C**) Peak $\Delta F/F$ responses to action potentials, as a function of the total number of photons detected per spike in cultured neurons. Isocontours (dashed lines) of spike-detection fidelity, d', were determined from measured brightness and optical waveforms, as in (B). Error bars, SEM. (**D**) Concurrent optical (colored) and juxtacellular electrical (black) recordings in an anesthetized mouse from V1 cells expressing Ace2N-4AA-mNeon. Magenta trace (lower right) shows the two magenta spikes in adjacent trace. Across 837 spikes, the electrical and optical traces were in perfect accord. (Inset) Two different neocortical neurons imaged by two-photon microscopy. A maximum projection of a dual-color image stack (top) acquired in a live mouse shows an Ace2N-4AA-mNeon–labeled cell and a pipette, filled with red dye, that recorded somatic electrical activity. An image acquired in a brain slice (bottom) after in vivo experimentation shows the membrane localization of Ace2N-4AA-mNeon. Scale bars, 40 μm. (**E**) Histogram of timing errors for spikes detected optically as in (D), using the electrical trace to provide the actual spike time (N = 837 spikes from three cells). Red line, Gaussian fit. Error bars, SD, estimated as counting errors. Illumination: 15, 25, and 25 mW · mm^{-2}, respectively, for studies in culture, brain slice, and live mice. Image acquisition rates: 440 Hz, 440 Hz, and 1000 Hz, respectively.

with values determined by Ca^{2+} imaging in the same neurons (Fig. 3E) and with previous studies (*16*, *19*). There were also light-sensitive V1→LM neurons that responded at the onset or offset of visual illumination regardless of the grating orientation (fig. S8).

We also studied sensory-driven neural dynamics in live fruit flies, in which electrical recordings are often challenging. Beyond in vivo imaging of fast somatic spike trains, GEVIs have the potential to reveal fast voltage dynamics in genetically identified dendrites and axons. To illustrate, we imaged fast dynamics in the olfactory system and first examined local neurons (LNs) of the olfactory glomeruli (*20*), in which we used the R55D11-GAL4 fly driver line (*21*) to express an Ace2N variant with two extra amino acids in the linker domain (Ace2N-2AA-mNeon) (Fig. 4A, fig. S6, and table S2). The baseline spike rate in the absence of odor stimulation was $7.4 \pm 2.8\ s^{-1}$ (N = 8 neurons from 8 flies), comparable to electrophysiological measurements (*20*). In response to odor stimuli, we observed fast, evoked spike trains in single trials at firing rates significantly above baseline ($P < 10^{-3}$; Wilcoxon signed rank test) (Fig. 4B). The peak odor-evoked spike rate was $65 \pm 7\ s^{-1}$; i.e., the individual spikes fired

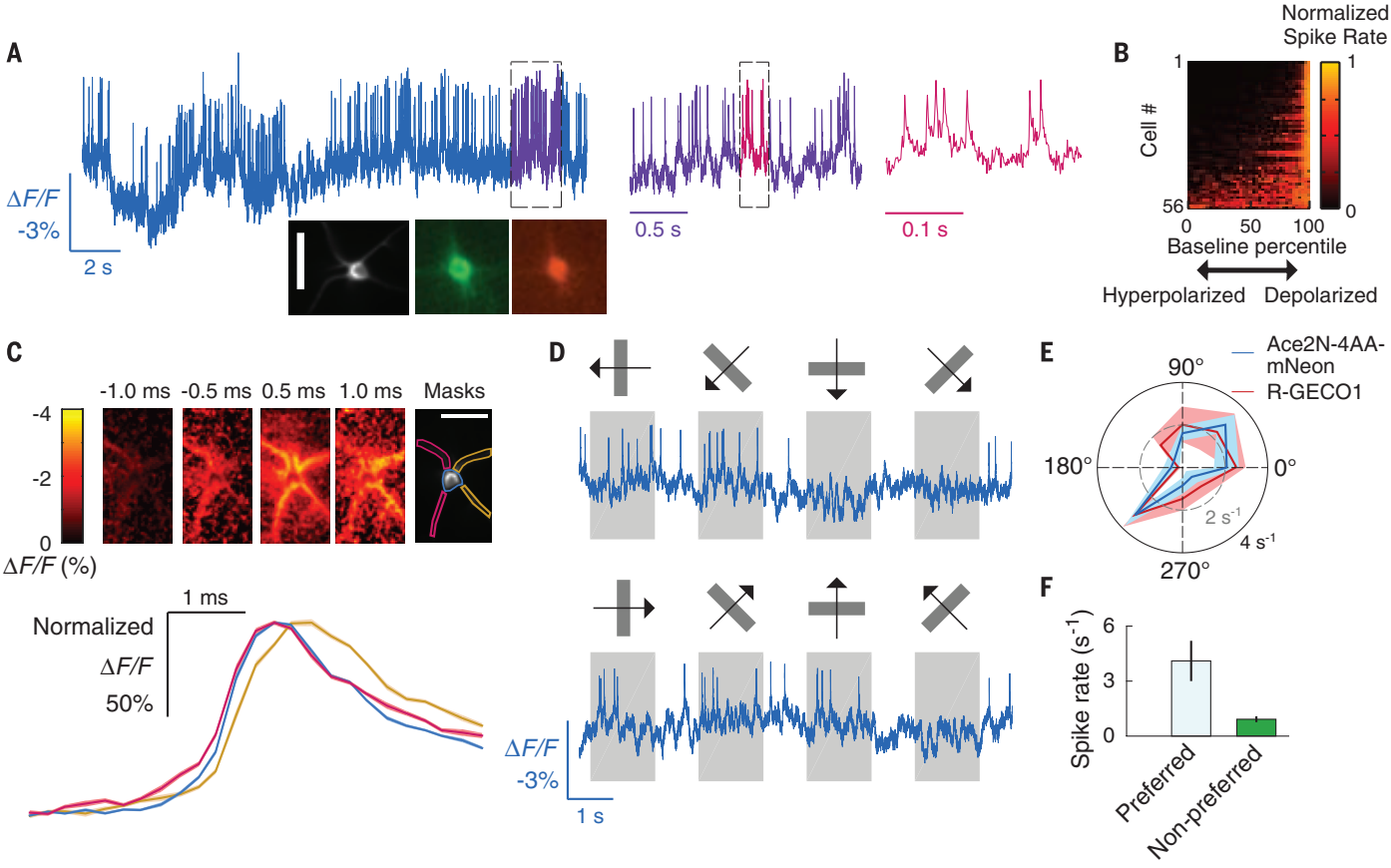

Fig. 3. Imaging single action potentials and subthreshold membrane voltage fluctuations in layer 2/3 visual cortical neurons of awake mice. (**A**) Optical voltage trace acquired in an awake mouse, showing spiking by a V1 layer 2/3 neuron expressing Ace2N-4AA-mNeon via the SAD-Ace2N-4AA-mNeon-RGECO1 virus. Dashed boxes indicate intervals shown at successively expanded time scales. (Insets) Image acquired in vivo of the cell that provided the optical trace and a pair of fluorescence images taken in a fixed tissue slice of an identically labeled V1 neuron from the same preparation expressing Ace2N-4AA-mNeon (green) and RGECO1 (red). Scale bar, 40 μm. (**B**) Periods of reduced spiking arose when Ace2N-4AA-mNeon reported a hyperpolarization. To track each cell's membrane voltage apart from its spikes, we applied a median filter (50-ms window) to the trace. For nonparametric comparisons, we matched each spike to the voltage at which the spike occurred, quantified as a percentile of the cell's full range of membrane voltages over the full recording. For each cell, the plot shows the spike rate (normalized to each cell's peak rate) at voltages across all percentiles. (**C**) (Top) Spike-triggered average image frames, for the cell in (A), showing the mean dendritic activation before and after firing an action potential. Times are relative to the spike peak at the soma. The left two dendrites activated before the right two dendrites. We calculated mean time traces for the soma and the left and right dendrite pairs using the spatial masks shown. (Bottom) Mean fluorescence time courses ($\Delta F/F$) for each of the three masks, normalized to the same maximum. The traces confirm the left-to-right activation pattern; the right dendrites exhibit a voltage peak 0.25 to 0.5 ms after the left dendrites. The $\Delta F/F$ image series and time traces were sampled in 0.25-ms time bins, using data from 1900 spikes mutually aligned to their peaks. Shaded regions on the time traces denote SEM and are barely discernible. (**D**) Example optical traces from a cortical V1→LM neuron in an awake mouse, showing visually evoked responses to moving gratings (orientations and motion directions marked above each trace). Spiking responses to the cell's preferred grating orientation (second column) differed from the activity suppression in response to the orthogonal orientation (fourth column). (**E**) Mean spike rates of the cell in (D), determined from the optical voltage trace in response to gratings moving in different orientations (10 trials per stimulus). Solid black and dashed gray circles indicate spike rates of 4 s^{-1} and 2 s^{-1}, respectively. Ca^{2+} imaging using RGECO1 in the same cell yielded similar orientation tuning. Evoked Ca^{2+} signals were integrated over 1 s and normalized so that Ca^{2+} and spiking responses to the preferred orientation (225°) were plotted at the same radius on the polar plot. Shaded areas indicate SEM. (**F**) Mean ± SEM spike rates in response to gratings at the preferred orientation were higher than to those oriented orthogonally ($P < 0.01$ for each of seven cells; permutation test; 10^5 permutations). Frame acquisition rate: 1 kHz for voltage imaging and 20 Hz for Ca^{2+} imaging. Illumination intensity: 20 and 10 mW · mm^{-2}, respectively, for voltage and Ca^{2+} imaging. Labeled neurons were ~150 μm below the brain surface.

about an order of magnitude faster than Ca^{2+} imaging can resolve.

As in mice, we performed dual optical and electrical recordings to verify the spike trains, this time using whole-cell patch-clamp electrodes to access LN neurons' intracellular potentials in intact fly brain explants (Fig. 4C, left). Across 18,141 recorded spikes, the spike trains provided by Ace2N-2AA-mNeon perfectly matched those from the patch-clamp recordings (N = 4 fly brains) and had spike-timing errors of 0.19 ± 0.002 ms (SEM; N = 18,141 spikes), close to the theoretical

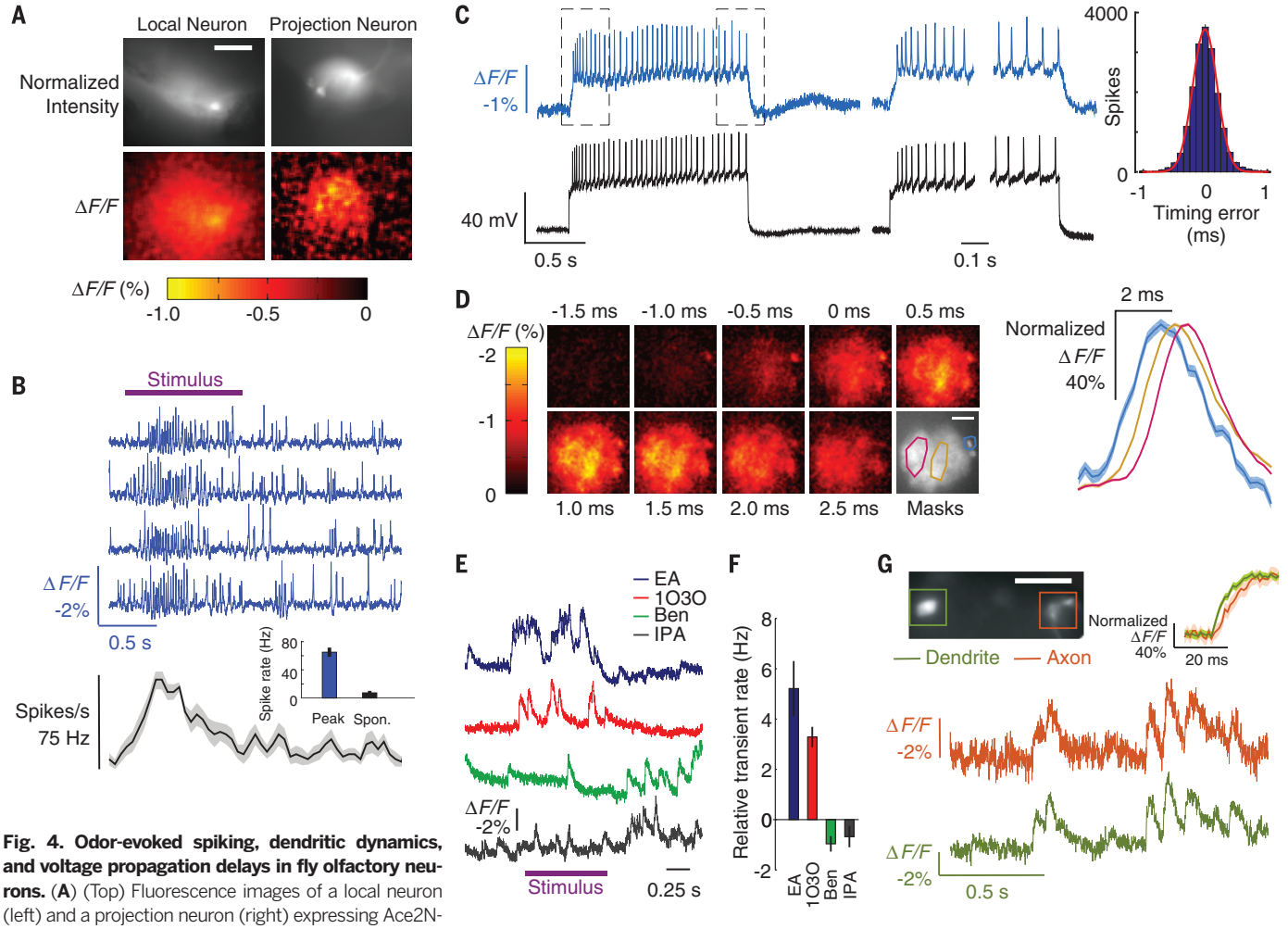

Fig. 4. Odor-evoked spiking, dendritic dynamics, and voltage propagation delays in fly olfactory neurons. (**A**) (Top) Fluorescence images of a local neuron (left) and a projection neuron (right) expressing Ace2N-2AA-mNeon in the fly antenna lobe. (Bottom) Spatial maps of the fluorescence response ($\Delta F/F$) at the peak of an odor-evoked transient. Scale bar, 40 μm. (**B**) (Top) Optical voltage traces (blue traces) from the local neuron in (A) reveal increased spiking during 5% benzaldehyde odor presentation (purple bar). (Bottom) Odor-evoked spike rate as a function of time, averaged over five trials (shaded area denotes SEM). (Inset) Mean peak spike rate during odor presentation was higher than baseline rates without odor [$P < 10^{-3}$; Wilcoxon signed-rank test; N = 8 neurons and 8 flies (20 × UAS-Ace2N-2AA-mNeon/+; R55D11-GAL4/+)]. (**C**) (Left) Concurrent optical voltage and whole-cell patch electrical recordings in whole brain explants, from the same cell type as in (B). Spikes were evoked by current injection. (Middle) Paired optical and electrical traces, taken from periods enclosed by dashed boxes in the left panel. Spikes are clearly distinguished in the optical traces from both the plateau of subthreshold depolarization and each rise to spike threshold. (Right) Histogram of timing errors for the spikes detected optically, relative to the spike times in the whole-cell patch recordings (N = 18,141 spikes from 4 flies). Red line is a Gaussian fit. Standard deviation of the timing errors was 0.19 ± 0.002 ms. Error bars estimating the SD as counting errors are too small to be seen. (**D**) (Left) Spike-triggered average image frames for the cell in (C), showing the mean activation in the neural processes before and after firing a somatic spike, as determined from spike times in the electrical recording. Depolarization started at about –1.0 ms in the soma (located in the upper right of each image) and propagated right to left across the dendritic tree during a spike. We calculated mean time traces for the soma and two subportions of the dendrites using the spatial masks in the lower right panel (cyan line encloses the soma; red and gold lines enclose dendritic regions). Scale bar, 40 μm. (Right) $\Delta F/F$ for each of the three spatial masks, normalized to the same maximum. The traces confirm the right-to-left activation pattern; the left dendrites exhibited a voltage peak 0.5 to 0.7 ms after the right dendrites. Mean $\Delta F/F$ image series and traces were sampled in 0.25-ms bins, using data from 1300 spikes, temporally aligned to the spike peaks. Shaded regions denote SEM and are only discernible for the soma. (**E**) Odor-evoked, optical voltage traces from the DL3 projection neuron dendrites of (A), with significant rises in activity over baseline for some [10% ethyl acetate (EA) and 3-octanol (1O3O); $P < 0.04$ for both EA and 1O3O), but not other odors (10% benzaldehyde (BEN) and isopropanol (IPA); P = 1 and 0.4 for BEN and IPA, respectively; Wilcoxon signed rank tests; N = 6 flies (20 × UAS-Ace2N-2AA-mNeon/+; R26B04-GAL4/+)]. (**F**) Odor-evoked dendritic activation levels, relative to baseline levels. (**G**) (Top) Example fly expressing Ace2N-2AA-mNeon in DL3 cells in which we concurrently imaged dendrites and axons. (Bottom) Optical traces from both regions show concurrent activity. (Inset) Averaged traces aligned to onset of dendritic activity reveal a ~4-ms propagation delay between dendrites and axons (N = 30 transients; shaded regions denote SEM). Scale bar, 50 μm. Illumination, 20 mW · mm^{-2}. Frame acquisition rate, 1 kHz. For display only, each optical trace in (B) was high-pass filtered by subtracting a median-filtered (50-ms window) version of the trace. Traces in (E) were processed the same way for display, but with a 1-s filter window.

optimum of 0.11 ± 0.03 ms (Fig. 4C, right). Subthreshold dynamics were readily apparent in the optical traces, including plateau potentials and the rising and falling voltage waveforms surrounding action potentials. Ace2N-2AA-mNeon also reported the submillisecond-scale dynamics of spike back-propagation into the dendritic tree, revealing ~0.5- to 1.0-ms delays between the initiating voltage peak at the soma and those in the dendrites (Fig. 4D and movie S2).

We next imaged olfactory projection neurons (PNs), which generally have more selective odor tuning than LNs (*22*, *23*). We used live flies and focused on R26B04-GAL4–labeled PN dendritic arbors (Fig. 4A), which exclusively innervate the DL3 glomerulus (*21*). In response to specific odors, the arbors exhibited fast, odor-evoked voltage dynamics with temporal structure at the 10- to 100-ms time scale (Fig. 4, E and F). We compared these dynamics to those seen by Ca^{2+} imaging using the GCaMP6f indicator (fig. S9). The odor-tuning profiles determined from the two modalities were in broad agreement, but voltage imaging with Ace2N revealed both small-amplitude responses and fast temporal signals that GCaMP6f failed to convey (fig. S9). Finally, we imaged the PN dendritic arbors and axonal boutons simultaneously. Odor-evoked voltage signals in the two structures were similar, but there was a 3.7 ± 0.4 ms (mean ± SEM; N = 3 flies) propagation delay from dendrites to axons (Fig. 4G). Neither Ca^{2+} imaging nor electrical recordings have been capable of revealing this type of fast, intracellular signal propagation in a live animal.

By virtue of their bright emissions, fast (<1 ms) kinetics, and targeted expression, Ace2N GEVIs open a wide range of experimental avenues in optical neurophysiology. The capabilities to track fast-spiking, subthreshold, and both sensory-evoked and back-propagating dendritic voltage activity in vivo allow direct visualization of many temporal features of neural dynamics, plasticity induction, and coding that have long been inaccessible. When combined with chronic animal preparations (*9*), it will be possible to track these phenomena over multiple days. Ace2N sensors resolved sensory-evoked spike trains with firing rates as high as ~75 s^{-1} (the fastest we encountered) with ~0.2-ms timing accuracy. Whereas in vivo Ca^{2+} imaging usually resolves successive spikes if they are ~50 to 250 ms apart and has ~20- to 100-ms timing accuracy for isolated spikes (*1*, *2*), Ace2N sensors directly reveal the constituent spikes in spike bursts, a widespread and important means of neural signaling (*24*, *25*). The Ace2N sensors' timing precision is also key to resolving long-standing debates over the temporal attributes of neural coding (*26*, *27*).

The retrograde labeling strategy we used to express the Ace2N indicator in live mice also holds importance for future work, in that every soma we imaged had an axon at the virus injection site. This allowed us to target the subclass of V1 neurons with projections to area LM. A logical next step in the study of V1 would be systematic voltage imaging of visually evoked spiking across all 15 subclasses of V1 neurons, as categorized by their axonal projections (*18*). There are long-standing in vivo electrophysiological methods for identifying cells with specific axonal projections (*28*), but they are technically onerous to an extent that has precluded widespread and routine use. Voltage imaging is now poised to make commonplace the study of neural dynamics in live mammals in chosen anatomical projection pathways.

Until now, subthreshold neural voltage dynamics have usually been inaccessible in live animals, especially in fine neural processes in which intracellular recordings are nearly prohibitive. As shown here, Ace-mNeon reveals fast dendritic activity, including stimulus-evoked dynamics and spike back-propagation. This is especially important for studies of flies and other species in which fine neurites are vital to information processing (*29*). There is also rising appreciation of the importance of dendritic computation in mammalian neurons (*30*, *31*). Ace2N should allow direct observations of such phenomena in vivo.

For our in vivo imaging studies, we used wide-field epifluorescence microscopy, 1-kHz imaging rates, and sparse fluorescence labeling. Fluorescent V1→LM neural somata were usually ~150 μm below the brain surface and separated by ~40 to 60 μm (fig. S7). This separation enabled high-fidelity tracking of neural spiking despite the lack of optical sectioning and the consequent background fluorescence. Comparable performance should also be feasible in deep brain areas by using microendoscopes to access deep tissues (*9*). Studies of both surface and deep neural ensembles would benefit from improved scientific-grade cameras for fast imaging (1 kHz) at cellular resolution over broader fields of view than are possible today. For comparison, Ca^{2+} imaging studies (10 to 20 Hz) capture specimen areas larger by a factor of 100 than those sampled here at 1 kHz (*9*).

In principle, microscopy modalities with optical sectioning should also allow denser fluorescence labeling patterns and deeper optical penetration through thick tissue. A challenge, however, is that nearly all extant in vivo microscopy modalities with sectioning involve laser scanning, with pixel dwell times typically ~0.1 to 2 μs for frame rates of ~10 to 20 Hz. Given the importance of detecting as many signal photons as possible with voltage imaging, conventional laser scanning is plainly insufficient at the faster frame rates used for in vivo voltage imaging (~0.5 to 1 kHz). The introduction of Ace2N indicators for in vivo voltage imaging puts a premium on the innovation of microscopes that provide optical sectioning without conventional laser scanning. The emergence of scanless forms of optical sectioning microscopy holds particular interest for the further development of in vivo voltage imaging capabilities (*32*, *33*). Even with existing optical hardware, Ace-mNeon's capacities for targeted imaging of cells of identified types or axonal projections, resolution of fast spike trains, accurate spike-timing estimation, and observation of subthreshold and dendritic voltage dynamics open many questions to empirical study that hitherto could not be examined in live animals.

REFERENCES AND NOTES

1. T. W. Chen *et al.*, *Nature* **499**, 295–300 (2013).
2. M. Inoue *et al.*, *Nat. Methods* **12**, 64–70 (2015).
3. D. S. Peterka, H. Takahashi, R. Yuste, *Neuron* **69**, 9–21 (2011).
4. T. Knöpfel, *Nat. Rev. Neurosci.* **13**, 687–700 (2012).
5. H. Tsutsui, S. Karasawa, Y. Okamura, A. Miyawaki, *Nat. Methods* **5**, 683–685 (2008).
6. L. Jin *et al.*, *Neuron* **75**, 779–785 (2012).
7. F. St-Pierre *et al.*, *Nat. Neurosci.* **17**, 884–889 (2014).
8. A. Lundby, H. Mutoh, D. Dimitrov, W. Akemann, T. Knöpfel, *PLOS ONE* **3**, e2514 (2008).
9. E. J. Hamel, B. F. Grewe, J. G. Parker, M. J. Schnitzer, *Neuron* **86**, 140–159 (2015).
10. D. R. Hochbaum *et al.*, *Nat. Methods* **11**, 825–833 (2014).
11. S. P. Tsunoda *et al.*, *Biophys. J.* **91**, 1471–1479 (2006).
12. N. C. Shaner *et al.*, *Nat. Methods* **10**, 407–409 (2013).
13. Y. Gong, M. J. Wagner, J. Zhong Li, M. J. Schnitzer, *Nat. Commun.* **5**, 3674 (2014).
14. P. Zou *et al.*, *Nat. Commun.* **5**, 4625 (2014).
15. B. A. Wilt, J. E. Fitzgerald, M. J. Schnitzer, *Biophys. J.* **104**, 51–62 (2013).
16. Materials and methods are available as supplementary materials on *Science* Online.
17. F. Osakada *et al.*, *Neuron* **71**, 617–631 (2011).
18. Q. Wang, A. Burkhalter, *J. Comp. Neurol.* **502**, 339–357 (2007).
19. C. M. Niell, M. P. Stryker, *J. Neurosci.* **28**, 7520–7536 (2008).
20. Y. H. Chou *et al.*, *Nat. Neurosci.* **13**, 439–449 (2010).
21. A. Jenett *et al.*, *Cell Reports* **2**, 991–1001 (2012).
22. R. I. Wilson, G. C. Turner, G. Laurent, *Science* **303**, 366–370 (2004).
23. S. R. Olsen, V. Bhandawat, R. I. Wilson, *Neuron* **54**, 89–103 (2007).
24. J. E. Lisman, *Trends Neurosci.* **20**, 38–43 (1997).
25. A. Mathy *et al.*, *Neuron* **62**, 388–399 (2009).
26. Y. Zuo *et al.*, *Curr. Biol.* **25**, 357–363 (2015).
27. K. Diba, A. Amarasingham, K. Mizuseki, G. Buzsáki, *J. Neurosci.* **34**, 14984–14994 (2014).
28. R. H. Hahnloser, A. A. Kozhevnikov, M. S. Fee, *Nature* **419**, 65–70 (2002).
29. A. Borst, J. Haag, D. F. Reiff, *Annu. Rev. Neurosci.* **33**, 49–70 (2010).
30. S. L. Smith, I. T. Smith, T. Branco, M. Häusser, *Nature* **503**, 115–120 (2013).
31. M. E. Sheffield, D. A. Dombeck, *Nature* **517**, 200–204 (2015).
32. B. O. Watson *et al.*, *Front. Neurosci.* **4**, 29 (2010).
33. R. Prevedel *et al.*, *Nat. Methods* **11**, 727–730 (2014).

ACKNOWLEDGMENTS

We gratefully acknowledge research funding from the Defense Advanced Research Projects Agency, an NIH Pioneer award, an NIH BRAIN Initiative U01 grant, and the Stanford *CNC* Program. We thank J. Li for animal husbandry. Genetic sequence data are in the supplementary materials. We licensed mNeonGreen from Allele Biotechnology & Pharmaceuticals (San Diego), which charges $100 to $300 per laboratory for a materials transfer agreement.

SUPPLEMENTARY MATERIALS

www.sciencemag.org/content/350/6266/1361/suppl/DC1
Materials and Methods
Figs. S1 to S9
Tables S1 and S2
Movies S1 and S2
References (*34*–*40*)

9 March 2015; accepted 10 November 2015
Published online 19 November 2015
10.1126/science.aab0810

RESEARCH INVESTMENT

Wrapping it up in a person: Examining employment and earnings outcomes for Ph.D. recipients

Nikolas Zolas,[1] Nathan Goldschlag,[1] Ron Jarmin,[1] Paula Stephan,[2,3] Jason Owen-Smith,[4] Rebecca F. Rosen,[5] Barbara McFadden Allen,[6] Bruce A. Weinberg,[7,3,8]* Julia I. Lane[1,5,8,9,10]

In evaluating research investments, it is important to establish whether the expertise gained by researchers in conducting their projects propagates into the broader economy. For eight universities, it was possible to combine data from the UMETRICS project, which provided administrative records on graduate students supported by funded research, with data from the U.S. Census Bureau. The analysis covers 2010–2012 earnings and placement outcomes of people receiving doctorates in 2009–2011. Almost 40% of supported doctorate recipients, both federally and nonfederally funded, entered industry and, when they did, they disproportionately got jobs at large and high-wage establishments in high-tech and professional service industries. Although Ph.D. recipients spread nationally, there was also geographic clustering in employment near the universities that trained and employed the researchers. We also show large differences across fields in placement outcomes.

Ten years ago, Jack Marburger challenged academics to provide scientific evidence about the impact of research investments (*1*). The United States Congress has been even more insistent: requiring the National Science Foundation to "better articulate the value of grants to the national interest." The aim of the current study is to investigate the labor market outcomes of doctoral recipients.

Little is known about where research-funded Ph.D.'s go when they graduate and enter the private sector, and even less is known about the characteristics of the businesses that employ them. Thus, it has been difficult to capture the human dimension of the impact of research on the economy. What little evidence there is has been based on an analysis of patent clusters (*2*, *3*); the geographic and industry placement of new Ph.D.'s (*4*–*6*); or on bibliometric approaches linking grants, patents, and publications (*7*, *8*). One noteworthy exception has been expensive—the United Kingdom spent more than £34 million (U.S. $51 million) in explicit costs, and much more in implicit costs, to generate almost 7000 case studies. Unfortunately, they lack a common framework or shared standards of evidence and presentation. Consequently, the extent to which this type of information provides rigorous, systematic, aggregate insights into economic value is far from clear (*9*).

We drew on recent investments to build administrative data that cover researchers supported by both federally and nonfederally funded grants in eight major universities that are members of the Committee on Institutional Cooperation (CIC) (*10*). Participating universities were Indiana, Iowa, Michigan, Minnesota, Ohio State, Purdue, Penn State, and Wisconsin. Those data, derived from the CIC's UMETRICS project (*11*), provided the share of time charged to funded research projects by all people employed under them (from undergraduate and graduate students to postdocs to staff and faculty), as well as purchases for those projects. Graduate students were linked to their dissertations (from ProQuest) and to all subsequent employers and earnings in the United States through matches to Census Bureau data.

We documented the 2010–2012 earnings and placement outcomes of people receiving doctorates in 2009–2011. The universities have provided identifiers that allow the UMETRICS data to be linked to administrative and survey data housed at the U.S. Census Bureau under strict confidentiality protocols. The data are protected by law and are for statistical use only (anonymized unique identifiers are used for match keys), and all results are reviewed to ensure that no identifiable information is disclosed. We performed two distinct, but related, analyses of the jobs obtained by doctoral recipients. The first describes the characteristics of the establishments and firms where people obtained jobs. The second emphasizes the earnings of individuals at those jobs. It should be noted at the start that these analyses are designed to be descriptive and do not demonstrate causation.

Placement data were obtained from links to two files derived from administrative data and augmented by survey data: (i) the Business Register (BR), which is the universe of U.S. nonagricultural firms and associated establishments, and (ii) the Longitudinal Business Database (LBD), which contains longitudinally linked data for all firms and associated establishments with paid employees in the United States (*12*, *13*). These files were used to describe the characteristics of the establishments and firms that employ the UMETRICS doctoral recipients covered by the data (an establishment is the physical place where business is conducted and the unit of observation at which industry and geographic location are defined; firms can own one or more establishments). The matched data were used to describe the sector and detailed industry classification of each establishment at which the recipients worked, the geographic location of their place of work, as well as characteristics related to productivity, such as size and payroll per worker (*14*). Age was determined at the firm level, and establishments owned by R&D performing firms were identified from the Business Research & Development and Innovation Survey

Table 1. Postgraduation employment of UMETRICS doctoral recipients who were paid by research grants and left the university between 2009 and 2011. The national workforce distribution is calculated from all employment in all establishments covered by the Census's LBD between 2010 and 2012.

	Doctoral recipients placed in sector (%)				
	Industry		Academia	Government	All
Locale and small	R&D firms	Non-R&D firms			
Placed within sector	17.0	21.7	57.1	4.1	100.0
National sample (*M*)	10.8	75.0	10.7	3.5	100.0
Of those in sector, percent placed:					
Within 50 miles	10.1	23.5	8.9	18.2	12.7
Within state	16.6	36.0	18.0	25.8	22.0

[1]U.S. Census Bureau, 4600 Silver Hill Road, Washington, DC 20233, USA. [2]Department of Economics, Box 3992, Georgia State University, Atlanta, GA 30302-3992, USA. [3]National Bureau of Economic Research, 1050 Massachusetts Avenue, Cambridge, MA 02138-5398, USA. [4]University of Michigan, 500 South State Street, no. 3001, Ann Arbor, MI 48103-1382, USA. [5]New York University, 70 Washington Square South, New York, NY 10012, USA [6]Committee on Institutional Cooperation (CIC), 1819 South Neil, Suite D, Champaign, IL 61820, USA. [7]Department of Economics, Ohio State University, 1945 North High Street, Columbus, OH 43210, USA. [8]Institute for the Study of Labor (IZA), Schaumburg-LippeStrasse 5-9, 53113 Bonn, Germany. [9]University of Strasbourg, 61 Avenue de la Forêt Noire, 67 085 Strasbourg, France. [10]American Institutes for Research, 1000 Thomas Jefferson Street, Washington, DC 20007, USA.
*Corresponding author. E-mail: weinberg.27@osu.edu

Downloaded from www.sciencemag.org on December 14, 2015

(*15*). The variables we analyzed, the level at which they were measured, and their source are listed in table S1.

Individual earnings data were derived from links to administrative records. Details of the data construction and links are in the supplementary materials (SM), including fig. S1 and table S2, A and B. De-identified versions of the UMETRICS data will be made available to the scholarly research community through a confidentially protected virtual digital enclave being developed at the Institute for Research on Innovation and Science (IRIS) (iris.isr.umich.edu) (*10*). Data integrated with census data on people and on their employers and their employer's characteristics will be made available at the Federal Statistical Research Data Centers through a partnership between IRIS and the U.S. Census Bureau (www.census.gov/fsrdc) under strict confidentiality protections.

There were 3197 graduate students on research payrolls at the sample universities in the period 2009–2011 who received a doctoral degree during that period and who were employed at a different institution in subsequent years. The major sectors into which they flowed in the year after their separation from university employment are summarized in Table 1 and compared with the sectors of employment for the U.S. workforce as a whole, which provides a benchmark (but not a formal control) group. The majority of graduate students (57.1%) went to academia—presumably many to postdoctoral positions. A large percentage (38.7%) found jobs in industry, notably, about 17% in establishments owned by firms that perform research and development (R&D) (for comparison, 10.8% of the U.S. workforce is employed in such establishments) and about 21.7% in establishments owned by firms that do not perform R&D (versus 75.0% of the U.S. workforce). Only a small percentage (4.1%) entered government.

Evidence that research funding to these universities provides training to a workforce that participates in a national (and likely international) labor market is shown in Table 1. For each of the universities in our sample, more than one in five doctoral recipients stayed in the state in which the university was located,

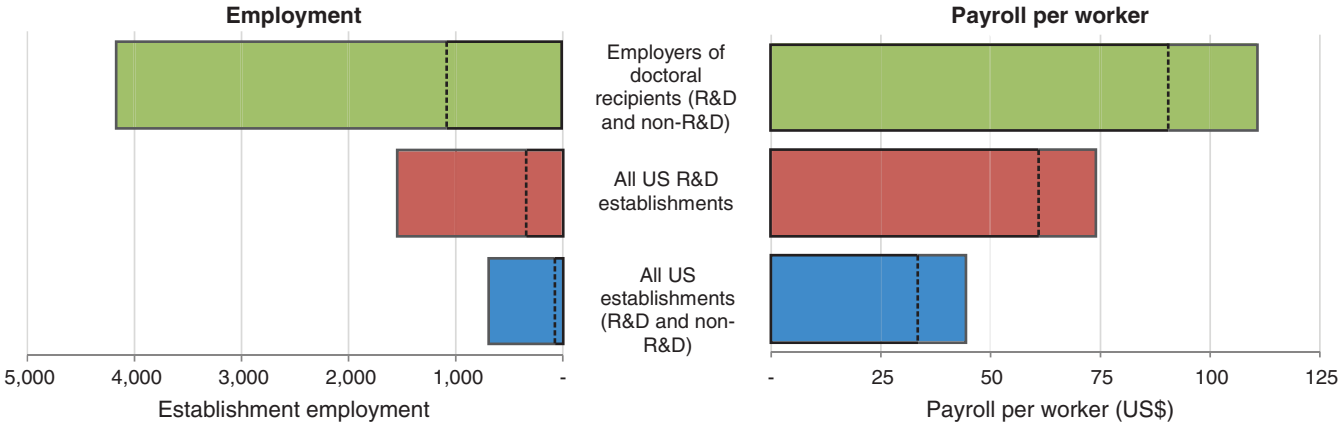

Fig. 1. UMETRICS doctoral recipients are placed at establishments that are larger and have higher payrolls per worker. Medians are dashed inner lines, and means are solid outer lines. The standard deviations in employment at establishments that employed UMETRICS doctoral recipients, at all U.S. establishments owned by R&D performing firms, and all U.S. establishments are 6407, 3661, and 2362, respectively; the standard deviations in annual payroll per worker are $120,199; $56,252; and $44,327, respectively; the differences in employment size and payroll per worker are statistically significant. Annual payroll per worker is the average payroll (the total payroll divided by the number of employees) across all employees at the three types of establishments—all U.S. establishments, all U.S. establishments owned by firms that perform R&D, and the establishments that employed UMETRICS doctoral recipients (regardless of whether they are owned by firms that perform R&D). National and R&D establishments are weighted by total establishment employment, whereas doctoral recipient establishments are weighted by the number of doctoral recipients employed. Values for annual payroll per worker are U.S.$1 ×1000.

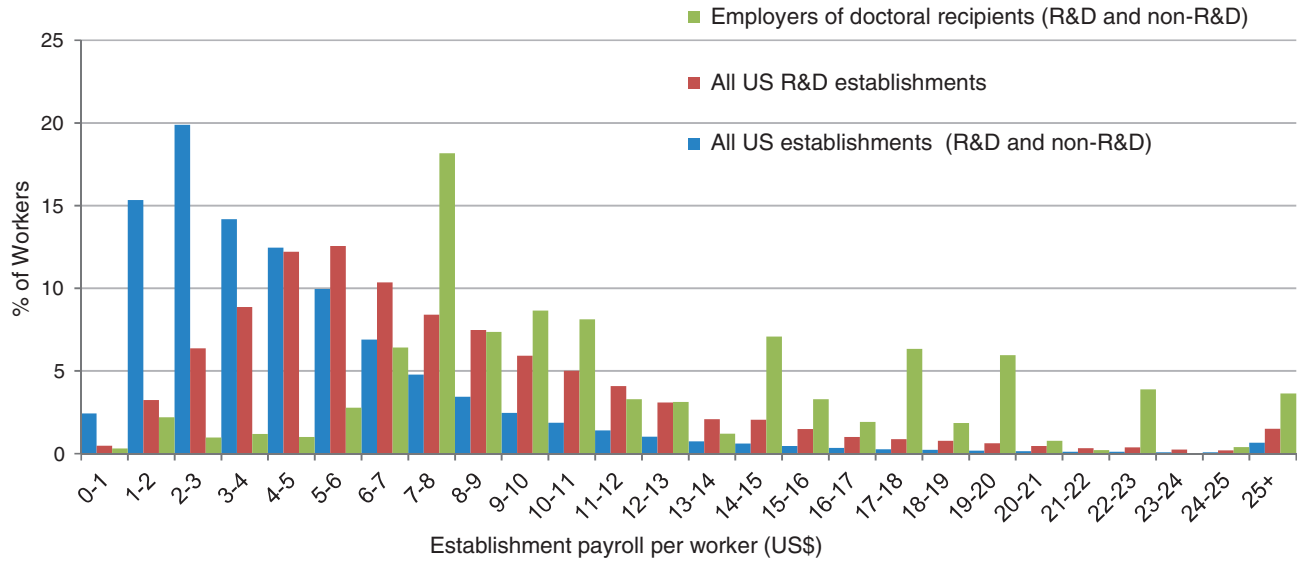

Fig. 2. Annual payroll per worker at establishments that employed UMETRICS doctoral recipients, establishments owned by firms that perform R&D, and all U.S. establishments. Values for average annual payroll per employee are U.S.$1 ×10,000.

and about 13% stayed within 50 miles of the university. More doctoral recipients stayed in the university's state than moved to any other single state, with the exception of California, which received more students from two of our eight universities. The results are substantially unchanged when the sample was restricted to those supported only by federal research grants (table S3).

The data permit an even deeper examination of the geographic destinations of the doctoral recipients. For example, 19% of the doctoral recipients who left their university's state headed for California, which has only 12% of the U.S. population. We expect that this is partially due to the fact that more R&D is conducted in California than in any other state. The states to which people moved are shown in fig. S2, and a comparison of the locations of Ph.D. recipients to R&D and population by state are shown in table S4. The other major destination states in terms of numbers of graduates among people who leave the state where they trained were Illinois, New York, Texas, North Carolina, Massachusetts, Pennsylvania, and Washington (state), which either have a large share of R&D relative to their populations or are very populous.

It is also possible to examine the specific industries that were most likely to employ the sample of doctoral recipients paid by research grants (table S5); results for doctoral recipients supported by federally funded projects are reported in table S6. The employers were much more likely to be in industries such as engineering, or high-tech and professional service fields (including medicine) than U.S. employers at large: For example, the shares of doctoral recipients employed in pharmaceutical and medicine manufacturing, semiconductors, and computer systems design were between 4 and 19 times the U.S. average. Uncommon employment destinations for doctoral recipients were restaurants and eating places and grocery stores.

The establishment-level data also permitted an examination of the differences between the employers of the UMETRICS doctoral recipients being studied, the typical employer across the U.S. as a whole, and the typical U.S. establishment owned by a firm performing R&D (Fig. 1). Because the distribution of establishments is highly skewed, it is informative to provide information on both the means and the medians. The median establishment that employed the doctoral recipients in our sample has more employees (at 1084) than the national median (at 73) or even than establishments owned by firms performing R&D (341) (Fig. 1). We used payroll per worker (constructed by dividing total payroll by the number of employees) to measure the average earnings at establishments. The median establishment that employed UMETRICS doctoral recipients also tended to have a higher payroll per worker (over $90,000) than the median U.S. establishment, which has a payroll per worker of just over $33,000, or the median establishment owned by a firm performing R&D, which has a payroll per worker of just less than $61,000. The same results hold when we used the mean as the measure of central tendency.

The data were rich enough to go beyond summary statistics and to characterize the distribution of each measure for all establishments employing the workers under study. In particular, we calculated the payroll per worker for each establishment (regardless of R&D status) employing individuals in our sample, all U.S. establishments, and all U.S. establishments owned by firms performing R&D (regardless of whether they employ the doctoral recipients in our sample) and report the distribution of each in Fig. 2. Although only 8.3% of the U.S. workforce and 24% of workers at establishments owned by firms performing R&D worked at establishments with payrolls per worker in excess of $100,000, more than half (51%) of the sample of doctoral recipients do. The results are consistent with the hypothesis that doctoral recipients are placed in establishments with characteristics usually associated with greater productivity.

It is possible to examine individual earnings outcomes, as well as the placement outcomes described above. The data also permit the statistical analysis of the relation between a researcher's field of study (based on ProQuest dissertation data) and subsequent placement and individual earnings.

The results of the analysis of individual earnings outcomes in the year after Ph.D. receipt are reported in (Fig. 3). Descriptive statistics and regression results are shown in tables S7 and S8. Although earnings are an imperfect measure of the value of skills, especially for people still investing in their human capital, the labor economics literature finds a strong correlation between skills and earnings (*16*). The two fields with the highest earnings are mathematics and/or computer sciences and engineering, with mean earnings in excess of $65,000. Although mean earnings for doctoral recipients are low in biology at $36,000, this may be due to many taking jobs as postdoctoral researchers in life sciences. If the sample is subset to only include industry earnings, the average earnings increase by one quarter (although the gap varies by field), with the highest earnings in mathematics and/or computer sciences (almost $90,000) and engineering (almost $80,000).

Placements are reported in the four right panels of Fig. 3. Doctoral recipients with degrees in engineering are most likely to go to work in industry, followed by those with degrees in math and/or computer science. New degree holders in engineering are by far the most likely to go to establishments that are owned by firms performing R&D. In all fields, doctoral recipients going into industry are likely to go into establishments with high payroll per worker [above the median for the establishments within their six-digit industry code (see SM)]. The recent

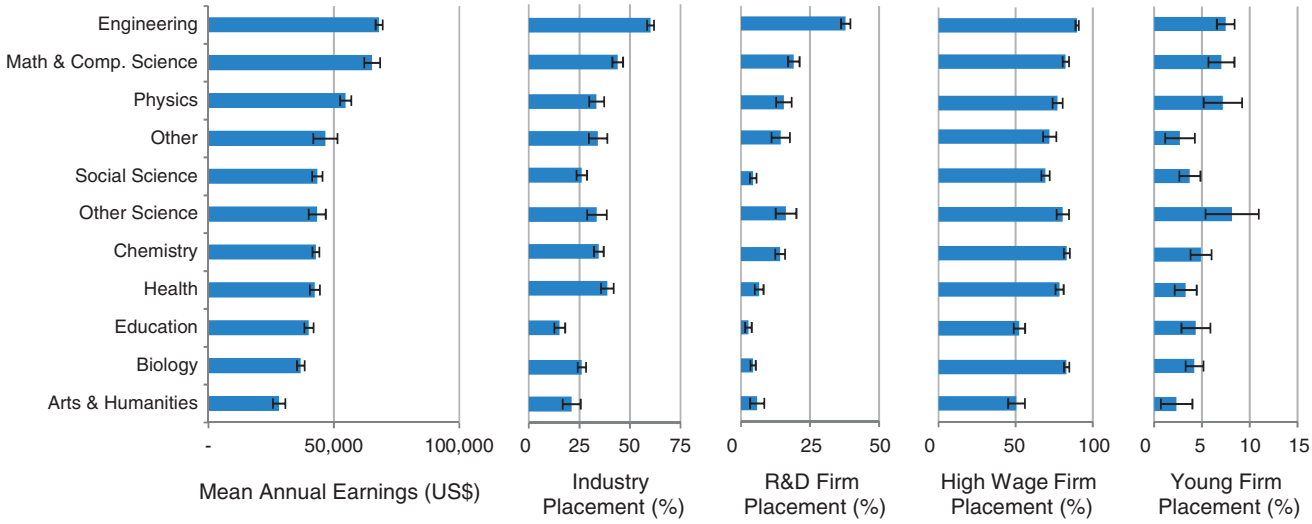

Fig. 3. The annual earnings and placement of doctoral recipients supported by grants vary by field. Young firms are defined to be those <5 years old. High–payroll per worker establishments are defined as those with a payroll per worker above the median for the establishments within their six-digit industry. Means and standard errors (error bars) for each variable.

economics literature has emphasized the importance of young firms in contributing to economic growth (*17*, *18*). We examine placements and find that engineers, physicists, and computer scientists are most likely to go to establishments of young firms.

Just as it was possible to show the distribution of average payroll per worker for employers, it is also possible to describe the distribution of individual earnings. One year after leaving the university, doctoral recipients placed in industry had considerably higher earnings than those who went to government or academia, and considerably more doctoral recipients placed in academia had earnings below $50,000 per year (Fig. 4). There is suggestive evidence that at least part of that may be due to doctoral recipients taking postdoctoral research positions; there is a noticeable heaping of the earnings distribution at just under $50,000 for those in biology, chemistry, and health disciplines. However, the earnings growth (albeit from a lower base) was still robust in all sectors 2 years after doctoral recipients left the university, as shown by the distribution of earnings growth.

This work takes a first step toward describing the links between research funding and the economy by tracing the flows of doctoral recipients employed by research grants subsequent to their separation from the university that employed them. The analysis shows that many doctoral recipients who were employed by funded research projects moved into the nonacademic sector and that, when they do, they disproportionately get jobs at establishments with high payroll per worker and in high-tech and professional service industries. Although the results are descriptive and not causal, the findings are consistent with sociological research regarding knowledge flows. A major way in which knowledge is transmitted from research institutions to the economic marketplace is through the placement of people at businesses that draw on that knowledge (*10*). As research has shown, and as Oppenheimer pointed out, the best way to send knowledge is to wrap it up in a person (*19*). Higher earnings and placement in large establishments with high payroll per worker, and in establishments owned by firms performing R&D, all characteristics correlated with higher productivity, are consistent with that view (*20*).

As with any initial examination of new data, there are a number of issues and future extensions to note. There is a need to develop a statistical framework to make causal inferences, which involves identifying appropriate counterfactuals or quasi-experimental variation. The Census Bureau links will make it possible to study both longer-term career trajectories and the characteristics of businesses started by researchers and to compare those with the careers of different types of workers and other business startups in the United States. In addition, the type of analysis we do here for Ph.D. recipients can be extended to study the career outcomes of other groups involved in research—particularly postdoctoral researchers, graduate students who do not get doctoral degrees, undergraduate students, research staff, and people employed by nonfederal projects. As the database expands, researchers can begin to study how outcomes relate to whether funding is federal or nonfederal.

There are important caveats, however. Although extensible to all research universities, the institutions we studied should not be viewed as representative of all academic research institutions. They are large public institutions in the Midwest, and many have large engineering programs and medical schools. Also, the use of U.S.-based administrative and survey data limits the ability to track students who leave the United States. The analysis is explicitly descriptive in nature and is not intended to make any causal assertions. However, because the data will be available at IRIS and the Federal Statistical Research Data Centers, the research community can build on this infrastructure to advance the science of science and to provide policy-makers with research-backed tools to assess the effects of investments in science.

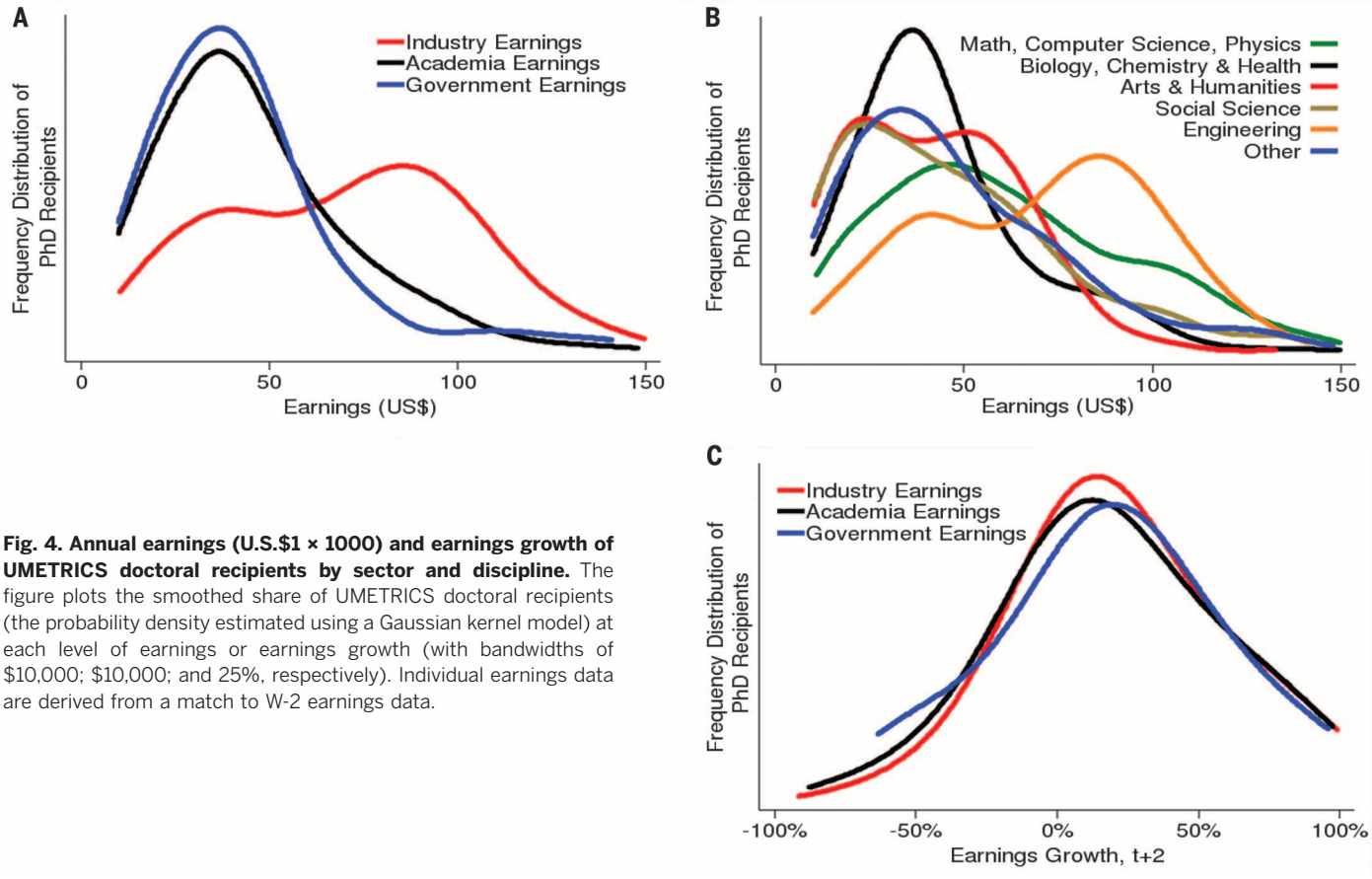

Fig. 4. Annual earnings (U.S.$1 × 1000) and earnings growth of UMETRICS doctoral recipients by sector and discipline. The figure plots the smoothed share of UMETRICS doctoral recipients (the probability density estimated using a Gaussian kernel model) at each level of earnings or earnings growth (with bandwidths of $10,000; $10,000; and 25%, respectively). Individual earnings data are derived from a match to W-2 earnings data.

REFERENCES AND NOTES

1. J. Marburger, *Science* **308**, 1087 (2005).
2. A. B. Jaffe, M. Trajtenberg, R. Henderson, *Q. J. Econ.* **108**, 577–598 (1993).
3. S. Kantor, A. Whalley, *Rev. Econ. Stat.* **96**, 171–188 (2014).
4. P. Shu, "The long-term impact of business cycles on innovation: Evidence from the Massachusetts Institute of Technology" (HBS Working Paper, Harvard Business School, Cambridge, MA, 2015).
5. H. Sauermann, M. Roach, *PLOS ONE* **7**, e36307 (2012).
6. A. J. Sumell, P. E. Stephan, J. D. Adams, in *Science and Engineering Careers in the United States: An Analysis of Markets and Employment*, R. B. Freeman, D. L. Goroff, Eds. (Univ. of Chicago, Chicago, 2009), pp. 257–287.
7. B. Cronin, C. Sugimoto, *Scholarly Metrics Under the Microscope* (ASIST Titles, Information Today Inc, Medford, NJ, 2014).
8. J. Lane, *Nature* **464**, 488–489 (2010).
9. D. Sayer, "Five reasons why the REF is not fit for purpose." *Guardian*, 15 December 2014; www.theguardian.com/higher-education-network/2014/dec/15/research-excellence-framework-five-reasons-not-fit-for-purpose
10. J. I. Lane, J. Owen-Smith, R. F. Rosen, B. A. Weinberg, *Res. Policy* **44**, 1659–1671 (2015).
11. B. A. Weinberg *et al*., *Science* **344**, 41–43 (2014).
12. R. S. Jarmin, J. Miranda, The Longitudinal Business Database (Working Paper no. 02-17, Center for Economic Studies, U.S. Census Bureau, 2002); https://ideas.repec.org/p/cen/wpaper/02-17.html.
13. S. Davis, J. Haltiwanger, R. Jarmin, C. J. Krizan, J. Miranda, A. Nucci, K. Sandusky, in *Producer Dynamics: New Evidence from Micro Data*, T. Dunne, J. B. Jensen, M. J. Roberts, Eds. (Univ. of Chicago Press, Chicago, 2009), pp. 329-368.
14. C. Syverson, *J. Econ. Lit.* **49**, 326–365 (2011).
15. National Science Foundation Committee of Visitors, "Business R&D Innovation Survey" (NSF, Arlington, VA, 2013).
16. G. S. Becker, *Human Capital: A Theoretical and Empirical Analysis, with Special Reference to Education* (Univ. of Chicago Press, Chicago, 2009).
17. R. Decker, J. Haltiwanger, R. Jarmin, J. Miranda, *J. Econ. Perspect.* **28**, 3–24 (2014).
18. J. Haltiwanger, R. S. Jarmin, J. Miranda, *Rev. Econ. Stat.* **95**, 347–361 (2013).
19. P. Stephan, in *Innovation Policy and the Economy*, vol. 7, J. Lerner, S. Stern, Eds. (MIT Press, Cambridge, MA, 2007), pp. 71–98.
20. K. B. Whittington, J. Owen-Smith, W. W. Powell, *Adm. Sci. Q.* **54**, 90–122 (2009).

ACKNOWLEDGMENTS

This research was supported by NSF SciSIP Awards 1064220 and 1262447; NSF Education and Human Resources Division of Graduate Education Awards 1348691, 1547507, 1348701, 1535399, and 1535370; NSF National Center for Science and Engineering Statistics award 1423706; NIH P01AG039347; and the Ewing Marion Kauffman and Alfred P. Sloan Foundations. Data were generously provided by the Committee on Institutional Cooperation and its member institutions. We thank W. Cheng, C. Conrad, C. Jones, E. Klochikhin, and J. Tokle for research support; G. Carr, M. Harrison, D. Mayo, M. Sweet, J. Van Horn, and S. Willis for help with data issues; and J. Walsh, R. Weiss, and C. Whitacre for their continuing support. The research agenda draws on work with many coauthors, but particularly work with J. Mairesse and M. Pezzoni. Opinions expressed are those of the authors to do not necessarily represent the views of the Census Bureau.

SUPPLEMENTARY MATERIALS

www.sciencemag.org/content/350/6266/1367/suppl/DC1
Materials and Methods
Figs. S1 and S2
Tables S1 to S8
References (*21*–*32*)

18 May 2015; accepted 4 November 2015
10.1126/science.aac5949

SOCIAL BEHAVIOR

Sexual fidelity trade-offs promote regulatory variation in the prairie vole brain

Mariam Okhovat,[1] Alejandro Berrio,[1] Gerard Wallace,[1] Alexander G. Ophir,[2] Steven M. Phelps[1]*

Individual variation in social behavior seems ubiquitous, but we know little about how it relates to brain diversity. Among monogamous prairie voles, levels of vasopressin receptor (encoded by the gene *avpr1a*) in brain regions related to spatial memory predict male space use and sexual fidelity in the field. We find that trade-offs between the benefits of male fidelity and infidelity are reflected in patterns of territorial intrusion, offspring paternity, *avpr1a* expression, and the evolutionary fitness of alternative *avpr1a* alleles. DNA variation at the *avpr1a* locus includes polymorphisms that reliably predict the epigenetic status and neural expression of *avpr1a*, and patterns of DNA diversity demonstrate that *avpr1a* regulatory variation has been favored by selection. In prairie voles, trade-offs in the fitness consequences of social behaviors seem to promote neuronal and molecular diversity.

Social behavior emerges from the complex, dynamic, and often strategic interactions of individuals—a complexity that places it among the most challenging and interesting behaviors to study. Neuroscience has elucidated many mechanisms of social behavior (*1*, *2*). In parallel, evolutionary biology has outlined how social interaction can promote variation within a species (*3*–*5*). Frequency- or density-dependent selection, for example, maintains individual differences in the parental care of sunfish (*3*), the territorial defense of lizards (*4*), and the cannibalistic behavior of tadpoles (*5*). Among humans, similar forces have been proposed to explain differences in personality, resilience, and psychiatric risk (*6*–*8*). Given that social diversity is central to behavioral ecology, social psychology, and mental health, it is surprising that we know so little about natural variation in the social brain, how it emerges from the interaction of genetic and epigenetic processes, or how it has been sculpted by evolutionary forces.

We explored individual differences in neuronal gene expression in the monogamous prairie vole, *Microtus ochrogaster*, a small North American rodent whose males and females form pair bonds and share parental care (*9*). Prairie vole pair-bonding is governed by multiple modulators and brain regions (*2*, *10*, *11*). Of these genes, the vasopressin 1a receptor (V1aR, encoded by *avpr1a*) is particularly well studied (*2*, *11*–*15*). V1aR expression can vary profoundly across individual prairie voles (*12*), and its abundance in a spatial-memory circuit predicts sexual fidelity in males (*13*, *14*) but not females (supplementary materials), a finding consistent with male-specific vasopressin effects in other contexts (*15*). We used the relationship between *avpr1a* expression and male fidelity to examine how social forces contribute to brain diversity. Specifically, we asked whether the fitness consequences of male sexual fidelity promote genetic and epigenetic variation in *avpr1a*.

Although prairie voles are socially monogamous, they are not sexually exclusive (*16*). Approximately 25% of young are conceived outside a pair bond (termed extra-pair fertilizations, or EPFs). Male fidelity is often thought to depend on spatial strategies that balance the demands of mate-guarding against the value of mating multiply (*17*, *18*). To examine the relationship between space use and sexual fidelity among male prairie voles, we estimated the intensity of a male's space use by fitting kernel density estimates to animal positions measured over several weeks by radiotelemetry (Fig. 1, A and B, and fig. S1). By overlaying these maps of space-use intensity, we could estimate how often males encounter other individuals either at home or in neighboring territories. We found that the spatial behavior of EPF males differs from that of males who sire young only with a partner (intra-pair fertilizations, IPF). EPF males have larger home ranges ($P < 0.05$; Fig. 1C), and they more frequently encounter extra-pair females ($P < 0.0001$; Fig. 1D), intrude on territories ($P < 0.01$; Fig. 1E), and are intruded upon ($P < 0.01$; Fig. 1F). The rate at which a male intrudes on a neighbor's territory is correlated with the rate at which he encounters extra-pair females [Pearson's correlation coefficient (r) = 0.69, $P < 0.0001$], but also with the rate at which he is intruded upon by other males (r = 0.83, $P < 0.0001$; Fig. 1G). Overall, the data suggest that venturing away from a male's core home range increases encounters with both extra-pair females and their aggressive mates; these intrusions may offer the opportunity for extra-pair paternity, but they also increase the rates at

[1]Department of Integrative Biology, University of Texas at Austin, 1 University Station, Campus Code C0930, Austin, TX 78712, USA. [2]Department of Psychology, Cornell University, 224 Uris Hall, Ithaca, NY 14853, USA.
***Corresponding author. E-mail: sphelps@mail.utexas.edu**

which a male's home range is visited by neighboring males. This pattern is consistent with data suggesting that pair-bonded EPF males are more likely to be cuckolded (*14*). Increasing the extra-pair female encounter rate seems to come at the expense of intra-pair mate-guarding.

Among prairie voles, we find that neuropeptide receptors show profound variation in nodes of a spatial memory circuit including the hippocampus, laterodorsal thalamus (LDThal), and retrosplenial cortex (RSC; Fig. 1H). Remarkably, variation in each of these regions predicts aspects of space use and paternity in the field (*13*, *19*). The relationship between spatial memory and sexual fidelity is not clear, but males with low V1aR in RSC or LDThal have been hypothesized to have a poor memory for locations of aggressive interactions, a cognitive strategy that could promote territorial intrusion and extra-pair encounters (*14*). In contrast, a male with abundant V1aR may better monopolize a mate but might encounter fewer extra-pair females. To look for evidence of fitness trade-offs that could promote forebrain diversity, we examined the relationship between

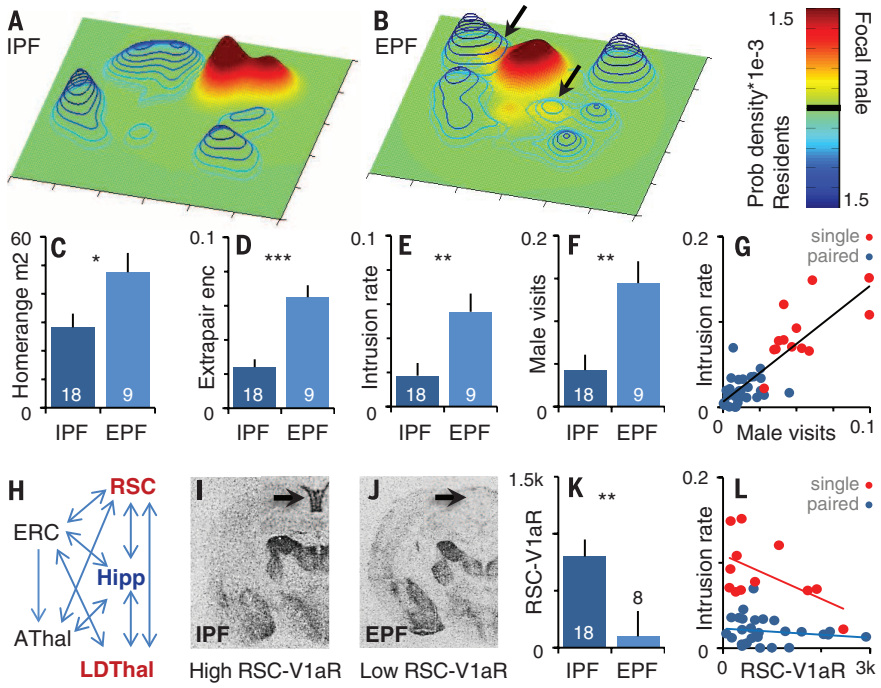

Fig. 1. Male sexual fidelity predicted by patterns of space use, social interaction, and V1aR. (**A** and **B**) Intensity of male space use. The *x* and *y* axes are enclosure dimensions (20 m × 30 m); the height and color of the peaks indicate probability densities. A focal male is indicated as a solid peak; nonfocal males are indicated as blue-contoured peaks. Single males are not shown. Arrows indicate the regions of likely intrusion by the focal male. (**C** to **F**) EPF and IPF males differ in space use. (**G**) Rates of intrusion and of male visitation are correlated. (**H**) Regions of a spatial-memory circuit (*31*) vary in receptors for vasopressin (red) or oxytocin (blue) (*13*, *19*). Abbreviations are as follows: ERC, entorhinal cortex; Hipp, hippocampus; AThal, anterior thalamus. (**I** to **K**) Autoradiograms for V1aR in the RSC. RSC-V1aR abundance (in dissociations per minute per milligram of tissue) predicts sexual fidelity and (**L**) intrusion rate. All bars show mean ± SE. $^{*}P \leq 0.05$, $^{**}P \leq 0.01$, $^{***}P \leq 0.001$.

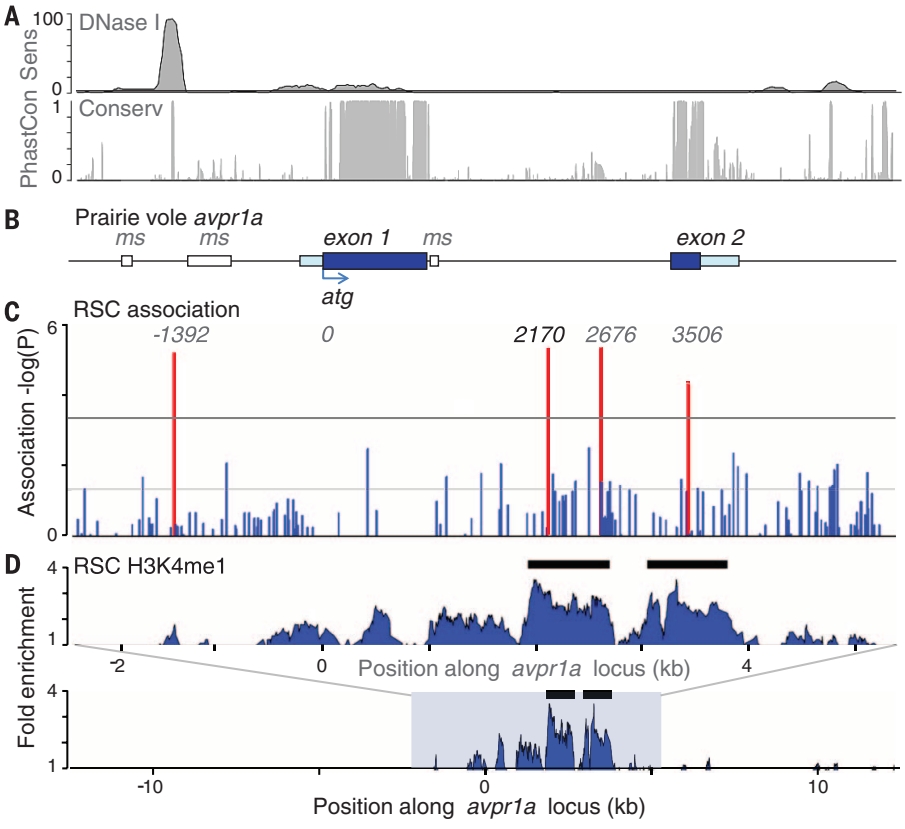

Fig. 2. SNPs in regulatory regions of the *avpr1a* locus predict RSC-V1aR. (**A**) DNAse I hypersensitivity in *Mus* brain and mammalian conservation (*22*). (**B**) Structure of prairie vole *avpr1a* locus (exons, blue; microsatellites, white). (**C**) Association of *avpr1a* SNPs with RSC-V1aR abundance. Each bar is a SNP; the *x* axis depicts position along the *avpr1a* locus; the *y* axis depicts strength of association [$-\log_{10}(P)$]. The lower horizontal gray line shows uncorrected $\alpha = 0.05$; the upper horizontal gray line shows corrected $\alpha = 0.00054$. (**D**) Fold enrichment by H3K4me1 ChIP-seq compared to input chromatin. Horizontal bars mark peaks corresponding to putative enhancers.

RSC-V1aR and our measures of space use. As reported previously, faithful IPF males have more RSC-V1aR than EPF males [$P < 0.001$, Fig. 1, I to K; (*13*)]. Low levels of RSC-V1aR were also associated with high intrusion rates (RSC, $P < 0.01$; pairing status, $P < 0.0001$; RSC × status, $P < 0.05$; Fig. 1L) and poor mate-guarding (male visits received: RSC, $P < 0.05$; pairing status, $P < 0.0001$; RSC × status, $P > 0.10$). V1aR levels in another node in this circuit (the LDThal) also predicted sexual fidelity and space use, whereas brain regions associated with pair-bonding and aggression (the ventral pallidum and lateral septum) did not [supplementary materials (*13*)]. These data suggest that trade-offs between the fitness benefits of intra-pair and extra-pair paternity could contribute to diversity in this memory circuit.

In order for selection to have promoted neuronal diversity, such variation must be heritable. We asked whether single-nucleotide polymorphisms (SNPs) in *avpr1a* predicted individual differences in V1aR abundance. We sequenced ~8 kb of the *avpr1a* locus (Fig. 2 and fig. S2) from lab-reared males with substantial field data [Fig. 1 (*13*)] and from wild-caught adults. Of 151 SNPs, 4 tightly linked polymorphisms predicted RSC-V1aR (Fig. 2, multiple-test corrected $\alpha = 5.4 \times 10^{-4}$). These SNPs were upstream of the coding sequence (SNP –1392, $P = 6.3 \times 10^{-6}$), in the intron (SNPs 2170 and 2676, $P = 4.7 \times 10^{-6}$), and in the second exon (SNP 3506, $P = 5.0 \times 10^{-5}$). We refer to the genotypes defined by these linked SNPs as HI (high)– and LO (low)–RSC alleles. The effects of HI and LO alleles were stronger among lab-reared animals ($P < 0.0001$) than wild-caught animals ($P < 0.05$; genotype × rearing $P = 0.002$; fig. S3), which suggests that population structure or developmental environment may influence cortical V1aR. We also found that a distinct SNP predicted V1aR in the LDThal (SNP 5168, $P = 3.6 \times 10^{-4}$), but none of the 151 SNPs predicted V1aR in the ventral pallidum or lateral septum (fig. S4). Thus, V1aR levels in regions implicated in spatial memory and sexual fidelity were linked to *avpr1a* sequence variation, whereas regions important in pair-bonding and aggression were not.

We examined the stability and specificity of the HI- and LO-RSC associations with a breeding design that controlled for potential confounds of our initial study. We obtained a new genetic stock from a third site >100 miles from prior sites. Heterozygous HI/LO parents were crossed to produce siblings that differed in their genotypes but shared a common genetic background, rearing environment, and lack of sexual experience. We again found that HI and LO alleles influenced V1aR in the RSC ($P < 0.0001$; Fig. 3A), but not in other brain regions (fig. S5). Thus, our data demonstrate a replicable, robust, and specific association between the HI-RSC allele and high RSC-V1aR expression. However, differences between wild-caught and lab-reared animals (fig. S3), as well as previously reported developmental manipulations (*20*), suggest that epigenetic variation may also be at play.

If individual differences in RSC-V1aR abundance are due to differences in the regulation of *avpr1a*, then HI/HI and LO/LO genotypes should differ in *avpr1a* transcript abundance. We dissected the RSC of the lab crosses reported above and used quantitative polymerase chain reaction to quantify *avpr1a* mRNA. Genotypes differed significantly in *avpr1a* transcript abundance (ΔCt versus β-*actin*, $P < 0.001$, Fig. 3B). Moreover, individual

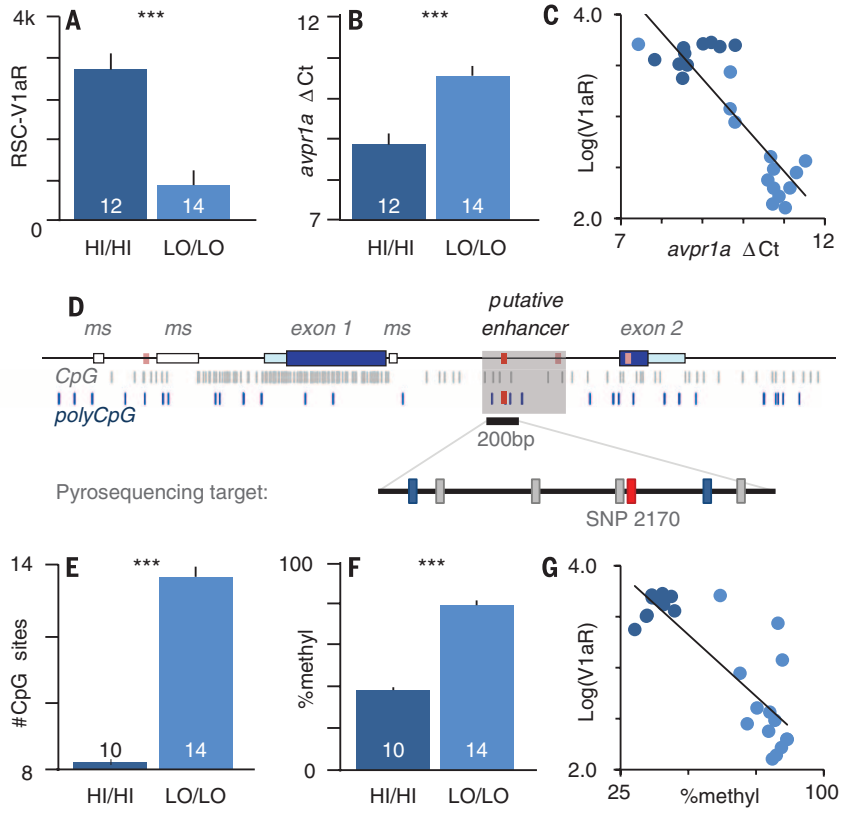

Fig. 3. Genotype differences in regulation of *avpr1a*. (**A**) Homozygotes differ in abundance of V1aR (dissociations per minute per milligram) and (**B**) *avpr1a* mRNA in the RSC. (**C**) RSC *avpr1a* transcript abundance correlates with V1aR protein. (**D**) Fixed (gray) and polymorphic (blue) CpG sites along *avpr1a*. The red bars are SNPs associated with RSC-V1aR. The shaded gray box indicates a putative intron enhancer. A cluster of CpG sites were selected for pyrosequencing, including polymorphic CpG SNP 2170 in red. (**E**) HI/HI males have fewer CpG sites in the intron and (**F**) lower levels of enhancer methylation. (**G**) RSC enhancer methylation correlates with V1aR abundance (R^2 = 0.70, $P < 0.0001$). Bars are means ± SE. ***$P \leq 0.001$.

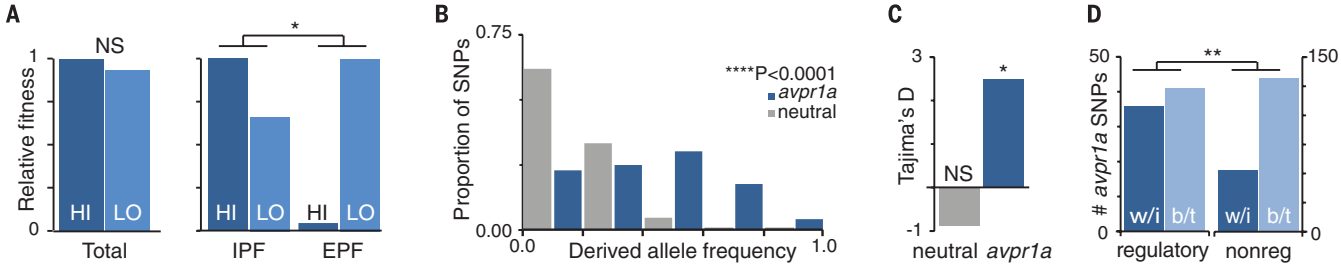

Fig. 4. Selection maintains regulatory variation at *avpr1a*. (**A**) Context-dependent selection on HI-RSC and LO-RSC alleles in the field. (**B**) *avpr1a* has more intermediate frequency alleles than do neutral markers. (**C**) Tajima's D value is significantly positive for *avpr1a* but not for neutral loci. (**D**) Regulatory regions of *avpr1a* had higher ratios of within:between species differences than nonregulatory regions. *$P < 0.05$, **$P < 0.01$, not significant = $P > 0.10$.

differences in *avpr1a* mRNA were strongly associated with RSC-V1aR protein [linear regression coefficient (R^2) = 0.75, $P < 0.0001$, Fig. 3C].

To determine whether any RSC-associated SNPs were within DNA sequences that might contribute to *avpr1a* regulation, we performed chromatin immunoprecipitation sequencing (ChIP-seq) targeting the histone modification H3K4me1, a marker for regulatory sequences known as enhancers (*21*). We dissected RSC samples from eight new lab-reared animals. Within a 25-kb sequence centered on the *avpr1a* translation start site (Fig. 2D), the H3K4me1 mark was specifically associated with two regions within the *avpr1a* locus [$P < 1 \times 10^{-7}$, false discovery rate (Q) < 0.0001; supplementary materials]. One putative enhancer was in the center of the intron, including both intron SNPs of the HI/LO alleles; the second overlapped the second exon and included the fourth linked SNP (Fig. 2C). Three of the polymorphisms that define the HI and LO alleles are within putative enhancer regions, and the fourth is within a conserved deoxyribonuclease I (DNAse I) hypersensitive site [Fig. 2A (*22*)]. Thus, all four RSC-associated SNPs coincide with markers of transcriptional regulation.

We next asked whether differences in RSC *avpr1a* transcript and V1aR protein abundance reflected differences in the epigenetic state of the *avpr1a* locus. We focused on the putative intron enhancer: This sequence had strong evidence of H3K4me1 enrichment and included the two SNPs most strongly linked to RSC-V1aR. SNP 2170 proved to be a G/T polymorphism that altered the presence of a CpG site, a common target of DNA methylation (*23*). Moreover, this CpG/CpT polymorphism is linked to a cluster of CpG polymorphisms within the enhancer (Fig. 3D). HI-RSC alleles have fewer CpG sites than LO alleles ($P < 0.0001$, Fig. 3E), suggesting fewer opportunities for methylation. We isolated DNA from the RSC, treated it with bisulfite, and performed pyrosequencing of this enhancer. HI/HI animals had less enhancer methylation than LO/LO animals ($P < 0.0001$, Fig. 3F). Genotypes also differed in enhancer methylation if we focused solely on nonvariable CpG sites [mean (μ) ± SE, HI/HI 67.6 ± 1.6%, LO/LO 75.6 ± 1.3%; $P = 0.001$]. Moreover, *avpr1a* enhancer methylation is significantly associated with RSC-V1aR abundance ($P < 0.0001$, Fig. 3G). Methylation at noncoding CpG sites is known to recruit methyl-binding proteins, histone de-acetylases, and other silencing proteins (*24*); our data suggest that SNP 2170 and neighboring CpG polymorphisms may alter the function of an intron enhancer by changing the number of CpG sites available for methylation.

Our molecular data indicate that specific alleles are robust predictors of RSC-V1aR, and they suggest mechanisms by which specific SNPs might exert influence on *avpr1a* expression. If genetic differences in RSC-V1aR are adaptive—a "balanced polymorphism" of the brain—we might expect differences in how HI- and LO-RSC alleles gain fitness. Using data from lab-reared animals monitored in the field (Fig. 1), we calculated the number of embryos that each male sired either with a partner (IPFs) or non-partner (EPFs) and estimated the relative fitness of HI and LO alleles in each context. Although the alleles had similar fitness overall, selection favored HI alleles in the context of IPFs and LO alleles in the context of EPFs (Fig. 4A, $P < 0.05$). Thus, fluctuations in the defensibility of females could profoundly influence the strength and direction of selection on HI and LO alleles. Prairie voles exhibit wide fluctuations in population density, ranging from ~25 to 600 voles per hectare in a year (*25*); high densities increase the rate of extra-pair interactions (*26*) and reduce the defensibility of prairie vole females (*27*). Manipulative studies will be needed to test whether fluctuations in population density or allele frequency promote variation in *avpr1a* and related behaviors.

If genetic variation at *avpr1a* produces variation in memory regions, and this in turn influences space use and sexual fidelity, then over time we expect selection to have influenced patterns of *avpr1a* nucleotide variation. We tested for a history of balancing selection by comparing the frequencies of SNPs at *avpr1a* to three putatively neutral nuclear loci among our original wild-caught samples. We found that the *avpr1a* locus was strongly skewed toward an excess of intermediate-frequency alleles, a classic signature of balancing selection (Fig. 4B, likelihood ratio = 120.3, df = 4, $P = 4.7 \times 10^{-25}$). Similarly, *avpr1a* had a positive Tajima's D value ($P < 0.05$) (*28*), whereas our neutral loci had negative values ($P > 0.10$, Fig. 4C). Lastly, a Hudson Kreitman Aguade test (*29*) comparing the number of within- and between-species differences indicated an excess of standing variation within regulatory regions (defined by H3K4me1 ChIP-seq and DNAse hypersensitivity $P < 0.01$, Fig. 4D). We conclude that balancing selection has actively maintained regulatory variation at the *avpr1a* locus. This regulatory variation seems to be specifically associated with brain regions related to memory and space use.

These data provide a remarkably coherent perspective on the origin and maintenance of diversity in the social brain. V1aR levels in memory structures predict whether males will intrude on neighbors and gain extra-pair paternity, or exclude intruders and improve intra-pair paternity. Nucleotide polymorphisms within regulatory sequences robustly and specifically predict V1aR variation in these same brain regions. Within the RSC, we find that low-expressing alleles differ in CpG abundance and methylation status. Because CpG sites can be gained or lost easily [~25% of single nucleotide differences between humans and chimps, for example, consist of the gain or loss of a CpG site (*30*)], we hypothesize that CpG polymorphisms may often shape heritable variation in environmental sensitivity. Genetic markers for this neuronal phenotype exhibit strong evidence of balancing selection. Together these data suggest that trade-offs in the fitness consequences of spatial behaviors promote diversity in the social brain. By focusing on what would seem to be the simplest of social phenotypes—the neural expression patterns of a single gene—we gain insights into the complex interplay of forces that shape both gene function and social evolution.

REFERENCES AND NOTES

1. R. Adolphs, *Nat. Rev. Neurosci.* **4**, 165–178 (2003).
2. L. J. Young, Z. Wang, *Nat. Neurosci.* **7**, 1048–1054 (2004).
3. M. R. Gross, *Philos. Trans. R. Soc. London Ser. B* **332**, 59–66 (1991).
4. B. Sinervo, C. M. Lively, *Nature* **380**, 240–243 (1996).
5. D. W. Pfennig, *Evolution* **46**, 1408–1420 (1992).
6. K. J. H. Verweij *et al*., *Evolution* **66**, 3238–3251 (2012).
7. B. J. Ellis, M. J. Essex, W. T. Boyce, *Dev. Psychopathol.* **17**, 303–328 (2005).
8. M. C. Keller, G. Miller, *Behav. Brain Sci.* **29**, 385–404, discussion 405–452 (2006).
9. L. L. Getz, B. McGuire, T. Pizzuto, J. E. Hofmann, B. Frase, *J. Mammal.* **74**, 44–58 (1993).
10. C. S. Carter, L. L. Getz, M. Cohen-Parsons, *Adv. Stud. Behav.* **16**, 109–145 (1986).
11. B. S. Cushing, K. M. Kramer, *Neurosci. Biobehav. Rev.* **29**, 1089–1105 (2005).
12. S. M. Phelps, L. J. Young, *J. Comp. Neurol.* **466**, 564–576 (2003).
13. A. G. Ophir, J. O. Wolff, S. M. Phelps, *Proc. Natl. Acad. Sci. U.S.A.* **105**, 1249–1254 (2008).
14. S. M. Phelps, A. G. Ophir, in *Cognitive Ecology II*, R Dukas, J. M. Ratcliffe, Eds. (Univ. of Chicago Press, Chicago, IL, 2009), chap. 9.
15. G. J. De Vries, G. C. Panzica, *Neuroscience* **138**, 947–955 (2006).
16. A. G. Ophir, S. M. Phelps, A. B. Sorin, J. O. Wolff, *Anim. Behav.* **75**, 1143–1154 (2008).
17. S. T. Emlen, L. W. Oring, *Science* **197**, 215–223 (1977).
18. H. Kokko, D. J. Rankin, *Philos. Trans. R. Soc. Ser. B* **361**, 319–334 (2006).
19. S. M. Phelps, P. Campbell, D.-J. Zheng, A. G. Ophir, *Neuropharmacology* **58**, 17–28 (2010).
20. K. L. Bales *et al*., *Neuroscience* **144**, 38–45 (2007).
21. N. D. Heintzman *et al*., *Nat. Genet.* **39**, 311–318 (2007).
22. K. R. Rosenbloom *et al*., *Nucleic Acids Res.* **41** (D1), D56–D63 (2013).
23. A. Razin, A. D. Riggs, *Science* **210**, 604–610 (1980).
24. X. Nan *et al*., *Nature* **393**, 386–389 (1998).
25. L. L. Getz, J. E. Hofmann, B. McGuire, T. W. Dolan, *J. Mammal.* **82**, 22–34 (2001).
26. B. McGuire, T. Pizzuto, L. L. Getz, *Can. J. Zool.* **68**, 391–398 (1990).
27. C. A. Streatfeild, K. E. Mabry, B. Keane, T. O. Crist, N. G. Solomon, *Anim. Behav.* **82**, 1387–1398 (2011).
28. F. Tajima, *Genetics* **123**, 585–595 (1989).
29. R. R. Hudson, M. Kreitman, M. Aguadé, *Genetics* **116**, 153–159 (1987).
30. Chimpanzee Sequencing and Analysis Consortium, *Nature* **437**, 69–87 (2005).
31. J. P. Aggleton, *Proc. Biol. Sci.* **281**, 20140565 (2014).

ACKNOWLEDGMENTS

The authors thank Z. Dehghani, L. O'Connell, and A. Sidik for help with molecular work. T. Juenger, M. Ryan, M. Wayne, and three anonymous reviewers provided valuable feedback. Funded by NSF grant IOS-0316451, NIH grant R21 HD059092, and NSF grant IOS-1355188 to S.M.P. Data presented in this manuscript are available in the Dryad Digital Repository (accession no. doi:10.5061/dryad.74s05). Sequencing data from our ChIP-seq experiment are available through the National Center for Biotechnology Information (GEO accession no. GSE73670).

SUPPLEMENTARY MATERIALS

www.sciencemag.org/content/350/6266/1371/suppl/DC1
Materials and Methods
Supplementary Text
Figs. S1 to S5
Tables S1 to S4
References (*32*–*45*)

14 May 2015; accepted 3 November 2015
10.1126/science.aac5791

AGING

Cell nonautonomous activation of flavin-containing monooxygenase promotes longevity and health span

Scott F. Leiser,[1] Hillary Miller,[1]* Ryan Rossner,[1]* Marissa Fletcher,[1] Alison Leonard,[1] Melissa Primitivo,[1] Nicholas Rintala,[1] Fresnida J. Ramos,[1] Dana L. Miller,[2] Matt Kaeberlein[1]†

Stabilization of the hypoxia-inducible factor 1 (HIF-1) increases life span and health span in nematodes through an unknown mechanism. We report that neuronal stabilization of HIF-1 mediates these effects in *Caenorhabditis elegans* through a cell nonautonomous signal to the intestine, which results in activation of the xenobiotic detoxification enzyme flavin-containing monooxygenase-2 (FMO-2). This prolongevity signal requires the serotonin biosynthetic enzyme TPH-1 in neurons and the serotonin receptor SER-7 in the intestine. Intestinal FMO-2 is also activated by dietary restriction (DR) and is necessary for DR-mediated life-span extension, which suggests that this enzyme represents a point of convergence for two distinct longevity pathways. FMOs are conserved in eukaryotes and induced by multiple life span–extending interventions in mice, which suggests that these enzymes may play a critical role in promoting health and longevity across phyla.

In nematodes, as in mammals, hypoxia-inducible factor (HIF) proteins have a central role in responding to changes in environmental oxygen (*1*). HIF proteins are transcription factors regulated by oxygen-dependent proteasomal degradation and are stabilized under low-oxygen conditions to modulate expression of hundreds of target genes to produce the hypoxic response (*2*). In mammals, constitutive stabilization of HIF through loss of the E3 ubiquitin ligase von Hippel-Lindau (VHL) protein leads to a disease characterized by angiomas and renal carcinomas (*3*), whereas in *Caenorhabditis elegans*, loss of the VHL homolog gene, *vhl-1*, improves proteostasis and increases life span (*4*, *5*). This difference likely reflects the fact that somatic cells of adult *C. elegans* are postmitotic, with little or no potential for tumor development, and raises the possibility that specific targets of HIF-1 that promote healthy aging in *C. elegans* may function similarly in mammals.

To understand how hypoxic signaling slows aging in worms, we identified genes downstream of HIF-1 that promote longevity and health span. We took advantage of the large reduction in age-associated autofluorescence observed in animals in which *vhl-1* is not expressed (*vhl-1* knockout) (*4*) to screen for known HIF-1 target genes required for this phenotype (fig. S1). Our screen identified 24 RNA interference (RNAi) clones that substantially increased autofluorescence in *vhl-1* animals, eight of which also reduced the long life span of *vhl-1* mutant animals (table S1 and fig. S2). Six of these RNAi clones had no effect on the life span of the wild-type reference strain (N2 Bristol), which indicated that they may function specifically to enhance longevity when HIF-1 is stabilized.

Having established a set of HIF-1 target genes necessary for the full longevity effect of activation of HIF-1, we tested whether any of these genes were sufficient to enhance longevity and health span. We used the Mos1 transposase–mediated single-copy insertion system (*6*) to overexpress a single copy of each of the six genes from the ubiquitous *eft-3* promoter (fig. S3). Depletion of the xenobiotic detoxification enzyme flavin-containing monooxygenase-2 (*fmo-2*) by RNAi showed it to be required for full life-span extension in *vhl-1* knockout animals (Fig. 1A). FMO-2 was also sufficient to extend life span on its own (Fig. 1B and fig. S3). Ubiquitous FMO-2 overexpression (FMO-2 OE) also improved multiple measures of health span, including enhanced maintenance of motility (measured by the ability to swim, or thrash, in liquid), pharyngeal pumping, and decreased age-associated autofluorescence (Fig. 1, C and D and fig. S4). FMO-2 OE animals did not show the decreased brood size or delay in development observed in animals lacking *vhl-1*; thus, these negative consequences of HIF-1 activation likely result from other HIF-1 targets and are separable from life-span and health-span extension (fig. S4).

Maintaining proteostasis is critical for healthy aging (*7*), and both dietary restriction (DR) and stabilization of HIF-1 enhance proteostasis in *C. elegans* (*4*, *8*). To determine whether FMO-2 enhances proteostasis, we examined the effect of FMO-2 OE on resistance to proteotoxic stress. The most notable effect of FMO-2 OE was resistance to proteotoxic stress within the endoplasmic reticulum (ER), as evidenced by reduced growth inhibition in response to treatment of animals

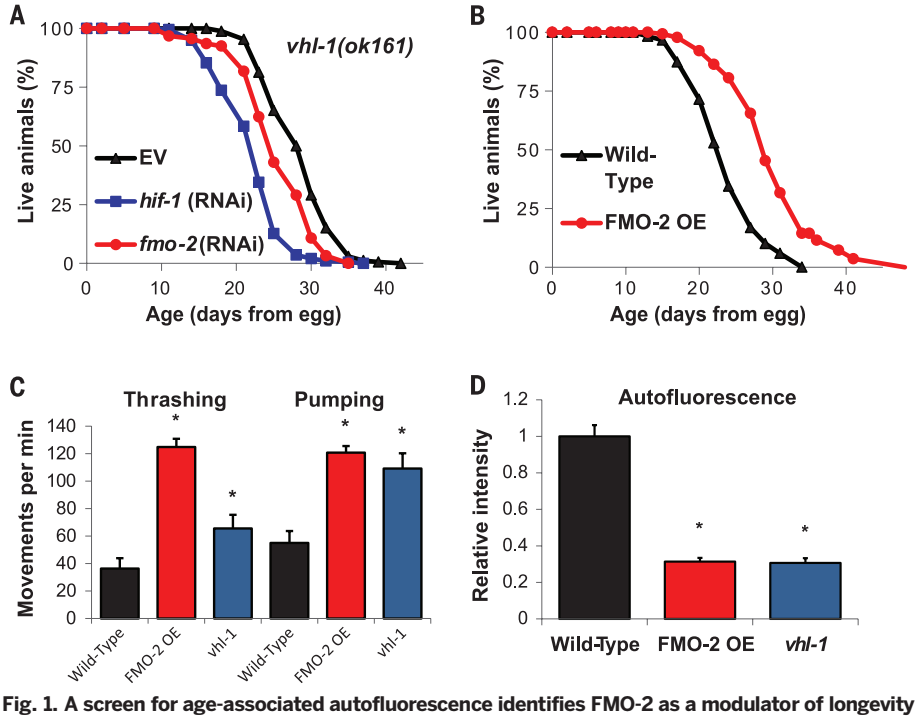

Fig. 1. A screen for age-associated autofluorescence identifies FMO-2 as a modulator of longevity and health span in the hypoxic-response pathway. (**A**) Life spans of *vhl-1(ok161)* animals on empty vector (EV), *hif-1* RNAi, or *fmo-2* RNAi. (**B**) Life spans of wild-type worms and worms overexpressing FMO-2 ubiquitously (*eft-3* promoter, FMO-2 OE). (**C** and **D**) Thrashing, pumping, and autofluorescence measurements of wild-type, FMO-2 OE worms, and *vhl-1(ok161)* mutant worms during adulthood (days 10, 13, and 5, respectively). Statistically different (*$P < 0.05$) from wild type by individual *t* test for each strain. Error bars represent SEM; $N \geq 3$ for all experiments.

[1]Department of Pathology, University of Washington, Seattle, WA 98195, USA. [2]Department of Biochemistry, University of Washington, Seattle, WA 98195, USA.
*These authors contributed equally to this work. †Corresponding author. E-mail: kaeber@uw.edu

Downloaded from www.sciencemag.org on December 14, 2015

with tunicamycin (up to 10 μg/ml) and reduced mortality of animals treated with dithiothreitol (DTT, 7 mM) (Fig. 2, A and B). FMO-2 OE animals were also resistant to general proteotoxic stress induced by high temperature (Fig. 2C), reductive proteotoxic stress from 2-carboxyethyl phosphine hydrochloride treatment, and transgenic expression of an aggregation-prone polyglutamine peptide fused to yellow fluorescent protein (Q35::YFP) (*9*) (fig. S5).

We examined the interaction between *fmo-2* and other important longevity pathways. Life-span extension from stabilization of HIF-1 is genetically distinct from that regulated by both the insulin-like signaling pathway and DR (*4*, *5*, *10*). Life extension in FMO-2 OE animals appears not to require the rest of the hypoxic-response pathway, insulin-like signaling, or the phase II detoxification pathway, because it was not lost in *hif-1*, *daf-16*, or *skn-1* mutants, respectively (fig. S6). Thus, FMO-2 does not act through these transcription factors to promote longevity. Similarly, *fmo-2* appears not to be necessary for life-span extension produced by known aging-related pathways, because loss of *fmo-2* alone had only a modest effect on life span and did not prevent life-span extension in response to reduced insulin-like signaling caused by *daf-2* RNAi or inhibition of mitochondrial respiration caused by *isp-1* RNAi (fig. S7). However, *fmo-2* was required for life-span extension induced by DR, when the technique of periodic feeding and fasting, or sDR, is used (*11*) (Fig. 2D). To further explore the possibility that FMO-2 acts in both the hypoxic response and DR, we confirmed that *fmo-2* is transcriptionally induced by food deprivation by monitoring a reporter for *fmo-2* transcription fused with green fluorescent protein (*fmo-2p*::GFP) (Fig. 2, E and F). Unlike that caused by hypoxia (*12*), induction of *fmo-2* in response to fasting was not dependent upon HIF-1 (Fig. 2, E and F). This is consistent with our observation that life-span extension from DR does not require *hif-1* (*4*) and raises the possibility that DR and the hypoxic response converge on FMO-2 to promote longevity through distinct signal transduction pathways.

The simplest way HIF-1 might increase *fmo-2* expression is to bind the *fmo-2* promoter directly and promote transcription. Previous reports, and our results with transcriptional reporters, both indicate that FMO-2 is expressed predominantly in the intestine (*13*). In agreement with this, overexpression of FMO-2 under an intestinal promoter was sufficient to promote longevity (Fig. 3A). To test whether HIF-1 also acts in the intestine to promote longevity, we used transgenic nematodes with a nondegradable HIF-1 variant (*14*), referred to hereafter as HIF-1^S. Intestinal HIF-1^S had no effect on longevity (fig. S8), whereas neuronal HIF-1^S was sufficient to increase life span (Fig. 3B). Expressing HIF-1^S in neurons was also sufficient to rescue additional defects in *hif-1* knockout animals, including failure to develop in hypoxia (0.5% oxygen) (Fig. 3C and fig. S9), loss of vulval integrity during aging (fig. S10), and life-span extension from

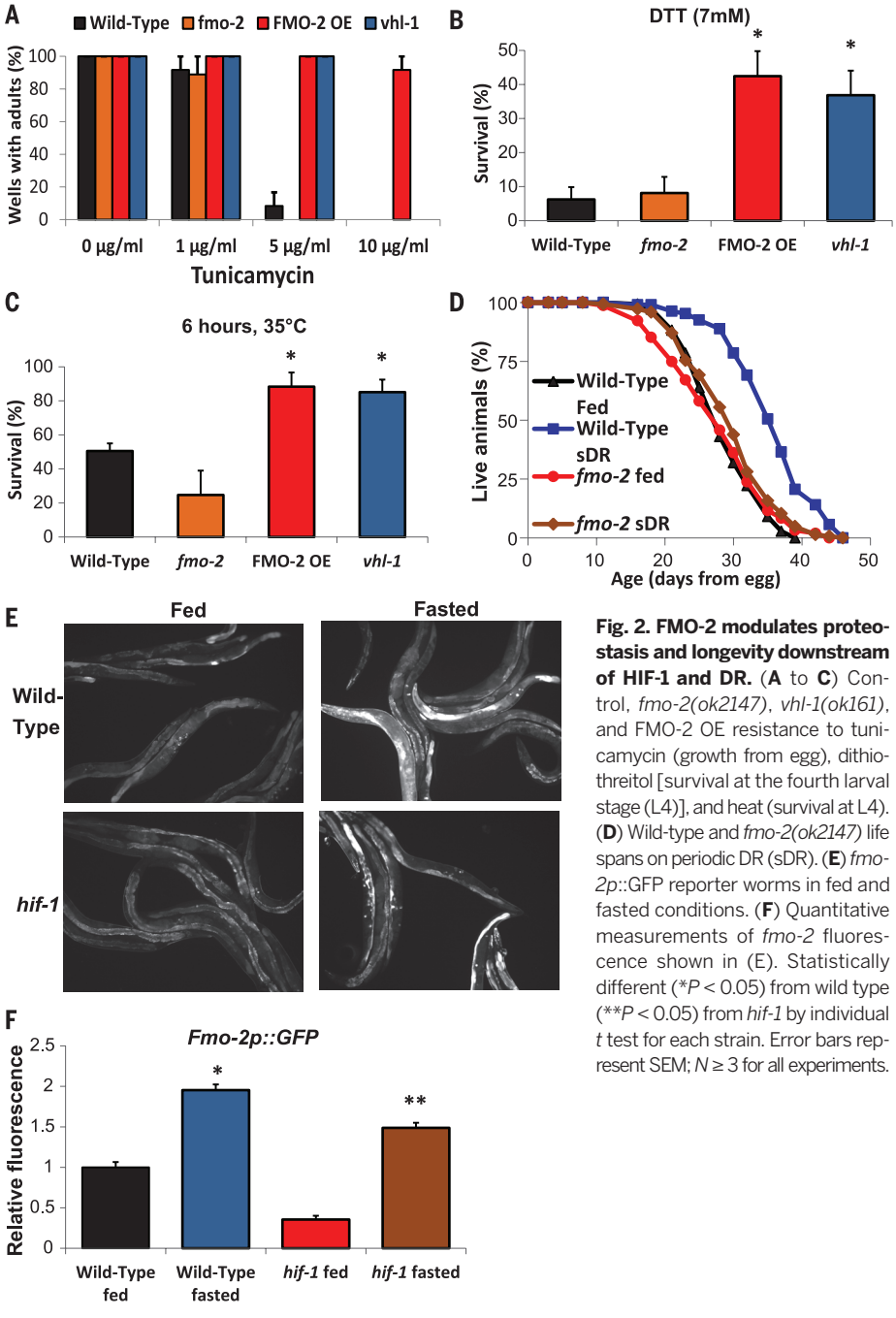

Fig. 2. FMO-2 modulates proteostasis and longevity downstream of HIF-1 and DR. (**A** to **C**) Control, *fmo-2(ok2147)*, *vhl-1(ok161)*, and FMO-2 OE resistance to tunicamycin (growth from egg), dithiothreitol [survival at the fourth larval stage (L4)], and heat (survival at L4). (**D**) Wild-type and *fmo-2(ok2147)* life spans on periodic DR (sDR). (**E**) *fmo-2p*::GFP reporter worms in fed and fasted conditions. (**F**) Quantitative measurements of *fmo-2* fluorescence shown in (E). Statistically different (*$P < 0.05$) from wild type (**$P < 0.05$) from *hif-1* by individual *t* test for each strain. Error bars represent SEM; $N \geq 3$ for all experiments.

hypoxia during adulthood (fig. S11) (*15*, *16*). Neuronal HIF-1^S in animals lacking HIF-1 in other tissues was also sufficient to extend life span (Fig. 3D), which indicated that stabilization of HIF-1 in neurons alone is sufficient to extend life span in *C. elegans*, even without HIF-1 in other cell types.

Neuronal overexpression of *fmo-2* had no detectable effect on longevity (fig. S8). Thus, HIF-1 and FMO-2 appear to promote longevity and health span by acting in distinct tissues: HIF-1 in neurons and FMO-2 in intestine. Consistent with this model, transcription of *fmo-2* was significantly induced in the intestine by stabilization of HIF-1 in neurons in a background where *hif-1* is knocked out in all other tissues [*hif-1(ia04)*; neuro-HIF-1^S] as measured by both quantitative reverse transcription polymerase chain reaction (QRT-PCR) and by fluorescence in a reporter strain (Fig. 3E and fig. S12). In agreement with these results, depletion of *fmo-2* with RNAi prevented life-span extension in this strain (Fig. 3F), despite the inefficiency of RNAi in neurons (*17*), which indicated that neuronal HIF-1 signaling to intestinal FMO-2 is probably necessary for the longevity benefit.

Having established a connection between neuronal HIF-1 signaling and intestinal FMO-2 activation, we explored potential signal transduction pathways by depleting signaling components

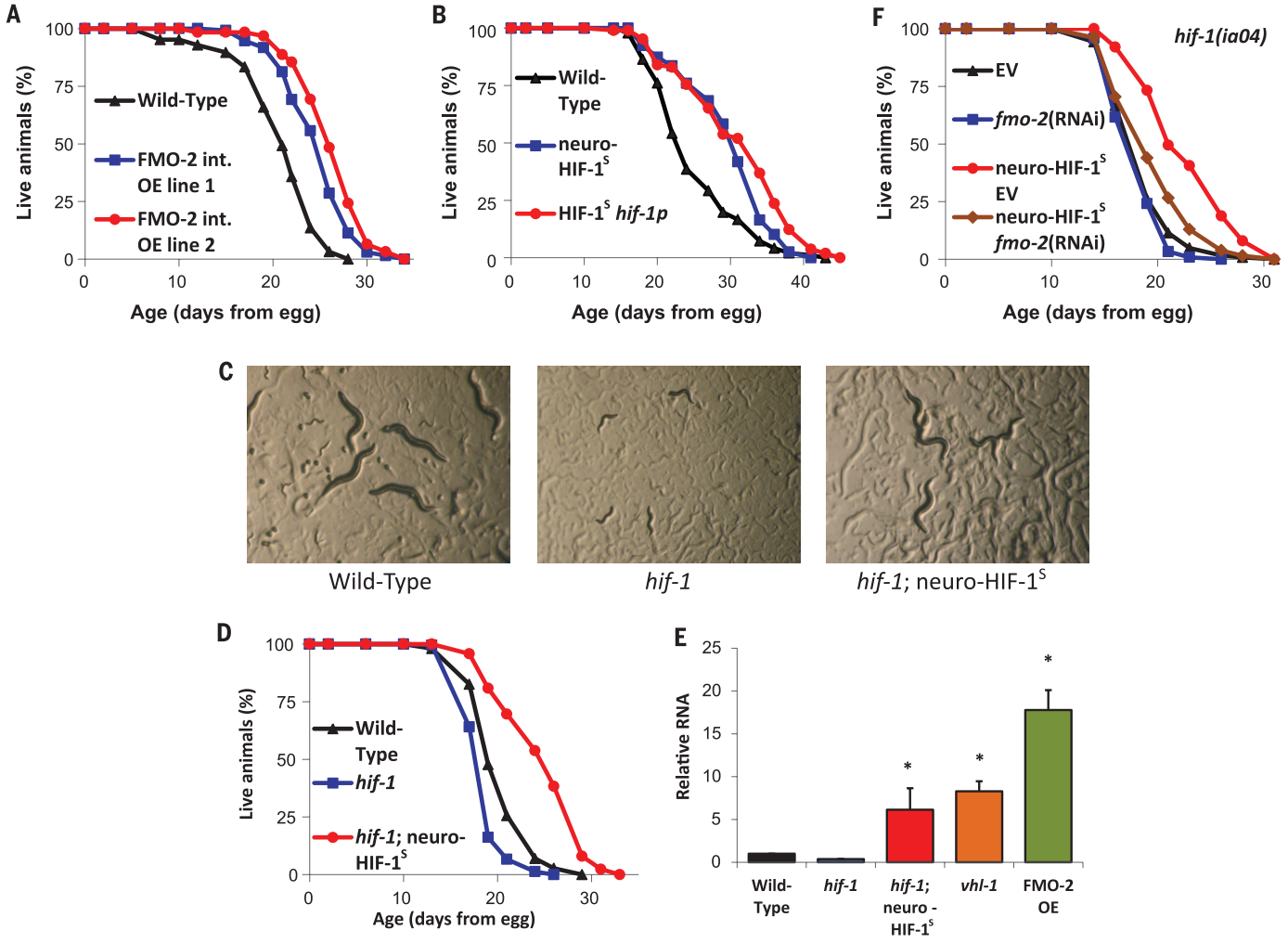

Fig. 3. Neuronal HIF-1 activates intestinal *fmo-2* to increase longevity. (**A**) Life spans of worms overexpressing FMO-2 under an intestinal *(vha-6p)* promoter. (**B**) Life spans of control worms and worms expressing HIF-1^S under neuronal (*unc-14p*) and ubiquitous (*hif-1p*) promoters. (**C**) Growth in hypoxia (0.5% oxygen) of wild-type, *hif-1(ia04)*, and *hif-1(ia04)*::neuro-HIF-1^S worms after 6 days from egg. (**D**) Life spans of control, *hif-1(ia04)*, and *hif-1(ia04)* worms with stabilized neuronal HIF-1. (**E**) QPCR measurement of *fmo-2* transcript in multiple strains. (**F**) Life spans of *hif-1(ia04)* and *hif-1(ia04)* worms with stabilized neuro-HIF-1^S in control (EV) and *fmo-2* RNAi. Statistically different (*P < 0.05) from wild type or (**P < 0.05) from *hif-1* by individual t test for each strain. Error bars represent SEM, $N \geq 3$ for all experiments.

and transcription factors chosen on the basis of previous reports and *in silico* promoter analysis (*18*, *19*). Although most of the factors examined had no effect (fig. S13), the serotonergic signaling pathway was both necessary and sufficient for the cell nonautonomous effect of HIF-1 signaling in neurons on expression of FMO-2 in intestine and subsequent longevity benefit of FMO-2. The 5-hydroxytryptamine$_7$ receptor *ser-7* and the rate-limiting enzyme in serotonin production, *tph-1,* were both required for the activation of FMO-2 in hypoxia and the longevity benefit from neuronal HIF-1^S or *vhl-1* mutation (Fig. 4, A to C, and fig. S14). In agreement with this, HIF-1^S expressed under the serotonergic *tph-1* promoter was sufficient to improve longevity to an extent comparable to that of pan-neuronal expression (Fig. 4D). A transcription factor with predicted binding to the *fmo-2* promoter, HLH-30, was necessary for either hypoxia or starvation to fully induce transcription of an FMO-2 reporter in the intestine (Fig. 4E). HLH-30 is necessary for life-span extension by DR (*20*), and our results indicate that it is also required to achieve maximal life-span extension from HIF-1 stabilization (Fig. 4F), although expression of HIF-1^S or deletion of *vhl-1* still partially increase life span in animals depleted of *hlh-30*.

Our results support a model in which the flavin-containing monooxygenase FMO-2 functions in the intestine to increase life span, improve health span, and enhance proteostasis in animals undergoing the hypoxic response or DR. Further, intestinal *fmo-2* is regulated cell nonautonomously through serotonergic signaling originating in neurons, and subsequent activation of the transcription factor HLH-30 in the intestine (Fig. 4G). FMO-2 is thus an enzyme both necessary and sufficient for a majority of the beneficial effects of either of these longevity pathways. The FMO-2 substrates important for healthy aging in *C. elegans* remain unknown. It will also be of interest to directly assess whether FMOs may function in mammalian aging. There are five mammalian FMO proteins (FMO-1 to 5) (*21*), similar to the five *C. elegans* FMOs (*13*), and all of these proteins came from a single ancestral FMO (*22*). In mammals, there is relatively limited information on the specific functions of each FMO beyond tissue-specific expression patterns and the role of FMO-3 in a single human disease, fish-odor syndrome (*23*). Mammalian FMOs also have a major role in regulating cholesterol and fat metabolism (*24*, *25*). Abundance of FMO proteins is increased in the tissues, particularly liver, of several long-lived mouse models including Snell dwarf mice, Ames dwarf mice, growth-hormone receptor knockout mice, Little mice, dietary-restricted mice, and rapamycin-fed mice (*26*). Indeed, FMO-3 mRNA is the most consistently induced mRNA under DR in mouse liver (*27*). Taken with the data presented here, these observations raise the possibility that activation of FMOs may be a conserved mechanism for enhancing protein homeostasis, improving health span, and extending life span and that appropriate

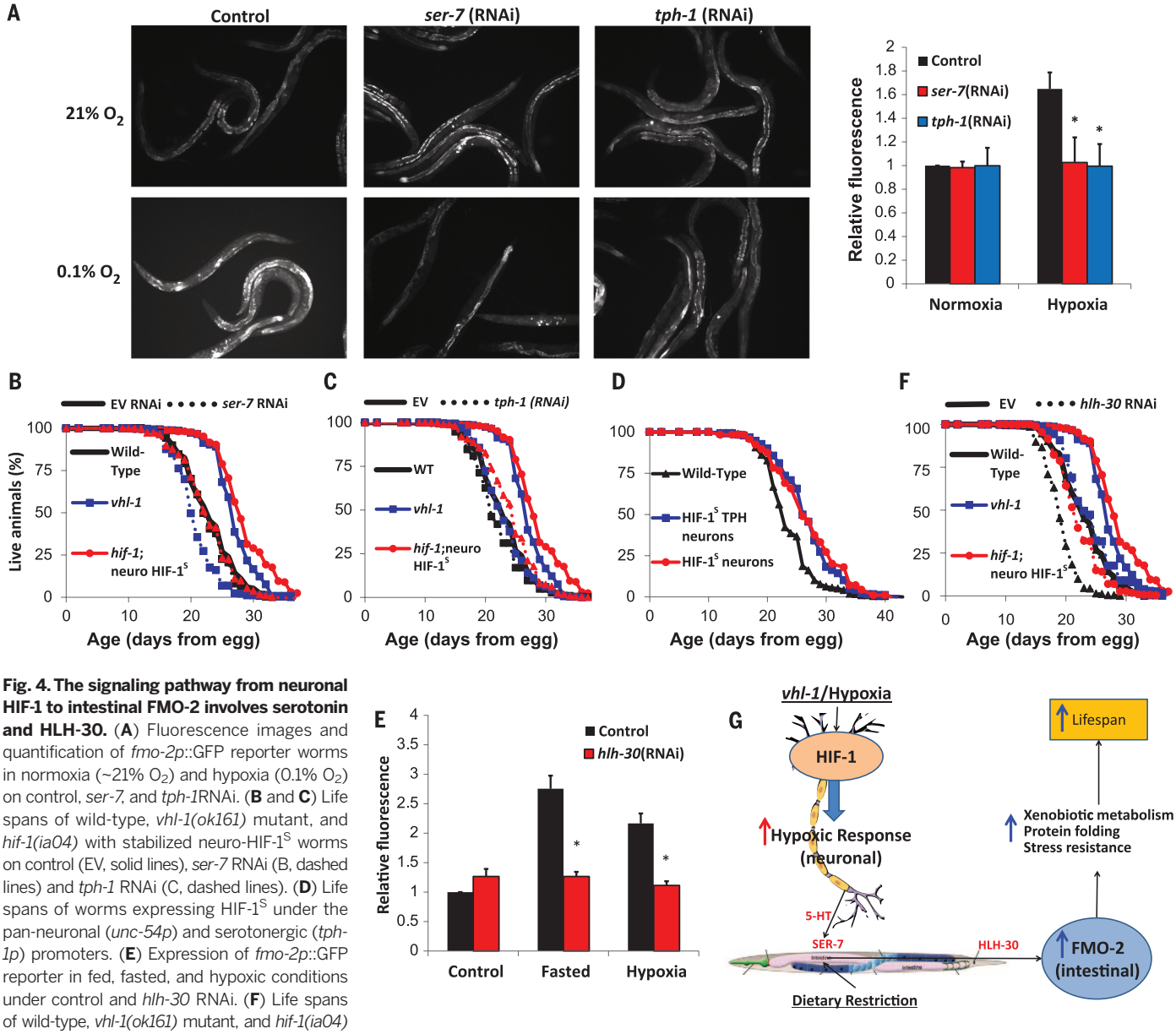

Fig. 4. The signaling pathway from neuronal HIF-1 to intestinal FMO-2 involves serotonin and HLH-30. (**A**) Fluorescence images and quantification of *fmo-2p*::GFP reporter worms in normoxia (~21% O_2) and hypoxia (0.1% O_2) on control, *ser-7*, and *tph-1*RNAi. (**B** and **C**) Life spans of wild-type, *vhl-1(ok161)* mutant, and *hif-1(ia04)* with stabilized neuro-HIF-1^S worms on control (EV, solid lines), *ser-7* RNAi (B, dashed lines) and *tph-1* RNAi (C, dashed lines). (**D**) Life spans of worms expressing HIF-1^S under the pan-neuronal (*unc-54p*) and serotonergic (*tph-1p*) promoters. (**E**) Expression of *fmo-2p*::GFP reporter in fed, fasted, and hypoxic conditions under control and *hlh-30* RNAi. (**F**) Life spans of wild-type, *vhl-1(ok161)* mutant, and *hif-1(ia04)* with stabilized neuro-HIF-1^S worms on control (EV, solid lines) and *hlh-30* RNAi (dashed lines) (**G**) Model of hypoxic response and DR converging on intestinal FMO-2. In graphs, statistical difference (*P < 0.05) from wild type by individual t test for each strain. Error bars represent SEM, $N \geq 3$ for all experiments.

activation of FMOs might promote healthy aging in mammals and people.

REFERENCES AND NOTES

1. H. Jiang, R. Guo, J. A. Powell-Coffman, *Proc. Natl. Acad. Sci. U.S.A.* **98**, 7916–7921 (2001).
2. Q. Ke, M. Costa, *Mol. Pharmacol.* **70**, 1469–1480 (2006).
3. M. Ivan, W. G. Kaelin Jr., *Curr. Opin. Genet. Dev.* **11**, 27–34 (2001).
4. R. Mehta *et al.*, *Science* **324**, 1196–1198 (2009).
5. R. U. Müller *et al.*, *J. Am. Soc. Nephrol.* **20**, 2513–2517 (2009).
6. C. Frøkjær-Jensen *et al.*, *Nat. Genet.* **40**, 1375–1383 (2008).
7. J. Labbadia, R. I. Morimoto, *F1000Prime Rep.* **6**, 7 (2014).
8. K. A. Steinkraus *et al.*, *Aging Cell* **7**, 394–404 (2008).
9. J. F. Morley *et al.*, *Proc. Natl. Acad. Sci. U.S.A.* **99**, 10417–10422 (2002).
10. Y. Zhang *et al.*, *PLOS ONE* **4**, e6348 (2009).
11. E. L. Greer *et al.*, *Curr. Biol.* **17**, 1646–1656 (2007).
12. C. Shen *et al.*, *J. Biol. Chem.* **280**, 20580–20588 (2005).
13. M. I. Petalcorin *et al.*, *Gene* **346**, 83–96 (2005).
14. R. Pocock, O. Hobert, *Nat. Neurosci.* **11**, 894–900 (2008).
15. S. F. Leiser *et al.*, *J. Gerontol. A Biol. Sci. Med. Sci.* **68**, 1135–1144 (2013).
16. D. L. Miller, M. B. Roth, *Curr. Biol.* **19**, 1233–1237 (2009).
17. R. S. Kamath, M. Martinez-Campos, P. Zipperlen, A. G. Fraser, J. Ahringer, *Genome Biol.* **2**, RESEARCH0002 (2001).
18. R. Pocock, O. Hobert, *Nat. Neurosci.* **13**, 610–614 (2010).
19. M. B. Gerstein *et al.*, *Science* **330**, 1775–1787 (2010).
20. L. R. Lapierre *et al.*, *Nat. Commun.* **4**, 2267 (2013).
21. S. K. Krueger, D. E. Williams, *Pharmacol. Ther.* **106**, 357–387 (2005).
22. D. Hernandez, A. Janmohamed, P. Chandan, I. R. Phillips, E. A. Shephard, *Pharmacogenetics* **14**, 117–130 (2004).
23. C. T. Dolphin *et al.*, *Nat. Genet.* **17**, 491–494 (1997).
24. S. Veeravalli *et al.*, *Biochem. Pharmacol.* **90**, 88–95 (2014).
25. D. M. Shih *et al.*, *J. Lipid Res.* **56**, 22–37 (2015).
26. M. J. Steinbaugh, L. Y. Sun, A. Bartke, R. A. Miller, *Am. J. Physiol. Endocrinol. Metab.* **303**, E488–E495 (2012).
27. W. R. Swindell, *BMC Genomics* **10**, 585 (2009).

ACKNOWLEDGMENTS

We thank C. Dolphin for the vector to make the *fmo-2p*::GFP reporter strains and A. Mendenhall for advice and help with injecting worms. Strains were provided by the *Caenorhabditis* Genetics Center. This work was supported by NIH grant R01AG038518 and an award from the Samsung Advanced Institute of Technology, Samsung Electronics Co., to M.K. and NIH grant K99AG045200 to S.F.L. S.F.L. and F.J.R. were supported by NIH Training Grant T32AG000057. S.F.L. was also supported by an American Federation for Aging Research Postdoctoral Fellowship. Additional support was provided by the University of Washington Healthy Aging and Longevity Research Institute, the University of Washington Nathan Shock Center of Excellence in the Basic Biology of Aging (NIH grant P30AG013280), and an award to M.K. from the M. J. Murdock Charitable Trust. D.L.M. is an Ellison Medical Foundation New Scholar in Aging and receives support from National Institute on Aging, NIH, R00AGA0033050. Additional data are available in the supplementary materials.

SUPPLEMENTARY MATERIALS

www.sciencemag.org/content/350/6266/1375/suppl/DC1
Materials and Methods
Figs. S1 to S14
Tables S1 to S3
References (*28*–*33*)

30 June 2015; accepted 3 November 2015
Published online 19 November 2015
10.1126/science.aac9257

SIGNAL TRANSDUCTION

Oscillatory stress stimulation uncovers an Achilles' heel of the yeast MAPK signaling network

Amir Mitchell,[1,2] Ping Wei,[1,3]* Wendell A. Lim[1,2,4]*

Cells must interpret environmental information that often changes over time. In our experiment, we systematically monitored the growth of yeast cells under various frequencies of oscillating osmotic stress. Growth was severely inhibited at a particular resonance frequency, at which cells show hyperactivated transcriptional stress responses. This behavior represents a sensory misperception: The cells incorrectly interpret oscillations as a staircase of ever-increasing osmolarity. The misperception results from the capacity of the osmolarity-sensing mitogen-activated protein kinase (MAPK) network to retrigger with sequential osmotic stresses. Although this feature is critical for coping with natural challenges, such as continually increasing osmolarity, it results in a trade-off of fragility to non-natural oscillatory inputs that match the retriggering time. These findings demonstrate the value of non-natural dynamic perturbations in exposing hidden sensitivities of cellular regulatory networks.

Cells have evolved complex signaling networks to monitor and respond to stimuli in their environment. As the cellular environment can dynamically change, evolution may select for sensory systems that are optimized for temporal patterns of stimulation that are frequently encountered by the organism. Such sensory systems may perform poorly when challenged by a non-natural stimulus pattern. Thus, exposing cells to time-variant inputs in controlled experiments can shed light on the mechanisms underlying cellular response, as well as the selection forces that shaped the biological system during evolution.

We systematically probed how the fitness of yeast cells responded to different dynamic patterns of osmotic stress. In *Saccharomyces cerevisiae*, the Hog1 mitogen-activated protein kinase (MAPK) pathway responds to increases in osmotic stress and ultimately leads to increased synthesis and retention of glycerol (*1*). Activation of the Hog1 MAPK is transient, even when osmotic stress persists (*2*). This adaptation allows cells to reset themselves and remain responsive to further increasing osmolarity that might occur with evaporation (*3*). Although MAPK signaling dynamics are well characterized, relatively little is known about the fitness of yeast cells when faced with different dynamic patterns of osmolarity.

We used time-lapse microscopy with single-cell resolution to monitor cell growth under dynamically controlled osmolarity profiles (Fig. 1A and supplementary materials and methods). Cells grown in microfluidic chambers were subjected to regular oscillations in osmolarity over a time span allowing for multiple rounds of cell division (amplitude range: 0 to 0.4 M KCl). We tracked colony growth when cells were exposed to continuous high osmolality (single-step increase) or to oscillations in osmolarity with a periodicity of 1, 8, or 32 min (Fig. 1B). Although the integrated osmolarity experienced by cells during these experiments was identical, cells grew considerably slower under the intermediate frequency of 8 min (movie S1). When tested under a wide range of oscillatory frequencies (0.5 to 128 min), cellular growth was drastically hampered in a

[1]Department of Cellular and Molecular Pharmacology, University of California, San Francisco (UCSF), San Francisco, CA 94158, USA. [2]Center for Systems and Synthetic Biology, UCSF, San Francisco, CA 94158, USA. [3]Center for Quantitative Biology, and Peking-Tsinghua Center for Life Sciences, Academy for Advanced Interdisciplinary Studies, School of Life Sciences, Peking University, Beijing 100871, China. [4]Howard Hughes Medical Institute (HHMI), UCSF, San Francisco, CA 94158, USA.
*Corresponding author. E-mail: lim@cmp.ucsf.edu (W.A.L.); pwei@pku.edu.cn (P.W.)

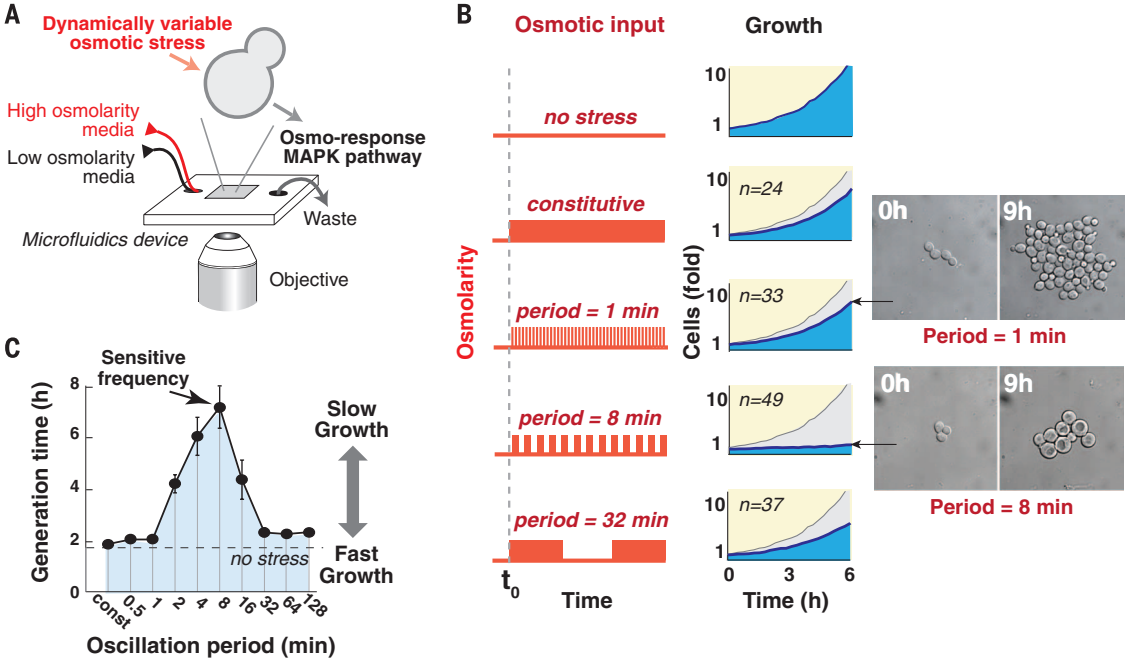

Fig. 1. Osmotic oscillations at an intermediate frequency cause slow proliferation. (**A**) Schematic of the flow chamber used in our experiment. (**B**) Cell growth under various frequencies of mild osmostress (0.4 M KCl). The graphs show the average number of progeny cells relative to the number of cells before stress is applied (*n* indicates the number of parental cells monitored). Growth without osmotic stress is depicted in gray. The insets at right show representative images of cells. (**C**) Systematic frequency scan of mild osmotic oscillations (0.4 M KCl). The graph shows the mean doubling time over a period of 8 hours. Each point marks the mean generation time calculated from at least 50 individual sets of progeny in two biological repeats. Error bars indicate SE.

Downloaded from www.sciencemag.org on December 14, 2015

narrow range of intermediate frequencies, with this inhibitory effect peaking at an 8-min resonance frequency (Fig. 1C). At this periodicity, cells were larger and contained large vacuoles (fig. S2).

To explore what cellular mechanisms might underlie the band-pass frequency selectivity of growth inhibition, we used a computational model developed to study the adaptive dynamics of yeast osmotic signaling (*3*) (Fig. 2A). Changes in the turgor pressure across the cell wall and membrane are sensed and culminate in phosphorylation of the MAPK Hog1. Phosphorylated Hog1 (Hog1-PP) regulates cytoplasmic proteins and gene expression, thus increasing internal glycerol concentrations and restoring turgor pressure. In response to a single-step osmotic shock, accumulation of Hog1-PP shows two phases: an induction phase that quickly peaks at 5 min, followed by slower adaptation within 30 min (Fig. 2B). However, if osmolarity stress is suddenly removed, Hog1-PP levels decrease almost immediately through action of protein phosphatases.

Because downstream changes in Hog1-PP–induced gene expression are expected to occur on a much slower time scale (hours) (*4*) as compared with MAPK adaptation (minutes), we can use the integral under the Hog1-PP curve as an approximation for the expected level of downstream transcriptional output (Fig. 2B). In response to a single-step increase in osmolarity, Hog1-PP shows a transient adaptive curve, and transcriptional output is expected to monotonically increase and reach a plateau once Hog1-PP returns to its basal level (protein levels will slowly decay afterward due to dilution and degradation). Similar downstream dynamics are not restricted to transcription but can manifest in any cellular activity that involves slow decay and hence acts as an integrator of MAPK signaling activity over time.

By tracking expected changes in osmotic stress–induced gene expression, this computational model can explain the stress sensitivity at the resonance frequency. We used the model to estimate response

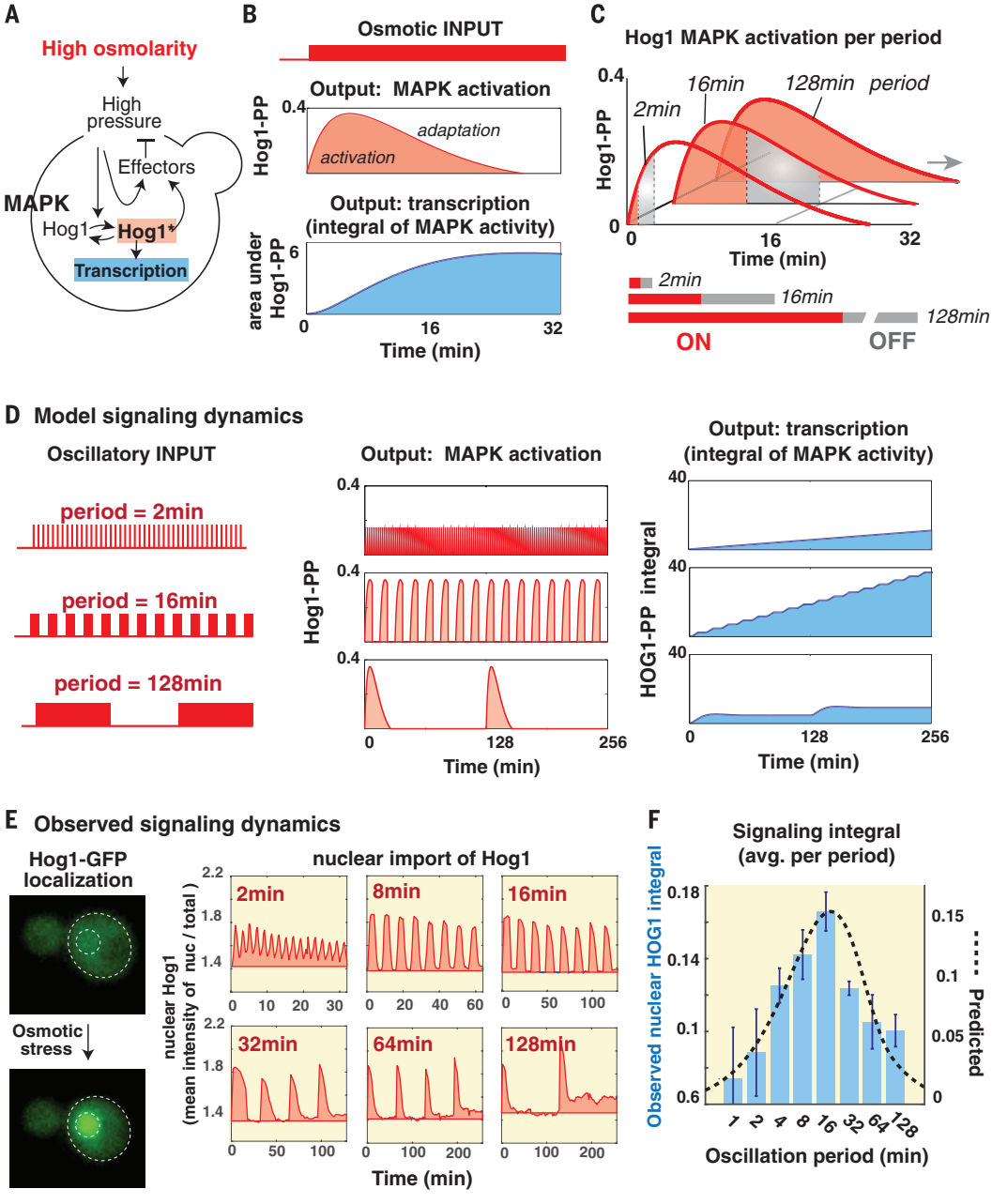

Fig. 2. Mathematical modeling of adaptive signaling of the osmotic pathway predicts downstream pathway hyperactivation at resonance stress frequency. (**A**) Schematic of the osmotic pathway (*3*). Changes in turgor pressure activate Hog1-dependent and Hog1-independent response arms that act to reduce deviation from the optimal turgor pressure. (**B**) Pathway activation according to the perfect-adaptation model (*3*). (Top) Predicted amounts of Hog1 phosphorylation in response to a 0.4 M increase in osmolality with induction and adaptation phases. (Bottom) Integral under the Hog1-PP curve, taken as an approximation of the accumulated transcriptional output. (**C**) Pathway activation at three representative pulse durations (ON and OFF intervals are marked in red and gray, respectively). The area under the predicted signaling curve (Top) was normalized to the entire pulse period (ON + OFF) (Bottom). (**D**) Model-predicted signaling and transcriptional dynamics under representative oscillation periods. (**E**) Experimentally observed signaling dynamics under representative oscillation periods, as measured by tracking Hog1-GFP nuclear localization. The graphs show the mean intensity ratio of nuclear Hog1-GFP over total Hog1-GFP in 40 to 100 cells (relative to the basal ratio at t = 0 min). (**F**) Measured signaling integral (normalized per minute) in a frequency scan. The blue bars show the average integral in two biological repeats (error bars indicate SD). The dashed black curve marks the model predictions.

dynamics for a cell exposed to a high-osmolarity pulse at three representative pulse durations (Fig. 2C). Under oscillations, the ON pulse is followed by an OFF pulse of the same length; therefore, the averaged transcriptional rate can be calculated from the integral under the signaling curve divided by the length of the full pulse period (ON + OFF duration). The model predicts that the normalized transcriptional output will maximize at an intermediate frequency of 16 min (as though the system contains a band-pass filter). The signaling dynamics have markedly different effects at different frequencies (Fig. 2D): Under a high-frequency stimulus, the signaling is terminated quickly, leading to very slow transcription. However, under an intermediate frequency, the signaling peaks in each oscillation. Because oscillations are still relatively frequent, signaling results in a high, ever-increasing transcriptional output. Under a low frequency, the signaling peaks and completely adapts. Yet because the encounters with stress are rare, this leads to a low overall transcriptional output. We experimentally tested this hypothesis by tracking Hog1–green fluorescent protein (GFP) localization under osmotic oscillations as a proxy for signaling dynamics (Hog1-GFP enters the nucleus when activated) (Fig. 2E). We observed a good agreement with the model predictions: The integral under the nuclear Hog1-GFP curve is maximized for an intermediate frequency of 16 min (Fig. 2F).

Thus, the model points to a plausible cellular mechanism: Adaptive signaling dynamics (the ability of the MAPK to reset and retrigger) may lead to downstream pathway hyperactivation at an intermediate resonance frequency. We used live-cell reporters (promoters linked to fluorescent proteins) to examine the transcriptional activity of the osmotic pathway and the intimately related invasive growth MAPK pathway that is triggered by starvation (Fig. 3A) (*5*, *6*). Note that despite sharing many common components, the individual pathways normally remain highly insulated from one another (*5*, *7*–*11*). Under a single-step osmotic stress, cells transiently induced the osmotic transcriptional response (peaking at 50-fold after 2 hours) (movie S1) with very little effect on the invasive-growth pathway (Fig. 3B). However, oscillatory osmolarity led to continuous induction of the osmotic response, culminating in pathway hyperactivation (450-fold increase after 8 hours) (movie S1). Moreover, the oscillations also led to full activation of the normally isolated invasive pathway (consistent with morphological changes observed for some cells) (fig. S2). A frequency scan showed that transcription of both pathways peaks at an intermediate frequency range (8 to 16 min) (Fig. 3C). The mating pathway, a third interwoven pathway, remains isolated (fig. S3) (*10*, *12*). Thus, stimulation at the resonance frequency led to hyperactivation of the osmotic response and misactivation of the invasive growth response (Fig. 3D).

To evaluate whether both osmotic hyperactivation and cross-talk with the invasive pathway

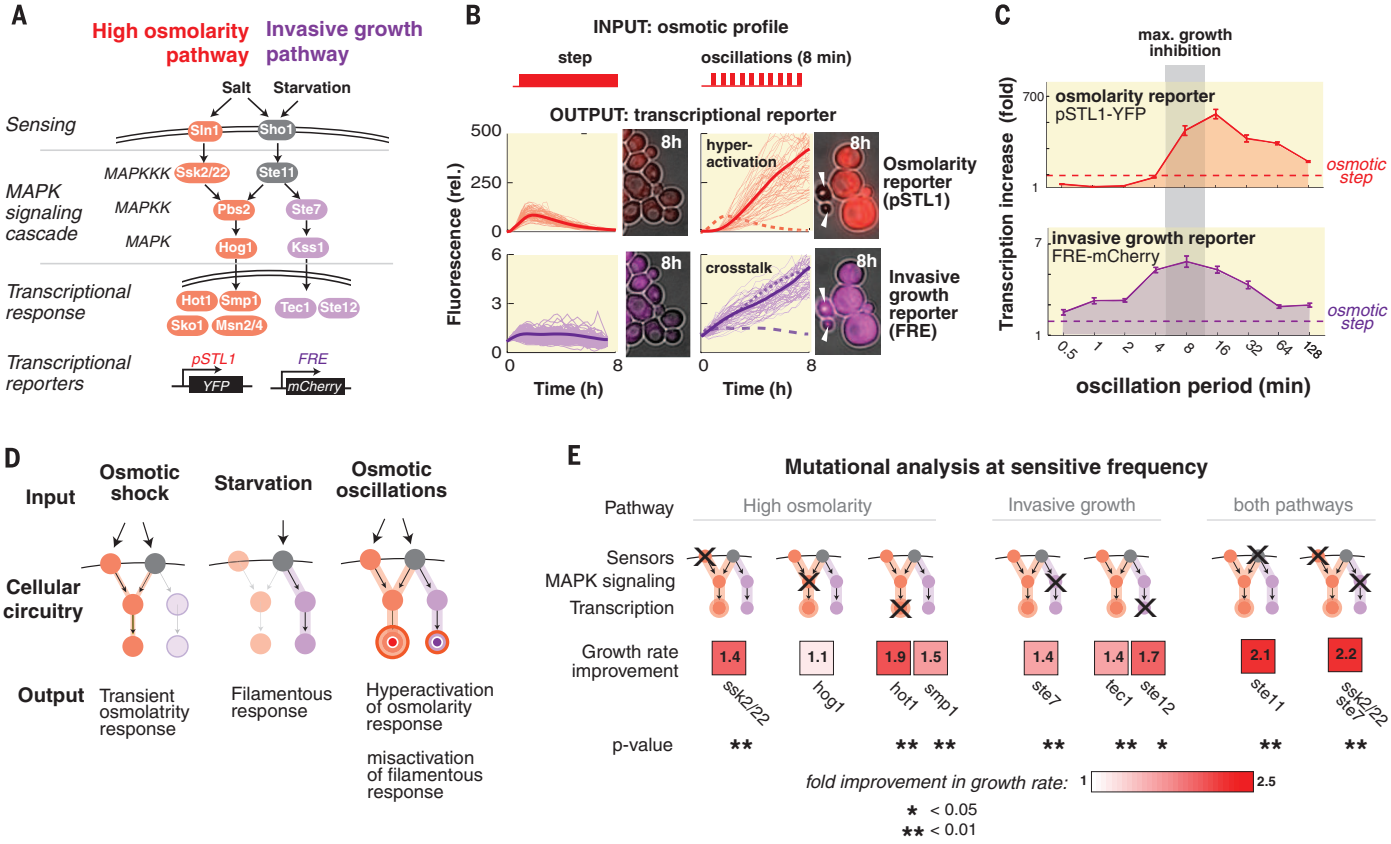

Fig. 3. Pathway hyperactivation and cross-talk underlie growth inhibition at the sensitive frequency. (**A**) Network diagram of the high-osmolality and invasive-growth pathways. YFP, yellow fluorescent protein. (**B**) Transcriptional output of the pathways in response to alternative inputs. The graphs show the mean fold induction in florescence per cell and the single-cell traces of cells within the interquartile range. The graph with the dotted purple line shows full pathway activation in response to butanol. Although pathway isolation is maintained under a step input profile, osmotic oscillations lead to hyperactivation of the osmotic response and full activation of the invasive-growth pathway. The microscopy images show representative cells 8 hours after their first exposure to stress. Arrowheads indicate cells that died during the stress period. (**C**) Transcriptional response at various frequencies of osmotic stress (0.4 M KCl). The activity of both reporters behaves as a band-pass filter, with peaked activity at intermediate frequencies (8 to 16 min). Error bars indicate SE of maximal fold fluorescence measured for 70 to 200 individual cells. (**D**) Frequency-dependent model of the MAPK network that explains growth inhibition at the resonance frequency. (**E**) Mutational analysis points to a contribution from both pathways in growth inhibition under osmotic oscillations (0.4 M, 8-min period). The color code marks the fold improvement of the deleted strain relative to the WT strain. Statistical significance was evaluated with the *t* test (comparing the mean growth rate of multiple progeny of the deleted strain and multiple progeny of the cocultured WT strain).

are detrimental to growth, we tested the phenotypes of specific mutations. We reasoned that deletions that weaken pathway activity might improve growth under oscillatory osmotic stress (Fig. 3E and fig. S5). Our measurements indicated that weakening the pathway by deletion of one of the osmosensing branches improved growth (complete knockout of the osmotic pathway did not improve growth because the core protective osmotic response is still necessary, even under oscillations). We also observed that knockout of invasive pathway genes is beneficial and that deletions targeting shared components in both pathways, such as Ste11 MAPK kinase kinase (*13*), are more advantageous than deletions targeting only one pathway.

Given the detrimental effects of pathway hyperactivation, we reasoned that an improved cascade could be engineered by adding a slow negative-feedback loop to the MAPK cascade. Ideally, this feedback would allow an initial osmotic response while dampening rapid retriggering (adding a longer refractory period). We implemented a feedback loop using OspF, a previously characterized bacterial effector protein that irreversibility inactivates phosphorylated Hog1 (*14*) (Fig. 4A). Monitoring the transcription in an engineered strain showed that the engineered pathway is still responsive to a single-step input but is not hyperactivated under oscillations (Fig. 4B and movie S2).

We then tested whether this network rewiring could improve growth under alternative dynamic stress inputs (Fig. 4C). Consistent with measurements of transcriptional activity, we observed that the engineered and wild-type (WT) strains had equal growth rates when exposed to a single step of osmotic stress but that the engineered negative-feedback strain grew considerably faster under osmotic oscillations. Nonetheless, when we compared strain growth under more natural types of dynamic stress profiles, we observed an opposite trend: Under a primed or gradually increasing osmolarity pattern, as may occur during evaporation of an aqueous niche, the WT strain grew faster. Thus, there is an inherent trade-off—our rewiring prevents detrimental pathway hyperactivation in response to oscillations but also leads to impaired growth in dynamic environments that truly require pathway reactivation (such as naturally occurring upward ramps of stress).

The detrimental sensitivity to osmotic oscillations can be viewed as an inherent limitation of the underlying biological system (Fig. 4D). In analogy to a sensory misperception phenomenon, the ability of oscillations to retrigger the osmotic response is misinterpreted by the cells as an infinite staircase increase in osmolality (*15*) that culminates in deleterious transcriptional hyperactivation. Thus, although the adaptive response allows the biological system to remain responsive in complex environments that it experiences in nature, it also creates an inherent "Achilles' heel" due to its failure to prevent pathway hyperactivation in non-natural oscillating environments. From an evolutionary perspective, this Achilles' heel is unimportant because the yeast are unlikely to experience oscillatory stress at the resonant frequency.

Our observations in yeast may have implications for the dynamic sensitivities of other biological systems, as many responses display adaptation or the ability to retrigger (*16*), and these may also have resonance frequency sensitivities. Our results may additionally be relevant for cellular signaling in disease, as mutations affecting cellular signaling are common in cancer, autoimmune disease, and diabetes. These mutations may rewire the native network and thus could modify its activation and adaptation dynamics. Such network rewiring in disease may lead to changes that can be most clearly revealed by simulation with oscillatory inputs or other non-natural patterns. The changes in network response behaviors could be exploited for diagnosis and functional profiling of disease cells or could potentially be taken advantage of as an Achilles' heel to

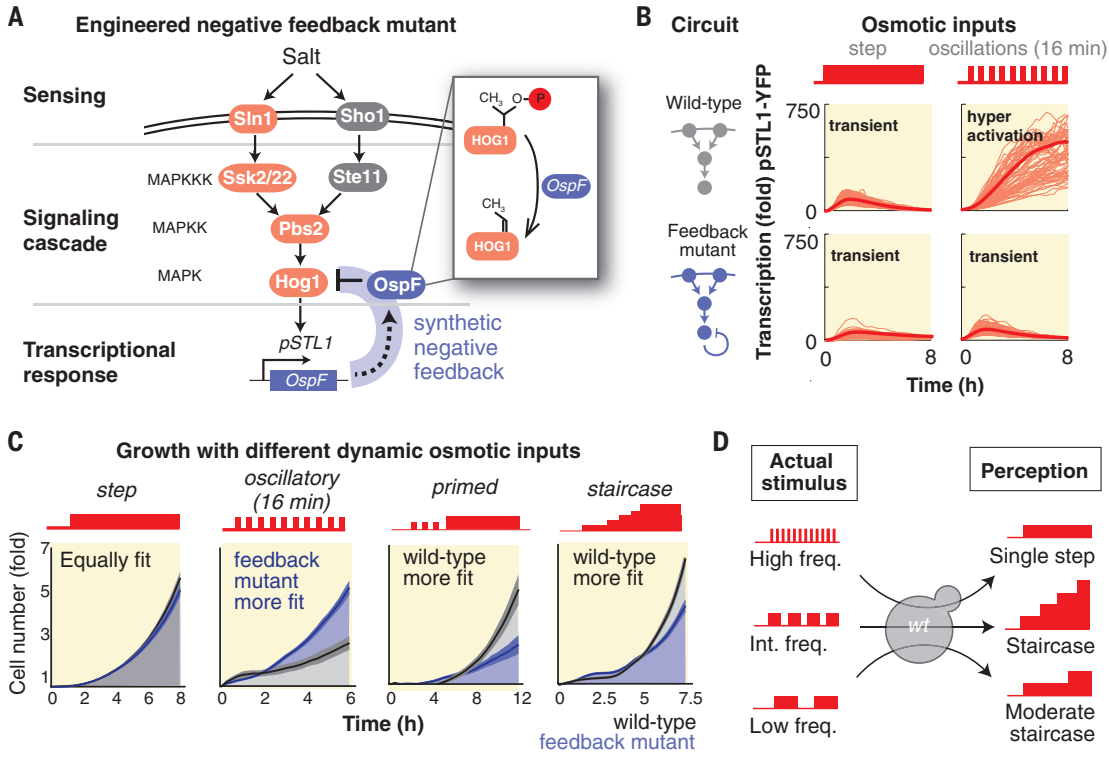

Fig. 4. Introducing a synthetic feedback loop resolves osmotic hyperactivation and relieves growth inhibition under osmotic oscillations but also reduces proliferation under more natural input dynamics. (**A**) Diagram of the genetic circuit that underlies the conditional negative feedback. The bacterial effector OspF (fused to an osmotic stress–responsive promoter) deactivates phosphorylated Hog1 by removing a hydroxyl group (*14*), leading to a longer delay in retriggering of the pathway. (**B**) Transcriptional response of the osmotic pathway in the WT strain and engineered strain. Both strains show a transient response after an osmotic shock but respond differently to an oscillating input. The graphs show the mean fold induction in florescence per cell and the single-cell traces of cells within the interquartile range. (**C**) Comparative growth assays of the WT and engineered strains under alternative inputs. (**D**) Growth inhibition under oscillatory input originates from the adaptive nature of the osmotic response. Although the signaling cascade effectively filters oscillatory inputs at a high frequency (*15*), oscillations at a lower frequency lead to repeated stimulation of the osmotic pathway. In this frequency range, the cascade circuitry perceives an oscillatory input as gradually increasing osmolarity and hence keeps the osmotic pathway continuously active to counteract the seemingly increasing high osmolality. Growth inhibition is maximized at an intermediate frequency because it is interpreted as the steepest stepwise (i.e., staircase) increase in osmolality, which leads to peaked levels of downstream hyperactivation.

selectively target cells bearing the diseased network (*17*).

REFERENCES AND NOTES

1. H. Saito, F. Posas, *Genetics* **192**, 289–318 (2012).
2. J. L. Brewster, T. de Valoir, N. D. Dwyer, E. Winter, M. C. Gustin, *Science* **259**, 1760–1763 (1993).
3. D. Muzzey, C. A. Gómez-Uribe, J. T. Mettetal, A. van Oudenaarden, *Cell* **138**, 160–171 (2009).
4. U. Alon, *An Introduction to Systems Biology: Design Principles of Biological Circuits* (Chapman & Hall/CRC, 2006).
5. H. D. Madhani, G. R. Fink, *Science* **275**, 1314–1317 (1997).
6. K. Furukawa, S. Hohmann, *Mol. Microbiol.* **88**, 5–19 (2013).
7. M. C. Good, J. G. Zalatan, W. A. Lim, *Science* **332**, 680–686 (2011).
8. M. Good, G. Tang, J. Singleton, A. Reményi, W. A. Lim, *Cell* **136**, 1085–1097 (2009).
9. H. D. Madhani, C. A. Styles, G. R. Fink, *Cell* **91**, 673–684 (1997).
10. S. M. O'Rourke, I. Herskowitz, *Genes Dev.* **12**, 2874–2886 (1998).
11. E. A. Elion, *J. Cell Sci.* **114**, 3967–3978 (2001).
12. J. G. Zalatan, S. M. Coyle, S. Rajan, S. S. Sidhu, W. A. Lim, *Science* **337**, 1218–1222 (2012).
13. F. Posas, H. Saito, *Science* **276**, 1702–1705 (1997).
14. P. Wei *et al*., *Nature* **488**, 384–388 (2012).
15. P. Hersen, M. N. McClean, L. Mahadevan, S. Ramanathan, *Proc. Natl. Acad. Sci. U.S.A.* **105**, 7165–7170 (2008).
16. J. E. Purvis, G. Lahav, *Cell* **152**, 945–956 (2013).
17. M. Behar, D. Barken, S. L. Werner, A. Hoffmann, *Cell* **155**, 448–461 (2013).

ACKNOWLEDGMENTS

We thank H. Youk, R. Almeida, S. Coyle, and M. Thomson for insightful discussions. This work was supported by NIH grants R01 GM55040, R01 GM62583, PN2 EY016546, and P50 GM081879; the NSF Synthetic Biology Engineering Research Center (SynBERC); and HHMI (to W.A.L.). This work was also supported in part by MOST grant 2015CB910300, National Natural Science Foundation of China grant 31470819, and Peking-Tsinghua Center for Life Sciences (to P.W.). A.M. is a European Molecular Biology Organization Fellow (ALTF 419-2010) and the recipient of a Program for Breakthrough Biomedical Research Postdoctoral Research Award (UCSF).

SUPPLEMENTARY MATERIALS

www.sciencemag.org/content/350/6266/1379/suppl/DC1
Materials and Methods
Figs. S1 to S5
Tables S1 and S2
References (*18*, *19*)
Movies S1 and S2

10 March 2015; accepted 8 November 2015
Published online 19 November 2015
10.1126/science.aab0892

TRANSCRIPTION

RNA polymerase II–associated factor 1 regulates the release and phosphorylation of paused RNA polymerase II

Ming Yu,[1]* Wenjing Yang,[2]* Ting Ni,[3] Zhanyun Tang,[1] Tomoyoshi Nakadai,[1] Jun Zhu,[2] Robert G. Roeder[1]†

Release of promoter-proximal paused RNA polymerase II (Pol II) during early elongation is a critical step in transcriptional regulation in metazoan cells. Paused Pol II release is thought to require the kinase activity of cyclin-dependent kinase 9 (CDK9) for the phosphorylation of DRB sensitivity–inducing factor, negative elongation factor, and C-terminal domain (CTD) serine-2 of Pol II. We found that Pol II–associated factor 1 (PAF1) is a critical regulator of paused Pol II release, that positive transcription elongation factor b (P-TEFb) directly regulates the initial recruitment of PAF1 complex (PAF1C) to genes, and that the subsequent recruitment of CDK12 is dependent on PAF1C. These findings reveal cooperativity among P-TEFb, PAF1C, and CDK12 in pausing release and Pol II CTD phosphorylation.

Thousands of developmentally regulated genes in metazoans harbor promoter-proximal paused RNA polymerase II (Pol II) 30 to 50 nucleotides downstream of their transcription start sites (TSS) (*1*–*3*). Paused Pol IIs are usually phosphorylated on C-terminal domain (CTD) Ser^5 and are associated with 5,6-dichloro-1-β-D-ribofuranosylbenzimidazole (DRB) sensitivity–inducing factor (DSIF) and negative elongation factor (NELF). Release of paused Pol II into productive elongation is believed to require phosphorylation of CTD Ser^2, conversion of DSIF into a positive elongation factor by phosphorylation of its SPT5 subunit, and disassociation of NELF (*1*). Although it was long believed that CTD Ser^2 phosphorylation was catalyzed predominantly by cyclin-dependent kinase 9 (CDK9), the mammalian ortholog of yeast Bur1, recent studies have identified CDK12 as the metazoan ortholog of Ctk1, the major CTD Ser^2 kinase in yeast, and suggested that CDK9 is a CTD Ser^5 kinase (*4*, *5*). The yeast Paf1 complex and the human PAF1 complex, of interest here, have been implicated in transcription elongation on DNA and chromatin templates, recruitment and activation of histone modifiers, mRNA 3′ formation, etc. (*6*, *7*). However, PAF1C has not been considered a critical elongation factor because depletions of PAF1C subunits in yeast and fly, while reducing the level of CTD Ser^2-phosphorylated elongating Pol II (*8*, *9*), did not affect the distribution of total Pol II on active genes (*8*, *10*).

To study the function of human PAF1C, we performed chromatin immunoprecipitation sequencing (ChIP-seq) experiments for PAF1C subunits PAF1, CDC73, LEO1, and CTR9, as well as total Pol II and CTD Ser^2-phosphorylated Pol II [Pol II (ser-2p)], in human acute myeloid leukemia THP1 cells. Similar to Pol II (ser-2p), the four PAF1C subunits occupied transcribed regions of most active genes and exhibited maximum occupancy downstream of transcription end sites (TESs) (Fig. 1, A to C, and fig. S1, A to F). LEO1 (fig. S1B) and CTR9 (fig. S1C) occupancies did not generally overlap with the promoter-proximal Pol II peaks, as reported previously (*2*). However, PAF1 and CDC73, the major scaffolding components within human PAF1C (*11*), did overlap with the promoter-proximal Pol II peaks (Fig. 1, B and C, and fig. S1, A, D, E, and F). Complementary strand-specific mRNA-seq analyses using RNA from THP1 cells identified 19,481 transcripts [reads per kilobase of transcript per million mapped reads (RPKM) > 1], corresponding to 10,664 genes, of which 9823 were bound by PAF1. Notably, the PAF1 binding signals on these genes positively correlated with corresponding mRNA levels (Fig. 1C and fig. S1, A to C), suggesting an involvement of PAF1C in Pol II transcription or transcription-coupled events.

In further functional analyses, we used two lentiviral short hairpin RNAs (shRNA #1 and shRNA #2, targeting different regions of the *PAF1*mRNA) to reduce the level of the key PAF1 subunit (*8*, *11*) in THP1 cells (Fig. 2A) and assessed global gene expression changes by RNA-seq. With false discovery rate < 0.01 and considering only relative expression change by a factor of >1.5, of the 9823 genes bound by PAF1, only 1351 showed changes in expression (table S1). The knockdown of PAF1 also resulted in an increased level of promoter-proximal paused Pol II that was not limited to genes whose mRNA levels were affected by PAF1 knockdown (Fig. 2, B and C). Considering only genes with a normalized promoter read count change of >2, 5851 exhibited increased Pol II pausing and only 344 exhibited

[1]Laboratory of Biochemistry and Molecular Biology, The Rockefeller University, New York, NY 10065, USA. [2]Systems Biology Center, National Heart, Lung, and Blood Institute, Bethesda, MD 20892, USA. [3]State Key Laboratory of Genetic Engineering and Ministry of Education Key Laboratory of Contemporary Anthropology, Collaborative Innovation Center of Genetics and Development, School of Life Sciences, Fudan University, Shanghai 200438, P.R. China.
*These authors contributed equally to this work. †Corresponding author. E-mail: roeder@rockefeller.edu

decreased Pol II pausing (table S2). The increased Pol II pausing, which led to an average factor of 2 increase in Pol II occupancy on promoters (Fig. 2C), was confirmed by comparison of the traveling ratio of total Pol II in control and knockdown cells (Fig. 2D).

The apparent and seemingly paradoxical increase of PAF1 occupancy near promoters in PAF1 knockdown cells relative to control cells (Fig. 2B) raised the possibility that the increased Pol II pausing might not be a direct effect of the decreased PAF1 chromatin association. However, normalization of the PAF1 levels to Pol II levels in control and knockdown cells revealed a relative decrease in PAF1 chromatin association in knockdown cells, suggesting that the increased Pol II pausing is indeed a direct effect of reduced PAF1 association at the promoter-proximal region (Fig. 2E). In a further validation of the ChIP-seq results for total Pol II, ChIP-seq for CTD Ser^5-phosphorylated Pol II revealed, as expected, a corresponding increase in Pol II (ser-5p) in PAF1 knockdown cells relative to control cells (Fig. 2F and fig. S2, A and B). Thus, PAF1C is a critical elongation factor that regulates elongation as early as the Pol II pausing release step.

To determine whether the facilitation of Pol II pausing release by PAF1C reflects a general mechanism that is not cell type–specific, we knocked down PAF1 (by shRNA #2) in human acute lymphoblastic leukemia CCRF-CEM cells and compared PAF1 and Pol II occupancies in control and knockdown cells. Surprisingly, and in contrast to the results in THP1 cells, PAF1 knockdown in these cells resulted in an increase in Pol II pausing on only 142 genes and a decrease in Pol II pausing on 1244 genes (fig. S3, A to E, and table S3). To rule out any off-target effects, the results were validated by PAF1 knockdown using shRNA #1 (fig. S3, F and G). With respect to the apparent cell-dependent or context-dependent variability in effects of PAF1C functions, we note that whereas PAF1C is generally considered a positive effector (*6*, *7*), there are earlier (*12*) and more recent (*13*) reports of PAF1C function as a negative regulator of Pol II pausing release. Therefore, the differential effects of PAF1 knockdown on Pol II pausing in THP1 cells (carrying the *MLL-AF9* fusion gene) and CCRF-CEM cells (bearing *TP53* mutations) likely reflect the distinct genetic backgrounds and physiological states of the two cell types. Thus, the diverse results in current and published studies (*12*, *13*) indicate variable context-dependent effects of PAF1C components as either positive or negative regulators, as further exemplified by a switch in the CDC73 subunit from a positive regulator (oncoprotein) to a negative regulator (tumor suppressor) by tyrosine phosphorylation (*14*).

The effect of PAF1 knockdown on Pol II pausing resembles that of pan-CDK inhibition by flavopiridol (*2*, *15*). To determine whether flavopiridol treatment affects Pol II pausing in part through PAF1C, we compared the genomic occupancy of Pol II and the LEO1 subunit of PAF1C in dimethyl sulfoxide (DMSO)– and flavopiridol-treated THP1 cells. Flavopiridol significantly increased global Pol II pausing (Fig. 2G) and markedly reduced the chromatin occupancy of LEO1 (Fig. 2H and fig. S4, A to B). These results implicate PAF1C as a key factor for the release of promoter-proxmal paused Pol II. The reduced occupancy of PAF1C as a result of flavopiridol treatment suggests that pan-CDK inhibition increases Pol II pausing in part through compromising the recruitment of PAF1C.

In yeast, Ser^2 and Ser^5 phosphorylation of the Pol II CTD, as well as phosphorylation of the Spt5 subunit of DSIF by Bur1 (ortholog of metazoan CDK9), are critical for the recruitment of PAF1C to target genes (*16*, *17*). To determine whether, as in yeast, CDK9 or SPT5 is required for the recruitment of PAF1C in THP1 cells, we performed independent SPT5 and CDK9 knockdown

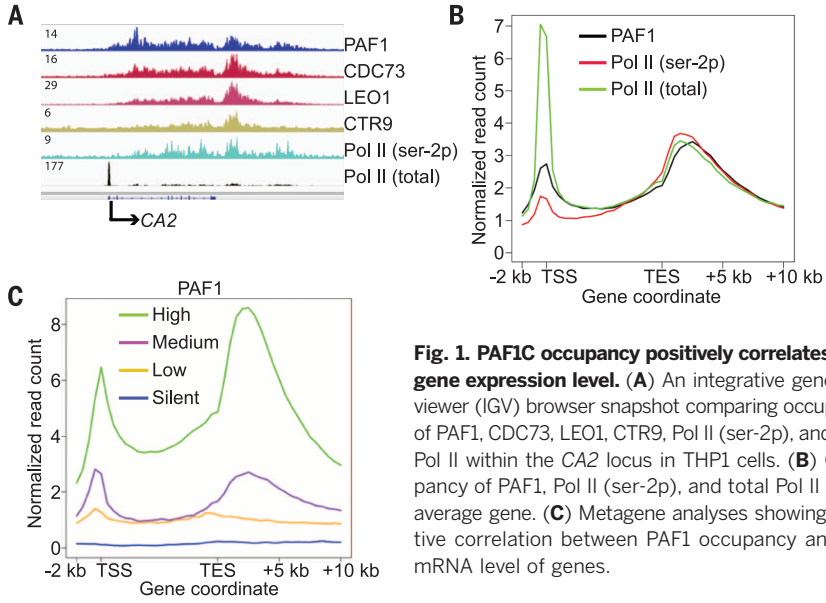

Fig. 1. PAF1C occupancy positively correlates with gene expression level. (**A**) An integrative genomics viewer (IGV) browser snapshot comparing occupancy of PAF1, CDC73, LEO1, CTR9, Pol II (ser-2p), and total Pol II within the *CA2* locus in THP1 cells. (**B**) Occupancy of PAF1, Pol II (ser-2p), and total Pol II on an average gene. (**C**) Metagene analyses showing positive correlation between PAF1 occupancy and the mRNA level of genes.

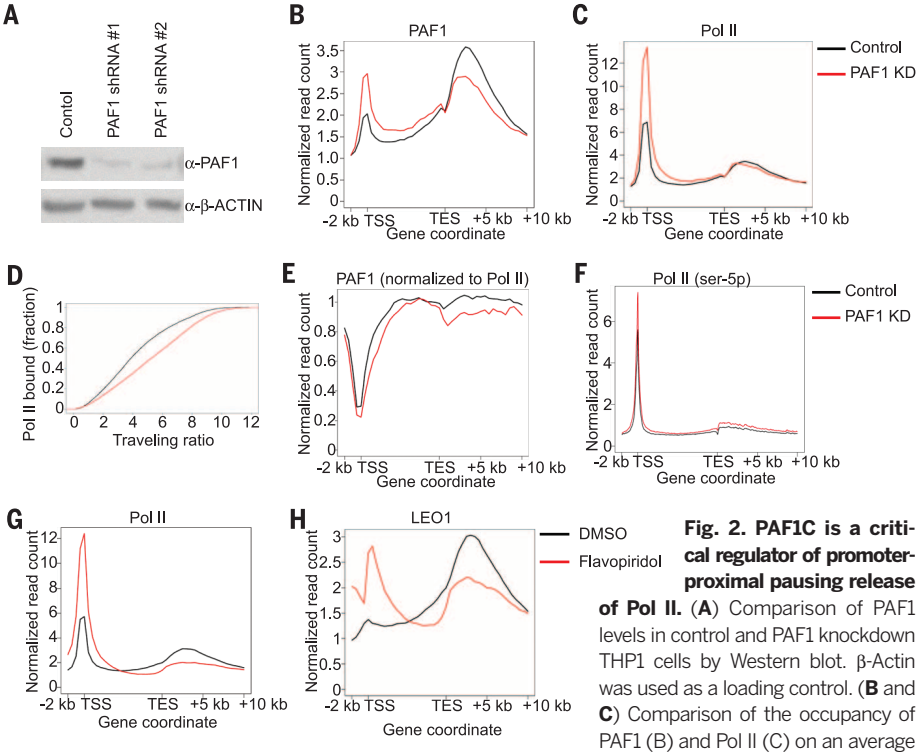

Fig. 2. PAF1C is a critical regulator of promoter-proximal pausing release of Pol II. (**A**) Comparison of PAF1 levels in control and PAF1 knockdown THP1 cells by Western blot. β-Actin was used as a loading control. (**B** and **C**) Comparison of the occupancy of PAF1 (B) and Pol II (C) on an average gene. (**D**) Comparison of the traveling ratios of genes bound by Pol II. (**E**) Comparison of the normalized occupancy of PAF1 on an average gene. (**F**) Comparison of the occupancy of Pol II (ser-5p) on an average gene. (**G** and **H**) Comparison of the occupancy of Pol II (G) and LEO1 (H) on an average gene in DMSO- and flavopiridol-treated THP1 cells.

analyses and evaluated the effects on Pol II and PAF1 occupancy. As anticipated (*2*), SPT5 knockdown reduced the occupancy of Pol II and PAF1 (fig. S5, A to D). Like flavopiridol treatment, CDK9 knockdown (~80%; Fig. 3, A and B) reduced PAF1 occupancy (Fig. 3C) but, unlike flavopiridol, had little effect on Pol II occupancy (Fig. 3D). In addition, and unexpectedly, CDK9 knockdown minimally increased global Pol II pausing (fig. S6A). However, a comparison of the levels of BRD4-associated CDK9 (CDK9-active complex) and LARP7-associated CDK9 [CDK9-inactive 7SK small nuclear ribonucleic protein (snRNP) complex] (*18*) in control and CDK9 knockdown THP1 cells revealed a preferential reduction of the CDK9 fraction in the 7SK snRNP complex relative to the CDK9 fraction in the BRD4 complex (fig. S6B). Thus, the minimal effect of the CDK9 knockdown on Pol II pausing may be due to the minimal effect on the kinase-active CDK9 fraction, and if that is the case, the regulation of PAF1C recruitment by CDK9 is likely independent of the CDK9 kinase activity.

In a further analysis of the role of CDK9 in PAF1C recruitment, a coimmunoprecipitation assay revealed strong association of endogenous PAF1 and P-TEFb (a complex of CDK9 and cyclin T1) in THP1 cells (Fig. 3E). The much stronger association between PAF1C and P-TEFb relative to the reported (*19*) PAF1-AF9 interaction (Fig. 3E) raised the possibility of an AF9-independent interaction between these two complexes. The PAF1 and CDC73 subunits of PAF1C, as well as Pol II, were reciprocally coimmunoprecipitated with CDK9 by a CDK9 antibody (Fig. 3F). More important, binding assays using purified P-TEFb and PAF1C complexes established a direct AF9-independent interaction between these two complexes (Fig. 3G), indicating that P-TEFb contributes to the recruitment of PAF1C through direct interaction.

These results raised the possibility that PAF1C may regulate promoter-proximal pausing release of Pol II in part by facilitation of P-TEFb extraction from 7SK snRNP. However, PAF1C was unable to release P-TEFb from 7SK snRNP in a release assay (fig. S7). To further analyze the functional consequences of the PAF1C-CDK9 interaction, we conducted ChIP-seq experiments for CDK9 in control and PAF1 knockdown cells. These revealed that (i) CDK9 is mainly associated with both enhancers and promoters (Fig. 3, H and I) (*20*, *21*), and (ii) PAF1 depletion reduces normalized CDK9 occupancy on promoters (Fig. 3, J and K), consistent with a previous report (*19*). The enhancer and promoter association of CDK9, along with Pol II imaging data (*21*), makes it less likely, as proposed in another study (*13*), that P-TEFb generally travels with Pol II during elongation. Therefore, we propose that (i) the interaction between PAF1C and P-TEFb is required mainly for the initial recruitment of PAF1C but may also stabilize the P-TEFb promoter association, and (ii) CDK9 and other kinases subsequently phosphorylate the CTD of Pol II (*16*) and the CTR of SPT5 (*17*), thus creating PAF1C binding sites on Pol II and the associated DSIF that enable PAF1C to facilitate release of paused Pol II into productive elongation.

In agreement with previous studies (*8*, *9*), we observed decreased Pol II CTD Ser^2 phosphorylation but increased CTD Ser^5 phosphorylation after PAF1 knockdown (fig. S8, A to C). Thus, PAF1C may be responsible either for the recruitment of CTD Ser^2 kinases or for the regulation of their activity. Recent studies have suggested that CDK12 is the predominant Ser^2 kinase (*4*) and that bromodomain-containing protein 4 (BRD4)

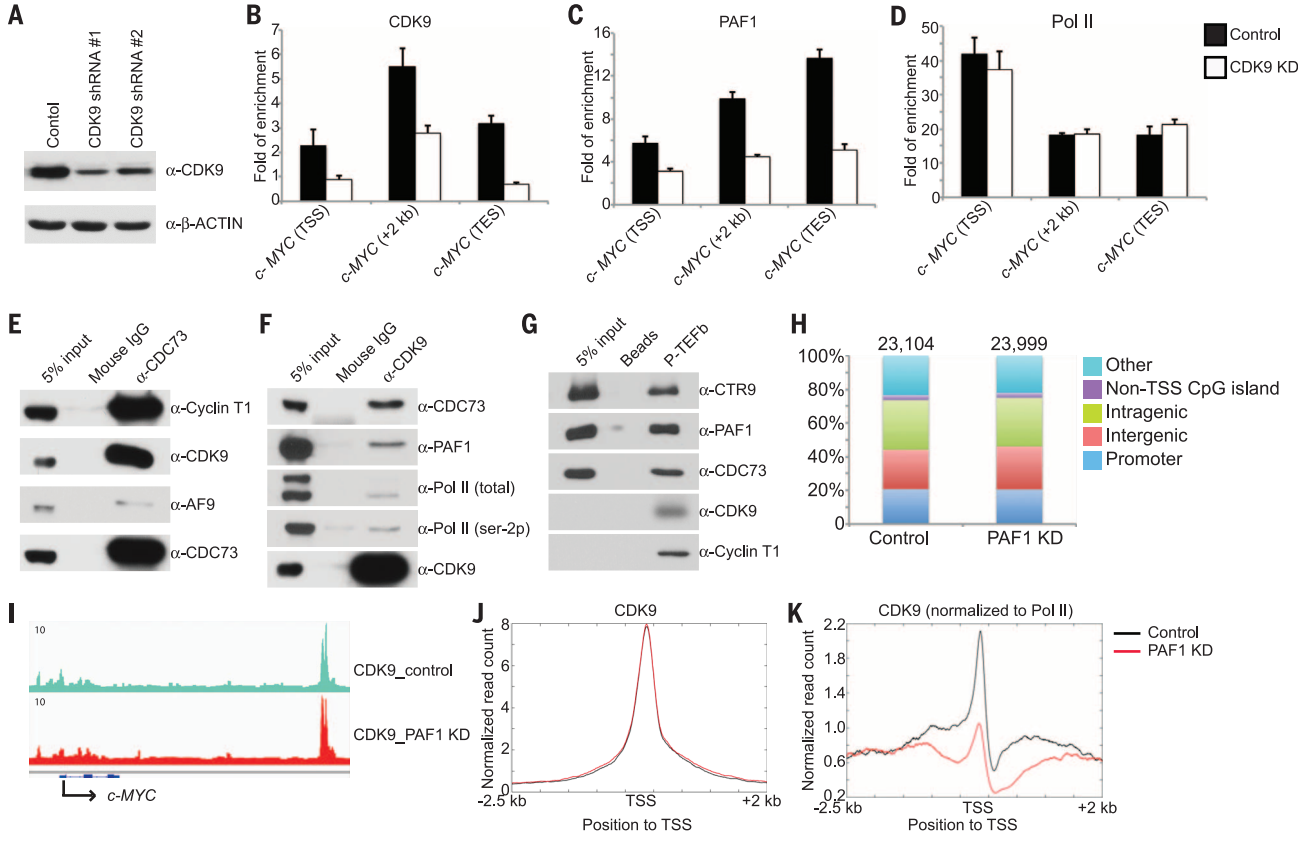

Fig. 3. P-TEFb contributes to the recruitment of PAF1C. (**A**) Comparison of CDK9 levels in control and CDK9 knockdown THP1 cells. (**B** to **D**) ChIP-qPCR data comparing the occupancy of CDK9 (B), PAF1 (C), and Pol II (D). Error bars indicate SD ($N = 3$). (**E**) Coimmunoprecipitation of P-TEFb and AF9 with CDC73. (**F**) Coimmunoprecipitation of PAF1, CDC73, total Pol II, and Pol II (ser-2p) with CDK9. (**G**) Pulldown assay using immobilized P-TEFb as bait and PAF1C as prey. (**H**) CDK9 peak distribution in control and PAF1 knockdown cells. Total peak numbers are shown at the top of each column. (**I**) An IGV browser snapshot comparing CDK9 occupancy within the *c-MYC* locus. (**J** and **K**) Comparison of CDK9 occupancy (J) and normalized CDK9 occupancy (K) on an average gene, respectively.

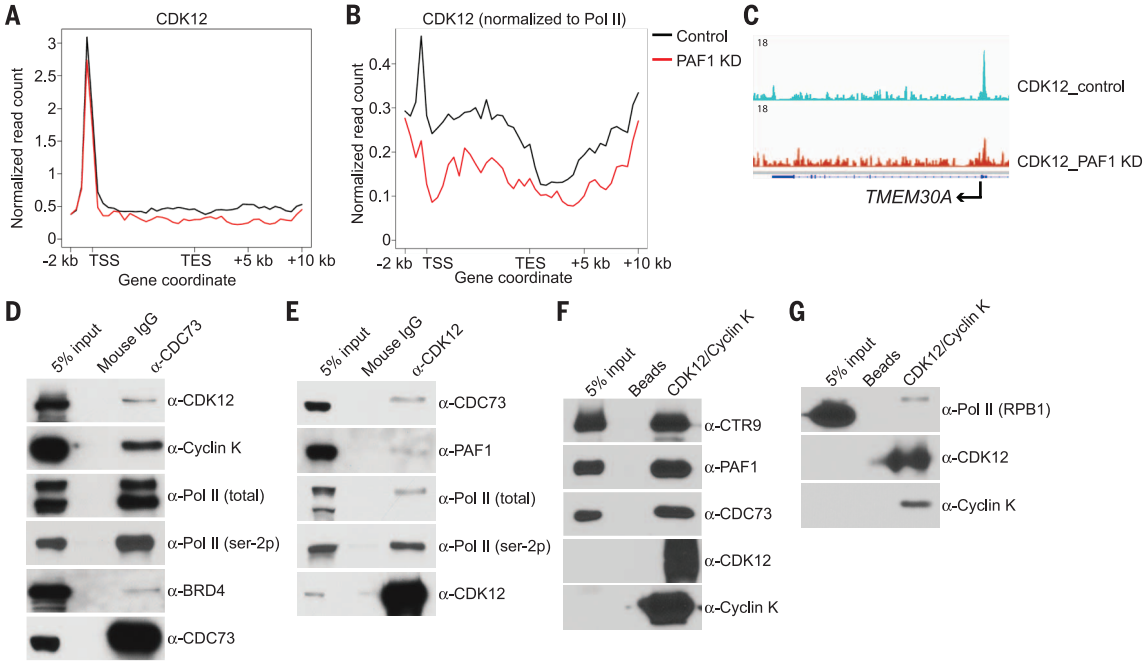

Fig. 4. PAF1C is responsible for the recruitment of CDK12. (**A** and **B**) Comparison of CDK12 occupancy (A) and normalized CDK12 occupancy (B) on an average gene in control and PAF1 knockdown THP1 cells, respectively. (**C**) An IGV browser snapshot comparing CDK12 occupancy within the *TMEM30A* locus. (**D**) Coimmunoprecipitation of CDK12, cyclin K, total Pol II, Pol II (ser-2p), and BRD4 with CDC73. (**E**) Coimmunoprecipitation of PAF1, CDC73, total Pol II, and Pol II (ser-2p) with CDK12. (**F** and **G**) Pulldown assays using immobilized CDK12–cyclin K complex as bait, and PAF1C (F) and purified Pol II (G) as prey, respectively.

is an atypical CTD Ser^2 kinase (*22*). A comparison of CDK12 and BRD4 occupancies on the *c-MYC* gene by ChIP-qPCR (quantitative polymerase chain reaction) revealed reduced occupancy of CDK12, but not BRD4, in PAF1 knockdown cells (fig. S9, A and B). Genomic analysis of the effect of PAF1C on CDK12 recruitment revealed a global decrease in CDK12 occupancy, especially when normalized to Pol II occupancy, in PAF1 knockdown cells (Fig. 4, A to C). These results are consistent with the reduced level of Pol II (ser-2p) and suggest a role for PAF1C-dependent recruitment of CDK12 in Pol II CTD Ser^2 phosphorylation.

Experiments to determine whether the PAF1C-dependent recruitment of CDK12 is through a direct interaction showed that CDK12 and cyclin K, as well as Pol II and BRD4, were coimmunoprecipitated with an antibody to the CDC73 subunit of PAF1C (Fig. 4D) and, reciprocally, that the PAF1 and CDC73 subunits of PAF1C, as well as Pol II, were coimmunoprecipitated with CDK12–cyclin K by an antibody to CDK12 (Fig. 4E). The PAF1C association with BRD4 was significantly weaker than its association with CDK12 (Fig. 4D), partially explaining why the recruitment of BRD4 is less dependent on PAF1C (fig. S9B). Analyses with purified recombinant CDK12–cyclin K and PAF1C complexes revealed a robust direct binding of PAF1C to CDK12–cyclin K under stringent conditions (Fig. 4F). A parallel binding assay with purified proteins under similar conditions revealed a very weak interaction of CDK12–cyclin K with Pol II (Fig. 4G) relative to the strong interaction with PAF1C (Fig. 4F). These results strongly suggest that (i) PAF1C, in addition to regulating the release of paused Pol II, is directly involved in the recruitment of CDK12, and (ii) along with the known interaction of human PAF1C with Pol II (*11*), the association of CDK12–cyclin K with Pol II is likely mediated by Pol II–bound PAF1C.

We next investigated whether CDK12–cyclin K affects the recruitment of PAF1C by comparing PAF1 and Pol II occupancy in control and cyclin K knockdown cells. Despite effecting a globally decreased Pol II (ser-2p) (fig. S8A) and reduced CDK12 occupancy, cyclin K knockdown had little effect on PAF1 or Pol II occupancy (fig. S10, A to D). These results, which agree with published data showing that a knockout of yeast Ctk1 (ortholog of CDK12) does not affect Paf1 occupancy (*23*), support a model in which Pol II–bound PAF1C recruits CDK12.

Our results indicate a critical role for PAF1C in Pol II pausing release, a direct role for P-TEFb in PAF1C recruitment, and a PAF1C-CDK12–cyclin K interaction that is important for CTD Ser^2 phosphorylation. These findings complement and extend previous results demonstrating functions for P-TEFb, DSIF/NELF, and Pol II CTD Ser^2 phosphorylation in Pol II pausing release and are summarized in an updated model (fig. S11) that will guide further mechanistic studies of both positive and negative functions of PAF1C in transcriptional control.

REFERENCES AND NOTES

1. K. Adelman, J. T. Lis, *Nat. Rev. Genet.* **13**, 720–731 (2012).
2. P. B. Rahl *et al.*, *Cell* **141**, 432–445 (2010).
3. L. J. Core, J. J. Waterfall, J. T. Lis, *Science* **322**, 1845–1848 (2008).
4. B. Bartkowiak *et al.*, *Genes Dev.* **24**, 2303–2316 (2010).
5. N. Czudnochowski, C. A. Bösken, M. Geyer, *Nat. Commun.* **3**, 842 (2012).
6. B. N. Tomson, K. M. Arndt, *Biochim. Biophys. Acta* **1829**, 116–126 (2013).
7. J. A. Jaehning, *Biochim. Biophys. Acta* **1799**, 379–388 (2010).
8. C. L. Mueller, S. E. Porter, M. G. Hoffman, J. A. Jaehning, *Mol. Cell* **14**, 447–456 (2004).
9. K. Nordick, M. G. Hoffman, J. L. Betz, J. A. Jaehning, *Eukaryot. Cell* **7**, 1158–1167 (2008).
10. K. Adelman *et al.*, *Mol. Cell. Biol.* **26**, 250–260 (2006).
11. J. Kim, M. Guermah, R. G. Roeder, *Cell* **140**, 491–503 (2010).
12. X. Bai *et al.*, *Cell* **142**, 133–143 (2010).
13. F. X. Chen *et al.*, *Cell* **162**, 1003–1015 (2015).
14. A. Takahashi *et al.*, *Mol. Cell* **43**, 45–56 (2011).
15. I. Jonkers, H. Kwak, J. T. Lis, *eLife* **3**, e02407 (2014).
16. H. Qiu, C. Hu, N. A. Gaur, A. G. Hinnebusch, *EMBO J.* **31**, 3494–3505 (2012).
17. Y. Liu *et al.*, *Mol. Cell. Biol.* **29**, 4852–4863 (2009).
18. B. M. Peterlin, D. H. Price, *Mol. Cell* **23**, 297–305 (2006).
19. N. He *et al.*, *Proc. Natl. Acad. Sci. U.S.A.* **108**, E636–E645 (2011).
20. J. Lovén *et al.*, *Cell* **153**, 320–334 (2013).
21. A. Ghamari *et al.*, *Genes Dev.* **27**, 767–777 (2013).
22. B. N. Devaiah *et al.*, *Proc. Natl. Acad. Sci. U.S.A.* **109**, 6927–6932 (2012).
23. S. H. Ahn, M. Kim, S. Buratowski, *Mol. Cell* **13**, 67–76 (2004).

ACKNOWLEDGMENTS

We thank G. Morin for providing the cyclin K cDNA, and S. Malik, S. Murphy, and M. Guermah for critical reading of the manuscript. Supported by a Leukemia and Lymphoma Society SCOR grant (R.G.R.), the intramural research program of the National Heart, Lung, and Blood Institute (W.Y. and J.Z.), and a National Science Foundation of China grant (T. Ni). ChIP-seq and RNA-seq data have been submitted to GEO under accession number GSE62171.

SUPPLEMENTARY MATERIALS

www.sciencemag.org/content/350/6266/1383/suppl/DC1
Materials and Methods
Supplementary Text
Figs. S1 to S11
Tables S1 to S5
References (*24–29*)

12 August 2015; accepted 21 October 2015
10.1126/science.aad2338

CANCER IMMUNOTHERAPY

Immunogenicity of somatic mutations in human gastrointestinal cancers

Eric Tran, Mojgan Ahmadzadeh, Yong-Chen Lu, Alena Gros, Simon Turcotte,* Paul F. Robbins, Jared J. Gartner, Zhili Zheng, Yong F. Li, Satyajit Ray, John R. Wunderlich, Robert P. Somerville, Steven A. Rosenberg†

It is unknown whether the human immune system frequently mounts a T cell response against mutations expressed by common epithelial cancers. Using a next-generation sequencing approach combined with high-throughput immunologic screening, we demonstrated that tumor-infiltrating lymphocytes (TILs) from 9 out of 10 patients with metastatic gastrointestinal cancers contained $CD4^+$ and/or $CD8^+$ T cells that recognized one to three neo-epitopes derived from somatic mutations expressed by the patient's own tumor. There were no immunogenic epitopes shared between these patients. However, we identified in one patient a human leukocyte antigen–C*08:02–restricted T cell receptor from $CD8^+$ TILs that targeted the $KRAS^{G12D}$ hotspot driver mutation found in many human cancers. Thus, a high frequency of patients with common gastrointestinal cancers harbor immunogenic mutations that can potentially be exploited for the development of highly personalized immunotherapies.

Genetic aberrations underpin all cancers. These genetic alterations are specific to cancers and are not present in normal tissues; thus, treatments that specifically target the protein product of these genetic alterations may provide clinical benefit in the absence of normal tissue toxicities. Cancer immunotherapies such as adoptive cell therapy with tumor-infiltrating lymphocytes (TILs) or immune checkpoint inhibitors have demonstrated clinical activity in patients with metastatic melanoma, smoking-induced lung cancer, renal cell carcinomas, and cancers with DNA mismatch-repair deficiency (*1*–*7*). Increasing correlative evidence suggests that some of these clinical responses are likely mediated by T cells that target somatic mutations expressed by the patients' tumors (*7*–*13*). In a direct demonstration of the therapeutic potential of immune targeting of cancer mutations, we recently identified mutation-specific $CD4^+$ T cells in a patient with metastatic epithelial cancer originating from the bile ducts and observed objective regression of lung and liver metastases ongoing now at 20 months after treating the patient with a highly enriched population of these mutation-specific T cells (*14*). This patient's tumors contained only 26 mutations, which indicates that the immune system can mount a clinically relevant antimutation T cell response against cancers with a low mutation load (*14*). However, immune checkpoint blockade therapies are ineffective against the majority of metastatic gastrointestinal (GI) cancers (*2*, *7*), which on average have a lower number of mutations as compared with those of melanoma, smoking-induced lung cancers, and cancers with DNA mismatch-repair deficiencies (*7*, *15*, *16*). This suggests that mutation-reactive T cells may be rare or absent in the majority of these patients. If so, this would likely pose major challenges for the development of immunotherapies that target mutations in many patients with GI cancers. Thus, we aimed to determine whether immunogenic mutations are common in patients with metastatic GI cancers.

To this end, we used whole-exome or whole-genome sequencing to identify somatic mutations present in the metastatic tumors derived from nine additional patients with cancers originating from the colon, rectum, esophagus, bile ducts, or pancreas (Table 1 and table S1). The number of mutations ranged from 10 to 155 (Table 1 and tables S2 to S9) when using previous methods to call mutations (*17*). However, to evaluate any low-coverage and low-confidence mutations, we relaxed the mutation call criteria for most samples (*17*) and thus evaluated between 38 and 264 putative mutations (Table 1). In parallel, we generated multiple TIL cultures from the metastatic lesions of each patient. To test whether any of the TIL cultures from each patient recognized their own tumor mutations, we used a tandem minigene (TMG) approach as previously described (*8*, *14*, *17*). Briefly, these TMGs comprise a string of minigenes, which are genetic constructs that encode an identified mutation flanked on each side by the 12 wild-type amino acids from the parent protein, except in the case of frameshift mutations, in which the cDNA was translated until the next stop codon. After in vitro transcription, the TMG RNAs are then individually transfected into autologous antigen-presenting cells (APCs), allowing for the potential processing and presentation of all mutated epitopes by each of the patient's major histocompatibility complex (MHC) class I and class II molecules, followed by a coculture with the different TIL cultures. Because we and others cannot consistently grow tumor cell lines from metastatic gastrointestinal cancers, this approach enables the reliable screening of tumor-specific antigens (the mutanome) without the requirement of a tumor cell line.

In a representative patient with metastatic colon cancer (patient 4007), 23 TIL cultures derived from individual tumor fragments of a single metastatic liver lesion were initially screened for reactivity against 17 TMG constructs, which together encoded 264 minigenes (table S10). We evaluated both the secretion of the effector cytokine interferon-γ (IFN-γ) using the enzyme-linked immunospot (ELISPOT) assay and up-regulation of the T cell activation marker 4-1BB using flow cytometry because these approaches can provide complementary and nonredundant information about antigen-specific T cell responses. Five of 23 and 4 of 23 TIL cultures contained variable levels of reactivity against TMG-7 (TIL cultures 4, 6, 16, 22, and 23) and TMG-14 (TIL cultures 7, 8, 16, and 18), respectively, as determined with IFN-γ ELISPOT (Fig. 1A, top). Flow cytometric analysis of the T cell activation marker 4-1BB suggested that the reactivities against TMG-7 and TMG-14 were mediated by $CD8^+$ T cells (Fig. 1A, bottom). To identify which mutated antigens were being recognized in TMG-7 and TMG-14, we first enriched the TMG-7– and TMG-14–reactive cells by sorting and expanding the $CD8^+$ T cells from TIL cultures 8, 16, and 23 that up-regulated 4-1BB upon stimulation with TMG-7 or TMG-14 (Fig. 1B). These enriched TMG-7– and TMG-14–reactive cells were then cocultured with autologous dendritic cells (DCs) that were individually pulsed with the mutated peptides encoded by TMG-7 or TMG-14, respectively (table S10). TMG-14–reactive $CD8^+$ T cells from both TIL cultures 8 and 16 recognized the $SKIV2L^{R653H}$ mutation, whereas the TMG-7–reactive $CD8^+$ T cells from TIL culture 23 recognized the $H3F3B^{A48T}$ mutation (Fig. 1C). We sequenced the T cell receptors (TCRs) of the two $SKIV2L^{R653H}$-mutation–reactive T cell populations and found that they did not share the same TCR sequences (table S19). The T cell responses were mutation-specific because genetic engineering of autologous open repertoire peripheral blood T cells with the TMG-7– and TMG-14–reactive TCRs (table S20) conferred reactivity to the mutated $H3F3B^{A48T}$ and $SKIV2L^{R653H}$ peptides, respectively, with no reactivity observed against the wild-type peptides (Fig. 1D). Thus, our screening approach enabled the identification of patient-specific mutation-reactive $CD8^+$ T cells.

For patient 3995 with metastatic colon cancer, in addition to the identification of patient-specific, mutation-reactive $CD8^+$ T cells against $RNF213^{N1702S}$ and $TUBGCP2^{P293L}$ (fig. S1), we also detected a low-level $CD8^+$ TIL reactivity against the $KRAS^{G12D}$ hotspot mutation (Fig. 2A). We purified by means of fluorescence-activated cell sorting (FACS) and expanded the low frequency

Surgery Branch, National Cancer Institute, National Institutes of Health, Bethesda, MD 20892, USA.
*Present address: Department of Surgery, Université de Montréal, and Institut du Cancer de Montréal, Centre de Recherche du Centre Hospitalier de l'Université de Montréal, Montréal, QC H2X 0A9, Canada. †Corresponding author. E-mail: sar@mail.nih.gov

Downloaded from www.sciencemag.org on December 14, 2015

of $KRAS^{G12D}$-reactive $CD8^+$ T cells (Fig. 2B) and confirmed that the enriched population indeed specifically recognized APCs when pulsed with the mutated $KRAS^{G12D}$ peptide or when transfected with full-length $KRAS^{G12D}$ RNA (Fig. 2C). Genetic engineering of autologous open-repertoire T cells with the TCR isolated from the $KRAS^{G12D}$-specific T cells (Fig. 2C and table S20) redirected human leukocyte antigen (HLA)–C*08:02–restricted reactivity to COS-7 cells transfected with $KRAS^{G12D}$ (Fig. 2D) as well as $KRAS^{G12D}$-expressing pancreatic cancer cell lines (Fig. 2E). In addition to the secretion of IFN-γ, the KRAS-mutation reactive TILs specifically produced tumor necrosis factor (TNF) and displayed cytolytic potential against pancreatic cancer cell lines expressing HLA-C*08:02 and $KRAS^{G12D}$ (Fig. 2F). The $KRAS^{G12D}$ mutation did not appear to be immunogenic in all patients for we did not detect KRAS-mutation reactive TILs in the two patients, 4032 and 4069, whose tumors harbored $KRAS^{G12D}$ (tables S8 and S9). These two patients did not express the HLA-C*08:02 allele (table S23), although they did express other MHC-I alleles predicted to bind the $KRAS^{G12D}$ mutation with moderate affinity (table S24). Thus, in addition to distinct patient-specific immunogenic mutations, we also identified an immunogenic mutation in the shared $KRAS^{G12D}$ driver mutation.

We used similar approaches to test whether mutation-reactive TILs could be detected in the seven remaining patients with metastatic colon, rectum, esophagus, bile duct, and pancreatic cancer and found mutation-reactive T cells in six patients (Table 1, figs. S2 to S7, and supplementary text). Our strategy of lowering the mutation-call threshold led to the identification of one immunogenic mutation that would not have been identified if we had used previous, more stringent methods to call mutations (the ZFYVE27 mutation in patient 4069) (Table 1 and tables S9 and S18). Both the number of mutation-reactive TIL cultures and the frequency of mutation-reactive T cells were often highly variable (Table 1 and figs. S1 to S7). Some of the immunogenic mutations identified in this report were in genes with known biological relevance to tumorigenesis, such as KRAS, PHLPP1, and API5 (Table 1) (*18*–*20*). All of the identified mutations recognized by $CD8^+$ T cells encompassed minimal T cell epitopes that were predicted to rank among the top 2% of peptides that bound to one or more of the patients' MHC-I molecules (tables S21 and S23), and some of these epitopes were tested and found to be recognized by the appropriate T cells (figs. S4F; S6, C, E, J, and K; and S7C). Most of the mutations recognized by $CD4^+$ T cells were encompassed within epitopes that were also predicted to bind with moderate affinity to at least one of the patients' own HLA-II alleles (tables S22 and S23). Whole-transcriptome analysis revealed that the immunogenic mutations were in genes demonstrating a wide range of expression levels [2.9 to 185.4 fragments per kilobase of transcript per million mapped reads (FPKM)] within the metastatic lesions (tables S21 and S22).

To determine the endogenous frequency of the mutation-reactive T cells (table S19) infiltrating the metastatic lesions, we performed TCR-Vβ deep sequencing on the cryopreserved metastatic tumor lesions. As shown in Table 1 and fig. S8, the frequency of the identified mutation-reactive T cells infiltrating the metastatic lesions was variable, ranging from 0.009 to 1.25% of all T cells within a given tumor. Of the 17 identified mutation-reactive TCRs, four ranked within the top 10 most frequent TCRs within the tumor (rank range, 3 to 2718) (Table 1). The low ranking of some mutation-specific TCRs could suggest poor clonal expansion, survival, and/or infiltration

Table 1. Mutation-reactive T cells in metastatic GI cancers. NE, not evaluated.

Patient ID	Age/sex	Tumor type	Number of mutations†	Number of mutations assessed‡	Number of TIL cultures assessed	Number of TIL cultures with mutation reactivity§	Mutated protein recognized	Amino acid change	T cell type	Frequency of mutation-reactive TCR in tumor (%)	Rank of mutation-reactive TCR in tumor
3737*	45/F	Bile duct	26	25	5	5	ERBB2IP	E805G	CD4	0.009	2718
								E805G	CD4	0.375	10
3812	44/M	Bile duct	48	179	5	0	—	—	—	—	—
3942	46/F	Rectal	155	144	6	2	NUP98	A359D	CD8	0.67	5
						4	KARS	D356	CD8	0.020	1143
						3	GPD2	E426K	CD4	0.037	862
3948	48/M	Esophageal	84	211	5	2	PLEC	E1179K	CD4	NE	NE
						2	XPO7	P274S	CD4	NE	NE
						2	AKAP2	Q418K	CD4	NE	NE
3971	49/M	Colon	118	118	23	11	CASP8	F67V	CD8	1.25	3
3978	46/F	Bile duct	39	38	9‖	1¶	ITGB4	S1002I	CD4	NE	NE
3995	50/M	Colon	58	154	19‖	2	TUBGCP2	P293L	CD8	0.023	1056
						15	RNF213	N1702S	CD8	0.60	15
						2	KRAS	G12D	CD8	0.055	527
4007	52/M	Colon	134	264	23	4	SKIV2L	R653H	CD8	0.090	121
								R653H	CD8	0.014	887
						5	H3F3B	A48T	CD8	1.19	4
4032	46/M	Colon	101	222	24	12	API5	R243Q	CD8	0.083	126
								R243Q	CD8	0.059	187
						1	RNF10	E572K	CD8	0.030	423
						7	PHLPP1	G566E	CD8	0.081	129
4069	57/M	Pancreatic	10	97	15	1	ZFYVE27	R6H	CD8	0.088	278

*Patient 3737 was previously reported in (*14*). †As determined by Personal Genome Diagnostics (PGDx) from whole-exome sequencing (*17*). ‡As determined when mutation call criteria was relaxed (*17*). The mutation call criteria was not relaxed for patients 3737, 3942, and 3978. §Reactivity was determined with IFN-γ ELISPOT or flow cytometry for 4-1BB or OX40 up-regulation upon coculture with mutated TMGs or peptides. ‖The indicated number of TIL cultures includes T cell populations that were sorted and expanded from a tumor digest based on PD-1 expression as described in the supplementary materials. ¶Identified from a FACS-purified TIL population as described in the supplementary text.

of these T cells in the tumor environment. The antigens recognized by the other TCRs in the tumor are unknown but could be comprised of nonmutated tumor antigens, nontumor antigens, and/or other mutated antigens not identified by our assays. Often, only a minority of TIL cultures derived from the same metastatic lesion harbored detectable levels of IFN-γ–producing mutation-reactive T cells, and different TIL cultures were enriched for T cells reactive to different mutations (Fig. 1, Table 1, and figs. S1 to S7). This heterogeneity and relatively low frequency of neo-epitope T cell reactivity may be a function of the intratumoral genomic heterogeneity observed in human cancers (*21*, *22*) and may partially explain the lack of efficacy observed in patients with metastatic GI cancers treated with immune-based therapies.

In vivo antitumor activity can theoretically be achieved by T cells targeting either passenger and/or driver mutations, so long as a sufficient number of tumor cells express the targeted mutation (or mutations). The immunological targeting of driver mutations (*23*–*25*) may be desirable over passenger mutations, and it is thus pertinent that we identified a HLA-C*08:02–restricted TCR that recognizes the shared $KRAS^{G12D}$ driver mutation. Because the adoptive transfer of autologous peripheral blood lymphocytes—genetically engineered to express tumor-reactive TCRs or chimeric antigen receptors—can elicit regression of widespread cancer in some patients with metastatic disease (*1*), the isolated TCR may extend TCR gene therapy to HLA-C*08:02 patients whose tumors express $KRAS^{G12D}$. The $KRAS^{G12D}$ mutation is expressed in ~45% of pancreatic adenocarcinomas (*26*), ~13% of colorectal cancers (*27*), and at lower frequencies in other common solid cancers, and the HLA-C*08:02 allele is expressed in up to ~8 and ~11% of American Caucasoid and Black ethnicities, respectively. Thus, in the United States alone, thousands of patients with GI cancers each year would potentially be eligible for immunotherapy with this single $KRAS^{G12D}$-reactive TCR.

Together with our recent Report demonstrating the existence of mutation-reactive $CD4^+$ T cells in a patient with metastatic cholangiocarcinoma (*14*), we have found that 9 out of 10 patients with metastatic GI cancers elicit T cell responses against at least one somatic mutation expressed by their tumors. The neo-epitope T cell responses identified in our patients were elicited against epithelial tumors with relatively low to moderate mutation burdens that are not susceptible to effective therapy with current checkpoint modulators (*2*, *7*). Of our 10 patients described in Table 1, four have been treated with enriched populations of T cells targeting predominantly one mutated antigen expressed by their autologous tumor. Patient 3737 (*14*) continues to experience tumor regression ongoing at 20 months posttreatment, whereas patient 4069 had a transient regression of multiple lung metastases, and 4007 and 4032 had no objective response. For patient 3737, over 23% of the circulating T cells at 1 month after treatment comprised the adoptively transferred mutation-specific T cells, whereas limited persistence (less than 1%, and even undetectable in some cases) of the mutation-reactive T cells was observed in the blood of the other three patients treated with an enriched population of mutation-specific T cells. These results suggest a need for enhancing the potency and persistence of adoptively transferred mutation-specific T cells through strategies such as the introduction of mutation-specific TCRs into naïve or central memory T cells with high proliferative capacity, the targeting of driver mutations, the

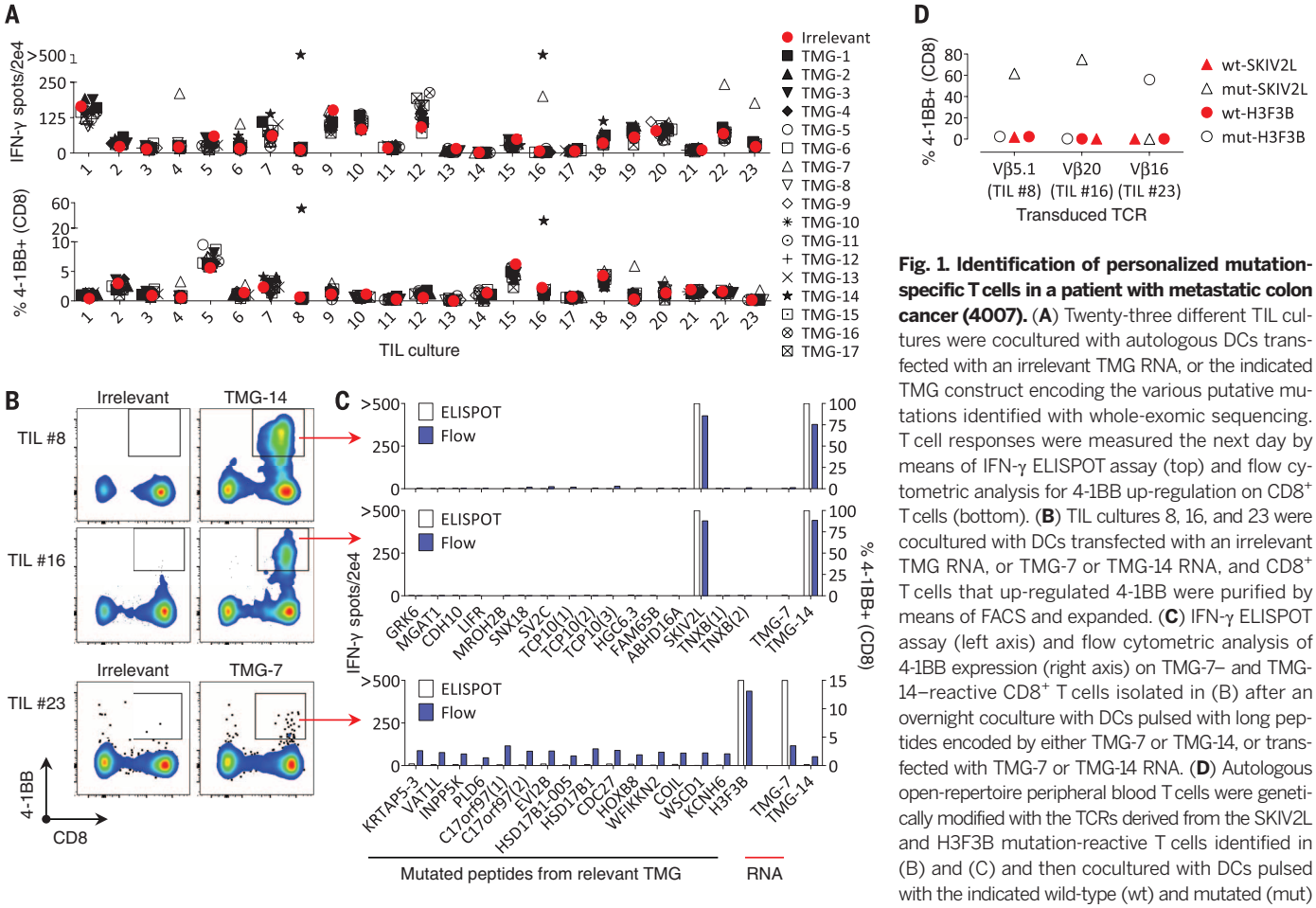

Fig. 1. Identification of personalized mutation-specific T cells in a patient with metastatic colon cancer (4007). (**A**) Twenty-three different TIL cultures were cocultured with autologous DCs transfected with an irrelevant TMG RNA, or the indicated TMG construct encoding the various putative mutations identified with whole-exomic sequencing. T cell responses were measured the next day by means of IFN-γ ELISPOT assay (top) and flow cytometric analysis for 4-1BB up-regulation on $CD8^+$ T cells (bottom). (**B**) TIL cultures 8, 16, and 23 were cocultured with DCs transfected with an irrelevant TMG RNA, or TMG-7 or TMG-14 RNA, and $CD8^+$ T cells that up-regulated 4-1BB were purified by means of FACS and expanded. (**C**) IFN-γ ELISPOT assay (left axis) and flow cytometric analysis of 4-1BB expression (right axis) on TMG-7– and TMG-14–reactive $CD8^+$ T cells isolated in (B) after an overnight coculture with DCs pulsed with long peptides encoded by either TMG-7 or TMG-14, or transfected with TMG-7 or TMG-14 RNA. (**D**) Autologous open-repertoire peripheral blood T cells were genetically modified with the TCRs derived from the SKIV2L and H3F3B mutation-reactive T cells identified in (B) and (C) and then cocultured with DCs pulsed with the indicated wild-type (wt) and mutated (mut) long peptides. Flow cytometric analysis is gated on live $CD8^+$ T cells, and TCR transduction efficiencies ranged between 60 and 80%. Plate-bound antibody to CD3 (OKT3) was used as a positive control in all coculture assays. ">" ELISPOT assay is not accurate above ~500 spots. Data from (B) to (D) are representative of at least two independent experiments.

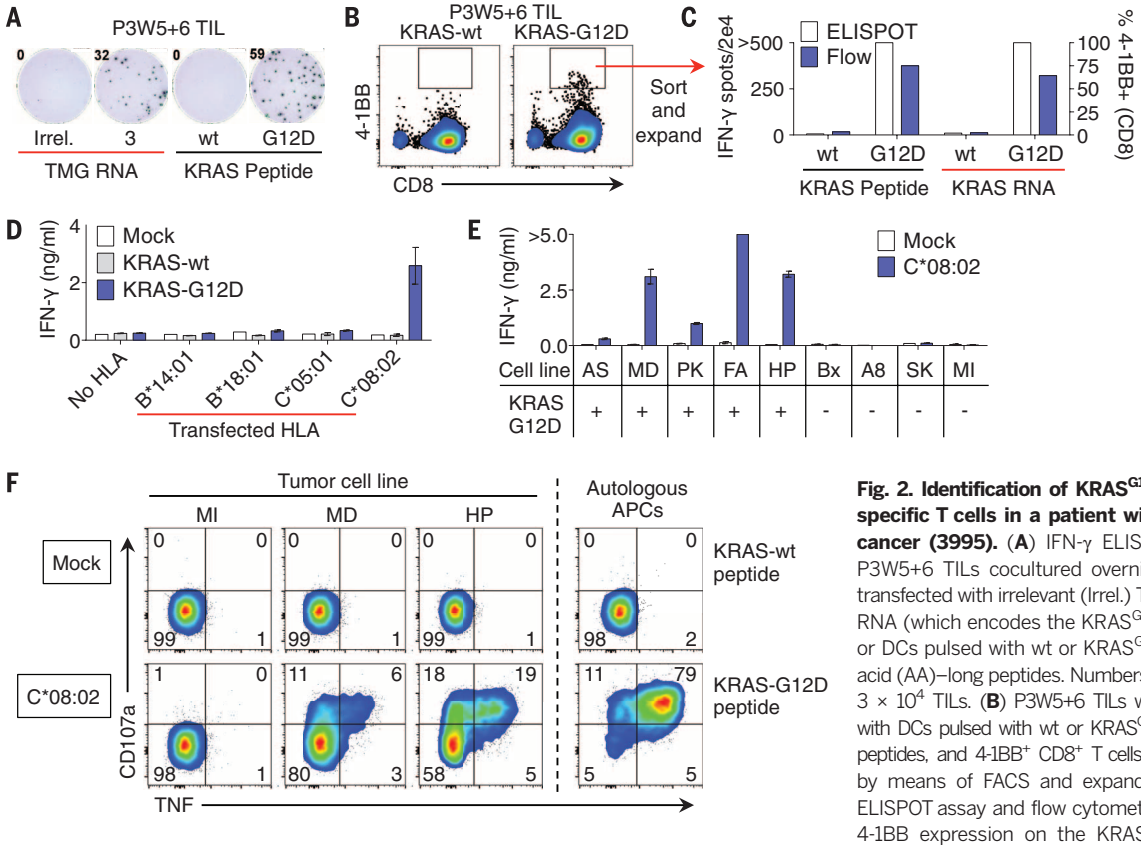

Fig. 2. Identification of KRAS^{G12D}-mutation–specific T cells in a patient with colorectal cancer (3995). (**A**) IFN-γ ELISPOT assay of P3W5+6 TILs cocultured overnight with DCs transfected with irrelevant (Irrel.) TMG or TMG-3 RNA (which encodes the KRAS^{G12D} minigene), or DCs pulsed with wt or KRAS^{G12D} 24–amino acid (AA)–long peptides. Numbers are spots per 3 × 10^4 TILs. (**B**) P3W5+6 TILs were stimulated with DCs pulsed with wt or KRAS^{G12D} 24-AA-long peptides, and 4-1BB$^+$ CD8$^+$ T cells were purified by means of FACS and expanded. (**C**) IFN-γ ELISPOT assay and flow cytometric analysis of 4-1BB expression on the KRAS^{G12D}-enriched CD8$^+$ T cells from (B) cocultured overnight with DCs pulsed with wt or KRAS^{G12D} 24-AA-long peptides, or DCs transfected with full-length wt or KRAS^{G12D} RNA. (**D**) IFN-γ enzyme-linked immunosorbent assay (ELISA) of T cells genetically modified with the KRAS^{G12D}-reactive TCR cocultured with COS-7 cells cotransfected with nothing (Mock) or the indicated KRAS gene along with nothing (No HLA), or the HLA-B and -C alleles expressed by the patient. (**E**) IFN-γ ELISA of T cells genetically modified with the KRAS^{G12D}-reactive TCR cocultured with various pancreatic cancer cell lines transduced with nothing (Mock) or the HLA-C*08:02 allele. The presence or absence of endogenously expressed KRAS^{G12D} is shown. AS, ASPC-1; MD, MDA-Panc48; PK, PK-45p; FA, FA6-2; HP, HPAC; Bx, BxPC-3 (KRAS-wt); A8, A818.8 (KRAS^{G12R}); SK, SK-PC3 (KRAS^{G12V}); MI, MIA PaCa-2 (KRAS^{G12C}). (**F**) KRAS^{G12D}-reactive TILs enriched from (B) were cocultured for 6 hours with pancreatic cancer cell lines transduced with nothing (Mock) or the HLA-C*08:02 allele, and flow cytometry was used to assess CD107a expression and TNF production by means of intracellular cytokine staining. Autologous APCs (peripheral blood mononuclear cells) pulsed overnight with wt or KRAS^{G12D} 24-AA-long peptides were used as control target cells. Data are gated on CD8$^+$ T cells expressing the KRAS^{G12D}-reactive TCR Vβ5.2. ">" ELISPOT assay is not accurate above ~500 spots. Error bars are ±SD. All data are representative of at least two independent experiments.

simultaneous targeting of multiple mutations, and/or combining adoptive cell therapy with other immunomodulators such as checkpoint inhibitors. Nonetheless, the observation that virtually all patients with metastatic GI cancers harbor tumor-mutation–specific T cells provides opportunities for the development of personalized vaccine and/or adoptive cell therapies that target immunogenic tumor mutations expressed by common epithelial cancers.

REFERENCES AND NOTES

1. S. A. Rosenberg, N. P. Restifo, *Science* **348**, 62–68 (2015).
2. S. L. Topalian *et al.*, *N. Engl. J. Med.* **366**, 2443–2454 (2012).
3. F. S. Hodi *et al.*, *N. Engl. J. Med.* **363**, 711–723 (2010).
4. O. Hamid *et al.*, *N. Engl. J. Med.* **369**, 134–144 (2013).
5. M. A. Postow *et al.*, *N. Engl. J. Med.* **372**, 2006–2017 (2015).
6. J. D. Wolchok *et al.*, *N. Engl. J. Med.* **369**, 122–133 (2013).
7. D. T. Le *et al.*, *N. Engl. J. Med.* **372**, 2509–2520 (2015).
8. Y. C. Lu *et al.*, *Clin. Cancer Res.* **20**, 3401–3410 (2014).
9. Y. C. Lu *et al.*, *J. Immunol.* **190**, 6034–6042 (2013).
10. P. F. Robbins *et al.*, *Nat. Med.* **19**, 747–752 (2013).
11. N. van Rooij *et al.*, *J. Clin. Oncol.* **31**, e439–e442 (2013).
12. A. Snyder *et al.*, *N. Engl. J. Med.* **371**, 2189–2199 (2014).
13. N. A. Rizvi *et al.*, *Science* **348**, 124–128 (2015).
14. E. Tran *et al.*, *Science* **344**, 641–645 (2014).
15. M. S. Lawrence *et al.*, *Nature* **499**, 214–218 (2013).
16. B. Vogelstein *et al.*, *Science* **339**, 1546–1558 (2013).
17. Materials and methods are available as supplementary materials on *Science* Online.
18. K. H. Noh *et al.*, *Cancer Res.* **74**, 3556–3566 (2014).
19. M. Chen *et al.*, *Cancer Cell* **20**, 173–186 (2011).
20. A. D. Cox, C. J. Der, *Small GTPases* **1**, 2–27 (2010).
21. M. Gerlinger *et al.*, *N. Engl. J. Med.* **366**, 883–892 (2012).
22. A. Sottoriva *et al.*, *Proc. Natl. Acad. Sci. U.S.A.* **110**, 4009–4014 (2013).
23. M. K. Gjertsen, J. Bjorheim, I. Saeterdal, J. Myklebust, G. Gaudernack, *Int. J. Cancer* **72**, 784–790 (1997).
24. B. Linard *et al.*, *J. Immunol.* **168**, 4802–4808 (2002).
25. M. S. Sharkey, G. Lizée, M. I. Gonzales, S. Patel, S. L. Topalian, *Cancer Res.* **64**, 1595–1599 (2004).
26. K. L. Bryant, J. D. Mancias, A. C. Kimmelman, C. J. Der, *Trends Biochem. Sci.* **39**, 91–100 (2014).
27. C. P. Vaughn, S. D. Zobell, L. V. Furtado, C. L. Baker, W. S. Samowitz, *Genes Chromosomes Cancer* **50**, 307–312 (2011).

ACKNOWLEDGMENTS

We thank the Milstein Family Foundation for their generous support, Q. Wang and U. Rudloff for providing KRAS-genotyped pancreatic cancer cell lines, A. Mixon and S. Farid for flow cytometry support, M. El-Gamil for reagents, T. Prickett for RNA-sequencing assistance, and other members of the Surgery Branch for helpful discussions and technical support. The data presented in this manuscript are tabulated in the main paper and in the supplementary materials. The raw whole-exome and genome sequence data are available through the National Center for Biotechnology Information Bioproject database, Bioproject PRJNA298330. E.T., Y-C.L., and S.A.R. have filed a patent application (U.S. application no. 62/218,688) that relates to the KRAS^{G12D}-mutation reactive TCR. This research was supported by the Center for Cancer Research intramural research program of the National Cancer Institute.

SUPPLEMENTARY MATERIALS

www.sciencemag.org/content/350/6266/1387/suppl/DC1
Materials and Methods
Supplementary Text
Figs. S1 to S8
Tables S1 to S24
References (*28*–*35*)

30 July 2015; accepted 15 October 2015
Published online 29 October 2015
10.1126/science.aad1253

VITAMIN C RESEARCH

Vitamin C selectively kills *KRAS* and *BRAF* mutant colorectal cancer cells by targeting GAPDH

Jihye Yun,[1] Edouard Mullarky,[1,2] Changyuan Lu,[3] Kaitlyn N. Bosch,[1] Adam Kavalier,[3] Keith Rivera,[4] Jatin Roper,[5] Iok In Christine Chio,[4] Eugenia G. Giannopoulou,[6]* Carlo Rago,[7] Ashlesha Muley,[1] John M. Asara,[8] Jihye Paik,[9] Olivier Elemento,[6] Zhengming Chen,[10] Darryl J. Pappin,[4] Lukas E. Dow,[1] Nickolas Papadopoulos,[7] Steven S. Gross,[3] Lewis C. Cantley[1]†

More than half of human colorectal cancers (CRCs) carry either *KRAS* or *BRAF* mutations and are often refractory to approved targeted therapies. We found that cultured human CRC cells harboring *KRAS* or *BRAF* mutations are selectively killed when exposed to high levels of vitamin C. This effect is due to increased uptake of the oxidized form of vitamin C, dehydroascorbate (DHA), via the GLUT1 glucose transporter. Increased DHA uptake causes oxidative stress as intracellular DHA is reduced to vitamin C, depleting glutathione. Thus, reactive oxygen species accumulate and inactivate glyceraldehyde 3-phosphate dehydrogenase (GAPDH). Inhibition of GAPDH in highly glycolytic *KRAS* or *BRAF* mutant cells leads to an energetic crisis and cell death not seen in *KRAS* and *BRAF* wild-type cells. High-dose vitamin C impairs tumor growth in *Apc/Kras*^{G12D} mutant mice. These results provide a mechanistic rationale for exploring the therapeutic use of vitamin C for CRCs with *KRAS* or *BRAF* mutations.

Activating *KRAS* and *BRAF* mutations are found in approximately 40% and 10% of human colorectal cancers (CRCs), respectively (*1*). BRAF is a direct target of KRAS, and both activate the mitogen-activated protein kinase (MAPK) pathway. Clinical studies indicate that activating mutations in *KRAS* and *BRAF* predict resistance to epidermal growth factor receptor (EGFR)–targeting agents (*2*–*4*). Thus, novel therapies for *KRAS* or *BRAF* mutant CRCs are urgently needed.

Glucose uptake, as measured by [^{18}F]fluorodeoxyglucose positron emission tomography (FDG-PET), correlates with *KRAS* or *BRAF* mutations and GLUT1 overexpression in CRCs (*5*, *6*), consistent with our previous finding that *KRAS* or *BRAF* mutant CRC cells rewire glucose metabolism, in part by up-regulating *GLUT1* expression (*7*). These data suggest a strategy for targeting *KRAS* or *BRAF* mutant cancers by exploiting the selective expression of *GLUT1* and the metabolic liability that comes with increased reliance on glycolysis.

Dietary vitamin C is transported across cellular membranes by sodium vitamin C cotransporters (SVCTs) and facilitative glucose transporters (GLUTs) (*8*, *9*). Whereas SVCTs transport vitamin C directly into the cell, GLUTs—mainly GLUT1 and GLUT3—transport the oxidized form of vitamin C, dehydroascorbate (DHA). After import, DHA is reduced to vitamin C at the expense of glutathione (GSH), thioredoxin, and nicotinamide adenine dinucleotide phosphate (NADPH) (*10*). Given that GLUT1 levels in *KRAS* and *BRAF* mutant cells are elevated, we hypothesized that the increase in DHA uptake could disrupt redox homeostasis and compromise cellular viability. To test our hypothesis, we used a panel of isogenic CRC cell lines harboring wild-type or mutant alleles of *KRAS* (HCT116 and DLD1) or *BRAF* (VACO432 and RKO) (*7*).

In cell culture media, vitamin C is oxidized to DHA (half-life ~70 min) unless reducing agents are added (fig. S1) (*11*). Using ^{14}C-radiolabeled vitamin C, we tested which form of vitamin C (reduced or oxidized DHA) is preferentially imported. Both HCT116 and VACO432 cells took up [^{14}C]vitamin C efficiently (Fig. 1A). However, adding GSH to the media to prevent oxidation of vitamin C to DHA abrogated [^{14}C]vitamin C uptake (Fig. 1A). Furthermore, [^{14}C]vitamin C uptake was significantly decreased in both HCT116 and VACO432 cells treated with a GLUT1-specific inhibitor, STF31, and in GLUT1 knockout cells (Fig. 1, A and B). Glucose competed with DHA for uptake in CRC cells (fig. S2). These results indicate that CRC cells preferentially import DHA, rather than vitamin C, and that this uptake is mediated by GLUT1 (fig. S3, A and B).

Given the increased expression of GLUT1 in mutant cells, we investigated whether *KRAS* or *BRAF* mutations influenced vitamin C uptake. We found that the mutant lines took up significantly more [^{14}C]vitamin C than did their wild-type counterparts (Fig. 1, B and C). Overexpression of GLUT1 in wild-type cells was sufficient to increase [^{14}C]vitamin C uptake to levels commensurate with those of the mutants (Fig. 1B and fig. S3C). Moreover, *KRAS* and *BRAF* mutant cells imported DHA faster than they did [^{14}C]vitamin C (fig. S4), consistent with the observation that vitamin C must first be oxidized to DHA to enter cells through GLUT1. Together, these results indicate that GLUT1 is the primary means of vitamin C uptake in CRC cells and that elevated GLUT1 expression in *KRAS* or *BRAF* mutant cells drives increased DHA uptake.

We next asked whether the increased uptake of DHA in *KRAS* and *BRAF* mutant cells could affect their survival and growth. When plated at a low density and grown in low-glucose medium (2 mM), all cell lines grew at similar rates and formed colonies (fig. S5). However, 24 to 48 hours of vitamin C treatment inhibited *KRAS* and *BRAF* mutant cell growth and colony formation, with reduced effects on their wild-type counterparts (Fig. 2A and fig. S5). Because of the competitive nature of DHA import, mutant lines were most sensitive to vitamin C under low-glucose conditions (2 mM). Nonetheless, selective cytotoxicity against the mutant lines was achieved even under higher-glucose conditions (5 to 20 mM) when treating with less than 1 mM vitamin C (fig. S6), indicating that vitamin C can selectively kill mutant cells under physiological glucose concentration (5 to 10 mM).

Plasma vitamin C concentrations greater than 10 mM are easily achieved in humans and in our murine pharmacokinetic study (fig. S7) without significant toxicity (*12*, *13*). Vitamin C was cytotoxic rather than cytostatic, as evidenced by increased staining for the apoptotic marker annexin V in the mutants (fig. S8A). Adding GSH to the culture medium was sufficient to rescue the death of each mutant line (Fig. 2A). *PIK3CA* is one of three frequently mutated oncogenes in CRCs in addition to *KRAS* and *BRAF*. Unlike *KRAS* or *BRAF*, the *PIK3CA* genotype did not predict vitamin C sensitivity (fig. S8B). Notably, although overexpression of *GLUT1* in wild-type cells increased vitamin C uptake (Fig. 1B), it did not sensitize wild-type cells to vitamin C (fig. S8C); these results indicate that high GLUT1 expression alone, without oncogene-induced metabolic reprograming, is not sufficient to make cells susceptible to vitamin C–dependent toxicity.

We next explored whether vitamin C altered the growth of *KRAS* and *BRAF* mutant CRC cells in mice. Mice bearing established xenografts derived from parental HCT116 and VACO432 cell lines were treated twice a day via intraperitoneal (ip) injection of high-dose vitamin C (4 g/kg) or

[1]Meyer Cancer Center, Department of Medicine, Weill Cornell Medical College, New York, NY 10065, USA. [2]Biological and Biomedical Sciences Graduate Program, Harvard Medical School, Boston, MA 02115, USA. [3]Department of Pharmacology, Weill Cornell Medical College, New York, NY 10065, USA. [4]Cold Spring Harbor Laboratory, Cold Spring Harbor, NY 11724, USA. [5]Molecular Oncology Research Institute and Division of Gastroenterology, Tufts Medical Center, Boston, MA 02111, USA. [6]Department of Physiology and Biophysics, Weill Cornell Medical College, New York, NY 10065, USA. [7]Ludwig Center for Cancer Genetics and Therapeutics and Howard Hughes Medical Institute, Johns Hopkins Kimmel Cancer Center, Baltimore, MD 21231, USA. [8]Division of Signal Transduction, Beth Israel Deaconess Medical Center and Department of Medicine, Harvard Medical School, Boston, MA 02115, USA. [9]Department of Pathology and Laboratory Medicine, Weill Cornell Medical College, New York, NY 10065, USA. [10]Department of Biostatistics and Epidemiology, Weill Cornell Medical College, New York, NY 10065, USA.
*Present address: Department of Biological Sciences, New York City College of Technology, City University of New York, Brooklyn, NY 11201, USA, and Arthritis and Tissue Degeneration Program and David Z. Rosensweig Genomics Research Center, Hospital for Special Surgery, New York, NY 10021, USA.
†Corresponding author. E-mail: lcantley@med.cornell.edu

Downloaded from www.sciencemag.org on December 14, 2015

phosphate-buffered saline (PBS; vehicle control) for 3 to 4 weeks, at which point control mice had to be killed because of tumor size. Vitamin C treatment significantly reduced tumor growth relative to vehicle control treatment (Fig. 2B). *KRAS* and *BRAF* wild-type isogenic HCT116 and VACO432 cell lines cannot form xenograft tumors in mice. To directly test the impact of *Kras* mutation on the sensitivity of tumors to vitamin C treatment, we generated a transgenic model of intestinal cancer, driven by either *Apc* mutation, or combined *Apc* and *Kras* (G12D) mutations. Compound mutant mice were generated by crossing available Apc^{flox} mice (*14*), *LSL-*$Kras^{G12D}$ mice (*15*), and *Lgr5-EGFP-creER*^{T2} (*16*) animals, enabling intestinal restricted alteration of *Apc* and *Kras*. Tumors were induced with a single ip injection of low-dose tamoxifen (20 mg/kg) and treated daily thereafter with high-dose vitamin C (ip, 4 g/kg) for 5 to 7 weeks. Whereas $Apc^{flox/flox}$ mice showed no difference in polyp burden after vitamin C treatment, $Apc^{flox/flox}$/$Kras^{G12D}$ mice had significantly fewer and smaller small intestine polyps (76 versus 165 in control group), confirming that vitamin C selectively affected *Kras* mutant tumors (Fig. 2C and fig. S9). Consistent with experiments in CRC lines, tumors from $Apc^{flox/flox}$/$Kras^{G12D}$ mice showed higher GLUT1 expression and greater vitamin C uptake than did tumors from $Apc^{flox/flox}$ mice (Fig. 2, D and E, and fig. S10).

To investigate the mechanism by which vitamin C is selectively toxic to *KRAS* and *BRAF* mutant cells, we used liquid chromatography–tandem mass spectrometry (LC-MS/MS)–based metabolomics to profile metabolic changes after vitamin C treatment (*17*). In untreated *KRAS* and *BRAF* mutant lines, the relative intracellular metabolite levels of glycolysis and the nonoxidative arm of the pentose phosphate pathway (PPP) were increased relative to their isogenic wild-type counterparts (fig. S11). Addition of a MEK1/2 (MAPK kinase) inhibitor to the parental *KRAS* or *BRAF* mutant cells also decreased glycolytic and PPP metabolite levels, indicating that the increased metabolite levels were driven by oncogene-induced MAPK activity (fig. S12) (*18*). Notably, within 1 hour of vitamin C treatment, the metabolic profile of the mutant cells changed markedly. Glycolytic intermediates upstream of glyceraldehyde 3-phosphate dehydrogenase (GAPDH) accumulated while those downstream were depleted, which suggests that GAPDH was inhibited (Fig. 3A and fig. S13). Also, oxidative PPP metabolites increased (Fig. 3A and fig. S13), indicating that the blockage may shift glycolytic flux into the oxidative PPP. Indeed, vitamin C treatment stimulated oxidative PPP-dependent $^{14}CO_2$ production from [1-^{14}C]glucose in both *KRAS* and *BRAF* mutant cells, and to a lesser degree in wild-type cells (fig. S14A). Decreased NADPH/$NADP^+$ ratios are known to activate glucose-6-phosphate dehydrogenase allosterically to enhance oxidative PPP flux. The increased flux is an attempt to restore cytosolic NADPH back to homeostasis to mitigate oxidative stress (*19*). We reasoned that DHA uptake may deplete cellular GSH and NADPH as they are consumed in reducing DHA to vitamin C. If the capacity of this pathway to restore GSH levels is exceeded, cellular reactive oxygen species (ROS) increase because GSH is the major cellular antioxidant (*20*). Indeed, the ratio of reduced to oxidized glutathione decreased as intracellular vitamin C increased (Fig. 3B and fig. S14B). Cysteine, the major limiting precursor for GSH biosynthesis, was also depleted after vitamin C treatment (fig. S13). As expected, vitamin C treatment induced a substantial increase in endogenous ROS in *KRAS* and *BRAF* mutant cells (Fig. 3C).

Given that cancer cells with *KRAS* or *BRAF* mutations are heavily dependent on glycolysis for survival and growth, and that pyruvate (the end product of glycolysis) is a major carbon source for the mitochondrial TCA cycle (*7*, *21*), we hypothesized that inhibition of GAPDH, a glycolytic enzyme, might deplete adenosine triphosphate (ATP) and thereby induce an energetic crisis ultimately leading to cell death. Vitamin C treatment caused a rapid decrease in the glycolytic rate in *KRAS* and *BRAF* mutant cells, but not in wild-type cells, as determined by the extracellular acidification rate, a proxy for lactate production (Fig. 3D and fig. S15). Accordingly, vitamin C induced a significant drop in ATP levels, with a concomitant increase in adenosine monophosphate (AMP) levels (Fig. 3E and fig. S16A). Within 1 hour, AMP-activated protein kinase (AMPK), a marker for energy stress, was activated; activation was strongest in the mutant lines (Fig. 3F). The cell-permeable reducing agent and glutathione precursor *N*-acetylcysteine (NAC) rescued both AMPK activation and cell death in the mutant lines (Fig. 3, F and G). Consistent with the in

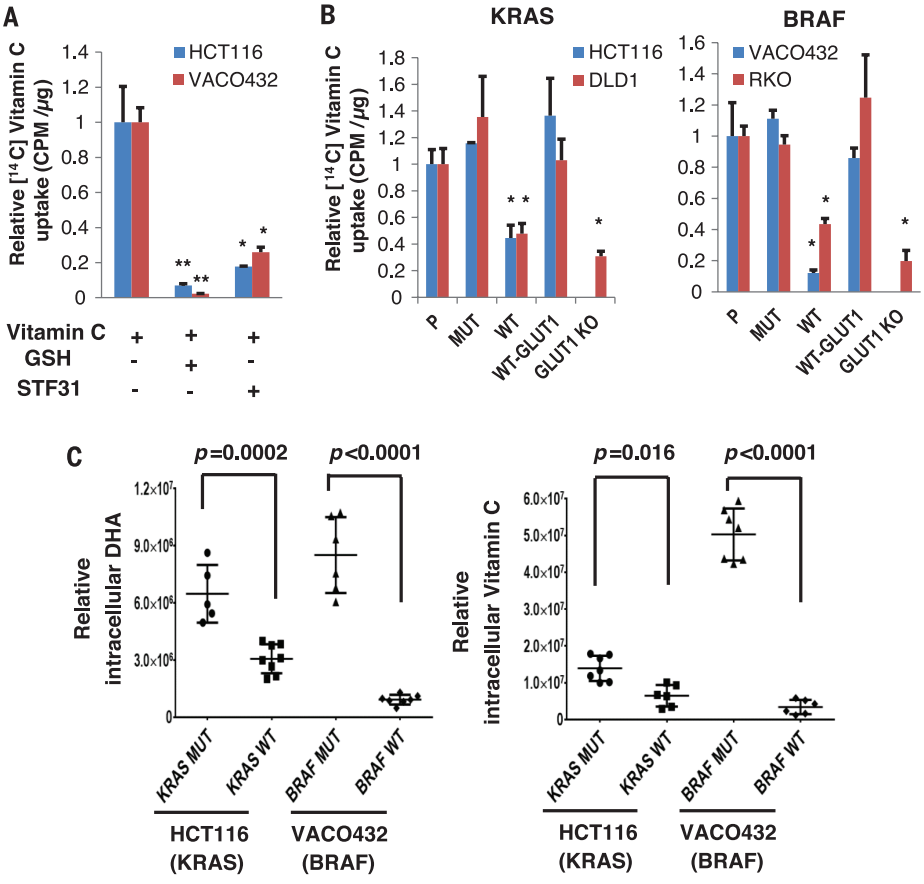

Fig. 1. *KRAS* and *BRAF* mutant cells predominantly take up DHA, the oxidized form of vitamin C, via GLUT1. (**A**) DHA, but not vitamin C, is transported into CRC cells via GLUT1. [^{14}C]Vitamin C was added to the culture media (2 mM glucose) for 30 min, followed by measurement of scintillation counts per minute (CPM) per microgram of protein input. Treating cells with GSH or STF31 (GLUT1 inhibitor) significantly reduced vitamin C uptake in all cases when compared to no GSH or STF31 treatment. One-way analysis of variance (ANOVA) followed by Dunnett's posttest for multiple comparisons. *P < 0.01, **P < 0.001, n = 3. (**B**) [^{14}C]Vitamin C uptake was monitored in 2 mM glucose and signal normalized to total protein. P, parental cells; WT-GLUT1, exogenously expressed *GLUT1* in wild-type cells; GLUT1 KO, *GLUT1* knockout cells. Asterisks indicate significant decreases in vitamin C uptake of wild-type or GLUT1 KO cells relative to the parental lines, *KRAS* or *BRAF* mutant cells (MUT), and WT-GLUT1. One-way ANOVA followed by Dunnett's posttest. *P < 0.01, n = 3. (**C**) LC/MS analysis of intracellular vitamin C and DHA in *KRAS* or *BRAF* isogenic cell lines derived from HCT116 and VACO432, respectively. Cells were treated with 1 mM (HCT116) or 2 mM (VACO432) vitamin C for 1 hour before extracting vitamin C and DHA (Student's t test, n = 6). All data represent means ± SD.

vitro results, supplementing drinking water with NAC over the course of vitamin C treatment abolished the ability of vitamin C to reduce xenograft growth (Fig. 3H). Similarly, pyruvate and oxaloacetate, both of which can enter the TCA cycle and thus provide ATP, rescued energy stress and cell death, as did Trolox (a water-soluble analog of the antioxidant vitamin E) (Fig. 3G and fig. S16, B and C). Rotenone, a complex I inhibitor, attenuated the ability of pyruvate to rescue vitamin C–induced cytotoxicity (fig. S17), indicating that the lack of mitochondrial substrates caused by glycolytic inhibition also contributes to ATP depletion in mutant cells (*21*).

We next sought to determine the mechanism by which vitamin C inhibits GAPDH. GAPDH is known to have an active-site cysteine (Cys^{152}) that is targeted by ROS (*22*). The active-site cysteine can undergo reversible S-glutathionylation in which the oxidized cysteine forms a mixed disulfide with GSH (Cys-GSH), or undergo further irreversible oxidations that include sulfonic acid (Cys-SO_3H) (*23*, *24*). Both cases result in loss of GAPDH activity. We measured GAPDH S-glutathionylation after vitamin C treatment by immunoprecipitating endogenous GAPDH and blotting with an antibody that recognizes S-glutathionylation under nonreducing conditions. In both *KRAS* and *BRAF* mutant lines, GAPDH S-glutathionylation levels were higher in vitamin C–treated cells than in vehicle-treated cells by a factor of 2 to 3 (Fig. 4A). However, GAPDH sulfonylation was not detected with a GAPDH-SO_3H antibody (Fig. 4B). GAPDH activity was assayed in lysates of vitamin C treated cells to confirm inhibition by S-glutathionylation (fig. S18). Treatment with vitamin C for 1 hour decreased GAPDH activity by 50% in both *KRAS* and *BRAF* mutant cells. Combining NAC with vitamin C fully rescued GAPDH activity (fig. S18).

We reasoned that the 50% reduction in GAPDH activity after vitamin C treatment could be explained by S-glutathionylation (Fig. 4A). However, given that the GAPDH substrates were added to the lysates to perform the activity assay, and in light of the striking accumulation (by as much as a factor of 19) of the GAPDH substrate glyceraldehyde-3-phosphate (G3P) (Fig. 3A and fig. S13), we suspected that additional mechanisms may contribute to GAPDH inhibition. This led us to examine the levels of the NAD^+ substrate required for GAPDH-dependent oxidation of G3P.

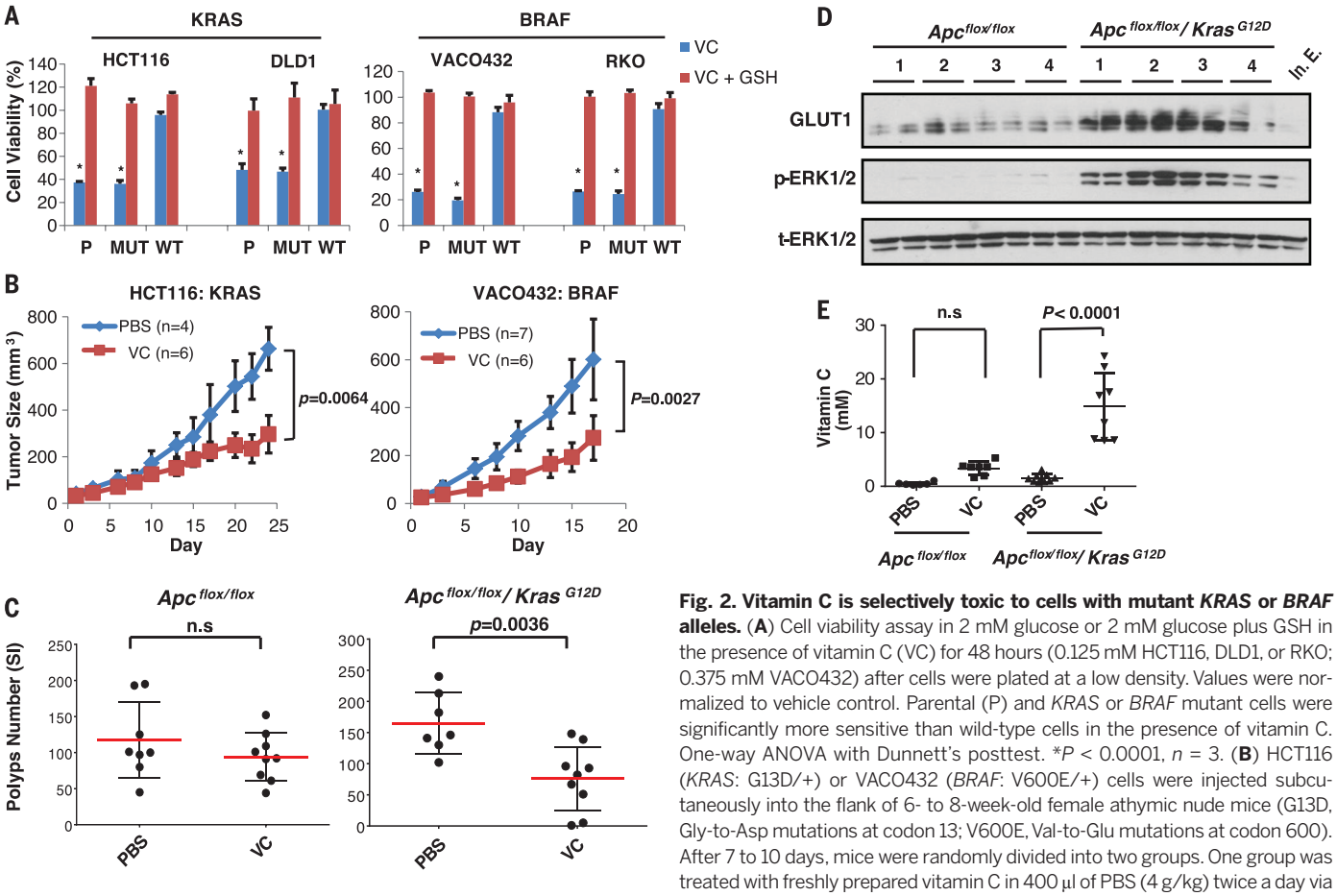

Fig. 2. Vitamin C is selectively toxic to cells with mutant *KRAS* or *BRAF* alleles. (**A**) Cell viability assay in 2 mM glucose or 2 mM glucose plus GSH in the presence of vitamin C (VC) for 48 hours (0.125 mM HCT116, DLD1, or RKO; 0.375 mM VACO432) after cells were plated at a low density. Values were normalized to vehicle control. Parental (P) and *KRAS* or *BRAF* mutant cells were significantly more sensitive than wild-type cells in the presence of vitamin C. One-way ANOVA with Dunnett's posttest. *$P < 0.0001$, $n = 3$. (**B**) HCT116 (*KRAS*: G13D/+) or VACO432 (*BRAF*: V600E/+) cells were injected subcutaneously into the flank of 6- to 8-week-old female athymic nude mice (G13D, Gly-to-Asp mutations at codon 13; V600E, Val-to-Glu mutations at codon 600). After 7 to 10 days, mice were randomly divided into two groups. One group was treated with freshly prepared vitamin C in 400 μl of PBS (4 g/kg) twice a day via ip injection (HCT116, $n = 6$; VACO432, $n = 6$). Control group mice were treated with PBS with the same dosing schedule (HCT116, $n = 4$; VACO432, $n = 7$). Tumor sizes were measured two or three times per week in an unblinded manner. Experiments were repeated twice independently. (**C**) At 7 weeks of age, $Apc^{flox/flox}$ mice and $Apc^{flox/flox}$/LSL-$Kras^{G12D}$ mice were treated with a single ip injection of low-dose tamoxifen (20 mg/kg) to activate the stem cell–specific *Cre* and facilitate loss of *Apc* and activation of the *Kras* G12D allele. Three weeks after tamoxifen injection, $Apc^{flox/flox}$ mice (8 male, 9 female) and $Apc^{flox/flox}$/LSL-$Kras^{G12D}$ mice (7 male, 9 female) were divided into two groups [vitamin C (4 g/kg) or PBS] and treated daily with ip injections (five or six times per week). As a result of weight loss and the increased level of fecal occult blood as measured by the Hemoccult II SENSA test, all $Apc^{flox/flox}$ mice were killed at 6 weeks after treatment. $Apc^{flox/flox}$/LSL-$Kras^{G12D}$ male mice were killed at 5 weeks after treatment and $Apc^{flox/flox}$/LSL-$Kras^{G12D}$ female mice were killed at 7 weeks after treatment; average polyp numbers in the PBS group for female and male mice were similar. $Apc^{flox/flox}$/LSL-$Kras^{G12D}$ mice experiments were repeated twice. Polyp numbers and volumes were determined in whole-mount tissue after methylene blue staining, using a dissecting microscope in an unblinded manner. (**D**) Immunoblots of GLUT1 protein, phospo-ERK1/2, and total ERK in tumors from $Apc^{flox/flox}$ mice ($n = 4$) and $Apc^{flox/flox}$/LSL-$Kras^{G12D}$ mice ($n = 4$). Two separate polyps per mouse (pairs) were used for immunoblots. In. E., normal intestinal epithelial cells. (**E**) Absolute amounts of intracellular vitamin C were measured in tumors derived from $Apc^{flox/flox}$ mice and $Apc^{flox/flox}$/LSL-$Kras^{G12D}$ mice treated with either vitamin C (4 g/kg) or PBS. Samples were harvested 1 hour after treatment. Two-way ANOVA ($P = 0.0002$) followed by Tukey's test for multiple comparisons. All data represent means ± SD; n.s., not significant.

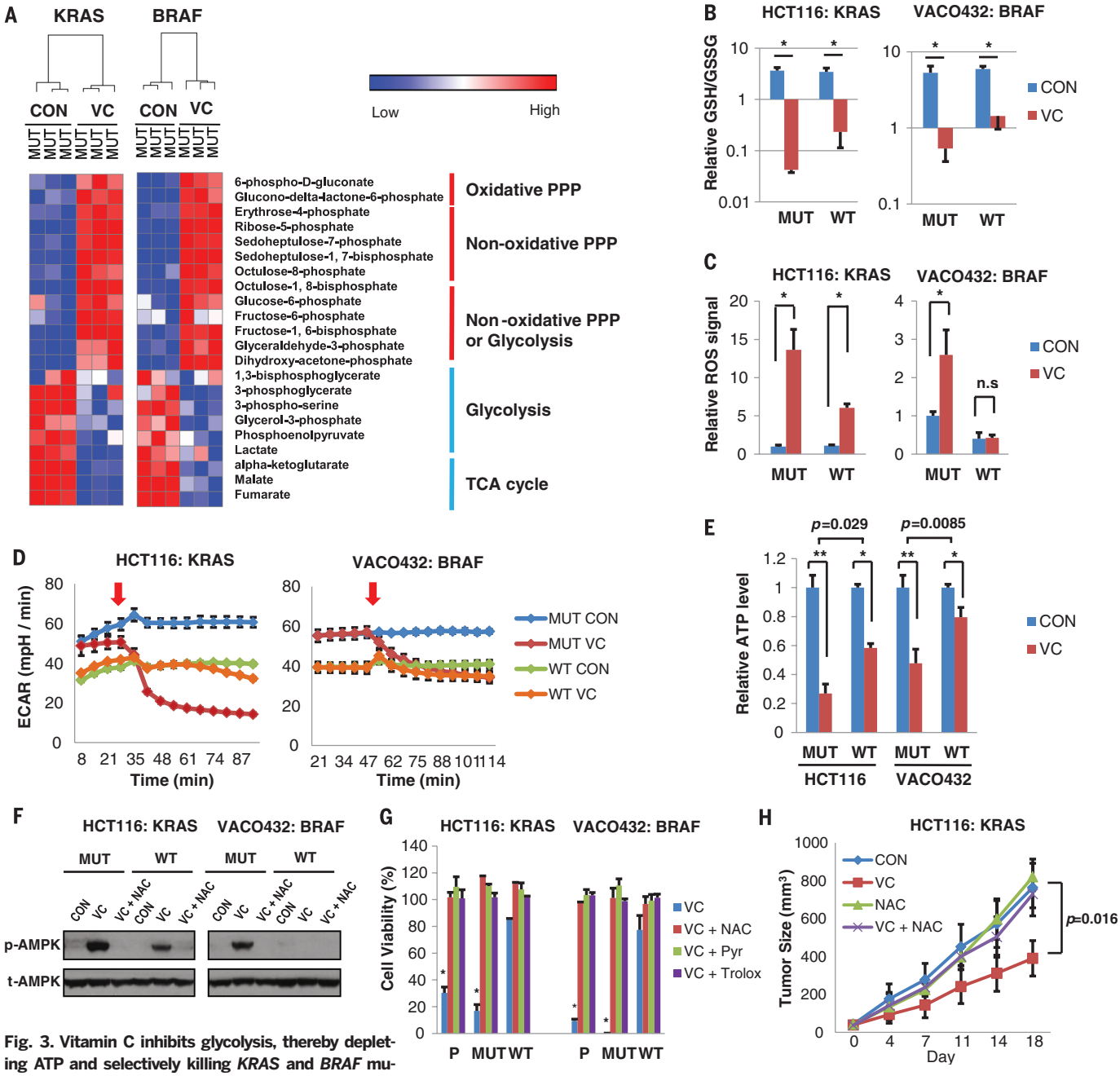

Fig. 3. Vitamin C inhibits glycolysis, thereby depleting ATP and selectively killing *KRAS* and *BRAF* mutant cells. (**A**) Heat map depicting significantly changed glycolytic and pentose phosphate pathway (PPP) metabolite levels in mutant cells after 1 hour of vitamin C (VC) or vehicle (CON) treatment, as analyzed by LC-MS/MS. Red, increase; blue, decrease; TCA, tricarboxylic acid cycle. (**B**) Relative ratios of reduced to oxidized glutathione (GSH/GSSG) in *KRAS* and *BRAF* isogenic cell lines determined by LC-MS/MS as in (A). The ratio was significantly decreased after vitamin C treatment in *KRAS* or *BRAF* mutant cells as well as wild-type cells (Student's *t* test, $*P < 0.002$, $n = 3$), but the extent was greater in the mutant cells than in the wild-type cells. (**C**) After 1 hour of vitamin C treatment, cells were incubated with the ROS-sensitive fluorescent dye DCF-DA for 30 min and fluorescence measured by flow cytometry. Asterisks indicate significant increases in ROS after vitamin C treatment (Student's *t* test, $*P < 0.01$, $n = 3$). (**D**) The extracellular acidification rate (ECAR) was monitored in *KRAS* and *BRAF* isogenic cell lines. Red arrows indicate the time of vitamin C or vehicle (CON) addition ($n = 6$). (**E**) ATP levels were determined in *KRAS* and *BRAF* isogenic cell lines after 1 hour of vitamin C treatment. Although ATP levels were significantly decreased in all cells (Student's *t* test, $*P < 0.05$, $**P < 0.002$, $n = 3$), the decrease was much more pronounced in *KRAS* or *BRAF* mutant cells (two-way ANOVA). (**F**) Cells were treated with vitamin C alone or combined with NAC for 1 hour before immunoblotting for Thr^{172} phosphorylation (p-AMPK) or total AMPK (t-AMPK). (**G**) Cells were treated with vitamin C alone or combined with NAC, pyruvate (Pyr), or Trolox for 48 hours and viability measured with a CellTiter-Glo assay (Promega). Cell viability in parental (P) and *KRAS* or *BRAF* mutant cells relative to wild-type cells was significantly decreased with vitamin C alone but not with vitamin C combination treatments. One-way ANOVA with Dunnett's posttest. $*P < 0.0001$, $n = 3$. (**H**) Eight-week-old female athymic nude mice with subcutaneous tumors from parental HCT116 cells were treated with vitamin C alone (4 g/kg), NAC alone (30 mM in drinking water), vitamin C plus NAC, or PBS twice a day via ip injection. Tumor sizes were measured once per week in an unblinded manner. Experiments were repeated twice independently. Relative to PBS, vitamin C treatment alone significantly decreased tumor growth ($P = 0.016$), but adding NAC to the vitamin C treatment abolished this effect ($P = 0.845$). Mixed effect analysis followed by Tukey's test. In (A) to (F), 1 and 2 mM vitamin C were used for HCT116 and VACO432 cells, respectively; for viability assays at low cell densities (G), 0.125 and 0.375 mM vitamin C were used for HCT116 and VACO432 cells, respectively. All data represent means ± SD.

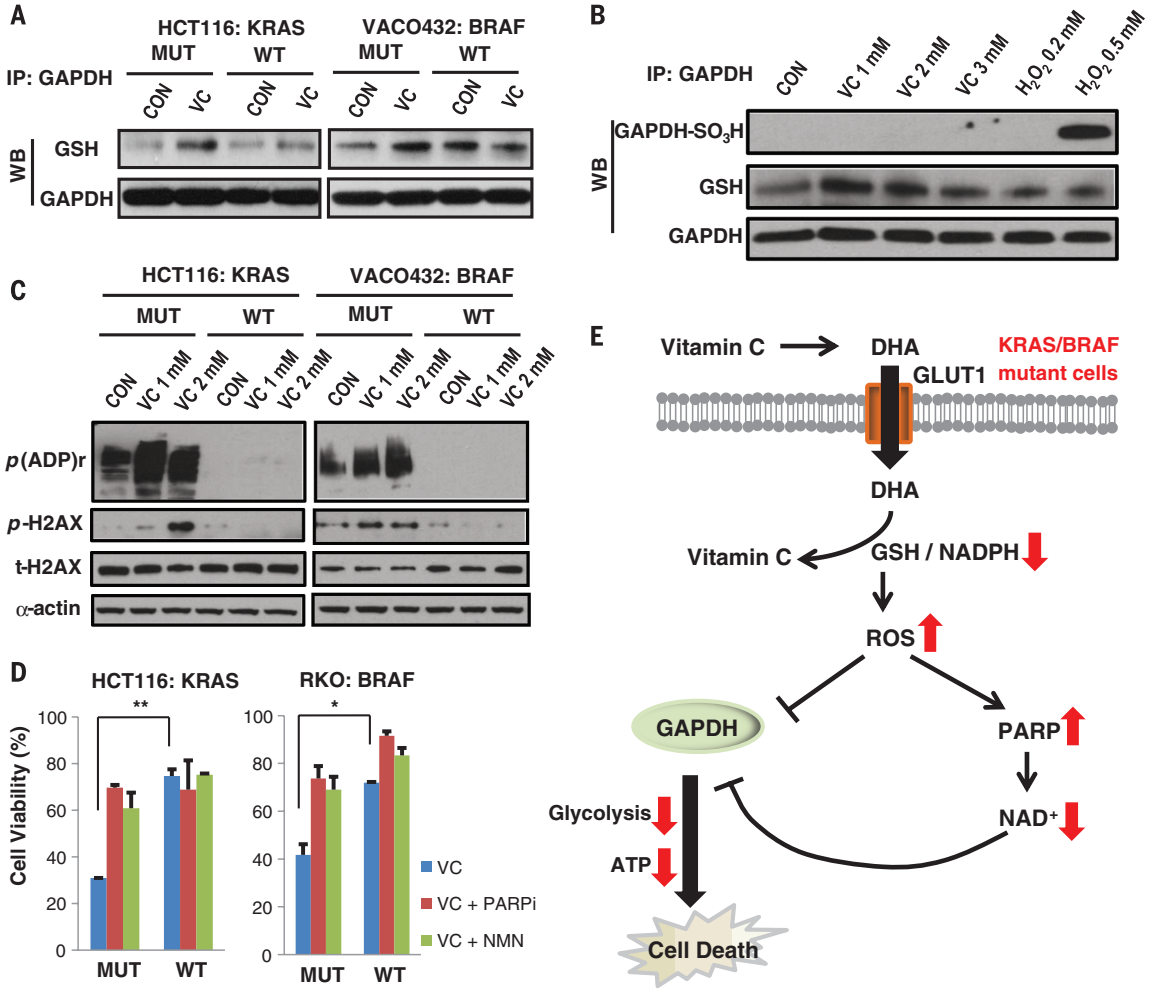

Fig. 4. Vitamin C–induced ROS inhibits GAPDH by cysteine S-glutathionylation and depletion of NAD$^+$. (**A**) Cells were incubated with vehicle (CON) or vitamin C for 1 hour (HCT116, 1 mM; VACO432, 2 mM). Cell extracts were prepared in the presence of iodoacetic acid to prevent S-thiolation during extraction, immunoprecipitated with a GAPDH antibody, and analyzed by nonreducing SDS–polyacrylamide gel electrophoresis and probed with an antibody that recognizes S-glutathionylation. IP, immunoprecipitation; WB, Western blot. (**B**) HCT116 cells were incubated with vehicle, vitamin C, or H_2O_2 for 1 hour. Immunoprecipitations with a GAPDH antibody were performed the same way as in (A) and immunoblots were probed with a GAPDH-SO_3H antibody. (**C**) Immunoblots for p(ADP)r (ADP-ribose polymers), Ser^{139}-phosphorylated H2AX, total H2AX, and β-actin on lysates from cells treated with vehicle (CON) or vitamin C for 1 hour. (**D**) Cells were treated with vitamin C alone (0.125 mM) or vitamin C plus 10 μM olaparib (VC + PARPi) or 1 mM β-nicotinamide mononucleotide (VC + NMN). Viability after 48 hours of treatment was measured using a CellTiter-Glo assay and normalized to untreated controls. Asterisks indicate significant differences relative to *KRAS* or *BRAF* mutant cells treated with vitamin C alone. Two-way ANOVA followed by Tukey's test. *$P < 0.01$, **$P < 0.001$, $n = 3$. (**E**) Schematic showing how vitamin C selectively kills *KRAS* or *BRAF* mutant cells.

In contrast to G3P levels, intracellular NAD$^+$ levels were significantly diminished after vitamin C treatment (fig. S19). PARP activation due to ROS-induced DNA damage consumes NAD$^+$ to form adenosine diphosphate (ADP)–ribose polymers on acceptor proteins. We observed PARP activation and phosphorylation of H2AX, a marker of DNA damage, shortly after vitamin C treatment (Fig. 4C); this finding suggests that PARP activation may diminish NAD$^+$ levels, thereby further inhibiting GAPDH activity by depleting substrate availability (*25*). To investigate whether PARP activation or NAD$^+$ depletion contributes to vitamin C–induced cytotoxicity in *KRAS* and *BRAF* mutant cells, we treated cells with a PARP inhibitor, olaparib, or a cell-permeable NAD$^+$ precursor, nicotinamide mononucleotide (NMN), before vitamin C treatment. Cell viability after vitamin C treatment was partially rescued by inhibiting PARP or supplementing with NMN (Fig. 4D). Taken together, these results indicate that in *KRAS* and *BRAF* mutant cells vitamin C–induced endogenous ROS inhibits GAPDH by both post-translational modifications and NAD$^+$ depletion, ultimately leading to an energetic crisis and cell death (Fig. 4E).

High-dose vitamin C cancer therapy has a controversial history. Although some early clinical studies indicated that vitamin C had antitumor activity (*26*, *27*), others have shown little effect (*28*, *29*). Recent studies suggest that the contradictory clinical data may be explained, at least in part, by differences in administration route; the millimolar vitamin C plasma concentrations cytotoxic to cancer cells are only achievable via intravenous administration, not via oral administration (*30*, *31*). Given these findings, a growing number of phase I and phase II clinical trials are reevaluating intravenous infusion of vitamin C to treat various cancers (*12*, *13*, *32*, *33*). However, despite the previous studies demonstrating that high-dose vitamin C is cytotoxic to cancer cells in vitro (*34*–*36*) and that it delays tumor growth in xenograft models (*37*, *38*), the mechanism by which vitamin C kills cancer cells while sparing normal cells has been unclear. Our findings address this fundamental question by suggesting that the oxidized form of vitamin C, DHA, is the pharmaceutically active agent, and that the selective toxicity of vitamin C to tumor cells stems from high GLUT1 expression combined with *KRAS* or *BRAF* oncogene-induced glycolytic addiction. Although it is unclear whether the results we have observed in our cell culture and mouse studies will translate to human tumors, our findings on the mechanism of action of vitamin C may warrant future investigation in clinical trials.

REFERENCES AND NOTES

1. J. S. Sebolt-Leopold, R. Herrera, *Nat. Rev. Cancer* **4**, 937–947 (2004).
2. A. Lièvre *et al.*, *Cancer Res.* **66**, 3992–3995 (2006).
3. F. Di Nicolantonio *et al.*, *J. Clin. Oncol.* **26**, 5705–5712 (2008).
4. C. S. Karapetis *et al.*, *N. Engl. J. Med.* **359**, 1757–1765 (2008).
5. K. Kawada *et al.*, *Clin. Cancer Res.* **18**, 1696–1703 (2012).
6. S. W. Chen *et al.*, *Clin. Nucl. Med.* **39**, 685–689 (2014).
7. J. Yun *et al.*, *Science* **325**, 1555–1559 (2009).

8. H. Tsukaguchi *et al*., *Nature* **399**, 70–75 (1999).
9. J. C. Vera, C. I. Rivas, J. Fischbarg, D. W. Golde, *Nature* **364**, 79–82 (1993).
10. C. L. Linster, E. Van Schaftingen, *FEBS J.* **274**, 1–22 (2007).
11. J. C. Vera, C. I. Rivas, R. H. Zhang, C. M. Farber, D. W. Golde, *Blood* **84**, 1628–1634 (1994).
12. C. M. Stephenson, R. D. Levin, T. Spector, C. G. Lis, *Cancer Chemother. Pharmacol.* **72**, 139–146 (2013).
13. L. J. Hoffer *et al*., *Ann. Oncol.* **19**, 1969–1974 (2008).
14. M. Kuraguchi *et al*., *PLOS Genet.* **2**, e146 (2006).
15. E. L. Jackson *et al*., *Genes Dev.* **15**, 3243–3248 (2001).
16. N. Barker *et al*., *Nature* **457**, 608–611 (2009).
17. M. Yuan, S. B. Breitkopf, X. Yang, J. M. Asara, *Nat. Protoc.* **7**, 872–881 (2012).
18. H. Ying *et al*., *Cell* **149**, 656–670 (2012).
19. M. Ralser *et al*., *J. Biol.* **6**, 10 (2007).
20. A. Pastore, G. Federici, E. Bertini, F. Piemonte, *Clin. Chim. Acta* **333**, 19–39 (2003).
21. S. E. Weinberg, N. S. Chandel, *Nat. Chem. Biol.* **11**, 9–15 (2015).
22. N. R. Hwang *et al*., *Biochem. J.* **423**, 253–264 (2009).
23. D. Shenton, C. M. Grant, *Biochem. J.* **374**, 513–519 (2003).
24. V. Ravichandran, T. Seres, T. Moriguchi, J. A. Thomas, R. B. Johnston Jr., *J. Biol. Chem.* **269**, 25010–25015 (1994).
25. C. C. Alano *et al*., *J. Neurosci.* **30**, 2967–2978 (2010).
26. E. Cameron, L. Pauling, *Proc. Natl. Acad. Sci. U.S.A.* **73**, 3685–3689 (1976).
27. E. Cameron, L. Pauling, *Proc. Natl. Acad. Sci. U.S.A.* **75**, 4538–4542 (1978).
28. E. T. Creagan *et al*., *N. Engl. J. Med.* **301**, 687–690 (1979).
29. C. G. Moertel *et al*., *N. Engl. J. Med.* **312**, 137–141 (1985).
30. S. J. Padayatty *et al*., *Ann. Intern. Med.* **140**, 533–537 (2004).
31. M. Levine *et al*., *Proc. Natl. Acad. Sci. U.S.A.* **93**, 3704–3709 (1996).
32. D. A. Monti *et al*., *PLOS ONE* **7**, e29794 (2012).
33. J. L. Welsh *et al*., *Cancer Chemother. Pharmacol.* **71**, 765–775 (2013).
34. Q. Chen *et al*., *Proc. Natl. Acad. Sci. U.S.A.* **102**, 13604–13609 (2005).
35. W. Tian *et al*., *J. Biol. Chem.* **289**, 3339–3351 (2014).
36. S. B. Vuyyuri *et al*., *PLOS ONE* **8**, e67081 (2013).
37. J. Kim *et al*., *Free Radic. Biol. Med.* **53**, 1607–1615 (2012).
38. Y. Ma *et al*., *Sci. Transl. Med.* **6**, 222ra218 (2014).

ACKNOWLEDGMENTS

We thank B. Vogelstein and K. W. Kinzler for helpful suggestions; the Cantley lab members, B. Hopkins, F. Karreth, C. Lyssiotis, and G. DeNicola for comments on the manuscript; and M. Yuan, S. Breitkopf, J. Wong, and O. Mashadova for technical assistance. We apologize for publications not cited because of space limitations. L.C.C. owns equity in, receives compensation from, and serves on the board of directors and scientific advisory board of Agios Pharmaceuticals. Agios Pharmaceuticals is identifying metabolic pathways of cancer cells and developing drugs to inhibit such enzymes in order to disrupt tumor cell growth and survival. Supported by the Damon Runyon Cancer Research Foundation (J.Y. and I.I.C.C.), KL2 Career Development Awards (J.Y.), the U.S. Department of Defense (J.P.), National Cancer Institute grants P01 CA120964-07 and P01 CA117969-09 (L.C.C.), and NIH grant P01 CA120964 (J.M.A.). The authors declare no competing financial interests.

SUPPLEMENTARY MATERIALS

www.sciencemag.org/content/350/6266/1391/suppl/DC1
Materials and Methods
Figs. S1 to S19
References (*39*, *40*)

15 December 2014; accepted 16 October 2015
Published online 5 November 2015
10.1126/science.aaa5004

NEW ENGLAND BioLabs® Inc.

Even more *from* less.

NEBNext® Ultra™ II DNA Library Prep Kit for NGS

Are you challenged with trying to get higher library yields using ever-decreasing input amounts? Each component in the NEBNext Ultra II DNA Library Prep Kit from NEB® has been reformulated, resulting in a several-fold increase in library yield with as little as 500 picograms of input DNA. These advances deliver unprecedented performance, while enabling lower inputs and fewer PCR cycles. Get even more from less with NEBNext Ultra II.

Visit **NEBNextUltraII.com** to learn more and request a sample.

The NEBNext Ultra II DNA Library Prep Kit for Illumina® produces the highest yield libraries from a broad range of input amounts.

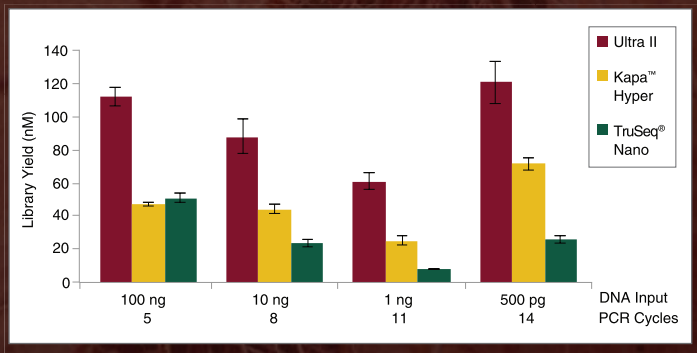

Libraries were prepared from Human NA19240 genomic DNA using the input amounts and numbers of PCR cycles shown. Manufacturers' recommended protocols were followed, with the exception that size selection was omitted.

NEW ENGLAND BIOLABS®, NEB® and NEBNEXT® are registered trademarks of New England Biolabs, Inc.
ULTRA™ is a trademark of New England Biolabs, Inc.
KAPA™ is a trademark of Kapa Biosystems. ILLUMINA® and TRUSEQ® are registered trademarks of Illumina, Inc.

Gordon Research Conferences

www.grc.org

Everyone remembers their first GRC... Make a memory at the Frontiers of Science in **Hong Kong**!

The Chinese University of Hong Kong

Advanced Health Informatics
The Use of Big Data in Health Related Research
July 17-22, 2016

Fibroblast Growth Factors in Development & Disease +GRS
FGF Signalling: From Molecular Understanding to Therapeutic Targeting
June 5-10, 2016

Ocean Biogeochemistry
The Biologically-Driven Ocean Carbon Pumps
June 12-17, 2016

Single Molecule Approaches to Biology +GRS
Single-Molecule Microscopy: Life at a Higher Resolution
July 3-8, 2016

Structural Nanomaterials
Interfacial and Surface Effects on Structural Nanomaterial Properties
July 10-15, 2016

Three Dimensional Electron Microscopy
Advancing and Reshaping Structural Biology with Electron Cryo-Microscopy
June 19-24, 2016

The Hong Kong University of Science and Technology

Advanced Materials for Sustainable Infrastructure Development
The Science and Technology of Sustainable Concrete
July 31 - August 5, 2016

Genomic Instability +GRS
DNA Packaging, Replication, and Repair
July 24-29, 2016

Hybrid Electronic & Photonic Materials and Phenomena
Fundamentals of Organic and Inorganic Semiconductors and Their Integration in Hybrid Electronic and Photonic Devices
June 19-24, 2016

Molecular & Cellular Neurobiology +GRS
Novel Approaches and New Advancement in Neural Development, Plasticity, and Diseases
June 12-17, 2016

Nasopharyngeal Carcinoma
Global Lessons on Cancer Pathogenesis from Insights into a Geographically Restricted Tumor of the Nasopharynx
June 26 - July 1, 2016

Personalized Medicine
Realizing Personalized Medicine Through Integrative Medicine, Science and Technology
July 10-15, 2016

Solar Energy Conversion
Materials, Physics and Devices in Solar Energy Conversion
July 17-22, 2016

Tissue Niches & Resident Stem Cells in Adult Epithelia
Regulation of Tissue Homeostasis by Signaling in the Stem Cell Niche
August 7-12, 2016

GRS A Gordon Research Seminar (GRS) for graduate students and post-docs will be held on the Saturday and Sunday just prior to these 4 GRCs.

Image: The Jockey Club Institute for Advanced Study at HKUST, one of the host sites for GRC meetings in Hong Kong.

PACIFICHEM 2015

GRC will be at Pacifichem: The 2015 International Chemical Congress of Pacific Basin Societies, which will take place December 15-20 in Honolulu, Hawaii.

New Conference Proposals: We are now accepting proposals for new GRCs to start in 2018. Check the "Proposing a New Gordon Conference" page on our web site for more information. Proposals for new conferences to take place in Hong Kong are particularly welcome!

“A multi-course meal for the mind”

– The Globe and Mail

NAUTILUS

Save 37% on *Nautilus* Prime
Use Coupon Code: **AAAS9**

nautil.us/aaas/9

Liquid Chromatography System

Proteomics laboratories can benefit from the new nano LC system with dedicated columns as front-end for liquid chromatography mass spectrometry (LC-MS). The EASY-nLC 1200 system provides effortless separation performance and high-throughput capacity and is designed for robust and reliable operation at 1200 bar. New maintenance-free ceramic valves decrease system downtime, and tool-free nanoViper connections provide fast and reproducible fluidic connections over the complete flow path. New software features enhance performance and usability, simplifying operation and maintenance and offering users at various levels of expertise a fully integrated solution that consistently generates high-quality data. The new Acclaim PepMap nano LC columns are designed to handle the 1200 bar-pressure capability of the EASY-nLC 1200. In particular, the new 75 cm format provides high peak capacity intended to increase sensitivity and resolution.

Thermo Fisher Scientific
For info: 800-556-2323
www.thermoscientific.com/nanolcms

Gel Imager

The Imagel Gel Doc system for iPhone or Android is the smart way to quickly grab your gel images. Just hook up your smartphone to the compact hood and start to collect images of all your gels quickly and easily. The Imagel can be used with three different light sources. Use the blue light-emitting diode (LED) transilluminator for DNA applications that use Green DNA, GelGren, SYBR Green, SYBR Safe, SYBR Gold, and for protein applications using LavaPurple. An ultraviolet transilluminator will let you work with AmberDNA, ethidium bromide, SYBR, Oriole, fluorescent gel stain, GelRed, SYPRO Ruby, Coomassie, Fluor Orange, and Krypton. Also, using a white light source you can capture images of proteins using Coomassie Blue, copper, silver, or zinc stains. The Imagel is very simple to use—just snap a photo and save on your phone or upload to the cloud for hosting, sharing, and image analysis and annotation features.

Gel Company/Aplegen
For info: 415-247-8760
www.gelcompany.com

Gel Documentation System

The HeroDoc Plus is a compact gel documentation system for imaging gels and blots. The compact darkroom/hood assembly will sit comfortably on any laboratory bench within its small footprint. A unique lift-up hood and a built-in ultraviolet (UV) protection shield enable the user to do preparative work easily and safely. Should the user wish to raise the shield, an automatic cutoff switch will protect the user from any harmful effects of UV light. A high sensitivity, charge-coupled device (CCD) camera combined with a distortion-free, software-controlled lens ensures quality image capture from 10 milliseconds up to 60 minutes. This is more than adequate for most fluorescent gel and blot image capture. Illumination comes from a massive 28 cm × 22 cm filter midrange transilluminator, while built-in white and blue light light-emitting diodes (LEDs) provide epi-illumination as standard. Multilanguage, HeroStore image capture and control software effortlessly enables the user to acquire images of gels and blots.

Hero
For info: +44-(0)-1223-515440
www.herolab.de

ChIP-Validated Antibodies

ChIP-validated antibodies further enhance the high-performance application solutions that Chromatrap can provide researchers. The use of high-quality and specific chromatin immunoprecipitation (ChIP)-validated antibodies is essential for the success of a ChIP assay. The antibody must recognize and bind to native protein that is bound to DNA. Antibodies from other applications do not always work well in ChIP. These top-quality validated antibodies are now offered alongside the expanding range of kits for ChIP assays of every type. Chromatrap currently offers a range of ChIP kits for quantitative polymerase chain reaction (qPCR) or sequencing and has now launched the first nine antibodies in its validated antibody program, which are H3, RNA pol II (S), RNA pol II (S5), H3K9me3, 5mC, AcH3, AcH4, AR, and Sin3a. Chromatrap validated antibodies are available in 100 uL aliquots at a concentration of 1 mg/ml.

Chromatrap
For info: +44-(0)-1978-666222
www.chromatrap.com

Imaging System

The Omega Lum W analysis system can be used for gel, multicolor R, G, B, and chemiluminescent imaging. This compact package sits neatly on any laboratory bench ready to image gels, Western blots, or multiplexing multicolored blots at the click of a button. At the heart of any gel documentation system is a quality camera, and the Omega Lum W comes with one of the best. A massive 8.4 megapixel, scientific grade, cooled charge-coupled device (CCD) camera combined with an f/0.95 motorized lens and six-position filter wheel gives the system outstanding power and performance. This combination provides the highest sensitivity and signal capture for perfect imaging, giving amazingly low background and a wide dynamic range for accurate quantification. One of the system's key features is the SmartCapture Technology. This unique automated control eliminates the need for filter selection and focus adjustment, thereby helping the user to obtain high-quality images every time.

Eikonix
For info: +44-(0)-1223-515440
www.eikonix.com

Electronically submit your new product description or product literature information! Go to www.sciencemag.org/products/newproducts.dtl for more information.

Newly offered instrumentation, apparatus, and laboratory materials of interest to researchers in all disciplines in academic, industrial, and governmental organizations are featured in this space. Emphasis is given to purpose, chief characteristics, and availability of products and materials. Endorsement by *Science* or AAAS of any products or materials mentioned is not implied. Additional information may be obtained from the manufacturer or supplier.

Your Next Breakthrough Begins Here.

You are a high academic achiever, looking to establish your research on the world stage. You need a university that is recognised globally for its transformative research and education.

Founded in 1592, Trinity College Dublin has an international reputation for intellectual rigour, excellence and research-led teaching. It is recognised as Ireland's number 1 university in the QS World University Rankings, THE World University Rankings, and Academic Ranking of World Universities (Shanghai).

Our three faculties are inviting gifted candidates from around the world to join us as one of 40 new **Ussher Assistant Professors**. We will offer you a dynamic environment to develop work of global consequence.

See if there is an opportunity for you at **tcd.ie/ussher**

Trinity College Dublin.
A history of driving the future.

Trinity College Dublin
Coláiste na Tríonóide, Baile Átha Cliath
The University of Dublin

Faculty of Arts, Humanities and Social Sciences
Faculty of Engineering, Mathematics and Science
Faculty of Health Sciences

R&D SYSTEMS
a bio-techne brand

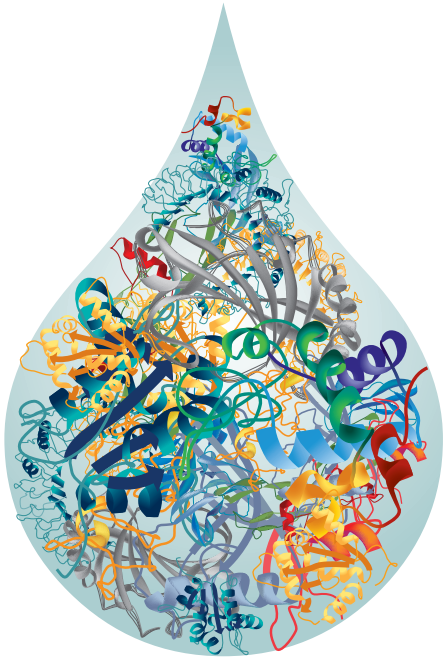

What's in Your Sample?

Find Your Answers!

rndsystems.com/
Immunoassays

ScienceCareers online @sciencecareers.org

Science Careers Advertising

For full advertising details, go to ScienceCareers.org and click For Employers, or call one of our representatives.

Tracy Holmes
Worldwide Associate Director
Science Careers
Phone: +44 (0) 1223 326525

THE AMERICAS

E-mail: advertise@sciencecareers.org

Fax: +1 (202) 289 6742

Tina Burks
Phone: +1 (202) 326 6577

Nancy Toema
Phone: +1 (202) 326 6578

Online Job Posting Questions
Phone: +1 (202) 312 6375

EUROPE / INDIA / AUSTRALIA / NEW ZEALAND / REST OF WORLD

E-mail: ads@science-int.co.uk

Fax: +44 (0) 1223 326532

Sarah Lelarge
Phone: +44 (0) 1223 326527

Kelly Grace
Phone: +44 (0) 1223 326528

Online Job Posting Questions
Phone: +44 (0) 1223 326528

JAPAN

Katsuyoshi Fukamizu (Tokyo)
E-mail: kfukamizu@aaas.org
Phone: +81 3 3219 5777

Hiroyuki Mashiki (Kyoto)
E-mail: hmashiki@aaas.org
Phone: +81 75 823 1109

CHINA / KOREA / SINGAPORE / TAIWAN / THAILAND

Ruolei Wu
Phone: +86 186 0082 9345
E-mail: rwu@aaas.org

All ads submitted for publication must comply with applicable U.S. and non-U.S. laws. *Science* reserves the right to refuse any advertisement at its sole discretion for any reason, including without limitation for offensive language or inappropriate content, and all advertising is subject to publisher approval. *Science* encourages our readers to alert us to any ads that they feel may be discriminatory or offensive.

ScienceCareers
FROM THE JOURNAL SCIENCE AAAS

ScienceCareers.org

UNIVERSITY OF CALIFORNIA
UC RIVERSIDE

The Malleable Nervous System: From Molecule to Circuit to Behavior

(Up to 8 Open Rank Tenure Track/Tenured Faculty Positions)

The University of California at Riverside (UCR) is embarking on a major new hiring initiative that will add 300 tenure-track positions in 33 cross-disciplinary areas selected through a peer-reviewed competition (clusterhiring.ucr.edu). Over the next three years, UCR will hire multiple faculty members in each area and invest in research infrastructure to support their work. This initiative will build critical mass in vital and emerging fields of scholarship, foster truly cross-disciplinary work and further diversify the faculty at one of America's most diverse research universities. In a major Neuroscience initiative, we seek to hire up to 8 tenure-track or tenured faculty members as part of a cross campus multi-disciplinary effort to study the nervous system (from development, to function, to aging, degeneration and repair). We seek researchers that collectively span multi-disciplinary levels of investigation (molecular mechanisms to circuit analysis to complex behaviors) using state of the art techniques (molecular, optogenetics, behavioral, educational, computational, imaging, genetic and research of clinical populations) applied to experimental model systems of health, injury and disease (invertebrate, vertebrate or human systems). Our goal is to recruit a team of collaborative individuals with an outstanding record, committed to excellence in research, that complement existing campus strengths. Applicants for tenured positions should also demonstrate notable scientific contributions and sustained extramural support. *Successful candidates must also have clear potential or demonstrated ability to work successfully with and benefit a diverse student body. UCR is a world-class research university with an exceptionally diverse undergraduate student body. Its mission is explicitly linked to providing routes to educational success for underrepresented and first-generation college students. A commitment to this mission is a preferred qualification.*

Depending on research focus, training background and career achievements, successful candidates will be appointed at the rank of assistant, associate or full professor within College of Natural and Agricultural Sciences, Bourns College of Engineering, College of Humanities, Arts and Social Sciences, Graduate School of Education or the School of Medicine. To foster development of collaborative research across hiring units, the successful candidates will participate in a campus wide seminar program and annual research retreat. Particular strengths on the campus pertinent to this recruitment include sensory processing, neurodevelopmental and neurodegenerative disorders, glial-neuronal interactions, cognitive neurotherapeutics, functional imaging, assessment and interventions of clinical populations, child development, circuits, neurobiology and endocrinology of behavior. Successful candidates will be also expected to contribute to teaching at both the graduate and undergraduate levels depending upon the college/department to which the candidate is assigned. *Advancement through the faculty ranks at the University of California is through a series of structured, merit-based evaluations, occurring every 2-3 years, each of which includes substantial peer input.*

The University of California, Riverside is centrally located within the Southern California area and situated in an historic citrus growing area surrounded by mountain ranges. Riverside is an hour away from ski slopes, surfing, or hiking in mountain wilderness or desert environments, and housing in the area is very affordable. The campus is located in close proximity to a host of high profile universities, research institutes, and biotech industries in Southern California. Applicants must hold a Ph.D., M.D., Pharm D., or equivalent degree and qualify for a tenure track or tenured faculty appointment at the University of California. Applications will be reviewed beginning **January 1st, 2016** and the positions will remain open until filled. The University of California is an Equal Opportunity/Affirmative Action Employer with a strong institutional commitment to the achievement of excellence and diversity among its faculty and staff. All qualified applicants will receive consideration of employment without regard to race, color, religion, sex, national origin, age, disability; protected veteran status, or any other characteristic protected by law. *We encourage applications from scholars committed to excellence and seeking to help redefine the research university for the next generation.*

To Apply: Please submit the following items electronically through the APRecruit system: Cover Letter, Curriculum vitae, statement of research accomplishments and goals, statement of teaching expertise.

Choose the appropriate link based on qualifications
Assistant Professor - https://aprecruit.ucr.edu/apply/JPF00498
Associate/Full Professor - https://aprecruit.ucr.edu/apply/JPF00490

Chongqing

A research boom in China's municipalities

In recent years, as China's cities have been transformed with gleaming skyscrapers, an Olympic stadium, and an iconic TV tower, the country has increasingly flexed its new economic might in the scientific arena as well. The government's investment in research grew to 1.98% of gross domestic product (GDP) in 2012, according to the World Bank—surpassing that of the European Union. That injection of resources, together with a strong base of well-educated researchers at home and abroad, has transformed Beijing and Shanghai into scientific powerhouses and jump-started opportunities in second-tier cities like Tianjin and Chongqing. **By Shawna Williams**

China's recent boom in scientific research and development is especially evident in its four municipalities: cities that are effectively their own province, administered directly by the central government. Those cities are Beijing, Tianjin, Shanghai, and Chongqing. Each is a priority target for government-led development efforts and home to top universities and government research institutes, and while Beijing and Shanghai offer an unrivaled array of opportunities in the sciences, Chongqing and Tianjin boast strengths of their own.

Beijing

China's capital is home to dozens of institutes of the Chinese Academy of Sciences (CAS); universities, including Peking University and Tsinghua University, which are widely considered China's best; and a wealth of private and state-owned companies. "As an innovation center, Beijing provides many opportunities in hospitals, universities, big companies, and small businesses," says **Luming Li**, who heads the National Engineering Laboratory for Neuromodulation (NELN) at Tsinghua University. In his work developing brain stimulation methods to treat neurological diseases such as Parkinson's, Li works closely with colleagues at Beijing's Tiantan Hospital—known for its neurosurgery expertise—and Beijing PINS Medical Co., Ltd., which brings products that NELN develops to the market. Li says NELN is unique in forging ties between clinicians, researchers, and industry that shorten the time needed to develop new devices. For example, researchers in his group all observe neurosurgeries at the hospital and learn to "speak the same language as surgeons," he says.

Synergistic opportunities also abound for researchers in less applied fields than Li's, according to **Junjie Hu**, a principal investigator (PI) at CAS's Institute of Biophysics. Hu, who was previously on the faculty of Nankai University in Tianjin, says, "I have more collaborations here, and I think [there are many such opportunities in the] scientific community in Beijing . . . because of its size." There are several other CAS institutes nearby, he says, and within his own institute, he has access to experts in powerful microscopy techniques with whom he can consult, as well as access to the microscopes themselves. Hu thinks it's these resources that have enabled the Institute of Biophysics to recruit four of the seven China-based researchers who were named International Early Career Scientists by the Howard Hughes Medical Institute in 2012.

Lingli Liu

Lingli Liu, a PI at CAS's Institute of Botany in Beijing, agrees that the city provides fertile ground for collaborations both at home and abroad. "Because Beijing has so many scientists, it's very convenient for us to collaborate with each other, and there are also many international conferences here," she explains. In addition, graduate students tend to be drawn to Beijing, which makes it easier to recruit them, she says. Another of the institute's selling points is that "students have a chance to work on advanced research and to interact with leading scientists who visit from all over the world," says Liu. And they can apply for one- or two-year scholarships to do research abroad.

Similar strengths are making the Institute of Biophysics increasingly attractive to graduate students, Hu says. Compared to the year 2000, when he graduated from college and left China for graduate school at New York University, "The research in China today is totally different," he says. "Nowadays I think the gap [between China and other countries] is growing smaller and smaller and there are more and more labs doing good research [that students] can choose from." There are also better opportunities for postdoctoral fellows than in the past, he adds, citing the institute's industry-sponsored postdoc packages that promise good pay and emphasize independence. continued>

PHOTO (TOP): © SEAN PAVONE/SHUTTERSTOCK.COM

Upcoming Features

Faculty Careers—January 29 ■ *Postdoc Careers—March 25* ■ *Cancer Research—April 8*

"Since clinical needs are important sources of ideas in biomedical engineering research, it is [beneficial] to have close collaborations and frequent communication [with] clinicians."
— Tao Yin

Tianjin

Just a short ride from Beijing by high-speed rail, the port city of Tianjin boasts mainland China's highest per-capita GDP, according to the Xinhua News Agency. That's partly because of the Tianjin Binhai New Area, a high-tech district lying outside central Tianjin but inside the municipality, and the home of 219 Fortune 500 companies, according to *China Daily.* One campus of the Tianjin University of Science and Technology is also located at Binhai, where the dominant industries include microelectronics, chemical engineering, and energy. **Zhi Yao**, director of the Department of Immunology at Tianjin Medical University (TMU), says the city currently offers many career opportunities in biomedicine, aerospace, information technology, and the petrochemical industry.

Yao projects that more than 300 professors and instructors will be hired at TMU over the next five years. The new hires will have ample opportunity to interact with top colleagues from abroad, as TMU has already awarded 119 honorary and visiting professorships to foreign scholars, says Yao. A new campus is being built to provide more space for teaching and research for new and current faculty.

Hiring is also among the strategic priorities at Tianjin University, which plans to hire about 400 new staff in 2016, including faculty, research staff, and postdoctoral fellows, according to President **Jiajun Li**. He sees many opportunities in Tianjin's industries as well, particularly in the chemical industry and in manufacturing, construction, energy, environmental protection, new materials, information technologies, instrumentation, biomedicine, and marine engineering.

Although industry provides some of Tianjin's most promising opportunities for scientists and engineers, the hiring and funding outlook is also good at Tianjin's Institute of Biomedical Engineering, an outpost of the Chinese Academy of Medical Sciences. **Tao Yin**, a professor of biomedical engineering at the institute, has found China's funding environment to be favorable for his work there, with most grants coming through the Ministry of Science and Technology and the National Natural Science Foundation. For students who would like to enter his field, Yin suggests acquiring extensive knowledge to "broaden their research horizons," because biomedical engineering is multidisciplinary. He adds that "since clinical needs are important sources of ideas in biomedical engineering research, it is [beneficial] to have close collaborations and frequent communication [with] clinicians."

Shanghai

Medical immunology is another area with strong grant funding in China, says **Xuetao Cao**, director of the National Key Laboratory of Medical Immunology in Shanghai. He credits strong government support with enabling the laboratory to develop powerful tools for both basic research and cancer immunotherapy studies. In the coming year, he predicts the laboratory will hire three to four PIs to continue to push the work forward.

Cao's laboratory is one of many potential destinations for those seeking research positions in Shanghai. China's largest city and financial capital, Shanghai is also a leader in science and engineering. The municipality is home to multiple CAS institutes and top universities, notably Fudan and Shanghai Jiao Tong, and several high-tech industrial development zones.

Jie Zhang, the president of Shanghai Jiao Tong University, has his sights set on making his institution one of the best in the world. "In China, with a population of 1.3 billion, every student competes to get into one of the top five universities," he explains. "The goal [at Shanghai Jiao Tong] is to give those students the same quality education in China that they would get at a U.S. institution." With that goal in mind, the university created different tracks to reward professors for excellence in teaching, not solely for the quantity and quality of their publications, as occurs at many Chinese universities. In the current academic year, Zhang projects that Shanghai Jiao Tong will hire 80 tenure-track faculty through global recruitment and through promoting current faculty. Eight years ago, Zhang also founded the university's Zhiyuan College, which emphasizes interdisciplinary education and hands-on research for the most talented students. All faculty are adjunct, which Zhang says enables the college to employ exceptionally innovative scientists who are jointly appointed to other departments within the university. He sees Zhiyuan College as a pilot program and hopes to eventually expand its educational model, which earned him a National Award for Higher Education in 2014, to the entire university.

Shanghai's educational environment has seen a lot of positive change since his days as a student, says **Weijun Pan**, who completed his Bachelor's in 1999 at East China University of Science and Technology and a Ph.D. at the Shanghai Institutes for Biological Sciences (SIBS). Following his studies in Shanghai, Pan went abroad for postdoctoral training at Yale University and the National Institutes of Health. Now a PI at SIBS' Institute of Health Sciences, he says that today's students have many more opportunities than he did to research abroad while completing a Ph.D. in Shanghai, and to interact with foreign researchers who visit the city. For example, of the eight institutes that comprise SIBS, one is a co-venture of CAS and the Institut Pasteur in France, and another is a collaboration between CAS and the Max Planck Society in Germany—both have recruited faculty from abroad as well as within China. And SIBS students can apply for scholarships to work in an overseas collaborator's lab for a year or two, Pan says.

Pan says that having the combination of a Thousand Young Talents award from the central continued>

PHOTO: YIN/TAO

TBSI 清华-伯克利深圳学院
Tsinghua-Berkeley Shenzhen Institute

ACADEMIC AND RESEARCH POSITIONS AVAILABLE
DEGREE PROGRAMS OPEN FOR APPLICATION
TSINGHUA-BERKELEY SHENZHEN INSTITUTE

Situated in the beautiful Xili University Town, Shenzhen, Guangdong, China, Tsinghua-Berkeley Shenzhen Institute (hereinafter referred to as TBSI) was jointly established by Tsinghua University, University of California at Berkeley, and Shenzhen Municipal Government. The vision of TBSI is to build a world-class transformative research and education partnership to fuel economic growth with accelerated innovation through transdisciplinary and translational research. The institute consists of three multidisciplinary research centers in Environmental Science and New Energy Technology, Data Science and Information Technology, and Precision Medicine and Healthcare, and is now recruiting faculty and researchers globally to conduct innovative and cutting-edge researches.

Positions and Requirements

Available Positions: Tenure-track Faculty (Assistant/Associate/Full Professors) and Postdoctoral Researchers
Applicants must have a Ph.D. degree from an accredited university, demonstrated ability for independent research and graduate teaching, and have significant research achievements. Candidates applying for faculty positions should demonstrate pioneering research achievements, international peer recognition, and capability to lead the research group to reach advanced level.
The positions are open to candidates in the following areas: Environmental Science and Engineering, Mechanical Engineering, Instrument Science and Technology, Material Science and Engineering, Electrical Engineering, Information and Telecommunication Engineering, Control Science and Engineering, Computer Science and Engineering, Physics, Chemistry, Biology, Management Science and Engineering, Logistics Engineering and Management, Sociology, etc.

Salary and Benefit

TBSI provides competitive annual salary ranging from CNY 400,000 to CNY 1,200,000 for the faculty positions. TBSI will also assist the faculty and researchers to apply for housing compensation up to CNY 1,500,000 sponsored by the Shenzhen Phoenix Talents Recruiting Project and other Shenzhen High Level Talents Plans.
The postdoctoral researchers will receive a total compensation package of CNY 300,000 per year (two-year contract). The postdoctoral researchers will be co-advised by Tsinghua and Berkeley professors and split the time to work in Shenzhen and Berkeley, respectively.

Ph.D. and M.Sc. Programs

TBSI provides three cross-disciplinary Ph.D. programs and two M.Sc. programs with novel graduate curriculum for the cultivation of future entrepreneurs and world leaders in science and technology. Students are co-advised by faculty members of both Tsinghua and UC Berkeley, and newly recruited full-time TBSI faculties in the three interdisciplinary research centers. They are also encouraged to interact with industry advisors to identify unique first-hand research problems that are both academically challenging and social-economically important. Upon meeting program requirements and passing in the dissertation defense and review, students will be awarded Diploma and Ph.D. Degree or M.Sc. Degree by Tsinghua University.
For more information about TBSI degree programs and scholarship, please refer to the official website: *http://www.tbsi.edu.cn*

Contact Us

1. Faculty or Postdoctoral Positions
To apply for the academic and research positions, please send the following documents to Ms. Fang via email *fangrui@sz.tsinghua.edu.cn*, or telephone +86-755-26038130.

a. Curriculum Vitae
b. Application form (Please download from the official website)
c. 3 to 5 representative publications
d. Contact information of 5 to 10 preferred reviewers including mailing address, e-mail address, and phone number
e. Research Plan

2. Ph.D. and M.Sc. Programs
The 2016 fall admission is now open. To apply for the Ph.D. and M.Sc. programs, please contact Ms. Liu at +86 755 26035839, or send email to *lareina_liu@sz.tsinghua.edu.cn*

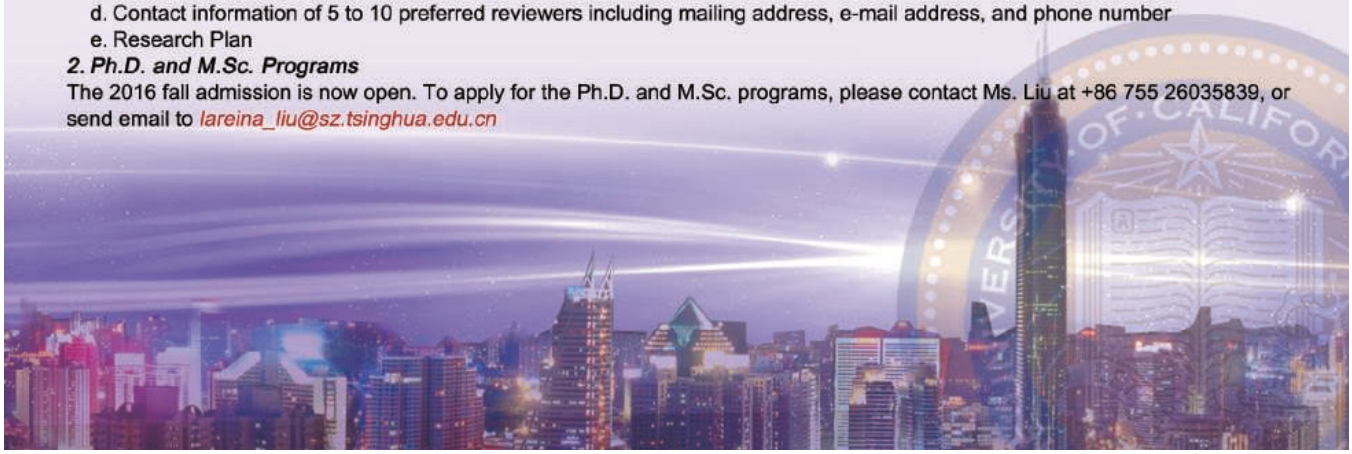

Science Careers online @sciencecareers.org
FOCUS ON CHINA

Featured Participants

Chongqing Cancer Hospital
www.cqch.cn/list.php?tid=365

Institute of Biomedical Engineering, Chinese Academy of Medical Sciences & Peking Union Medical College
www.bme.org.cn (in Chinese)

Institute of Biophysics, Chinese Academy of Sciences
english.ibp.cas.cn

Institute of Botany, Chinese Academy of Sciences
english.ib.cas.cn

The Institute of Health Sciences, Shanghai Institutes for Biological Sciences, Chinese Academy of Sciences
www.ihs.ac.cn/eng/eindex.asp

National Key Laboratory of Medical Immunology
www.immunol.org (in Chinese)

NELN, Tsinghau University
www.neuromodulation.cn

Ruijin Hospital
www.rjh.com.cn/chpage/c1352

School of Electrical Engineering, Chongqing University
cee.cqu.edu.cn/enindex.asp

Shanghai Jiao Tong University
en.sjtu.edu.cn

Southwest University
www.swu.edu.cn/english

Tianjin Medical University
www.tijmu.edu.cn/s/2/t/250/p/3/c/1080/list.htm

Tianjin University
www.tju.edu.cn/english

Jie Zhang

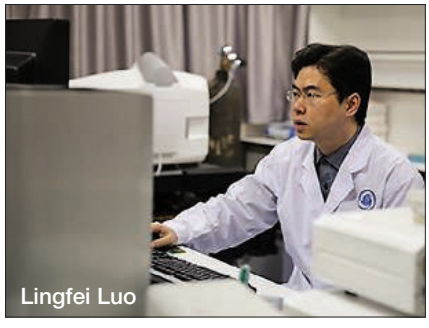
Lingfei Luo

government and funds from the Institute of Health Sciences provided a startup package almost equivalent to what he would have expected from a U.S. institution. And because SIBS' eight institutes share resources, it's "easy for me to find advanced instruments," he says.

Shanghai will soon have another institute specializing in translation, thanks to a $157 million investment from the National Development and Reform Commission of the People's Republic of China. **Guang Ning**, the deputy director at Ruijin Hospital, is involved in launching a new National Centre for Translational Medicine that will open in 2017 with 300 beds devoted to translational and clinical research. "The translational medicine center also includes a biobank for hundreds of thousands of patient samples and an 'omics analyses center for genomic and metabolic data," he says, as well as space for pharmaceutical industry collaborators. The center will have two sites, Ning says, one at Ruijin, a teaching hospital affiliated with the Shanghai Jiao Tong University School of Medicine, and one on campus. He adds that the hiring process has already begun for 50 PIs and 12 scientists, who he expects will be a mixture of clinicians and basic scientists.

Chongqing

Chongqing, the only inland municipality, may be best known to Westerners as the starting point for many Yangtze River cruises, or to history buffs as the capital of the Republic of China through much of the Second Sino-Japanese War (1937–1945). Formerly a part of Sichuan Province, it retains that province's laid-back reputation to some extent. But with its designation as a municipality in 1997 and a corresponding increase in resources from the central government, the city is regaining eminence. And Chongqing's strong growth has staying power: It was the only city near the top of The Economist Intelligence Unit's (EIU's) report on rapidly growing Chinese cities in both 2010 and 2015. The 2015 EIU report projects that Chongqing's real GDP will grow by nearly 9% between 2014 and 2019—the third-largest projected rate for any Chinese city. Its fast growth means that "Chongqing offers more working opportunities compared to other Chinese cities," says **Chenguo Yao**, deputy director of the Department of High Voltage and Insulation in the School of Electrical Engineering at Chongqing University.

Much of that opportunity lies in Chongqing's many universities and teaching hospitals. Among these, Chongqing Cancer Hospital's 70-acre campus is unique in its combination of medical treatment, scientific research, cancer screening and education programs for the public, teaching, and postsurgical physical therapy, says neurosurgeon **Xing Cheng**. He cites a dynamic environment and passionate colleagues as advantages of his job, but acknowledges that finding positions at his and other teaching hospitals is "highly competitive."

In contrast, **Lingfei Luo**, who studies organ development in zebrafish at Southwest University, says the employment picture is bright in his field. Luo earned his Master's and Ph.D. in a cooperative program of the University of Göttingen and the Max Planck Institute for Biophysical Chemistry in Germany, followed by a postdoc at the Max Planck Institute. He later spent a year at the University of California, San Francisco as a visiting scientist. Luo was drawn back to Chongqing because it is his hometown, but the decision has also paid off for his career, he says, observing that it is easier for early-career scientists to win grant funding in China than in the United States or Europe. "The biomedical community is growing very fast. Every large university has a number of positions available."

With their wealth of opportunities in the sciences, China's municipalities offer something for almost everyone: Those who prefer a large and active community of fellow researchers might opt for Beijing or Shanghai, while those looking for careers in specific fields, such as biomedicine or energy, would do better to seek a position in Chongqing or Tianjin. Any of the municipalities are sure to provide a front-row seat as China's research and development capabilities continue to expand.

Shawna Williams is a freelance writer based in Baltimore, Maryland.

DOI: 10.1126/science.opms.r1500162

吉林大学

Faculty Positions Available at Jilin University

Jilin University (JLU) is one of the main research-oriented comprehensive universities in China under the direct jurisdiction of the Ministry of Education and is strongly supported by state key projects such as the "211 Project" and the "985 Project". Jilin University has eight campuses, seven of them are located in Changchun, the capital city of Jilin province and one is located in Zhuhai, Guangdong province. The university has 43 colleges which cover 13 academic categories of disciplines, including Philosophy, Economics, Law, Education, Literature, History, Science, Engineering, Agriculture, Medicine, Management, Military Science and Arts. There are also 4 first-level national disciplines and 15 second-level national disciplines. Jilin University offers 125 bachelor's, 302 Master's and 242 doctor's degree programs. At present, there are 6,630 faculty members, including 2,255 associate professors, 2,051 full professors (1,213 doctoral advisors) and 25 members of the Chinese Academy of Sciences and Chinese Academy of Engineering(16 adjunct academicians).

[Recruitment Programs]

Long-term

Position	Employee Benefit Package(Unit:1,000yuan)		
	Salary	Relocation Allowance	Research Funds
Thousand Talents Plan(Long Term)	800-1000 /year	1500	4000-10000
Thousand Talents Plan (Young Professionals)	200-500 /year	1150	2000-6000
Changjiang Scholars Program (Distinguished Professors)	600+ /year	400	500-2000
Changbai Mountain Scholars of Jilin Province (Distinguished Professors)	250+ /year	350	200-1000
Oversea Doctor Recruitment Program	80+ /year	78-250	30-350
Postdoctoral Research Fellow	80-300 /year		

Short-term

Position	Employee Benefit Package(Unit:1,000yuan)		
	Salary	Relocation Allowance	Research Funds
Thousand Talents Plan(Short Term)	100 /month	500	1500-3000
Changjiang Scholars Program (Chair Professors)	30 /month		250-1000
Changbai Mountain Scholars of Jilin Province (Chair Professors)	15 /month		

[Benefits and Supports]

Housing
Jilin University has 790 relocation apartments, which are available to new oversea talents. These apartments are nicely decorated and close to the campus.

Education
The children of oversea talents have the full access to the university affiliated education system such as kindergartens, elementary schools and middle schools. In particular, the middle school attached to Jilin University is the best middle school in this area, which provides international standard education.

Health Care
Oversea talents are eligible for 5 first-rate university affiliated hospitals. Oversea talents have the priority of quality health care and resources by superb medical treatment and advanced equipment.

Environment
Changchun is not only one of "The Happiest City in China" but also the city with upmost human interest. Changchun is served by a comprehensive public transportation system. Faculty members can have a comfortable lifestyle at a relative low cost. Changchun is one of the four "National Garden Cities" due to its high urban greening rate.

Internationalization
Jilin University has established partnerships with 236 outstanding universities and other institutions across 39 countries. We offer a wide variety of programs and courses for international students. Currently we have about 2,200 international students studying at Jilin University.

[Contact Us]

Xu Hao, Zheng Nuo

Email:
talent@jlu.edu.cn

Tel:
+86-431-85167448

Qualified applicants are invited to email their CV or contact us..

For more information about the university, please visit:
http://www.jlu.edu.cn

东北大学

自强不息·知行合NEU

Recruitment of Global Talents Northeastern University

General Information

Northeastern University, located in Shenyang, the central city of Northeast China, is one of China's key universities first joining in "211" and "985" Project. NEU is directly funded by Chinese Ministry of Education, and co-financed by both Liaoning Province and Shenyang City.Established in 1923, it has long been a base for scientific research in the fields of mining, material science, metallurgy, and mechanical sciences.Now NEU has made headway in some of the newly rising and cross-disciplinary areas such as automation, computer science, and other high-tech disciplines. As a comprehensive and research-oriented university, NEU consists of 17 major academic schools, covering engineering, science, law, liberal art, education, management, and medical research; it includes 3 key national laboratories, 3 National Engineering Laboratories, and 4 national engineering (technology) research centers.

Recruitments: positions, qualifications and offers.

Position 1 Dean, School of Robotics and Engineering

Responsibilities

Successful candidate shall take full charge of the school, responsible for departmental teaching, research,disciplinary development, team-building, and administrative work. The first term of employment is four years.

Qualifications

It is desired that candidates generally be under the age of 55; domestic applicants are supposed to hold a Ph.D. degree and full professorship (research fellow included); overseas candidates with a Ph.D. degree should hold a tenured professorship (associate professor included)in a well-known university or hold a fellowship in acorresponding institutionoverseas.

Offers

Successful applicants will be offered highly competitive salary and benefits. Specific offers are negotiable.

*Please contact us no later than December 30, 2015.

Position 2 "1000-talents Plan"

Qualifications

Candidates should be eligible for the national "1000-talents Plan".Successful candidates are supposed to apply for the program with NEU as the author's institution. (For detailed information of the "1000-talents Plan", please visit the website:<http://www.1000plan.org/qrjh/section/2>).

Offers

1)a supporting research fund of no less than RMB10,000,000 by NEU;
2) alump sum of RMB 1,000,000 will be allocated as research fund by the State;
3) an annual salary of RMB 800,000 by NEU;
4) NEU willfacilitate research team-building;
5) NEU helps arrange house-renting.

Position 3 Chang Jiang Scholar; National Science Fund for Distinguished Young Scholars

Qualifications

Candidates should be eligible for Chang Jiang Scholar. Successful candidates are supposed to apply for the program with NEU as the author's institution.(For detailed information of the Chang Jiang Scholarprogram, please visit the website:<http://www.changjiang.edu.cn/news/17/list.htm>).

Offers

1) a supporting research fund of no less than RMB5,000,000 by NEU;
2) housing subsidy of no less than RMB 1,200,000 by NEU;
3) anannual bonus of RMB 200,000 per person will be provided by the State;
4) NEU willfacilitate research team-building;
5) If requested, NEU will help arrange employment for the spouse of talent commensurate to his/her educational and professional background.

Position 4 "1000 Plan Professorship for Young Talent"; Outstanding Young Scholars

NEU is hunting for Special-Term Professorship for Young Talent.

Qualifications

Candidates should be under 40 years old, majoring in engineering or natural sciences, with Ph.D. degree from a world-renowned university; candidates are supposed to have at least 3 years of research experience; if a candidate hold a Ph.D. from Mainland China, he or she is supposed to have at least 5 years of research and teaching experience abroad. Applicants should have a position in a well-known university or other corresponding institutions overseas.

Offers

1)successful candidates will be entitled to supervise Ph.D. students;
2) an annual salary of RMB 350,000 by NEU;
3) a research fund of RMB 3,000,000 – 5,000,000by NEU;
4) a relocation fee of RMB 500,000by NEU.

Position 5 Special-Term Associate Professorship

Qualifications: excellent overseas PhD graduates.

Offers

1)successful candidates will be entitled to supervise Ph.D. students;
2) an annual salary of RMB 250,000 by NEU.
3) NEU will provide ways for associate professor to get promoted to full professorship, based on research output.

Position 6 Post-Doc

Qualifications: excellent overseas PhD graduates from the world's top 100 universities.

Offers

up to RMB 300,000 funds per annum;

For PhD graduates, applications for regular positions (professor, associate professor, lecturer) are open all year round.

Contact person: Zheng Zhonghua, Ma Yiming
Tel: +86-24-83688005, +86-24-83686962
Fax: +86-24-23890977
Email: zhonghuaz@mail.neu.edu.cn
Address: R1308, Complex Building, NO. 3-11, Wenhua Road, Heping District, Shenyang, China
Recruitment website: http://202.118.27.233/home/home.asp
School website: http://www.neu.edu.cn/

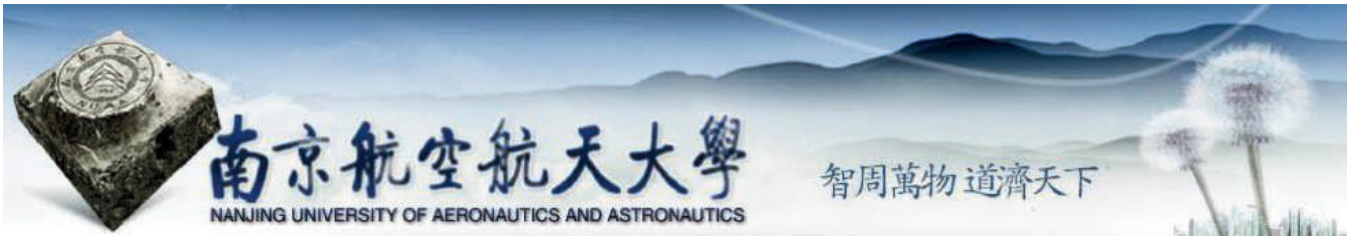

NUAA Hunting for Talents from Home and Abroad

Nanjing University of Aeronautics and Astronautics(NUAA), established in 1952, enjoys a well-balanced development of multiple disciplines in Natural Sciences, Humanities, Social Sciences, Management, etc. with the characteristics of Aeronautics, Astronautics and Civil Aviation. NUAA is among the first batch of national key universities entitled to award doctoral degree, master's degree. It has been listed as one of the "National Project 211" universities, qualified to be “Dominant Discipline Innovation Platform of 985 Project” .

NUAA will provide teachers and researchers with a good academic environment, satisfactory working and living conditions and a stage on which they can put their talents to good use.

Contacts

Ms. ZHAO , Mr. CAO
Personnel Division, NUAA
Address: 29# Yudao St. Nanjing, Jiangsu Province, Postcode: 210016
Tel: +86-25-84892461
Email: rencai@nuaa.edu.cn
Web: http://www.nuaa.edu.cn/nuaanew
http://rsc.nuaa.edu.cn

河海大學
HOHAI UNIVERSITY

Hohai University Calls for Global Talents

Hohai Univeristy, one of the oldest higher institutions in China, is a national key university under the direct administration of the Ministry of Education of China. Specialized in the water-related science and engineering technology, Hohai has grown into a multi-discipline university in coordinated development, supported by Project 211 and Project of Innovative Platforms for Key Disciplines from the Chinese central government.

In order to implement the strategy "Reinvigorating the university through talents" and achieve the goal "Water characteristics, World class" for building a university of high research level, Hohai University seeks talents perennially from the prestigious universities and institutes abroad for the following positions:

1. Recruitment Program of Global Experts/Changjiang Scholars Program

The successful applicants will be eligible for work allowance, research grant, research assistants, laboratory and office for research purposes, residential apartment or equivalent housing subsidy. In addition, assistance will be provided in securing a job position for the spouse, and obtaining school admissions for the child(ren) if required. Salaries and benefits are open to further negotiation for applicants with exceptional qualifications.

For details regarding these positions, please contact:

Ms. Qiao, or Mr. Li

Talent Recruitment office of Hohai University

Tel: +86-25-83786484

Email: rscrcb@hhu.edu.cn

2. Full-time Teachers of College of Oceanography

College of Oceanography currently houses a postdoctoral research center of marine sciences, a graduate program in the first-tier discipline of marine sciences, a doctorate program in the second-tier discipline of physical oceanography, and an undergraduate program of marine sciences. Priority will be given in the near future to developing the disciplines of physical oceanography, marine resources and environment, marine ecology, seawater desalination, ocean remote sensing, and marine equipments.

3. Other Positions

A variety of positions are offered in other colleges and schools of Hohai University. Outstanding PhDs, post doctors, researchers and full-time teachers are encouraged to consult the faculty recruitment plan of 2016 at the university.

website http://rsc.hhu.edu.cn/ for detailed information.

Hohai University will provide the successful applicants with salaries and benefits ranged in categories and grades, including work allowance, research grant, resettlement subsidy, and housing subsidy. Prominent talents will be eligible for various personnel growth programs like Youth Professors, Excellent Innovative Talents, Championship Talents, and Hohai Scholars.

Contact Information

Person of contact: Ms. Xu, or Mr. Wu

Address: Human Resources Department of Hohai University

No.1 Xikang Rd., Nanjing, 210098, P. R. China

Tel: +86-25-83786205

Email: rscrsk@hhu.edu.cn

Fax: +86-25-83786767

Thanks for attention!

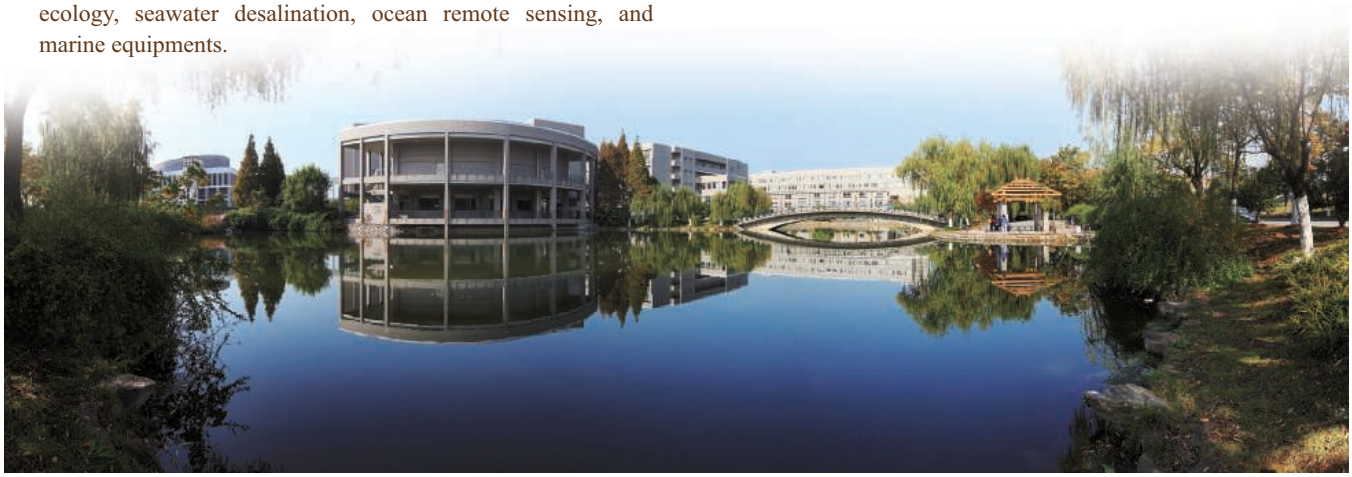

暨南大學
JINAN UNIVERSITY

Faculty Positions Available at Jinan University

Jinan University, first university of overseas Chinese founded by the state, with the largest foreign student among the country currently, is the national "211 Project" of key comprehensive university directly under the guidance of Overseas Chinese Affairs Office of State Council. In June 2015, Jinan University was listed as high-level university construction by Guangdong provincial Party Committee and the provincial government.

Professor/Associate professor/Postdoctors, The Institute of Atmospheric Environment Safety and Pollution Control

The Institute of Atmospheric Environment Safety and Pollution Control (IAESPC), directly administrated by JNU, is seeking outstanding professors, associate professors and postdoctors in the fields of atmospheric pollution, human health and mass spectrometry instrumentation.
Prof. Zhen Zhou, the director of IAESPC, is the expert of "National 1000-Talents Program"(2009). IAESPC has 3 research teams focusing on the fields aforementioned. Besides, the institute also has a super city air quality monitoring station, an engineering center on on-line source apportionment of PM2.5 and a research base, all of which are of the first-class in China. Presently, 30+ million has been investigated for high-level instruments and facilities, and the total area of labs/offices is more than 1000 m^2.
The requirements for the candidates are specified as follows:
Research Areas: Atmosphericenvironment; Atmospheric chemistry; Human health; Instrumentation (e.g., mass spectrometry, electronics, machinery).
Requirements:
1.Professors (≤55-year): Experts of"National 1000-Talents Program", "Changjiang Scholars Program","National Distinguished Young Scholars",and professors/senoior researchers/PI in well-known universities/research institutes/companies at home and aboard.
2.Associate professors (≤ 40-year):Experts of"National Excellent Young Scholars", "National 1000-Young-TalentsProgram", and excellent young researchers in well-known universities/research institutes/companies at home and aboard.
3.Excellent postdoctorsfrom top universities all over the world.
4.Nationality: All over the world.
5.Application materials: CV, representative research achievements, and a 5-year research plan.
Contact person: HaifengFu Tel/Fax: +86 (0)20-85220220/-85225991
Email: Odqs@jnu.edu.cn http://dqs.jnu.edu.cn/ (IAESPC); http://www.tofms.net/ (the Research Base)

Faculty Positions Available in School of Medicine

Jinan University School of Medicine is to become a world- class medical school. Now we are searching Senior Scientists (full professor or associate professor) for the Department of basic science in medicine,the Department of Public health ,the Department of Nursing, the Department of Dentistry and the Department of integration medicine.
Applicants should :
* have a doctoral degree in the relevant research field, and a proven record of research excellence;
* have team work spirits and coordination skills,leadership ability;
* top-priority will be given to candidates hold a professorship/associate professorship in a renowned overseas university (or research institutes).

Compensation and benefit:
* general compensation and benefits are on line with current standards of Jinan University
* generous start-up packages
* successful applicants who meet relevant criteria will be nominated for the various talent programs of the Chinese government and the Guangdong Province

Please submit your curriculum vitae including a cover letter declaring the targeted research area via post or email to:
Ms.Emily Huang(***E-mail:thyzh@email.jnu.edu.cn***;Tel:+86-20-85228912)
Mr. Huanmin Luo (***E-mail: tlhm@jnu.edu.cn***; Tel: +86-20-85220500)

Worldwide Search for Talent Research Staff in the College of Life Science and Technology

Fields:
Biomaterial, Biomedical Engineering, Drug Delivery, Medical Apparatus and Instruments, Proteomics, Biochemistry and Molecular Biology, Aquatic Ecology, Hydrobiology, Marine Microalgae Biology, Marine Plankton Ecology, Stem cell and Regenerative medicine, System biology and Bioinformatics, Epigenetics in Aging, Healing and Regeneration, Transgenic and knockout model, Molecular Immunology, and Cell Biology
Requirements:
Applicant should obtaineda PhD or equivalentdegree of related disciplinary and published top papers in the field as first author or corresponding author. Applicants must have a demonstrated record of scholarly accomplishment and ability to conduct outstanding research and education that are appropriate to the interests of the college. Preference will be given to candidates who had approved national research grants.
Salary and Conditions of Service:
Remuneration package will be driven by market competitiveness and individual performance. Detailed information could be discussed via a telephone or face-to-face interview.
Required Documents:
1. A latest personal CV
2. A list of approved grants, published papers (with information of impact factors and citations by other papers) and awards.
3. Copies of degree, grants, awards and patents (if applicable).
4. Future research plan at Jinan University.

Information and Application:
Tel: +86-20-85221436, 85226272 Contact persons: Mr. Zhu, Mr. Zhang or Ms. Li ***E-mail:osky@jnu.edu.cn***
Address: Room 108, College of Life Science and Technology, Jinan University, No. 601 Huangpu Avenue West, Guangzhou, 510632, China.

ScienceCareers online @sciencecareers.org
FOCUS ON CHINA

ScienceCareers online @sciencecareers.org
FOCUS ON CHINA

北京交通大学
BEIJING JIAOTONG UNIVERSITY

Job Vacancies at Beijing Jiaotong University

Beijing Jiaotong University (hereinafter referred to as BJTU) was founded in 1896 and it is the birthplace for modern China's education in railway management and telecommunication. The university is located in Haidian District of Beijing, the resort of universities and next to Zhongguancun, the "silicon valley" of China. Under the direct administration of the Ministry of Education, BJTU is one of the first universities being selected into the "National 211 Project" and the "985 Strength Discipline Innovation Platform" Project, one of the first institutions authorized to confer master's and doctoral degrees.

After the development of over 100 years, the university builds up its strengths in information and management and features in transportation science and technology. Now a completed and coordinated disciplinary cultivation system has been formed including disciplinary categories such as engineering, management, economics, science, art, law and philosophy. The university has 51 research platforms such as National Evaluation and Research Center of Railway Transportation Safety. In 2012, five disciplines rank the TOP 10 in the Third Round of National Discipline Evaluation among which System Science ranks No.1 for three consecutive rounds. The university has been among the top 100 for 3 consecutive years in "QS University Ranking of BRICS" and among the top 30 of the listed Chinese universities. Six disciplines including Architecture and Civil Engineering, Accounting and Finance, Computer Science, Electrical Engineering, Mechanical Engineering, Aeronautical Engineering and Mathematics are listed among TOP 400 by QS.

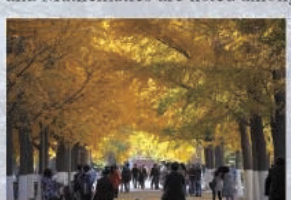

As the renowned research institute in the field of high-speed railway, heavy haul railway and urban railway system, the university has achieved a lot of "No.1" in the history of railway transportation development and witnessed the breakthrough of key technologies of high-speed railway in China. BJTU as the leading organization has established the Collaborative Innovation Center of Urban Transit Safety, which has been selected into the first batch of national Project on Innovation Capability Promotion of Higher Education Institutions in China (2011 Project). BJTU has become one of the most innovative and influential universities along with the development of railway transportation in China.

BJTU has established long-term partnership with more than 200 universities and famous multinational enterprises from over 40 countries. International research platforms such as China-Russia, China-US and China-UK High-Speed Railway Research Centers have been established. The establishment and development of the Russia-China Jiaotong Institute and the Hanergy School of Renewable Energy have witnessed pragmatic progress. BJTU has also set up Confucius Institutes in Leuven, Belgium, Houston, U.S. and Campinas, Brazil.

In order to fulfill the goal of building "world top-class university with distinctive features" and serve the National "Belt and Road" Initiative and "Going Global" Strategy of high- speed railway, the university has been carrying out the strategy of "strengthening the university via talents introduction" so as to improve the disciplinary influence and research innovation. We are expecting your participation!

1. Disciplines for Recruitment

Information and Communication Engineering, Traffic and Transportation Engineering, Applied Economics, Civil Engineering, System Science, Statistics, Optical Engineering, Mechanical Engineering, Computer Science and Technology, Electrical Engineering and other related disciplines.

2. Requirements

(1) BJTU "Excellent One Hundred Talents" Project

Qualifications: First Level: Academicians of the Chinese Academy of Sciences and Chinese Academy of Engineering, Experts recruited by The Thousand Talents Plan and outstanding scholars with same academic level. Second Level: Distinguished Professors under the Yangtze River Scholar Program, "National Outstanding Youth" or leading scholars with same academic level. Third Level: talents under the Recruitment Program for Young Professionals or top-notch scholars with same academic level. Fourth Level: scholars who have achieved outstanding academic outcomes and are able to reach the third level within 3 to 5 years.

Salaries and Conditions: Payment for the first level scholars will be determined through negotiation, and for others are listed in the following table.

Levels	Annual Salary (ten thousand yuan/year)	Start-up Research Funding and Funding for Disciplinary Development (ten thousand yuan)	Labs and Offices (Square meters)
Second Level	45-50	Natural Science 300-500 Humanities & Social Sciences 60-100	Natural Science 150-300 Humanities & Social Sciences 50-100
Third Level	35-40	Natural Science 100-300 Humanities & Social Sciences 40-60	Natural Science 50-150 Humanities & Social Sciences 40-80
Fourth Level	25-30	Natural Science 30-100 Humanities & Social Sciences 20-30	Independent space 15-20

(2) Outstanding Young Talents

We are seeking to recruit outstanding young talents who have obtained Ph. D degree or with more than two years' research experience in famous universities (research institutes) abroad. We offer funding of 100,000 to 200,000 yuan (science and engineering) and 50,000 to 100,000 yuan (humanities and social sciences) for start-up research, settling-in allowance of 30,000 to 50,000 yuan and renting allowance of 3500-4500 yuan/month for 3 years. Those with outstanding achievements can be selected into BJTU "Cultivation Program for Young Talents", who will enjoy 3 years' cultivation allowance of 3000-5000 yuan/month and other supporting measures.

3. How to apply

Please send your C.V to rczp@bjtu.edu.cn and specify the vacancy you are applying for.

4. Contact

Website: http://www.bjtu.edu.cn/ Channel of Recruitment
Address: Beijing Jiaotong University, Shangyuancun No.3, Haidian District, Beijing
Post: 100044
Contact: ZHANG Yi (Ms.)
Tel: +86-10-51683432
Fax: +86-10-51684704
Email: rczp@bjtu.edu.cn

東北林業大學
Northeast Forestry University

学参天地 德合自然

2015~2017 High-level Talent Introduction Announcement of Northeast Forestry University

Established in 1952 and located in Harbin – beautiful "Ice City", Northeast Forestry University is in national "211 Project" directly under the Ministry of Education of the People's Republic of China and key construction projects of "Advantage Discipline Innovation Platform". It is a multidisciplinary university integrating agriculture, science, industry, economics, management, culture, law, medicine and art with forestry science as advantage and forestry engineering as specialty.

To further improve the overall level of teaching staff and achieve a research university with international view, we are hereby looking for talents sincerely and mainly introducing excellent domestic and foreign talents with important complementary and supporting functions for the construction of subjects and talent team.

I. Subject Areas for Recruitment:

Agriculture, General Computing, Computer Science, Information Science and Technology, Architecture, Planning, Cell & Molecular Biology, Bioinformatics, Ecology, Genetics, Microbiology & Virology, Plant Science, Zoology & Animal Science, Civil Engineering & Construction, Electrical & Electronics Engineering, Materials Science, Mechanical Engineering, Polymer Science & Technology, Veterinary Medicine, Business, Economics, Finance, and Accounting, Analytical Chemistry, Chemical Engineering, Inorganic Chemistry, Organic Chemistry, Physical Chemistry, Botany.

II. Recruitment Plan

1. Leading Talents or Teams: to introduce leading talents or teams with international advanced level and competitive capacity in distinctive preponderant disciplines of the university and national key disciplines.
2. Distinguished Young Scholars: distinguished domestic and foreign young scholars have published high cited academic paper in the top-level publication of related field, with the potential to be selected into talent projects such as Thousands of People Plan, National Science Fund for Distinguished Young Scholars, Thousand Youth Talents Plan and Tens of Thousands of People Plan, or personnel with academic title of associate professor in overseas famous colleges and universities and above or personnel equivalent to the level of researchers in overseas famous research institutes; age under 40, and 45 for the excellences .
3. Excellent Young Scholars: excellent domestic and foreign young scholars have published high cited academic paper in the top-level publication of related secondary discipline, with the potential to be selected into talent projects such as Provincial Science Fund for Distinguished Young Scholars, Longjiang Scholars and Provincial Excellent Young and Middle-aged Experts; ageunder 35, and 40 for the excellences.
4. Young Backbone: domestic and foreign young backbone have published high cited academic paper in the top-level publication of related secondary discipline, with the ability of winning National Science Foundation of China and Philosophy and Social Science Foundation of China and great development potential in academy and scientific research; age: under 35.
5. Excellent Young Teachers: doctors with strong ability of teaching and scientific research; age: under 35.

III. Treatment

1. Leading Talents: appointed to the post of professor;
2. Distinguished Young Scholars: appointed to the post of professor;
3. Excellent Young Scholars: appointed to the post of professor or associate professor;
4. Young Backbone: appointed to the post of associate professor or lecturer;

The university will provide salary standard, scientific research start-up fund and house purchase subsidies according to the level of talent introduction.

IV. Further Details and Contact Information

Please check the following links for more details about the recruitment plan:
http://www.gkzp.nefu.edu.cn
For official website, please check:
http://www.nefu.edu.cn
Contact Person:
Mr. Zhang Chunlei (Tel: +86-451-82190165)
Ms. Guan Bingbing or Mr. Ni Songyuan(+86-451-82192070,82191327)
Email: nefugzc@nefu.edu.cn

FOCUS ON CHINA
ScienceCareers online @sciencecareers.org

宁波大学
NINGBO UNIVERSITY

Ningbo University invites you to apply for faculty positions

About Ningbo University

Founded in 1986 by Sir Yue-Kong Pao and autographed the name by Deng Xiaoping, Ningbo University (NBU) is a young and dynamic university located in the beautiful city of Ningbo by East China Sea, with five campuses covering 160 hectares of land. As a leading comprehensive university in Zhejiang Province, NBU offers programs in economics, law, education, liberal arts, history, science, engineering, agriculture, medicine, and management. The university now receives public funding, as well as continuous support and generous donations from many overseas Chinese and their families including Sir Yue-Kong Pao, Sir Run-Run Shaw, Chao An Chung, Hans Tang, Yue-shu Pao, Cao Guangbiao, Li Dashan, Zhu Xiushan, etc.

Academic Excellence

NBU consists of 22 faculties and offers 75 undergraduate programs, 116 master programs, and 12 Ph.D. programs. It enrolls 31,645 students including 26,527 full-time undergraduates and 5,118 graduate students. Currently NBU has around 1,400 full-time faculty members and 1,000 administrative staff members. Among them there are 5 academicians, 284 full professors, and 721 associate professors.

Research Achievements

With 77 research institutes and 14 key laboratories, NBU is the center of varieties of research and teaching activities. The research and development initiatives of the university, especially in marine science, information science and technology, engineering mechanics, and material science have contributed greatly to the economic development of the region and have been recognized by numerous national awards. The university library has a CNKI Network Administrative Service Center, and a collection of approximately 1,700,000 books and 11500GB digital resources.

International Programs

NBU maintains close links to 47 well-known institutions of higher education in Canada, Germany, France, Great Britain, USA, Sweden, Japan, South Korea and Australia. For example, the Sino-Canada joint-educational program is welcomed by international students with 100% satisfaction.

QUALIFICATIONS

Candidates should at least have (a) a Ph.D. degree in a related discipline, (b) adequate teaching ability and a strong passion for teaching, (c) an outstanding research background and influential publication record in recent three years, and (d) an ability to conducthigh-quality research and attract external funding.

REMUNERATION & CONDITIONS OF SERVICE

Salary offered will be commensurate with qualifications and experience. Remuneration package will be highly competitive. Forapplicants with titles of professor or associate professor, salary and housing compensation can be negotiated on the individual basis.For newly graduate PhD and Postdoctoral, initial appointment will be made on a fixed-term contract, with a housing compensation of 600,000 RMB upon fulfillment of the contract requirements. Re-engagement thereafter is subject to mutual agreement.

APPLICATION

Please submit completed application form, CV and cover letter via email to rsc@nbu.edu.cn. Application forms can be downloaded from http://www.nbu.edu.cn/shizi Recruitment stays open until positions are filled unless otherwise specified. Please visit http://rsc.nbu.edu.cn for more details.

INFORMATION ON POSITIONS

SCHOOL OF MARINE SCIENCE

Professor/Associate Professor
Marine Biotechnology/ Marine Sciences/Medicinal Chemistry/ Ocean Engineering/Marine planning and remote sensing /Sea port and environmental ecology/Marine Geographic Information Science

Faculty of Electrical Engineering and Computer Science

Professor/ Associate Professor Wireless Communications / New Generation Communication Networks / Underwater Acoustic Communication / Multimedia Information Processing / Embedded Systems / Integrated Circuit Design / Electronic Design Automation / Database System / Big Data Processing / Software and Theory / Information Security / Mobile Computing / Graphics and Image processing / Power system and Its Automation / Power Electronics / Pattern recognition and Intelligent system / Sensor and Intelligent detection

FACULTY OF SCIENCE

Professor/Associate Professor/Assistant Professor
Condensed Matter Physics/Microelectronics/Optoelectronics/Solar Cell
Department of Mathematics/Computational Mathematics/Probability and Statistics / Financial Mathematics

FACULTY OF MECHANICAL ENGINEERING AND MECHANICS

Professor/Associate Professor/Assistant Professor
Mechanics/Vehicle Engineering/ Mechanical Engineering/Industrial Design

INTERNATIONAL COLLEGE

Professor/Assistant Professor
Accounting

SCHOOL OF MATERIALS SCIENCE AND CHEMICAL ENGINEERING

Assistant/Associate/Full Professors
Polymer Science/Chemical Engineering/Materials Science

SCHOOL OF LAW

Professor/Associate Professor/Assistant Professor
Criminal Law/Criminal Procedure Law/Civil Procedure Law/Civil Law/Electronic Commerce Law

COLLEGE OF TEACHER EDUCATION

Professor/Associate Professor/Assistant Professor
Curriculum and Teaching Methodology/Higher Education/Preschool Education/Educational Economy and Management/Cognitive Psychology/Educational Psychology/Clinical Psychology/School Psychology/Experimental Psychology/Personality Psychology/Social Psychology/Management Psychology/Computer Graphics and Digital Image Processing/Electronic Music, Game Development/3D Animation and Game Development

FACULTY OF MARITIME AND TRANSPORTATION

Professor/Associate Professor/Assistant Professor
Department of Logistics and Transportation/Department ofMaritime Technology/Department of Marine Engineering/Department of Naval Architecture and Ocean Engineering

FACULTY OF PHYSICAL EDUCATION

Assistant Professor
Sport Management/Sport Sociology/Human Movement/Sport Training/Sport Physiology

MEDICAL SCHOOL

Professor / Associate Professor
Mechanism And Prevention Of Alzheimer's Disease; Oncology; Genetics; Human Anatomy; Histology And Embryology; Cell Biology; Immunology; Microbiology; Parasitology; Analytical Chemistry; Occupational And Environmental Health; Toxicology

COLLEGE OF ARTS

Professor / Associate Professor / Assistant Professor
Performance Of All Areas, Musicology (Ethnomusicology), Music Composition
Art Design Of All Areas, Digital Arts, Fine Art, Art History,Art/Music Industry, Art/Music Therapy

SCHOOL OF ARCHITECTURE, CIVIL ENGINEERING AND ENVIRONMENT

Professor /Associate Professor /Assistant Professor
Architecture Design/Urban Design/ Urban Planning/Architecture Technology/Human Geography/ Physical Geography/Cartography and Geographic Information System/Environmental Technology/Applied Environmental Microbiology/ Civil Engineering/Engineering Management

Global Talent Recruitment of Northeast Normal University

I. About Northeast Normal University

Founded in 1946, Northeast Normal University (NENU) is located in the beautiful city of Changchun, Jilin Province. It is a "Project 211" national key university under the direct jurisdiction of the Ministry of Education.

NENU currently runs 71 undergraduate programs in 23 colleges (or divisions), 34 primary disciplines which confer master degrees, 22 primary disciples which confer PhD. degrees, and 20 post-doctoral research stations. It enrolls more than 25,000 full-time students including about 15,000 undergraduates and about 10,000 graduate students. Currently, NENU has 1,516 full-time faculty members, among whom 470 full professors and 570 associate professors.

NENU boasts 1 "Project 985" innovation platform for teacher's education in advantageous disciplines, 5 secondary state-level key disciplines, 8 "Project 211" key disciplines, 32 "The 12th Five-Year Plan" primary disciplines with special features in Jilin Province, 2 key research bases for humanity and social science of Ministry of Education, 1 national engineering laboratory, 1 key provincial and ministrial base for laboratories, 1 national and local joint engineering laboratory, 5 key laboratories of the Ministry of Education. History, Chinese, and Biology are among the national bases for talent cultivation and scientific research in both basic subjects of art and science. The total of 11 disciplines, apart from military and medicine, form a comprehensive disciplinary structure.

II. Positions & Qualifications

1. Thousand Talent Program for Innovative Scientists (Short & Long Term)

An applicant should be under the age of 55 and possess an overseas doctorate, holding a Professor or other equivalent positions. The applicant is required to possess one of the following qualifications: having published influential papers in international key journals in the previsous 5 years; having won significant international scientific or technological awards; having expertise in experimental research and scientific engineering construction.

2. Thousand Talent Program for Young Outstanding Scientists

Candidates should be under the age of 40 and major in natural sciences or engineering technology with doctorate. Applicants should have a 3-year overseas working experience in scientific research and a formal teaching or research position in an overseas university or other corresponding institutions.

3. Chang Jiang Scholars Program (Distinguished Professors/ Chair Professors)

Applicants should hold a Professor or other equivalent positions with doctorate. Applicants should be under the age of 45 if in the field of natural sciences and engineering technology, and under 55 if in the field of humanities and social sciences.

4. Chang Jiang Scholars Program (Young Scientists)

Applicants should hold an Associate Professor or higher positions with doctorate. Applicants should be under the age of 38 if in the field of natural sciences and engineering technology, and under 45 if in the field of humanities and social sciences.

5. Distinguished Professors/Chaired Professors as Scholars in NENU

Applicants should hold a Professor or any other equivalent positions with doctorate if from China. Or they should hold an Assistant Professor or an equivalent (or higher) position if from abroad. Applicants should be under the age of 45 if in the field of natural sciences, and under 50 if in the field of philosophy and social sciences.

6. Professors, Associate Professors & Outstanding PhD Graduates

More than 100 positions are offered across over 80 disciplines. For detailed information, please refer to the website: http://zhaopin.nenu.edu.cn .

III. Renumeration & Conditions of Service

1. For the first five positions, successful applicants will be offered allowance for specific post and favorable research space. Assistance will also be given to facilitate their application of funds for various scientific researches, and their construction of academic team and disciplinary platform.

2. Successfully selected full-time applicants will be offered relocation fee, housing compensation, and startup funding. In addition, their children's admission to kindergarten or school will be solved.

IV. Application

Please submit materials including: CV (with educational background and working experience); major academic achievements (e.g. experience of presiding scientific research projects, papers and books published, awards and patients); a brief description of future plan.

V. Contact Us

Address: Human Resource Department, No. 5268 Renmin Street, Changchun City, Jilin Province, China.

Postcode: 130024
Tel: +86-431-85099718 / 85098029
Fax: +86-431-85683843
Website: http://zhaopin.nenu.edu.cn
E-mail: zhaopin@nenu.edu.cn

FOCUS ON CHINA
ScienceCareers online @sciencecareers.org

中国矿业大学
CHINA UNIVERSITY OF MINING AND TECHNOLOGY
可持续能源研究院

Global Recruitment for Executive Vice Director and PI

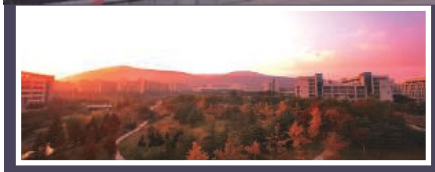

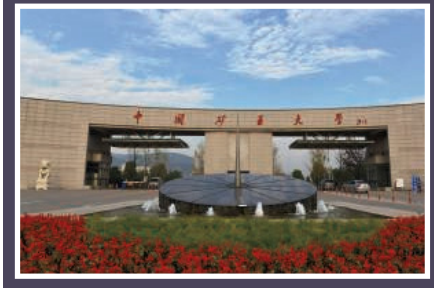

Applications are invited for:

Institute of Sustainable Energy (ISE), CUMT

China University of Mining and Technology (CUMT) is one of the top national comprehensive universities in China. The Institute of Sustainable Energy (ISE) of CUMT is a newly established research institute directed by **Carlo Rubbia**, the 1984 Nobel Laureate of Physics, and **C. C. Chan**, Fellow of Royal Academy of Engineering (UK) and Academician of Chinese Academy of Engineering. ISE's goal is to conduct research on next generation energy systems, and build an international top class research center in the areas of sustainable energy.

ISE is currently focusing on the following three research fields: **a)Zero Emission Energy Systems**–such as spontaneous transformation of CH_4 into Hydrogen and solid Black Carbon without CO_2 emissions and Innovative Renewable energy systems; **b)Innovative Energy Storage Systems and Intelligent Distributed Energy Recourse Systems**-systems essentially based on renewables (solar, wind, nuclear, etc.), advanced power electronics, advanced energy storage systems, genius smart control systems and smart integration of energy and information; **c)Long Distance G-Watt Electric Power Transmission**-a transmission of electric power up to 5000 km with a novel type of super conductivity (MgB_2).

ISE is now accepting applicants for:

1)Vice Director – Executive: A full-time faculty who is familiar with international research regulations and responsible for the operation and management of ISE under direction of Prof. Carlo Rubbia and Prof. C.C. Chan.

2)Principle Investigators (PI): Professor grade (tenure), or similar positions in colleges or institutes. PI will be responsible to build and lead a team in each research field narrated above. Researchers with team leading experience is essential.

Qualified candidates are expected to develop innovative and competitive programs in those three research fields. Adequate research funds, competitive salaries, welfares and benefits will be offered for the positions above. The salary will be no less than the tenure salary in world well known universities. Applicants shall send your curriculum vitae, brief research proposal and submit an application form to the contact email below. Researchers specialized in other research fields are also welcomed to apply faculty positions in CUMT.

The expiration date of the applications is Feb 29, 2016.Applications are open from now. Applicants will be replied within 15 working days since application received. Interviews will be conducted in mid Mar. 2016 with the participation of Professors Carlo Rubbia, C.C.Chan and consultant experts team from CUMT. CUMT will offer a round-trip air tickets for each applicant accepted for the interview.

For more information, please contact:

Mr. Gao,Vice Director of Talent Introduction Office,CUMT
Email: gaoding@cumt.edu.cn or kdrc@cumt.edu.cn.
Tel: +86-516-83590278; Fax: +86-516-83590211
Add: (221116) Department of Personnel, China University of Mining and Technology, No. 1 Daxue Rd, Xuzhou, Jiangsu, China.

University website: http://www.cumt.edu.cn/
Job vacancy website: http://pd.cumt.edu.cn/
Application form download URL: http://pd.cumt.edu.cn/39/3c/c352a276796/page.htm

國防科学技術大学
National University of Defense Technology

Calls for Talents All Over the World

The National University of Defense Technology (NUDT) is a comprehensive national key university under the dual supervision of the Ministry of Defense and the Ministry of Education as designated by Project 211 and Project 985. The University is located in Changsha, a magnificent city enjoying thousands of years of history. Over the past 60 years, NUDT has accomplished a large number of advanced scientific achievements, among which listed the Galaxy series and Tianhe series of supercomputer systems, Beidou Satellite Navigation System, Medium and Lower Speed Maglev, Core Routers and Unmanned Vehicles. The University has played an important part in building an innovation oriented country. After Tianhe-1 Supercomputing System, developed by NUDT, shocked the world as the first Chinese supercomputer topping the TOP500 list of fastest supercomputers, Tianhe-2 has retained the supremacy of TOP500 for 6 times and reigned as World's Best Supercomputer from 2013- 2015.

In order to accelerate the establishing of a leading university, NUDT now welcomes outstanding scholars and technicians all over the world to our multidisciplinary faculty positions.

Positions Available

1.1000-Talent Plan

The Innovative Talents Long Term Program

This program aims at recruiting world-class scholars under age 55 if in a field of natural sciences, or under 60 in a field of humanities and social sciences as full-time professors at NUDT. Applicants should have acquired doctoral degree(s) and have worked either as professors or at equivalent positions in world-renowned oversea universities or research institutes.

Successful applicants should spend at least 9 months per year undertaking research and teaching on NUDT campus for 3 consecutive years after being selected for the Program.

The Innovative Talents Short Term Program

This program aims at recruiting world-class scholars under age 55 if in a field of natural sciences, or under 60 in a field of humanities and social sciences as part-time professors at NUDT. Applicants should have acquired doctoral degree(s) and have worked either as professors or at equivalent positions in world-renowned oversea universities or research institutes.

Successful applicants should spend at least 3 months per year undertaking research and teaching on NUDT campus for 3 consecutive years after being selected for the Program.

Foreign Experts Program of 1000-Talent Plan

This program is designed for world-class scholars of non-Chinese ethnicity under age 65. Applicants should have worked either as professors or at equivalent positions in world-renowned oversea universities or research institutes. Successful applicants should spend at least 3 months per year undertaking research and teaching on NUDT campus for 3 consecutive years after being selected for the Program.

1000-Young-Talent Program

This program is one type of "1000-Talent Plan" especially for young scholars under age 40. Generally, applicants should have official teaching or research positions in world-renowned overseas universities or institutes. Three or more years of overseas post-doctoral research experience is required if the doctoral degrees were acquired overseas, while five or more years required if degrees obtained in Mainland China. Special offers are granted to those who have made distinguished research achievements.

2.Chang Jiang Scholars Program

Distinguished Professors

Applicants should be under age 45 if in a field of natural sciences, or under 55 in a field of humanities and social sciences. Applicants should have worked either as associate professors (or with above academic titles), or at equivalent positions in world-renowned universities or research institutes.

Chair Professors

Applicants should have worked either as professors or at equivalent positions in world-renowned overseas universities or research institutes. Successful applicants should spend at least 2 months per year undertaking research and teaching on NUDT campus for 3 consecutive years after being selected for the Program.

3.University Distinguished Guest Professors

Applicants should be academicians of CAS or CAE, or have worked either as professors or at equivalent positions in world-renowned overseas universities or research institutes, and should have outstanding contribution to their domains of specialties or with world recognized achievements. Successful applicants should spend at least 3 months per year undertaking research and teaching on NUDT campus for 3 consecutive years after being selected for the Program.

4.Elite Young Scholars

This program is designed for the great cohort of innovative and promising scientific minds under age 40, willing to work at NUDT as full-time faculty. Applicants should have obtained doctoral degrees at world-renowned overseas or domestic universities or research institutes, willing to exert their strength and passion for research excellence and self-fulfillment.

Research Fields in Demand

Physical Oceanography
Marine Meteorology
Data Assimilation
Marine Information Engineering
Underwater Acoustic Engineering
Oceanic Circulation
Numerical Modeling of Marine Hydrodynamics
Aerospace Propulsion Theory and Engineering
Materials Science and Engineering
Mechanics
Statistics
Atomic and Molecular Physics
Condensed Matter Physics
Quantum Communication
Quantum Information
Network Science
Synthetic Biology
Mechanical Engineering
Control Science and Engineering
Instrument Science and Technology
Satellite Navigation and Positioning
Space-based Information Aquisition and Processing
Management Science and Engineering
Applied Mathematics
Computer Science and Technology
Software Engineering
Microelectronics and Solid-State Electronics
Optical Engineering
Physical Electronics
Foreign Languages and Literature
Philosophy
International Relations

Salary and Support

Successful applicants will be offered sufficient research support, adequate laboratory space, highly competitive salary, startup funding and social benefits, and extensive opportunities for collaboration both within NUDT and with partner institutions. Relocation or establishment of your own research team will be supported.

Contact Us

All the position demands are long-term effective. Any further inquiries will be welcomed via emails. Interested applicants are invited to submit documents including a cover letter, a CV, a brief future research plan, 2 recommendation letters, 3 pieces of representative works to our Talent Affairs Office:

Mr.Ke Tel:+86-731-84572216 +86-18707498661
Fax: +86-731-84572217
E-mail: rcb@nudt.edu.cn
Address: Talent Affairs Office, Human Resources Department, National University of Defense Technology, 137 Yanwachi Street, Changsha, Hunan, People's Republic of China.

Southwest Jiaotong University, Chengdu, China Invites Applications for the Academic Positions

西南交通大學 Southwest Jiaotong University

Southwest Jiaotong University (SWJTU), founded in 1896 and located in Chengdu, the capital of Sichuan province-China's dynamically growing West. SWJTU is an elite university with national key multi-disciplinary "211" and "985 Feature" projects directly managed by the Ministry of Education, featuring comprehensive study and research programs/disciplines for 19 faculties and institutes/centers. SWJTU is a leading university which excels in engineering with disciplines in sciences and arts. This comprehensive 1st-class renowned university has complete graduate and undergraduate divisions with more than 2,600 academic members and staffs, and 15 doctoral/43 master/75 undergraduate programs and 11 post-doctoral stations in addition to more than 30 key laboratories at the national and provincial levels.

SWJTU is currently on the strategic "Developing and Strengthening the University by Introducing and Cultivating talents" campaign. Thus,you arecordially invited to apply for the following academic positions.

More information is available at http://www.swjtu.edu.cn/

Available Disciplines

Civil Engineering/Surveying Science and Engineering/Mechanical Engineering
Science of Transportation and Logics/Science of Information and Communication
Electrical Engineering/Computer Science and Technology
Materials Science and Technology/Mechanics/Management Science and Technology
Managing Technology and Innovation/Environmental Science/Architecture
Physics Science/Mathematics Science/Life Science/Medical Science
Chemical Science/Humanities and Social Science

Positions and Requirements

A.High-level Talented Leaders

Candidates should be qualified to be listed in national top talents programs such as ***Program of Global Experts, Top Talents of National Special Support Program, "Chang Jiang Scholars", China National Funds for Distinguished Young Scientists and National Award for Distinguished Teacher.***
Candidates are preferable no more than 50 years old. Exceptions could be made in the most-needed areas of disciplinary development.
Candidates working in the universities/institutes,meeting the above requirements, are preferable to be no more than 45 years old.

B.Young Leading Scholars

Candidates are preferable to be listed or qualified for the following programs:
•National Thousand Young Talents Program
•The Top Young Talents of National Special Support Program(Program for Supporting Top Young Talents)
•Science Foundation for the Excellent Youth Scholars
Eligible candidates should have team spirit and leadership, outstanding academic achievements, a broad academic vision and international cooperation experiences and have the potential of becoming a leading academic researcher.

C. Excellent Young Academic Backbones

Candidates, preferable under 40 years old, are expected to graduate from 1st-calss universities/institutes in China or internationally. Those who are professors, associate professors and other equivalent positions with talents from 1st-class universities/institutes overseas could be employed as professors and associate professors as well.

D. Excellent Doctors and Post Doctoral Fellows

Candidates, preferable under 35 years old,are expected to become excellent academic researchers from 1st-class universities in China or internationally.

Salary and Fringe Benefits

Salary will be highly competitive, commensurate with qualifications and experiences. University offers a comprehensive fringe benefit package for eligible appointees, includingthe settling-in allowances, subsidy of rental residence, start-up funds of scientific research, assistance in establishing scientific platform and research group as well as international-level training and promotion.

University also helps the eligible appointees, on your children's education.As for outstanding returnees, special treatments can be discussed personally.

Application Procedure

Please send full resume, copies of academic credentials, a publication list with abstracts of selected published papers, a research plan, a teaching statement, together with names of three referees to the Human Resources Department. For inquiries, please contact Mr. Yu Wang, Ms. Ye Zeng or Mr. Yinchuan Li
Telephone number: +86-28-66367238/66366202

Email: talent@swjtu.edu.cn

Address: Human Resources Department, SWJTU, Western Park of High-Tech Zone, Chengdu, Sichuan, China, 611756

复旦大学生物医学研究院 Institutes of Biomedical Sciences Fudan University

Faculty Positions Available in Institutes of Biomedical Sciences, Fudan University

The Institutes of Biomedical Sciences (IBS) at Fudan University, established in 2005, pursues cutting-edge biomedical research from an interdisciplinary and inter-institutional perspective. Under the consistent and strong supports from Fudan University and various China government funding agencies, Fudan IBS has now developed into a vibrant research institution consisting of Epigenetics Research Center, Systems Biology of Medicine Research Center, Molecular Cell Biology Research Center, with the intension to initiate innovative research fields that are centered in China and emphasizing translational medicine.

Principle Investigators

Applicants should have a strong research profile to establish and conduct innovative research in the areas of Epigenetics, Molecular Cell Biology, Bioinformatics and Big-data Analysis, Proteomics, Electron Microscopy 3D Reconstruction, Structure Biology, Small Active Molecule for Drug Screening, Translational Medicine for Cancer, Cardiovascular Diseases, Birth Defect and Stem Cell Technology.

As an eligible candidate for professorship, you should have:

- PhD degree from overseas and more than 3 years working experience abroad or doctorate degree obtained in China with 5 years working experience.
- High-profiled publications as corresponding author.
- ≤ 40-years old is preferred

Treatment

The university will provide munificent salary, internationally competitive start-up support, laboratory construction and organizing the research team.

For more information, please check:http://www.ibsfudan.org

Contact person:

Ms. Lingjing Bao
Email: ljbao@fudan.edu.cn
Tel: +86-21-54237007

華南農業大學 South China Agricultural University

Faculty Positions Available at South China Agriculture University

One of the national key universities, South China Agricultural University is a “211 Project” university sponsored by both Guangdong Province and the Ministry of Agriculture. SCAU has a history of 106 years. Chairman Mao Zedong autographed the former school name which was known as "South China Agricultural College”. The campus is located in Guangzhou, known as “City of Flowers", covering an area of 8250 mu (550 hectares) with beautiful scenery. It is a good place for working.

In 2015, South China Agricultural University was listed in the first batch of high-level universities. SCAU embraces disciplines well coordinated in agriculture, engineering, liberal arts, sciences, economy, management, and law studies. Advantages in agricultural sciences will be maintained, and priority in life sciences continued. The university is to step into the top-class universities in China and become internationally recognized.

We warmly welcome outstanding scholars to cooperate with us and create a better future.

I. Recruitment program for topnotch talents and teams (long-term effective)

1、Academicians of the Chinese Academy of Sciences, Academicians of the Chinese Academy of Engineering.

2、The Thousand Talents Plan , Specially-Appointed Professors and Chair Professors of The Ministry of education " Chang Jiang Scholars Program " Award Scheme.

3、Guangdong province introducing leading talents, Guangdong province introducing innovative scientific research team,Specially- Appointed Professors and Chair Professors of Guangdong higher education institutions (Zhujiang Scholars).

4、School-level academic leaders, academic leaders and excellent post-doctoral returnees.

II.Conditions and supporting measures

The university provides transitional housing for all introducing talents and offer special remuneration and working conditions. (http://www.scau.edu.cn/zhaoping/xqxx.htm).

National and provincial recruitment conditions comply with national and provincial related regulations. For more detailed requirements of recruitment, recruitment procedures, support measures and other information, please refer to "South China Agricultural University home page-jobs" (http://www.scau.edu.cn/zhaoping/xqxx.htm).

III. Recruit ordinary overseas doctors

The university recruits many overseas doctors every year. For detailed announcement programs and position requirements, please refer to"South China Agricultural University home page-job" (http://www.scau.edu.cn/zhaoping/xqxx.htm)

IV. Contact

1、South China Agricultural University Web: http://www.scau.edu.cn
Postcode: 510642 Address: Personnel Office, South China Agricultural University, No.483 Wushan Road, Tianhe District, Guangzhou, Guangdong, China

2、Contact person: Mr. Zhang, Mr. Zhou
Phone number: (0086)-020－85280043
Email: rsk@scau.edu.cn

Recruitment of Global Talents, Jiangsu University (Zhenjiang, Jiangsu, China)

江苏大学
JIANGSU UNIVERSITY
全国重点大学

Jiangsu University (JSU) is a comprehensive university especially reputed for its strength in engineering. The research fields cover 10 primary academic categories including engineering, nature science, medicine, management, economics, law, literature, philosophy, pedagogy and art. JSU has 13 post-doctoral research stations, 9 primary (or first-level) disciplines for doctoral degrees, 42 doctoral programs, 2 national key academic disciplines, and 1 national key academic discipline under cultivation. Four disciplines have been ranked as global top 1% in Essential Science Indicators (ESI), including Engineering, Materials Science, Clinical Medicine and Chemistry. According to the Evaluations of China's Universities in 2015 by China Academy of Management Science, JSU is ranked 55th.

Jinshan Scholar (金山学者)

Candidates are supposed to be listed in national top talents programs, such as "Recruitment Program of Global Experts", "Chang Jiang Scholars Program", and "China National Funds for Distinguished Young Scientists".
In general, candidates should be less than 50 years old, hold Ph.D. in renowned universities home and abroad, and have been appointed as associate professor and above (or equivalent).

Jinshan Distinguished Professor (金山特聘教授)

Candidates are supposed to be listed in or qualified to apply for the following programs, such as Distinguished Professor of Jiangsu Province, High-level Innovation Talents, and Innovation Team Leader of Jiangsu Province.
Candidates should have team spirits, abundant research experiences, and outstanding academic achievements, and have been appointed as assistant professors and above (or equivalent).

Excellent Doctors and Post Doctoral Fellows (海外优秀博士和博士后)

Candidates are expected to be excellent academic researchers from high-level universities, less than 35 years old, and have strong scientific research abilities.

Salary, Benefits and Support

JSU offers competitive salaries, sufficient research start-up funds, fringe benefits, medical/dental insurance, and retirement etc. For high-level talents, JSU still offers an apartment (or purchase subsidies) with individual property after serving JSU for 10 years.

Contact Us

More information at http://www.ujs.edu.cn/site1/node15/ Phone: +86-511-88789659 +86-511-88780061 E-mail: hr@ujs.edu.cn, rsk@ujs.edu.cn.

徐州医学院招聘海外高层次人才

Teaching and Research Positions

Xuzhou Medical College, situated in the city of Xuzhou, was founded in 1958.It is now the center of medical education, medical service and medical research in Northern Jiangsu and in the whole Huaihai economic zone.

XZMC offers 20 undergraduate programs, such as Clinical Medicine, Anesthesiology, Medical Imageology, Pharmacology, Stomatology, Nursing, Biomedical Engineering, Public Adminis- tration, etc., 2 first-level discipline doctoral programs, namely Clinical Medicine and Biology and 5 first-level discipline master's programs, namely Clinical Medicine, preclinical medicine, Biology, Pharmacology, public health and preventive medicine. Still, the college has post-doctoral research centre.

I.Disciplines for Application:

Biology, Basic Medicine, Pharmacy, Clinical Medicine,Public Health and Preventive Medicine, Stomatology, etc..

II.Requirements for overseas applicants:

1)Doctoral degree holder
2)Professor or associate professor

III. More information and to apply visit website:

http://rsc.xzmc.edu.cn/

IV. Contact:

Mr. Du Gang or Mr. Li Yuandong
Personnel Department, Xuzhou Medical College
209 Tongshan Road, Xuzhou, Jiangsu Province, 221004, China
Tel/Fax:+86-516-83262043,83262032
Email: szb@xzmc.edu.cn rsc@xzmc.edu.cn

南京工業大學
NANJING TECH UNIVERSITY

海外领军人才招聘

Overseas Talents Recruitment

Nanjing Tech University, with a history of more than one hundred years, is a multidisciplinary university with its focus on fundamental and applied cutting edge research and high-level education. In April, 2013, Nanjing Tech University was officially announced as one of the first round of 14 "2011 Plan" universities. Nanjing Tech University, located in Nanjing, Capital City of Jiangsu Province, has an ambitious agenda to ensure that science and engineering remain at the forefront both nationally and internationally. Catering to the national demand and aiming at building a top-notch university with open mind, innovative effort and entrepreneurial spirit, Nanjing Tech University is striding forward towards a "comprehensive, research-oriented and globalized" university for a brighter future. We are now seeking outstanding academic and research leaders in the following and related fields:

- Basic disciplines from within the Physical Sciences
- Cutting edge disciplines from within the Life Sciences
- Applied disciplines from within the Information Sciences
- Humanities represented by Management Sciences

Applicants should have a Ph.D. with at least 3-year research experience from leading universities or institutes. Candidates should demonstrate an internationally recognized research record and outstanding achievements. Successful candidates are expected to develop vigorous research programs and lead an independent research team. Successful Candidates will be offered with a highly competitive salary and benefits, and other support includes generous start-up funds, spacious laboratories and sufficient relocation fee. For complete application instructions, please visit: http://rczyb.njtech.edu.cn.

Nanjing Tech University will also provide distinguished candidates with very strong continuing support to apply for programs such as "1000 Plan Professorship for Young Talent", "Chang Jiang Scholars" for young talent , and Specially-Appointed Professor of Jiangsu. Qualified applicants are invited to send a cover letter and CV to talent@njtech.edu.cn.

Contacts: Mr. Wang and Mrs. Tang
Tel: +86-25-58139145, Fax: +86 25 58139148
E-mail: hr@njtech.edu.cn
Address: Room 401, Administration Building, 30 Puzhu South Road, Nanjing, Jiangsu, China 211816

南京财经大学
Nanjing University Of Finance & Economics

Faculty Positions Available at Nanjing University Of Finance & Economics

Nanjing University of Finance and Economics (NUFE), one of the key comprehensive universities in Jiangsu Province, is oriented to the disciplines of economics and management, coupled with those of law, engineering, humanities, and science.
NUFE now has a postdoctoral research station in applied economics, a doctoral program in "Development and Policies of Modern Food Circulation Industry", 12 graduate programs of first-level disciplines, 9 professional graduate programs, and 46 undergraduate programs.
For more information, please visit our website at www.njue.edu.cn.

We sincerely invite you to join us at the following disciplines: Economics, Management, Law, Engineering, Science, Literature, Art.

Benefits and Support

Program	Relocation Fee (unit:1000 yuan)	Startup Funds (unit:1000 yuan)
Outstanding Program	2000-3000	200
Climing Program	600-1000	100
Cultivating Program	200-1000	30-50
Excellent Doctors	0-400	30

Payment, benefits and support offered are subject to individual academic achievement, and will be considered on a case-by-case basis.

Contact us

Mr. Wu Dengke: 9119961041@njue.edu.cn , 86-25-86718679,
Mr. He Haixin: 1692576295@qq.com , 86-25-86718678

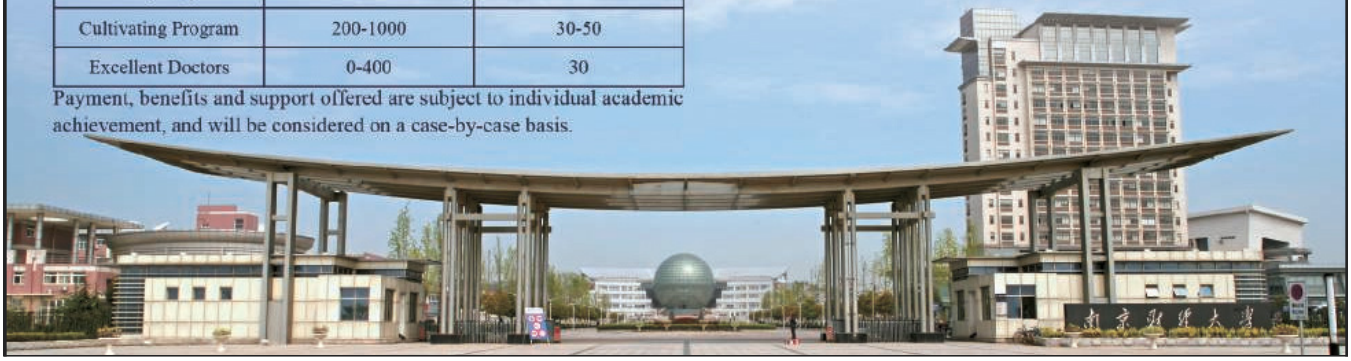

Faculty Positions Available at Hangzhou Dianzi University

杭州电子科技大学
HANGZHOU DIANZI UNIVERSITY

About HDU:

Hangzhou Dianzi University（HDU）, located in Hangzhou, a well-known city for its history and culture, is one of the advanced universities in Zhejiang Province, China. There are more than 28000 full-time students and over 2200 faculty and staffs in campus, 2 academician, 5 sharing academicians, 1 young middle-aged outstanding experts, 5 distinguished experts of the "Thousand-talent Project" awarded by the Organization Department of the Central Committee of the CPC, 3 of New Century's Talent Project, 4 holders of the National Outstanding Youth Fund, 10 of the New Century's Excellent Talents Project supported by the Ministry of Education, and a large number of famous scholars and middle-aged experts with profound academic accomplishments. HDU has developed into a significant institution for its personnel training, scientific research and community service, and holds the lead among the universities in Zhejiang Province in every aspect as the school scale, the education level, the teaching quality and efficiency in school management.

HDU website: http://www.hdu.edu.cn

Vacancies:

Mechanical Engineering, Electric Engineering, Marine Equipment & Technology, Control Theory & Control Engineering, Biomedical Engineering, Instrument Science & Technology , Electronic Science & Technology, Computer Application Technology, Information & Communication Engineering, Economics, Business Administration, Material & Environmental Engineering, Digital Media, Artistic Designing, Journalism , Law, Mathematics, Physics, English Language and Literature and so on. (Link Recruitment of Personnel Department of HDU for further Information).

Qualifications:

Applicants with PHD degree from prestigious domestic and overseas universities; Professors or assistant professors/researchers of the equivalent titles, having been working at overseas prestigious universities or research institutes.

Salary, Benefits and Support:

Successful applicant will be offered a competitive package, including sufficient laboratory space, startup funding and competitive salary commensurate with experience, in addition to a housing allowance, and other employee benefits.HDU is recruiting overseas talents all year around. Applicants may refer to the recruitment in our website http://renshi.hdu.edu.cn for further information. For those exceptionally qualified talents, the salary could be negotiated in person.

Contact:

Interested individuals should send curriculum vitae by e-mail to rsc@hdu.edu.cn.Or contact us by telephone:86-(0)571-86915031, fax：86-(0)571-86915029.

Website: http://renshi.hdu.edu.cn

西南石油大學

Faculty Positions available at Southwest Petroleum University

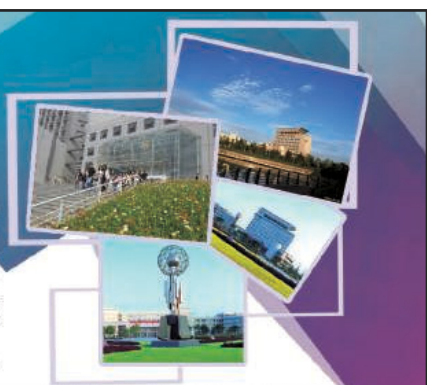

Southwest Petroleum University (SWPU) is located in Chengdu City, the capital city of Sichuan province. Founded in 1958, SWPU was co-built by the central and local government and is administered mainly by Sichuan Provincial Government.

The university is composed of 16 schools and 1 new energy and unconventional natural gas and oil institute. It specializes in disciplines as oil and gas engineering, geological resources and geological engineering, geology, mechanical engineering, chemical engineering and technology and materials science and engineering, along which the petroleum and natural gas engineering discipline is top-ranked in China.

There are 81 scientific research bases, including 1 state key laboratory (SKL), 1 national university Science Park, 1 national technology transfer institution and 2 international cooperation laboratories.

SWPU has been involved in over 2,000 provincial or ministerial scientific programs, among which there are National Science Foundation for Distinguished Young Scholars, Science Foundation for Outstanding Young Scholars, National 973 Program, National 863 Program, National Science and Technology Support Plan, National Key S&T Special Projects, National Social and Scientific Foundation and New Century Talents Scheme.

The university has won more than 360 provincial or ministerial prizes such as the special award, the first and second prizes for National Progress in Science and Technology. Since the 11th Five-Year Plan of SWPU, almost 4,000 research results have been successfully applied or transformed in production sites.

Currently, there are 2,303 faculty and staff members and 220 senior professional technicians, including 2 academicians of the Chinese Academy of Engineering, 3 winners of National Science Foundation for Distinguished Young Scholars, 2 distinguished professors of Chang Jiang Scholars Program and 225 experts awarded at the provincial/ ministerial level. Aiming at building a high-level university with top disciplines it is urgent to introduce advanced international talents.

1. Research Background

Petroleum and Natural Gas Engineering, Geological Resources and Geological Engineering, Geology, Mechanical Engineering, Chemical Engineering and Technology, Materials Science and Engineering, Instrument Science and Technology, Control Science and Engineering, Electrical Engineering and Automation, Management Economics, Environmental Science and Engineering, Civil Engineering, Computer Science and Technology or related disciplines and majors.

2. Qualification

A doctoral degree obtained overseas or PhD graduates, professors or academic leaders with overseas experience.

3. Application

A CV and other records of qualification are required.
Candidates will be interviewed and selected on merit.

4. Compensation

Candidates recruited can be provided with re-settlement allowance, funds for laboratory construction and scientific research. Salary and payment are negotiable.

5. Contact us for more information

Address: 8 Xindu Avenue, Xindu District, Chengdu City, Sichuan Province, P.R.C. Post Code: 610500
Website: www.swpu.edu.cn
Tel: +86-28-83032172
Email: swpu_rsc@swpu.edu.cn

四川大學
生命科学学院

Global Talent Recruitment at College of Life Sciences, Sichuan University, Chengdu, China

Sichuan University, with a history of 120 years, is an elite university supported by 985 and 211 projects from the Ministry of Education. Located in Chengdu, a famous historic and cultural city in west China, it is designated as a key comprehensive research university.

The college of Life Sciences at Sichuan University (http://life.scu.edu.cn) has more than 90 years of history and currently has 140 faculty and staff members. There are broad and diverse research programs spanning from basic and applied biological sciences (including microorganisms, ecology, plants and animals) to bio-medical research (cancer, genetics, immunology, stem cell research, aging etc). The college has intensive collaborations with West China College of Medicine and institutions abroad. We aim to recruit candidates for China's national talent plans with priorities in the fields of

(1) Plants and important economic crops
(2) Wildlife conservation and domestic animals
(3) Cell biology and molecular genetics
(4) Evolution and Ecological studies

We offer competitive salary, housing benefit and startup research funding package.

●NationalThousand Young Talent Plan:Candidates under age of 40 should have outstanding academic achievements, good team spirit with potential for leadership.

●High-level Leadership Talents: Candidates should hold a Professor or equivalent position, able to work full time during the tenure, qualified to apply for the National Thousand Talent Plan, National Foreign Experts of Thousand Talent Plan or Chang Jiang Scholars.

●Young Principal / Associate Investigators: Candidates under age of 35 should have excellent academic achievements, good team spirit with potential as a leading academic researcher.

●Post-Doctoral Fellows and Research-track scientist positions: Candidates under age of 30 should have good academic achievements, excellent team spirit with potential as a principle investigator.

Contacts:
Ms.Tan Furong
TEL: 86-28-85412053 or 85412279
Email: **tanfurong@scu.edu.cn**
Address: College of Life Sciences, Sichuan University, No.29 Wangjiang Road, Chengdu, Sichuan 610065, China

---

南通大學
NANTONG UNIVERSITY

Faculty Positions Available at Nantong University
南通大学诚聘优秀人才

Nantong University was approved to establish by Jiangsu Provincial Government and China's Ministry of Transportation in 1912. As a comprehensive university, Nantong University has leading graduate, professional, and undergraduate programs in a variety of fields, including programs in literature, science, economics, law, education, history, engineering, medical science, and management. Nantong is located at the estuary of Yangtze River. And Shanghai and Suzhou across the river , Nantong is integrated into "Shanghai one-hour" and "Yangtze River Delta region three-hour" traffic circle. Nantong University is now recruiting top-level personnel world-wide.

Ⅰ. Requirements

1. Applicants should be nominated as a member of the Chinese Academic of Sciences.
2. Applicants should be qualified to apply for country-level talents programs, such as "The Recruitment Program of Global Experts", "Chang Jiang Scholars Program" or "The National Science Fund for Distinguished Young Scholars".
3. Applicants should be qualified to apply for ministerial and provincial-level qualification, such as "The Recruitment Program of Global Youth Experts", "National Science Fund for Excellent Young Scholars", "Jiangsu Innovation and Creation Talents Program" and "Jiangsu Distinguished Professor".
4. Applicants should have got PhD from world-wide well-known universities and have post-doctoral research experience.

Ⅱ. Compensation

In order to bring in top-level personnel, the university provides great compensation, of which, the annual salary is RMB500,000+ and RMB400,000+ for country-level experts and provincial-level experts respectively. There is no ceiling on the compensation which can be determined on the case-by-case basis. Purchase Subsidies and scientific research fund can also be negotiated. For details please visit the website of the Personnel Department of Nantong University at http://rsc.ntu.edu.cn.

Ⅲ. Resume and Contacts

Applicants should submit (i) a curriculum vitae (including current research projects and future plans) (ii) copy of diploma(iii)recommendation letters.
Telephone Number: 086-513-85012806
Email: rck@ntu.edu.cn/ zhaopin@ntu.edu.cn
Contact Persons: Ms. Cheng

Warmly welcome you to apply for all top-level talents projects such as "Chang Jiang Scholars Program", "The Recruitment Program of Global Experts", "Jiangsu Innovation and Creation Talents Program" and "Jiangsu Distinguished Professor" in the name of Nantong University.

Faculty Positions Available in China Pharmaceutical University

China Pharmaceutical University (CPU), founded in 1936, is one of the "211 Project" key universities with top-ranking pharmacy-related disciplines and innovative platforms affiliated to the Ministry of Education of China. Located in Nanjing, Jiangsu Province, CPU was China's first independent school of pharmacy. It consists of 12 pharmacy-related schools and departments. With its sound atmosphere in pharmaceutical research and education, CPU has been taking its leading position in China. It once won National 1st Prize in pharmaceutical education for three times consecutively during 12 years. More than 17 national, provincial or ministerial key laboratories guarantee researchers to receive and fulfill various key funding projects in innovative drug development.

CPU boasts a highly qualified and experienced team of faculty and an advanced research platform. To further facilitate our development, CPU focuses on the construction of talent teams. With our favorable teaching and research environment, we sincerely invite outstanding scholars to join us. For more information about CPU, please visit http://www.cpu.edu.cn/.

Major disciplines open for recruitment:

1. Pharmacy disciplines: Pharmacology, Biology, Medicinal Chemistry, Pharmaceutics, Pharmacognosy and Plant Science.
2. Pharmacy-related disciplines, including but not limited to: Stem Cells, Bioinformatics, Molecular Diagnostics, Omics and Clinical Pharmacy.

Positions and Remuneration:

We provide competitively favorable offers for all our positions. Further information is available at: http://rsc.cpu.edu.cn/s/15/t/185/6c/51/info27729.htm.

Contact Information:

Qualified applicants can email their CV, which should include the basic personal information, education background, publication, interested position and statement of research interests to rcb@cpu.edu.cn. Applications will be reviewed on a rolling basis until the positions are filled.
Tel: +86-25-86185091

中国华北高校招聘

Recruitment for Universities in Shanxi,Hebei and Tianjin,China

太原理工大學 www.tyut.edu.cn

山西大學 www.sxu.edu.cn

河北工業大學 www.hebut.edu.cn

中國民航大學 www.cauc.edu.cn

Looking for more positions? Please send your CV to acabridge@163.com
or call the direct line: 86-10-62603334

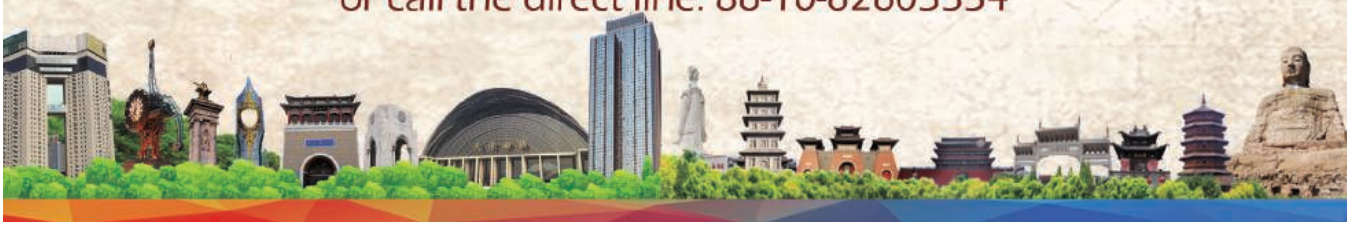

中国•北京高校招聘

Recruitment for Universities in Beijing, China

www.edu.cn/zhaopin

SCAN
北京理工大學
www.bit.edu.cn

SCAN
華北電力大學
www.ncepu.edu.cn

北京郵電大學
www.bupt.edu.cn

北京工業大學
www.bjut.edu.cn

北京工商大學
www.btbu.edu.cn

SCAN
首都師范大學
www.cnu.edu.cn

Looking for more positions? Please send your CV to
acabridge@163.com or call the direct line: 86-10-62603334

中国东北高校招聘

Recruitment for Universities in Northeast China

大连理工大学
软件学院
ssdut.dlut.edu.cn

哈尔滨工程大学
www.hrbeu.edu.cn

东北林业大学
www.nefu.edu.cn

东北师范大学
www.neu.edu.cn

Looking for more positions? Please send your CV to
acabridge@163.com or call the direct line: 86-10-62603334

www.edu.cn/dbzp

中国安徽高校招聘

Recruitment for Anhui Universities of China

长江三角洲城市群

国际6大世界级城市群之一

One of the world's 6 major world cities: the Yangtze River Delta city group

中国科学技术大学
www.ustc.edu.cn

安徽大学
www.ahu.edu.cn

合肥工业大学
www.hfut.edu.cn

Looking for more positions? Please send your CV to acabridge@163.com or call the direct line: 86-10-62603334

www.edu.cn/ahzp

中国华南高校招聘

Recruitment for Universities in Southern China

秀美河山，旅游胜地

改革开放的先行者

The beautiful rivers and mountains, tourist attractions,
the pioneer of reform and opening up.

中山大學 www.zsu.edu.cn

華南理工大學 www.scut.edu.cn

廣東海洋大學 www.gdou.edu.cn

海南大學 www.hainu.edu.cn

廣西大學 www.scut.edu.cn

Looking for more positions? Please send your CV to
acabridge@163.com or call the direct line: 86-10-62603334

www.edu.cn/hnzp

中国华中高校招聘

Recruitment for Universities in Central China

湖南大學
www.hnu.edu.cn

湘潭大學
www.xtu.edu.cn

武漢大學
www.whu.edu.cn

華中師范大學
www.ccnu.edu.cn

Looking for more positions? Please send your CV to

acabridge@163.com or call the direct line: 86-10-62603334

www.edu.cn/hzzp

中国苏鲁高校招聘

Recruitment for Universities in Shandong and Jiangsu,China

山東大學 www.sdu.edu.cn

中國石油大學 www.upc.edu.cn

中國礦業大學 www.cumt.edu.cn

南京財經大學 www.njue.edu.cn

Looking for more positions? Please send your CV to

acabridge@163.com or call the direct line: 86-10-62603334

www.edu.cn/slzp

中国西北高校招聘

Recruitment for Universities in Northwest China

一帶一路：中國夢與世界夢的交滙橋梁

One Belt and One Road:The bridge between the Chinese dream and the world dream

西安交通大學 www.xjtu.edu.cn

陕西師范大學 www.snnu.edu.cn

西安電子科技大學 www.xidian.edu.cn

西北工業大學 www.nwpu.edu.cn

Looking for more positions? Please send your CV to acabridge@163.com or call the direct line: 86-10-62603334

www.edu.cn/xbzp

中国西南高校招聘

Recruitment for Universities in Southwest China

钟灵毓秀，杰归西南

Welcome your joining in southwest China's colleges and universities

西南大學
www.nefu.edu.cn

重庆大学
www.cqu.edu.cn

电子科技大学
www.uestc.edu.cn

四川農業大學
www.sicau.edu.cn

Looking for more positions? Please send your CV to acabridge@163.com or call the direct line: 86-10-62603334

www.edu.cn/xnzp

Postdoctoral Fellow/Staff Scientist

Chinese National Clinical Research Center for Metabolic Diseases at Rui-Jin Hospital in the heart of downtown Shanghai is a large complex including the Shanghai Institute of Endocrine and Metabolic Diseases and the Department of Endocrine and Metabolic Diseases. The center is pioneering both basic and translational science, housing research teams dedicated to studying endocrine tumors, diabetes, and obesity, among other areas. It is to become the most important clinical and research center in the field of endocrine and metabolic diseases in China.

The center is currently seeking a full time Postdoctoral Fellow or Staff Scientist to carry out basic and translational research in the fields of endocrine and metabolic diseases.

Applicants should have a Ph.D., MD., or equivalent degree. Curriculum vitae containing a summary of past research accomplishments, a statement of research interests and names of references should be submitted via email to:
Dr. Yan Xu, xuyanrr@aliyun.com.

Max Planck Institute for the Physics of Complex Systems

CBG Max Planck Institute of Molecular Cell Biology and Genetics | center for systems biology dresden | mpipks

Postdoc Positions

The Center for Systems Biology Dresden calls for applications for several open postdoc positions within the prestigious

ELBE Postdoctoral Fellowship Program

in the following areas

- Computer Science, Computational Science, and Applied Mathematics
- Bioinformatics and Computational Biology
- Biological Physics, Biophysics, and Theoretical Biology

We seek outstanding candidates with a degree in the listed areas and a strong interest in working in a multidisciplinary environment towards developing and using computational and physical methods to address key questions in biology and to transform data into knowledge.

The Center for Systems Biology Dresden is a joint activity by the Max Planck Institute of Molecular Cell Biology and Genetics (MPI-CBG) and the Max Planck Institute for the Physics of Complex Systems (MPI-PKS). The center is a highly interactive and collaborative workplace with an international atmosphere where English is the working language, and has a strong commitment to interdisciplinary training and career development. The center provides access to cutting-edge computer infrastructure, genome sequencing technology and wet lab facilities. The MPI-CBG has been awarded one of the "Best Places To Work Postdocs" in 2011.

ELBE Fellowships are awarded on a competitive basis to outstanding young researchers with a doctoral degree. To foster collaboration, fellows are usually affiliated with two hosting groups working in different disciplines.

Dresden was awarded "City of Science" in 2006 and is one of the leading scientific centers in Europe with 3 Max Planck and 13 other research institutes, and the Dresden University of Technology as one of eleven Universities of Excellence in Germany. Dresden has half a million inhabitants and is considered one of the most beautiful cities of Germany, located 2 hours from Berlin and Prague.

The Max Planck Society is an equal opportunity employer: handicapped individuals are strongly encouraged to apply. The Center for Systems Biology, the MPI-CBG and the MPI-PKS aim to increase the number of women in scientific positions. Female candidates are therefore particularly welcome.

Deadline for applications is February 10, 2016. For details about the application procedure, please visit our website http://mpg-sysbio.de/index.php?id=jobs

MAX-PLANCK-GESELLSCHAFT

ScienceCareers online @sciencecareers.org

Deputy Director, Office of Extramural Research
National Institutes of Health
Department of Health and Human Services

The National Institutes of Health (NIH) in Bethesda, Maryland, the world's largest medical research facility and an operating division of the U.S. Department of Health and Human Services (HHS), seeks applications from exceptional candidates for the position of Deputy Director, Office of Extramural Research (OER), Office of the Director (OD).

This position reports to the NIH Deputy Director for Extramural Research/Director (DDER), OER and will coordinate activities across NIH, among other federal agencies and external organizations.

Leadership Responsibilities: On behalf of the DDER, the Deputy Director for the OER (DDOER) is responsible for the oversight and management of highly complex, cross-cutting, and sensitive assignments that include:

- leading and serving on trans-NIH activities to formulate, implement, and evaluate relevant extramural programs, policies, procedures, and priorities;
- representing the NIH on government-wide committees, task forces, and working groups;
- developing plans for future initiatives and preparing and/or presenting position papers on extramural issues of broad impact;
- directly engaging in legislative issues including actual testimony and preparing legislative testimony for use by the NIH;
- collaborating with other OD offices to address scientific and policy issues that affect extramural grantees; and
- serving as the Agency Extramural Research Integrity Officer.

Additional Responsibilities: The DDOER serves as the second authority for the OER and directs the OER Office of Communications Analysis and Planning. In this role, the DDOER allocates budgets and provides supervisory oversight for 28 staff.

Position Requirements: Candidates must have an M.D., Ph.D., or equivalent degree in a field relevant to the position. This position will be filled under a Title 42(f) excepted service appointment. An integral function of this position is bringing the appropriate individuals from across the NIH to coalesce around critical matters requiring immediate response, with the flexibility to move quickly from one issue to another with independence and authority. As such, the position requires professional interaction with the extramural scientific community. In addition, the DDOER must possess the ability to gain support of constituents that often may have competing interests, both internal and external to the NIH, on key public health policy issues. This is a highly visible position with significant impact on the NIH extramural community.

Salary/Benefits: Salary is competitive and will be commensurate with the experience of the candidate. A recruitment or relocation bonus may be available, and relocation expenses may be paid. A full package of Federal Civil Service benefits is available, including: retirement, health and life insurance, long-term care insurance, leave, and a Thrift Savings Plan (401K equivalent). The successful candidate is subject to a background investigation and public financial disclosure requirements.

How to Apply: Applicants must submit a current curriculum vitae, bibliography, and full contact details for three references. In addition, applicants are asked to prepare two statements: a vision statement and a statement that addresses the specific qualification requirements (please limit both statements to two pages each). Send application package by email to **T42OER@od.nih.gov** **OR** via mail to:

Tamla Ransford
National Institutes of Health
Office of Extramural Research
6705 Rockledge Drive, MSC 7986, Suite 5016, Room 5110
Bethesda, MD 20892 (or 20817 for overnight delivery services)

For additional information about this vacancy, contact Tamla Ransford at 301-451-7784. All applications must be postmarked by the closing date. OER will begin accepting applications on **December 4, 2015** and plans to have the position open for 30 days. To learn more information about the OER, please visit **http://grants.nih.gov**.

HHS and NIH are Equal Opportunity Employers

kialm

INSERM IS RECRUITING: 93 TENURE POSITIONS ARE OFFERED TO RESEARCHERS M/F DEDICATED TO BIOMEDICAL RESEARCH

Inserm is the only French public research institute to focus entirely on human health.
Its researchers are committed to studying all diseases, whether common or rare. Through its diversity of approaches, Inserm provides a unique environment for researchers. More than 13 000 researchers, engineers and technicians work in the 289 Inserm laboratories housed in hospitals, universities and research campuses, all over France.

Application modalities: visit our website : http//www.eva2.inserm.fr
Application deadline: January 8th, 2016 - 4.00.pm (GMT+1)

Instituts thématiques Inserm
Institut national de la santé et de la recherche médicale

DePaul University

Assistant Professor
Endocrinology

A joint-appointment, tenure-track opening for a faculty position in endocrinology is available in the Departments of Biological Sciences (primary appointment) and Health Sciences (secondary appointment) at DePaul University starting September 2016. Successful candidate will be broadly trained in endocrinology with a strong commitment to undergraduate education. We especially encourage applications from individuals using cell/molecular approaches to study endocrinology. Ph.D. required; postdoctoral and previous teaching experience preferred. Teaching responsibilities will include Human Biology, and some combination of Cell Biology, General Biology, and a graduate/advanced undergraduate course in Endocrinology. Start-up funds are provided. The Departments are housed in spacious and well-equipped teaching, research and support facilities, including a 2,000 sq. ft. state-of-the-art staffed animal care facility. Visit http://csh.depaul.edu/departments/biological-sciences/Pages/default.aspx and http://csh.depaul.edu/departments/health-sciences/Pages/default.aspx for more information about each department. Review of applications will **begin immediately** and ends **January 20, 2016** or until position is filled.

Applicants should apply online with a cover letter, curriculum vitae, statement of research interests (2 page maximum), statement of teaching interests with educational philosophy (2 page maximum), and general list of equipment and supply needs with cost estimates. In addition, we request three letters of reference – please supply the on-line system with the e-mail addresses of three individuals. Any queries should be sent to **Dr. Joanna S. Brooke** at **jbrooke@depaul.edu**. To apply, please visit the following URL: **https://facultyopportunities.depaul.edu/postings/298**

As an Equal Employment Opportunity (EEO) Employer, DePaul University provides job opportunities to qualified individuals without regard to race, color, ethnicity, religion, sex, sexual orientation, national origin, age, marital status, physical or mental disability, parental status, housing status, source of income or military status, in accordance with applicable federal, state and local EEO laws.

ScienceCareers online @sciencecareers.org

Faculty Positions in CHEMICAL SCIENCE PROGRAM

The Physical Science and Engineering (PSE) Division (http://pse.kaust.edu.sa) at King Abdullah University of Science and Technology (KAUST) invites qualified applicants to apply for faculty positions at all ranks (Assistant, Associate, and Full Professor) in the Chemical Science Program.

KAUST offers superb research facilities which include the Analytical, the Nanofabrication and Thin film and the Imaging and Characterization core laboratories, generous assured research funding and internationally competitive salaries.

The science produced in PSE is about understanding, modeling, and manipulating matter at all scales: nano, meso, and macroscopic levels; in all forms: bulk, thin films, divided colloids, fluid flows, earth as system etc. and in interaction with external stimuli: light, heat, fluids, etc. or stresses. The knowledge created serves to design and engineer materials, technologies and systems.

The Chemical Science Program is concerned with chemistry in all its facets including those addressed in KAUST Research Centers, particularly in Catalysis, Membrane, and Solar Energy (http://chems.kaust.edu.sa).

The Chemical Science program is currently recruiting in the following areas:

Heterogeneous Catalysis for KAUST Catalysis Research Center: Candidates are expected to have a strong expertise on "catalysis by design" especially on multistep reactions, on the association of various types of catalytic concepts or tools e.g. acid base, -oxidation, -cascade, -confinement effect, -green and sustainable chemistry -in situ, in operando spectroscopies.

Reactor design and process engineering of catalytic reactions for KAUST Catalysis Research Center in relation with the Chemical and Biological Engineering Program: This position should be focusing on "reactor design" and establishment of a 'scale up platform': It will complement the existing areas of expertise in Chemical Science Program and put a greater focus on bridging chemistry and chemical engineering: 'from the bench to the processes': Strong experience with industrial partners is needed.

Polymer Engineering/Processing: Emphasis will be placed on a) the design, characterization, properties and modification of polymeric materials, b) the compounding and processing of polymeric materials and c) the structure property relationships and applications.

Applicants should have a proven track record to establish a high impact research program and have a commitment to high quality teaching at the graduate level.

To learn more about the PSE Division and complete the online application form, visit **http://apptrkr.com/705565**

Application requirements include the following:

- Updated curriculum vitae with a full list of publications
- Statement of research
- Statement of teaching interests
- Contact details of at least four potential referees

Applications received by January 31, 2016 will receive full consideration but positions will remain open until filled.

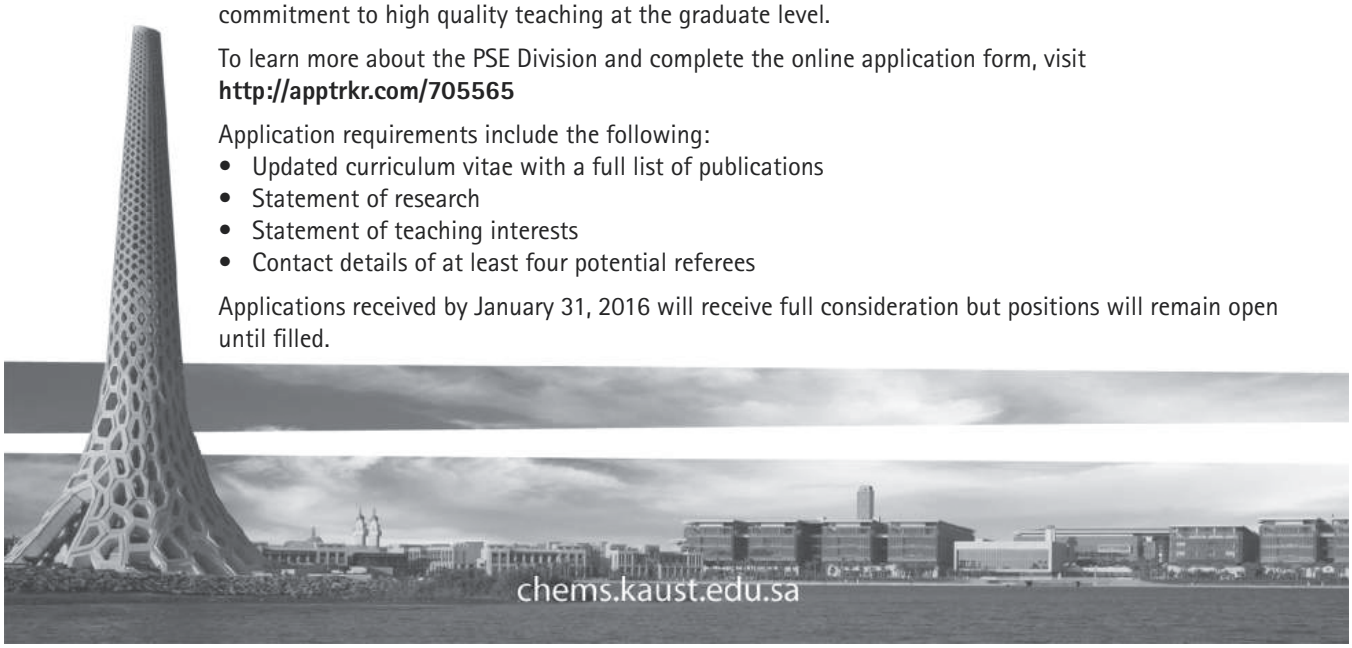

ScienceCareers online @sciencecareers.org

UCLA

Associate/Full Professor Faculty Position in Life Sciences
Director of Bioscience Undergraduate Research Career Programs

Building on four successive years of hiring leading research scientists with strong commitments to promoting success of underrepresented minority students, the Division of Life Sciences in the UCLA College of Letters and Sciences is recruiting for a new position, the Director of Bioscience Undergraduate Research Career Programs. We seek a visionary leader with a strong record of scholarly publication, research funding, and undergraduate teaching, and who is passionately committed to the advancement of under-represented minorities in the sciences. This new Director will work with the Assistant Vice Provost for Undergraduate Research and multiple dedicated PhD level staff of the Undergraduate Research Center-Sciences to shape the direction and vision for undergraduate programs focused on underrepresented student success and careers in the life sciences. In addition to serving as PI and faculty director of UCLA's NIH Maximizing Access to Research Careers (MARC) Program, the new Director will provide leadership on a portfolio of new and/or existing programs, with the scope of programs negotiated based on the interests, vision and expertise of the candidate. Administrative support will be provided and teaching loads adjusted so that the successful candidate can maintain his/her research excellence and externally funded research programs while serving as Director. The successful candidate will hold an Academic Senate appointment as an Associate or Full Professor in one of the following Life Sciences Departments (www.lifesciences.ucla.edu): Ecology and Evolutionary Biology; Integrative Biology and Physiology; Microbiology, Immunology, and Molecular Genetics; Molecular, Cell and Developmental Biology; Institute for Society and Genetics; or Psychology, and candidates must hold a PhD in one of these fields. The candidate will be expected to hold the Director position for five-year renewable terms, reporting administratively to the Dean and Vice Provost for Undergraduate Education. UCLA offers competitive salaries, research set-up funds, and recruitment allowances.

Questions should be sent to: **Professor Paul Barber (paulbarber@ucla.edu)**. Application packages should be submitted online through **https://recruit.apo.ucla.edu/apply/JPF01842** and include the following: (1) curriculum vitae; (2) statement of research interests; (3) statement of experience/vision related to administration of Undergraduate research Career Programs; (4) statement of commitment to mentorship, including formal and informal mentorship activities targeting underrepresented and underserved populations; and (5) cover letter that includes names of referees that can be contacted for letters. All items should be distinct documents. Review of applications will begin on 2 January 2016, and continue until position is filled.

Individuals with a history of mentoring students under-represented in the sciences are encouraged to apply and to describe their experience in a cover letter

Located in an urban setting, **UCLA** is California's largest university with a diverse student body of 38,000 undergraduate and graduate students, approximately 25% that come from underrepresented minority groups. UCLA College of Letters and Science is home to many innovative programs focused on student success in sciences and promotes excellence in STEM teaching through the Center for Education Innovation & Learning in the Sciences. Interdisciplinary programs in Life Sciences are enhanced by the Medical, Nursing, Dental and School of Public Health along with 7 other professional schools with renowned faculty offering more than 323 degree programs and majors UCLA is home to a number of NIH, NSF, and HHMI funded training programs focused on increasing success for underrepresented students in science, medical and allied health fields, and currently serves as the coordinating center for NIH BUILD grants. As a campus with a continually growing diverse student body, we encourage applications from women, minorities, and individuals with a commitment to mentoring under-represented demographics in the sciences.

The University of California is an Equal Opportunity/Affirmative Action Employer. All qualified applicants will receive consideration for employment without regard to race, color, religion, sex, sexual orientation, gender identity, national origin, disability, age or protected veteran status. For the complete University of California nondiscrimination and affirmative action policy see: UC Nondiscrimination and Affirmative Action Policy (http://policy.ucop.edu/doc/4000376/NondiscrimAffirmAct).

University of New Hampshire

Assistant Professor of Animal Science-Nutrition

The Department of Biological Sciences, College of Life Sciences and Agriculture, University of New Hampshire, Durham, invites applicants for an academic-year, tenure-track faculty position in Animal Science at the Assistant Professor rank. The position has an anticipated start date of August 2016. We seek a nutritionist specializing in agriculturally important, non-ruminant animals (e.g. poultry, swine) to complement existing research and teaching strengths in Animal Science and Sustainable Agriculture and Food Systems. Research foci may include: creating and determining the nutritional potential of alternative feeds, including those derived from human food waste; developing novel feeding strategies and temporary pasture systems (e.g. legumes, seed/tuber crops); and/or evaluating species and breed suitability for extensive culture, limited confinement, and/or low-cost housing systems. Evaluation endpoints may include effects on growth, physiology, health, body composition, and/or palatability. Research should have direct and beneficial impact on regional stakeholders and be relevant to the small-scale, diversified agricultural production systems typical of the northeastern United States.

To apply, and to view a full job description and minimum qualifications required, visit the following web site: **https://jobs.usnh.edu**. For full consideration, applications must be received by January 4, 2016.

UNH is an AA/EEO Employer. UNH is committed to excellence through the diversity of its faculty and staff and encourages women and minorities to apply.

IOWA STATE UNIVERSITY

Tenure-Track Faculty Position in Limnology

The Department of Ecology, Evolution & Organismal Biology (EEOB) seeks a limnologist specializing in the biogeochemistry, eutrophication, food webs, and/or restoration of lakes. The successful candidate is expected to contribute to the growth of aquatic sciences at ISU, establishing a major, externally funded research program and contributing to undergraduate and graduate education, including teaching in aquatic ecology. The successful candidate is expected to focus on the limnology of Iowa lakes and to continue partnerships with the Iowa Department of Natural Resources related to limnology and aquatic ecology. This is a 9 month position in the College of Agriculture and Life Sciences at the rank of assistant professor, with a primary (tenure home) appointment in EEOB (85%) and a secondary appointment (15%) in the Department of Natural Resource Ecology and Management (NREM).Candidates must hold a Ph.D. by the time of appointment and are expected to establish a successful, externally funded research program and to teach at the undergraduate and graduate levels.

All applications must be submitted electronically at **www.iastatejobs.com** (search vacancy **ID#: 500207**). Please be prepared to attach a letter of application, including concise teaching and research statements, curriculum vitae, and up to three reprints. Arrange to have three confidential letters of recommendation submitted as per instructions in the on-line application system. The position will remain open until filled. Full consideration will be given to applications received by **January 15, 2016**. Iowa State University is an EO/AA Employer. For additional information please email **limnol@iastate.edu**.

Iowa State University is an EO/AA Employer. All qualified applicants will receive consideration for employment without regard to race, color, religion, sex, national origin, disability, or protected Vets status. Iowa State University is an AAU-member comprehensive, land grant, Carnegie Doctoral/Research Extensive University with an enrollment of over 36,000 students. The university is located in Ames, IA, one of the nation's most highly rated metropolitan areas of its size (http://www.iastate.edu/about/ames.php) and is only 35 miles north of Des Moines. ISU is committed to achieving inclusive excellence through a diverse workforce and is dedicated to supporting work-life balance through an array of flexible policies.

Faculty Positions in CHEMICAL AND BIOLOGICAL ENGINEERING PROGRAM

جامعة الملك عبدالله للعلوم والتقنية
King Abdullah University of Science and Technology

The Physical Science and Engineering (PSE) Division (http://pse.kaust.edu.sa) at King Abdullah University of Science and Technology (KAUST) invites qualified applicants to apply for faculty positions at all ranks (Assistant, Associate and Full Professor) in the Chemical and Biological Engineering program (CBE).

KAUST offers superb research facilities which includes the BioScience and Bioengineering and Analytical Core laboratories, generous assured research funding and internationally competitive salaries.

The science produced in PSE focuses on understanding, modeling and manipulating matter at all scales (nano, meso and macroscopic levels), in all forms (bulk, thin films, divided colloids, fluid flows, the earth as system, etc.) and in interaction with external stimuli (light, heat, fluids, stresses, etc.). The knowledge produced serves to help design and engineer cutting-edge materials, technologies and systems.

The CBE program offers opportunities to develop real-world solutions to global challenges by leveraging basic discoveries in the chemical and biological sciences. Three KAUST research centers are associated with CBE: KAUST Catalysis Center (http://kcc.kaust. edu.sa), Advanced Membranes and Porous Materials (http://ampm.kaust.edu.sa), and the Clean Combustion Research Center (http://ccrc.kaust.edu.sa).

The CBE Program has open Faculty positions in the following areas of expertise:

Process Modeling and Design for Advanced Membranes and Porous Materials Research Center
- Solid academic/industrial background
- Conduct design, optimization and cost analysis of membrane and conventional separation processes
- Teach advanced principles of process design and control

Biomolecular Engineering (Senior-level Position)
- Development and leadership of the Biomolecular Engineering program
- Well-established research in areas such as biomaterials, tissue engineering, bioprocess engineering or biomedical engineering

Reactor Design and Process Engineering for KAUST Catalysis Center
- Specialize in heterogeneous or photo catalysis
- Scale up reactors in the field of water splitting, high temperature catalytic processes and processes for air-sensitive catalysts
- Expertise in academia, industry or both

Applicants should have a proven track record to establish a high-impact research program, and should have a commitment to high-quality teaching at the graduate level.

To learn more about the PSE Division and complete the online application form, visit **http://apptrkr.com/705548**

Application requirements include the following:
- Updated curriculum vitae with a full list of publications
- Statement of research
- Statement of teaching interests
- Contact details of at least four potential referees.

Applications received by January 31, 2016 will receive full consideration but positions will remain open until filled.

ScienceCareers online @sciencecareers.org

By **Jessica W. Tsai**

The M.D.-Ph.D. double agent

It was 2 o'clock on a Saturday morning. I felt exhausted, overwhelmed, and defeated. Still wearing my scrubs from the day before, I stared blankly at the wall in the dark room, holding the once-again botched Western blot, signifying hours lost to what should have been a simple task in my Ph.D. work. I quickly bicycled home, knowing that I needed to be at the hospital in a few short hours to fulfill my additional responsibilities—as a third-year medical student. Even in the sixth year of my M.D.-Ph.D. program, my two worlds were constantly colliding. Despite these challenges, the journey to becoming a physician-scientist is one I am so glad I undertook.

My love of both molecular biology and human physiology began in my fourth-grade science class. I remember the astonishment of dissecting an earthworm; learning about the mishmash of organelles within our cells; and examining the small atherosclerotic plaques brought in by our class guest speaker, a cardiologist. When I started college, I knew I would major in something science-related—the thought of medical school had crossed my mind—but I wavered on my future plans, unable to decide whether I wanted to pursue an M.D. or a Ph.D. I had no idea what the phrases "M.D.-Ph.D." or "physician-scientist" even meant until I joined a lab as an undergraduate researcher and began working with an M.D.-Ph.D. neuroscientist who also saw patients as a neurologist. He clued me in to the possibility of pursuing both degrees, which seemed like an ideal option for me. But I found there were very few resources for students interested in this path.

"My clinical and scientific lives were constantly dueling for my time."

Even after I joined the Medical Scientist Training Program, a nationwide National Institutes of Health–supported M.D.-Ph.D. program, I still did not quite know what I was getting myself into. No one had mentioned that I would feel that my clinical and scientific lives were constantly dueling for my time. Working in the lab after leaving the hospital meant less time to prepare for medical rounds and shelf exams, yet preparing more for rounds meant not completing the experiments I needed to earn my Ph.D.—not to mention finding time to relax, sleep, and catch up with family and friends.

I am by no means an expert, as I am a pediatrics intern still learning the ropes. However, now that I am a little further along in my training, I offer one piece of advice to aspiring physician-scientists: Find mentors. Surround yourself with clinicians who appreciate science and the way that scientists think, and scientists who value clinical applications of their research. And, of course, find physician-scientists, including those who balance both research and medicine; others who have chosen to pursue just one; and those who have explored alternative career paths such as startups, advocacy, and journalism.

I was lucky to find outstanding mentors who understood the tensions between science and medicine. During my Ph.D., my adviser allowed me to spend half a day each week seeing patients so that I could maintain my clinical skills while still challenging me to become a thoughtful, thorough, analytical scientist. My clinical mentor always made it a point to ask me about my basic science research, and he even attended my thesis defense.

My M.D.-Ph.D. training was incredibly grueling, extremely humbling, and so very rewarding. The best part is that so much more learning lies ahead. The tools and training I gleaned from earning a Ph.D. have allowed me to think critically; to question everything; and to be industrious, innovative, and flexible. Medical training has equipped me with the capacity to make astute medical decisions, emphasizing the importance of teamwork, empathy, and humanism. And now, I have found peace with this duality. The patients and families I take care of motivate and inspire me. They remind me every day why we need more physician-scientists who can identify important and frustrating clinical questions, find creative solutions in the laboratory, and ultimately improve patient care by bridging science and medicine. ■

Jessica W. Tsai is a resident physician in pediatrics at Boston Children's Hospital and Boston Medical Center and a member of STEM Education Advocacy Group. Send your story to SciCareerEditor@aaas.org.

ILLUSTRATION: ROBERT NEUBECKER

Downloaded from www.sciencemag.org on December 14, 2015

Published by AAAS